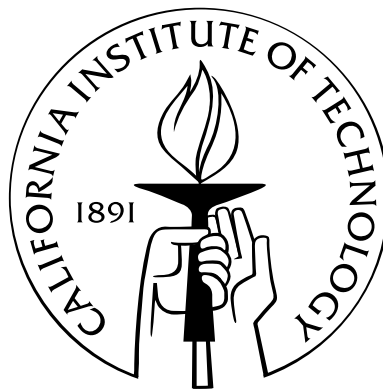


Semiconductor Optical Microcavities for Chip-Based Cavity QED

Thesis by
Kartik Srinivasan

In Partial Fulfillment of the Requirements
for the Degree of
Doctor of Philosophy



California Institute of Technology
Pasadena, California

2006
(Defended May 3, 2006)

© 2006

Kartik Srinivasan

All Rights Reserved

To my friends and family

Acknowledgements

The work described in this thesis would not have been possible without the contributions of a number of people. First and foremost, I would like to thank my advisor, Professor Oskar Painter, for the time and energy he has invested in my research and training as a scientist. Oskar's genuine enthusiasm and passion for physics are remarkable, as is his willingness to provide his students with tangible help with their research. In addition to his role as my advisor, I have also enjoyed his friendship over the years.

Since my undergraduate days at Caltech, I have benefited from the guidance of Professors Kerry Vahala and William Bridges. Professor Vahala gave me my first introduction to an optics research lab as a sophomore and my first industry job at XPonent Photonics after I graduated with my bachelor's degree, and my subsequent choices in research have been greatly influenced by these rewarding experiences and his mentorship. Professor Bridges served as my undergraduate advisor, and I appreciate the time and care he put into what is a largely unrecognized role.

There are a number of other researchers at Caltech and abroad that have played a part in shaping my time in graduate school. I appreciate the interactions I have had with Professors Amnon Yariv and Hideo Mabuchi, who are two scientists that I admire as researchers and teachers. During my first three years in graduate school, I greatly enjoyed a collaboration with the quantum cascade laser group at Bell Laboratories, and in particular, Dr. Raffaele Colombelli (now at Université Paris-Sud) and Professor Federico Capasso (now at Harvard). I would also like to thank Dr. Jianxin Chen of Bell Laboratories and Professors Andreas Stintz and Sanjay Krishna of the University of New Mexico, whose expertise in material growth has allowed us to undertake experiments that could not have been done at Caltech alone. Finally, I would like to acknowledge the Hertz Foundation for my graduate fellowship, and recognize the effort they put into identifying and funding promising students.

Oskar has assembled a talented and personable group of individuals with whom it has been a pleasure to work. I would particularly like to thank my officemate Paul Barclay. Paul and I have very

similar research interests, and I think we have been able to learn a lot from each other. Similarly, I have enjoyed interacting with Matt Borselli, who has been a great sounding board for ideas, and Tom Johnson, whom I have known since our time working together at XPonent. The four of us were Oskar's first graduate students, and the hard work and tedium of building a research lab was made easier because it was done with good friends. More recently, I have enjoyed collaborating with Chris Michael and Ben Lev (a student in Hideo's group), as well as interacting with Raviv Perahia, David Henry, Matt Eichenfield, Orion Crisafulli, and Jessie Rosenberg.

The biggest influence in my life has been my parents, and I want to thank my mom Kalpagam and my dad V.K. for their unconditional love and support, and the example they set for me. I also want to thank my older sister Jahnavi, who I have always looked up to. My oldest sister Meera and her husband Jon have lived 15 minutes away from me for the past ten years, and during that time, they have always kept their home open to me. I truly appreciate everything they have done for me, and the affection of my nieces Kiran and Jaya.

Finally, there a large number of friends from my undergraduate days that I should thank in detail, but will instead just thank as a group. I would, however, like to single out one person, Hanna Kim, for all her friendship and support over the years.

Abstract

Optical microcavities can be characterized by two key quantities: an effective mode volume V_{eff} , which describes the per photon electric field strength within the cavity, and a quality factor Q , which describes the photon lifetime within the cavity. Cavities with a small V_{eff} and a high Q offer the promise for applications in nonlinear optics, sensing, and cavity quantum electrodynamics (cavity QED). Chip-based devices are particularly appealing, as planar fabrication technology can be used to make optical structures on a semiconductor chip that confine light to wavelength-scale dimensions, thereby creating strong enough electric fields that even a single photon can have an appreciable interaction with matter. When combined with the potential for integration and scalability inherent to microphotonic structures created by planar fabrication techniques, these devices have enormous potential for future generations of experiments in cavity QED and quantum networks.

This thesis is largely focused on the development of ultrasmall V_{eff} , high- Q semiconductor optical microcavities. In particular, we present work that addresses two major topics of relevance when trying to observe coherent quantum interactions within these semiconductor-based systems: (1) the demonstration of low optical losses in a wavelength-scale microcavity, and (2) the development of an efficient optical channel through which the sub-micron-scale optical field in the microcavity can be accessed. The two microcavities of specific interest are planar photonic crystal defect resonators and microdisk resonators.

The first part of this thesis details the development of photonic crystal defect microcavities. A momentum space analysis is used to design structures in graded square and hexagonal lattice photonic crystals that not only sustain high Q s and small V_{eff} s, but are also relatively robust to imperfections. These designs are then implemented in a number of experiments, starting with device fabrication in an InAsP/InGaAsP multi-quantum-well material to create low-threshold lasers with Q s of 1.3×10^4 , and followed by fabrication in a silicon-on-insulator system to create passive resonators with Q s as high as 4.0×10^4 . In the latter experiments, an optical fiber taper waveguide is used to couple light into and out of the cavities, and we demonstrate its utility as an optical

probe that provides spectral and spatial information about the cavity modes. For a cavity mode with $Q \sim 4 \times 10^4$, we demonstrate mode localization data consistent with $V_{\text{eff}} \sim 0.9(\lambda/n)^3$.

In the second part of this thesis, we describe experiments in a GaAs/AlGaAs material containing self-assembled InAs quantum dots. Small diameter microdisk cavities are fabricated with $Q \sim 3.6 \times 10^5$ and $V_{\text{eff}} \sim 6(\lambda/n)^3$, and with $Q \sim 1.2 \times 10^5$ and $V_{\text{eff}} \sim 2(\lambda/n)^3$. These devices are used to create room-temperature, continuous-wave, optically pumped lasers with thresholds as low as $1 \mu\text{W}$ of absorbed pump power. Optical fiber tapers are used to efficiently collect emitted light from the devices, and a laser differential efficiency as high as 16% is demonstrated. Furthermore, these microdisk cavities have the requisite combination of high Q and small V_{eff} to enable strong coupling to a single InAs quantum dot, in that the achievable coupling rate between the quantum dot and a single photon in the cavity is predicted to exceed the decay rates within the system. Quantum master equation simulations of the expected behavior of such fiber-coupled devices are presented, and progress towards such cavity QED experiments is described.

Contents

Acknowledgements	v
Abstract	vii
List of Figures	xix
List of Tables	xxi
Acronyms	xxii
Preface	1
List of Publications	34
 I Development of Ultrasmall Volume, High-Q Photonic Crystal Microcavities	 38
 1 Semianalytic Methods for Studying Localized Modes Within Two-Dimensional Photonic Crystals	 40
1.1 Symmetry-based analysis	40
1.1.1 Introduction	40
1.1.2 Hexagonal lattice photonic crystals	42
1.1.2.1 X-point	45
1.1.2.2 J-point	47
1.1.2.3 Conduction band donor modes	49
1.1.2.4 Valence band acceptor modes	54
1.1.3 Square lattice photonic crystals	57
1.1.3.1 X-point	58

1.1.3.2	M-point	61
1.1.3.3	Conduction band donor modes	62
1.1.3.4	Valence band acceptor modes	65
1.1.4	Comparison with FDTD simulations	66
1.2	Wannier-like approach for describing localized modes in photonic crystals	70
1.2.1	Introduction	70
1.2.2	Wannier theorem for photons in periodic dielectric structures	71
1.2.3	Envelope function calculation	79
1.2.3.1	Donor modes at the X -point	79
1.2.3.2	Acceptor modes at the J -point	87
2	Momentum Space Design of High-Q Photonic Crystal Microcavities	93
2.1	Introduction	93
2.2	Momentum space consideration of vertical radiation loss	94
2.3	Summary of the symmetry analysis of defect modes in hexagonal and square lattices	96
2.3.1	Hexagonal lattice	98
2.3.2	Square lattice	100
2.4	Initial FDTD simulation results	102
2.4.1	Hexagonal lattice	103
2.4.2	Square lattice	104
2.5	Momentum space design of the defect geometry in a square lattice	105
2.6	Tailoring of the defect geometry for the $\mathbf{H}_{A_2}^{a,a1}$ mode in the hexagonal lattice	112
2.7	Defect modes in a compressed hexagonal lattice	115
2.7.1	Preliminary analysis	115
2.7.2	FDTD results	119
2.8	Summary	121
3	High-Q Photonic Crystal Microcavities in InAsP/InGaAsP Multi-Quantum-Well Membranes	125
3.1	Introduction	125
3.2	Fabrication of PC cavities in InP-based multi-quantum-well membranes	127
3.2.1	Mask creation	128
3.2.2	InAsP/InGaAsP membrane etch and undercut	129

3.3	Photoluminescence measurements	133
3.4	Summary	136
4	Optical-Fiber-Based Measurement of an Ultrasmall Volume, High-Q Silicon Photonic Crystal Microcavity	138
4.1	Introduction	138
4.2	Fabrication	139
4.3	Measurement setup	140
4.4	Measurement results	143
4.4.1	Polarization	143
4.4.2	High- Q measurements	145
4.4.3	Spatial localization measurements	147
4.5	Applications to quantum optics	151
4.6	Fabrication-tolerant high- Q cavities	152
4.7	Fiber tapers as an optical probe for photonic crystal microcavities	157
4.8	Efficient optical fiber coupling to photonic crystal microcavities and microdisks	161
4.8.1	PC microcavities	161
4.8.2	Microdisk cavities	163
II	Fiber-Coupled Microdisk Cavities with Embedded Quantum Dots	165
5	Optical Loss and Lasing Characteristics of AlGaAs Microdisk Cavities with Embedded Quantum Dots	167
5.1	Introduction	167
5.2	Overview of microdisk cavity modes	168
5.2.1	Analytic approximation	168
5.2.2	Finite-element method simulations	171
5.2.3	Standing wave whispering gallery modes	172
5.3	Fabrication	174
5.4	Cavity Q measurements in the 1400 nm band	176
5.5	Initial measurements of lasing behavior	178

6	Photoluminescence Measurements of Quantum-Dot-Containing Microdisks Using Optical Fiber Tapers	181
6.1	Preliminary discussion and experimental methods	182
6.2	Measurement of cavity Q in the 1200 nm wavelength band	185
6.3	Improved collection efficiency with fiber tapers	187
6.4	Fiber-pumped microdisk lasers	193
6.5	Discussion and future applications	194
7	Cavity Q, Mode Volume, and Lasing Threshold in Small Diameter Microdisks with Embedded Quantum Dots	196
7.1	Simulations	196
7.2	Passive measurement of cavity Q	201
7.3	Measurements of lasing behavior	202
8	Prospects for Strong Coupling Between a Single Quantum Dot and Standing Wave Whispering Gallery Modes of a Semiconductor Microdisk Cavity	207
8.1	Introduction	207
8.2	Modal coupling of two whispering gallery modes due to surface scattering	210
8.3	Quantum master equation model	213
8.4	Solutions to the steady state quantum master equation in the weak driving regime	218
8.4.1	$\beta > g > (\kappa, \gamma_{\perp})$	219
8.4.2	$g > \beta > (\kappa, \gamma_{\perp})$	222
8.4.3	$\kappa > g > \beta > \gamma_{\perp}$	223
8.4.4	$\gamma_{\parallel} > g > \beta > \kappa$	224
8.4.5	$g > \kappa > \beta > \gamma_{\perp}$	224
8.4.5.1	Steady state analysis	224
8.4.5.2	Time-dependent analysis	225
8.4.6	$\beta = 0; g > \kappa > \gamma_{\perp}$	228
8.5	Potential for low power switching in the microdisk-QD system	229
9	Conclusions and Future Outlook	233

Appendixes

A	Quantum Cascade Photonic Crystal Surface-Emitting Injection Lasers	237
A.1	Introduction	237
A.2	Basic design and fabrication	238
A.3	Electroluminescence and lasing measurements	240
B	Finite-Difference Time-Domain Simulations	245
C	Fabrication Notes	249
C.1	Process flow and general considerations	249
C.2	Si-based devices	252
C.3	AlGaAs-based devices	254
C.4	ICP-RIE etching of quantum cascade heterostructures	257
D	Cavity Q and Related Quantities	260
E	Resonator-Waveguide Coupled Mode Theory	263
E.1	Traveling wave mode resonator	263
E.2	Standing wave mode resonator	268
F	Laser Rate Equations	270
G	The Jaynes-Cummings Model	274
G.1	The Jaynes-Cummings Hamiltonian and eigenvalue spectrum	274
G.2	The damped, driven Jaynes-Cummings model	278
G.2.1	Driving field	278
G.2.2	Dissipation terms and the quantum master equation approach	280
H	The Purcell Factor F_p and Atom-Photon Coupling Rate g	284
H.1	The Purcell factor	284
H.2	Atom-photon coupling rate	287
	Bibliography	289

List of Figures

1	Schematic of quantum-dot-photon coupling in a photonic crystal cavity.	3
1.1	Illustration of a two-dimensional photonic crystal cavity in a slab waveguide structure.	41
1.2	Bandstructure and real and reciprocal space representations of a hexagonal lattice photonic crystal	43
1.3	X-point valence and conduction band modes in a hexagonal lattice photonic crystal .	47
1.4	J-point valence and conduction band modes in a hexagonal lattice photonic crystal .	49
1.5	Example defect cavity geometries in the hexagonal lattice.	50
1.6	Conduction band donor modes in a hexagonal lattice photonic crystal	53
1.7	Valence band acceptor modes in a hexagonal lattice photonic crystal	55
1.8	X-point valence band acceptor modes in a hexagonal lattice photonic crystal	57
1.9	Bandstructure and real and reciprocal space representations of a square lattice photonic crystal	58
1.10	X-point valence and conduction band modes in a square lattice photonic crystal . . .	60
1.11	M-point valence and conduction band modes in a square lattice photonic crystal . . .	62
1.12	Conduction band donor modes in a square lattice photonic crystal	64
1.13	Valence band acceptor modes in a square lattice photonic crystal	66
1.14	FDTD-generated spectrum of a single defect PC cavity	67
1.15	Dipole-like modes in a photonic crystal cavity.	69
1.16	Graded hexagonal lattice donor- and acceptor-type cavities.	85
1.17	Comparison of donor modes in a graded hexagonal lattice cavity as generated by the Wannier/symmetry analysis and FDTD simulations.	86
1.18	Comparison of acceptor modes in a graded hexagonal lattice cavity as generated by the Wannier/symmetry analysis and FDTD simulations.	92
2.1	2D hexagonal PC slab waveguide structure and cladding light cone.	95

2.2	Real and reciprocal space representations of 2D hexagonal and square lattice photonic crystals.	96
2.3	Spatial Fourier transform of E_x of the x -dipole donor mode in a hexagonal lattice. . .	97
2.4	Fundamental TE-like (even) guided mode bandstructure for hexagonal and square lattices.	98
2.5	Illustration showing the mode coupling for the $\mathbf{H}_{A2}^{e,d1}$ mode in \mathbf{k} -space through the $\widetilde{\Delta\eta}$ perturbation.	107
2.6	$\widetilde{\Delta\eta}(\mathbf{k}_\perp)$ for dielectric structure of table 2.7.	108
2.7	Properties of the graded square lattice.	109
2.8	(a) $\widetilde{\Delta\eta}(\mathbf{k}_\perp)$ for single enlarged hole design in hexagonal lattice ($r/a = 0.30$, $r'/a = 0.45$). (b) $\widetilde{\Delta\eta}(\mathbf{k}_\perp)$ for graded hexagonal lattice design shown in table 2.9.	114
2.9	(a) Real and reciprocal space versions of a compressed 2D hexagonal lattice. (b) Fundamental TE-like guided mode bandstructures for a compressed hexagonal lattice.	116
2.10	Modal characteristics of a simple defect mode in a compressed hexagonal lattice ($d/a = 0.75$).	120
3.1	FDTD-calculated properties of the graded square lattice PC cavity design.	126
3.2	Angled view SEM image of the SiO ₂ etch mask	128
3.3	Cross-sectional SEM images of InP ICP-RIE etches.	130
3.4	Wet etch characteristics of the InP sacrificial layer.	131
3.5	Comparison of CAIBE and ICP-RIE etches of InP-based PC lasers.	132
3.6	Top view SEM image of a fabricated PC cavity.	133
3.7	Schematic of the photoluminescence measurement setup.	134
3.8	L-L curves and subthreshold emission spectra from PC microcavity lasers under different pump conditions.	135
3.9	Localization and polarization measurements of the PC microcavity laser mode. . . .	136
4.1	SEM images of Si PC microcavities.	140
4.2	Zoomed-in SEM images of a Si PC microcavity.	141
4.3	Measurement setup for fiber taper probing of PC microcavities.	142
4.4	Polarization measurements of PC microcavity modes using the fiber taper.	144
4.5	Summary of the graded square lattice PC cavity design.	145
4.6	Q measurements in a PC microcavity using the fiber taper.	146

4.7	PC microcavity mode localization measurements using the fiber taper.	148
4.8	Mode localization measurements of a higher order mode in the graded square lattice PC microcavity.	150
4.9	Resolution of the fiber taper.	151
4.10	Grade in the normalized hole radius for different square lattice PC cavities.	155
4.11	Q measurements for two of the PC cavity devices of fig. 4.10 and table 4.1.	157
4.12	Fiber-coupled PC microcavity using an intermediate PC waveguide.	162
4.13	SEM image of a Si microdisk cavity.	164
5.1	Schematic and photoluminescence of a 1DWELL epitaxy.	175
5.2	SEM images of DWELL-containing microdisk cavities	176
5.3	Q measurements of $4.5\ \mu\text{m}$ diameter AlGaAs microdisk cavities in the 1400 nm band	177
5.4	Photoluminescence measurements of $4.5\ \mu\text{m}$ diameter microdisk cavities with em- bedded quantum dots.	179
6.1	Experimental setup for studying the QD-microdisk devices with fiber tapers.	184
6.2	Passive measurements of DWELL-containing AlGaAs microdisks in the 1200 nm band.	187
6.3	Comparison of free-space and fiber taper collection.	188
6.4	(a) L-L curves for free-space pumping and fiber taper collection at different taper positions. (b) Scatter plot of the differential efficiency for fiber taper (filled circles) and free-space collection (open circles) for a number of different microdisk lasers. . .	190
6.5	Light-in-light-out characteristic for lasing and non-lasing modes.	191
6.6	Light-in-light-out curve and subthreshold spectrum for fiber-pumped microdisk laser.	194
7.1	SEM image and finite element calculation of the electric field intensity for a $D \sim 2\ \mu\text{m}$ diameter microdisk.	197
7.2	Finite-element simulation results for Q_{rad} and V_{eff} (and the implied g and κ) as a function of disk diameter.	198
7.3	Calculated $g/\max(\gamma_{\perp}, \kappa)$ as a function of microdisk diameter.	199
7.4	Comparison of finite-element-calculated electric field intensity in disks with vertical and slanted sidewalls.	200
7.5	PL spectrum from the $1.3\ \mu\text{m}$ 1DWELL epitaxy and Q measurement for a $2\ \mu\text{m}$ diameter microdisk fabricated from this material.	202

7.6	Light-in-light-out curve for a $2\ \mu\text{m}$ diameter quantum-dot-embedded microdisk device operated with free-space collection.	203
7.7	Comparison of L-L curves from a $2\ \mu\text{m}$ diameter quantum-dot-embedded microdisk using free-space and fiber-based collection.	204
7.8	Rate equation model fit to experimental data from a fiber taper coupled microdisk laser.	205
8.1	Illustrations of the various experimental configurations utilized in studying coupling between a semiconductor microdisk and a single QD.	209
8.2	Calculated doublet mode spectra for different parameter regimes.	212
8.3	Finite-element method calculated V_{eff} of traveling wave modes of a microdisk cavity.	219
8.4	Normalized transmitted and reflected signal for a QD coupled to a microdisk cavity, calculated through numerical solution of the steady state quantum master equation under weak driving, for $g/2\pi=6\ \text{GHz}$, $\beta/2\pi=9.6\ \text{GHz}$, $\kappa/2\pi=1.2\ \text{GHz}$, and $\tau_{\text{sp}}=1\ \text{ns}$.	220
8.5	Calculated normalized transmitted and reflected signal for a QD coupled to a microdisk cavity, using identical parameters as those used in fig. 8.4, but with $\beta/2\pi=-9.6\ \text{GHz}$	221
8.6	Calculated normalized transmitted and reflected signal for a QD coupled to a microdisk cavity, using identical parameters as those used in fig. 8.4, but with $\beta/2\pi=i*9.6\ \text{GHz}$ ($i = \sqrt{-1}$).	222
8.7	Calculated normalized transmitted and reflected signal for a QD coupled to a microdisk cavity, for the regimes (a) $g > \beta > (\kappa, \gamma_{\perp})$, (b) $\kappa > g > \beta > \gamma_{\perp}$, (c) $\gamma_{\parallel} > g > \beta > \kappa$, and (d) $g > \kappa > \beta > \gamma_{\perp}$	223
8.8	Normalized transmitted signal for a QD coupled to a microdisk cavity, calculated as a function of time through numerical integration of the quantum master equation under weak driving.	225
8.9	Number of intracavity photons in the microdisk clockwise and counterclockwise propagating WGMs, calculated by numerical integration of the quantum master equation.	226
8.10	Calculated normalized transmitted and reflected signal for a QD coupled to a microdisk cavity, for $\beta=0$	228

8.11	Steady state solutions to the semiclassical Maxwell-Bloch equations and quantum master equation, showing normalized intracavity field amplitude $ X_{ss} $ as a function of normalized drive field Y	230
8.12	Steady state solutions to the semiclassical Maxwell-Bloch equations and quantum master equation, showing cavity reflection as a function of average number of intracavity drive photons and input drive power, for varying cavity decay rates.	231
8.13	Steady state solutions to the semiclassical Maxwell-Bloch equations and quantum master equation, showing normalized intracavity field amplitude $ X_{ss} $ as a function of normalized drive field $ Y $, for a system with large non-radiative dephasing (linewidth ~ 5 meV).	232
8.14	Steady state solutions to the quantum master equation, showing cavity reflection as a function of average number of intracavity drive photons and input drive power, for a system with large non-radiative dephasing (linewidth ~ 5 meV)	232
A.1	Schematic, SEM image, in-plane bandstructure, and subthreshold and lasing spectra for a QC-PCSEL.	239
A.2	Surface plasmon mode and cross sectional SEM image of a QC PCSEL device.	240
A.3	Multi-wavelength emission in a QC-PCSEL array.	241
A.4	Polarized emission patterns and FDTD-simulations for a QC-PCSEL device.	242
A.5	Measurements and FDTD simulations of the QC-PCSEL far field emission pattern	243
B.1	Setup for FDTD simulations.	246
B.2	FDTD spectra and mode field patterns for TM-polarized donor type defect modes in a square lattice photonic crystal.	247
C.1	Process flow for fabrication of microphotonic devices such as photonic crystals.	250
C.2	SEM images of the Si ICP-RIE etch with varying gas flow and RF power.	253
C.3	Angled and top view SEM images of the Si etch used in fabrication of high- Q PC cavities.	253
C.4	Top view and cross sectional SEM images of AlGaAs PC cavities fabricated using an SiO ₂ etch mask.	254
C.5	SEM images of AlGaAs photonic crystals using direct pattern transfer from an electron beam mask.	255

C.6	SEM images of photonic crystal patterns in a SiN_x mask and subsequent transfer into AlGaAs.	256
C.7	SEM images of photonic crystal and microdisk patterns when the SiN_x etch does not turn out properly, most likely because of too low a flow of C_4F_8	257
C.8	SEM images of a typical QC-PCSEL device after the semiconductor etch, but before the deposition of electrical contacts.	259
E.1	Schematic for single mode coupling between a resonator and waveguide.	263
G.1	Schematic for atom-field coupling and block diagonal form for the Hamiltonian in the Jaynes-Cummings model.	276
G.2	Energy level spectrum for the Jaynes-Cummings model ($\omega_f = \omega_a$).	277

List of Tables

1	Optical microcavities in 2002	4
2	Optical microcavities in 2006	32
1.1	Point group character tables for the hexagonal lattice.	44
1.2	Point group character tables for the square lattice.	59
1.3	FDTD calculations of modes in a single defect hexagonal lattice PC cavity	68
1.4	Hexagonal PC parameters for the donor- and acceptor-type defect cavities.	85
1.5	Donor mode (X -point) ground state Wannier envelope parameters.	85
1.6	FDTD calculated mode envelope parameters.	87
1.7	Acceptor mode (J -point) ground state Wannier envelope parameters	91
2.1	Symmetry classification and dominant Fourier components for the \mathbf{H} -field of conduction band donor modes in a hexagonal lattice.	99
2.2	Symmetry classification and dominant Fourier components for the \mathbf{H} -field of valence band acceptor modes in a hexagonal lattice.	100
2.3	Symmetry classification and dominant Fourier components for the \mathbf{H} -field of conduction band donor modes in a square lattice.	101
2.4	Symmetry classification and dominant Fourier components for the \mathbf{H} -field of valence band acceptor modes in a square lattice.	101
2.5	Candidate donor and acceptor modes in a square lattice.	102
2.6	Characteristics of the $\mathbf{H}_{A_2''}^{a,a1}$ resonant mode in a hexagonal lattice	104
2.7	Characteristics of the $\mathbf{H}_{A_2}^{e,d1}$ resonant mode in a square lattice	105
2.8	Field characteristics of the graded square lattice shown in fig. 2.7(a).	110
2.9	FDTD simulation results for graded hexagonal lattice geometries	113
2.10	Key geometrical quantities associated with the standard and compressed hexagonal lattices.	117

2.11	FDTD simulation results for graded compressed hexagonal lattice geometries.	121
3.1	Epitaxy for $1.3\ \mu\text{m}$ PC microcavity lasers	127
4.1	Theoretical and experimental Q factors for PC cavities with r/a profiles shown in fig. 4.10.	156
5.1	Epitaxy for 1-DWELL microcavity lasers.	175
7.1	Finite-element calculated $\text{TE}_{p=1,m}$ modes of a $D = 2\ \mu\text{m}$ microdisk.	201

Acronyms

cQED, or **cavity QED** Cavity quantum electrodynamics

DBR Distributed Bragg reflection

DWELL Epitaxy consisting of a layer of quantum dots embedded in a quantum well (dot-in-a-well)

EL Electroluminescence

FEMLAB Commercial software, written by the Comsol Group, for solving partial differential equations by the finite element method

FDTD Finite-difference time-domain

FSR Free spectral range

ICP-RIE Inductively coupled plasma reactive ion etch

MBE Molecular beam epitaxy

MQW Multi-quantum-well

NA Numerical aperture

OSA Optical spectrum analyzer

PC Photonic crystal

PCWG Photonic crystal waveguide

PECVD Plasma enhanced chemical vapor deposition

PL Photoluminescence

Q Quality factor

QC Quantum cascade

QC-PCSEL Quantum cascade photonic crystal surface-emitting laser

QD Quantum dot

SEM Scanning electron microscope

SOI Silicon-on-insulator

TE Transverse electric polarization, defined in this thesis to have electric field components predominantly in-plane and a magnetic field primarily out-of-plane

TM Transverse magnetic polarization, defined in this thesis to have magnetic field components predominantly in-plane and an electric field primarily out-of-plane

V_{eff} Effective mode volume

WGM Whispering gallery mode

WG Waveguide

Preface

The intent of this preface is to present an informal history of my research as a graduate student at Caltech. It is my hope that this introduction will provide a readable overview of my research, which will be described in much greater technical detail in the bulk of the thesis. In addition, I hope that this section will help the reader understand the logic behind our choices in research topics. On a personal note, the work described in this thesis has consumed an enormous amount of my time and energy, and I would like to take this opportunity to document some aspects of our research that are not included in journal papers. This includes tasks such as infrastructure building, which take place in any graduate career, but are particularly prevalent when you work for a newly minted faculty member. Finally, I will use this preface as a means to discuss how our work fits in with the work of others, and will attempt to provide the reader with some sense of the progress that has been made subsequent to our contributions in a given area.

Starting graduate school

Although I officially started graduate school in September, 2001, my introduction to optical microcavities and photonic crystals began a couple of months earlier, in discussions with Dr. Oskar Painter, who had not yet joined the faculty at Caltech, but whom I already knew through our work at XPonent Photonics (a start-up company in nearby Monrovia, CA). Oskar gave me the opportunity to work with him on a couple of papers he was writing. The first was a review article on how one can tailor the properties of photonic crystal microcavities [1], while the second was a short letter on the polarization properties of a pair of modes within a single defect, hexagonal lattice photonic crystal microcavity [2]. Along with a careful reading of his thesis [3] and Joannopoulos's and Sakoda's books on photonic crystals [4, 5], working on these papers gave me a thorough introduction to photonic crystal (PC) microcavities. During this time, Oskar and I had several discussions as to what type of research he would pursue upon starting at Caltech (as a Visiting Associate in the fall of 2001, and as an Assistant Professor in January, 2002). I committed to joining his group, confident that I would have the opportunity to engage in the electromagnetic design, fabrication, and optical

characterization of microphotonic devices.

The two projects that Oskar and I discussed in greatest detail were the development of high quality factor (Q) photonic crystal microcavities, and efficient evanescent coupling between optical fiber tapers and photonic crystal waveguides (PCWGs). We agreed that I would pursue the former topic, while my officemate Paul Barclay, who joined Oskar's group a few weeks after I did, would focus on the latter. From my experiences at XPonent Photonics, I was already very familiar with the finite-difference time-domain (FDTD) method for electromagnetic simulations [6], which is well suited for studying the loss properties of wavelength-scale devices. As a result, there were very few barriers to plunging into research during my first year of graduate school.

Designing photonic crystal microcavities

One of the most interesting and useful aspects of photonic crystal microcavities is their ability to confine light to an extremely small mode volume (V_{eff}), approaching a cubic half-wavelength in the material [7, 8]. These ultrasmall volumes correspond to extremely large per photon electric field strengths, which translate to strong light-matter interactions. This is at the heart of a number of potential applications in quantum optics, nonlinear optics, laser physics, and sensing/detection. The advantages of an ultrasmall volume are most potent when combined with a high cavity quality factor (Q), which corresponds to a long photon lifetime within the cavity. One specific application of interest to us is strong coupling in cavity quantum electrodynamics (cavity QED, or cQED), which examines the coherent interaction of a quantized electromagnetic field with a two-level system, such as an atom or a semiconductor quantum dot (which, at a first level of approximation, is a two-level system). Strong coupling places very strict requirements on the cavity used: the atom-photon coupling rate g , which scales as $1/\sqrt{V_{\text{eff}}}$, must exceed the atom decay rate γ_{\perp} and the cavity decay rate κ , which scales as $1/Q$. The strong coupling regime (fig. 1) is one in which coherent interactions between a single atom and a single photon can take place, and is at the core of many applications of cavity QED in quantum information processing and computing.

Within the optical domain, cavity QED experiments have typically taken place in a system consisting of a single atom coupled to a mode of a high-finesse Fabry-Perot cavity [9]. Over the past several years, there has been a real push to extend this work to semiconductor-based systems, where the Fabry-Perot cavity would be replaced by some semiconductor microcavity, and the atom would be replaced by a semiconductor quantum dot [10]. There are a number of motivating factors behind this drive, as semiconductor-based systems offer significant experimental simplification in comparison to the atom-Fabry-Perot systems. In particular, the semiconductor microcavities are

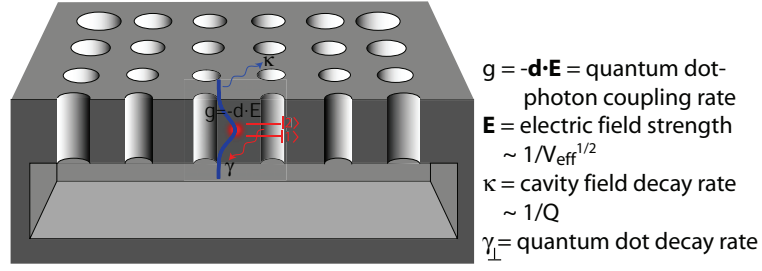


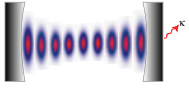
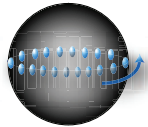
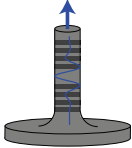
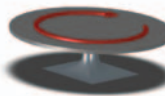
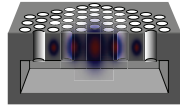
Figure 1: Schematic of quantum-dot-photon coupling in a photonic crystal cavity.

monolithic elements that should not require active stabilization, and a semiconductor quantum dot can be naturally integrated in a microcavity during the initial growth of the material comprising the device. Furthermore, the quantum dot is physically trapped within the device, eliminating the infrastructure required to trap atoms. Finally, these devices are potentially scalable and easy to integrate, as a result of the planar processing techniques by which they are created.

As I mentioned above, one of the key properties of semiconductor microcavities is the very small volumes to which they confine light. These small volumes lead to a very strong coupling rate to even a single quantum dot, so that $g/2\pi \sim 10$ GHz for $V_{\text{eff}} \sim (\lambda/n)^3$. For comparison, typical coupling rates in an atom-Fabry-Perot system are on the order of 10–100 MHz. Nevertheless, even for coupling strengths of several GHz, a cavity $Q \sim 10^4$ is needed to be within the strong coupling regime. As of a couple of years ago, these Q s were not accessible to ultrasmall volume semiconductor microcavities.

Indeed, when I first started this work, the performance of photonic crystal (PC) microcavities, in terms of Q , was significantly worse than it is today. The highest predicted Q s from simulations were on the order of 10^4 [7, 11], and the highest experimentally demonstrated Q s were an order of magnitude less at 2,800 [12]. Nevertheless, PC microcavities still seemed to be a preferred architecture, as the experimentally demonstrated Q s in semiconductor microdisk cavities ($\sim 12,000$ in ref. [13] and $\sim 20,000$ in ref. [14]) were not sufficiently high to compensate for their increased modal volumes (over 10 times larger than those of the PC microcavities). Micropost cavities [15, 16] had experimentally demonstrated Q s that were even lower than those of the PC cavities, for slightly larger mode volumes. Table 1 presents, to the best of my knowledge, the state of the art for microcavities in early 2002 (in this table, I have only considered experimentally demonstrated results). The cavities are generally classified into two types; large mode volume, ultra-high Q structures such as Fabry-Perot cavities and microspheres, and wavelength-scale, relatively low- Q

Table 1: Q and V_{eff} for several experimentally demonstrated microcavity structures, as of 2002

Fabry-Perot	Microsphere	Micropost	Microdisk	Photonic Crystal
				
Geometry	Material	Q	$V_{\text{eff}}((\lambda/n)^3)$	Reference
Fabry-Perot	Air (w/dielectric mirrors)	10^9	10^5	[17, 18]
microsphere	SiO_2	10^9	10^4	[19, 20]
micropost	GaAs/AlGaAs	2×10^3	5	[15]
microdisk	GaAs/AlGaAs	1.2×10^4	6	[13]
photonic crystal	InP/InGaAsP	500	0.3	[8]
	GaAs/AlGaAs	2.8×10^3	0.4	[12]

structures such as semiconductor microdisks, microposts, and photonic crystals. As our interests were focused on cavity QED with semiconductor quantum dots, we were most interested in the development of semiconductor microcavities. The PC cavities appeared to be the most promising candidate, as their ultrasmall volumes implied that the requisite Q s for achieving strong coupling would be less than what would be necessary in a micropost or microdisk.

In approaching the design of PC microcavities, Oskar and I set the following goal: a theoretical $Q \gtrsim 5 \times 10^4$ for $V_{\text{eff}} \sim (\lambda/n)^3$. These numbers were chosen because they would be sufficient, in the ideal case, to allow for strong coupling experiments in cQED. More important than these numbers, we wanted to understand and elucidate the causes for radiation loss in these devices, and to develop a fairly general framework that could be used to design high- Q PC cavities. Of particular interest to us was the development of designs that would be robust to perturbations such as those that one might encounter in the fabrication of the cavities. This seemed to us to be a crucial point, as relatively small discrepancies between a fabricated device and the intended structure would, in many designs, cause the maximum achievable Q to degrade by almost an order of magnitude, such as in ref. [12].

As I describe in chapter 2, the natural way to study losses in these devices is in momentum space. In particular, by considering the Fourier components of the cavity mode, one can understand the sources of loss; small momentum components lead to vertical radiation losses, while in-plane losses occur when the cavity mode contains components in regions of momentum space for which

the photonic lattice is no longer reflective. Taking the spatial Fourier transform of a generated cavity mode serves as a diagnostic for understanding the source of loss in a given design. In addition to our paper on this topic [21], which was published in July, 2002, Vučković and co-workers published a paper during the same month that also noted the relationship between vertical radiation loss and the presence of small momentum components within the spatial Fourier transform of the cavity mode [22].

Rather than just having a diagnostic tool for understanding the performance of a given design, we were also interested in the development of the designs. Knowing which parts of momentum space are to be avoided is the first step toward this. As a second step, we chose to consider modes of a specific odd symmetry, as this leads to zero DC Fourier components and an automatic reduction in vertical radiation loss. We combined this with a methodology for tailoring the defect regions in these cavities in such a way so as to avoid problematic regions in Fourier space, and used FDTD simulations to quantitatively calculate the properties of the designs we generated. We were able to meet our goals, and develop designs in both square and hexagonal lattice photonic crystals with Q s as high as 10^5 and $V_{\text{eff}} \sim (\lambda/n)^3$ [21, 23]. These designs used a grading of the hole radius in the cavity, both to help achieve high- Q s and to make the cavity robust to perturbations to the design. We did not attempt to optimize our results, as Q s of 10^5 were sufficient for the initial experiments of interest to us, and more importantly, at the time, the experimentally demonstrated Q s for PC cavities were significantly lower than what had been predicted theoretically, so it was unclear whether further design optimization would be beneficial.

In addition to using FDTD, we were able to develop a number of semianalytic tools to aid in the cavity design (chapter 1). One of the most useful tools was a simple symmetry-based analysis that used the basic tools of point group theory to classify the symmetries of PC defect cavity modes and determine their dominant Fourier components [1, 3]. The results of this analysis meshed perfectly with the cavity design principles described above, and we relied upon it heavily in our high- Q designs [21, 23]. In particular, this analysis identified the modes within defect cavities in square and hexagonal lattice photonic crystals that satisfied our symmetry criterion for reducing vertical radiation loss. Oskar and I wrote a separate article that fully details the development of this symmetry-based analysis [24], which was published in July, 2003. In the same month, we published another article [25], which details the development of a Wannier-like equation that yields the envelope for resonant modes within PC defect cavities. These two methods are very complementary. The group theory analysis identifies and classifies the symmetries of defect modes within PC cavi-

ties, but has nothing to say about the localization of the modes. The Wannier analysis, on the other hand, describes the localizing effect of the PC lattice on the defect modes. When combined with the symmetry analysis, this Wannier method qualitatively matches the results of the FDTD simulations.

After these initial publications [21, 23, 24, 25], we did not return to the topic of PC microcavity design, but several research groups across the world continued to work on this topic, and have succeeded in developing designs with predicted Q factors in excess of 10^6 [26, 27, 28, 29, 30]. Momentum space design principles remain the basis for most of these works, albeit in combination with new geometries such as modified photonic crystal waveguides [28, 30], and the use of inverse design and optimization methods [31, 29] to help reduce the dependence on the trial-and-error approach that dominated early cavity design work. From my perspective, the Wannier and symmetry-based methods remain attractive starting points for any cavity design (whether or not the focus is on high- Q structures), as they provide a wealth of information with very little computational expense, and can be used to build physical insight on how to appropriately tailor the cavity geometry for the application of interest. Ultimately, FDTD or some other numerical simulation method will be used to calculate the cavity properties in detail, and it is likely that some further amount of tweaking of the cavity design will be required. During this step, the aforementioned optimization and inverse design methods will be of great use.

Building the cleanroom and characterization lab

While developing the PC cavity design techniques, I also spent a great deal of time helping Oskar plan the setup of our labs. Oskar, Paul, and I were able to attend meetings with the project manager in charge of building our labs, and we carefully designed a cleanroom facility and a characterization lab that would be able to support the experiments that we had planned for the first few years of the research group. The centerpiece of the cleanroom would be an Oxford Instruments Plasma Technology (OIPT) inductively coupled plasma reactive ion etch (ICP-RIE) tool clustered to a plasma-enhanced chemical vapor deposition (PECVD) tool. This tool, along with a Hitachi cold cathode, field emission scanning electron microscope (SEM), would allow us to do all of the fabrication steps necessary for creation of optical devices such as the photonic crystal waveguides and cavities that Paul and I were studying. The ICP-RIE/PECVD and SEM would be located in a Class 1000 portion of the cleanroom, and would be adjacent to service chaises that would house the support equipment for the machines (such as vacuum pumps, chillers, gas lines, and bottles). In addition, the cleanroom would contain a Class 100 section that would house fume hoods, a spinner, and a mask aligner for doing optical lithography. Our characterization lab would initially contain se-

tups that would allow for the fabrication of tapered optical fibers, optical probing of microfabricated devices in the telecommunications band ($\lambda \sim 1.5 \mu\text{m}$) using these tapers, and microphotoluminescence measurements of light-emitting devices. Within the period of September 2001–June 2002, we ordered the bulk of all of the equipment to be housed in the cleanroom and characterization labs, and helped install basic equipment such as the optical tables. By June 2002, I had finished the bulk of our work on the design of high- Q PC microcavities as well as coursework for the year, so that I could focus exclusively on lab work. That summer, we installed the SEM and ICP-RIE, the latter of which required a considerable amount of setup time. Oskar, Paul, Tom Johnson (another graduate student of Oskar’s who had just joined the group), and I did all of the stainless steel and PVC plumbing required to service the machines and their accompanying vacuum pumps. By August, we were ready to begin using the tools that we had spent the last couple of months installing.

In August 2002, Oskar and I flew to Murray Hill, New Jersey, to meet with members of the quantum cascade laser group at Bell Laboratories, headed by Dr. Federico Capasso. Our primary collaborator at Bell Laboratories was Dr. Raffaele Colombelli, and he and Dr. Mariano Troccoli met with us and discussed a project that they and Oskar had initiated earlier, which was the incorporation of photonic crystal microcavities within a quantum cascade heterostructure to create electrically injected microcavity laser arrays operating at mid-infrared wavelengths. Initially, our role was primarily to provide photonic crystal design expertise. However, after visiting Raffaele and Mariano, we learned that they were having great difficulty etching the quantum cascade heterostructures using their plasma etching system. Oskar and I agreed to attempt this part of the fabrication at Caltech, while Bell Labs would remain responsible for material growth, all other device fabrication steps, and subsequent device characterization.

Developing fabrication processes

After returning from Bell Labs, I began work in the cleanroom in earnest. Having had some experience in the development of plasma etching processes, I took the lead on developing the ICP-RIE etch recipes, while Paul was in charge of getting the electron beam lithography to work. For Paul, this meant starting with a code that had originally been written by a Caltech undergraduate, Oliver Dial, to control the scan coils and stage of a Hitachi SEM. Paul needed to update the code for our SEM (a different model than that originally used), data acquisition card, and operating system. For me, the ICP-RIE etching would involve building upon my previous experience in plasma processing to develop recipes for etching silicon and InP-based materials. We had decided on silicon-on-insulator (SOI) as a platform for near-infrared (near-IR) PCs, due to its low optical

losses in this wavelength range and the ready availability of high quality wafers from commercial vendors such as SOITEC. InP-based materials were of potential interest for future experiments with PC microcavity lasers in quantum-well-based materials, including the quantum cascade photonic crystal laser project we had agreed to work on with Bell Laboratories.

The development of fabrication processes for creating micro-optical devices is really at the heart of the work that I have done in graduate school. Very simply put, the physical phenomena that we have been interested in require superior device performance. For example, as described above, to reach the strong coupling regime in cQED, wavelength-scale PC microcavities with Q s in excess of 10^4 are required. Thus, all fabrication-induced losses (such as roughness-induced scattering and etch-induced absorption) had to be minimized as much as possible.

The process flow for fabricating a device such as a photonic crystal microcavity typically consists of 1) deposition of a hard mask layer, 2) coating of the sample in electron beam resist and subsequent electron beam lithography, 3) plasma etching (also known as dry etching) of the mask layer, and 4) plasma etching of the primary material layer (typically a semiconductor layer in the applications we consider). For some devices, such as the passive PC resonators and optically pumped lasers described in this thesis, these steps are followed by a wet etch step to undercut the devices. For more complicated structures, such as electrically contacted devices, a number of additional fabrication steps are required. In appendix C, I provide a qualitative overview of some of the considerations that must be taken into account when developing dry etch processes for microphotonic structures.

The first material system that we had significant success with was the quantum cascade material, a heterostructure containing dozens of InP-based layers. The requirements on this etch were relatively strict; we needed to etch $4 - 5 \mu\text{m}$ deep holes (with a radius of $\sim 1 \mu\text{m}$) that were as vertical as possible. In this case, we had the fortune of starting with a very good etch mask, consisting of a 500 nm thick SiO_2 PC mask that had been fabricated by our colleagues at Bell Labs. The process we developed for etching the semiconductor layers, which will be described briefly in appendixes A and C, was able to meet our requirements, and gave us the first indication that we would be able to fabricate world-class structures with our system.

At the same time, we also worked towards fabricating near-IR PCs in silicon and InP. Our group was exclusively responsible for the fabrication of these devices, so that we needed to develop the electron beam lithography and all subsequent etches. By September 2002, Paul had succeeded in adapting the control software to allow us to do the lithography with our SEM, and we began by

using polymethylmethacrylate (PMMA) as our electron beam resist. We were able to do reasonably good lithography with this resist, but its performance under dry etching was very poor. There was no question that we would need to use a dielectric mask before transferring the PC pattern into the semiconductor layer (either Si or InP), but the performance of the PMMA under dry etching was so bad that it seemed unlikely that we would be able to suitably etch our dielectric mask (SiO_2) with it. For about four months, we struggled with the fabrication, and attempted to use a two-level mask consisting of a Au metal layer on top of SiO_2 , with the hope that the PMMA would be more robust to the etch that would transfer the PC pattern to Au, at which point the Au would serve as a strong etch mask for the SiO_2 layer. Although we made some progress, none of our results were up to our expectations, and we did not attempt to optically characterize any of the devices created using these processes.

In January 2003, we switched electron beam resists to ZEP-520A, manufactured by Zeon Chemicals. Oskar had heard of this resist while at a conference, and in looking at its specifications, we realized that it was developed to be significantly more dry etch resistant than PMMA. Paul and I were quickly able to recalibrate our lithography for this new resist, and the resulting PC patterns looked very good. For the time being, we decided to exclusively focus on Si fabrication, and furthermore, we scrapped the original process we were working on (an Ar/Cl_2 etch) and started from scratch, using a $\text{SF}_6/\text{C}_4\text{F}_8$ chemistry. As briefly described in chapter 4 and in more detail in appendix C, this chemistry etches silicon beautifully, particularly for our purposes, where deep etches were not required (in such instances, a cryogenic temperature etch or the Bosch process etch are typically used). We were quickly able to develop an etch that produced smooth, vertical sidewalls. Equally important, this was a low power etch, so that the ZEP electron beam mask suffered minimal etch damage. As a result, we tried using this electron beam resist as the only etch mask for the silicon layer, foregoing the dielectric mask that we had previously attempted to use. This worked extremely well, so that creation of testable PC devices was imminent. Paul and I calibrated the electron beam lithography to create patterns that matched our designs (for waveguides and cavities, respectively), and the final processing step, undercutting of the sample, was relatively simply accomplished through a hydrofluoric acid wet etch to remove the underlying SiO_2 layer of the SOI material. By the end of February 2003, we were ready to test our devices.

Our plan was to use optical fiber taper waveguides as a method for coupling light into and out of these PC devices, and to study the characteristics of this coupling to understand the device properties. Such coupling had previously been demonstrated to *silica* devices such as microsphere

cavities [32, 20], and these works served as an inspiration for our research. However, our devices were significantly different from what had been used in previous demonstrations; we were working with high-index semiconductor microphotonic elements in which the modal fields, particularly in the PC microcavities, were significantly more spatially localized. Overcoming the refractive index mismatch between the fiber taper and the PCWG was at the heart of Paul’s work, as they had been designed [33] to have a phase velocity (and hence effective refractive index) equal to that of light propagating through the optical fiber. As a result, it was clear that phase matched coupling should be achievable. When combined with the significant field overlap between the taper and PCWG modes, this would enable efficient power transfer to take place over the length of the waveguide. For the PC cavities, we did not employ any specific technique to overcome the refractive index mismatch. Instead, we were essentially hoping that the field overlap between the fiber taper mode and the cavity mode would be strong enough to enable some amount of coupling between the two devices; efficient power transfer was not our initial goal. Rather, we simply hoped to have enough coupling to be able to use the taper as a means to learn about the modes of these PC cavities.

Quantum cascade photonic crystal microcavity lasers

As I touched on above, while working on the high- Q PC cavity project, I also had the opportunity to collaborate with Bell Labs on a project involving the integration of PC cavities with quantum cascade heterostructures. As this project lies somewhat outside the focus of the rest of this thesis, I have chosen to include a summary of the technical details within appendix A. Nevertheless, this work presented an exciting opportunity for us, both in terms of collaborating with a very accomplished group of scientists at Bell Labs and also in terms of the technical potential of the project.

The basic goal of the project was to create quantum cascade, photonic crystal surface-emitting lasers, or QC-PCSELs. These devices were of interest to us for a number of reasons. For quantum cascade lasers, they offered the potential for direct surface emission, a non-trivial property due to the transverse magnetic (TM) polarization of the intersubband transitions in QC lasers, but a highly desirable one for applications such as trace gas sensing (one of the most important applications of QC lasers). In addition, PC cavities offered the promise of device miniaturization and integration, allowing for the realization of multi-wavelength laser arrays on a single chip, again of great potential for sensing applications. For PC microcavities, success would represent the first demonstration of an electrically injected PC microcavity laser, and an important milestone for PC devices.

The PC microcavity design we initially decided to employ was a very simple geometry within the hexagonal lattice, as our initial goal was simply to demonstrate lasing from a QC-PCSEL, with-

out particular regard for how high the Q of the cavity was (of course, the Q needed to be high enough for gain to overcome loss in the cavity). By the time I started working on the project in earnest in August 2002, the main obstacle was not in design but in fabrication of the devices, and in particular, the dry etch of the quantum cascade heterostructure. As mentioned above, by the end of 2002, we had developed a suitable dry etch, and Raffaele and Mariano had worked out all of the other processing steps. Toward the end of 2002 and in early 2003, they began measurements on fabricated devices, and lasing action was observed. After carefully examining the data, it became clear that the cavity modes that we observed in electroluminescence measurements were not due to defect modes, but were rather due to band-edge states (low group velocity modes) in the photonic lattice. From the perspective of what we had set out to demonstrate, this distinction was relatively unimportant as the band-edge modes were still confined within the microcavity structure and had reasonable far-field distributions. However, for future applications, the increased localization and higher Q s of the defect modes are of considerable interest.

To verify our understanding of these devices, the initial electroluminescence data, which showed the tuning of the cavity resonances as a function of the cavity geometry (lattice constant and hole size) as well as lasing for certain modes that were well aligned with the QC material gain, was supplemented by additional measurements of the laser mode's polarization and far-field distribution. These experimental measurements were complemented by FDTD simulations and simple symmetry-based arguments, and by May 2003, we had a good understanding of how the devices were functioning. Our principal results were presented in ref. [34], and subsequent publications presented detailed discussions of device fabrication [35] and lasing mode identification [36].

Around the time of completion of this first round of work, there was a redistribution of the Bell Labs group to different universities (Raffaele went to Université Paris-Sud as a research faculty member, Mariano became a postdoc in Federico Capasso's newly formed research group at Harvard, and Claire Gmachl became a faculty member at Princeton). On our end at Caltech, I continued to work on the cavity design some [37], but otherwise stopped working on the project to focus all of my efforts on the near-IR high- Q microcavities. Raviv Perahia has taken over the project at Caltech, and has been working on developing the capability to do a larger chunk of the fabrication at Caltech (including the electron beam lithography and dielectric mask etching), and on new etch recipes to handle different QC heterostructures. Initial efforts will be focused on achieving room temperature operation of the devices (the first devices operated at ~ 10 K), through improvement of a number of device characteristics, including the QC material quality, the cavity design and fabrication, and the

efficiency of current injection.

First attempts at taper coupling and near-IR photonic crystal microcavity lasers

While I worked with Paul and Oskar on developing the fabrication processes to implement our photonic crystal cavity and waveguide designs, Matt Borselli took the lead on building a station to fabricate optical fiber tapers and a second station for probing microphotonic structures with them. The former essentially consists of a pair of motorized stages that pull on the fiber (in opposite directions) while it is being heated by the flame from a hydrogen torch. The characterization setup consists of a motorized xy stage upon which the sample sits, and a motorized z stage upon which the optical fiber taper is attached. A scanning tunable laser is used as the input to the fiber taper, and the transmission past the microphotonic element is detected by a simple InGaAs photodetector. By February 2003, these two setups were ready to be used in conjunction with our newly fabricated silicon devices.

My initial attempts at probing our PC cavities with fiber tapers were unsuccessful and somewhat discouraging; we were not able to see any spectral characteristics of our cavity modes within the taper's transmission spectrum. After spending about a week testing a number of different devices, we became concerned that the technique was simply ill suited for our application; the coupling between the waveguide mode of the fiber taper and our ultrasmall volume PC cavity mode was just too small for appreciable power transfer to take place. While I contemplated this possibility, Paul took over the testing setup and was almost immediately successful in seeing coupling between his PCWGs and the fiber tapers. His initial results in this area were sent out for publication in late March, 2003 [38], and demonstrated some of the basic principles of this technique. Over the next few months, Paul continued to study taper coupling to PCWGs, and was able to not only demonstrate highly efficient power transfer to the PCWG mode of interest [39], but also the utility of fiber tapers as a probe for the spatial and dispersive properties of PCWGs [40].

Soon after our initial failure at taper coupling to PC cavities, I decided that it was worthwhile to pursue another route to an experimental demonstration of our high- Q designs. One method that had been commonly used for studying the Q s of semiconductor microcavities was the use of an active material to create a light-emitting structure whose emission properties could be studied [41, 13, 8, 14, 12, 42]. I was aware that this method had some limitations, such as the need to pump the structure to material transparency in order to achieve a true estimate of the bare cavity Q , but it was nevertheless an already established technique that would, at the least, give us a strong indication as to whether we were able to create PC cavities with a $Q > 10^4$. Furthermore, active

devices such as microcavity lasers were an area of research that we had planned on investigating at some point, and we had in fact already ordered and set up many of the components necessary to do microphotoluminescence measurements. Of course, one drawback was that active devices would require the development of new etch processes. More importantly, as of January 2003, we did not have access to any material from which such devices could be fabricated.

Luckily, in February 2003, Claire Gmachl put us in touch with Dr. Jianxin Chen, a Bell Labs scientist with expertise in the growth of InP-based quantum well structures. Jianxin had in fact already grown $1.3\ \mu\text{m}$ InAsP/InGaAsP multi-quantum-well laser material that was very close in design to what was of interest to us. We agreed to collaborate on this project, and by mid-April, Jianxin had provided us with laser material from which we could make our PC microcavity devices.

Starting in March, I began focusing on InP-based PC microcavity lasers in earnest (chapter 3). The fabrication promised to be challenging, as InP is typically considered to be a much more difficult material to dry etch than Si. Although there are other possible chemistries that can be used, we were committed to an Ar/Cl₂ etch due to its relative cleanliness, which is an absolute necessity for us as we use a single ICP-RIE to etch a number of different material systems with a number of different gas chemistries. While clean, one problem with the Ar/Cl₂ chemistry is that the InCl_x etch byproducts are not volatile at room temperature, so that the material will not etch cleanly unless steps are taken to increase the volatility. The most common way to do this is through heating; in our QC work, this heating was accomplished by the plasma itself. Although the material that we etched in the QC project was very similar to the material we wanted to etch for these near-IR PC microcavity lasers, it quickly became clear that we could not use the same etch. The QC etch is very nonlinear in time, resulting from the finite amount of time (at least a couple of minutes) required for the etch to heat the sample to some sufficiently high temperature. For the QC lasers, this was not a problem, as we had a 500 nm thick SiO₂ etch mask that could withstand the etch for several minutes. Such a thick etch mask was possible due to the mid-IR operating wavelength ($\lambda \sim 8\ \mu\text{m}$) of these devices, which allows the use of a chemically amplified photoresist (which is relatively dry etch resistant) as an electron beam resist. For the near-IR ($\lambda \sim 1.3\ \mu\text{m}$) PC microcavity lasers, we had to use an electron beam resist with much better resolution (such as ZEP 520A), due to the much smaller feature sizes. These resists are much less dry etch resistant, limiting the thickness of dielectric mask that could be used.

Fortunately, we had another option to heat the sample and increase the InCl_x volatility, which was to directly increase the temperature of the ICP-RIE lower electrode using a resistive heating

element that the tool came equipped with. We quickly added the necessary plumbing to allow us to run the ICP-RIE in this heated wafer table mode, which would let us achieve temperatures in excess of 250 °C. Initial tests indicated that temperatures greater than $\sim 150^\circ\text{C}$ would be sufficient for achieving the volatility necessary to etch the InP cleanly.

Of course, such elevated temperatures precluded any possibility of directly etching into the InP using only the electron beam resist as a mask, as we did with silicon. We decided to use SiO_2 as an etch mask, and for the next several weeks, I spent a considerable amount of time and energy in trying to develop etch recipes for both the SiO_2 mask and for the InP-based heterostructure layers. I was eventually able to develop a reasonable SiO_2 etch, although it was somewhat fickle in its performance, and has remained so to this day. One difficulty in etching so many different materials in one chamber is that it is hard to be certain that you are starting your etch from some well-known initial condition. As a result, it is very important for us to develop relatively robust processes. Nevertheless, the SiO_2 etch seemed to be at least adequate, and the subsequent InP etch did not take long to optimize once we committed to using elevated temperatures. By early May 2003, all of the steps, including the subsequent wet etching steps to release the PC membranes (which are somewhat more complicated for these structures than the SOI ones), had been worked out to make the lasers. Chapter 3 discusses the development of these fabrication procedures in detail.

Oskar and I tested the initial rounds of devices together, and we were immediately rewarded with lasing action in photoluminescence measurements of the first devices we tested. Over the next couple of weeks, we tested many devices, and were able to measure cavity Q s of 1.3×10^4 at material transparency. This principal result was very exciting, and represented about a 5 times increase in Q over what had been demonstrated for a PC microcavity to date [12]. In addition, we were encouraged to see that our measured Q s were essentially limited by the resolution of the spectrometer, and furthermore, were very reproducible from device to device. These results, along with studies of the lasing mode polarization, light-in-light-out characteristic, and approximate mode localization, were submitted for publication in late May, and were published in September [43]. In addition, we wrote a detailed article describing the fabrication of these devices [44], which, along with our new cavity designs, was clearly instrumental in their superior performance. This point was particularly apparent to us as Oskar's own graduate research involved fabrication of PC microcavity lasers in InP-based multi-quantum-wells, and the discrepancy between our new fabrication processes and the fabrication processes he had used (which employed a chemically-assisted ion beam etch) was quite pronounced.

We initially had many plans for continuing work on these InP multi-quantum-well lasers, including studying laser performance as a function of the number of quantum wells in the device, developing surface passivation methods to reduce non-radiative recombination, and starting a program to investigate some interesting phenomena in microcavity physics (such as enhanced radiative rates due to the Purcell effect or measurements of the spontaneous emission coupling factor). These plans were never followed up on, however. Initially, we were more interested in giving the taper coupling approach another try, and in the long term, quantum-dot-based materials seemed to be a more suitable choice for some of the microcavity physics experiments. As a result, we stopped efforts of InP-based near-IR PC lasers after this initial round of success. Nevertheless, the Q s that we demonstrated remain the highest values that have been demonstrated for an InP-based PC microcavity (to the best of my knowledge), and quantum-well-based lasers do have potential for various applications, such as fluid-based sensing [45, 46, 47] where the additional quantum confinement provided by quantum dots is not needed. Furthermore, the fabrication processes developed can certainly be used in combination with structures incorporating InP-based quantum dots in an InP-based matrix [48].

Fiber taper probing of silicon photonic crystal microcavities

After completing work on the high- Q PC microcavity lasers in June 2003, we returned the idea of using the fiber tapers to investigate the cavities. We felt that there were many good technical reasons for doing so. In particular, Q measurements involving emission from a light-emitting material are complicated by the need to pump the material to transparency; in practice, the pump level at which this condition is achieved can be hard to experimentally identify. In addition, these emission-based measurements are limited by the resolution of the spectrometer used; for us, this was ~ 0.1 nm, but even for instruments with a longer path length, achieving resolutions better than 0.01 nm can be difficult. Other resolving instruments, such as Fabry-Perot optical filters could possibly be used, but would rely upon collecting a significant amount of emitted power from the PC cavities, a non-trivial feat. A strictly passive measurement, which we proposed, would instead probe the cavity transmission (or reflection) through the fiber taper as a function of the wavelength of the input probe light. The wavelength resolution in such a measurement would then be limited by the probe laser's linewidth, which could be less than 10 MHz (< 0.1 pm). Passive measurements of PC microcavities had certainly been done in the past [49], in experiments where an in-plane waveguide had been fabricated to couple light into and out of the cavity. However, such experiments had their

own difficulties; coupling light into a PCWG is itself non-trivial, and furthermore, somewhat inflexible in that a waveguide must be fabricated for each cavity on the chip, and the waveguide position, and therefore the waveguide-cavity coupling, is fixed and cannot be adjusted. On the other hand, an optical fiber taper waveguide can be fabricated with very little loss ($< 10\%$), and a single device could be used to probe all of the PC cavities on a chip, in a rapid and flexible manner. In that sense, we envisioned the taper acting as an optical probe for chip-based resonant microphotonic elements.

Furthermore, Paul's experiences in coupling between tapers and PCWGs convinced us that our initial failures in coupling to cavities were not fundamental, but were rather due to simple technical difficulties that could easily be remedied. In particular, he discovered some problems with how our detectors were set up, which would have prevented us from measuring modest changes in the transmitted signal. As the taper-PC cavity coupling was not expected to be particularly strong (unlike the taper-PCWG coupling), this was a vitally important discovery. At the time of our previous attempt at taper-PC cavity coupling, we also had not properly calibrated our SEM, so that our measurements of the dimensions of our cavity (such as the hole radius and lattice spacing) were overestimated by around 10%. As the scanning range of the laser source used in the taper probing measurements was around 5% of the center wavelength ($\lambda=1595$ nm), it was certainly important to know the cavity geometry to a reasonably high degree of accuracy.

Thus, when we began our second attempt at taper coupling to the PC cavities (chapter 4), we were much better prepared. We were immediately able to see some amount of coupling between a taper and the first set of new SOI PC cavities that we fabricated, and were able to confirm that the modes were localized defect states. In particular, we were able to demonstrate coupling to the high- Q mode of interest from our design work (chapter 2), and by July 2003, we had used the taper probing technique to measure cold-cavity Q s as high as 25,000. This measurement technique worked extremely well; we could easily probe all of the devices on a chip with a single taper, and the cold-cavity Q could be accurately determined by measuring the linewidth of the cavity resonance (within the taper's transmission spectrum) when the taper was positioned several hundred nanometers away from the cavity (to reduce taper loading effects).

In addition to using the taper to determine the resonant wavelength and Q of the cavity modes, we also began to consider its use as a tool to study the spatial properties of the modes. In particular, by varying the taper's position with respect to the cavity, the position-dependent coupling could be ascertained. This coupling was clearly a function of the overlap between the taper and cavity fields, and would thus, at some level, describe the spatial localization of the cavity mode. We

fabricated new devices that could be probed along both axes of the cavity, and took measurements of this position-dependent coupling as the taper was moved along each of these axes. This data was then compared to the results of a simple coupled mode theory [50] that took into account the analytically determined taper field and FDTD-calculated cavity field, and the experimental data and numerical results matched very well. In early September 2003, we submitted a paper detailing the taper-based measurements of a Si PC microcavity with an experimentally measured $Q \sim 40,000$ and spatial localization consistent with $V_{\text{eff}} \sim 0.9(\lambda/n)^3$ to the journal *Nature*. Although the Q s that we measured were only a factor of 3 times larger than what we had demonstrated in the multi-quantum-well laser cavities, we felt that the taper probing technique, which confirmed the simultaneous demonstration of high- Q and ultrasmall V_{eff} in our PC microcavities, added a significant amount of content to the work. The demonstrated Q and V_{eff} values were particularly exciting from the perspective of cQED, where they would satisfy the strong coupling requirements for both neutral alkali atoms and self-assembled semiconductor quantum dots, with the potential for coupling rates on the order of tens of GHz, which would exceed both the cavity and atom (quantum dot) decay rates.

About three weeks later, we learned that *Nature* had just decided to accept another paper, by Susumu Noda's group at Kyoto University, Japan, detailing the experimental demonstration of high Q s in PC microcavities, and therefore would not consider publication of our work. The Kyoto group work [51], which was published at the end of October 2003, showed measurements of Q s as high as 45,000 in an SOI PC microcavity, using the in-plane waveguide coupling approach. Our rejected manuscript was submitted to *Physical Review* in September 2003, and was eventually published as a *Rapid Communication* in *Physical Review B* in August 2004 [52]

On the surface, the Kyoto work and our work seem to be very similar, but I have always felt that within the context of PCs and optical microcavities, there are several important differences. As I have already mentioned, our work was partly focused on the application of fiber taper probing to wavelength-scale semiconductor microcavities, and in demonstrating that the fiber taper could serve as a useful tool for studying both the spectral and spatial properties of the cavity modes (in particular, measuring both Q and V_{eff}). In addition, although both designs employed Fourier space methods to reduce vertical radiation loss from the cavities, there were some important differences. Upon glancing upon the geometry of the cavities, the most glaring difference would seem to be in the complexity of the design; the Kyoto group design simply consists of three missing holes and two shifted holes within a hexagonal lattice PC. In contrast, our design incorporated a graded

square lattice in which the hole radius continuously changed as a function of position within the lattice. While we did use this to achieve our highest Q s, it was not completely essential for obtaining reasonably high Q s. We were previously able to show, in our simulation work, that Q s of $\sim 40,000$ could be achieved in simple square lattice cavities in which the defect consisted of the reduction in size of two air holes in the lattice. In addition to increasing this maximum achievable Q to $\sim 10^5$, part of the reason for incorporating the grade in hole radius was to make the design robust to fabrication imperfections, so that Q s in excess of 10^4 could be achieved even when the cavity significantly deviated from the prescribed geometry. On the other hand, the Kyoto group design (as well as other designs involving the fine tuning of a small number of holes in the PC lattice) required very precise control of the cavity geometry to achieve high Q s; small variations in the geometry could easily reduce the Q by a factor of 10.

We spent the next couple of months exploring this idea more quantitatively, fabricating and testing different devices and comparing the results to simulations. We amassed the data from several devices, and were able to conclude that our design was indeed robust to fabrication imperfections, from both an experimental and a theoretical standpoint. In particular, we were able to show that the cavity Q could remain above 20,000 even in the presence of variations in the cavity geometry that caused the resonant frequency to vary by $\sim 10\%$ of its nominal value. These geometrical variations included perturbations that broke the desired symmetry of the structure, as well as variations in the hole radius that were significantly different from the intended grade in hole radius. As described in chapter 4, there are relatively simple physical explanations for this robustness, which I believe can be incorporated as principles in future designs of high- Q PC microcavities. We published some of these ideas and numerical and experimental data on the robustness of our cavities in an article in *Optics Express* in April 2004 [53]. Although robustness has not necessarily gained widespread recognition as an important element of PC cavity designs, I think that eventually it will, particularly as optimization and inverse design techniques [31, 29] become more commonly used, as robustness can possibly be entered as a condition within such algorithms. Certainly, from the perspective of an experimentalist, I can attest to the practical utility of having every device on the chip support a high- Q mode, rather than an isolated number of devices that precisely match the nominal design.

At this point, although we had been able to show the versatility of the fiber taper as a probe for the spectral and spatial properties of PC microcavities, as described in detail in a review article [54], one important thing that we had not yet demonstrated was highly efficient coupling to the cavities. Our results thus far had been limited to maximum coupling depths of around 10%-20%. On the one

hand, such levels of coupling were fairly high because the taper is such a low-loss device; coupling losses to an in-plane waveguide using standard end-fire coupling approaches can easily be in excess of 3 dB per coupling junction (for a total of 6 dB, or 75 %). On the other hand, phase matched coupling, such as that which had been achieved for silica microsphere and microtoroid cavities [20, 55, 56], and by Paul for PCWG [38, 39, 40], could achieve coupling efficiencies approaching 100 %. There was thus significant room for improvement.

The strategy we adopted, in work led by Paul, was to first couple light from the taper to the PCWG, which we had shown could be very efficient, and then couple light from the PCWG to the PC cavity. This had been our plan from the outset, as the PCWGs had been specifically designed to mode match to our PC cavities [33]. In addition to potentially allowing for very high coupling efficiencies, this technique had the advantage of more optimally loading the cavity than direct taper probing does, so that the loaded Q s can typically be much higher. Paul's results [57] showed a loaded Q of 3.8×10^4 for $\sim 44\%$ coupling efficiency to a cavity with an unloaded Q of 4.7×10^4 . In comparison, for direct taper coupling, the loaded Q was $\sim 2.0 \times 10^4$ for a coupling depth of about 10 % to a cavity with an unloaded Q of 4.0×10^4 . Having achieved these impressive results by May 2004, Paul then worked on an initial demonstration of what could be done with these fiber-coupled PC cavities by studying the nonlinear response of these devices. He was able to show evidence of optical bistability at very low input powers of a couple hundred microWatts, corresponding to femtoJoule internal cavity energies. These results were published in February 2005 [57], and were soon followed by several additional studies of nonlinear optics in silicon PC microcavities (see ref. [58] and its follow-up articles, for example).

Since the initial publications on high- Q PC cavities from our group [43, 52, 53] and the Kyoto group [51], there has continued to be impressive progress in the experimental demonstration of higher and higher Q PC cavities. The Kyoto group was able to fine tune their initial design to achieve Q s of $\sim 10^5$ [59], and more recently, have employed an entirely different design to achieve $Q \sim 6.0 \times 10^5$. This very interesting and impressive result relies upon the slight modification (through adjustment of the lattice constant) of a PCWG mode to form a cavity that has very little vertical radiation loss, and still has $V_{\text{eff}} \sim 1-2(\lambda/n)^3$ [28]. Even more recently, the group of Masaya Notomi at NTT Laboratories has used a similar design (this time adjusting the size and position of some of the PCWG holes) to achieve $Q \sim 9.0 \times 10^5$ [30]. One key to these designs is that the PCWG modes, in principle, have no vertical radiation loss, so that they serve as a good starting point from which the cavity design can be built. Another key is that strong localization in these PC lattices can

be achieved through very weak perturbations to the lattice, which allows for the creation of defect modes that do not contain lossy Fourier components (such as those within the cladding light cone). In some ways, these results mirror, and of course amplify, what we have been able to see in our graded lattice PC designs, particularly in regards to the idea that a seemingly weak modification to the PC lattice can still confine light to an ultrasmall volume, which was perhaps not appreciated in the earliest PC cavity work. This can be seen in the evolution of PC cavity designs, starting from Oskar's original work [7, 8] employing a single missing air hole in a hexagonal PC lattice, to some of our designs that graded the lattice hole radius, to these latest designs that utilize small modifications to a PCWG.

Switching to AlGaAs: Even more fabrication

As soon as we achieved our first results on passive probing of high- Q Si PC microcavities in June 2003, we began to consider their potential use in cavity QED experiments. There were two specific experiments of interest to us, involving trapped neutral atoms and self-assembled quantum dots, respectively. Of course, our group does not have expertise in either atomic physics or material growth, so both projects would require a collaboration with other groups. At Caltech, we are fortunate to have two research groups in the physics department, those of Professors Hideo Mabuchi and H. Jeff Kimble, that are world leaders in atomic physics and its application to cQED. Hideo's group, in particular, had already begun to consider the potential for incorporating PC cavities with magnetostatic atom chips to create integrated devices in a scalable architecture [60]. Hideo's student, Benjamin Lev, had already developed the ability to trap and guide neutral Cs atoms on microfabricated atom chips [61]. However, despite some initial design work [31], their group had not yet experimentally demonstrated high- Q s in their PC microcavities, and perhaps more importantly, had not been able to effectively address the issue of coupling light into and out of the devices.

In early July 2003, Paul, Oskar, and I met with Ben and Hideo to discuss the potential for a collaboration, and we agreed that it was something of interest to all parties. Initially, there was not that much that we could do on our end, as Paul and I still had much work to do in establishing the efficacy of the taper probing for PC microcavities. Nevertheless, it was useful for us to meet with Ben on a periodic basis, to learn about his atom trapping setup, and to understand what some of the biggest obstacles in this experiment would be. The basic proposal and some simple simulations for the experiment that we planned to do, optical detection of single atom transits through a PC microcavity, were put together in article that we coauthored with Ben and was published in July 2004 [62].

It was immediately apparent that the one issue that was most pressing on our end was the demonstration of a high- Q , ultrasmall V_{eff} at the near-visible wavelengths at which atomic cavity QED experiments are conducted. The Si microcavities we had developed would not be option, as Si is opaque at wavelengths below $1\ \mu\text{m}$. InP-based structures were a possibility, but we instead decided to go with GaAs-based devices, as that would be the most likely host material for any future experiments with semiconductor quantum dots (QDs). For the atomic physics experiments, pure GaAs was not a possibility, as it too was opaque at the Cs transition wavelength of interest (the D2 transition at $\lambda \sim 852.3\ \text{nm}$). Instead, we would use an AlGaAs structure (with an Al percentage of $\sim 30\%$) which in principle, would be transparent at 852 nm. As the refractive index of the AlGaAs structure would be very close to that of Si, the PC cavity design would not change, with the exception of the proper scaling for operating at shorter wavelengths. The fabrication, however, would be completely different. Although optimization of device fabrication in yet another material system was not a very attractive project for me, it was certainly a necessity for us to be able to move forward with cavity QED experiments. Indeed, we placed more importance on this than on any efforts to improve on the performance of our Si PC microcavities.

After taking my candidacy examination in February 2004, I began calibration of etch processes for AlGaAs-based microcavities. By this point, we had begun a collaboration with Professors Andreas Stintz and Sanjay Krishna at the Center for High Technology Materials at the University of New Mexico. Andreas and Sanjay are experts at material growth and in particular, have a good deal of experience in growing self-assembled QDs for applications such as lasers and hyperspectral detectors. They had agreed to provide us with both pure $\text{Al}_{0.3}\text{Ga}_{0.7}\text{As}$ waveguides for the Cs cavity QED experiments and QD-containing waveguides for the creation of microcavity lasers and eventual studies of single photon, single QD interactions.

In a very qualitative sense, AlGaAs tends to etch somewhat less easily than Si but more easily than InP. As a result, it was not clear as to whether we would have to use a dielectric mask in our processing, or if we could transfer the PC pattern directly from the electron beam resist as we had done in the Si devices. Other groups had used the direct transfer approach, but the air holes used in their devices were significantly larger than what ours would be, so that achieving a vertical etch for our devices would be somewhat more difficult. Furthermore, the demonstrated Q s for AlGaAs PC microcavities had been relatively modest [12, 63] (a few thousand at best), and in order to improve upon this, we wanted to optimize the fabrication processes as much as possible, even if this meant resorting to the added steps required to use a dielectric etch mask.

As I discuss in appendix C, we eventually settled on a process that made use of a SiN_x dielectric etch mask for the subsequent dry etch of the AlGaAs layer. The key here is that the SiN_x can be etched using a recipe similar to that we used for etching Si. This low power etch minimally damages the electron beam resist, allowing for the initial cavity pattern to be faithfully reproduced in the dielectric layer. By August 2004, we were in a position to start testing devices.

Over the previous several months, Matt had begun research on Si microdisk cavities. This was a natural follow-up to our Si PC cavity work in many ways. The etch processes needed to fabricate the devices would be identical to what we had already developed, and the devices could be tested using the fiber taper waveguides. At that point the highest demonstrated Q s for small mode volume devices were on the order of 10^4 [13, 14].

Matt's results, which were published in October 2004 [64], were truly impressive; he was able to measure Q s as high as $\sim 5 \times 10^5$ for a mode volume of $\sim 6(\lambda/n)^3$. These results, in terms of the metrics Q/V_{eff} and $Q/\sqrt{V_{\text{eff}}}$, which are relevant to processes such as enhanced spontaneous emission and strong atom-photon coupling, were actually better than what we (or any other group) had achieved in PC cavities. For applications requiring the introduction of another material to couple to the optical field, such as cavity QED with neutral atoms or colloidal quantum dots, the microdisk geometry was not optimal, as its peak electric field lies buried within the semiconductor layer. However, for experiments involving embedded materials, such as semiconductor quantum dots (which was to be my primary focus), they are completely suitable. Furthermore, one particularly attractive aspect of Matt's results was that coupling depths of $\sim 50\%$ could be achieved while still maintaining a loaded $Q > 10^5$. Thus, not only could the fiber taper be used to probe the Q and spatial localization of the microdisk modes, it could serve as an efficient coupler as well. Although Paul had already established the method for efficiently coupling to our high- Q PC microcavities by this point, the simplicity of being able to directly couple to the microdisk while still maintaining a high- Q was certainly appealing.

In my estimation, the microdisks seemed to be a good starting point for future experiments. For much of the work we intended to do, including microcavity-quantum-dot lasers and chip-based cavity QED involving single quantum dot, single photon interactions, the cavity geometry is by itself not necessarily important; all of the important device properties are encapsulated by the cavity's Q , V_{eff} (more precisely, the peak electric field strength at the location of the emitter), and η_0 , a parameter that defines the collection efficiency of photons from the cavity. Matt's results had clearly shown that the microdisks were very competitive in these regards. In addition, from a purely practical

standpoint, high quality microdisks are in many ways much easier to fabricate than PC cavities (in terms of the requirements on sidewall angle, as one example). Thus, when starting new experiments, it seemed like an appropriate strategy was to first use microdisk cavities as a way to observe the basic physical phenomena of interest. Ultimately, PC cavities have a number of interesting properties that are somewhat unique to them (for example, very high spontaneous emission coupling factors), and they are certainly interesting from the perspective of future experiments involving integration of multiple devices on a chip, where the truly planar geometry of the PCs is a significant advantage. We thus planned to begin experiments by using microdisk cavities, and would switch to PC cavities when many of the experimental details had been worked out, or when we were interested in studying phenomena that would be specific to them.

Quantum dot microdisk lasers

Fabrication of the AlGaAs microdisk cavities was accomplished through largely the same fabrication steps as what we had developed for the PC cavities. The primary differences were slight adjustments in the etch chemistries for the SiN_x and AlGaAs dry etches, to make the disk sidewalls as smooth as possible, even at the expense of sidewall verticality. The reason for this is that for most microdisk geometries, sidewall angle is not nearly as important an influence on Q as it is for PC cavities, but sidewall roughness is. Another important element of the microdisk fabrication is a resist reflow process that Tom had developed for the Si microdisk cavities. This process largely eliminates radial variations in the mask, thereby improving the circularity of the disk and reducing surface scattering losses. Matt and Tom had recently used this technique to demonstrate Q s as high as 5×10^6 in a $60 \mu\text{m}$ radius disk, and they also made devices that exhibited $Q \sim 1.25 \times 10^6$ for $V_{\text{eff}} \sim 14(\lambda/n)^3$ [65].

The first devices I tested were microdisks fabricated in a passive Al_{0.3}Ga_{0.7}As waveguide (no quantum dots), for potential use in the neutral Cs atom cavity QED experiments. At the desired operation wavelength of $\lambda \sim 852 \text{ nm}$, the devices did not perform as well as hoped, and we did not observe Q s greater than $\sim 2 \times 10^4$. On the other hand, the devices performed much better at longer wavelengths, with $Q \sim 1.5 \times 10^5$ exhibited in the 1500 nm band. Over the next several months, this behavior was observed repeatedly, both by me and by Paul, who took over our group's portion of the neutral atom cavity QED project upon completion of his work on nonlinear optics in Si PC cavities [57]. Our working hypothesis is that deep impurity states (caused by O₂ incorporation, for example) in the AlGaAs are causing absorption at wavelengths above the semiconductor bandgap (around 700 nm for Al_{0.3}Ga_{0.7}As) but below $1 \mu\text{m}$. There is some support for this theory in literature, through

measurements of waveguide loss [66]. We are currently working with Kevin Hennessy in the group of Professor Evelyn Hu at UC Santa Barbara to study this phenomenon a bit more closely, with Chris Michael taking the lead on this project from our end. If true, this will have a significant impact on QD-microcavity devices, as much of the current work is being done at wavelengths below $1\ \mu\text{m}$.

Our measurements within the $1500\ \text{nm}$ band were quite promising as far as our QD-based devices were concerned, as they were grown by Andreas and Sanjay to operate in the $1.2\text{-}1.3\ \mu\text{m}$ band. The most immediate application for these devices would be room-temperature lasers. We began this investigation, described in chapter 5, by fabricating disks in an epitaxy containing three stacked layers of quantum dots. Such an epitaxy (often times containing even more layers of dots) is often used in QD laser research as a result of the increased amount of gain relative to a single layer of QDs. We were quickly able to demonstrate optically pumped lasing from such devices, and the thresholds were quite low, close to the predicted transparency level for the material. These low thresholds were consistent with the cavities sustaining very high Q s. Indeed for a cavity $Q \gtrsim 3 \times 10^4$, the modal gain from a single layer of dots was predicted to be sufficient to achieve lasing. This would be a significant demonstration, as at that point, no other microcavity-based device had been able to demonstrate room temperature lasing from a single layer of QDs (due to the relatively high Q s required).

We were soon able to demonstrate optically pumped lasing from a single layer of QDs, at room temperature, for both pulsed and continuous wave pumping. The threshold pump values were again quite close to the predicted transparency levels, indicating that the cavity Q s were most likely much larger than the minimum value ($Q \sim 3 \times 10^4$) needed for lasing. As this value is already higher than what could be resolved with our spectrometer (which has a resolution limit of around $0.1\ \text{nm}$), this would typically be all that could be quantitatively said about the cavity Q using standard measurement techniques. There is the possibility of fitting the lasing data with a rate equation model with the Q as a free parameter, but such fits depend upon a number of different parameters, such as the QD radiative lifetime, internal efficiency, and collection efficiency, which will not necessarily be precisely known, and the estimated Q s will have a relatively large uncertainty.

Using the fiber taper probing technique in conjunction with knowledge about the microdisk mode structure allowed us to learn a great deal more, however. In particular, we used the taper to probe the cavity modes within the $1.4\ \mu\text{m}$ wavelength band, which was far enough red detuned from the emission wavelength that we did not expect to see any effects related to the absorption by the QD gain material, thus giving us an accurate estimate of the cold-cavity Q s of the modes. This would give us the desired information about the quality of our fabrication, and would let us know whether

our cavities were good enough for future experiments, such as those in cQED. It would also give us additional information about the lasing modes we had studied through photoluminescence. Of course, a mode that we study in the $1.4\ \mu\text{m}$ band is not the same mode that is lasing. However, by carefully studying the cavity's spectrum and comparing it to simulation results, we can study a mode within the $1.4\ \mu\text{m}$ band that has the same polarization and vertical and radial order as the lasing mode, and only differs in its azimuthal mode number (i.e., the number of lobes in the azimuthal direction). As long as the radiation loss that occurs when the mode tunnels around the disk perimeter is not the dominant loss mechanism, modes whose azimuthal orders are only slight different will behave very similarly; in fact, modes at the longer wavelength will have lower radiation-limited Q s. As losses due to mechanisms such as surface scattering, surface absorption, and bulk absorption are not expected to be drastically different between the $1.2\ \mu\text{m}$ and $1.4\ \mu\text{m}$ bands, the Q measured in the $1.4\ \mu\text{m}$ band can give a good estimate of the Q expected for the lasing mode in the $1.2\ \mu\text{m}$ band.

Using this taper coupling technique, we were able to demonstrate Q s as high as 3.6×10^5 . These Q s were over a factor of 10 higher than anything that had been demonstrated in an AlGaAs microcavity. The high- Q resonances we saw were actually doublets, corresponding to standing wave modes that form when the traditional clockwise and counterclockwise modes of the disk are coupled and split by surface scattering. Such doublet modes were also seen by Matt in his investigation of Si disks [64], and are indicative of a cavity loss rate that is low enough that coherent coupling between the propagating modes of the disk can occur. For our disk geometries (255 nm thick and $4.5\ \mu\text{m}$ in diameter), $V_{\text{eff}} \sim 6(\lambda/n)^3$. For optimal coupling to a single quantum dot, this corresponded to a QD-cavity coupling rate $g/2\pi \sim 11\ \text{GHz}$, which would greatly exceed (by over a factor of 10) the demonstrated cavity decay rate $\kappa/2\pi \sim 0.4\ \text{GHz}$ and typical QD decay rates of $\gamma_{\perp}/2\pi \sim 1\ \text{GHz}$. These results indicated the potential for strong coupling in this system.

In addition to the V_{eff} and cold-cavity Q of these cavities, we were also able to demonstrate relatively efficient coupling to them, with power transfers very similar to what Matt had demonstrated in the Si microdisks. We measured coupling depths as great as 60 % for a loaded $Q \sim 10^5$. This was a key result; it indicated that we could still achieve strong coupling (with $g/\kappa \sim 10$) while also obtaining efficient coupling into and out of a coupled QD-microdisk system. For future experiments, this will be of great importance. Experiments in quantum optics will involve very low light levels, and efficient light collection is necessary from a detection standpoint, particularly at wavelengths greater than $1\ \mu\text{m}$, where InGaAs detectors, which suffer from significantly poorer performance characteristics than the Si detectors used at shorter wavelengths, are used. From the standpoint of

future work in quantum information processing, applications in linear optics quantum computing [67, 68] require a near-unity collection efficiency of single photon pulses. Although not currently at that level, our results were a significant step towards these goals, and the path to more efficient coupling through tailoring of the disk geometry was apparent. Indeed, Matt and Tom have since demonstrated critical coupling in the Si microdisks.

This first set of results on optical loss and lasing characteristics in AlGaAs microdisk cavities with embedded quantum dots was submitted for publication in December 2004, and was published in April 2005 [69]. At this point, we began to seriously consider the possibility of doing cavity QED experiments in these resonators. By this point, vacuum Rabi splitting due to the interaction of a single QD with a microcavity had just been demonstrated by three groups [70, 71, 72], through measurements of the spontaneous emission from the devices. Although our devices had the potential for exhibiting Rabi splitting with a greater ratio of g/κ , it was clear to us that the most important contribution that we could make was to develop cavity QED experiments using the fiber taper as an input-output channel, as it appeared to be the key to opening up a number of future experiments and device applications. This would require us to set up a number of different pieces of equipment in the lab, such as a spectrometer with a very sensitive detector for studying the emission from single QDs, a laser source for doing near-resonant pumping and spectroscopy of the coupled QD-microcavity system, and the integration of the fiber-coupled devices in a liquid He cryostat. The last point was particularly important and challenging, as it had not yet been demonstrated and was essentially at the heart of our proposed experiments.

While waiting for some of the experimental equipment to arrive, we decided to further investigate the performance of our microdisk-QD lasers at room temperature (chapter 6). In particular, we were interested in explicitly demonstrating the utility of the fiber taper for future measurements of QD-containing microdisks. To this point, we had used the taper as means to probe the microdisk Qs, but there obviously was significant potential for using the taper as means to collect the emission from optically pumped devices, and furthermore, as a way to pump the devices as well (to this point, our pumping and collection was done through standard free-space optics). To most explicitly compare the efficiency of fiber taper collection with free-space collection, we revamped our photoluminescence measurement setup to allow for the microdisks to simultaneously be probed with optical fiber tapers while still allowing for standard free-space pumping and collection. This allowed us to continue to pump the devices with a free-space beam while comparing the amount of collected power through the free-space optics with that collected through the fiber taper. The differ-

ence was quite dramatic; whereas before we were only able to collect hundreds of picoWatts from our lasers, we were now able to collect as much as a couple hundred nanoWatts from the devices. To most precisely quantify our results, we compared the differential efficiency ξ of the laser with and without the fiber taper collection, and saw that the taper collection improved ξ by almost two orders of magnitude. By collecting a significant fraction of the laser emission, we put ourselves in the position to more quantitatively study some aspects of the laser's behavior, particularly subthreshold, where the poor collection typically obtained through free-space optics makes careful investigations of device behavior difficult.

Not only is the collected power significantly greater when using the fiber tapers, but the number and variety of modes that are observed is strikingly different. This is not too surprising; for microdisks, free-space collection essentially relies upon imperfections in the disk to scatter light vertically into our collection optics. This is a relatively inefficient process, and becomes increasingly more inefficient as device fabrication improves and higher and higher Q devices are realized. The fiber taper, on the other hand, directly evanescently couples light out of the disk WGMs, and can be a very efficient process. Although loading due to the taper does degrade the cavity Q , the key point is that this loading is efficient in that the added loss is primarily due to coupling into an observable channel (the fiber taper); the lost photons are collected into the fiber and are free to interact with some other part of the system, such as another cavity or photon counting detectors. This is not the same as loss due to absorption, for example, where the lost photons are not detectable and are of no benefit. This point is somewhat obvious in that it is true for all cavities; in a simple Fabry-Perot cavity, for example, one typically degrades the reflectivity of one of the mirrors to allow for light to be coupled out of the cavity. Despite the simplicity of this concept, it is nevertheless often misunderstood in the literature.

In the early part of 2005, we gained access to two new laser sources, which allowed us to do two additional measurements. The first laser source was a 980 nm external cavity laser that had been built by some members of our lab; we were able to use this as a source for optically pumping our microdisks directly through the fiber taper. We were thus able to make purely fiber-coupled devices that no longer relied upon any free-space optics. From a technological standpoint, the device simply consists of a fiber input, to be hooked up to an optical pump source, and a fiber output, through which the emitted laser light would propagate. Such purely fiber-coupled devices had been previously demonstrated by the Vahala group at Caltech in the context of erbium-doped glass microsphere and microtoroid cavities [73, 74]; our work extended this to the regime of wavelength-

scale, semiconductor-based devices, for which interesting gain materials such as quantum well and quantum dot layers can be incorporated. The second laser source we acquired was a 1250 nm scanning tunable laser. The primary purpose of this laser was for future experiments employing near-resonant pumping of QDs at cryogenic temperatures (Andreas and Sanjay had recently grown new samples for us that emit at $\sim 1.32 \mu\text{m}$ at room temperature and $\sim 1.25 \mu\text{m}$ at 4 K). For the time being, we were able to use it in conjunction with our current devices (which emitted at $\sim 1.2 \mu\text{m}$) to measure the cavity Q at a wavelength that was much closer to the peak of the QD emission spectrum. Because the wavelength dependence of surface state and material absorption in AlGaAs is not particularly well known, and in addition, we had already seen strong differences in the cavity Q s between the 850-1000 nm band and the 1400 nm band, it was important for us to be sure that the Q s would still be high at wavelengths relevant to future cavity QED experiments. We were indeed able to measure $Q > 2 \times 10^5$ at $\sim 1250 \text{ nm}$, with the discrepancy in Q between the 1400 nm band and the 1250 nm band likely being due to absorption from the tail end of the inhomogeneous QD spectrum.

We wrote a relatively detailed paper on the various results concerning photoluminescence measurements using optical fiber tapers and submitted it for publication in June 2005; it was published a few months later in November [75]. We subsequently continued our study of these QD-microdisk devices by considering how device performance (cavity Q , V_{eff} , and lasing threshold) scales in going to smaller sized disks. In particular, we were interested in seeing how these microdisks could compare to devices such as photonic crystal microcavities, both in theory and in practice. On the theoretical end, we employed a finite element eigenfrequency solver method to calculate the radiation-limited quality factor Q_{rad} and mode volume V_{eff} of the first order radial modes of $D=1.5$ - $3 \mu\text{m}$ diameter microdisks in the 1200-1400 nm band. These simulations had been developed using the FEMLAB software by Matt, who had in turn received some assistance from Sean Spillane (a graduate student in Professor Vahala's group who had previously used FEMLAB to study micro-toroid resonators). From the simulations, we were able to see that standing wave modes in the microdisks could have $Q_{\text{rad}} > 10^5$ for $V_{\text{eff}} \sim 2(\lambda/n)^3$, corresponding to a disk diameter of $\sim 1.5 \mu\text{m}$. Furthermore, Q_{rad} sharply increases as the diameter increases, so that $Q_{\text{rad}} > 10^8$ can be achieved for $V_{\text{eff}} \sim 3.5(\lambda/n)^3$. Such values are quite comparable to the highest values predicted for 2D photonic crystal microcavities [28, 30]. From these simulation results, we could then calculate the predicted coupling and decay rates for interactions with a single QD. One significant difference between QD-based cavity QED and atomic-based cavity QED is in the emitter decay rates; a typical QD might

have a radiative decay rate $\gamma_{\text{sp}}/2\pi \sim 0.2$ GHz, but due to non-radiative dephasing, the total decay rate $\gamma_{\perp}/2\pi$ will often be closer to 1 GHz (a neutral Cs atom, on the other hand, has a transverse decay rate $\gamma_{\perp}/2\pi \sim 2.6$ MHz). An equivalent cavity decay rate would correspond to $Q \sim 10^5$; this indicates that there is some optimum diameter at which the ratio of the QD-microcavity coupling rate g to the maximum decay rate in the system (either γ_{\perp} or the cavity decay rate κ) is maximum. From our simulations, this diameter is ~ 1.5 - $2 \mu\text{m}$.

We then fabricated $2 \mu\text{m}$ diameter microdisks and studied their Q s and lasing properties using the taper coupling techniques we had already established. These devices were fabricated in the latest material that Andreas and Sanjay had grown, which had been optimized for room temperature emission at $\sim 1.32 \mu\text{m}$ and low temperature (4K) emission at $\sim 1.25 \mu\text{m}$. By taper testing the devices in the $1.4 \mu\text{m}$ band, we were able to demonstrate Q s as high as 1.2×10^5 for $V_{\text{eff}} \sim 2.2(\lambda/n)^3$. We also observed room-temperature, continuous-wave lasers with threshold pump powers as low as $1 \mu\text{W}$ of absorbed power, and used the fiber taper to create devices with differential collection efficiencies as high as 16 %. From a pure device performance standpoint, these devices were outstanding; the demonstrated lasing thresholds were orders of magnitude smaller than what had been demonstrated by other groups for microcavity-QD lasers. This is a result of the ultrasmall volume of these cavities and the correspondingly small number of QDs that need to be inverted (all the more so because we are only using a single layer of QDs); the ability to achieve lasing from such a small amount of gain is made possible by having a high cavity Q . Our study of these small diameter microdisks with embedded quantum dots was submitted for publication in November 2005, and published in February 2006 [76].

Towards cavity QED experiments

The most recent devices we had fabricated showed significant promise for cavity QED experiments, and over the past few months, we have begun to equip our lab to do such work. This includes setting up a continuous flow liquid He cryostat, which would allow us to reduce our sample temperatures to ~ 4 K, a necessity in order to reduce non-radiative dephasing in the QDs, as well as a 0.5 m spectrometer system with a liquid-nitrogen-cooled InGaAs detector. Even with such a detector, single QD detection at wavelengths above $1 \mu\text{m}$ is very difficult, due to the already-mentioned poorer performance of InGaAs detectors relative to Si detectors.

With this equipment in place, we are in principle in the position to observe vacuum Rabi splitting in the spontaneous emission from a single QD in a semiconductor cavity, as has been recently demonstrated by three groups at the end of 2004 [70, 71, 72]. This is not to say that such a demon-

stration will be trivial; we certainly have to work hard to optimize our photoluminescence setup to be sure that we can observe single QD emission, but the techniques for doing so have been established by many research groups, although fewer have done so at the longer wavelengths at which our devices operate. We are most interested in performing a slightly different experiment, however, where Rabi splitting will be observed in the transmission (or reflection) past the cavity. This will be a unique experiment as a result of our capability to efficiently couple light into and out of the cavity, which can allow us measure the cavity response as opposed to spontaneous emission. In this sense, it will make our semiconductor-based system quite analogous to the neutral atom cavity QED experiments, where Rabi splitting is typically observed in the cavity's transmission spectrum [77, 78]. Most important, however, is the potential of this fiber-coupled system for observations beyond vacuum Rabi splitting, such as photon blockade [79] or few photon nonlinear optics. Chapter 8 presents a further discussion of some of these topics.

As our goal was to make the fiber taper an integral part of our cavity QED experiments, it was necessary to figure out how to best integrate it within our liquid He cryostat. In some ways, our problem paralleled the problem that Paul and Ben were facing in trying to integrate fiber-coupled microcavities into a UHV chamber for neutral atom cavity QED. They had decided that the appropriate way to tackle this latter problem was to try to robustly mount the taper to our microcavity chip with a UV-curable epoxy. This would result in a fiber-pigtailed device that, ideally, would be portable and easy to integrate in existing setups. Paul spent many weeks tackling this challenging, yet tedious task. There was little room for error, as a taper movement on the order of a micron would eliminate coupling to the cavity. A number of different methods and strategies were tried but were at best partially successful. Towards the end of the summer of 2005, however, he developed a technique that affixed the taper to on-chip support structures using microdroplets of UV-curable epoxy. This technique worked amazingly well, to the point that it was easier to break the support structures free from the rest of the chip than it was to remove the taper was from the support structures. Paul submitted these results, along with some impressive measurements of $Q \sim 4 \times 10^6$ for a SiN_x microdisk with $V_{\text{eff}} \sim 15(\lambda/n)^3$, for publication in April 2006 [80]. These SiN_x microdisks are transparent at $\lambda \sim 852$ nm, making them suitable for the Cs atom cavity QED experiments.


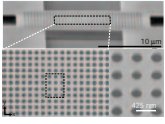

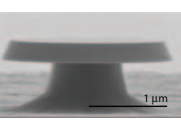

In the summer of 2005, Christopher Michael began working full-time in our group, and began working with me on the QD-microcavity project. In particular, he took the lead on trying to adapt the mounting techniques that Paul had developed for our low temperature setup. Of course, the primary concern here was the behavior of the UV epoxy at low temperatures. Chris was quickly able to

reproduce Paul’s mounting results for our AlGaAs microdisks at room temperature, and we had no significant difficulties in physically integrating the taper-coupled device into our cryostat. During the cooldown, however, the taper came free at around 200 K. Chris and I made multiple additional attempts at cooling down mounted samples over the next few weeks, and tried a number of heat-curable epoxies that in principle had good low temperature performance. None of these attempts succeeded, however. One important point is that the microdroplets of epoxy that we were using were significantly less than what any of these epoxies had been tested at during manufacturing. By mid-November 2005, we began to re-assess the situation.

Because Paul and Ben were tackling a similar problem, it seemed to make sense to try to leverage their recent success. In doing so, we overlooked the important point that Paul and Ben were doing taper mounting, rather than active positioning with mechanical stages, in part out of necessity, as they needed to make a device that was of low enough profile to avoid impeding any of the cooling and trapping laser beams within their vacuum chamber. This was not an all an issue for our QD work. Although the experiments using taper-mounted devices would potentially be relatively simple and elegant (and inexpensive), it is certainly not necessary, particularly in early experiments where the primary focus is on the physical phenomena we hope to see. We thus began to explore the possibility of incorporating a positioning setup within the cryostat. By the end of December 2005, I had worked out a design that would significantly modify our cryostat and let us integrate piezo-actuated stages into the chamber. The cryostat manufacturers (Janis research) began construction of the modified parts in early 2006, and we ordered a set of piezo-actuated stages that were specifically engineered for operation at low temperatures and high vacuums.

While waiting for the new equipment to arrive, I began to more quantitatively investigate some of the phenomena we might expect to see in our experiments. This gave me the opportunity to learn some of the quantum master equation and quantum trajectory formalisms common to quantum optics research. Using the Quantum Optics Toolbox for Matlab developed by Sze Tan [81, 82], we began to simulate a coupled QD-microdisk system using the Q and V_{eff} values we would expect for our devices. One question of particular interest to us was how, if at all, the QD-microcavity interaction would differ in our devices, which had Q s that were high enough that surface scattering would couple the propagating modes of the disk and create standing wave modes. One immediate consequence of having standing wave modes is that their mode volumes are approximately half that of the traveling wave modes; the peak electric field strength for a standing wave mode is therefore $\sqrt{2}$ times larger than that for a traveling wave mode. Of course, another consequence is that the

Table 2: Experimentally demonstrated optical microcavities as of early 2006. The scanning electron microscope (SEM) images are for devices fabricated in the Painter research group (Si μ disk image courtesy of M. Borselli and SiN_x μ disk image courtesy of P.E. Barclay).

InP PC	Si PC	Si μdisk	AlGaAs μdisk	SiN_x μdisk
				
Geometry	Material	Q	$V_{\text{eff}}((\lambda/n)^3)$	Reference
photonic crystal	InP/InGaAsP	1.3×10^4	1.2	[43]
	Si	9.0×10^5	1.7	[30]
	Si	6.0×10^5	1.2	[28]
	GaAs/AlGaAs	2.0×10^4	1.0	[71]
microdisk	Si	1.3×10^6	14	[64]
		5.0×10^6	188	[65]
	GaAs/AlGaAs	3.6×10^5	6	[69]
		1.2×10^5	2.2	[76]
	SiN _x	3.6×10^6	15	[80]
microtoroid	SiO ₂	1.0×10^8	500	[56]
		4.0×10^8	160	[83]
micropost	GaAs/AlGaAs	1.3×10^4	16	[84]
		2.8×10^4	79	[84]
	AlGaAs/AlO _x	4.8×10^4	51	[85]

new standing wave field would have nodes for which the QD-cavity interaction would be zero. We wanted to understand a bit more quantitatively how the system's spectral response would behave within different parameter regimes, where the quantities of interest are the QD-photon coupling rate g , the cavity decay rate κ , the QD decay rate γ_{\perp} , and the amplitude and phase of the backscattering parameter β . Finally, the per photon electric field strengths within these cavities are so large that nonlinear optics at the single photon level becomes a possibility. Our initial consideration of these topics are the focus of chapter 8.

In table 2, I have updated table 1 to report overall progress in the field that has occurred during the time of my graduate research. This table, which contains experimentally demonstrated values for Q and V_{eff} for a number of different microcavity geometries in different materials, is a good indication of the large amount of effort that has been placed on developing microphotonic struc-

tures with low optical losses (other types of devices, such as PC waveguides, have also exhibited markedly reduced losses over the last few years, although I have not included these structures within the table).¹ In addition to the semiconductor microcavities that I have focused on in this thesis, there has been significant progress in the development of chip-based dielectric cavities, such as the SiO₂ microtoroid cavities first demonstrated by Deniz Armani in Professor Kerry Vahala's group at Caltech [56], which exhibit Q s in excess of 100 million, and the SiN_x cavities demonstrated by Paul in our group [80], which have Q s of a few million and mode volumes that are significantly reduced in comparison to the microtoroid geometries. As these structures are fabricated in materials that are transparent throughout the visible and near-IR spectrum (unlike high-index semiconductors such as Si, GaAs, and InP), they have potential for integration with a number of systems, including colloidal quantum dots, impurity states in crystalline films, and alkali atoms, which all have optical transitions at less than 1 μ m. In general, the results of table 2 indicate that the field has significantly and rapidly matured, through a combination of progress in fabrication technology, our understanding of how to design these devices, and in the development of tools with which these devices can be probed. For quantum optics applications, this means that we are finally in the position to take advantage of the intense electric fields that are supported by these ultrasmall volume microcavities, in order to study coherent light-matter interactions in solid-state systems.

The organization of this thesis is as follows. Part I details the design and experimental realization of ultrasmall volume, high quality factor photonic crystal microcavities. Measurements of InP-based multi-quantum-well lasers and passive Si resonators are presented. Part II is focused on microdisk resonators in the AlGaAs system. These microdisks contain an integral layer of InAs quantum dots, and measurements of the loss properties and lasing characteristics of these devices are presented. Simulations of the predicted behavior of these structures in the strong coupling regime of cavity QED are also considered. Finally, the appendixes contain relevant background material for the topics discussed within the body of the thesis.

¹In addition to the cavities described in this table, there have been significant efforts in developing new cavity geometries. These include defect cavities in full three-dimensional photonic crystals [86] and other types of cavities employing the distributed Bragg reflection confinement mechanism, including circular Bragg resonators [87, 88] and Bragg "onion" resonators [89].

List of Publications

Listed below are publications that took place during my time in graduate school. They have been divided into two sections, to separate those that are most closely related to this thesis from those that are not.

Publications most closely related to this thesis

- K. Srinivasan and O. Painter, Momentum space design of high-Q photonic crystal optical cavities, *Optics Express*, **10**(15), pp. 670-684 Jul. 29, 2002.
- K. Srinivasan and O. Painter, Fourier space design of high-Q cavities in standard and compressed hexagonal lattice photonic crystals, *Optics Express*, **11**(6), pp. 579-593, Mar. 24, 2003.
- O. Painter and K. Srinivasan, Localized defect states in two-dimensional photonic crystal slab waveguides: a simple model based upon symmetry analysis, *Physical Review B*, **68**, 035110, Jul. 2003.
- O. Painter, K. Srinivasan, and P. E. Barclay, A Wannier- like equation for localized resonant cavity modes of locally perturbed photonic crystals, *Physical Review B*, **68**, 035214, Jul. 2003.
- K. Srinivasan, P. E. Barclay, O. Painter, J. Chen, A.Y. Cho, and C. Gmachl, Experimental demonstration of a high-Q photonic crystal microcavity, *Applied Physics Letters*, **83**(10), pp. 1915-1917, Sep. 8, 2003.
- R. Colombelli, K. Srinivasan, M. Troccoli, O. Painter, C. Gmachl, D. M. Tennant, A. M. Sergent, D. L. Sivco, A. Y. Cho, and F. Capasso, Quantum cascade surface-emitting photonic crystal laser, *Science*, **302**(5649), pp. 1374-1377, Nov. 21, 2003.

- K. Srinivasan, P. E. Barclay, and O. Painter, Fabrication-tolerant high quality factor photonic crystal microcavities, *Optics Express*, **12**(7), pp. 1458-1463, Apr. 5, 2004.
- K. Srinivasan, P. E. Barclay, O. Painter, J. Chen, and A. Y. Cho, Fabrication of high quality factor photonic crystal microcavities in InAsP/InGaAsP membranes, *Journal of Vacuum Science and Technology B*, **22**(3), pp. 875-879, May, 2004.
- K. Srinivasan, O. Painter, R. Colombelli, C. Gmachl, D. M. Tennant, A. M. Sergent, D. L. Sivco, A. Y. Cho, M. Troccoli, and F. Capasso, Lasing mode pattern of a quantum cascade photonic crystal surface-emitting microcavity laser, *Applied Physics Letters*, **84**(21), pp. 4164-4166, May 24, 2004.
- B. Lev, K. Srinivasan, P. E. Barclay, O. Painter, and H. Mabuchi, Feasibility of detecting single atoms using photonic bandgap cavities, *Nanotechnology*, **15**, S556-S561 2004.
- K. Srinivasan, P. E. Barclay, M. Borselli, and O. Painter, Optical-fiber-based measurement of an ultrasmall volume high-Q photonic crystal microcavity, *Physical Review B, Rapid Communications*, **70**, 081306(R), Aug. 25, 2004.
- M. Borselli, K. Srinivasan, P. E. Barclay, and O. Painter, Rayleigh scattering, mode coupling, and optical loss in silicon microdisks, *Applied Physics Letters*, **85**(17), pp. 3693-3695, Oct. 25, 2004.
- P. E. Barclay, K. Srinivasan, and O. Painter, Nonlinear response of silicon photonic crystal microresonators excited via an integrated waveguide and fiber taper, *Optics Express*, **13**(3), pp. 801-820, Feb. 7, 2005.
- K. Srinivasan, P.E. Barclay, and O. Painter, Photonic crystal microcavities for chip-based cavity QED, *Physica Status Solidi b*, **242**(6), pp. 1187-1191, March 24, 2005.
- K. Srinivasan, M. Borselli, T. J. Johnson, P. E. Barclay, O. Painter, A. Stintz, and S. Krishna, Optical loss and lasing characteristics of high-quality-factor AlGaAs microdisk resonators with embedded quantum dots, *Applied Physics Letters*, **86**, 151106, April 6, 2005.
- K. Srinivasan, P. E. Barclay, M. Borselli, and O. Painter, An optical fiber-based probe for photonic crystal microcavities, *IEEE Journal on Selected Areas in Communications (special issue on photonic crystals)*, **23**(7), pp. 1321-1329, July 2005.

- K. Srinivasan, A. Stintz, S. Krishna, and O. Painter, Photoluminescence measurements of quantum-dot-containing semiconductor microdisk resonators using optical fiber taper waveguides, *Physical Review B*, **72**, 205318, Nov. 10, 2005.
- K. Srinivasan, M. Borselli, O. Painter, A. Stintz, and S. Krishna, Cavity Q, mode volume, and lasing threshold in small diameter AlGaAs microdisks with embedded quantum dots, *Optics Express*, **14**(3), pp. 1094-1105, Feb. 6, 2006.

Other related publications

- O. Painter, K. Srinivasan, J. D. O'Brien, A. Scherer, and P. D. Dapkus, Tailoring of the resonant mode properties of optical nanocavities in two-dimensional photonic crystal slab waveguides, *Journal of Optics A-Pure and Applied Optics*, **3**(6), pp. S161-S170, Nov. 2001
- O. Painter and K. Srinivasan, Polarization properties of dipolelike defect modes in photonic crystal nanocavities, *Optics Letters*, **27**(5), pp. 339-341, Mar. 1 2002
- P. E. Barclay, K. Srinivasan, M. Borselli, and O. Painter, Experimental demonstration of evanescent coupling from optical fiber tapers to photonic crystal waveguides, *Electronics Letters*, **39**(11), pp. 842-844, May 29, 2003
- P. E. Barclay, K. Srinivasan, and O. Painter, Design of photonic crystal waveguides for evanescent coupling to optical fiber tapers and for integration with high-Q cavities, *Journal of the Optical Society of America B-Optical Physics*, **20**(11), pp. 2274-2284, Nov. 2003
- D. M. Tennant, R. Colombelli, K. Srinivasan, M. Troccoli, O. Painter, C. Gmachl, F. Capasso, A. M. Sergent, D. L. Sivco, and A. Y. Cho, Fabrication methods for a quantum cascade photonic crystal surface emitting laser, *Journal of Vacuum Science and Technology B*, **21**(6), pp. 2907-2911, Nov/Dec. 2003
- R. Colombelli, K. Srinivasan, M. Troccoli, O. Painter, C. Gmachl, D. M. Tennant, A. M. Sergent, D. L. Sivco, A. Y. Cho, and F. Capasso, Fabrication technologies for quantum cascade photonic-crystal microlasers, *Nanotechnology*, **15**, pp. 675-681, 2004
- P. E. Barclay, K. Srinivasan, M. Borselli, and O. Painter, Efficient input and output fiber coupling to a photonic crystal waveguide, *Optics Letters*, **29**(7), pp. 697-699, Apr. 1, 2004

- P. E. Barclay, K. Srinivasan, M. Borselli, and O. Painter, Probing the dispersive and spatial properties of planar photonic crystal waveguide modes via highly efficient coupling from optical fiber tapers, *Applied Physics Letters*, **85**(1), pp. 4-6, Jul. 5, 2004
- K. Srinivasan and O. Painter, Design of two-dimensional photonic crystal defect states for quantum cascade laser resonators, (<http://arxiv.org/abs/physics/0410068>), Oct. 11, 2004

Part I

Development of Ultrasmall Volume, High- Q Photonic Crystal Microcavities

The first part of this thesis details work on planar photonic crystal microcavities. Chapter 1 discusses two semi-analytic tools for studying modes within these structures, while chapter 2 reviews a methodology for design of high quality factor cavities, and presents cavity designs within different photonic crystal lattices. Finally, chapters 3 and 4 describe the experimental implementation of these designs within an InP-based multi-quantum-well material and within silicon, respectively. The former chapter presents photoluminescence measurements of the InP-based devices, while the latter chapter utilizes an optical fiber taper waveguide to passively probe the properties of the silicon resonators.

Chapter 1

Semianalytic Methods for Studying Localized Modes Within Two-Dimensional Photonic Crystals

The design of photonic crystal (PC) based optical elements has often relied on numerical simulations using methods such as finite-difference time-domain (FDTD) [6, 7]. While FDTD provides a wealth of detailed information about the system under consideration, it has the drawback of being rather computationally intensive and time consuming. In this chapter, I detail two approximate analytic methods that are of great use in studying planar PC cavities (fig. 1.1). The first is a group-theory-based analysis [24] that provides information about the symmetries and dominant Fourier components of defect modes within hexagonal and square lattice PC cavities. The second method [25] is a Wannier-like equation analysis that describes how the photonic lattice provides localization for the cavity modes. Taken together, these two techniques can provide approximate modal field patterns that reproduce many of the detailed features of the cavity modes generated by FDTD simulations. They thus serve as a starting point from which a more detailed analysis or optimization of the cavity design can proceed.

1.1 Symmetry-based analysis

1.1.1 Introduction

The work described in this section is largely based on ref. [24], and is presented here in a slightly different form, where I have omitted some results that are not utilized in the rest of this thesis in favor of more detailed derivations of some basic results. The principal thrust of the analysis is contained in sections 1.1.2 and 1.1.3, which outline the application of group theory in producing

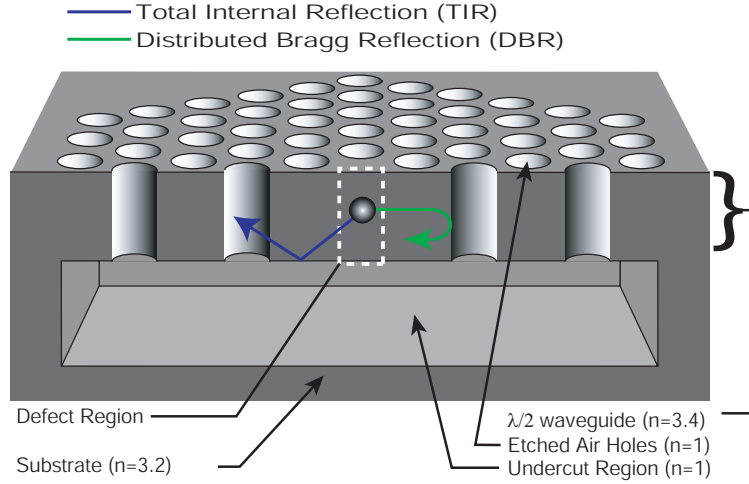


Figure 1.1: Illustration of a two-dimensional photonic crystal cavity in a slab waveguide structure.

an approximate description of the resonant modes of the defect cavities in hexagonal and square host photonic lattices. Section 1.1.4 then presents the results of FDTD simulations, confirming the results of the approximate group theory analysis while providing detailed properties of the defect mode resonances beyond the scope of the simple symmetry analysis.

The spatial symmetries within Maxwell's equations are determined by the translation and rotary-reflection symmetries of the dielectric function, $\epsilon(\mathbf{r})$ [90]. The theory of space groups [91] can then be used to predict and categorize the resonant modes of defects within PC structures. A two-step process is implemented here. First, modes of the unperturbed slab waveguide are used as a symmetry basis to generate approximate field patterns for the PC modes at the high symmetry points of the first Brillouin zone (IBZ) boundary. The curvature of the photonic bands at these points are such that peaks and valleys are created in the energy-momentum dispersion surface. It is these peaks and valleys that are the seeds from which localized states are formed. The second step in our approach then utilizes the PC band-edge states created from the unperturbed slab waveguide mode symmetry basis to generate approximate forms for the localized defect modes lying within the bandgap.

The host PC structures that we consider consist of a symmetric planar geometry with a two-dimensionally patterned core layer surrounded by spatially uniform cladding layers. A structure which has been the basis of many previously fabricated devices is depicted in cross section in fig. 1.1. The semiconductor core dielectric material has an approximate refractive index of 3.4, and the cladding in these membrane-type structures is air with a refractive index of 1. For the structures

studied in this and following sections, the ratio of the core thickness, d , to lattice constant, a , is chosen so as to maintain the single-mode nature of the vertical waveguide for wavelengths within the first-order guided-mode bandgap of the PC lattice. The modes of a symmetric slab waveguide, patterned or unpatterned, separate into modes of even or odd parity with respect to a mirror plane in the middle of the dielectric slab. Of interest here are the *fundamental* guided modes. Limiting our analysis to the fundamental guided modes of the PC slab effectively reduces the spatial dimension of the problem from three to two.

Within the mirror plane of the waveguide in these symmetric quasi-2D systems, the fundamental even and odd modes can be represented by scalar fields H_z and E_z , respectively. As has been described elsewhere [4], for connected 2D lattices such as those investigated here, the extent of the photonic bandgap for modes with electric field polarization in the plane of the 2D patterning (TE) is larger than for modes with normal electric field polarization (TM). For this reason, we will focus our attention on the fundamental even modes of the 2D PC waveguides which are TE-like (although the fundamental even and odd modes of the patterned slab are not purely TE or TM, they are significantly TE-like or TM-like in nature). An extension to TM-like modes has been presented in ref. [37], as it finds specific application in the study of quantum cascade photonic crystal lasers, due to the TM polarization of the intersubband transitions within quantum cascade heterostructures. In the analysis below, we consider two of the most common 2D geometries for the host PC lattice, the square lattice and the hexagonal or trigonal lattice. We begin with an analysis of the hexagonal lattice.

1.1.2 Hexagonal lattice photonic crystals

The point group symmetry of a 2D hexagonal PC is D_{6h} , with a single horizontal mirror plane (σ_h) lying in the waveguide center. Narrowing our scope to TE-like modes of a symmetric slab, the point group symmetry of the hexagonal PC system can be effectively reduced to $C_{6v}=D_{6h}/\sigma_h$. A plot of the approximate in-plane bandstructure for the fundamental TE-like guided modes of a half-wavelength thick hexagonally patterned slab waveguide is given in fig. 1.2(a).¹ This bandstructure was calculated through the plane wave expansion technique, as reviewed in ref. [5].

Within the mirror plane of the slab, the magnetic field pattern for the (fundamental) TE-like eigenmodes of the unpatterned slab waveguide can be written as $\mathbf{H}_{\mathbf{k}_\perp}(\mathbf{r}_\perp) = \hat{z}e^{-i(\mathbf{k}_\perp \cdot \mathbf{r}_\perp)}$, where \mathbf{k}_\perp

¹In this calculation a 2D hexagonal PC with host dielectric constant given by the effective index of the fundamental TE mode of the half-wavelength thick slab is analyzed [7].

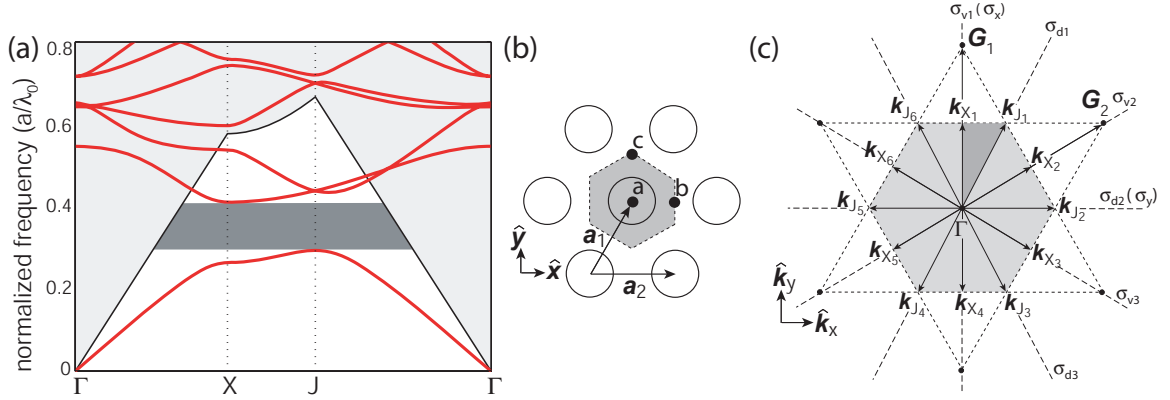


Figure 1.2: (a) Fundamental TE-like guided mode bandstructure ($r/a = 0.36$, $n_{\text{slab}} = n_{\text{eff}} = 2.65$). The bandgap extends over a normalized frequency of 0.29-0.41. The air (cladding) light line is shown as a solid black line. (b)-(c) Illustration of the real and reciprocal spaces of the two-dimensional hexagonal PC. The high-symmetry points of the hexagonal lattice, referenced to the center of an air hole, are $\mathbf{a} = (0, 0)$, $\mathbf{b} = (a/2, 0)$, and $\mathbf{c} = (0, a/\sqrt{3})$. (b) Real space. $|\mathbf{a}_1| = |\mathbf{a}_2| = a$. (c) Reciprocal space. $|\mathbf{G}_1| = |\mathbf{G}_2| = 4\pi/\sqrt{3}a$, $|\mathbf{k}_X| = 2\pi/\sqrt{3}a$, $|\mathbf{k}_J| = 4\pi/3a$.

and \mathbf{r}_\perp are in-plane wavenumber and spatial coordinates, respectively (in order to simplify notation we drop the \perp label in the equations that follow). Upon patterning the slab waveguide, coupling occurs between waveguide modes with similar unperturbed frequencies and identical propagation constants modulo a reciprocal lattice vector \mathbf{G} . This follows from the approximate conservation of frequency and the exact conservation of crystal momentum. Of particular interest for the resonant cavity designs and devices described below are those modes which comprise the frequency bands defining the first order bandgap. The Bloch modes at the band-edges defining the first order bandgap are predominantly formed from modes of the unpatterned waveguide with in-plane wavevector lying at the boundary of the IBZ; other unpatterned waveguide modes with additional in-plane momentum equal to some integer multiple of a reciprocal lattice vector contribute much less, owing to their large (unperturbed) frequency difference. For the symmetry analysis described here we will be satisfied with considering the contribution from only the degenerate lowest frequency unpatterned waveguide modes at the first zone boundary.

The high symmetry points within and on the boundary of the IBZ of the hexagonal lattice are (see fig. 1.2(c)): the six X points ($\{\pm(0, 1)k_X, \pm(\sqrt{3}/2, 1/2)k_X, \pm(\sqrt{3}/2, -1/2)k_X\}$), the six J points ($\{\pm(1/2, \sqrt{3}/2)k_J, \pm(1/2, -\sqrt{3}/2)k_J, \pm(1, 0)k_J\}$), and the Γ point $= (0, 0)$. The first-order bandgap of the hexagonal lattice (see fig. 1.2(a)) is defined from above by the X point and below by the J point. In analogy to the electronic bands in semiconductor crystals, the high frequency

Table 1.1: Point group character tables for the hexagonal lattice.

C_{6v}	E	C_2	$2C_3$	$2C_6$	$3\sigma_d$	$3\sigma_v$
A_1''	1	1	1	1	1	1
A_2''	1	1	1	1	-1	-1
B_1''	1	-1	1	-1	1	-1
B_2''	1	-1	1	-1	-1	1
E_1	2	-2	-1	1	0	0
E_2	2	2	-1	-1	0	0
$S^{a,d1}$	3	-3	0	0	1	-1
$S^{a,a1}$	2	0	2	0	-2	0
$S^{a,a2}$	3	3	0	0	-1	-1

C_{2v}	E	C_2	$\sigma_x(\sigma_{v1})$	$\sigma_y(\sigma_{d2})$
A_1	1	1	1	1
A_2	1	1	-1	-1
B_1	1	-1	-1	1
B_2	1	-1	1	-1
$S^{a,d1}$	3	-3	-1	1
$S^{b,d1}$	3	1	-1	1
$S^{a,a1}$	2	0	0	-2
$S^{a,a2}$	3	3	-1	-1
$S^{b,a1}$	3	3	-1	-1

C_{3v,σ_d}	E	$2C_3$	$3\sigma_d$	C_{3v,σ_v}	E	$2C_3$	$3\sigma_v$
A_1'	1	1	1	A_1'''	1	1	1
A_2'	1	1	-1	A_2'''	1	1	-1
E	2	-1	0	E	2	-1	0
				$S^{c,d1}$	3	0	-1
				$S^{c,a1}$	2	-1	0

band defining the first-order bandgap is called the conduction band, and the low frequency band is the valence band [4]. In the approximate analysis of the defect states to follow we will need to include all the degenerate satellite peaks (conduction band) and valleys (valence band). The group of the wavevector, which defines the point group symmetry of a plane wave modulo \mathbf{G} within the dielectric lattice, is C_{2v} , C_{3v} , and C_{6v} for the X , J , and Γ points of the hexagonal lattice, respectively. Character tables [92] for these groups are given in table 1.1.

1.1.2.1 X-point

For the frequency bands defining the first-order bandgap, the unpatterned waveguide modes which are most strongly coupled together to form the Bloch modes at the X -point are given by $\mathbf{H} = \hat{z} e^{-i\mathbf{k}_{X_i} \cdot \mathbf{r}}$, where $i = 1, 2, \dots, 6$. The unperturbed frequencies of these modes are degenerate and can be written as $\omega_o^X \approx c|\mathbf{k}_X|/n_{\text{eff}}$, where n_{eff} is an effective index taking into account the vertical waveguiding perpendicular to the slab.

The star of \mathbf{k} ($\star\mathbf{k}$) at the X -point, formed from the independent satellite X -points within the IBZ, consists of wavevectors $\{\mathbf{k}_{X_1}, \mathbf{k}_{X_2}, \mathbf{k}_{X_3}\}$, with all other X -points being equivalent to one of these vectors modulo a reciprocal lattice vector. A symmetry basis for the modes of the patterned slab waveguide at the X_1 -satellite point can be found by applying the symmetry operations of the group of the wave vector ($G_{o\mathbf{k}_X} = C_{2v}$) to the seed vector $\mathbf{H}_{\mathbf{k}_{X_1}}$. In this case, the basis is simply $(\mathbf{H}_{\mathbf{k}_{X_1}}, \mathbf{H}_{-\mathbf{k}_{X_1}})$.

Using these basis vectors, we calculate the 2×2 matrices that represent the different point group operations of C_{2v} , noting that the magnetic field transforms like a pseudovector [93] (unlike the electric field). This yields the following:

$$S_E^X = \begin{pmatrix} 1 & 0 \\ 0 & 1 \end{pmatrix} \quad S_{C_2}^X = \begin{pmatrix} 0 & 1 \\ 1 & 0 \end{pmatrix} \quad S_{\sigma_x}^X = \begin{pmatrix} -1 & 0 \\ 0 & -1 \end{pmatrix} \quad S_{\sigma_y}^X = \begin{pmatrix} 0 & -1 \\ -1 & 0 \end{pmatrix}. \quad (1.1)$$

The character values for these operations are $\chi_E=2$, $\chi_{C_2}=0$, $\chi_{\sigma_x}=-2$, and $\chi_{\sigma_y}=0$. These character values are consistent with a reducible representation that decomposes as $A_2 \oplus B_1$. The projection operators [92] onto these IRREP spaces are calculated as:

$$P_{A_2} = \frac{1}{4} \left\{ 1 \begin{pmatrix} 1 & 0 \\ 0 & 1 \end{pmatrix} + 1 \begin{pmatrix} 0 & 1 \\ 1 & 0 \end{pmatrix} + (-1) \begin{pmatrix} -1 & 0 \\ 0 & -1 \end{pmatrix} + (-1) \begin{pmatrix} 0 & -1 \\ -1 & 0 \end{pmatrix} \right\} = \frac{1}{2} \begin{pmatrix} 1 & 1 \\ 1 & 1 \end{pmatrix} \quad (1.2)$$

$$P_{B_1} = \frac{1}{4} \left\{ 1 \begin{pmatrix} 1 & 0 \\ 0 & 1 \end{pmatrix} + (-1) \begin{pmatrix} 0 & 1 \\ 1 & 0 \end{pmatrix} + (-1) \begin{pmatrix} -1 & 0 \\ 0 & -1 \end{pmatrix} + (1) \begin{pmatrix} 0 & -1 \\ -1 & 0 \end{pmatrix} \right\} = \frac{1}{2} \begin{pmatrix} 1 & -1 \\ -1 & 1 \end{pmatrix} \quad (1.3)$$

Applying these projection operators to the seed vector $\mathbf{H}_{\mathbf{k}_{X_1}}$ yields:

$$\begin{aligned} \mathbf{H}_{A_2}^{X_1} &= \hat{z} \cos(\mathbf{k}_{X_1} \cdot \mathbf{r}^a), \\ \mathbf{H}_{B_1}^{X_1} &= \hat{z} \sin(\mathbf{k}_{X_1} \cdot \mathbf{r}^a), \end{aligned} \quad (1.4)$$

where A_2 and B_1 label the IRREP spaces of C_{2v} (see table 1.1), and the index a is used to denote the location of the origin within the hexagonal lattice (marked in fig. 1.2(b)). As the magnetic field of $\mathbf{H}_{A_2}^{X_1}$ overlaps strongly with the air holes of the hexagonal PC (its electric field lying largely in the dielectric) it represents the lower frequency “valence” band mode, while $\mathbf{H}_{B_1}^{X_1}$ represents the “conduction” band mode. This is a result of the tendency for modes with electric field concentrated within regions of high dielectric constant to be lower frequency than those with electric field concentrated in low dielectric regions [4].

In order to fully define the modes at the X -point all modes of the $\star\mathbf{k}$ must be included. In the case of the X -point this corresponds to successive rotations by $\pi/6$ (C_6 rotation). The result is the following set of degenerate valence band modes,

$$VB_a^X = \begin{pmatrix} v_{X_1} \\ v_{X_2} \\ v_{X_3} \end{pmatrix} = \hat{z} \begin{pmatrix} \cos(\mathbf{k}_{X_1} \cdot \mathbf{r}^a) \\ \cos(\mathbf{k}_{X_2} \cdot \mathbf{r}^a) \\ \cos(\mathbf{k}_{X_3} \cdot \mathbf{r}^a) \end{pmatrix}, \quad (1.5)$$

and degenerate conduction band modes,

$$CB_a^X = \begin{pmatrix} c_{X_1} \\ c_{X_2} \\ c_{X_3} \end{pmatrix} = \hat{z} \begin{pmatrix} \sin(\mathbf{k}_{X_1} \cdot \mathbf{r}^a) \\ \sin(\mathbf{k}_{X_2} \cdot \mathbf{r}^a) \\ \sin(\mathbf{k}_{X_3} \cdot \mathbf{r}^a) \end{pmatrix}. \quad (1.6)$$

fig. 1.3 shows the magnetic field amplitude for each of the valence and conduction band modes at all the satellite X -points of the hexagonal lattice.

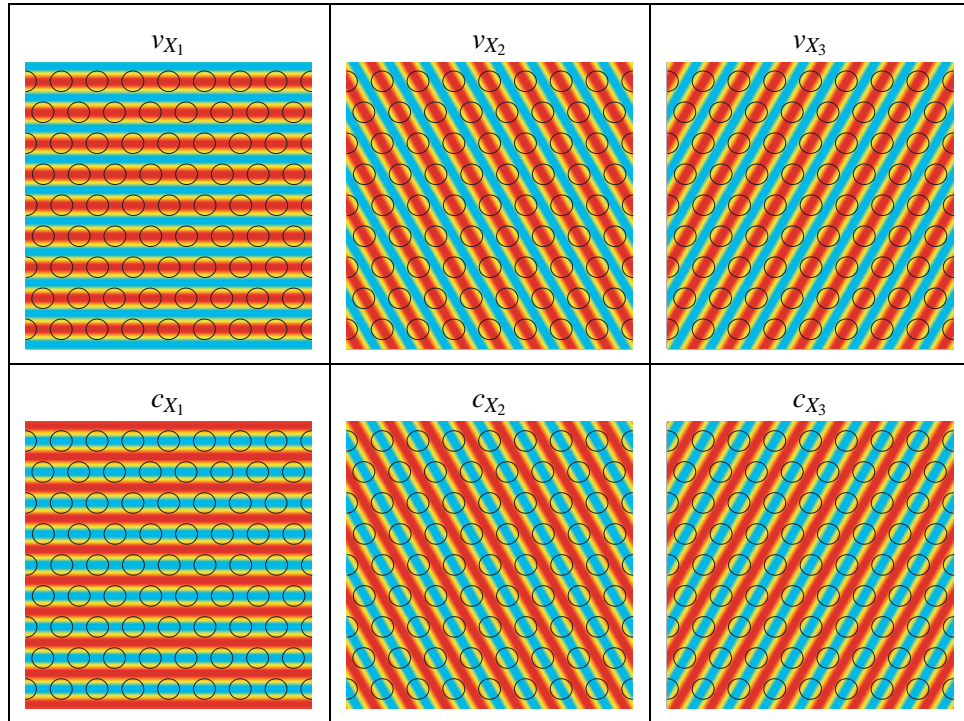


Figure 1.3: Magnetic field (amplitude) patterns of the valence band modes (top) and conduction band modes (bottom) of the hexagonal lattice at the three different X -points generated by the symmetry bases VB_a^X and CB_a^X .

1.1.2.2 J-point

A similar procedure may be performed in order to determine approximate forms for the TE-like valence and conduction band modes of the hexagonal lattice at the J -point of the IBZ. Approximate forms for the valence band edge and conduction band edge modes at the J -point are (with point a taken as the origin):

$$VB_a^J = \begin{pmatrix} v_{J_1} \\ v_{J_2} \end{pmatrix} = \hat{z} \begin{pmatrix} e^{-ik_{J_1} \cdot \mathbf{r}^a} + e^{-ik_{J_3} \cdot \mathbf{r}^a} + e^{-ik_{J_5} \cdot \mathbf{r}^a} \\ e^{-ik_{J_2} \cdot \mathbf{r}^a} + e^{-ik_{J_4} \cdot \mathbf{r}^a} + e^{-ik_{J_6} \cdot \mathbf{r}^a} \end{pmatrix}, \quad (1.7)$$

$$CB_a^J = \begin{pmatrix} c1_{J_1} \\ c2_{J_1} \\ c1_{J_2} \\ c2_{J_2} \end{pmatrix} = \hat{z} \begin{pmatrix} e^{-ik_{J_1} \cdot \mathbf{r}^a} + e^{-ik_{J_3} \cdot \mathbf{r}^a} - 2e^{-ik_{J_5} \cdot \mathbf{r}^a} \\ e^{-ik_{J_1} \cdot \mathbf{r}^a} - e^{-ik_{J_3} \cdot \mathbf{r}^a} \\ e^{-ik_{J_2} \cdot \mathbf{r}^a} + e^{-ik_{J_4} \cdot \mathbf{r}^a} - 2e^{-ik_{J_6} \cdot \mathbf{r}^a} \\ e^{-ik_{J_2} \cdot \mathbf{r}^a} - e^{-ik_{J_4} \cdot \mathbf{r}^a} \end{pmatrix}. \quad (1.8)$$

Figure 1.4 shows the magnetic field amplitude for each of the valence and conduction band modes at the J -point of the hexagonal lattice. Although not obvious from first inspection of equations (1.7) and (1.8), the plots in these two tables show that the modes of the symmetry basis VB_a^J have a magnetic field amplitude predominantly overlapping the air holes while the magnetic field amplitude of the modes of CB_a^J overlap the dielectric regions, a property that allows us to classify the modes as valence and conduction band, respectively. This result is also quite encouraging, given the fact that our symmetry basis is quite primitive and yet can reproduce this property of the valence and conduction band modes so critical to the formation of a frequency bandgap.

The approximate valence and conduction band edge modes derived above all have their origin at the center of an air hole of the lattice. The hexagonal lattice has two other high-symmetry points around which one may center a defect, points b and c shown in fig. 1.2(b). Unlike point a , points b and c are of lower symmetry than the point group of the hexagonal lattice. A defect centered about point b will be limited to a point group of symmetry C_{2v} , and those about point c to point group C_{3v,σ_v} . The point group symmetry operations for each of these types of defects are centered about different points within the lattice. So as to be clear about the position of the origin to be used for point symmetry operations, we label the Bloch mode symmetry bases with an index corresponding to the location of the origin around which it is expanded. For example, VB_b^X is the X -point valence band basis of equation (1.5) written in a shifted coordinate system with point b at the origin. In the equations to follow, \mathbf{r}^a , \mathbf{r}^b , and \mathbf{r}^c are coordinate systems with origin located at point a , b , and c of the hexagonal lattice, respectively.

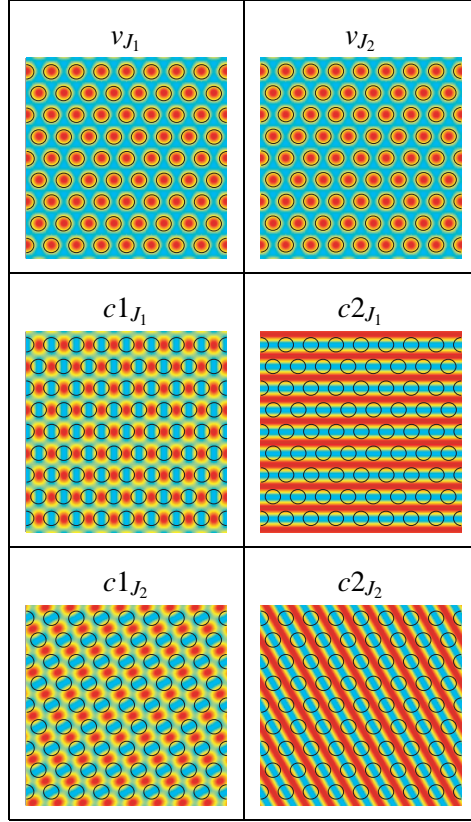


Figure 1.4: Magnetic field (amplitude) patterns of the valence band (top) and conduction band (middle and bottom) modes of the hexagonal lattice at the J -point, generated by the symmetry bases VB_a^J and CB_a^J .

1.1.2.3 Conduction band donor modes

In an attempt to form localized resonances, the dielectric constant in a small region of a periodic photonic crystal lattice may be altered from its unperturbed value, breaking the regular periodicity of the lattice and mixing the Bloch modes. If the perturbation corresponds to a local increase in the dielectric constant (fig. 1.5(a)), the localized modes are formed predominantly from the conduction band, specifically the modes at the band edge. This is a result of the tendency for mode frequencies to decrease with increasing dielectric constant [4], pulling the conduction band edge modes into the bandgap of the photonic crystal near the defect. This type of localized mode is termed a donor mode in analogy to the electronic defect states in crystalline materials [94].

For the hexagonal PC lattice the minimum in the conduction band occurs at the X -point (see fig. 1.2(a)). Therefore, the appropriate symmetry basis to use for describing localized donor modes are the degenerate conduction band edge modes of CB_a^X , CB_b^X , and CB_c^X for defect regions centered around points a , b , and c .

Let us consider the formation of conduction band donor modes within defects that maintain the full C_{6v} symmetry of the lattice. Using the symmetry basis CB_a^X , we calculate the matrix represen-

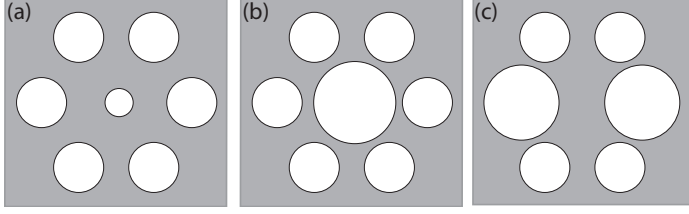


Figure 1.5: Example defect cavity geometries in the hexagonal lattice. (a) Donor-type cavity, (b) Acceptor-type cavity, (c) Y-split acceptor-type cavity.

tation of the point group operators:

$$E_{CB^X} = \begin{pmatrix} 1 & 0 & 0 \\ 0 & 1 & 0 \\ 0 & 0 & 1 \end{pmatrix} C_{2,CB^X} = \begin{pmatrix} -1 & 0 & 0 \\ 0 & -1 & 0 \\ 0 & 0 & -1 \end{pmatrix} C_{3,CB^X} = \begin{pmatrix} 0 & -1 & 0 \\ 0 & 0 & -1 \\ 1 & 0 & 0 \end{pmatrix} C_{3,CB^X}^{-1} = \begin{pmatrix} 0 & 0 & 1 \\ -1 & 0 & 0 \\ 0 & -1 & 0 \end{pmatrix} \quad (1.9)$$

$$C_{6,CB^X} = \begin{pmatrix} 0 & 0 & -1 \\ 1 & 0 & 0 \\ 0 & 1 & 0 \end{pmatrix} C_{6,CB^X}^{-1} = \begin{pmatrix} 0 & 1 & 0 \\ 0 & 0 & 1 \\ -1 & 0 & 0 \end{pmatrix} \sigma_{d_1,CB^X} = \begin{pmatrix} 0 & -1 & 0 \\ -1 & 0 & 0 \\ 0 & 0 & 1 \end{pmatrix} \sigma_{d_2,CB^X} = \begin{pmatrix} 1 & 0 & 0 \\ 0 & 0 & -1 \\ 0 & -1 & 0 \end{pmatrix} \quad (1.10)$$

$$\sigma_{d_3,CB^X} = \begin{pmatrix} 0 & 0 & 1 \\ 0 & 1 & 0 \\ 1 & 0 & 0 \end{pmatrix} \sigma_{v_1,CB^X} = \begin{pmatrix} -1 & 0 & 0 \\ 0 & 0 & 1 \\ 0 & 1 & 0 \end{pmatrix} \sigma_{v_2,CB^X} = \begin{pmatrix} 0 & 0 & -1 \\ 0 & -1 & 0 \\ -1 & 0 & 0 \end{pmatrix} \sigma_{v_3,CB^X} = \begin{pmatrix} 0 & 1 & 0 \\ 1 & 0 & 0 \\ 0 & 0 & -1 \end{pmatrix} \quad (1.11)$$

The character values for these operations are $\chi_E=3$, $\chi_{C_2}=-3$, $\chi_{C_3}=0$, $\chi_{C_6}=0$, $\chi_{\sigma_d}=1$, and $\chi_{\sigma_v}=-1$. These character values are consistent with a reducible representation that decomposes as $S^{a,d1} = E_1 \oplus B_1''$, as listed in table 1.1. For the B_1'' representation, the calculation of the projection operator is done using the same method as was used to calculate the projectors for the conduction band modes at the X -point. For the E_1 representation, there is an additional step because it is a two-dimensional representation. Recalling that E_1 can be spanned by the coordinate pair (x,y) , we write out two-

dimensional matrices for E_1 :

$$E_E = \begin{pmatrix} 1 & 0 \\ 0 & 1 \end{pmatrix} \quad E_{C_2} = \begin{pmatrix} -1 & 0 \\ 0 & -1 \end{pmatrix} \quad E_{C_3} = \begin{pmatrix} \frac{-1}{2} & \frac{\sqrt{3}}{2} \\ \frac{-\sqrt{3}}{2} & \frac{1}{2} \end{pmatrix} \quad E_{C_3^{-1}} = \begin{pmatrix} \frac{-1}{2} & \frac{-\sqrt{3}}{2} \\ \frac{\sqrt{3}}{2} & \frac{-1}{2} \end{pmatrix} \quad (1.12)$$

$$E_{C_6} = \begin{pmatrix} \frac{1}{2} & \frac{\sqrt{3}}{2} \\ \frac{-\sqrt{3}}{2} & \frac{1}{2} \end{pmatrix} \quad E_{C_6^{-1}} = \begin{pmatrix} \frac{1}{2} & \frac{-\sqrt{3}}{2} \\ \frac{\sqrt{3}}{2} & \frac{1}{2} \end{pmatrix} \quad E_{\sigma_{d1}} = \begin{pmatrix} \frac{-1}{2} & \frac{\sqrt{3}}{2} \\ \frac{\sqrt{3}}{2} & \frac{1}{2} \end{pmatrix} \quad E_{\sigma_{d2}} = \begin{pmatrix} 1 & 0 \\ 0 & -1 \end{pmatrix} \quad (1.13)$$

$$E_{\sigma_{d3}} = \begin{pmatrix} \frac{-1}{2} & \frac{-\sqrt{3}}{2} \\ \frac{-\sqrt{3}}{2} & \frac{1}{2} \end{pmatrix} \quad E_{\sigma_{v1}} = \begin{pmatrix} -1 & 0 \\ 0 & 1 \end{pmatrix} \quad E_{\sigma_{v2}} = \begin{pmatrix} \frac{1}{2} & \frac{\sqrt{3}}{2} \\ \frac{\sqrt{3}}{2} & \frac{-1}{2} \end{pmatrix} \quad E_{\sigma_{v3}} = \begin{pmatrix} \frac{1}{2} & \frac{-\sqrt{3}}{2} \\ \frac{-\sqrt{3}}{2} & \frac{1}{2} \end{pmatrix} \quad (1.14)$$

The diagonal elements of these matrices are then used in the calculation of the two projectors within this subspace. Overall, we arrive at the following projection operators for the conduction band donor modes:

$$P_{B_1''}^{CB^X} = \frac{1}{3} \begin{pmatrix} 1 & -1 & 1 \\ -1 & 1 & -1 \\ 1 & -1 & 1 \end{pmatrix} \quad P_{E_{1,1}}^{CB^X} = \frac{1}{6} \begin{pmatrix} 4 & 2 & -2 \\ 2 & 1 & -1 \\ -2 & -1 & 1 \end{pmatrix} \quad P_{E_{1,2}}^{CB^X} = \frac{1}{2} \begin{pmatrix} 0 & 0 & 0 \\ 0 & 1 & 1 \\ 0 & 1 & 1 \end{pmatrix} \quad (1.15)$$

Note that the coefficients in front of these projection matrices are eventually dropped as the approximate solutions that we give are not absolutely normalized, although the relative amplitudes of the different Fourier components are certainly kept (and are captured by the projection matrices themselves, without the prefactors). Using these projection operators on CB_a^X , a set of basis functions for the localized conduction band donor modes centered about point a of the hexagonal lattice is found:

$$\begin{aligned}
\mathbf{H}_{B_1''}^{a,d1} &= \hat{z} \left(\sin(\mathbf{k}_{X_1} \cdot \mathbf{r}^a) - \sin(\mathbf{k}_{X_2} \cdot \mathbf{r}^a) + \sin(\mathbf{k}_{X_3} \cdot \mathbf{r}^a) \right) \\
\mathbf{H}_{E_1,1}^{a,d1} &= \hat{z} \left(2 \sin(\mathbf{k}_{X_1} \cdot \mathbf{r}^a) + \sin(\mathbf{k}_{X_2} \cdot \mathbf{r}^a) - \sin(\mathbf{k}_{X_3} \cdot \mathbf{r}^a) \right) \\
\mathbf{H}_{E_1,2}^{a,d1} &= \hat{z} \left(\sin(\mathbf{k}_{X_2} \cdot \mathbf{r}^a) + \sin(\mathbf{k}_{X_3} \cdot \mathbf{r}^a) \right),
\end{aligned} \tag{1.16}$$

Similar techniques are used to find the character values of representation $S^{b,d1}$ of the CB_b^X basis under C_{2v} and representation $S^{c,d1}$ of the CB_c^X basis under C_{3v,σ_v} , and they are given in table 1.1. From the character tables we find that these representations decompose as $S^{b,d1} = A_1 \oplus A_2 \oplus B_1$ and $S^{c,d1} = E \oplus A_2'''$. We then use the appropriate projection operators to find basis functions for the localized conduction band donor modes centered about point b :

$$\begin{aligned}
\mathbf{H}_{A_1}^{b,d1} &= \hat{z} \left(\cos(\mathbf{k}_{X_2} \cdot \mathbf{r}^b) - \cos(\mathbf{k}_{X_3} \cdot \mathbf{r}^b) \right) \\
\mathbf{H}_{A_2}^{b,d1} &= \hat{z} \left(\cos(\mathbf{k}_{X_2} \cdot \mathbf{r}^b) + \cos(\mathbf{k}_{X_3} \cdot \mathbf{r}^b) \right) \\
\mathbf{H}_{B_1}^{b,d1} &= \hat{z} \left(\sin(\mathbf{k}_{X_1} \cdot \mathbf{r}^b) \right),
\end{aligned} \tag{1.17}$$

and point c :

$$\begin{aligned}
\mathbf{H}_{A_2'''}^{c,d1} &= \hat{z} \left(\sin\left(\mathbf{k}_{X_1} \cdot \mathbf{r}^c - \frac{\pi}{3}\right) - \sin\left(\mathbf{k}_{X_2} \cdot \mathbf{r}^c + \frac{\pi}{3}\right) \right. \\
&\quad \left. + \sin\left(\mathbf{k}_{X_3} \cdot \mathbf{r}^c - \frac{\pi}{3}\right) \right) \\
\mathbf{H}_{E,1}^{c,d1} &= \hat{z} \left(2 \sin\left(\mathbf{k}_{X_1} \cdot \mathbf{r}^c - \frac{\pi}{3}\right) + \sin\left(\mathbf{k}_{X_2} \cdot \mathbf{r}^c + \frac{\pi}{3}\right) \right. \\
&\quad \left. - \sin\left(\mathbf{k}_{X_3} \cdot \mathbf{r}^c - \frac{\pi}{3}\right) \right) \\
\mathbf{H}_{E,2}^{c,d1} &= \hat{z} \left(\sin\left(\mathbf{k}_{X_2} \cdot \mathbf{r}^c + \frac{\pi}{3}\right) + \sin\left(\mathbf{k}_{X_3} \cdot \mathbf{r}^c - \frac{\pi}{3}\right) \right),
\end{aligned} \tag{1.18}$$

Figure 1.6 shows plots of the amplitude of the \hat{z} -component of the magnetic field for each of the localized donor modes centered about point a , as generated by the symmetry analysis. In these plots (and in all plots generated from the symmetry analysis to follow), the localization of each mode has been taken into account by multiplying a two-dimensional Gaussian envelope function with each

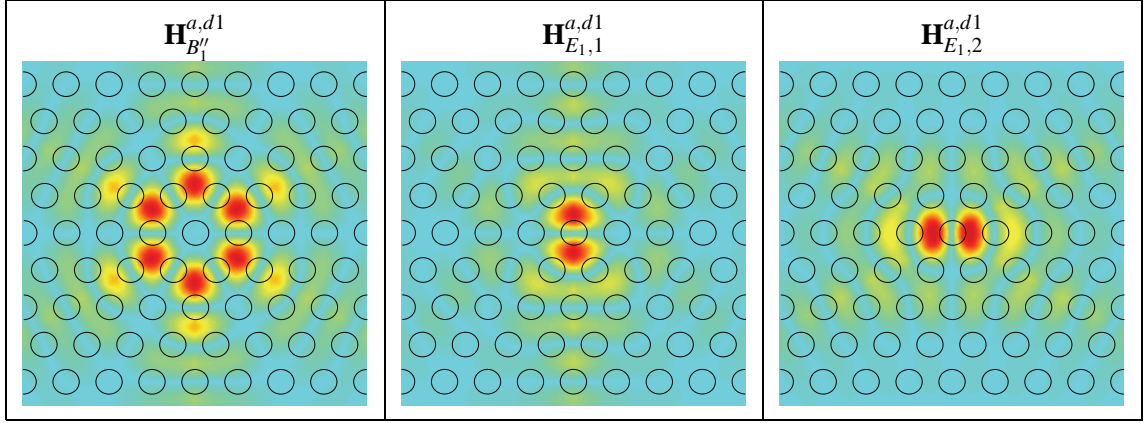


Figure 1.6: Magnetic field amplitude of the symmetry analysis conduction band donor modes centered about point a of the hexagonal lattice.

dominant Fourier component, where the two axes of the Gaussian envelope are taken as parallel and perpendicular to the direction of the Fourier component. This set of envelope function transforms as the identity under symmetry operations of the group of the wavevector, and as such does not alter the transformation properties of each \mathbf{k} component. Consequently, the IRREP classification of the defect modes given above is maintained. This particular choice of envelope function, apart from symmetry, is rather arbitrary, only chosen to capture the localized nature of the defect modes and highlight the dominant Fourier components. In section 1.2, a Wannier-like equation for the envelope of localized photon states is studied and shown to have ground state solutions invariant under those elements of the group of the wavevector that are also symmetries of the defect perturbation. The ground state envelope solutions then leave the IRREP classification of the above analysis for the defect modes unchanged.

Returning to equation (1.16) describing the localized donor modes about point a of the hexagonal lattice, we note that the $(d1, B_1'')$ donor mode transforms like a hexapole, whereas the degenerate $(d1, E_1)$ modes transform as an (x, y) -dipole pair. By introducing defect regions with lower symmetry than the host photonic lattice one is able to remove degeneracies in the localized mode spectrum. The effects of this symmetry lowering can be simply determined using group theory by virtue of the compatibility relations between the IRREPs of the full and reduced symmetry groups:

$$\begin{aligned}
C_{6v} &\rightarrow C_{2v} \\
\mathbf{H}_{B_1'}^{a,d1} &\rightarrow \mathbf{H}_{B_1}^{a,d1,1} \\
\mathbf{H}_{E_1,1}^{a,d1} &\rightarrow \mathbf{H}_{B_1}^{a,d1,2} \text{ (x-dipole)} \\
\mathbf{H}_{E_1,2}^{a,d1} &\rightarrow \mathbf{H}_{B_2}^{a,d1} \text{ (y-dipole)}.
\end{aligned} \tag{1.19}$$

In the case of cavities with C_{2v} symmetry, group theory predicts the splitting of the degenerate dipole-like modes into x and y dipole-like modes with differing frequencies. This has been studied in numerical simulations and experimental measurements of such devices [2].

1.1.2.4 Valence band acceptor modes

If the dielectric constant had been reduced in a small region within the photonic lattice, by enlarging an air hole for instance (fig. 1.5(b)), then instead of pulling the conduction band modes down into the photonic crystal bandgap the valence band modes are pushed up into the bandgap. In this case modes localized to the defect region are formed predominantly from mixtures of Bloch modes from the valence band edge. This type of defect mode is termed an acceptor mode, again in analogy to the electronic states in a crystal [94]. For the hexagonal lattice the maximum of the valence band occurs at the J -point (see fig. 1.2(a)). The obvious symmetry basis to use to describe the acceptor modes is the set of degenerate valence band modes at the J -point, VB_a^J in the case of defects centered around point a , and VB_b^J and VB_c^J for defects about points b and c , respectively.

The characters of the representation $S^{a,a1}$ of VB_a^J under the C_{6v} point symmetry group, the representation $S^{b,a1}$ of VB_b^J under C_{2v} , and the representation $S^{c,a1}$ of VB_c^J under C_{3v,σ_v} are given in table 1.1. $S^{a,a1}$ decomposes into irreducible blocks $A_2'' \oplus B_2''$, $S^{b,a1} = A_2 \oplus B_2$, and $S^{c,a1} = E$. Using the projection operators, the basis functions VB_a^J are coupled together to form the following acceptor modes about point a :

$$\begin{aligned}
\mathbf{H}_{A_2''}^{a,a1} &= \hat{z} \left(\cos(\mathbf{k}_{J_1} \cdot \mathbf{r}^a) + \cos(\mathbf{k}_{J_3} \cdot \mathbf{r}^a) + \cos(\mathbf{k}_{J_5} \cdot \mathbf{r}^a) \right) \\
\mathbf{H}_{B_2''}^{a,a1} &= \hat{z} \left(\sin(\mathbf{k}_{J_1} \cdot \mathbf{r}^a) + \sin(\mathbf{k}_{J_3} \cdot \mathbf{r}^a) + \sin(\mathbf{k}_{J_5} \cdot \mathbf{r}^a) \right).
\end{aligned} \tag{1.20}$$

Similarly, projecting the basis functions VB_b^J onto the IRREPs of C_{2v} and the basis functions VB_c^J

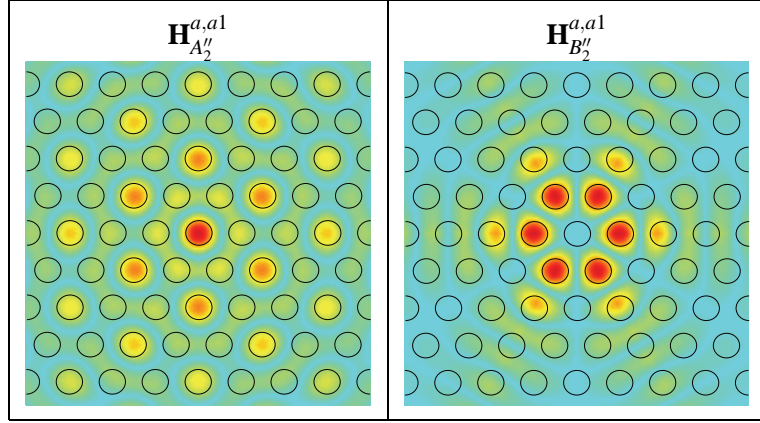


Figure 1.7: Magnetic field amplitude of the symmetry analysis valence band acceptor modes centered about point a of the hexagonal lattice.

onto the IRREPs of C_{3v,σ_v} , we get for the acceptor modes about point b :

$$\begin{aligned}\mathbf{H}_{A_2}^{b,a1} &= \hat{z} \left(\cos(\mathbf{k}_{J_1} \cdot \mathbf{r}^b) + \cos(\mathbf{k}_{J_3} \cdot \mathbf{r}^b) - \cos(\mathbf{k}_{J_5} \cdot \mathbf{r}^b) \right) \\ \mathbf{H}_{B_2}^{b,a1} &= \hat{z} \left(\sin(\mathbf{k}_{J_1} \cdot \mathbf{r}^b) + \sin(\mathbf{k}_{J_3} \cdot \mathbf{r}^b) - \sin(\mathbf{k}_{J_5} \cdot \mathbf{r}^b) \right),\end{aligned}\tag{1.21}$$

and the acceptor modes about point c :

$$\begin{aligned}\mathbf{H}_{E,1}^{c,a1} &= \hat{z} \left(\cos\left(\mathbf{k}_{J_1} \cdot \mathbf{r}^c + \frac{2\pi}{3}\right) + \cos\left(\mathbf{k}_{J_3} \cdot \mathbf{r}^c - \frac{2\pi}{3}\right) \right. \\ &\quad \left. + \cos(\mathbf{k}_{J_5} \cdot \mathbf{r}^c) \right) \\ \mathbf{H}_{E,2}^{c,a1} &= \hat{z} \left(\sin\left(\mathbf{k}_{J_1} \cdot \mathbf{r}^c + \frac{2\pi}{3}\right) + \sin\left(\mathbf{k}_{J_3} \cdot \mathbf{r}^c - \frac{2\pi}{3}\right) \right. \\ &\quad \left. + \sin(\mathbf{k}_{J_5} \cdot \mathbf{r}^c) \right).\end{aligned}\tag{1.22}$$

Figure 1.7 shows plots of the \hat{z} -component of the magnetic field for each of the localized acceptor modes centered about point a of the hexagonal lattice generated by the symmetry analysis.

In modified cavities with C_{2v} symmetry, $\mathbf{H}_{A_2''}^{a,a1}$ and $\mathbf{H}_{B_2''}^{a,a1}$ transform as A_2 and B_2 IRREPs, respectively:

$$\begin{aligned}
C_{6v} &\rightarrow C_{2v} \\
\mathbf{H}_{A_2''}^{a,a1} &\rightarrow \mathbf{H}_{A_2}^{a,a1}, \\
\mathbf{H}_{B_2''}^{a,a1} &\rightarrow \mathbf{H}_{B_2}^{a,a1}.
\end{aligned} \tag{1.23}$$

For defect regions that strongly perturb the photonic lattice it is possible that a larger number of localized defect modes will form than can be described by the limited symmetry basis used above. This is the case for the Y -split cavity described in ref. [24] and illustrated in fig. 1.5(c), where the defect region is composed of two enlarged holes and has a relatively deep potential well for acceptor modes. As a result, in the FDTD simulations of the Y -split cavity, an additional shallow acceptor type mode (Y - $A2_0$), not covered by the VB_a^J symmetry basis, is present.

In order to more fully capture the possible defect modes in a deep potential well, the symmetry basis can be expanded in a number of ways [24]. The method we adopt here is based upon the observation that, for defect regions which provide a deep potential well, it is possible that defect modes will form which are composed of unperturbed photonic crystal modes located not just at the edge of the bandgap, but also at other nearby (in frequency) high-symmetry k -points within the IBZ. In order to represent these additional localized resonant modes the unperturbed photonic crystal modes at the additional high-symmetry k -points must be included in the symmetry basis. For the hexagonal lattice the valence band at the X -point is close in frequency to the bandgap edge at the J -point (see fig. 1.2(a)). The symmetry basis for the X -point valence band edge is the triply degenerate VB_a^X basis set. The representation of VB_a^X under C_{6v} , labeled $S^{a,a2}$, has the character values shown in table 1.1 and decomposes into irreducible spaces E_2 and A_2'' . The acceptor type modes formed from the X -point valence band modes in a symmetric defect cavity centered about point a in the lattice are:

$$\begin{aligned}
\mathbf{H}_{A_2''}^{a,a2} &= \hat{z} \left(\cos(\mathbf{k}_{X_1} \cdot \mathbf{r}^a) + \cos(\mathbf{k}_{X_2} \cdot \mathbf{r}^a) + \cos(\mathbf{k}_{X_3} \cdot \mathbf{r}^a) \right), \\
\mathbf{H}_{E_2,1}^{a,a2} &= \hat{z} \left(2 \cos(\mathbf{k}_{X_1} \cdot \mathbf{r}^a) - \cos(\mathbf{k}_{X_2} \cdot \mathbf{r}^a) - \cos(\mathbf{k}_{X_3} \cdot \mathbf{r}^a) \right), \\
\mathbf{H}_{E_2,2}^{a,a2} &= \hat{z} \left(\cos(\mathbf{k}_{X_2} \cdot \mathbf{r}^a) - \cos(\mathbf{k}_{X_3} \cdot \mathbf{r}^a) \right).
\end{aligned} \tag{1.24}$$

The Y -split cavity does not have C_{6v} symmetry, but rather C_{2v} symmetry. This reduction of

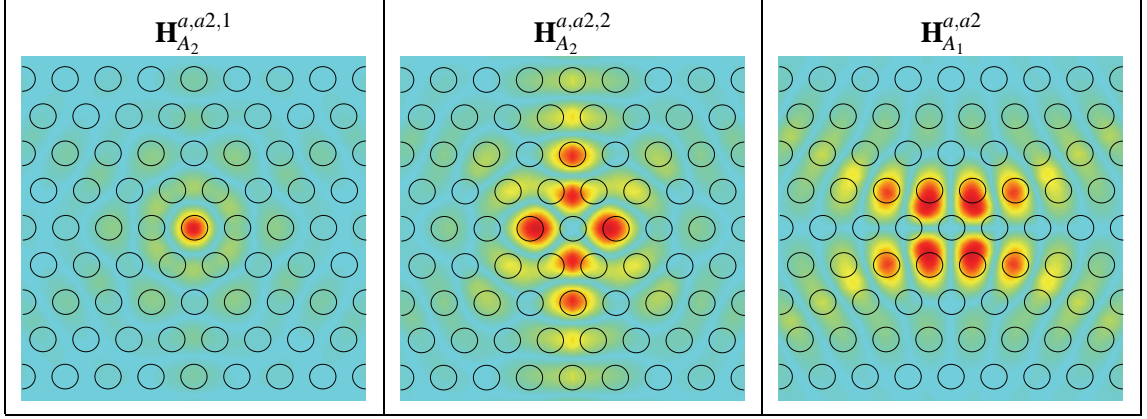


Figure 1.8: Magnetic field amplitude of the symmetry analysis acceptor modes formed from the valence band modes at the X-point of the hexagonal lattice.

symmetry causes the E_2 IRREP space to split into $A_1 \oplus A_2$, and the A_2'' space to transfer over into an A_2 IRREP space:

$$\begin{aligned}
 C_{6v} &\rightarrow C_{2v} \\
 \mathbf{H}_{A_2''}^{a,a2} &\rightarrow \mathbf{H}_{A_2}^{a,a2,1}, \\
 \mathbf{H}_{E_2,1}^{a,a2} &\rightarrow \mathbf{H}_{A_2}^{a,a2,2}, \\
 \mathbf{H}_{E_2,2}^{a,a2} &\rightarrow \mathbf{H}_{A_1}^{a,a2}.
 \end{aligned} \tag{1.25}$$

Figure 1.8 shows the magnetic field patterns of the acceptor modes predicted by the symmetry analysis to form out of the valence band at the X-point. The shallow acceptor mode ($Y\text{-}A2_0$) found in FDTD simulations of the Y-split cavity [24] transforms as the A_2 IRREP under C_{2v} symmetry operations. The dominant Fourier component within the FDTD generated field pattern of $Y\text{-}A2_0$ is \mathbf{k}_{X_1} , from which we can conclude that this mode is given by $\mathbf{H}_{A_2}^{a,a2,2}$ as opposed to $\mathbf{H}_{A_2}^{a,a2,1}$.

1.1.3 Square lattice photonic crystals

As with the hexagonal lattice we concern ourselves here with only the fundamental even modes (TE-like) of the slab waveguide. The point group symmetry of the square lattice photonic crystal can then be reduced to $C_{4v}=D_{4h}/\sigma_h$. A plot of the approximate in-plane bandstructure for the fundamental TE-like guided modes of a half-wavelength thick slab waveguide with a square array patterning of air holes is given in fig. 1.9(a).

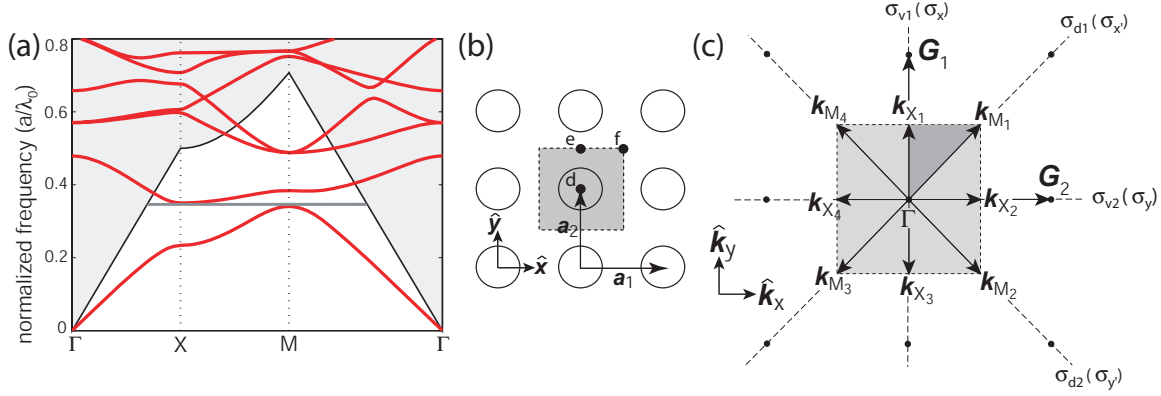


Figure 1.9: (a) Fundamental TE-like guided mode bandstructure ($r/a = 0.35$, $n_{\text{slab}} = n_{\text{eff}} = 2.65$) for a square lattice of air holes. The bandgap is seen to be much smaller for the square lattice than in the case of the hexagonal lattice. The air (cladding) light line is shown as a solid black line. (b)-(c) Illustration of the real and reciprocal spaces of the two-dimensional PC with a square array of air holes. The high-symmetry points of the square lattice, referenced to the center of an air hole, are $\mathbf{d} = (0, 0)$, $\mathbf{e} = (0, a/2)$, and $\mathbf{f} = (a/2, a/2)$. (b) Real space. $|\mathbf{a}_1| = |\mathbf{a}_2| = a$. (c) Reciprocal space. $|\mathbf{G}_1| = |\mathbf{G}_2| = 2\pi/a$, $|\mathbf{k}_X| = \pi/a$, $|\mathbf{k}_M| = \sqrt{2}\pi/a$.

The high symmetry points on the boundary or within the IBZ are (see fig. 1.9(c)): the four X points ($\{\pm(1, 0)k_X, \pm(0, 1)k_X\}$), the four M points ($(\pm\sqrt{2}/2, \pm\sqrt{2}/2)k_M$), and the Γ point $= (0, 0)$. The first-order band edges of the square lattice (see fig. 1.9(a)) are defined from above by the X point (conduction band edge) and below by the M point (valence band edge). The group of the wave vector at the X , M , and Γ points is C_{2v} , C_{4v} , and C_{4v} , respectively. Character tables [92] for the two groups are given in table 1.2.

1.1.3.1 X-point

A symmetry basis for the modes of the square lattice PC at the X -point can be found by applying the symmetry operations of the group of the wave vector ($G_{\mathbf{k}_X} = C_{2v}$) to the seed vector $\mathbf{H}_{\mathbf{k}_{X_1}}$. In this case, the basis is simply $(\mathbf{H}_{\mathbf{k}_{X_1}}, \mathbf{H}_{-\mathbf{k}_{X_1}})$. Projecting this symmetry basis onto the IRREP spaces of C_{2v} yields:

$$\begin{aligned}\mathbf{H}_{A_2}^{X_1} &= \hat{z} \cos(\mathbf{k}_{X_1} \cdot \mathbf{r}) \\ \mathbf{H}_{B_1}^{X_1} &= \hat{z} \sin(\mathbf{k}_{X_1} \cdot \mathbf{r}),\end{aligned}\tag{1.26}$$

where A_2 and B_1 label the IRREP spaces of C_{2v, σ_v} (see table 1.2). With the origin at the center of an

Table 1.2: Point group character tables for the square lattice.

C_{4v}	E	C_2	$2C_4$	$2\sigma_v$	$2\sigma_d$
A_1''	1	1	1	1	1
A_2''	1	1	1	-1	-1
B_1''	1	1	-1	1	-1
B_2''	1	1	-1	-1	1
E	2	-2	0	0	0
S^M	4	0	0	0	-2
$S^{d,d1}$	2	-2	0	0	0
$S^{f,d1}$	2	2	0	-2	0

C_{2v,σ_d}	E	C_2	$\sigma_{x'}(\sigma_{d1})$	$\sigma_{y'}(\sigma_{d2})$
A_1'	1	1	1	1
A_2'	1	1	-1	-1
B_1'	1	-1	-1	1
B_2'	1	-1	1	-1

C_{2v,σ_v}	E	C_2	$\sigma_x(\sigma_{v1})$	$\sigma_y(\sigma_{v2})$
A_1	1	1	1	1
A_2	1	1	-1	-1
B_1	1	-1	-1	1
B_2	1	-1	1	-1
S^{X1}	2	0	0	-2
$S^{e,d1}$	2	0	0	-2

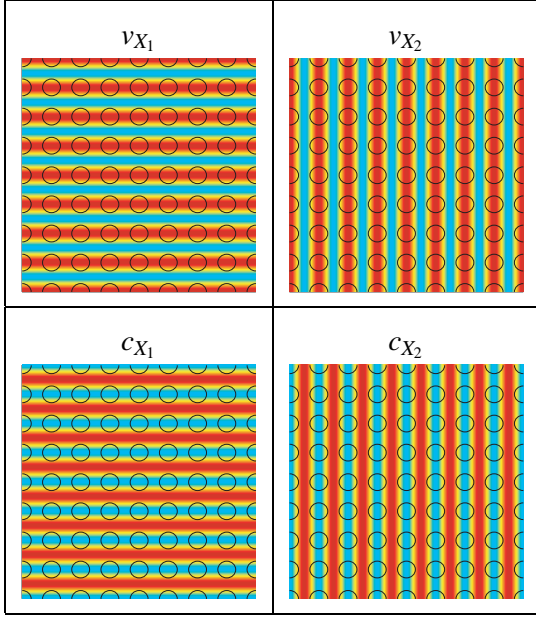


Figure 1.10: Magnetic field (amplitude) patterns of the valence band (top) and conduction band (bottom) modes of the square lattice at the X -points of the IBZ, generated by the symmetry basis VB_d^X and CB_d^X .

air hole of the lattice (point d of fig. 1.9), $\mathbf{H}_{A_2}^{X_1}$ corresponds to the “valence” band mode and $\mathbf{H}_{B_1}^{X_1}$ to the “conduction” band mode.

In order to fully define the modes at the X -point all modes of the $\star\mathbf{k}$ must be included. The result is the following set of degenerate valence band modes,

$$VB_d^X = \begin{pmatrix} v_{X_1} \\ v_{X_2} \end{pmatrix} = \hat{z} \begin{pmatrix} \cos(\mathbf{k}_{X_1} \cdot \mathbf{r}^d) \\ \cos(\mathbf{k}_{X_2} \cdot \mathbf{r}^d) \end{pmatrix}, \quad (1.27)$$

and degenerate conduction band modes,

$$CB_d^X = \begin{pmatrix} c_{X_1} \\ c_{X_2} \end{pmatrix} = \hat{z} \begin{pmatrix} \sin(\mathbf{k}_{X_1} \cdot \mathbf{r}^d) \\ \sin(\mathbf{k}_{X_2} \cdot \mathbf{r}^d) \end{pmatrix}. \quad (1.28)$$

The magnetic field amplitude patterns of the approximate valence and conduction band modes of the square lattice at the X -points of the IBZ are given in fig. 1.10.

1.1.3.2 M-point

A similar procedure may be performed in order to determine approximate forms for the TE-like valence and conduction band modes at the M -point of the IBZ. The symmetry basis, S^M , in this case includes all the M -points of the IBZ, $S^M = (\mathbf{H}_{\mathbf{k}_{M_1}}, \mathbf{H}_{\mathbf{k}_{M_2}}, \mathbf{H}_{-\mathbf{k}_{M_1}}, \mathbf{H}_{-\mathbf{k}_{M_2}})$. As determined from its character under C_{4v} (table 1.2), $S^M = E \oplus A_2'' \oplus B_1''$. The doubly degenerate IRREP E must represent a higher energy level band as the conduction and valence band edges are non-degenerate at the M -point as shown in fig. 1.9(a). Using only the A_2'' and B_1'' IRREPs, an approximate form for the valence band edge and conduction band edge modes at the M -point are calculated by projecting the symmetry basis onto these IRREP spaces. With the origin centered at point d , the valence and conduction band edge modes are:

$$VB_d^M = \begin{pmatrix} v_M \end{pmatrix} = \hat{z} \begin{pmatrix} \cos(\mathbf{k}_{M_1} \cdot \mathbf{r}^d) + \cos(\mathbf{k}_{M_2} \cdot \mathbf{r}^d) \end{pmatrix} \quad (1.29)$$

$$CB_d^M = \begin{pmatrix} c1_M \end{pmatrix} = \hat{z} \begin{pmatrix} \cos(\mathbf{k}_{M_1} \cdot \mathbf{r}^d) - \cos(\mathbf{k}_{M_2} \cdot \mathbf{r}^d) \end{pmatrix}. \quad (1.30)$$

Approximate modes for the degenerate higher frequency conduction bands represented by the IRREP E are, in one particular basis,

$$CB_d^{M,2} = \begin{pmatrix} c2_M \\ c3_M \end{pmatrix} = \hat{z} \begin{pmatrix} \sin(\mathbf{k}_{M_1} \cdot \mathbf{r}^d) - \sin(\mathbf{k}_{M_2} \cdot \mathbf{r}^d) \\ \sin(\mathbf{k}_{M_1} \cdot \mathbf{r}^d) + \sin(\mathbf{k}_{M_2} \cdot \mathbf{r}^d) \end{pmatrix}. \quad (1.31)$$

These higher frequency bands will be unimportant in our present analysis where we focus on the band edge modes defining the first order bandgap. The magnetic field amplitude patterns of the valence and conduction band modes at the M -point of the IBZ of the square lattice are given in fig. 1.11.

In the square lattice there are three different high-symmetry points around which one may center a defect. These points are labeled d , e , and f in fig. 1.9. Points d and f maintain the C_{4v} point group of the square lattice, and point e has a lowered symmetry given by the point group C_{2v, σ_v} . As was done for the hexagonal lattice, Bloch mode symmetry bases written with their origin at points d , e ,

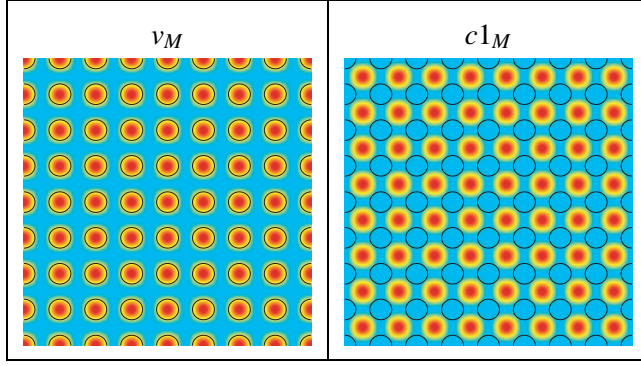


Figure 1.11: Magnetic field (amplitude) patterns of the valence and conduction band modes of the square lattice at the M -points of the IBZ generated by the symmetry analysis (VB_d^M and CB_d^M).

or f will be indexed as such. Coordinates centered about points d , e , and f of the lattice are also labeled as \mathbf{r}^d , \mathbf{r}^e , and \mathbf{r}^f , respectively.

1.1.3.3 Conduction band donor modes

For the square PC lattice the minimum in the conduction band occurs at the X -point (fig. 1.9(a)). The representations describing how the CB_d^X , CB_e^X , and CB_f^X symmetry bases transform under the appropriate point group are given by $S^{d,d1}$, $S^{e,d1}$, and $S^{f,d1}$, respectively. From their characters in table 1.2 we find that $S^{d,d1} = E$, $S^{e,d1} = A2 \oplus B2$, and $S^{f,d1} = A_2'' \oplus B_2''$. Projecting the symmetry bases onto the different IRREPs gives the following conduction band donor modes:

$$\begin{aligned} \mathbf{H}_{E,1}^{d,d1} &= \hat{z} \left(\sin(\mathbf{k}_{X_1} \cdot \mathbf{r}^d) \right) \\ \mathbf{H}_{E,2}^{d,d1} &= \hat{z} \left(\sin(\mathbf{k}_{X_2} \cdot \mathbf{r}^d) \right), \end{aligned} \tag{1.32}$$

centered about point d ,

$$\begin{aligned} \mathbf{H}_{A2}^{e,d1} &= \hat{z} \left(\cos(\mathbf{k}_{X_1} \cdot \mathbf{r}^e) \right) \\ \mathbf{H}_{B2}^{e,d1} &= \hat{z} \left(\sin(\mathbf{k}_{X_2} \cdot \mathbf{r}^e) \right), \end{aligned} \tag{1.33}$$

centered about point e , and

$$\begin{aligned}
\mathbf{H}_{A_2''}^{f,d1} &= \hat{z} \left(\cos(\mathbf{k}_{X_1} \cdot \mathbf{r}^f) + \cos(\mathbf{k}_{X_2} \cdot \mathbf{r}^f) \right) \\
\mathbf{H}_{B_2''}^{f,d1} &= \hat{z} \left(\cos(\mathbf{k}_{X_1} \cdot \mathbf{r}^f) - \cos(\mathbf{k}_{X_2} \cdot \mathbf{r}^f) \right),
\end{aligned} \tag{1.34}$$

centered about point f .

For the points d and f , defects may be formed with lower symmetry than the C_{4v} symmetry of the square lattice. We may use the compatibility relations between the IRREPs of the full and reduced symmetry groups to determine the new mode structure. For a defect of C_{2v} symmetry with mirror planes along the \hat{x} and \hat{y} directions of fig. 1.9(a) (C_{2v,σ_v}) we have the following reduction:

$$\begin{aligned}
C_{4v} &\rightarrow C_{2v,\sigma_v} \\
\mathbf{H}_{E,1}^{d,d1} &\rightarrow \mathbf{H}_{B_1}^{d,d1} \text{ (x-dipole)} \\
\mathbf{H}_{E,2}^{d,d1} &\rightarrow \mathbf{H}_{B_2}^{d,d1} \text{ (y-dipole)} \\
\mathbf{H}_{A_2''}^{f,d1} &\rightarrow \mathbf{H}_{A_2}^{f,d1,1} \\
\mathbf{H}_{B_2''}^{f,d1} &\rightarrow \mathbf{H}_{A_2}^{f,d1,2}.
\end{aligned} \tag{1.35}$$

If instead, the defect at points d and f contain the mirror planes σ_d , the symmetry is C_{2v,σ_d} and the compatibility relations give a mode decomposition:

$$\begin{aligned}
C_{4v} &\rightarrow C_{2v,\sigma_d} \\
\mathbf{H}_{E,1}^{d,d1} + \mathbf{H}_{E,2}^{d,d1} &\rightarrow \mathbf{H}_{B_1'}^{d,d1} \text{ (x'-dipole)} \\
\mathbf{H}_{E,1}^{d,d1} - \mathbf{H}_{E,2}^{d,d1} &\rightarrow \mathbf{H}_{B_2'}^{d,d1} \text{ (y'-dipole)} \\
\mathbf{H}_{A_2''}^{f,d1} &\rightarrow \mathbf{H}_{A_2'}^{f,d1} \\
\mathbf{H}_{B_2''}^{f,d1} &\rightarrow \mathbf{H}_{A_1'}^{f,d1}.
\end{aligned} \tag{1.36}$$

Magnetic field patterns of the different localized donor-type defect modes formed about point d , e , and f of the square lattice are given in fig. 1.12, where we have chosen to decompose the fields according to C_{2v,σ_v} .

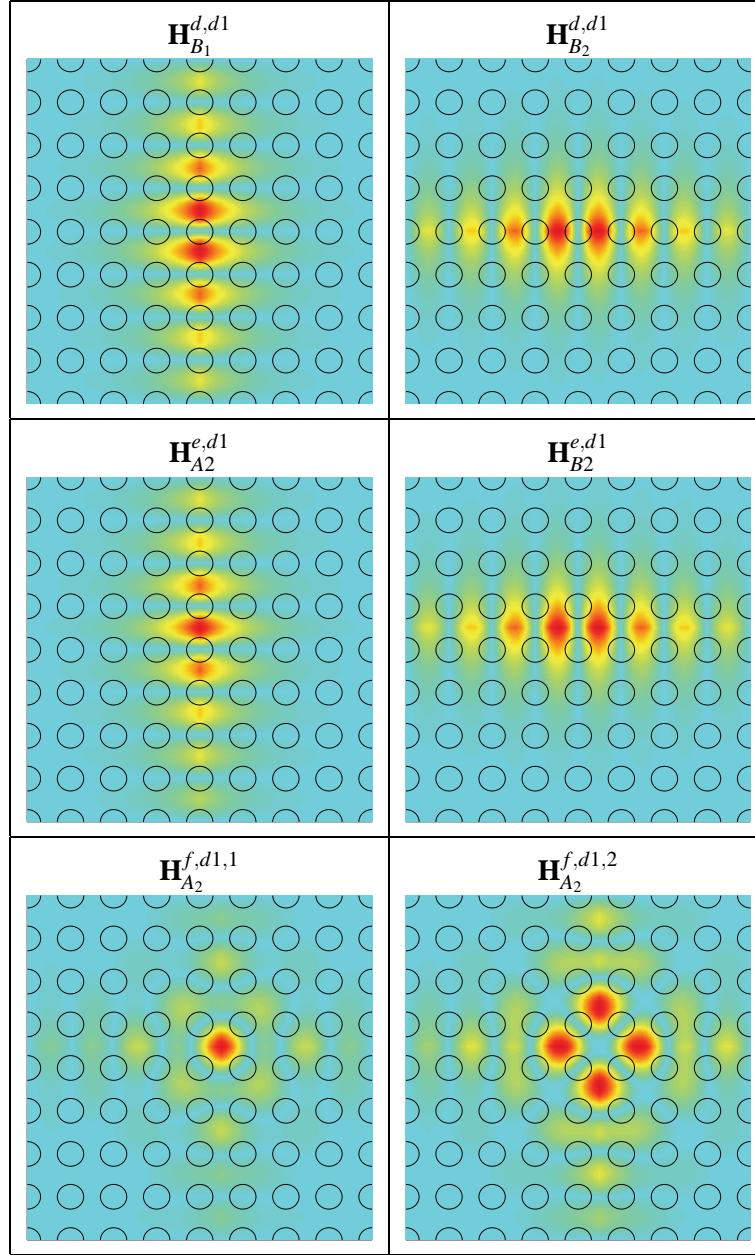


Figure 1.12: Magnetic field amplitude of the localized donor modes centered about points d , e , and f of the square lattice.

1.1.3.4 Valence band acceptor modes

For the square lattice the maximum of the valence band occurs at the M -point (fig. 1.9(a)). For the square lattice the valence band edge modes at the M -point consist of a single non-degenerate mode. This can be traced back to the fact that the M -point in the square lattice is highly symmetric, and the group of the wave vector mixes all four of the M -points on the IBZ boundary. The symmetries and fundamental momentum components of the possible acceptor modes formed from the M -point band edge modes (the approximate defect modes) are then trivially given by the single M -point valence band edge mode.

For the high-symmetry points d and f of the square lattice, assuming that the defect is symmetric enough so as to maintain the C_{4v} symmetry of the square lattice, the single acceptor mode is

$$\mathbf{H}_{A_2''}^{d,a1} = \hat{z} \left(\cos(\mathbf{k}_{M_1} \cdot \mathbf{r}^d) + \cos(\mathbf{k}_{M_2} \cdot \mathbf{r}^d) \right), \quad (1.37)$$

about point d , and

$$\mathbf{H}_{B_1''}^{f,a1} = \hat{z} \left(\cos(\mathbf{k}_{M_1} \cdot \mathbf{r}^f) - \cos(\mathbf{k}_{M_2} \cdot \mathbf{r}^f) \right), \quad (1.38)$$

about point f . The character of the representation S_e^{a1} of the M -point valence band edge mode under symmetry transformations C_{2v, σ_v} about point e is given in table 1.2. From its character, $S_e^{a1} = B_1$, the approximate acceptor mode of a defect centered about point e is

$$\mathbf{H}_{B_1''}^{e,a1} = \hat{z} \left(\sin(\mathbf{k}_{M_1} \cdot \mathbf{r}^e) - \sin(\mathbf{k}_{M_2} \cdot \mathbf{r}^e) \right). \quad (1.39)$$

For defects of reduced symmetry about points d and f we have the following compatibility relations:

$$\begin{array}{ll} C_{4v} \rightarrow C_{2v, \sigma_v} & C_{4v} \rightarrow C_{2v, \sigma_d} \\ \mathbf{H}_{A_2''}^{d,a1} \rightarrow \mathbf{H}_{A_2}^{d,a1} & \text{and } \mathbf{H}_{A_2''}^{d,a1} \rightarrow \mathbf{H}_{A_2'}^{d,a1} \\ \mathbf{H}_{B_1''}^{f,a1} \rightarrow \mathbf{H}_{A_1}^{f,a1}, & \mathbf{H}_{B_1''}^{f,a1} \rightarrow \mathbf{H}_{A_2'}^{f,a1}. \end{array} \quad (1.40)$$

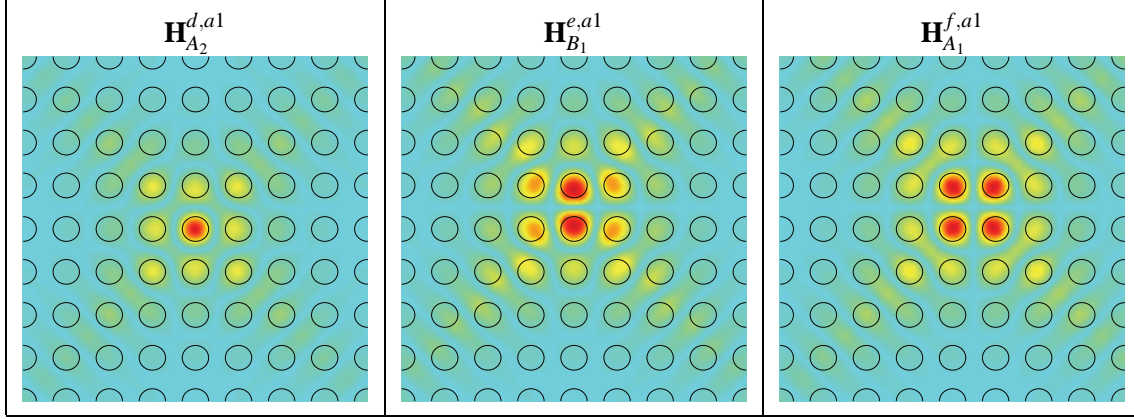


Figure 1.13: Magnetic field amplitude of the acceptor-type modes formed the valence band M -point modes of the square lattice.

Figure 1.13 shows the magnetic field patterns of the acceptor-type modes formed from the M -point of the IBZ of the square lattice for defects centered about points d , e , and f . Again, as for the donor modes, the modes are shown for the C_{2v,σ_v} symmetry basis.

1.1.4 Comparison with FDTD simulations

In order to establish the effectiveness of the above symmetry analysis of the modes of relatively localized defects within photonic crystals, we provide results of numerical calculations using the FDTD method. The FDTD simulation results provide information about the resonant frequency, radiation pattern, and modal loss of PC defect cavity resonant modes. The cavity studied in this section has been of particular relevance to the initial work on PC microcavity lasers performed by Painter et al. [3, 8].

The FDTD calculations (additional details provided in appendix B) were performed on a mesh with 20 points per lattice spacing. Excitation of the cavity modes was performed by an initial field (H_z) with a localized Gaussian profile, located in a position of low symmetry so as not to exclude any possible resonant modes. The even modes of the patterned slab waveguide were selected out by using an even mirror symmetry ($\sigma_h = +1$) in the middle of the slab waveguide. In order to choose a consistent mode basis (only important for degenerate modes), as well as to reduce computation time, a pair of vertical mirror planes (σ_x, σ_y) were used to filter out cavity modes according to their projection on the IRREPs of C_{2v} . Each cavity mode is thus labeled by the C_{2v} IRREP by which it transforms and an index corresponding to its energy (frequency) level.

The simplest cavity geometry that can be readily implemented consists of a single missing hole

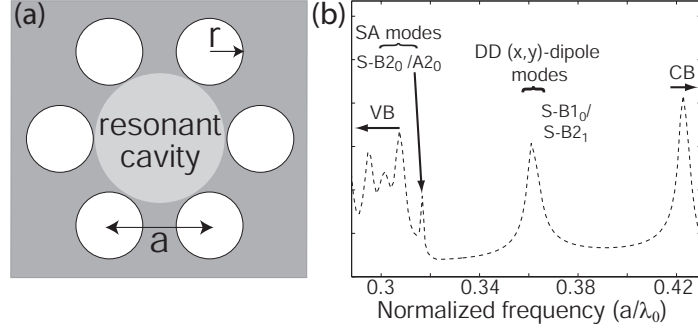


Figure 1.14: (a) S cavity (b) FDTD spectrum of a S -type defect cavity with $a = 515$ nm, $r/a = 0.36$ nominally, $n_{\text{slab}} = 3.4$, and $d/a = 0.409$.

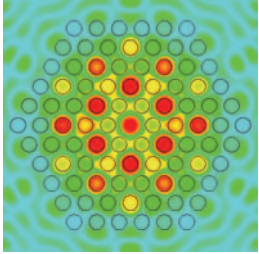
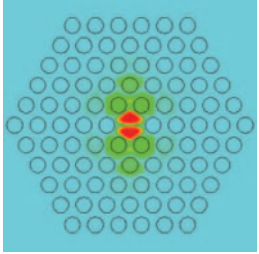
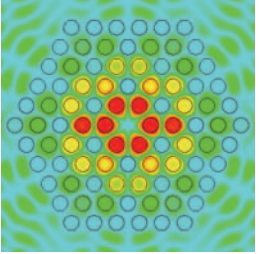
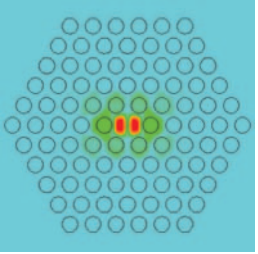
(schematically shown in fig. 1.14(a)). We will refer to this cavity as a symmetric or S cavity as it retains the full point group symmetry of the hexagonal lattice (C_{6v}). A FDTD-simulated spectrum of a defect cavity with a central missing hole and a linear grade in r/a (from the center outwards) of 0.38-0.34 is plotted in fig. 1.14(b) as a dashed line.² The spectrum is plotted versus normalized frequency, $\omega_n = a/\lambda_o$, where a is the lattice spacing and λ_o is the free-space wavelength. A normalized slab thickness, d/a , of 0.41 was used in the simulated structures to be consistent with the fabricated devices. To reduce computation time, the number of mirror periods (p) surrounding the central missing hole was limited to five in the simulations, save for the more extended modes for which cavities with eight periods were also simulated in order to more accurately estimate the modal losses present in the fabricated devices (see table 1.3).

In fig. 1.14, there appear to be two distinct resonance peaks within the guided mode bandgap of the TE-like modes. Performing a mode filter [7] using the C_{2v} mirror planes, we find that each resonance peak contains two different modes, yielding a total of four different localized modes whose magnetic field patterns within the mirror symmetry plane of the slab are shown in table 1.3. The two resonant modes (accidentally degenerate) associated with the peak near the valence band edge correspond to shallow acceptor (SA) modes which transform as the A_2'' and B_2'' IRREPs of C_{6v} ,³ and have the same dominant in-plane Fourier components as $\mathbf{H}_{A_2''}^{a1}$ and $\mathbf{H}_{B_2''}^{a1}$ of the symmetry analysis in section 1.1.2. The addition of these SA modes is a result of the linear grading in hole

²As a result of non-idealities in the fabrication process [95], the air holes near the center of the cavity are larger than those at the perimeter in the fabricated devices. A linear grading of the hole radius of 10% is quite common.

³Careful inspection of the FDTD generated magnetic field plot for these two modes shows that the mode patterns appear to have lower symmetry than that quoted in the text. This is a consequence of the way in which the modes were simulated, using vertical mirror planes to reduce the computation domain by a factor of four. Due to discretization of the computation grid, the mirror symmetry distorts the structure slightly, resulting in an asymmetry in the field pattern.

Table 1.3: Characteristics and magnetic field amplitude patterns of the resonant modes in a symmetric cavity with r/a linearly graded from 0.38 to 0.34 ($d/a = 0.409$, $n_{\text{slab}} = 3.4$, $p = 5$).

A2 $(-1, -1)$	B1 $(-1, +1)$	B2 $(+1, -1)$	
S-A2 ₀	S-B1 ₀	S-B2 ₀	S-B2 ₁
			
Label	Grp.	(σ_x, σ_y)	ω_n
S-A2 ₀ ($\mathbf{H}_{A_2'}^{a1}$)	SA	$(-, -)$	0.320
S-B1 ₀ ($\mathbf{H}_{E1,1}^{d1}$)	DD	dipole (\mathbf{x})	0.361
S-B2 ₀ ($\mathbf{H}_{B_2'}^{a1}$)	SA	$(+, -)$	0.322
S-B2 ₁ ($\mathbf{H}_{E1,2}^{d1}$)	DD	dipole (\mathbf{y})	0.360

radius, which forms a potential well for acceptor type modes. Of particular interest are the strongly localized pair of degenerate deep donor (DD) dipole-like modes near the center of the bandgap. From the plots of the electric field intensity of the x and y dipole modes shown in fig. 1.15(a)-(b), we see that the fundamental \mathbf{k} -components of the x and y dipole-like modes correspond nicely with the approximate field patterns predicted by the symmetry analysis (fig. 1.15(c)-(d)). Even the subtle difference in the in-plane radiation pattern of the x and y dipole modes as calculated numerically using FDTD is contained within the symmetry analysis as can be seen by the lack of a third standing wave component in the y -dipole ($\mathbf{H}_{E1,2}^{d1}$) mode.

A list of properties of the two SA and two DD localized defect modes is given in table 1.3. The numerically calculated losses of each cavity mode are represented by effective in-plane and out-of-plane quality factors [7], $Q_{||}$ and Q_{\perp} , respectively. A detailed analysis of quality factors within PC cavities will be discussed in detail in the following chapter.

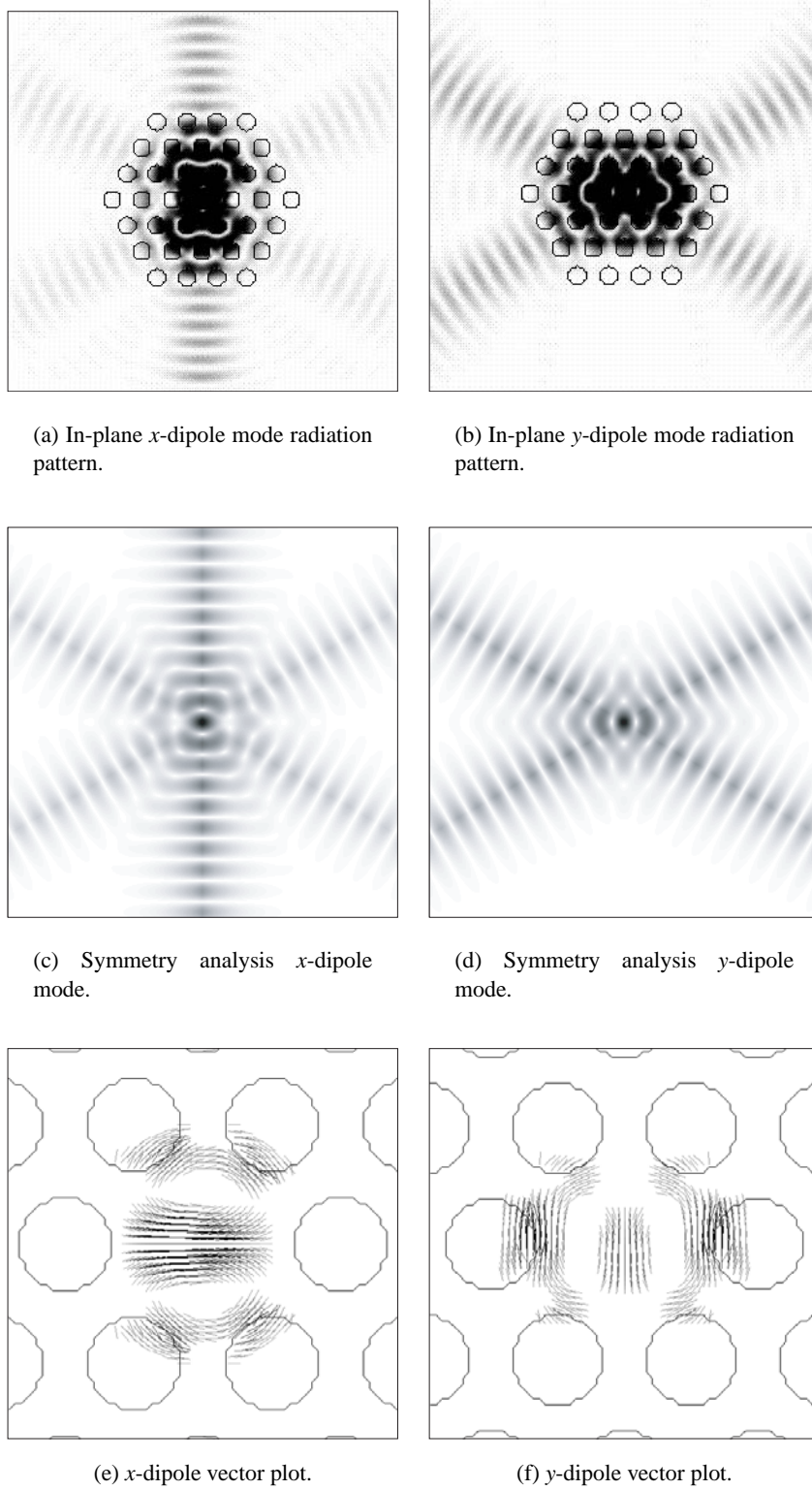


Figure 1.15: In-plane radiation losses (electric field amplitude saturated) of the x and y dipole mode (degenerate case) are shown in (a) and (b), respectively, as calculated by FDTD simulations. The electric field amplitude of the corresponding defect modes generated by the symmetry analysis are shown in (c) and (d) for comparison. In (e) and (f) the FDTD-generated vector plot of the electric field of the (x,y) -dipole modes in the middle of the slab waveguide are shown.

1.2 Wannier-like approach for describing localized modes in photonic crystals

1.2.1 Introduction

The work described in this section is largely based on ref. [25]. In analogy to the study of localized impurity states of electrons in periodic crystals [96, 97, 98, 99], we develop a Wannier-like wave equation to describe the envelope of resonant modes of localized perturbations within periodic dielectric structures. This has been done previously, in a more restrictive setting by Johnson et al. [100], and more recently in a general way by Charbonneau-Lefort et al. [101] and Istrate et al. [102] in the study of photonic crystal heterostructures. In these works, a wave equation for localized modes of non-uniform photonic crystals using an envelope approximation has been developed; however, in each case the envelope equation was formulated as a generalized Hermitian eigenvalue equation in terms of the electric field, and more importantly, only localized modes formed from non-degenerate satellite extrema were considered. In the analysis presented here we (i) consider the magnetic field and (ii) incorporate the mixing amongst the degenerate peaks or valleys of the orbit of \mathbf{k} in the bandstructure, resulting in a set of coupled Wannier-like equations describing a multi-envelope system. This allows us to more easily apply the envelope formalism to resonant cavity modes of PC slab waveguides, which in a two- or three-dimensional crystal mix Bloch modes near the degenerate satellite extrema of the orbit of \mathbf{k} . We also focus on the magnetic field as it can be approximately treated as a scalar for TE-like polarization modes of PC slabs⁴. From the shape and symmetry of the envelope of a localized resonant mode, and its relation to the underlying photonic bandstructure, one may better design features of planar 2D PC resonant cavities, such as in-plane and vertical emission, resonator-waveguide coupling, and the quality factor of resonant modes. In addition, the Wannier-like equation for localized defect modes more clearly and rigorously relates the curvature of the bandstructure to the formation of donor and acceptor modes for different types of local perturbations of a dielectric lattice.

This section is organized as follows. In section 1.2.2 we derive a set of coupled Wannier-like equations for the envelope functions of localized TE-like states in planar 2D PC structures, where as predicted by the Wannier theorem, the underlying bandstructure of the periodic dielectric structure gives rise to an effective mass tensor. We also derive an approximate form for the effective potential

⁴It should be noted that the envelope is always a scalar field, regardless of the vector nature of the electric or magnetic field.

in the Wannier envelope equation in terms of the local perturbation to the dielectric lattice. In section 1.2.3 we use the approximate symmetry basis for the TE-like Bloch modes at the valence and conduction band edge of the first-order bandgap in a 2D photonic crystal consisting of a hexagonal array of air holes derived in the previous section to obtain approximate relations for the effective mass tensor of the Wannier equation. In conjunction with the symmetry analysis, which determines the mixing amongst the degenerate satellite extrema, we find an approximate form for the localized donor and acceptor modes of a hexagonal lattice with a parabolically graded filling fraction. For comparison, FDTD calculations of the acceptor and donor modes of such a defect cavity are also presented.

1.2.2 Wannier theorem for photons in periodic dielectric structures

In studying the localized electronic states associated with impurities within a crystalline material, it is often helpful to transform Schrödinger's equation into Fourier space, simplify the set of coupled equations through the limited Fourier decomposition of the perturbing potential, and then transform back to real-space coordinates, where a wave equation for the envelope of the localized states is generated. The Wannier theorem [103] captures the essence of this procedure in using the underlying energy-(crystal)momentum dispersion generated by the periodic Coulombic potential of the crystal in a spatially coarse-grained theory of electron dynamics. One application of the Wannier theorem is in the calculation of bound electronic states of crystal impurities [96, 99, 97, 98, 104]. The basic form of the Wannier equation for the envelope of impurity states is

$$\left((E - E_n(\hbar^{-1}\hat{\mathbf{p}})) + \Delta V(\mathbf{r}) \right) \Gamma(\mathbf{r}) = 0, \quad (1.41)$$

where $E_n(\hbar^{-1}\hat{\mathbf{p}})$ is the energy-(crystal)momentum dispersion relation of the n th energy band with wavevector \mathbf{k} replaced by the canonical momentum operator $\hat{\mathbf{p}} = -i\hbar\nabla$, $\Delta V(\mathbf{r})$ is the impurity potential, and $\Gamma(\mathbf{r})$ is the envelope function describing the localized electronic state.

We would like to find a similar Wannier-like equation for the envelope of localized photon states in periodic dielectric lattices. Of particular interest are the localized resonant modes of planar 2D PCs formed in optically thin dielectric slabs (see fig. 1.1). The fundamental TE-like even modes and TM-like odd modes of a symmetric 2D patterned dielectric slab waveguide can be approximated by scalar fields. In what follows we shall focus on the TE-like modes (as discussed in ref. [25], a

similar theory may also be derived for the TM-like modes of the PC slab).

We begin with Maxwell's equations in a (lossless) dielectric medium free of currents and free charge,

$$\begin{aligned}
\nabla \times \mathbf{E} &= -i\omega\mu_0\mathbf{H}, \\
\nabla \times \mathbf{H} &= +i\omega n^2\epsilon_0\mathbf{E}, \\
\nabla \cdot (n^2\epsilon_0\mathbf{E}) &= 0, \\
\nabla \cdot \mu_0\mathbf{H} &= 0,
\end{aligned} \tag{1.42}$$

where \mathbf{E} and \mathbf{H} are the harmonic complex electric and magnetic fields, respectively, with time dependence $e^{+i\omega t}$ (the physical fields are found by taking the real part of the complex fields). The velocity of light in vacuum is represented by c , and we have assumed that the material is non-magnetic ($\mu = \mu_0$). We also assume here that the dielectric function does not depend on spatial or temporal frequency, $\epsilon(\omega, \mathbf{k}, \mathbf{r}) = \epsilon_0 n^2(\mathbf{r})$. From the above Maxwell relations, a wave equation for both the electric and magnetic fields can be generated:

$$\eta(\mathbf{r}) \left(\nabla \times \nabla \times \mathbf{E} \right) = \left(\frac{\omega}{c} \right)^2 \mathbf{E}, \tag{1.43}$$

$$\nabla \times \left(\eta(\mathbf{r}) \nabla \times \mathbf{H} \right) = \left(\frac{\omega}{c} \right)^2 \mathbf{H}, \tag{1.44}$$

where $\eta(\mathbf{r}) \equiv 1/n^2(\mathbf{r})$.

As we have discussed in the previous section, we separate modes into TE and TM polarizations, keeping in mind that this separation is only truly valid for purely 2D structures (for slab waveguides, the modes are only approximately TE and TM in nature). For TE modes the magnetic field is described by a scalar field, $\mathbf{H} = \hat{z}H_d$ (where the subscript d stands for “defect mode”). As we have assumed that the refractive index does not vary (or the variation can be approximately neglected) in the \hat{z} -direction, $\partial_z \eta(\mathbf{r}) = 0$. The Hermitian eigenvalue equation which results from equation (1.44) and $\nabla \cdot \mathbf{H} = 0$ is (in the 2D case we only consider variations with respect to the in-plane coordinates, $\nabla \equiv \nabla_\perp$),

$$\hat{L}_H^{\text{TE}} H_d = \Lambda_d H_d, \quad (1.45)$$

with the TE eigenoperator given by,

$$\hat{L}_H^{\text{TE}} = -(\nabla \eta) \cdot \nabla - \eta \nabla^2. \quad (1.46)$$

The form of TE eigenoperator is easily obtained from equation (1.44) by using standard vector calculus identities as found in ref. [93], for example. The eigenvalue, Λ_d , is related to the square of the frequency of the mode, $\Lambda_d = (\omega_d/c)^2$. $\eta = \eta_o + \Delta\eta$, where η_o is given by the inverse of the square of the refractive index of the unperturbed photonic crystal, $1/n_{2D}^2(\mathbf{r})$, and $\Delta\eta$ represents the localized perturbation to $1/n_{2D}^2(\mathbf{r})$. The eigenoperator \hat{L}_H (we drop the TE superscript from here on) can be separated into an unperturbed photonic crystal part, $\hat{L}_{H,o} = -\nabla(\eta_o) \cdot \nabla - \eta_o \nabla^2$, and a perturbation part due to the defect, $\hat{L}'_H = -\nabla(\Delta\eta) \cdot \nabla - \Delta\eta \nabla^2$.

The (2D approximate) modes of the perfect crystal are eigenmodes of $\hat{L}_{H,o}$,

$$\hat{L}_{H,o} H_{l,\mathbf{k}} = \Lambda_{l,\mathbf{k}} H_{l,\mathbf{k}}, \quad (1.47)$$

where l labels the band index and \mathbf{k} labels the in-plane crystal momentum. As the $H_{l,\mathbf{k}}$ are Bloch waves they can be written as

$$H_{l,\mathbf{k}} = \frac{1}{L} h_{l,\mathbf{k}}(\mathbf{r}) e^{i\mathbf{k} \cdot \mathbf{r}}, \quad (1.48)$$

with L^2 equal to the area of the 2D photonic crystal and the set of periodic functions, $h_{l,\mathbf{k}}(\mathbf{r})$, at crystal momentum \mathbf{k} , satisfying their own set of orthogonality relations (normalized over the lattice unit cell v),

$$\langle h_{l',\mathbf{k}} | h_{l,\mathbf{k}} \rangle_v \equiv \frac{1}{v} \int_v d^2r h_{l',\mathbf{k}}^* h_{l,\mathbf{k}} = \delta_{l',l}. \quad (1.49)$$

In forming a defect state by perturbing the lattice in a localized region of space, the Bloch modes in proximity to the degenerate satellite extrema of a band edge, the $\{\mathbf{k}_i; i = 1, 2, \dots, M\}$ points of the $\star\mathbf{k}$ (from here on, the $\star\mathbf{k}$ refers implicitly to the orbit of this band edge), are most strongly coupled together [98]:

$$H_d(\mathbf{r}) = \sum_i c_i \sum_{\mathbf{k}} \tilde{\Gamma}_i(\mathbf{k} - \mathbf{k}_i) \frac{1}{L} h_{l,\mathbf{k}} e^{i\mathbf{k} \cdot \mathbf{r}}, \quad (1.50)$$

The $\tilde{\Gamma}_i$ are a set of Fourier space envelope functions, which in the spirit of the effective mass theory have amplitudes localized around $\mathbf{k} = \mathbf{k}_i$. Note that throughout this analysis the band of interest at the band edge is considered to be non-degenerate and we neglect *inter*-band mixing [98].

Assuming that the $h_{l,\mathbf{k}}$ do not vary significantly (using a similar argument as in ref. [97]) over the range of each Fourier space envelope function,

$$H_d(\mathbf{r}) \approx \sum_i c_i \frac{1}{L} h_{l,\mathbf{k}_i} e^{i\mathbf{k}_i \cdot \mathbf{r}} \left(\sum_{\Delta\mathbf{k}} \tilde{\Gamma}_i(\Delta\mathbf{k}) e^{i\Delta\mathbf{k} \cdot \mathbf{r}} \right), \quad (1.51)$$

where $\Delta\mathbf{k} \equiv \mathbf{k} - \mathbf{k}_i$. Writing the envelope functions in real space,

$$\Gamma_i(\mathbf{r}) = \sum_{\Delta\mathbf{k}} \tilde{\Gamma}_i(\Delta\mathbf{k}) e^{i\Delta\mathbf{k} \cdot \mathbf{r}}, \quad (1.52)$$

allows us to rewrite equation (1.51) as,

$$H_d(\mathbf{r}) \approx \sum_i c_i \frac{1}{L} h_{l,\mathbf{k}_i} e^{i\mathbf{k}_i \cdot \mathbf{r}} \Gamma_i(\mathbf{r}), \quad (1.53)$$

It is in this way that the real space envelope of localized defect modes can be interpreted in the Fourier domain [97] as a result of the *intra*-band mixing of the unperturbed Bloch modes of the crystal.

Returning to equation (1.45), we now proceed to find an eigenvalue equation for the envelope functions. Multiplying both sides of equation (1.45) by $H_{l',\mathbf{k}'}$, where \mathbf{k}' is chosen in a neighborhood of \mathbf{k}_i , and integrating over the in-plane spatial coordinates gives,

$$\sum_j c_j \sum_{\mathbf{k}} \tilde{\Gamma}_j(\mathbf{k} - \mathbf{k}_j) \langle H_{l',\mathbf{k}'} | (\Lambda_d - \Lambda_{l,\mathbf{k}} - \hat{L}'_H) H_{l,\mathbf{k}} \rangle = 0. \quad (1.54)$$

We rewrite \mathbf{r} as $\mathbf{R}_i + \mathbf{r}$, where \mathbf{R}_i gives the center of the i^{th} unit cell and \mathbf{r} is now confined to the interior of the unit cell. Using the orthonormality of the Bloch waves and the normalization of their periodic parts described in equation (1.49),

$$\begin{aligned} \langle H_{l',\mathbf{k}'} | (\Lambda_d - \Lambda_{l,\mathbf{k}}) H_{l,\mathbf{k}} \rangle &= (\Lambda_d - \Lambda_{l,\mathbf{k}}) \frac{1}{L^2} \sum_{i=1}^N e^{i(\mathbf{k}-\mathbf{k}') \cdot \mathbf{R}_i} \int_v d^2 r h_{l',\mathbf{k}'}^* h_{l,\mathbf{k}} e^{i(\mathbf{k}-\mathbf{k}') \cdot \mathbf{r}} \\ &= (\Lambda_d - \Lambda_{l',\mathbf{k}'}) \delta_{l',l} \delta_{\mathbf{k}',\mathbf{k}}. \end{aligned} \quad (1.55)$$

Note that a reciprocal lattice vector was not included in $\delta_{\mathbf{k}',\mathbf{k}}$ as both \mathbf{k}' and \mathbf{k} (through the localized nature of the $\tilde{\Gamma}_i$) are assumed to lie within a neighborhood of one of the wavevectors comprising the $\star\mathbf{k}$, which by definition are not linked by a reciprocal lattice vector. Equation (1.54) then becomes

$$\begin{aligned} &c_i (\Lambda_d - \Lambda_{l,\mathbf{k}'}) \tilde{\Gamma}_i(\mathbf{k}' - \mathbf{k}_i) \\ &- \sum_j c_j \sum_{\mathbf{k}} \langle H_{l',\mathbf{k}'} | \hat{L}'_H H_{l,\mathbf{k}} \rangle \tilde{\Gamma}_j(\mathbf{k} - \mathbf{k}_j) = 0. \end{aligned} \quad (1.56)$$

Fourier expanding the defect perturbation in reciprocal space,

$$\Delta\eta(\mathbf{r}) = \sum_{\mathbf{k}''} \tilde{\Delta\eta}_{\mathbf{k}''} e^{i\mathbf{k}'' \cdot \mathbf{r}}, \quad (1.57)$$

we can write the mode-mixing term $\langle H_{l',\mathbf{k}'} | \hat{L}'_H H_{l,\mathbf{k}} \rangle$ in equation (1.56) as:

$$\begin{aligned} \langle H_{l',\mathbf{k}'} | \hat{L}'_H H_{l,\mathbf{k}} \rangle &= - \sum_{\mathbf{k}''} \left(\sum_{i=1}^N e^{i(\mathbf{k}+\mathbf{k}''-\mathbf{k}') \cdot \mathbf{R}_i} \frac{\tilde{\Delta\eta}_{\mathbf{k}''}}{L^2} \int_v d^2 r e^{i(\mathbf{k}+\mathbf{k}''-\mathbf{k}') \cdot \mathbf{r}} h_{l',\mathbf{k}'}^* \left(i\mathbf{k}'' \cdot (\nabla + i\mathbf{k}) \right. \right. \\ &\quad \left. \left. + \nabla^2 + 2i\mathbf{k} \cdot \nabla - |\mathbf{k}|^2 \right) h_{l,\mathbf{k}} \right) \\ &= \sum_{\mathbf{G}} \sum_{\mathbf{k}''} \left(\tilde{\Delta\eta}_{\mathbf{k}''} K_{l',l}(\mathbf{k}', \mathbf{k}, \mathbf{G}) + \tilde{\Delta\eta}_{\mathbf{k}''}(i\mathbf{k}'') \cdot \mathbf{L}_{l',l}(\mathbf{k}', \mathbf{k}, \mathbf{G}) \right) \delta_{\mathbf{k}'-\mathbf{k}''+\mathbf{G},\mathbf{k}}, \end{aligned} \quad (1.58)$$

where the \mathbf{G} are reciprocal lattice vectors, and we have defined scalar and vector coupling matrix elements as

$$\begin{aligned} K_{l',l}(\mathbf{k}', \mathbf{k}, \mathbf{G}) &= -\frac{1}{v} \int_v d^2r e^{i\mathbf{G}\cdot\mathbf{r}} h_{l',\mathbf{k}'}^* (\nabla^2 + 2i\mathbf{k} \cdot \nabla - |\mathbf{k}|^2) h_{l,\mathbf{k}} \\ &\equiv -\langle h_{l',\mathbf{k}'} | e^{i\mathbf{G}\cdot\mathbf{r}} (\nabla^2 + 2i\mathbf{k} \cdot \nabla - |\mathbf{k}|^2) | h_{l,\mathbf{k}} \rangle_v, \end{aligned} \quad (1.59)$$

and

$$\begin{aligned} \mathbf{L}_{l',l}(\mathbf{k}', \mathbf{k}, \mathbf{G}) &= -\frac{1}{v} \int_v d^2r e^{i\mathbf{G}\cdot\mathbf{r}} h_{l',\mathbf{k}'}^* (\nabla + i\mathbf{k}) h_{l,\mathbf{k}} \\ &\equiv -\langle h_{l',\mathbf{k}'} | e^{i\mathbf{G}\cdot\mathbf{r}} (\nabla + i\mathbf{k}) | h_{l,\mathbf{k}} \rangle_v. \end{aligned} \quad (1.60)$$

Substituting equation (1.58) into equation (1.56) while keeping only terms that mix states within the l th band results in the following Fourier space representation of the magnetic field master equation:

$$\begin{aligned} c_i(\Lambda_d - \Lambda_{l,\mathbf{k}'}) \widetilde{\Gamma}_i(\mathbf{k}' - \mathbf{k}_i) - \sum_{\mathbf{G}} \sum_j c_j \sum_{\mathbf{k}''} \left(\left(\widetilde{\Delta\eta}_{\mathbf{k}''} K_{l,l}(\mathbf{k}', \mathbf{k}' - \mathbf{k}'' + \mathbf{G}, \mathbf{G}) \right. \right. \\ \left. \left. + \widetilde{\Delta\eta}_{\mathbf{k}''}(i\mathbf{k}'') \cdot \mathbf{L}_{l,l}(\mathbf{k}', \mathbf{k}' - \mathbf{k}'' + \mathbf{G}, \mathbf{G}) \right) \widetilde{\Gamma}_j((\mathbf{k}' - \mathbf{k}'' + \mathbf{G}) - \mathbf{k}_j) \right) = 0. \end{aligned} \quad (1.61)$$

For defect perturbations which are localized in \mathbf{k} -space as well as in real-space, the strongest mixing terms will be those with \mathbf{k}'' nearest the origin. As such, a further simplification can be made by including only those reciprocal lattice vectors \mathbf{G} which minimize the magnitude of \mathbf{k}'' in coupling the different neighborhoods of the $\star\mathbf{k}$ (satellite extrema). The local mixing of states within the neighborhood of each \mathbf{k}_i will thus be dominated by the Fourier components of $\widetilde{\Delta\eta}$ about the origin with $\mathbf{G} = 0$. Similarly, the mixing between neighborhoods of \mathbf{k}_i and \mathbf{k}_j , where $i \neq j$, will be dominated by a single \mathbf{G} which minimizes the magnitude of the vector $\mathbf{G} - (\mathbf{k}_j - \mathbf{k}_i)$. Writing this reciprocal lattice vector as $\mathbf{G}_{j,i}$ and only including the dominant coupling terms in equation (1.61) collapses the sum over \mathbf{G} and yields,

$$\begin{aligned}
& c_i \left((\Lambda_d - \Lambda_{l,\mathbf{k}'}) \tilde{\Gamma}_i(\mathbf{k}' - \mathbf{k}_i) - \sum_{\mathbf{k}''} \left(\tilde{\Delta}\eta_{\mathbf{k}''} K_{l,l}(\mathbf{k}_i, \mathbf{k}_i, \mathbf{0}) + \tilde{\Delta}\eta_{\mathbf{k}''}(i\mathbf{k}'') \cdot \mathbf{L}_{l,l}(\mathbf{k}_i, \mathbf{k}_i, \mathbf{0}) \right) \right. \\
& \left. \tilde{\Gamma}_i((\mathbf{k}' - \mathbf{k}'') - \mathbf{k}_i) \right) - \sum_{i \neq j} c_j \sum_{\mathbf{k}''} \left(\left(\tilde{\Delta}\eta_{\mathbf{k}''} K_{l,l}(\mathbf{k}_i, \mathbf{k}_j, \mathbf{G}_{j,i}) + \tilde{\Delta}\eta_{\mathbf{k}''}(i\mathbf{k}'') \cdot \mathbf{L}_{l,l}(\mathbf{k}_i, \mathbf{k}_j, \mathbf{G}_{j,i}) \right) \right. \\
& \left. \tilde{\Gamma}_j((\mathbf{k}' - (\mathbf{k}'' - \mathbf{G}_{j,i})) - \mathbf{k}_j) \right) = 0,
\end{aligned} \quad (1.62)$$

where we have neglected the variation of $K_{l,l}$ and $\mathbf{L}_{l,l}$ within the local neighborhoods of the $\mathbf{k}_i \in \star\mathbf{k}$.

Implicit in the derivation of equation (1.62) is that the $\tilde{\Gamma}_i$ are localized around the \mathbf{k}_i in reciprocal space. In order to make this explicit (which will be necessary when transforming back to real-space coordinates) we expand $\Lambda_{l,\mathbf{k}'}$ in the vicinity of each \mathbf{k}_i ,

$$\Lambda_{l,\mathbf{k}'} \approx (\Lambda_{l,o} + \Lambda'_{l,i}(\Delta\mathbf{k})) + O(\Delta k^3), \quad (1.63)$$

where $\Lambda_{l,o}$ is the top(bottom) of the band edge, $\Delta\mathbf{k} = \mathbf{k}' - \mathbf{k}_i$, and $\Lambda'_{l,i}$ only contains terms up to second-order in elements of $\Delta\mathbf{k}$ [98]. In the case of those \mathbf{k}_i located at an extrema of a given (non-degenerate) band the resulting dispersion relation may be written in the form, $\Lambda'_{l,i}(\Delta\mathbf{k}) = \Delta\mathbf{k} \cdot \mathbf{M}_{l,*}^{-1} \cdot \Delta\mathbf{k}$, where the matrix $\mathbf{M}_{l,*}$ is an effective mass tensor defined by the curvature of the band. Substituting equation (1.63) into equation (1.62) gives,

$$\begin{aligned}
& c_i \left((\Delta\Lambda_d - \Lambda'_{l,i}(\Delta\mathbf{k})) \tilde{\Gamma}_i(\Delta\mathbf{k}) - \sum_{\mathbf{k}''} \left(\tilde{\Delta}\eta_{\mathbf{k}''} K_{l,l}(\mathbf{k}_i, \mathbf{k}_i, \mathbf{0}) + \tilde{\Delta}\eta_{\mathbf{k}''}(i\mathbf{k}'') \cdot \mathbf{L}_{l,l}(\mathbf{k}_i, \mathbf{k}_i, \mathbf{0}) \right) \right. \\
& \left. \tilde{\Gamma}_i(\Delta\mathbf{k} - \mathbf{k}'') \right) - \sum_{i \neq j} c_j \sum_{\mathbf{k}''} \left(\left(\tilde{\Delta}\eta_{\mathbf{k}''} K_{l,l}(\mathbf{k}_i, \mathbf{k}_j, \mathbf{G}_{j,i}) + \tilde{\Delta}\eta_{\mathbf{k}''}(i\mathbf{k}'') \cdot \mathbf{L}_{l,l}(\mathbf{k}_i, \mathbf{k}_j, \mathbf{G}_{j,i}) \right) \right. \\
& \left. \tilde{\Gamma}_j((\Delta\mathbf{k} + \mathbf{G}_{j,i} - \Delta\mathbf{k}_{j,i}) - \mathbf{k}'') \right) = 0,
\end{aligned} \quad (1.64)$$

where $\Delta\Lambda_d = \Lambda_d - \Lambda_{l,o}$ is the eigenvalue referenced to the top(bottom) of the band edge, and $\Delta\mathbf{k}_{j,i} \equiv \mathbf{k}_j - \mathbf{k}_i$.

Equation (1.64) is the Fourier space representation of an approximate master equation for the localized magnetic field envelope functions of defect states. Transforming back to real space results in a set of coupled Wannier-like equations,

$$c_i \left((\Delta\Lambda_d - \Lambda'_{l,i}(\hbar^{-1}\hat{\mathbf{p}})) - \Delta\eta'_{l,i}(\mathbf{r}) \right) \Gamma_i(\mathbf{r}) - \sum_{i \neq j} c_j \left(e^{-i(\mathbf{G}_{j,i} - \Delta\mathbf{k}_{j,i}) \cdot \mathbf{r}} \Delta\eta'_{j,i}(\mathbf{r}) \right) \Gamma_j(\mathbf{r}) = 0, \quad (1.65)$$

$$\Delta\eta'_{j,i}(\mathbf{r}) = \Delta\eta(\mathbf{r}) K_{l,l}(\mathbf{k}_i, \mathbf{k}_j, \mathbf{G}_{j,i}) + \nabla(\Delta\eta(\mathbf{r})) \cdot \mathbf{L}_{l,l}(\mathbf{k}_i, \mathbf{k}_j, \mathbf{G}_{j,i}), \quad (1.66)$$

where $\hat{\mathbf{p}} = -i\hbar\nabla$ as in quantum mechanics, and $\Delta\eta'_{j,i}(\mathbf{r})$ is an effective perturbation potential.

Assuming that the amplitude of the relatively large Fourier components of $\Delta\eta(\mathbf{r})$ associated with mixing of states between neighborhoods of *different* satellite points of the $\star\mathbf{k}$ are much smaller than the amplitude of the small Fourier components which mix states within a given neighborhood of a point of the $\star\mathbf{k}$, we can treat the *inter- \mathbf{k}_i* mixing as a perturbation to the envelope functions formed from the local \mathbf{k} -space mixing [104]. This allows us to write an independent Wannier-like equation for each of the $\Gamma_i(\mathbf{r})$ envelope functions,

$$\left((\Delta\Lambda_d - \Lambda'_{l,i}(\hbar^{-1}\hat{\mathbf{p}})) - \Delta\eta'_{l,i}(\mathbf{r}) \right) \Gamma_i(\mathbf{r}) = 0. \quad (1.67)$$

Of most importance for the types of resonant cavities studied here are the ground state solutions to equation (1.67). This is due to the relatively localized nature of the defect regions. For delocalized defect regions extending over many lattice periods a more extensive set of envelope functions, including higher order functions with added nodes and antinodes must be included. Choice of such a set of envelope functions will depend on the geometry of the boundary of the defect [105]. For the present work then, we take $\Gamma_i(\mathbf{r})$ equal to the ground state envelope, $\Gamma_{i,o}(\mathbf{r})$.

As the ground state of a system is in general invariant under the symmetries of the Hamiltonian of that system [106, 104], the ground state envelope function should transform as the identity of the point group of the Wannier-like equation given in equation (1.67). The spatial symmetries of equation (1.67) are those of $\Lambda'_{l,i}(\hbar^{-1}\hat{\mathbf{p}})$ and $\Delta\eta'_{l,i}(\mathbf{r})$. As discussed in ref. [24], it then follows that the point symmetries of the Wannier-like equation for the ground state envelope functions are given by $G' \cap G'_{\mathbf{k}_i}$, where G' is the point group of the defect perturbation (independent of the crystal lattice) and $G'_{\mathbf{k}_i}$ is the point group isomorphic to the group of the wavevector (of the underlying Bravais lattice) at the point \mathbf{k}_i in the IBZ. With this knowledge the coefficients c_i of the defect state

in equation (1.53) can then be determined using symmetry arguments.

1.2.3 Envelope function calculation

We will consider two examples of how the Wannier-like equation of the previous section can be used to calculate an approximate envelope function for a localized photon state in a hexagonal lattice photonic crystal. The first example is a localized donor-type mode formed at the band edge occurring at the X -point of the reciprocal lattice where the bandstructure (fig. 1.2(a)) has a local minimum and is given by a simple paraboloid in a neighborhood of the X -point. The second example is that of a localized acceptor-type mode formed from the J -point where the bandstructure has a local maximum.

1.2.3.1 Donor modes at the X -point

We begin by recalling equations 1.5 and 1.6 of section 1.1.2.1, which give an approximate representation for the band edge modes at the X -point of the hexagonal lattice. In particular, we found

$$VB_X^a = \begin{pmatrix} v_{X_1} \\ v_{X_2} \\ v_{X_3} \end{pmatrix} = \hat{z} \begin{pmatrix} \cos(\mathbf{k}_{X_1} \cdot \mathbf{r}^a) \\ \cos(\mathbf{k}_{X_2} \cdot \mathbf{r}^a) \\ \cos(\mathbf{k}_{X_3} \cdot \mathbf{r}^a) \end{pmatrix}, \quad (1.68)$$

as an approximate form for the X -point valence band modes, and

$$CB_X^a = \begin{pmatrix} c_{X_1} \\ c_{X_2} \\ c_{X_3} \end{pmatrix} = \hat{z} \begin{pmatrix} \sin(\mathbf{k}_{X_1} \cdot \mathbf{r}^a) \\ \sin(\mathbf{k}_{X_2} \cdot \mathbf{r}^a) \\ \sin(\mathbf{k}_{X_3} \cdot \mathbf{r}^a) \end{pmatrix}. \quad (1.69)$$

as an approximate form for the X -point conduction band modes. Separating the plane wave and periodic parts of the above Bloch modes allows us to write,

$$\begin{aligned} v_{X_i} &= \frac{\hat{z}}{2}(1 + e^{-i2\mathbf{k}_{X_i} \cdot \mathbf{r}^a})e^{i\mathbf{k}_{X_i} \cdot \mathbf{r}^a}, \\ c_{X_i} &= \frac{\hat{z}}{i2}(1 - e^{-i2\mathbf{k}_{X_i} \cdot \mathbf{r}^a})e^{i\mathbf{k}_{X_i} \cdot \mathbf{r}^a}, \end{aligned} \quad (1.70)$$

with normalized periodic functions given by

$$\begin{aligned} h_{v,\mathbf{k}_{X_i}} &= (1/\sqrt{2})(1 + e^{-i2\mathbf{k}_{X_i} \cdot \mathbf{r}^a}), \\ h_{c,\mathbf{k}_{X_i}} &= (1/i\sqrt{2})(1 - e^{-i2\mathbf{k}_{X_i} \cdot \mathbf{r}^a}). \end{aligned} \quad (1.71)$$

We now use the above set of modes to calculate the local dispersion of the conduction band at the X -point. The Hermitian operator acting on the space of periodic functions at point \mathbf{k} in the reciprocal lattice, for the quasi-2D case studied here, is

$$\hat{L}_{H,\mathbf{k}} = -\nabla(\eta_o) \cdot (i\mathbf{k} + \nabla) + \eta_o(|\mathbf{k}|^2 - 2i\mathbf{k} \cdot \nabla - \nabla^2), \quad (1.72)$$

with associated eigenvalue equation given by,

$$\hat{L}_{H,\mathbf{k}} h_{l,\mathbf{k}} = \Lambda_{l,\mathbf{k}} h_{l,\mathbf{k}}. \quad (1.73)$$

As in “ $\mathbf{k} \cdot \hat{\mathbf{p}}$ ” theory for Bloch electrons in crystalline materials, we expand $\hat{L}_{H,\mathbf{k}}$ about point \mathbf{k}_o ,

$$\hat{L}_{H,\mathbf{k}} = \hat{L}_{H,\mathbf{k}_o} + \hat{L}'_{H,\Delta\mathbf{k}}, \quad (1.74)$$

with

$$\hat{L}'_{H,\Delta\mathbf{k}} \equiv \eta_o|\Delta\mathbf{k}|^2 + \Delta\mathbf{k} \cdot (-i\nabla(\eta_o) + 2\eta_o\mathbf{k}_o - 2i\eta_o\nabla). \quad (1.75)$$

Treating $\hat{L}'_{H,\Delta\mathbf{k}}$ as a perturbation to \hat{L}_{H,\mathbf{k}_o} , and expanding $h_{l,\mathbf{k}}$ in terms of the h_{l,\mathbf{k}_o} ,⁵ gives to second

⁵As discussed in ref. [107], the h_{l,\mathbf{k}_o} are not complete in the space of lattice periodic functions due to the divergenceless

order in elements of $\Delta\mathbf{k}$,

$$\begin{aligned} \Lambda_{l,\mathbf{k}\sim\mathbf{k}_o} &= \Lambda_{l,\mathbf{k}_o} + \Delta\mathbf{k} \cdot \langle h_{l,\mathbf{k}_o} | (-i\nabla(\eta_o) + 2\eta_o\mathbf{k}_o - 2i\eta_o\nabla) | h_{l,\mathbf{k}_o} \rangle_v + |\Delta\mathbf{k}|^2 \langle h_{l,\mathbf{k}_o} | \eta_o | h_{l,\mathbf{k}_o} \rangle_v \\ &+ \sum_{l' \neq l} \frac{|\Delta\mathbf{k} \cdot \langle h_{l',\mathbf{k}_o} | (-i\nabla(\eta_o) + 2\eta_o\mathbf{k}_o - 2i\eta_o\nabla) | h_{l,\mathbf{k}_o} \rangle_v|^2}{(\Lambda_{l,\mathbf{k}_o} - \Lambda_{l',\mathbf{k}_o})}. \end{aligned} \quad (1.76)$$

If \mathbf{k}_o corresponds to an extremal point within the bandstructure, then the linear $\Delta\mathbf{k}$ terms in equation (1.76) are identically zero. One can check that for the X -point conduction and valence band modes of equation (1.70), this is indeed the case. Substituting the periodic functions of the conduction and valence band modes of equation (1.71) into equation (1.76) gives the local X -point bandstructure of the conduction band as:

$$\begin{aligned} \Lambda_{c,\mathbf{k}\sim\mathbf{k}_{X_i}} &= \Lambda_{c,\mathbf{k}_{X_i}} + |\Delta\mathbf{k}|^2 \langle h_{c,\mathbf{k}_{X_i}} | \eta_o | h_{c,\mathbf{k}_{X_i}} \rangle_v \\ &+ \frac{|\Delta\mathbf{k} \cdot \langle h_{v,\mathbf{k}_{X_i}} | (-i\nabla(\eta_o) + 2\eta_o\mathbf{k}_{X_i} - 2i\eta_o\nabla) | h_{c,\mathbf{k}_{X_i}} \rangle_v|^2}{\Delta\Lambda_X}, \end{aligned} \quad (1.77)$$

where $\Delta\Lambda_X \equiv (\Lambda_{c,\mathbf{k}_X} - \Lambda_{v,\mathbf{k}_X})$.

Fourier expanding η_o ,

$$\eta_o = \sum_{\mathbf{G}} \tilde{\eta}_{o,\mathbf{G}} e^{i\mathbf{G} \cdot \mathbf{r}^a}, \quad (1.78)$$

allows the bandstructure to be evaluated in terms of the Fourier coefficients of the dielectric PC. Since η_o is a lattice periodic *real* function, \mathbf{G} are reciprocal lattice vectors and $\tilde{\eta}_{o,\mathbf{G}} = (\tilde{\eta}_{o,-\mathbf{G}})^*$. With the origin located at point a of the lattice (see fig. 1.2(a)), the hexagonal PC has C_{6v} symmetry. As a result the Fourier coefficients of the hexagonal lattice are all real (inversion symmetry of the lattice), and $\tilde{\eta}_{o,2\mathbf{k}_{X_i}} = \tilde{\eta}_{o,2\mathbf{k}_{X_j}}$, for all $\mathbf{k}_{X_i}, \mathbf{k}_{X_j} \in \star\mathbf{k}$. Also, as point a lies within the center of an air hole, the fundamental Fourier coefficients of the lattice, $\tilde{\eta}_{o,2\mathbf{k}_{X_i}}$, must be positive. Substituting equation (1.78) into equation (1.77) gives,

nature of the magnetic field. In order to form a complete basis one must include zero frequency unphysical solutions. As we neglect the contribution of remote bands in our analysis, which the zero frequency solutions certainly are, no significant additional error is to be expected.

$$\Lambda_{c,\mathbf{k}\sim\mathbf{k}_{X_i}} = \Lambda_{c,\mathbf{k}_X} + |\Delta\mathbf{k}|^2 \left(\tilde{\eta}_{o,\mathbf{0}} - \tilde{\eta}_{o,2\mathbf{k}_X} \right) + \frac{4|(\Delta\mathbf{k} \cdot \mathbf{k}_{X_i})|^2 (\tilde{\eta}_{o,\mathbf{0}})^2}{\Delta\Lambda_X}, \quad (1.79)$$

where the index i has been dropped from \mathbf{k}_{X_i} in those quantities that have the same value for each element of the $\star\mathbf{k}$.

The bandgap at the X -point, $\Delta\Lambda_X$, may also be approximately determined in terms of the Fourier coefficients $\tilde{\eta}_{o,\mathbf{G}}$. The magnetic field eigenoperator \hat{L}_H can be written as,

$$\hat{L}_H = -\tilde{\eta}_{o,\mathbf{0}}\nabla^2 - \sum_{\mathbf{G} \neq \mathbf{0}} \tilde{\eta}_{o,\mathbf{G}} e^{i\mathbf{G} \cdot \mathbf{r}} (\nabla^2 + i\tilde{\eta}_{o,\mathbf{G}} \mathbf{G} \cdot \nabla). \quad (1.80)$$

Treating $\Delta\eta_o = \sum_{\mathbf{G} \neq \mathbf{0}} \tilde{\eta}_{o,\mathbf{G}} e^{i\mathbf{G} \cdot \mathbf{r}}$ as a perturbation to the average dielectric $\tilde{\eta}_{o,\mathbf{0}}$, and considering only the coupling between the forward and backward normalized plane wave states at the X -point, $(|\mathbf{k}_{X_i}\rangle, |-\mathbf{k}_{X_i}\rangle)$, results in the following two band magnetic field eigenoperator:

$$\hat{L}_H^{X_i} = \begin{pmatrix} \tilde{\eta}_{o,\mathbf{0}}|\mathbf{k}_X|^2 & -\tilde{\eta}_{o,2\mathbf{k}_X}|\mathbf{k}_X|^2 \\ -\tilde{\eta}_{o,2\mathbf{k}_X}|\mathbf{k}_X|^2 & \tilde{\eta}_{o,\mathbf{0}}|\mathbf{k}_X|^2 \end{pmatrix}. \quad (1.81)$$

The eigenvalues of $\hat{L}_H^{X_i}$ are $\tilde{\eta}_{o,\mathbf{0}}|\mathbf{k}_X|^2 \pm (\tilde{\eta}_{o,2\mathbf{k}_X})|\mathbf{k}_X|^2$, which gives for the bandgap, $\Delta\Lambda_X = 2(\tilde{\eta}_{o,2\mathbf{k}_X})|\mathbf{k}_X|^2$.

Choosing a coordinate basis $\hat{\mathbf{x}}_i$ with \hat{x}_i orthogonal to \mathbf{k}_{X_i} and \hat{y}_i parallel to \mathbf{k}_{X_i} , allows us to write for the local bandstructure of the conduction band in the vicinity of the X_i -point,

$$\Lambda_{c,\mathbf{k}\sim\mathbf{k}_{X_i}} = \Lambda_{c,\mathbf{k}_X} + \frac{\Delta\mathbf{k}_{X_i}^2}{m_{c,X,x_i}^*} + \frac{\Delta\mathbf{k}_{y_i}^2}{m_{c,X,y_i}^*}, \quad (1.82)$$

with effective “masses”⁶ defined as,

⁶We use the term “mass” here in analogy to solid-state physics where the curvature of the bandstructure is related to the inverse of an effective electron mass. m^* as defined here is unitless.

$$\begin{aligned}\frac{1}{m_{c,X,x_i}^*} &= \tilde{\eta}_{o,\mathbf{0}} \left(1 - \frac{\tilde{\eta}_{o,2\mathbf{k}_X}}{\tilde{\eta}_{o,\mathbf{0}}} \right) \\ \frac{1}{m_{c,X,y_i}^*} &= \tilde{\eta}_{o,\mathbf{0}} \left(1 - \frac{\tilde{\eta}_{o,2\mathbf{k}_X}}{\tilde{\eta}_{o,\mathbf{0}}} + \frac{2\tilde{\eta}_{o,\mathbf{0}}}{\tilde{\eta}_{o,2\mathbf{k}_X}} \right).\end{aligned}\tag{1.83}$$

For a PC formed from dielectric materials with real refractive indices greater than that of vacuum, $0 \leq \eta_o(\mathbf{r}) \leq 1$. Consequently, $\tilde{\eta}_{o,\mathbf{0}} \geq 0$ and $\tilde{\eta}_{o,\mathbf{0}} \geq 2\tilde{\eta}_{o,\mathbf{G}}$ for all \mathbf{G} . The effective masses for the conduction band at the X -point are thus both positive.

Evaluating the scalar and vector coupling matrix elements using the X_i -point conduction band modes of equation (1.71) gives: $K_{l,l}(\mathbf{k}_{X_i}, \mathbf{k}_{X_i}, \mathbf{0}) = |\mathbf{k}_X|^2$ and $\mathbf{L}_{l,l}(\mathbf{k}_{X_i}, \mathbf{k}_{X_i}, \mathbf{0}) = \mathbf{0}$. Substituting these coupling matrix elements into equation (1.66), the effective Wannier potential is,

$$\Delta\eta'_{i,i}(\mathbf{r}) = |\mathbf{k}_X|^2 \Delta\eta(\mathbf{r}).\tag{1.84}$$

Lastly, upon substituting the local bandstructure of equation (1.82) and the effective Wannier potential of equation (1.84) into equation (1.67), we have for the Wannier equation of the conduction band envelope at the i th X -point:

$$\left((\Lambda_d - \Lambda_{c,\mathbf{k}_X}) - \left(\frac{-\nabla_{x_i}^2}{m_{c,X,x_i}^*} + \frac{-\nabla_{y_i}^2}{m_{c,X,y_i}^*} + |\mathbf{k}_X|^2 \Delta\eta(\mathbf{r}) \right) \right) \Gamma_{c,\mathbf{k}_{X_i}}(\mathbf{r}) = 0.\tag{1.85}$$

We now see from the Wannier-like equation for the conduction band edge at the X -point that as a result of the positive effective mass coefficients, localized resonant modes will form for perturbations to the hexagonal lattice in which $\Delta\eta(\mathbf{r})$ is locally reduced, that is for which the refractive index is locally *increased*.

Here we consider a defect which results in an approximate harmonic perturbation potential. By appropriately varying the hole radii of a photonic crystal consisting of a hexagonal array of air holes in a host dielectric material, the inverse of the filling fraction of the hexagonal crystal can be graded in a roughly parabolic fashion. The filling fraction of the lattice, f , as a function of air hole radius is,

$$f = 1 - \frac{2\pi}{\sqrt{3}} \left(\frac{r}{a} \right)^2, \quad (1.86)$$

where r is the hole radius and a is the nearest neighbor distance between holes of the hexagonal lattice. For a host dielectric material of refractive index n_o , the average dielectric constant of the patterned crystal is $\bar{\epsilon} = f(n_o)^2$. The slowly varying envelope of η_o ($\bar{\eta}_o$), neglecting rapid variations on the scale of the lattice spacing, is proportional to $1/f$, $\bar{\eta}_o = (n_o)^{-2}/f$. For an approximate harmonic potential then, the filling fraction of the lattice should vary as,

$$\frac{1}{f(\rho)} = \frac{1}{f_o} + k \left(\frac{\rho}{a} \right)^2, \quad (1.87)$$

with ρ representing the radial distance from the center of the defect, f_o the filling fraction given by the air hole radius at the center of the defect, and k the lattice grading coefficient. The filling fraction as used here is a local approximation, based upon the local hole radius, of the true filling fraction of a crystal lattice. The resulting slowly varying envelope of the effective Wannier potential is,

$$\overline{\Delta\eta'}_{i,i}(\rho) = k \left(\frac{\rho}{a} \right)^2 \left(\frac{|\mathbf{k}_X|}{n_o} \right)^2. \quad (1.88)$$

The ground state solution to equation (1.85) with the harmonic effective potential of equation (1.88) is the 2D Gaussian,

$$\Gamma_{c,\mathbf{k}_{X_i}}(\mathbf{r}) = \exp \left[- \left(x_i^2 / \kappa^2 + y_i^2 / \gamma^2 \right) \right], \quad (1.89)$$

with decay constants,

$$\begin{aligned} \frac{1}{\kappa^2} &= \frac{1}{2} (\bar{k} m_{c,X,x_i}^*)^{\frac{1}{2}}, \\ \frac{1}{\gamma^2} &= \frac{1}{2} (\bar{k} m_{c,X,y_i}^*)^{\frac{1}{2}}, \end{aligned} \quad (1.90)$$

where $\bar{k} = k(|\mathbf{k}_X|/an_o)^2$.

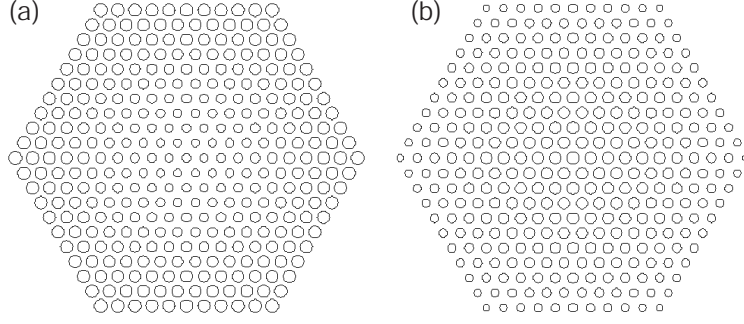


Figure 1.16: (a) Graded hexagonal lattice donor-type cavity, (b) graded hexagonal lattice acceptor-type cavity (parameters are given in table 1.4).

Table 1.4: Hexagonal PC parameters for the donor- and acceptor-type defect cavities.

cavity	n_o	$\left(\frac{r}{a}\right)_o$	f_o	k	\bar{k}/a^2	$\left(\frac{r}{a}\right)_e$	$\frac{\tilde{\eta}_{o,2k_Y}}{\eta_{o,0}}$
donor	2.65	0.25	0.77	0.01	0.019	0.4	0.294
acc.	2.65	0.35	0.56	-0.006	0.015	0.20	0.23

From equation (1.86), in order to obtain the parabolic grade in filling fraction, the normalized hole radius of the defect cavity must vary with ρ as,

$$\left(\frac{r}{a}\right)^2 = \frac{\sqrt{3}}{2\pi} \left(1 - f_o \frac{1}{1 + f_o k (\rho/a)^2}\right). \quad (1.91)$$

With grading parameters given in table 1.4, the donor-type defect cavity we consider here is plotted in fig. 1.16(a). The calculated parameters of the approximate envelope function for the donor modes of this defect cavity are given in table 1.5.

The point group symmetry of the donor-type defect cavity of fig. 1.16(a) centered about point

Table 1.5: Donor mode (X-point) ground state Wannier envelope parameters.

m_{c,X,x_i}^*	m_{c,X,y_i}^*	$\frac{\kappa}{a}$	$\frac{\gamma}{a}$
7.7	0.72	2.3	4.1

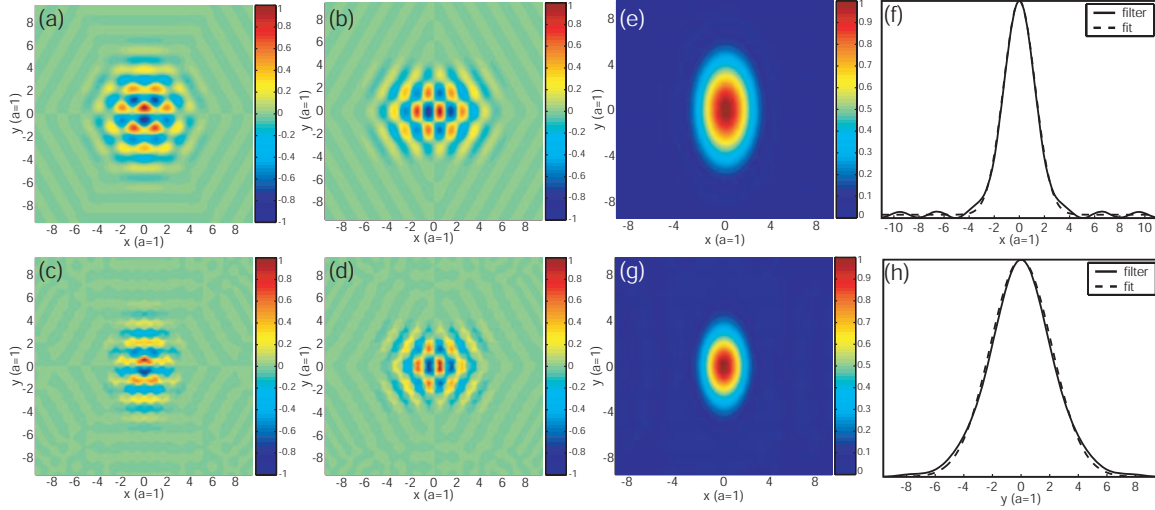


Figure 1.17: Magnetic field (\hat{z} -component) plot of the donor modes of the graded hexagonal donor-type cavity: (a) symmetry analysis $H_{E_1,1}^{a,d1}$ (x -dipole) mode, (b) symmetry analysis $H_{E_1,2}^{a,d1}$ (y -dipole) mode, (c) FDTD simulated x -dipole mode, and (d) FDTD simulated y -dipole mode. Comparison of: (e) Wannier and (g) FDTD envelope functions for $\mathbf{H}_{E_1,1}^{a,d1}$ (x -dipole) donor mode. (f) and (h) show line scans of the FDTD filtered envelope (solid line) along the \hat{x} - and \hat{y} -directions, respectively. The Gaussian fit to the FDTD envelope along these principal directions are also plotted (dashed line).

a of the hexagonal lattice is that of the underlying hexagonal lattice, C_{6v} . A set of basis functions for the localized conduction band donor modes was given in Equation 1.16, and has been rewritten here to include the conduction band envelope functions $\Gamma_{c,\mathbf{k}_{X_i}}$:

$$\begin{aligned}\mathbf{H}_{B_1''}^{a,d1} &= |c_{X_1}\rangle\Gamma_{c,\mathbf{k}_{X_1}} - |c_{X_2}\rangle\Gamma_{c,\mathbf{k}_{X_2}} + |c_{X_3}\rangle\Gamma_{c,\mathbf{k}_{X_3}}, \\ \mathbf{H}_{E_1,1}^{a,d1} &= 2|c_{X_1}\rangle\Gamma_{c,\mathbf{k}_{X_1}} + |c_{X_2}\rangle\Gamma_{c,\mathbf{k}_{X_2}} - |c_{X_3}\rangle\Gamma_{c,\mathbf{k}_{X_3}}, \\ \mathbf{H}_{E_1,2}^{a,d1} &= |c_{X_2}\rangle\Gamma_{c,\mathbf{k}_{X_2}} + |c_{X_3}\rangle\Gamma_{c,\mathbf{k}_{X_3}},\end{aligned}\tag{1.92}$$

In fig. 1.17(a)-(b) the magnetic field intensity is plotted for the dipole-like modes of the E_1 IRREP with envelope functions given by the $\Gamma_{c,\mathbf{k}_{X_i}}$ of equation (1.89). The calculated decay parameters for the Gaussian $\Gamma_{c,\mathbf{k}_{X_i}}$ are tabulated in table 1.5. Note that the coefficients of the expansion for each donor mode (c_i) are determined solely by the transformation properties of the basis CB_X^a ; the envelope functions transform effectively as the identity and do not modify the expansion coefficients.

For comparison, 2D FDTD simulations were performed on the donor-type cavity of fig. 1.16(a). Plots of the FDTD calculated magnetic field patterns (and their Fourier transforms) of the two modes most deep within the first order bandgap are given in fig. 1.17(c)-(d). The modes transform as the

Table 1.6: FDTD calculated mode envelope parameters.

mode	$\frac{\kappa}{a} (\frac{\kappa_x}{a})$	$\frac{\gamma}{a} (\frac{\kappa_y}{a})$
$\mathbf{H}_{E_{1,1}}^{a,d1}$	1.77	3.02
$\mathbf{H}_{A_2}^{a,a1}$	4.65	4.52
$\mathbf{H}_{B_2}^{a,a1}$	5.29	4.48

B_1'' and B_2'' IRREPs of the C_{2v} point group (the FDTD simulation was performed with mirror plane symmetries to reduce the size of the computation, thus projecting the modes onto the C_{2v} IRREPs), equivalent to the \hat{x} and \hat{y} basis of the C_{6v} IRREP E_1 (the basis chosen for modes $\mathbf{H}_{E_{1,1}}^{a,d1}$ and $\mathbf{H}_{E_{1,2}}^{a,d1}$). The FDTD generated field patterns show good correspondence with the field patterns of the approximate symmetry analysis (fig. 1.17(a)-(b)).

A more quantitative estimate of the envelope of the FDTD-generated localized modes can be obtained by considering the form of the approximate symmetry analysis modes of equation (1.92). Multiplying a donor mode which contains a dominant Fourier component at \mathbf{k}_{X_i} by $\cos(\mathbf{k}_{X_i} \cdot \mathbf{r}^a)$ will produce a term proportional to $\Gamma_{c,\mathbf{k}_{X_i}}$, thus shifting the envelope to the origin in Fourier space. Applying a low-pass spatial filter to the product of the mode and the cosine function will then leave only the envelope corresponding to $\Gamma_{c,\mathbf{k}_{X_i}}$. In fig. 1.17(f)-(h) we plot the result of such a procedure applied to the FDTD calculated $\mathbf{H}_{E_{1,1}}^{a,d1}$ (x -dipole) mode (fig. 1.17(e) shows a plot of the envelope calculated using the Wannier-like equation). The FDTD generated envelope is oriented parallel to \mathbf{k}_{X_1} , and as can be seen from fig. 1.17(f),(h) is Gaussian in nature. The fit decay parameters along \hat{x}_i and \hat{y}_i directions are given in table 1.6, and although smaller than estimated (table 1.5), they are in nearly the precise ratio predicted by the Wannier equation

1.2.3.2 Acceptor modes at the J -point

As mentioned above, the valence band edge of the fundamental bandgap for TE-like modes occurs at the J -point of the reciprocal lattice for the hexagonal PC. From section 1.1.2.2, the approximate form for the band edge states at the J -point is:

$$VB_J^a = \begin{pmatrix} v_{J_1} \\ v_{J_2} \end{pmatrix} = \hat{z} \begin{pmatrix} e^{i\mathbf{k}_{J_1} \cdot \mathbf{r}^a} + e^{i\mathbf{k}_{J_3} \cdot \mathbf{r}^a} + e^{i\mathbf{k}_{J_5} \cdot \mathbf{r}^a} \\ e^{i\mathbf{k}_{J_2} \cdot \mathbf{r}^a} + e^{i\mathbf{k}_{J_4} \cdot \mathbf{r}^a} + e^{i\mathbf{k}_{J_6} \cdot \mathbf{r}^a} \end{pmatrix}, \quad (1.93)$$

for valence band modes, and

$$CB_J^a = \begin{pmatrix} c1_{J_1} \\ c2_{J_1} \\ c1_{J_2} \\ c2_{J_2} \end{pmatrix} = \hat{z} \begin{pmatrix} e^{-i\mathbf{k}_{J_1} \cdot \mathbf{r}^a} + e^{-i\mathbf{k}_{J_3} \cdot \mathbf{r}^a} - 2e^{-i\mathbf{k}_{J_5} \cdot \mathbf{r}^a} \\ e^{-i\mathbf{k}_{J_1} \cdot \mathbf{r}^a} - e^{-i\mathbf{k}_{J_3} \cdot \mathbf{r}^a} \\ e^{-i\mathbf{k}_{J_2} \cdot \mathbf{r}^a} + e^{-i\mathbf{k}_{J_4} \cdot \mathbf{r}^a} - 2e^{-i\mathbf{k}_{J_6} \cdot \mathbf{r}^a} \\ e^{-i\mathbf{k}_{J_2} \cdot \mathbf{r}^a} - e^{-i\mathbf{k}_{J_4} \cdot \mathbf{r}^a} \end{pmatrix}. \quad (1.94)$$

for conduction band modes. The normalized periodic functions of the above Bloch modes are,

$$\begin{aligned} h_{v,\mathbf{k}_{J_1}} &= \frac{1}{\sqrt{3}}(1 + e^{-i2\mathbf{k}_{X_1} \cdot \mathbf{r}^a} + e^{-i2\mathbf{k}_{X_2} \cdot \mathbf{r}^a}), \\ h_{v,\mathbf{k}_{J_2}} &= \frac{1}{\sqrt{3}}(1 + e^{-i2\mathbf{k}_{X_2} \cdot \mathbf{r}^a} + e^{-i2\mathbf{k}_{X_3} \cdot \mathbf{r}^a}), \end{aligned} \quad (1.95)$$

$$\begin{aligned} h_{c1,\mathbf{k}_{J_1}} &= \frac{1}{\sqrt{6}}(1 + e^{-i2\mathbf{k}_{X_1} \cdot \mathbf{r}^a} - 2e^{-i2\mathbf{k}_{X_2} \cdot \mathbf{r}^a}), \\ h_{c1,\mathbf{k}_{J_2}} &= \frac{1}{\sqrt{6}}(1 + e^{-i2\mathbf{k}_{X_2} \cdot \mathbf{r}^a} - 2e^{-i2\mathbf{k}_{X_3} \cdot \mathbf{r}^a}), \end{aligned} \quad (1.96)$$

$$\begin{aligned} h_{c2,\mathbf{k}_{J_1}} &= \frac{1}{\sqrt{2}}(1 - e^{-i2\mathbf{k}_{X_1} \cdot \mathbf{r}^a}), \\ h_{c2,\mathbf{k}_{J_2}} &= \frac{1}{\sqrt{2}}(1 - e^{-i2\mathbf{k}_{X_2} \cdot \mathbf{r}^a}). \end{aligned} \quad (1.97)$$

The local bandstructure for the valence band at the J_1 -point, upon evaluating equation (1.76) using the approximate J_1 -point valence and conduction band modes above, is

$$\begin{aligned}
\Lambda_{v,\mathbf{k}\sim\mathbf{k}_{J_1}} &= \Lambda_{v,\mathbf{k}_J} + |\Delta\mathbf{k}|^2 \left(\tilde{\eta}_{o,\mathbf{0}} + 2\tilde{\eta}_{o,2\mathbf{k}_X} \right) \\
&\quad - \left(|\Delta\mathbf{k} \cdot \mathbf{k}_{J_2}|^2 \frac{\left(2(\tilde{\eta}_{o,\mathbf{0}})^2 + \frac{1}{2}(\tilde{\eta}_{o,2\mathbf{k}_X})^2 + 2(\tilde{\eta}_{o,\mathbf{0}})(\tilde{\eta}_{o,2\mathbf{k}_X}) \right)}{\Delta\Lambda_J} \right. \\
&\quad \left. + \frac{4}{3} |\Delta\mathbf{k} \cdot \mathbf{k}_{X_1}|^2 \frac{\left(2(\tilde{\eta}_{o,\mathbf{0}})^2 + \frac{1}{2}(\tilde{\eta}_{o,2\mathbf{k}_X})^2 + 2(\tilde{\eta}_{o,\mathbf{0}})(\tilde{\eta}_{o,2\mathbf{k}_X}) \right)}{\Delta\Lambda_J} \right) \\
&= \Lambda_{v,\mathbf{k}_J} + |\Delta\mathbf{k}|^2 \left(\tilde{\eta}_{o,\mathbf{0}} + 2\tilde{\eta}_{o,2\mathbf{k}_X} - \frac{|\mathbf{k}_J|^2 \left(2(\tilde{\eta}_{o,\mathbf{0}})^2 + \frac{1}{2}(\tilde{\eta}_{o,2\mathbf{k}_X})^2 + 2(\tilde{\eta}_{o,\mathbf{0}})(\tilde{\eta}_{o,2\mathbf{k}_X}) \right)}{\Delta\Lambda_J} \right),
\end{aligned} \tag{1.98}$$

where $\Delta\mathbf{k} = \mathbf{k} - \mathbf{k}_{J_1}$. To second order in the elements of $\Delta\mathbf{k}$, the local bandstructure around the J_1 -point of the valence band is centro-symmetric. As a result, the local bandstructure in the neighborhood of each of the J points of the $\star\mathbf{k}$ is also given by equation (1.98). In order to determine the sign of the curvature of the valence band, the bandgap at the J -point, $\Delta\Lambda_J$, is evaluated using a similar procedure as for the bandgap at the X -point. The three band eigenoperator, in the normalized plane wave basis of $(|\mathbf{k}_{J_1}\rangle, |\mathbf{k}_{J_3}\rangle, |\mathbf{k}_{J_5}\rangle)$, is:

$$\hat{L}_H^{J_1} = |\mathbf{k}_J|^2 \begin{pmatrix} \tilde{\eta}_{o,\mathbf{0}} & -\frac{1}{2}\tilde{\eta}_{o,2\mathbf{k}_X} & -\frac{1}{2}\tilde{\eta}_{o,2\mathbf{k}_X} \\ -\frac{1}{2}\tilde{\eta}_{o,2\mathbf{k}_X} & \tilde{\eta}_{o,\mathbf{0}} & -\frac{1}{2}\tilde{\eta}_{o,2\mathbf{k}_X} \\ -\frac{1}{2}\tilde{\eta}_{o,2\mathbf{k}_X} & -\frac{1}{2}\tilde{\eta}_{o,2\mathbf{k}_X} & \tilde{\eta}_{o,\mathbf{0}} \end{pmatrix}. \tag{1.99}$$

The eigenvalues of $\hat{L}_H^{J_1}$ consist of the single eigenvalue $\Lambda_{v,\mathbf{k}_J} = |\mathbf{k}_J|^2(\tilde{\eta}_{o,\mathbf{0}} - \tilde{\eta}_{o,2\mathbf{k}_X})$, and the double eigenvalue $\Lambda_{c,\mathbf{k}_J} = |\mathbf{k}_J|^2(\tilde{\eta}_{o,\mathbf{0}} + \tilde{\eta}_{o,2\mathbf{k}_X}/2)$. The bandgap at the J -point is then, $\Delta\Lambda_J = (3/2)\tilde{\eta}_{o,2\mathbf{k}_X}|\mathbf{k}_J|^2$. Substituting this value of $\Delta\Lambda_J$ into the equation (1.98) we have for the local bandstructure at each of the J -points,

$$\Lambda_{v,\mathbf{k}\sim\mathbf{k}_J} = \Lambda_{v,\mathbf{k}_J} + \frac{|\Delta\mathbf{k}|^2}{m_{v,J}^*}. \tag{1.100}$$

where the effective mass of the valence band is,

$$\frac{1}{m_{v,J}^*} = -\frac{1}{3}\tilde{\eta}_{o,0}\left(1 + 3\frac{\tilde{\eta}_{o,2\mathbf{k}_X}}{\tilde{\eta}_{o,0}} + \frac{4((\tilde{\eta}_{o,0})^2 - 2(\tilde{\eta}_{o,2\mathbf{k}_X})^2)}{(\tilde{\eta}_{o,0})(\tilde{\eta}_{o,2\mathbf{k}_X})}\right). \quad (1.101)$$

As expected for the valence band, the effective mass is negative at the J -point.

The scalar and vector coupling matrix elements, evaluated using the J_1 -point valence band mode of equation (1.95), are: $K_{v,v}(\mathbf{k}_{J_1}, \mathbf{k}_{J_1}, \mathbf{0}) = |\mathbf{k}_J|^2$ and $\mathbf{L}_{v,v}(\mathbf{k}_{J_1}, \mathbf{k}_{J_1}, \mathbf{0}) = \mathbf{0}$. The resulting effective Wannier potential at the J -point is given by,

$$\Delta\eta'_{i,i}(\mathbf{r}) = |\mathbf{k}_J|^2\Delta\eta(\mathbf{r}). \quad (1.102)$$

With the local bandstructure of equation (1.100) and the effective potential of equation (1.102), the Wannier equation of the valence band envelope at the J -point is:

$$\left((\Lambda_d - \Lambda_{v,\mathbf{k}_J}) - \left(\frac{-\nabla^2}{m_{v,J}^*} + |\mathbf{k}_J|^2\Delta\eta(\mathbf{r})\right)\right)\Gamma_{v,\mathbf{k}_J}(\mathbf{r}) = 0. \quad (1.103)$$

Due to the negative effective mass coefficient, localized resonant modes will form for local perturbations to the hexagonal lattice in which the refractive index is locally *decreased*. The acceptor-type defect is taken to consist of a grade in the radius of the air holes of the hexagonal crystal as defined in equation (1.91), with grading coefficient $k = -0.006$. The values of the parameters of the acceptor-type cavity are given in table 1.4 and a plot of the acceptor-type cavity is shown in fig. 1.16(b).

As was the case for the donor-type cavity, this grade in the hole radius results in an approximate parabolic potential well. Therefore, we take as our approximate ground state envelope function the Gaussian,

$$\Gamma_{v,\mathbf{k}_J}(\mathbf{r}) = \exp\left[-(\rho/\kappa)^2\right], \quad (1.104)$$

with $\rho = |\mathbf{r}_\perp|$ the in-plane radius, and κ a single parameter decay constant given by,

Table 1.7: Acceptor mode (J -point) ground state Wannier envelope parameters

$m_{v,J}^*$	$\frac{\kappa}{a} = \frac{\kappa_x}{a} = \frac{\kappa_y}{a}$
-0.68	4.44

$$\frac{1}{\kappa^2} = \frac{1}{2} (\bar{k} |m_{v,J}^*|)^{\frac{1}{2}}, \quad (1.105)$$

where $\bar{k} = |k|(|\mathbf{k}_J|/an_o)^2$. The value of κ/a as calculated for the acceptor-type defect of fig. 1.16(b) is given in table 1.7.

From equation (1.20), we have a form for acceptor modes formed at the J -point of the hexagonal lattice. Rewriting these equations to include the Wannier envelope functions, we arrive at:

$$\begin{aligned} \mathbf{H}_{A_2''}^{a,a1} &= |v_{J_1}\rangle \Gamma_{v,\mathbf{k}_J} + |v_{J_2}\rangle \Gamma_{v,\mathbf{k}_J} \\ &\propto \hat{z} (\cos(\mathbf{k}_{J_1} \cdot \mathbf{r}) + \cos(\mathbf{k}_{J_2} \cdot \mathbf{r}) + \cos(\mathbf{k}_{J_3} \cdot \mathbf{r})) \Gamma_{v,\mathbf{k}_J}, \\ \mathbf{H}_{B_2''}^{a,a1} &= |v_{J_1}\rangle \Gamma_{v,\mathbf{k}_J} - |v_{J_2}\rangle \Gamma_{v,\mathbf{k}_J} \\ &\propto \hat{z} (\sin(\mathbf{k}_{J_1} \cdot \mathbf{r}) + \sin(\mathbf{k}_{J_2} \cdot \mathbf{r}) + \sin(\mathbf{k}_{J_3} \cdot \mathbf{r})) \Gamma_{v,\mathbf{k}_J}, \end{aligned} \quad (1.106)$$

where the Γ_{v,\mathbf{k}_J} are equivalent for each element of the $\star\mathbf{k}$ due to the isotropic effective mass of the J -point valence band. A plot of the magnetic field (\hat{z} -component) for the symmetry basis modes $\mathbf{H}_{A_2''}^{a,a1}$ and $\mathbf{H}_{B_2''}^{a,a1}$ are given in fig. 1.18(a)-(b).

2D FDTD simulations of the acceptor-type cavity of fig. 1.16(b) and table 1.4 were also performed. The two deepest modes within the first order bandgap are found to be of A_2'' and B_2'' symmetry, the same symmetry as the modes predicted by the approximate analysis. Plots of the FDTD calculated magnetic field patterns of these modes are given in fig. 1.18(c)-(d), again showing a strong resemblance to the approximately generated field patterns. Figure 1.18(e)-(h) shows a series of plots of the envelope ($\Gamma_{v,\mathbf{k}_{J_1}}$) of the acceptor mode $\mathbf{H}_{A_2''}^{a,a1}$. The size and shape (isotropic) of the FDTD calculated mode envelope corresponds very nicely with the approximate Wannier envelope as can be seen by the Gaussian fits in fig. 1.18(f)-(h) and the values of the fit decay constants given in table 1.6. A similar envelope was extracted for mode $\mathbf{H}_{B_2''}^{a,a1}$, with its fit decay constants given in

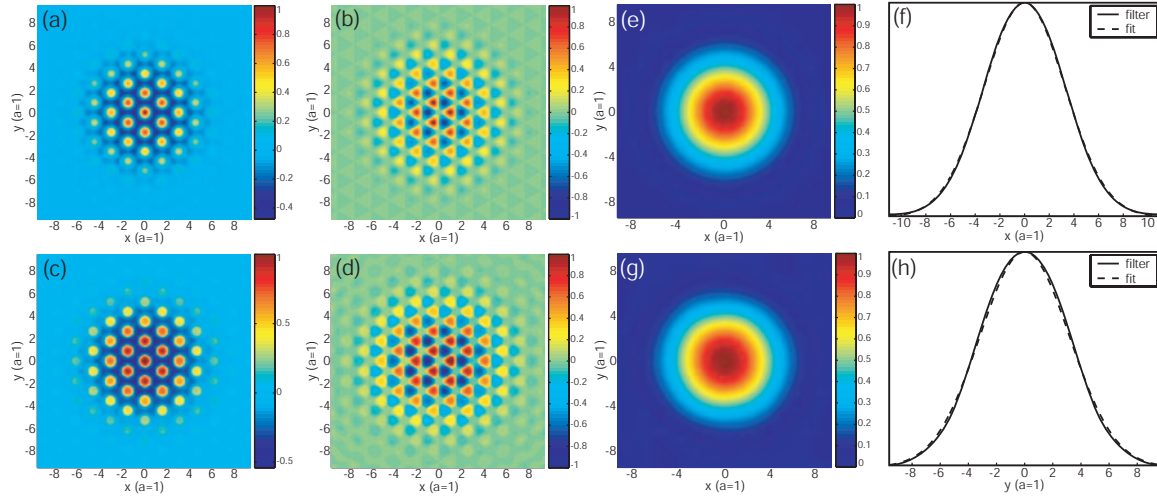


Figure 1.18: Magnetic field (\hat{z} -component) plots of the acceptor modes of the graded hexagonal lattice acceptor-type cavity: (a) symmetry analysis A_2'' mode, (b) symmetry analysis B_2'' mode, (c) FDTD A_2'' mode, and (d) FDTD B_2'' mode. Comparison of: (e) Wannier (see table 1.7) and (g) FDTD envelope functions for the $\mathbf{H}_{A_2}^{a,a1}$ acceptor mode. (f) and (h) show line scans of the FDTD filtered envelope (solid line) along the \hat{x} - and \hat{y} -directions, respectively. The Gaussian fit to the FDTD envelope along these principal directions are also plotted (dashed line).

table 1.6 as well.

Chapter 2

Momentum Space Design of High- Q Photonic Crystal Microcavities

2.1 Introduction

As I have discussed in the preface, there has been a considerable amount of interest in extending cavity QED experiments to the semiconductor regime. In these experiments, coherent interactions between a single quantum dot (QD) and a single photon within the semiconductor microcavity can take place if the system is in the so-called strong coupling regime [9], where the QD-cavity coupling strength g exceeds the QD dephasing rate γ_{\perp} and the cavity decay rate κ . As of just a few years ago (i.e, at the start of our work in the area), no semiconductor microcavity had been demonstrated that had the requisite combination of a high quality factor (Q) and small mode volume (V_{eff}) to achieve strong coupling ($\kappa \sim 1/Q$, $g \sim 1/V_{\text{eff}}^{1/2}$). Photonic crystal (PC) microcavities seemed to be a particularly appealing route to semiconductor-based strong coupling; the ultrasmall volumes to which they confined light (smaller than the modal confinement that had been achieved in micropost or microdisk cavities, for example) implied that the Q values needed to achieve strong coupling would be more modest than in other geometries. The focus of this chapter is on the design of PC microcavities with sufficiently high Q s for these applications. It is based largely on references [21] and [23], which were published in July 2002 and March 2003.

While the PC microcavities studied in ref. [8] had very small mode volumes and loss properties sufficient to sustain lasing, the measured Q values were still less than 1000. In particular, the radiation losses were predominantly out of plane, while the in-plane losses were in comparison small [7]. Although refinements in design [11] and fabrication [12] had since increased the total measured Q to as high as 2,800, applications in cavity QED require Q values on the order of 10^4 to

achieve strong coupling (assuming $V_{\text{eff}} \sim (\lambda/n)^3$).

The limitations on Q stem from a number of possible factors, including intrinsic material absorption, etch-induced surface roughness and surface-state absorption, and other fabrication irregularities that prevent ideal replication of a given design. These issues aside, the fundamental design of these cavities had left room for improvement, and as such, the focus of this chapter primarily lies here. Our main objective is to consider simple design rules that can be used to significantly reduce the vertical losses from these structures, while maintaining or even improving upon the in-plane losses. In section 2.2, we describe a simple picture which illustrates that the vertical radiation loss of a mode is characterized by the presence of momentum components within the light cone of the cladding of the host slab waveguide (WG). We then consider (section 2.3) the use of symmetry to eliminate in-plane momentum components (\mathbf{k}_\perp) at $\mathbf{k}_\perp = 0$ (DC), thereby reducing the vertical loss in the structure. Drawing heavily from chapter 1, we summarize the different defect modes available in hexagonal and square lattice PCs, and proceed to choose target symmetries for modes in these lattices based upon the constraints they impose on the dominant field components of the modes. In section 2.4, we propose simple defect geometries that support such modes and present the results of three-dimensional (3D) finite-difference time-domain (FDTD) calculations of their relevant properties. In section 2.5, we consider further improvements in the designs based on a Fourier space tailoring of the defect geometries that reduces coupling of the mode's dominant Fourier components to components that radiate. The results of FDTD simulations of these improved designs in a square lattice are presented, and show that a modal Q -factor approaching 10^5 can be achieved by a careful consideration of the mode and defect geometry in Fourier space. Similar considerations are given in sections 2.6 and 2.7, where we consider the design of high- Q defect modes within standard and compressed hexagonal lattice photonic crystals. Comparable results in terms of Q ($\sim 10^5$) and V_{eff} ($\sim (\lambda/n)^3$) are achieved in these lattices.

2.2 Momentum space consideration of vertical radiation loss

The optical cavities studied here are comprised of defects situated in 2D PC slab WGs (fig. 2.1). As a result, the in-plane confinement of the cavity modes is governed by the distributed Bragg reflection (DBR) of the surrounding photonic lattice. Leakage of light in the plane of the PC slab WG from the cavity is thus determined by the number of periods of the host lattice surrounding the defect and the width and angular extent of the in-plane guided mode bandgap. Vertical confinement, on the

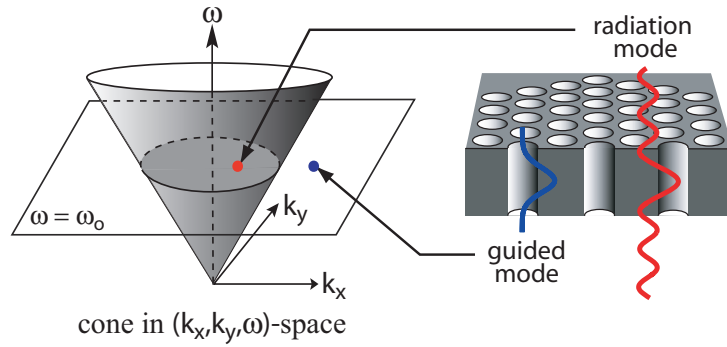


Figure 2.1: 2D hexagonal PC slab waveguide structure and cladding light cone.

other hand, is due to standard waveguiding by total internal reflection. Vertical radiation loss occurs when the magnitude of the in-plane momentum component, k_{\perp} , is inappropriate to support guiding. More concretely, we note that the energy-momentum dispersion relationship for a homogenous dielectric cladding (refractive index n) of the PC slab WG is $(n\omega/c)^2 = k_{\perp}^2 + k_z^2$, where ω is the angular frequency, k_z is the momentum normal to the slab, and c is the speed of light. For an air clad PC WG as studied here, $k_{\perp}^2 = (\omega/c)^2$ defines a cone in (k_x, k_y, ω) space, commonly referred to as the “light cone” (fig. 2.1). Modes that radiate vertically will have small in-plane momentum components that lie within the light cone of the cladding, thereby creating an oscillatory (radiating) field in the air instead of an evanescently decaying field. Equivalently, from a ray optics perspective, modes with in-plane momenta lying within the cladding light cone do not meet the total internal reflection condition at the semiconductor-air interface. This simple rule serves as our fundamental guideline in designing cavities that limit vertical radiation loss. In particular, we seek out structures that support resonant modes whose in-plane momentum components are primarily situated outside of the cladding light cone.

Before discussing methods to improve the vertical loss properties of PC defect cavities, it is instructive to consider the characteristics of the previously studied [7] dipole-like defect modes in a hexagonal lattice PC. Consider the x -dipole donor mode produced by a symmetric defect consisting of the removal of a single air hole from a hexagonal lattice of air holes in a 2D slab WG, as discussed in the previous chapter. Following the symmetry analysis presented in chapter 1, we see that this mode is composed of dominant Fourier components directed along $\pm\{\mathbf{k}_{X_1}, \mathbf{k}_{X_2}, \mathbf{k}_{X_3}\}$, where the \mathbf{k}_X directions are shown in the hexagonal PC reciprocal space lattice of fig. 2.2(a). The 2D spatial Fourier Transform (FT) of the x -dipole field component \mathbf{E}_x at the middle of the PC slab WG is given

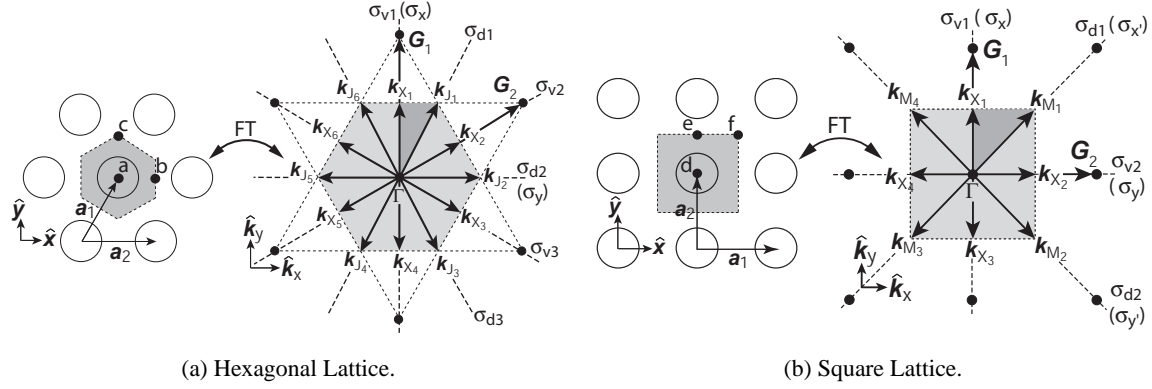


Figure 2.2: Real and reciprocal space lattices of (a) a 2D hexagonal lattice, and (b) a 2D square lattice. For the hexagonal lattice: $|\mathbf{a}_1| = |\mathbf{a}_2| = a$, $|\mathbf{G}_1| = |\mathbf{G}_2| = 4\pi/\sqrt{3}a$, $|\mathbf{k}_X| = 2\pi/\sqrt{3}a$, $|\mathbf{k}_J| = 4\pi/3a$. For the square lattice: $|\mathbf{a}_1| = |\mathbf{a}_2| = a$, $|\mathbf{G}_1| = |\mathbf{G}_2| = 2\pi/a$, $|\mathbf{k}_X| = \pi/a$, $|\mathbf{k}_M| = \sqrt{2}\pi/a$.

in fig. 2.3(a). It shows the E -field to be primarily composed of momentum components located about the X points, with $\pm\mathbf{k}_{X1}$ as the strongest components. Note that the field has a significant amplitude for momentum components lying within the light cone, the boundary of which is shown in fig. 2.3(a) as a dashed white circle. These low momentum components radiate and are the cause of the mode's relatively low effective vertical Q -factor ($Q_{\perp} \approx 1000$).

2.3 Summary of the symmetry analysis of defect modes in hexagonal and square lattices

There are a number of ways to limit the presence of small in-plane momentum components in the localized resonant modes of PC slab WG defect cavities. For example, the geometry of the defect and the surrounding holes can be tailored to reduce the magnitude of these components, as was done in ref. [11], where the authors report a predicted Q of 30,000. One particularly appealing way to limit the presence of small in-plane momentum components is to use symmetry to enforce specific boundary conditions on the Fourier space representation of the mode. A defect will support one or more resonant modes with symmetries that are compatible with the nature of the defect and the surrounding PC. Of particular interest are modes whose symmetry is odd about mirror planes normal to the dominant Fourier components of the mode. In the context of our symmetry analysis, the fields of the approximate TE-like modes have in-plane electric field polarization normal

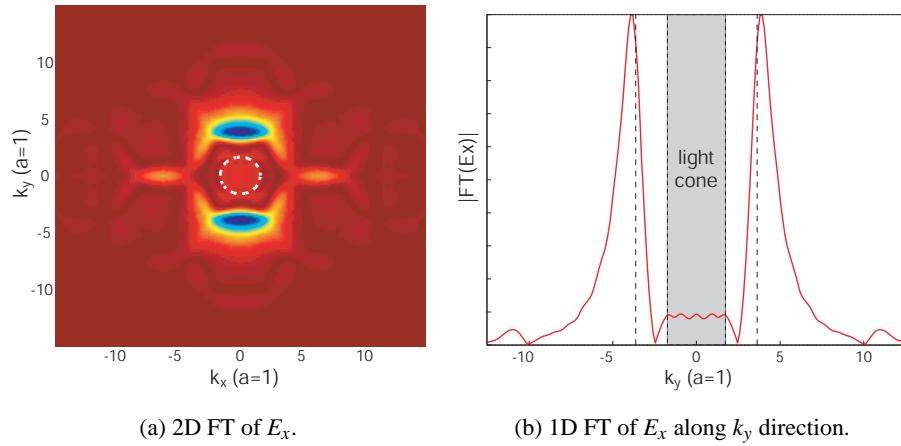


Figure 2.3: Spatial FT of x -dipole donor mode in a hexagonal lattice ($r/a = 0.30$) with a central missing air hole. (a) in 2D, (b) along the k_y direction with $k_x = 0$.

to the direction of their dominant Fourier components. In Fourier space, our choice of symmetry is equivalent to eliminating these in-plane electric field polarizations at $\mathbf{k}_\perp = 0$ (DC). This elimination of DC momentum components is the first step in reducing vertical radiation loss, and serves as our fundamental criterion for choosing the desired symmetry for our defect modes.¹ In addition, as we shall discuss later within this thesis (chapter 4), this use of a symmetry as a primary mechanism for reducing vertical radiation loss is also important from the standpoint of making cavities whose Q s are relatively robust to perturbations in their geometries.

The defect modes of a PC cavity are generally classified into donor- and acceptor-type modes [94], based upon whether the defect creates modes from the conduction band edge (donor modes) or valence band edge (acceptor modes). For the hexagonal lattice, whose real and reciprocal space depictions are given in fig. 2.2(a), the valence band edge is at the J -point and the conduction band edge is at the X -point (fig. 2.4(a)), while the square lattice of fig. 2.2(b) has its valence band edge at the M -point and conduction band edge at the X -point (fig. 2.4(b)). The dominant Fourier components and symmetry of a defect mode are determined by the type of mode (donor or acceptor) under consideration, the symmetry of the surrounding PC lattice, and the point group symmetry of the defect. The use of such an analysis to produce approximate forms for the modes in hexagonal and square lattice PC defect cavities was the focus of section 1.1, and as a result, here, we primarily incorporate the results of that chapter and describe their implications towards the

¹This can be viewed in the far-field as elimination of lower-order multi-pole radiation components, as has been considered by Johnson and co-workers [108]

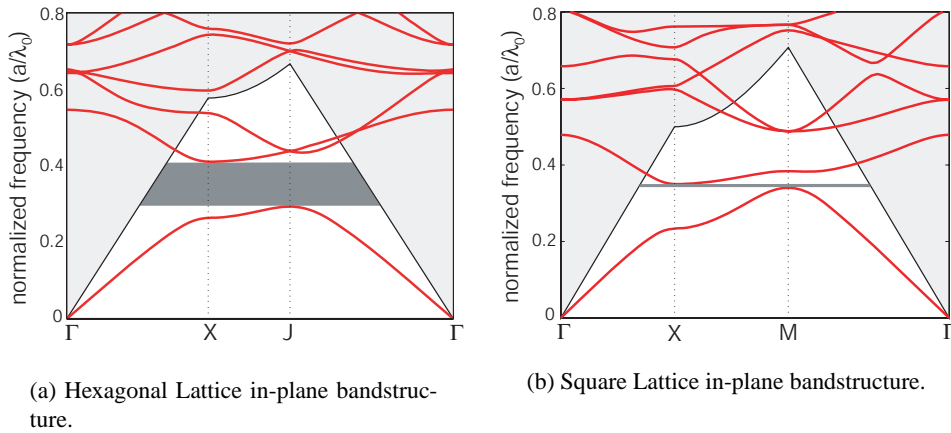


Figure 2.4: Fundamental TE-like (even) guided mode bandstructure for hexagonal and square lattices, calculated using a 2D plane-wave expansion method with an effective index for the vertical guiding: (a) hexagonal lattice with $r/a = 0.36$, $n_{\text{slab}} = n_{\text{eff}} = 2.65$, (b) square lattice with $r/a = 0.40$, $n_{\text{slab}} = n_{\text{eff}} = 2.65$.

design of high- Q defect resonators. The course of study is the following: we use the results of this group-theory-based analysis to determine the symmetry and dominant Fourier components for the available donor and acceptor type modes formed at different high symmetry points within hexagonal and square lattice PCs. Candidate modes for high- Q resonators are then chosen from these sets of available modes based upon the criteria placed on the mode's momentum components as described above. Within the mirror plane of the slab WG (coordinates \mathbf{r}_{\perp}) the TE modes are described by the field components \mathbf{E}_x , \mathbf{E}_y , and \mathbf{H}_z . Since the magnetic field is exactly scalar within this mirror plane, the criterion reduces to looking for modes in which the magnetic field pattern is spatially even in the directions of its dominant Fourier components. This is equivalent to having the in-plane electric field components spatially odd in these directions.

2.3.1 Hexagonal lattice

For a hexagonal lattice, the high symmetry points about which a defect may be formed are points a (C_{6v} symmetry), b (C_{2v} symmetry), and c (C_{3v,σ_v} symmetry) shown in fig. 2.2(a). Here, we consider donor and acceptor modes formed only at points a and b , as from the analysis presented in the previous chapter, those centered at point c do not contribute modes with the requisite symmetry and dominant Fourier components. We also examine reduced symmetry modes formed at point a , where the reduction of symmetry from C_{6v} to C_{2v} is accomplished by choosing a defect that

Table 2.1: Symmetry classification and dominant Fourier components for the \mathbf{H} -field of conduction band donor modes in a hexagonal lattice.

Defect Center	C_{6v} Modes	Fourier Comp.	$(\sigma_d, \sigma_v)^a$	C_{2v} Modes	$(\sigma_x, \sigma_y)^a$
(0,0)	$\mathbf{H}_{B_1'}^{a,d1}$	$\pm\{\mathbf{k}_{X_1}, \mathbf{k}_{X_2}, \mathbf{k}_{X_3}\}$	$(+, -)$	$\mathbf{H}_{B_1}^{a,d1,1}$	$(-, +)$
(0,0)	$\mathbf{H}_{E_1,1}^{a,d1}$	$\pm\{\mathbf{k}_{X_1}, \mathbf{k}_{X_2}, \mathbf{k}_{X_3}\}$	$(0, 0)$	$\mathbf{H}_{B_1}^{a,d1,2}$	$(-, +)$
(0,0)	$\mathbf{H}_{E_1,2}^{a,d1}$	$\pm\{\mathbf{k}_{X_2}, \mathbf{k}_{X_3}\}$	$(0, 0)$	$\mathbf{H}_{B_2}^{a,d1}$	$(+, -)$
$(a/2, 0)$	N/A ^b	$\pm\{\mathbf{k}_{X_2}, \mathbf{k}_{X_3}\}$	N/A	$\mathbf{H}_{A_1}^{b,d1}$	$(+, +)$
$(a/2, 0)$	N/A	$\pm\{\mathbf{k}_{X_2}, \mathbf{k}_{X_3}\}$	N/A	$\mathbf{H}_{A_2}^{b,d1}$	$(-, -)$
$(a/2, 0)$	N/A	$\pm\{\mathbf{k}_{X_1}\}$	N/A	$\mathbf{H}_{B_1}^{b,d1}$	$(-, +)$

^a Character values.

^b Not applicable. Modes centered at point b are of C_{2v} symmetry.

breaks the symmetry of the lattice and is compatible with C_{2v} . Based upon the analysis of chapter 1, we create table 2.1 for donor modes and table 2.2 for acceptor modes. These tables provide the labeling scheme for the C_{6v} and C_{2v} modes, the dominant Fourier components of the modes, and their transformation properties about the available mirror planes (the mirror plane properties are represented by their character values [92]).

Donor modes of C_{6v} symmetry, formed at point a in the lattice, have their dominant Fourier components in the $\pm\{\mathbf{k}_{X_1}, \mathbf{k}_{X_2}, \mathbf{k}_{X_3}\}$ directions, and we thus require that $\sigma_d = -1$, where the σ_{d_i} are the mirror planes labeled in fig. 2.2(a). However, $\sigma_d \neq -1$ for the modes listed in table 2.1. Reducing the symmetry of the mode to C_{2v} (through a modified defect at point a or re-centering to point b) results in modes with dominant Fourier components that are not orthogonal to the available mirror planes, or as in the case of the $\mathbf{H}_{B_1}^{b,d1}$ mode, have incorrect spatial symmetry.

Out of the C_{6v} acceptor modes in table 2.2, the $\mathbf{H}_{A_2'}^{a,a1}$ mode satisfies the symmetry criteria. The $\mathbf{H}_{A_2}^{b,a1}$ mode produced at position b does not quite satisfy our criteria, as two of the three pairs of dominant Fourier components ($\pm\{\mathbf{k}_{J_1}, \mathbf{k}_{J_3}\}$) are not orthogonal to the mirror planes; however, distortions of the lattice that preferentially select for the $\pm\mathbf{k}_{J_5}$ Fourier components over $\pm\mathbf{k}_{J_1}$ and $\pm\mathbf{k}_{J_3}$ can be made so that the symmetry condition is satisfied. Such lattice distortions are addressed in section 2.7. As a reference, the approximate form for the $\mathbf{H}_{A_2'}^{a,a1}$ mode, given previously in equation (1.20), is listed below:

Table 2.2: Symmetry classification and dominant Fourier components for the \mathbf{H} -field of valence band acceptor modes in a hexagonal lattice.

Defect Center	C_{6v} Modes	Fourier Comp.	(σ_d, σ_v)	C_{2v} Modes	(σ_x, σ_y)
$(0,0)$	$\mathbf{H}_{A_2''}^{a,a1}$	$\pm\{\mathbf{k}_{J_1}, \mathbf{k}_{J_3}, \mathbf{k}_{J_5}\}$	$(-, -)$	$\mathbf{H}_{A_2}^{a,a1}$	$(-, -)$
$(0,0)$	$\mathbf{H}_{B_2''}^{a,a1}$	$\pm\{\mathbf{k}_{J_1}, \mathbf{k}_{J_3}, \mathbf{k}_{J_5}\}$	$(-, +)$	$\mathbf{H}_{B_2}^{a,a1}$	$(+, -)$
$(a/2, 0)$	N/A	$\pm\{\mathbf{k}_{J_1}, \mathbf{k}_{J_3}, \mathbf{k}_{J_5}\}$	N/A	$\mathbf{H}_{A_2}^{b,a1}$	$(-, -)$
$(a/2, 0)$	N/A	$\pm\{\mathbf{k}_{J_1}, \mathbf{k}_{J_3}, \mathbf{k}_{J_5}\}$	N/A	$\mathbf{H}_{B_2}^{b,a1}$	$(+, -)$

$$\mathbf{H}_{A_2''}^{a,a1} = \hat{z} \left(\cos(\mathbf{k}_{J_1} \cdot \mathbf{r}_{\perp}^a) + \cos(\mathbf{k}_{J_3} \cdot \mathbf{r}_{\perp}^a) + \cos(\mathbf{k}_{J_5} \cdot \mathbf{r}_{\perp}^a) \right), \quad (2.1)$$

where \mathbf{r}_{\perp}^a denotes in-plane coordinates referenced to point a .

2.3.2 Square lattice

The square lattice of air holes in a dielectric slab, whose real and reciprocal space representations are shown in fig. 2.2(b), and whose TE-mode bandstructure is depicted in fig. 2.4(b), also provides a photonic lattice from which low-loss defect modes can be formed. Defects in a square lattice may be centered at the C_{4v} symmetry points d and f , or the C_{2v} symmetry point e . Again, following the analysis of chapter 1, we produce tables 2.3 and 2.4 for the square lattice defect modes.

Based on their properties under mirror reflection, the $\mathbf{H}_{A_2''}^{f,d1}$, $\mathbf{H}_{B_2''}^{f,d1}$, and $\mathbf{H}_{A_2}^{e,d1}$ donor modes all meet the symmetry condition we have placed on the modes. By suitable modification of the defect geometry, the symmetry of modes formed at points d and f can be reduced to C_{2v,σ_v} or C_{2v,σ_d} , where the subscript σ_v denotes symmetry with respect to the (σ_x, σ_y) mirror planes and the subscript σ_d refers to the $(\sigma_{x'}, \sigma_{y'})$ mirror planes (fig. 2.2(b)). The modes at f continue to satisfy the symmetry criteria under C_{2v,σ_v} , but no longer do so under C_{2v,σ_d} , as the σ_d mirror planes are not orthogonal to the modes' dominant Fourier components.

The acceptor states formed from the valence band edge at the M -point are analyzed in a similar fashion, and in this case, the modes at points d and f are candidates. The reduced symmetry C_{2v,σ_v} modes at points d and f are ruled out, while the C_{2v,σ_d} modes at these two high symmetry points

Table 2.3: Symmetry classification and dominant Fourier components for the \mathbf{H} -field of conduction band donor modes in a square lattice.

Defect center	C_{4v}	Fourier Comp.	(σ_d, σ_v)	C_{2v, σ_v}	(σ_x, σ_y)	C_{2v, σ_d}	$(\sigma_{x'}, \sigma_{y'})$
$(0,0)$	$\mathbf{H}_{E,1}^{d,d1}$	$\pm\{\mathbf{k}_{X_1}\}$	$(0,0)$	$\mathbf{H}_{B_1}^{d,d1}$	$(-,+)$	$\mathbf{H}_{B'_1}^{d,d1}$	$(-, -)$
$(0,0)$	$\mathbf{H}_{E,2}^{d,d1}$	$\pm\{\mathbf{k}_{X_2}\}$	$(0,0)$	$\mathbf{H}_{B_2}^{d,d1}$	$(+,-)$	$\mathbf{H}_{B'_2}^{d,d1}$	$(+, -)$
$(a/2, a/2)$	$\mathbf{H}_{A_2''}^{f,d1}$	$\pm\{\mathbf{k}_{X_1}, \mathbf{k}_{X_2}\}$	$(-, -)$	$\mathbf{H}_{A_2}^{f,d1,1}$	$(-, -)$	$\mathbf{H}_{A_2'}^{f,d1}$	$(-, -)$
$(a/2, a/2)$	$\mathbf{H}_{B_2''}^{f,d1}$	$\pm\{\mathbf{k}_{X_1}, \mathbf{k}_{X_2}\}$	$(-, +)$	$\mathbf{H}_{A_2}^{f,d1,2}$	$(-, -)$	$\mathbf{H}_{A_1'}^{f,d1}$	$(-, -)$
$(0, a/2)$	N/A ^a	$\pm\{\mathbf{k}_{X_1}\}$	N/A	$\mathbf{H}_{A_2}^{e,d1}$	$(-, -)$	N/A	N/A
$(0, a/2)$	N/A	$\pm\{\mathbf{k}_{X_2}\}$	N/A	$\mathbf{H}_{B_2}^{e,d1}$	$(+, -)$	N/A	N/A

^a Not applicable. Modes centered at point e are of C_{2v} symmetry.

Table 2.4: Symmetry classification and dominant Fourier components for the \mathbf{H} -field of valence band acceptor modes in a square lattice.

Defect Center	C_{4v}	Fourier Comp.	(σ_d, σ_v)	C_{2v, σ_v}	(σ_x, σ_y)	C_{2v, σ_d}	$(\sigma_{x'}, \sigma_{y'})$
$(0,0)$	$\mathbf{H}_{A_2''}^{d,a1}$	$\pm\{\mathbf{k}_{M_1}, \mathbf{k}_{M_2}\}$	$(-, -)$	$\mathbf{H}_{A_2}^{d,a1}$	$(-, -)$	$\mathbf{H}_{A_2'}^{d,a1}$	$(-, -)$
$(a/2, a/2)$	$\mathbf{H}_{B_1''}^{f,a1}$	$\pm\{\mathbf{k}_{M_1}, \mathbf{k}_{M_2}\}$	$(+, -)$	$\mathbf{H}_{A_1}^{f,a1}$	$(+, +)$	$\mathbf{H}_{A_2'}^{f,a1}$	$(-, -)$
$(0, a/2)$	N/A	$\pm\{\mathbf{k}_{M_1}, \mathbf{k}_{M_2}\}$	N/A	$\mathbf{H}_{B_1}^{e,a1}$	$(-, +)$	N/A	N/A

remain on the list. As a reference, the approximate forms for the candidate donor and acceptor modes are given in table 2.5 below.

Table 2.5: Candidate donor and acceptor modes in a square lattice.

Donor Modes	Acceptor Modes
$\mathbf{H}_{A_2''}^{f,d1} = \hat{z}(\cos(\mathbf{k}_{X_1} \cdot \mathbf{r}_{\perp}^f) + \cos(\mathbf{k}_{X_2} \cdot \mathbf{r}_{\perp}^f))$	$\mathbf{H}_{A_2''}^{d,a1} = \hat{z}(\cos(\mathbf{k}_{M_1} \cdot \mathbf{r}_{\perp}^d) + \cos(\mathbf{k}_{M_2} \cdot \mathbf{r}_{\perp}^d))$
$\mathbf{H}_{B_2''}^{f,d1} = \hat{z}(\cos(\mathbf{k}_{X_1} \cdot \mathbf{r}_{\perp}^f) - \cos(\mathbf{k}_{X_2} \cdot \mathbf{r}_{\perp}^f))$	$\mathbf{H}_{B_1''}^{f,a1} = \hat{z}(\cos(\mathbf{k}_{M_1} \cdot \mathbf{r}_{\perp}^f) - \cos(\mathbf{k}_{M_2} \cdot \mathbf{r}_{\perp}^f))$
$\mathbf{H}_{A_2}^{e,d1} = \hat{z}(\cos(\mathbf{k}_{X_1} \cdot \mathbf{r}_{\perp}^e))$	

2.4 Initial FDTD simulation results

The symmetry analysis presented in the previous section determined the modes satisfying our symmetry criteria, chosen to reduce vertical radiation losses from the PC slab WG. For a hexagonal lattice, we singled out the acceptor mode of equation (2.1), while for the square lattice, a number of options were available, as summarized in table 2.5. We begin the 3D FDTD analysis of high- Q PC resonant cavities by choosing particular defects in the hexagonal and square lattices that will support one of these modes. Results from the FDTD analysis will provide a measure of the benefits obtained in using modes of such symmetries, and will also give an indication of what further improvements are needed. This will lead naturally to the Fourier space tailoring of the lattice discussed in sections 2.5 and 2.6.

The FDTD calculations presented in this section (see appendix B for more details) were performed on a mesh with 20 points per lattice spacing (greater than 70 points per free space wavelength or 20 points per wavelength in the dielectric). Cavity modes were excited by an initial field (H_z) with a localized Gaussian profile, and even modes of the slab WG were preferentially selected by using an even mirror symmetry condition ($\sigma_h = 1$) in the middle of the slab. In order to maintain a single vertical mode of the PC slab waveguide (within the frequency band of interest), we choose a normalized slab thickness $d/a = 0.75$ in this section. Where appropriate, the mirror planes (σ_x, σ_y) were used to filter out cavity modes according to their projection onto the irreducible representations (IRREPs) of C_{2v,σ_v} . Mur's absorbing boundary conditions were used to terminate the FDTD simulation domain in all other directions. Q values are calculated by determining the power absorbed in the boundaries (P_{abs}) and the stored energy in the mode (U), and taking $Q = \omega_0 U / P_{abs}$, where ω_0 is the angular frequency of the mode. By distinguishing between power flow to vertical

and in-plane boundaries, effective Q values Q_{\perp} and Q_{\parallel} are calculated, with the total quality factor being determined by $1/Q = 1/Q_{\parallel} + 1/Q_{\perp}$ [7]. It should be noted that a number of other methods were also used to estimate the Q values, including the modal energy decay rate and the radiated power calculated from the near field momentum components lying within the cladding light cone, all resulting in consistent values. The effective volume [109, 110] of the cavity modes, V_{eff} in the tables below, is calculated using the peak in the electric field energy density and is given in units of cubic wavelengths in the material.² The explicit form of V_{eff} is:

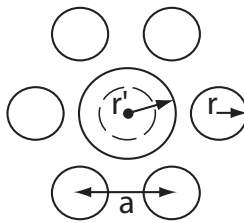
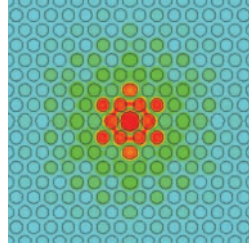
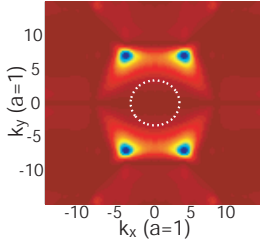
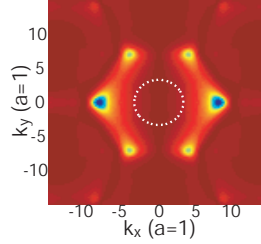
$$V_{\text{eff}} = \frac{\int_V \epsilon(\mathbf{r}) |\mathbf{E}(\mathbf{r})|^2 d^3\mathbf{r}}{\max[\epsilon(\mathbf{r}) |\mathbf{E}(\mathbf{r})|^2]} \quad (2.2)$$

2.4.1 Hexagonal lattice

The $\mathbf{H}_{A_2''}^{a,a1}$ mode, our candidate mode for study, is formed by enlarging holes in a manner consistent with the C_{6v} symmetry of the lattice, so that an acceptor mode is formed. We choose the defect geometry shown in table 2.6, where the central hole (about point a) is enlarged from radius r to r' . The defect is surrounded by a total of 8 periods of the hexagonal lattice in the \hat{x} -direction and 12 periods in the \hat{y} -direction. The magnetic field amplitude and Fourier-transformed momentum space electric field components $\tilde{\mathbf{E}}_x$ and $\tilde{\mathbf{E}}_y$ of mode $\mathbf{H}_{A_2''}^{a,a1}$ are given in table 2.6 for two different pairs of values (r, r') . The dominant Fourier components are seen to be $\pm\{\mathbf{k}_{J_1}, \mathbf{k}_{J_3}, \mathbf{k}_{J_5}\}$, as predicted by the symmetry analysis. Examining $\tilde{\mathbf{E}}_x$ and $\tilde{\mathbf{E}}_y$, it is also clear that, although the power within the light cone has been reduced in comparison to the x -dipole donor mode, it is still significant. This fact is evidenced in Q_{\perp} which, at 4,900 for $r/a = 0.35$ and $r'/a = 0.45$, is larger than that obtained for the x -dipole mode. By reducing the frequency, and consequently the radius of the light cone, the PC cavity with $r/a = 0.30$ and $r'/a = 0.45$ has an improved vertical Q of 8,800 (although its in-plane Q has degraded due to a reduction in the in-plane bandgap for smaller lattice hole radii).

²In our original papers [21, 23], we quoted modal volumes in terms of cubic wavelengths in air (λ^3); this unit has meaning in terms of describing the physical volume of the field. However, to compare differing cavity geometries across different material systems, the unit of cubic wavelengths in the material $((\lambda/n)^3)$ is more appropriate, and I have thus chosen this unit for all of the V_{eff} values quoted in this chapter and the rest of the thesis. In addition, certain phenomena, such as the enhanced radiative rate of an emitter within a cavity (the Purcell effect) are most straightforwardly calculated when the volume is quoted in units of $(\lambda/n)^3$. In other works within the field, mode volumes will sometimes be quoted in terms of cubic half-wavelength in the material $((\lambda/2n)^3)$, to provide a comparison against a theoretical cavity that can confine an optical mode to a half-wavelength in the material in all three dimensions (i.e., the optical analog of the particle in a 3D infinite square well from quantum mechanics).

Table 2.6: Characteristics of the $\mathbf{H}_{A_2''}^{a,a1}$ resonant mode in a hexagonal lattice (images are for a PC cavity with $r/a = 0.35$, $r'/a = 0.45$, $d/a = 0.75$, and $n_{\text{slab}} = 3.4$).

Geometry		$ \mathbf{H} $	$ \tilde{\mathbf{E}}_x $	$ \tilde{\mathbf{E}}_y $		
						
\mathbf{r}/a	\mathbf{r}'/a	$\omega_n = a/\lambda_o$	\mathbf{Q}_{\parallel}	\mathbf{Q}_{\perp}	\mathbf{Q}_{tot}	$\mathbf{V}_{\text{eff}}((\lambda/n)^3)$
0.35	0.45	0.265	34,100	4,900	4,300	0.54
0.30	0.45	0.248	5,300	8,800	3,300	0.84

2.4.2 Square lattice

We choose the $\mathbf{H}_{A_2}^{e,d1}$ mode as our candidate for study. This mode, centered in the dielectric at point e in the lattice, is appealing in that it has Fourier components primarily situated at $\pm \mathbf{k}_{X_1}$, while the other modes of correct symmetry have a larger number of Fourier components. This simplifies the design considerations of section 2.5. To create the mode, we consider the structure depicted in table 2.7. Defining point e as the origin, $(0,0)$, we see that the structure consists of a standard square lattice of air holes in which the two holes centered at $(0, \pm a/2)$ are decreased in size so as to create a donor mode of A_2 symmetry. In the FDTD simulations, the structure consists of 12 rows and 8 columns of air holes surrounding the defect holes.

Starting with $r/a = 0.30$, $r'/a = 0.28$, and $d/a = 0.75$, we produce a mode with normalized frequency $\omega_n = a/\lambda_o = 0.264$. The magnetic field amplitude and 2D spatial FTs ($\tilde{\mathbf{E}}_x$ and $\tilde{\mathbf{E}}_y$) of the mode are given in table 2.7. As the amplitude of $\tilde{\mathbf{E}}_y$ is small in comparison to that of $\tilde{\mathbf{E}}_x$, the mode is predominantly made up of components centered at $\pm \mathbf{k}_{X_1}$, as predicted. The effective vertical Q of this mode is approximately 54,000, easily exceeding the values obtained in ref. [8] for a mode of even symmetry. The small Q_{\parallel} (17,400) is a result of the weak defect perturbation and extended nature of the cavity mode ($V_{\text{eff}} = 2.11(\lambda/n)^3$). Improving the localization of the mode by lowering r'/a of the defect to 0.25 improves Q_{\parallel} to a value of 60,000 and lowers V_{eff} by a factor of almost two. Surprisingly, Q_{\perp} has also increased from 54,000 to 69,000 despite the stronger localization of the mode and its expected broadening in Fourier space. This rather counterintuitive result indicates

Table 2.7: Characteristics of the $\mathbf{H}_{A2}^{e,d1}$ resonant mode in a square lattice (images are for a PC cavity with $r/a = 0.30$, $r'/a = 0.28$, $d/a = 0.75$, and $n_{\text{slab}} = 3.4$).

Geometry		$ \mathbf{H} $	$ \tilde{\mathbf{E}}_x $	$ \tilde{\mathbf{E}}_y $		
\mathbf{r}/\mathbf{a}	\mathbf{r}'/\mathbf{a}	ω_n	\mathbf{Q}_{\parallel}	\mathbf{Q}_{\perp}	\mathbf{Q}_{tot}	$\mathbf{V}_{\text{eff}}((\lambda/n)^3)$
0.30	0.28	0.265	17,400	54,000	13,000	2.11
0.30	0.25	0.262	60,100	69,200	32,000	1.08

that a more detailed study of the effects of the defect geometry on cavity loss is required. This is the focus of the following section.

2.5 Momentum space design of the defect geometry in a square lattice

The results for the simple square lattice cavities studied in the previous section are quite encouraging, and we will thus begin by examining cavity design within these square lattice structures before returning to the hexagonal lattice in a later section. The results given thus far indicate that improving the loss properties of the defect mode resonators requires isolation of the mode's momentum components to regions outside the light cone to maintain a high Q_{\perp} , and to those regions for which the in-plane bandgap is substantial for a high Q_{\parallel} . To determine how to tailor the defect geometries to accomplish these goals, we consider a simple model to illustrate the couplings induced in Fourier space between the dominant momentum components of a given defect mode and those modes which radiate. We employ a two-step process where in the first step, the approximate form of the defect mode is taken based on symmetry arguments, as outlined in section 2.3, with the allowance for finite \mathbf{k} -space bandwidths in the dominant Fourier components due to the localization of the defect mode. We then consider couplings of this approximate symmetry mode to other modes of the PC slab WG through the dielectric perturbation $\Delta\eta(\mathbf{r})$, where $\eta = 1/\epsilon$ is the inverse of the dielectric profile of the lattice. The most important mode couplings from the perspective of increasing the Q are those

between the dominant Fourier components and “leaky cavity modes.” The leaky cavity modes consist of vertical radiation modes and guided modes of the PC slab WG which are not reflected by the PC and thus leak in-plane. $\Delta\eta$ induces the change $\delta\mathbf{H}^d(\mathbf{r})$ in the defect mode, and this change is written as a superposition over the set of nearly (frequency) degenerate guided and radiation modes of the PC slab WG. The coupling amplitude between the symmetry mode composed of the dominant Fourier components, $\mathbf{H}_o^d(\mathbf{r})$, and a leaky cavity mode, $\mathbf{H}_o^{lcm}(\mathbf{r})$, of the unperturbed PC slab is given by the following matrix element:

$$\int d^3r \left(\mathbf{H}_o^{lcm}(\mathbf{r}) \right)^* \left(\nabla \times \left(\Delta\eta(\mathbf{r}) \nabla \times \mathbf{H}_o^d(\mathbf{r}) \right) \right) \sim \int \frac{d^2k_\perp}{(2\pi)^4} \left(\tilde{H}_{z,o}^{lcm} \right)^* \left(\left[\tilde{\Delta\eta} * (|\mathbf{k}_\perp|^2 \tilde{H}_{z,o}^d) \right] + \left[(k_x \tilde{\Delta\eta}) * (k_x \tilde{H}_{z,o}^d) \right] + \left[(k_y \tilde{\Delta\eta}) * (k_y \tilde{H}_{z,o}^d) \right] \right) \quad (2.3)$$

where $*$ denotes convolution. In converting from the real space integral to momentum space, we have neglected the variation of $\eta(\mathbf{r})$ and $\Delta\eta(\mathbf{r})$ in the \hat{z} -direction, so that $\mathbf{H}_o^d(\mathbf{r}) \approx H_{z,o}^d(\mathbf{r}_\perp)$ (TE-like mode). From this equation, it is clear that the Fourier Transform of the dielectric perturbation, $\tilde{\Delta\eta}(\mathbf{k}_\perp)$, is the key quantity that couples Fourier components between the basis modes of the system. By tailoring this quantity appropriately, we can thus limit couplings that lead to in-plane and vertical leakage.

The formula given above is meant to be a qualitative guide to help build physical intuition; it is not a rigorous formula that can be expected to be quantitatively accurate. Such a formula can be conceived, however, by considering the Wannier analysis provided in the previous chapter. In particular, in equation (1.58), we showed that the mixing of the Bloch modes of the PC due to the presence of the defect perturbation, $\hat{L}'_H = -\nabla(\Delta\eta) \cdot \nabla - (\Delta\eta)\nabla^2$, is given by:

$$\langle H_{l',\mathbf{k}'} | \hat{L}'_H H_{l,\mathbf{k}} \rangle = \sum_{\mathbf{G}} \sum_{\mathbf{k}''} \left(\tilde{\Delta\eta}_{\mathbf{k}''} K_{l',l}(\mathbf{k}', \mathbf{k}, \mathbf{G}) + \tilde{\Delta\eta}_{\mathbf{k}''}(i\mathbf{k}'') \cdot \mathbf{L}_{l',l}(\mathbf{k}', \mathbf{k}, \mathbf{G}) \right) \delta_{\mathbf{k}' - \mathbf{k}'' + \mathbf{G}, \mathbf{k}}, \quad (2.4)$$

where $\tilde{\Delta\eta}_{\mathbf{k}''}$ is the \mathbf{k}'' th Fourier coefficient of $\Delta\eta(\mathbf{r})$, l and \mathbf{k} label the band index and crystal momentum of the $H_{l,\mathbf{k}}$ Bloch wave, the \mathbf{G} are reciprocal lattice vectors, and $K_{l',l}(\mathbf{k}', \mathbf{k}, \mathbf{G})$ and $\mathbf{L}_{l',l}(\mathbf{k}', \mathbf{k}, \mathbf{G})$ are scalar and vector coupling matrix elements, respectively, which depend upon the Bloch waves. As expected, this formula indicates the importance of the Fourier transform of the dielectric perturbation, $\tilde{\Delta\eta}(\mathbf{k}_\perp)$, in determining the coupling of different Bloch modes of the unperturbed crystal.

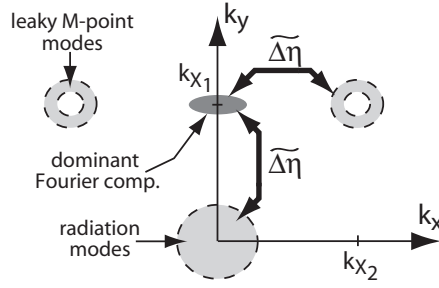


Figure 2.5: Illustration showing the mode coupling for the $\mathbf{H}_{A2}^{e,d1}$ mode in \mathbf{k} -space through the $\widetilde{\Delta\eta}$ perturbation.

Our candidate mode within the square lattice, $\mathbf{H}_{A2}^{e,d1}$, has dominant in-plane Fourier components at $\pm\mathbf{k}_{X1}$. We must therefore modify the defect so that $\widetilde{\Delta\eta}$ does not couple the $\pm\mathbf{k}_{X1}$ momentum components to those regions in \mathbf{k} -space which are “leaky.” In order to reduce radiation normal to the PC slab through coupling to the light cone, the amplitude of $\widetilde{\Delta\eta}$ in the neighborhood of $k_y = \pm\pi/a$ should be minimized. In addition, for the square lattice designs investigated here the bandgap between the conduction band edge at the X -point and the valence band edge at the M -point is at best very narrow, consequently, we look to reduce coupling between neighborhoods surrounding the X - and M -points. This implies that it will also be necessary to reduce the amplitude of $\widetilde{\Delta\eta}$ in the region about $k_x = \pm\pi/a$.

The crux of the argument described above is depicted in fig. 2.5, where lossy couplings are illustrated for the upper region of \mathbf{k} -space (the negative k_y region will behave identically in this case). Here we have assumed that the defect mode frequency lies below the conduction band edge at the X -point but slightly within the valence band near the M -point, resulting in an annular region of \mathbf{k} -space about the M -point which is strongly coupled to. With reference to this simple schematic, the Fourier components of $\widetilde{\Delta\eta}$ that lead to radiation losses from the defect cavity are approximately:

$$\begin{aligned} \widetilde{\Delta\eta} \left(|k_x| \lesssim (k_{lc} + \Delta_x), |k_y \pm |\mathbf{k}_{X1}|| \lesssim (k_{lc} + \Delta_y) \right) &\implies \text{coupling to light cone,} \\ \widetilde{\Delta\eta} \left(|k_x \pm |\mathbf{k}_{X2}|| \lesssim \Delta_x, |k_y| \lesssim \Delta_y \right) &\implies \text{coupling to leaky } M\text{-point.} \end{aligned} \quad (2.5)$$

where k_{lc} is the radius of the light cone, and Δ_x and Δ_y are the widths of the dominant Fourier peaks in the \hat{k}_x - and \hat{k}_y -directions, respectively.

Before attempting any design modifications, we first consider the simple defect geometry stud-

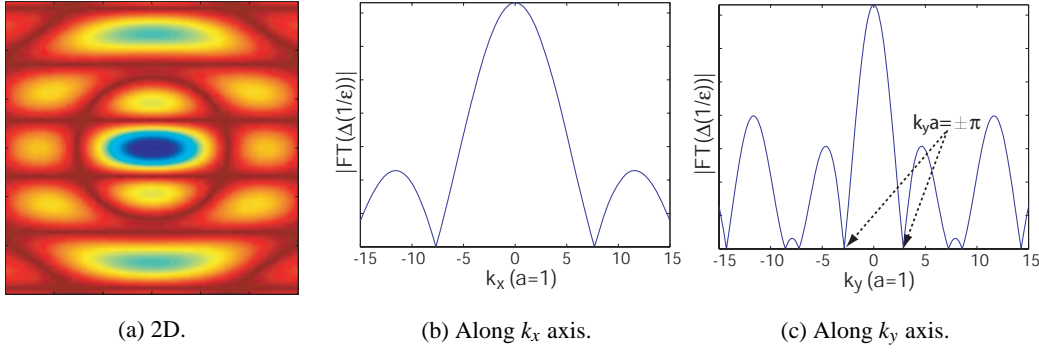


Figure 2.6: $\widetilde{\Delta\eta}(\mathbf{k}_\perp)$ for dielectric structure of table 2.7.

ied in section 2.4, where the holes located at $(0, \pm a/2)$ were reduced from the standard hole radius r to a radius r' . The perturbation $\Delta\eta$ is given by the difference in η with and without the defect holes, and thus simply consists of a pair of annuli, each of width $(r - r')$, centered at $(0, \pm a/2)$. The 2D spatial FT of this function can be obtained analytically [5], and is separable into the form

$$\widetilde{\Delta\eta}(\mathbf{k}_\perp) = F(k_\perp; r, r') \cos\left(\frac{k_y a}{2}\right), \quad (2.6)$$

where $F(k_\perp; r, r')$ is a function of the magnitude of the in-plane momentum, with r and r' as parameters. This function, along with one-dimensional (1D) slices along the k_x and k_y axes, is shown in fig. 2.6 (the figure shown is actually the direct FT of the structure used in FDTD calculations, to take into account any staircasing effects in the rendering of the holes; however, the difference between it and the analytic function are insignificant.). We notice, as is clear from examining equation (2.6), that $\widetilde{\Delta\eta} = 0$ at $k_y = \pm\pi/a$. Our choice of defect was thus a fortuitous one, as the zero amplitude of $\widetilde{\Delta\eta}$ at the X points eliminated coupling between the dominant Fourier components of the $\mathbf{H}_{A2}^{e,d1}$ mode and DC. Of course, a localized defect mode has a finite bandwidth in Fourier space about its dominant momentum components, and the light cone encompassing the radiation modes is of finite radius as well. As a result it is desirable to minimize the Fourier components of the dielectric perturbation over an extended region about $k_y = \pm\pi/a$. Note that $\widetilde{\Delta\eta}$ for the hexagonal lattice design of the previous section does not have zero amplitude at any of the \mathbf{k}_J , and thus the Q_\perp values are much smaller than those of the square lattice. To increase Q_\perp in the hexagonal lattice, future designs must therefore tailor the lattice in a way so that this amplitude is significantly reduced.

It is also necessary to modify the dielectric to improve Q_{\parallel} . The most straightforward way to immediately do so is to increase the r/a of the host PC, as that will provide a bandgap for an increased range of momentum values. This also tends to decrease Q_{\perp} , as the increased r/a will produce a mode of higher frequency, resulting in a cladding light cone of increased radius encompassing a larger range of momentum values. Fortunately, this does not necessarily have to hold for a general defect geometry. In particular, the hole radius can be kept relatively small in the region where the mode is primarily located, but can be graded outside this region to increase the in-plane reflectivity. The choice of grading can be determined by considering the need to limit the in-plane momentum components of the mode to regions in which the bandgap is substantial (note that for the simple two-hole design considered in section 2.4, $\widetilde{\Delta\eta}$ is quite large in this region of momentum space about $k_x = \pm\pi/a$). The benefit of this approach is that it does not necessarily result in increased vertical radiation loss, thus allowing for both a large Q_{\parallel} and Q_{\perp} .

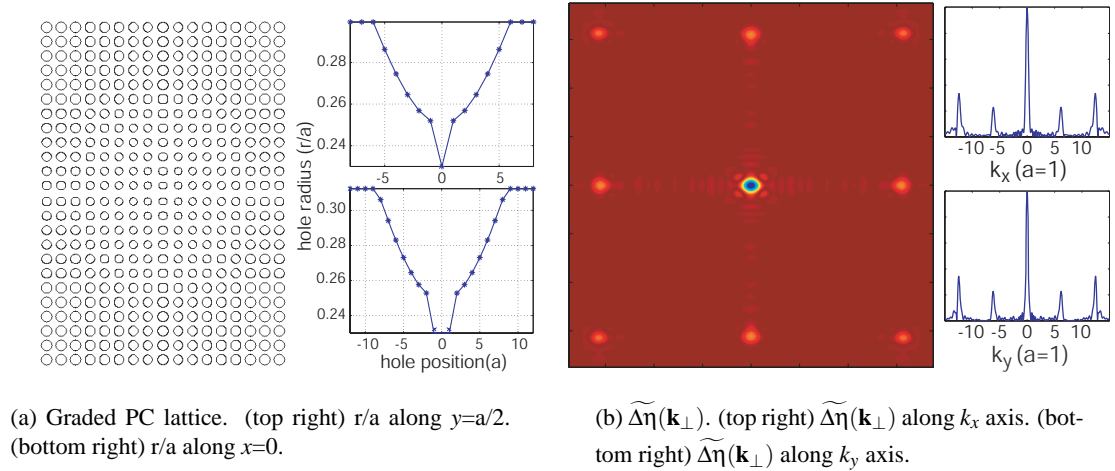
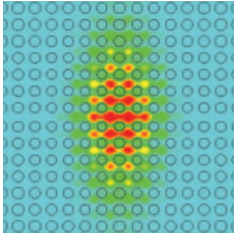
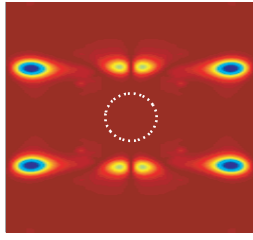
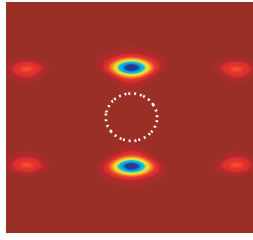
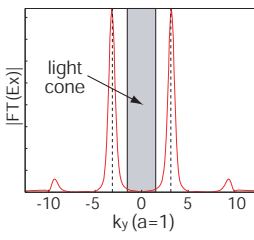


Figure 2.7: Properties of the graded square lattice.

Consider the graded lattice shown in fig. 2.7(a). The standard defect holes at $(0, \pm a/2)$ have $r/a = 0.23$, while their immediate neighbors have $r/a = 0.253$. The hole radii are then increased parabolically outwards for 5 periods in the \hat{x} -direction and 7 periods in the \hat{y} -direction, after which they are held constant. The nature of this grading is shown in fig. 2.7(a), where the r/a profiles are given for slices along $y = a/2$ and $x = 0$. Along these axes the maximum value r/a attains is 0.31, but along the diagonal directions r/a grows to be as large as 0.35. The dielectric perturbation, which now consists of a series of annuli of decreasing width from the center to the edges, has a FT

Table 2.8: Field characteristics of the graded square lattice shown in fig. 2.7(a).

$ \mathbf{H} $		$ \tilde{\mathbf{E}}_y $	$ \tilde{\mathbf{E}}_x $	$ \tilde{\mathbf{E}}_x $ along k_y axis	
					
\mathbf{d}/\mathbf{a}	ω_n	Q_{\parallel}	Q_{\perp}	Q_{tot}	$V_{\text{eff}}((\lambda/n)^3)$
0.75	0.245	470,000	110,000	89,000	1.23
0.85	0.239	422,000	128,000	98,000	1.28
0.95	0.235	296,000	139,000	95,000	1.33
1.05	0.231	280,000	145,000	96,000	1.38

given in fig. 2.7(b). Examining both the 2D image and the 1D line scans of the FT, we see that our grading has greatly diminished the amplitude of $\tilde{\Delta}\eta$ in the regions surrounding $k_y = \pm\pi/a$ and $k_x = \pm\pi/a$.

The FDTD simulations of the defect mode of this structure largely confirm the ideas described thus far. Q_{\perp} has increased to over 110,000, while Q_{\parallel} has improved even further to approximately 470,000, giving an overall $Q_{\text{tot}} \approx 89,000$. The predicted mode volume $V_{\text{eff}} \sim 1.2(\lambda/n)^3$, so that the combination of Q and V_{eff} achievable in this cavity is very promising from the standpoint of cavity QED experiments. This will be described in further detail in later chapters within this thesis.

The magnetic field amplitude and FT of the in-plane electric field components in table 2.8 provide further indication of the success of this design in suppressing radiation loss. In particular, consider the line scan of $\tilde{\mathbf{E}}_x$ along the k_y axis. It shows that the grading has met with success, as power has largely been eliminated within the light cone. This point is particularly striking when contrasted with the corresponding image shown in fig. 2.3(b) for the low Q x -dipole mode we took as our baseline. Note that $\tilde{\Delta}\eta(k_x = 0, k_y = \pm\pi/a)$ is identically zero regardless of the grade, due to the position of the defect holes with respect to the center of the defect, whereas $\tilde{\Delta}\eta(k_x = \pm\pi/a, k_y = 0)$ is not automatically zero. It may be advantageous to identically zero $\tilde{\Delta}\eta(k_x = \pm\pi/a, k_y = 0)$ as this will allow for the formation of a more localized mode that is still of high Q_{\parallel} . Such a mode would be centered at the f -point of the square lattice, and would either be the $\mathbf{H}_{A_2''}^{f,d1}$ or $\mathbf{H}_{B_2''}^{f,d1}$ mode.

Before concluding, there are a couple of points concerning the chosen lattice that are worth

mentioning. The first is that the initial jump in r/a between the defects at $(0, \pm a/2)$ and their neighbors is an important element of this design. Acting as a potential well, the jump helps confine the mode in real space, allowing r/a to increase quickly to a value for which the in-plane reflectivity is high without significantly increasing the modal frequency. The size of the jump is also important; if incorrectly sized the resulting dielectric perturbation contains larger Fourier amplitudes which couple the mode to the M -point for which the PC is no longer reflective and to the light cone in which light radiates vertically. An optimum defect design is found when a compromise is struck between the minimization of the Fourier components of $\widetilde{\Delta\eta}$ which couple the dominant momentum components of the defect mode to regions of \mathbf{k} -space which radiate, and the degree to which the dominant momentum components of the mode broaden due to in-plane confinement by the defect.

It should again be emphasized that the increased Q_{\perp} for these graded lattice designs is not solely the result of real-space delocalization of the mode, which has been an approach considered by other authors [108, 111]. It is instead largely due to the aforementioned reduction of amplitude for those Fourier components of the dielectric perturbation that couple the dominant momentum components of the defect mode to those which radiate. Of course, real-space localization plays a role in determining the spread in \mathbf{k} -space of the dominant Fourier components of the mode, and if this spread exceeds the size of the region about $\pm \mathbf{k}_{x_1}$ that $\widetilde{\Delta\eta}$ has been flattened, vertical radiation will result. An increase in the slab thickness also effects the performance of the structure. It causes a decrease in the frequency of the mode, thus increasing Q_{\perp} . It also slightly reduces the size of the in-plane bandgap, decreasing Q_{\parallel} . This is in fact seen in the results of FDTD simulations compiled in table 2.8.

Finally, we note that the criteria for choosing the geometries presented in this paper were entirely based on Q considerations, and optimization of the lattice grading to further increase Q can still be made. Changes may also be made to improve other aspects of the design. In particular, reducing the mode volume may be of importance to applications in quantum optics, while reducing the complexity of the design (in terms of the number and size of holes comprising the defect) may be of interest from a fabrication standpoint. Alternately, as we shall discuss in chapter 4, this graded lattice geometry is distinguished by supporting a mode whose Q is relatively insensitive to perturbations in the cavity geometry; one could envision making such robustness a prerequisite along with high- Q and small- V_{eff} in future designs of photonic crystal cavities. The approach to such designs can be aided through the Fourier space consideration of the dielectric perturbation as has been described in this section. Doing so will elucidate the potential lossy couplings that occur when the

defect mode is formed, and will help determine whether a given structure is able to sustain a high- Q mode.

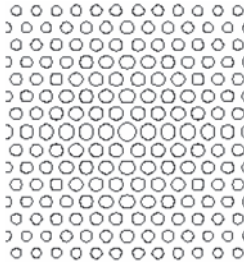
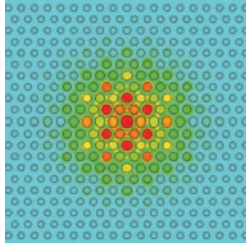
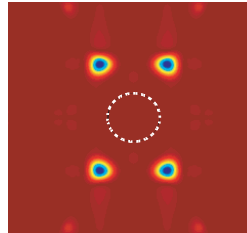
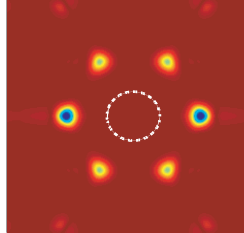
2.6 Tailoring of the defect geometry for the $\mathbf{H}_{A_2''}^{a,a1}$ mode in the hexagonal lattice

When comparing defect modes of a square lattice with those of a hexagonal lattice in the context of forming high- Q microcavities, there are a number of salient points that merit consideration. The first is that the square lattice designs adopted above provided a natural “geometric” advantage in that $\widetilde{\Delta\eta}(\mathbf{k}_\perp)$ (even in the simplest case of two reduced size air holes) was automatically zero at the dominant Fourier components ($k_x = 0, k_y = \pm\pi/a$), thereby reducing coupling between those components and small momentum components that radiate. Furthermore, these dominant Fourier components were in directions orthogonal to the available mirror planes of the system, maximizing the symmetry-based reduction of small momentum components as discussed in section 2.2. In the hexagonal lattice, it is difficult to obtain a similar set of circumstances. The only mode consistent with the symmetry criteria is the $\mathbf{H}_{A_2''}^{a,a1}$ mode, but defects that create such a mode have $\widetilde{\Delta\eta}(\mathbf{k}_\perp)$ that is non-zero at the mode’s dominant Fourier components ($\pm\{\mathbf{k}_{J_1}, \mathbf{k}_{J_3}, \mathbf{k}_{J_5}\}$). Conversely, a mode such as $\mathbf{H}_{A_2}^{b,d1}$, formed by a defect such as two reduced size holes at $(0, \pm a\sqrt{3}/2)$, could have $\widetilde{\Delta\eta}(\mathbf{k}_\perp) = 0$ at its dominant Fourier components ($\pm\{\mathbf{k}_{X_2}, \mathbf{k}_{X_3}\}$), but these Fourier components are oriented along directions that are not orthogonal to the available mirror planes of the system.

Despite these potential obstacles, it is certainly possible to design high- Q defect cavities in a hexagonal lattice. One advantage of the hexagonal lattice is that it exhibits a relatively large and complete in-plane bandgap for TE-like modes due to its nearly circular first Brillouin zone (IBZ) boundary. This essentially guarantees the ability to achieve high in-plane Q provided that the mode is suitably positioned within the bandgap, and that a sufficient number of periods of the photonic lattice are used (it is still important not to entirely neglect in-plane considerations in cavity designs as the mode volume can be affected significantly). To address vertical radiation losses, the defect geometry can be tailored to reduce couplings to the light cone, even though $\widetilde{\Delta\eta}(\mathbf{k}_\perp)$ does not necessarily have the automatic zeros it had in the case of the square lattice. Examining such tailorings is the focus of this section.

Our first goal is to reduce couplings between the dominant Fourier components of the $\mathbf{H}_{A_2''}^{a,a1}$ mode and the light cone. As was demonstrated above for the square lattice, this can be accomplished

Table 2.9: FDTD simulation results for graded hexagonal lattice geometries (images are for the first PC cavity listed below; $d/a=0.75$ in all designs).

Lattice		$ \mathbf{H} $	$ \widetilde{\mathbf{E}}_x $	$ \widetilde{\mathbf{E}}_y $			
							
$(\mathbf{r}/\mathbf{a})_c$	$(\mathbf{r}/\mathbf{a})_{nn}$	$(\mathbf{r}/\mathbf{a})_e$	ω_n	\mathbf{Q}_{\parallel}	\mathbf{Q}_{\perp}	\mathbf{Q}_{tot}	$\mathbf{V}_{eff}((\lambda/n)^3)$
0.36	0.325	0.225	0.250	400,000	180,000	123,000	2.41
0.40	0.380	0.30	0.271	1,540,000	76,000	72,000	1.67
0.36	0.355	0.225	0.252	800,000	107,000	94,000	1.18

through a grade in the hole radii as a function of distance from the center of the cavity. In this case, we reduce the hole radius as we move outwards from the central defect. An example of a graded lattice defect design is given in table 2.9, where only the central region of the cavity is shown to help the reader visualize the hole radii grading (the actual cavity used in FDTD simulations has 10 periods of the hexagonal lattice in each direction). The design consists of two levels of confinement. The first level of confinement has a centrally enlarged air hole ($(r/a)_c = 0.35$) followed by a relatively large decrease in hole radius ($(r/a)_{nn} = 0.325$) for the nearest neighbor holes. The hole radii are then parabolically decreased in moving radially outwards (down to $(r/a)_e = 0.225$ at the edge of the crystal), forming the second level of confinement. The effect this has on $\widetilde{\Delta\eta}(\mathbf{k}_{\perp})$ is evident in fig. 2.8(a)-(b), where we plot this function for the single enlarged hole design of the previous section and for the graded lattice design just described. It is clear that $\widetilde{\Delta\eta}(\mathbf{k}_{\perp})$ has been dramatically reduced at $\pm\{\mathbf{k}_{J_1}, \mathbf{k}_{J_3}, \mathbf{k}_{J_5}\}$, limiting the coupling between the dominant Fourier components and the light cone. The magnetic field amplitude and the Fourier transform of the mode's in-plane electric field components are shown in table 2.9. The resulting Q values and mode volume, as listed in table 2.9, are $Q_{\perp} = 1.8 \times 10^5$, $Q_{\parallel} = 4 \times 10^5$, and $V_{eff} = 2.41(\lambda/n)^3$. As previously mentioned, Q_{\parallel} could be made larger by simply increasing the number of periods in the photonic lattice; however, this will not have an appreciable effect on the mode volume, which is somewhat large in this case.

Having achieved a design with a high Q_{\perp} , we would like to modify it so as to reduce the mode

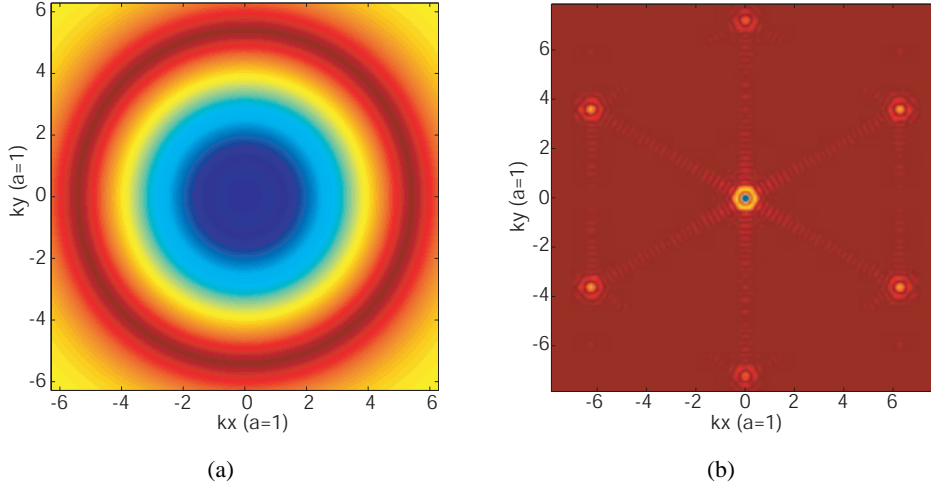


Figure 2.8: (a) $\widetilde{\Delta\eta}(\mathbf{k}_\perp)$ for single enlarged hole design in hexagonal lattice ($r/a = 0.30$, $r'/a = 0.45$). (b) $\widetilde{\Delta\eta}(\mathbf{k}_\perp)$ for graded hexagonal lattice design shown in table 2.9.

volume, which, at $V_{\text{eff}} = 2.41(\lambda/n)^3$, is roughly twice that which we had for square lattice designs. We employ two different modifications to do so; an increase in the average hole radius and a faster grade in the hole radii (the grading occurs over a smaller number of periods than in the first example), both of which should improve in-plane confinement. The results of these modifications are given in the second row of table 2.9; as expected, the in-plane Q has increased considerably, to a value of $Q_{\parallel} = 1.54 \times 10^6$, and the mode volume has decreased to $V_{\text{eff}} = 1.67(\lambda/n)^3$, but at the expense of a decreased vertical Q , now at $Q_{\perp} = 76,000$. The decreased Q_{\perp} is the result of a number of factors. The improved in-plane localization widens the mode in Fourier space, broadening the dominant Fourier components to the extent that they extend into the cladding light cone. The modified grade also changes the magnitude of $\widetilde{\Delta\eta}(\mathbf{k}_\perp)$ at $\pm\{\mathbf{k}_{J_1}, \mathbf{k}_{J_3}, \mathbf{k}_{J_5}\}$, increasing the amount of coupling between the mode's dominant Fourier components and the light cone. In addition, the increase in modal frequency correspondingly increases the radius of the cladding light cone.

As a final example, we consider adjusting the first level of confinement to reduce the mode volume. Starting with our original graded cavity design (the first design of table 2.9), the size of the holes adjacent to the central defect are increased to a value of $(r/a)_{nn} = 0.355$. The results are for the most part intermediate to the first two examples, with $Q_{\parallel} = 8 \times 10^5$ and $Q_{\perp} = 1.07 \times 10^5$. One important exception is that $V_{\text{eff}} = 1.17(\lambda/n)^3$ is actually much smaller than both of the original designs. Upon further consideration, this result is not too surprising; the smaller mode volume and

the relatively large Q_{\perp} are a result of the stronger yet more extended central perturbation to the photonic lattice.

2.7 Defect modes in a compressed hexagonal lattice

Although we have thus far focused on two regular photonic lattices, there are certainly a number of other lattices and structures that are of potential interest. In this section, we consider the use of a compressed hexagonal lattice. The lattice compression introduces additional degeneracies amongst the satellite extrema of the bandstructure, thus providing an additional level of design flexibility that in this case, allows us to efficiently localize defect modes both vertically and in the plane of the dielectric slab.

The defect modes of the previous section were centered about an air hole; for other applications, such as lasers, it may be of interest to have designs centered about a dielectric region, where strong overlap of the optical field with the semiconductor is desirable. Such a mode would be centered about the b -point in fig. 2.2(a). From the standpoint of designing a high- Q mode, the donor and acceptor modes formed at this point do not meet our symmetry criteria, as the dominant Fourier components of the modes (as listed in tables 2.1 and 2.2) are not orthogonal to the available mirror planes (σ_x and σ_y for the C_{2v} symmetry found at the b -point). This is a reflection of the fact that the \mathbf{k}_{X_i} are not mutually orthogonal (nor are the \mathbf{k}_{J_i}). Thus, our motivation behind distorting the photonic lattice is to modify the dominant Fourier components of the defect modes, with the potential of creating a mode, centered about the dielectric, whose properties are in accordance with our momentum space design rules.

2.7.1 Preliminary analysis

We would like to create a mode whose dominant Fourier components are orthogonal to σ_x and σ_y . Such a mode would have dominant Fourier components $\pm\mathbf{k}_{X_1}$ and/or $\pm\mathbf{k}_{J_2}$. Let us begin by considering acceptor modes. By compressing the lattice in the \hat{y} -direction, so that the spacing between two adjacent rows of holes is less than its usual value (changing it from $a\sqrt{3}/2$ to $\gamma a\sqrt{3}/2$, where γ is the compression factor), we intuitively expect the position of the band edges in that direction of Fourier space (corresponding to $\pm\mathbf{k}_{X_1}$) to increase in frequency, perhaps to the point where the valence band edge at X_1 is nearly degenerate with the valence band edge at the J -points. Of course, this qualitative justification leaves many questions unanswered (such as the position of

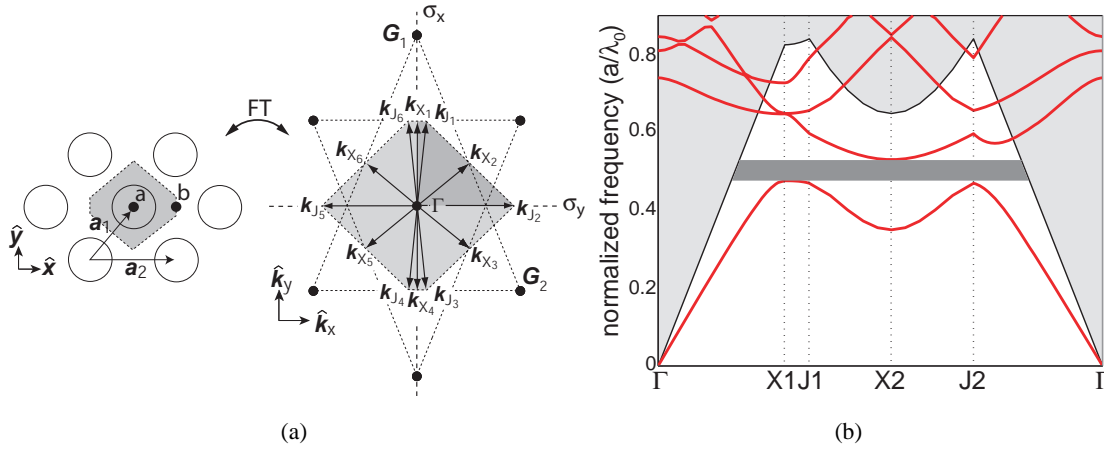


Figure 2.9: (a) Real and reciprocal space lattices of a compressed 2D hexagonal lattice. Refer to table 2.10 for more identification of key geometrical quantities; (b) fundamental TE-like (even) guided mode bandstructure for a compressed hexagonal lattice, calculated using a 2D plane-wave expansion method with an effective index for the vertical guiding; $r/a = 0.35$, $n_{\text{slab}} = n_{\text{eff}} = 2.65$, $\gamma = 0.7$.

the band edges at the other high symmetry points in the lattice). To properly answer these questions, we formulate a symmetry analysis of defect modes in compressed hexagonal lattices, using the methods of chapter 1.

Consider the real and reciprocal space representations of the compressed hexagonal lattice as illustrated in fig. 2.9(a). Compression has reduced the point group symmetry of the lattice to C_{2v} , and the irreducible Brillouin zone (IrBZ) is no longer a $30^\circ - 60^\circ - 90^\circ$ triangle, but is now a quadrilateral, traced between $\Gamma - X_1 - J_1 - X_2 - J_2 - \Gamma$. The modifications in various geometrical quantities associated with the real and reciprocal space compressed lattice are given in table 2.10. Note that, in particular, the group of the wavevector $G_{\mathbf{ok}}$ at the X and J points has been reduced in symmetry, and that $|\mathbf{k}_{X_1}| \neq |\mathbf{k}_{X_2}|$ (the \mathbf{k}_{J_i} are still equal in magnitude). Furthermore, $|\mathbf{k}_{X_1}|$ now approaches $|\mathbf{k}_J|$. Indeed, for a compression factor $\gamma = 1/\sqrt{3}$, the vectors coincide and the resulting lattice is in fact square. For compression factors between 0.8 and $1/\sqrt{3}$, the vectors are still quite close in magnitude, and we qualitatively expect that the lowest frequency band (the valence band) will be very nearly degenerate at the X_1 and J points. It is in this way that the compressed hexagonal lattices considered in this section are intermediate to the hexagonal and square lattices. In using the compressed hexagonal lattice we hope to take advantage of the large in-plane bandgap of the hexagonal lattice and the favorable symmetry of the square lattice.

Table 2.10: Key geometrical quantities associated with the standard and compressed hexagonal lattices.

Crystal Parameter(s)	Hexagonal Lattice	Compressed Hexagonal Lattice
G_a^a	C_{6v}	C_{2v}
G_b^b	C_{2v}	C_{2v}
$\{\mathbf{a}_1, \mathbf{a}_2\}$	$\{(\frac{a}{2}, \frac{a\sqrt{3}}{2}), (a, 0)\}$	$\{(\frac{a}{2}, \frac{a\sqrt{3}\gamma}{2}), (a, 0)\}$
$\{\mathbf{G}_1, \mathbf{G}_2\}$	$\{(0, \frac{4\pi}{a\sqrt{3}}), (\frac{2\pi}{a}, -\frac{2\pi}{a\sqrt{3}})\}$	$\{(0, \frac{4\pi}{a\sqrt{3}\gamma}), (\frac{2\pi}{a}, -\frac{2\pi}{a\sqrt{3}\gamma})\}$
$\pm X_1$	$(0, \pm \frac{2\pi}{a\sqrt{3}})$	$(0, \pm \frac{2\pi}{a\sqrt{3}\gamma})$
$\pm X_2$	$(\pm \frac{\pi}{a}, \pm \frac{\pi}{a\sqrt{3}})$	$(\pm \frac{\pi}{a}, \pm \frac{\pi}{a\sqrt{3}\gamma})$
$\pm X_3$	$(\pm \frac{\pi}{a}, \mp \frac{\pi}{a\sqrt{3}})$	$(\pm \frac{\pi}{a}, \mp \frac{\pi}{a\sqrt{3}\gamma})$
$\pm J_1$	$(\pm \frac{2\pi}{3a}, \pm \frac{2\pi}{a\sqrt{3}})$	$(\pm \frac{\pi}{a}(1 - \frac{1}{3\gamma^2}), \pm \frac{2\pi}{a\sqrt{3}\gamma})$
$\pm J_2$	$(\pm \frac{4\pi}{3a}, 0)$	$(\pm \frac{\pi}{a}(1 + \frac{1}{3\gamma^2}), 0)$
$\pm J_3$	$(\pm \frac{2\pi}{3a}, \mp \frac{2\pi}{a\sqrt{3}})$	$(\pm \frac{\pi}{a}(1 - \frac{1}{3\gamma^2}), \mp \frac{2\pi}{a\sqrt{3}\gamma})$
$G_{o, \mathbf{k}_{X_i}}^c$	C_{2v}	C_{2v}
$G_{o, \mathbf{k}_{J_1}}$	C_{3v}	$C_{1v} = \{e, \sigma_y\}$
$G_{o, \mathbf{k}_{J_2}}$	C_{3v}	$C_1 = \{e\}$
$G_{o, \mathbf{k}_{J_3}}$	C_{3v}	$C_{1v} = \{e, \sigma_y\}$

^a Point Group for defect at point a of lattice.

^b Point Group for defect at point b of lattice.

^c Group of the wavevector.

Using the 2D plane wave expansion method with an effective index to account for vertical waveguiding, we arrive at the bandstructure shown in fig. 2.9(b). The compression ratio (γ) has been set at a value of 0.7 for this calculation. We see that the valence band is nearly degenerate at points X_1 , J_1 , and J_2 , and thus, we expect an acceptor mode to be formed by mixing the valence band modes formed at all of these points in Fourier space. Following the symmetry analysis techniques described in chapter 1, we determine approximate forms for valence band modes at these points. Grouping all of them together, we arrive at the following expressions for modes formed about the high symmetry point a shown in fig. 2.9(a):

$$VB_a = \hat{z} \begin{pmatrix} \cos(\mathbf{k}_{X_1} \cdot \mathbf{r}_\perp^a) \\ e^{-i\mathbf{k}_{J_1} \cdot \mathbf{r}_\perp^a} + e^{-i\mathbf{k}_{J_3} \cdot \mathbf{r}_\perp^a} \\ e^{-i\mathbf{k}_{J_4} \cdot \mathbf{r}_\perp^a} + e^{-i\mathbf{k}_{J_6} \cdot \mathbf{r}_\perp^a} \\ e^{-i\mathbf{k}_{J_2} \cdot \mathbf{r}_\perp^a} \\ e^{-i\mathbf{k}_{J_5} \cdot \mathbf{r}_\perp^a} \end{pmatrix} \quad (2.7)$$

Note that the valence band modes formed about the high symmetry point b (found by taking $\mathbf{r}_\perp^b = \mathbf{r}_\perp^a - \mathbf{b}$) differ from these only by constant phase factors and hence the modes above can be used for investigations about b as well. Both the a and b points have C_{2v} symmetry, and the representation of the VB_a basis under C_{2v} , labeled $S^{a,a1}$, is given by $S^{a,a1} = 3A_2 \oplus 2B_2$, where A_2 and B_2 label irreducible representations (IRREPs) of C_{2v} . In our previous analysis, we were able to take such a representation and use projection operators on the basis functions to get approximate forms for the localized modes. In this case, we have no such luxury, as there is no way to distinguish between the modes of the different A_2 (or B_2) subspaces without some additional physical knowledge of the system. The best we can do is to form one projection operator for a composite A_2 subspace and another for a composite B_2 subspace. Doing so yields the following matrices, where the rows and columns are ordered in accordance with that which was chosen for the VB_a modes above:

$$P_{A_2} = \begin{pmatrix} 2 & 0 & 0 & 0 & 0 \\ 0 & 1 & 1 & 0 & 0 \\ 0 & 1 & 1 & 0 & 0 \\ 0 & 0 & 0 & 1 & 1 \\ 0 & 0 & 0 & 1 & 1 \end{pmatrix}, \quad P_{B_2} = \begin{pmatrix} 0 & 0 & 0 & 0 & 0 \\ 0 & 1 & -1 & 0 & 0 \\ 0 & -1 & 1 & 0 & 0 \\ 0 & 0 & 0 & 1 & -1 \\ 0 & 0 & 0 & -1 & 1 \end{pmatrix}. \quad (2.8)$$

By the form of these projection matrices, it is clear that the A_2 modes can potentially be formed from any of the degenerate band edge points $\{\pm\mathbf{k}_{X_1}, \pm\mathbf{k}_{J_1}, \pm\mathbf{k}_{J_2}, \pm\mathbf{k}_{J_3}\}$, while the B_2 modes do not include $\pm\mathbf{k}_{X_1}$. It is our hope to design defects that produce A_2 modes which only contain $\pm\mathbf{k}_{X_1}$ and $\pm\mathbf{k}_{J_2}$, to satisfy our symmetry criteria from section 2.2. To see if this can be the case, in the next section we consider FDTD simulations of defect cavities in this lattice.

Before moving on to discuss FDTD simulations, for the sake of completeness, let us briefly consider donor modes in this lattice. Such modes will be formed from the conduction band edge

located at point X_2 in fig. 2.9(b). Using a symmetry analysis similar to that described above, we determine the conduction band modes for the a and b high symmetry points:

$$CB_a = \hat{z} \begin{pmatrix} \sin(\mathbf{k}_{X_2} \cdot \mathbf{r}_\perp^a) \\ \sin(\mathbf{k}_{X_3} \cdot \mathbf{r}_\perp^a) \end{pmatrix}, \quad CB_b = \hat{z} \begin{pmatrix} \cos(\mathbf{k}_{X_2} \cdot \mathbf{r}_\perp^b) \\ \cos(\mathbf{k}_{X_3} \cdot \mathbf{r}_\perp^b) \end{pmatrix}, \quad (2.9)$$

where $\mathbf{r}_\perp^b = \mathbf{r}_\perp^a - \mathbf{b}$.

The representation of the CB_a basis under C_{2v} (the defect symmetry), labeled $S^{a,d1}$, is given by $S^{a,d1} = B_1 \oplus B_2$, while the representation of the CB_b basis under C_{2v} , labeled $S^{b,d1}$ is given by $S^{b,d1} = A_1 \oplus A_2$. Projecting the CB_a and CB_b bases onto the irreducible representations above, we get

$$\begin{aligned} \mathbf{H}_{B_1}^{a,d1} &= \hat{z} \begin{pmatrix} \sin(\mathbf{k}_{X_2} \cdot \mathbf{r}_\perp^a) - \sin(\mathbf{k}_{X_3} \cdot \mathbf{r}_\perp^a) \end{pmatrix}, \\ \mathbf{H}_{B_2}^{a,d1} &= \hat{z} \begin{pmatrix} \sin(\mathbf{k}_{X_2} \cdot \mathbf{r}_\perp^a) + \sin(\mathbf{k}_{X_3} \cdot \mathbf{r}_\perp^a) \end{pmatrix}, \\ \mathbf{H}_{A_1}^{b,d1} &= \hat{z} \begin{pmatrix} \cos(\mathbf{k}_{X_2} \cdot \mathbf{r}_\perp^b) - \cos(\mathbf{k}_{X_3} \cdot \mathbf{r}_\perp^b) \end{pmatrix}, \\ \mathbf{H}_{A_2}^{b,d1} &= \hat{z} \begin{pmatrix} \cos(\mathbf{k}_{X_2} \cdot \mathbf{r}_\perp^b) + \cos(\mathbf{k}_{X_3} \cdot \mathbf{r}_\perp^b) \end{pmatrix}, \end{aligned} \quad (2.10)$$

as approximate forms for the donor modes at points a and b .

2.7.2 FDTD results

As discussed in the previous sections, we are interested in forming an A_2 symmetry mode in the compressed hexagonal lattice, centered about the b -point, whose dominant Fourier components are situated at $\{\pm\mathbf{k}_{X_1}, \pm\mathbf{k}_{J_2}\}$, to be consistent with the symmetry criterion we have prescribed. The group theory analysis just presented has indicated that the modes of the correct symmetry are acceptor-type modes, and have $\{\pm\mathbf{k}_{X_1}, \pm\mathbf{k}_{J_1}, \pm\mathbf{k}_{J_2}, \pm\mathbf{k}_{J_3}\}$ as their potential dominant Fourier components. We thus begin our FDTD design in the compressed hexagonal lattice by analyzing the dominant Fourier components produced by a simple defect geometry.

Consider the defect geometry depicted in fig. 2.10(a), consisting of four enlarged holes surrounding the b -point in a compressed hexagonal lattice with compression factor $\gamma = 0.7$. FDTD simulations of such a design (choosing, for example, $r/a = 0.30$ and $r'/a = 0.35$), give the mag-

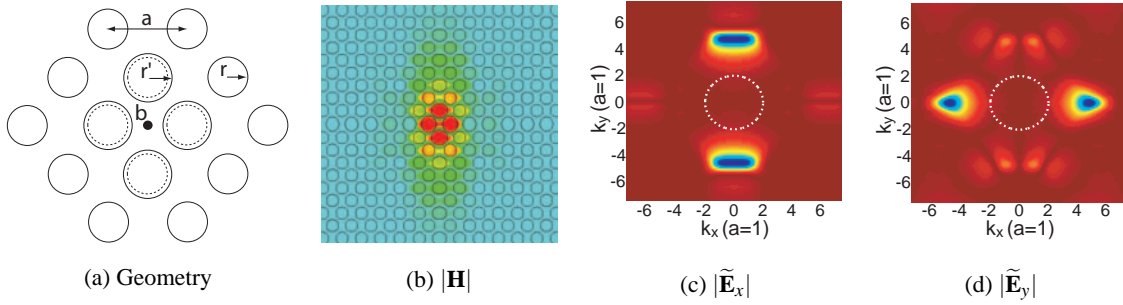


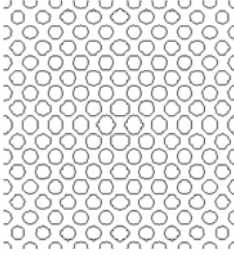
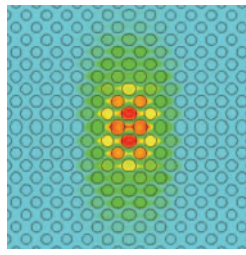
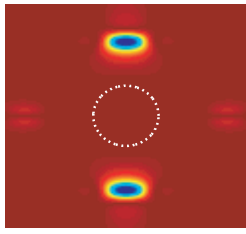
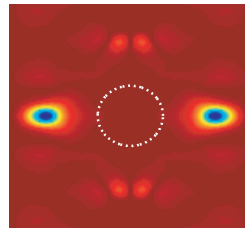
Figure 2.10: Modal characteristics of a simple defect mode in a compressed hexagonal lattice ($d/a = 0.75$).

netic field amplitude and Fourier transformed dominant electric field components shown in fig. 2.10(b)-(d). We see that our defect geometry has produced a mode with dominant Fourier components centered at $\{\pm \mathbf{k}_{X_1}, \pm \mathbf{k}_{J_2}\}$, as desired. Having produced a mode consistent with our symmetry criterion, our next step is to tailor the defect geometry so as to produce a high- Q mode.

The procedure followed is the same as what has been done in the square and hexagonal lattices, namely, we modify the lattice (and therefore $\widetilde{\Delta\eta}(\mathbf{k}_\perp)$) to reduce couplings between the mode's dominant Fourier components (in this case, $\{\pm \mathbf{k}_{X_1}, \pm \mathbf{k}_{J_2}\}$) and the light cone. We do so by starting with a defect consisting of the four enlarged holes surrounding the b -point (we choose $r'/a = (r/a)_c = 0.30$), and then parabolically decreasing the hole radius as we move away from the defect center (down to a value of $(r/a)_e = 0.225$ at the edge of the crystal). The resulting lattice is shown in table 2.11 (only the central region has been shown; in total there are 10 periods of air holes in \hat{x} and 8 periods in \hat{y} surrounding the defect center), along with the magnetic field amplitude and Fourier transformed electric field components for the defect mode. FDTD calculations predict $Q_\perp = 1.5 \times 10^5$, $Q_\parallel = 7.5 \times 10^5$, $Q_{tot} = 1.3 \times 10^5$, and $V_{\text{eff}} = 1.7(\lambda/n)^3$ for this design.

The modifications to the lattice have largely accomplished our objectives, as we have simultaneously achieved high vertical and in-plane Q s, while keeping the modal volume reasonably small (although this value is still larger than our previous designs). Improvements can still be made; for example, simulation results indicate that there are still momentum components present within the light cone of $\widetilde{\mathbf{E}}_y$; hence a further tailoring of the lattice in the \hat{x} -direction ($\widetilde{\mathbf{E}}_y$ has its dominant Fourier components along $\pm \mathbf{k}_{J_2}$) should help increase Q_\perp , though potentially at the expense of a larger mode volume.

Table 2.11: FDTD simulation results for graded compressed hexagonal lattice geometries.

Lattice		$ \mathbf{H} $	$ \widetilde{\mathbf{E}}_x $	$ \widetilde{\mathbf{E}}_y $		
						
$(\mathbf{r}/\mathbf{a})_c$	$(\mathbf{r}/\mathbf{a})_e$	ω_n	\mathbf{Q}_{\parallel}	\mathbf{Q}_{\perp}	\mathbf{Q}_{tot}	$\mathbf{V}_{\text{eff}}((\lambda/n)^3)$
0.30	0.225	0.323	755,000	152,000	127,000	1.72

2.8 Summary

The design of high- Q defect modes in a 2D PC slab WG has been developed through use of momentum space methods. Starting with the fundamental criterion that the reduction of vertical radiation losses requires an elimination of momentum components within the light cone of the slab waveguide, we proceed to present methods by which this is accomplished. The first is through a judicious choice of the mode's symmetry so that it is odd about mirror planes orthogonal to the mode's dominant Fourier components. To determine the precise nature of the symmetry for such modes in square and hexagonal lattices, we refer to the symmetry analysis of chapter 1, from which we produce a set of candidate modes that satisfy this momentum space criterion. Although symmetry alone can reduce vertical radiation loss, further modifications of the defect geometry based upon Fourier space considerations can be used to increase Q even further. Tailoring the lattice to avoid momentum space couplings which lead to in-plane and vertical radiation losses, we present graded square lattice structures for which Q_{\perp} exceeds 10^5 while maintaining Q_{\parallel} in the $3\text{--}5 \times 10^5$ range, demonstrating the possibility of producing high- Q modes in a planar PC slab WG by using these techniques. Similarly, we have used these techniques to produce cavity geometries within the regular and compressed hexagonal lattices that have total Q s in excess of 10^5 . The ability to create high- Q cavity geometries in three different lattices is an indication of the generality of this Fourier space-based approach.

As I have mentioned in the preface, after our contributions to the area of high- Q cavity design [21, 23], a number of groups have continued this work and have succeeded in developing designs

with predicted Q factors in excess of 10^6 [26, 27, 28, 29, 30]. Momentum space design principles remain the basis for most of these works, and in particular, the analysis of the spatial Fourier transform of the cavity mode field patterns has more or less become a standard approach in PC cavity design. The physical intuition behind the adoption of different cavity geometries is often thought of in different ways. The picture that we have followed is one that involves an examination of modal couplings in Fourier space, where the dielectric perturbation that forms the defect (or more precisely, its Fourier transform) is the key quantity that should be tailored to avoid the creation of modes that contain leaky Fourier components, where such problematic regions of Fourier space are well known to be the cladding light cone (for vertical radiation loss) and the range of angles and momenta for which the photonic lattice is not highly reflective (for in-plane losses). As a slightly different take on this, one can consider what the field profile of such a ‘good’ mode (i.e., one that does not contain small momentum components) looks like in real space, and then consider how to tailor the a given defect geometry to achieve this. This is essentially the approach taken in ref. [51]. More recently, some authors [28, 30] have used a PC waveguide mode as the starting point for creating PC cavities; that is, the cavity is formed through some localized modification to the geometry of a PC waveguide. This has been done by both changing the lattice constant within some region of the waveguide [28] and by shifting the position of some small number of holes within the structure [30]. Although there a number of different ways in which one can view these designs, a simple way to think about this is that a PC waveguide mode has the advantage of having a well-defined in-plane momentum along the waveguide (its propagation constant) which lies outside of the cladding light cone. It thus makes intuitive sense that there is a benefit to starting the cavity design with such a mode that, in principle, is free of radiation losses. As a side comment, this class of design is actually not that far astray from the graded square lattice cavity design presented in this chapter. The PCWG designed in ref. [33] is based upon our square lattice cavity design, where the grade in hole radius along the \hat{x} -axis is essentially kept, but the structure is not graded along the \hat{y} -axis (it has translational periodicity in this dimension). One could imagine creating a cavity that consists of a short section of this PCWG sandwiched between a pair of appropriately designed DBR mirrors that could, for example, be PCWGs with a different lattice constant or grade in hole radius. Such a design would, in principle, be very similar to those of refs. [28, 30]. This is actually relatively close to what has already been done, where the end mirrors can be thought of as the uniform PC lattice surrounding the graded section. The key to additional improvements would be to further tailor the geometry to better avoid radiation losses. At some level, this becomes somewhat difficult to do within the square

lattice because of the small in-plane bandgap, which means that in-plane losses can not be neglected (they often can be within the hexagonal lattice). In addition, it should be noted that the cavity design procedure adopted in this chapter is in part based on the utilization of modes of odd spatial symmetry in order to reduce vertical radiation losses, and as further described in chapter 4, to create a cavity design that is relatively robust to fabrication-induced imperfections. These restrictions could potentially be relaxed in future designs, in favor of other mechanisms for accomplishing the same goals. In particular, as the ability to precisely reproduce designs in fabricated structures improves, the necessity for a robust cavity design is reduced.

The momentum space analysis described in this chapter essentially tells us which portions of Fourier space to avoid to create high- Q structures; one might then expect that this could be used as the input to some type of automated computational technique that would generate the field patterns, and the associated dielectric functions, for modes that satisfy the criteria. Additional constraints on the mode volume and the robustness of the cavity geometry to imperfections, for example, could be added to such an analysis. Initial attempts to incorporate at least some amount of this inverse design approach, along with optimization methods for determining the highest possible Q and associated dielectric function within some region of parameter space, have been reported in refs. [31, 29]. Such approaches have a lot of merit in that they can eliminate the trial-and-error approach that is often used to design high- Q structures. This is particularly important in the design of these PC cavities, as FDTD simulations are often computationally intensive (a 3D simulation of the cavity field and the determination of its quality factor often takes one day of computing time on our Pentium III machines). However, one has to be mindful of the large parameter space over which such optimization techniques must, in principle, operate. At the most complex level, one can imagine that the only constraint on the physical structure is that the dielectric function at every grid point in the simulation can only be one of two values (that of the semiconductor material or that of air). Obviously, the simulation can be further constrained to only allow those dielectric functions that are physically realizable (some minimum feature size can be specified). Nevertheless, the number of potential configuration over which an optimization, for example, must be run is still quite considerable. The physical insight gained by techniques such as the group theory and Wannier analysis of chapter 1, as well as the momentum space design of this chapter, is thus very important from the standpoint of further constraining these problems by, for example, specifying the lattice to be considered, the high symmetry point about which a defect is to be formed, or the type of mode (donor or acceptor) to be considered. The specification of the lattice may be dictated by the desire to create modes of a

certain polarization, dominant emission direction, or location of the peak electric field, for example.

Chapter 3

High- Q Photonic Crystal Microcavities in InAsP/InGaAsP Multi-Quantum-Well Membranes

3.1 Introduction

With the high- Q photonic crystal microcavity designs of chapter 2 in hand, the next step is the experimental demonstration of these devices. There have typically been two experimental techniques that have been used to characterize PC microcavities. The first involves fabrication of the devices within an active (light-emitting) material, where the properties of the cavity modes are studied by optical pumping and examination of the characteristics of the resulting emission. This method has been used in a number of studies, including refs. [8, 12, 42]. Alternately, other authors [49] have chosen to fabricate the cavities within a passive (non-light-emitting) material, and have probed them by using accompanying microfabricated waveguides to couple light into and out of the cavities. In chapter 4, we will discuss the relative merits of these two approaches. For now, we will focus on our efforts on the first technique, where we have fabricated cavities in a InP-based multi-quantum-well (MQW) membrane and studied their emission characteristics. The results presented in this chapter are largely based on refs. [43] and [44]. The former paper details the primary results of our measurements, including the demonstration of $Q \sim 1.3 \times 10^4$ in a PC microcavity, which represented an improvement by almost a factor of 5 over what had been demonstrated to that point ($Q \sim 2,800$ in ref. [12]).¹ The second paper is a detailed description of the fabrication processes developed to create these InP-based structures, and in particular, highlights the advances in plasma etching that

¹ $Q \sim 4,000$ had also been demonstrated in a PC cavity, albeit a larger mode volume design where the defect consisted of several missing air holes [112].

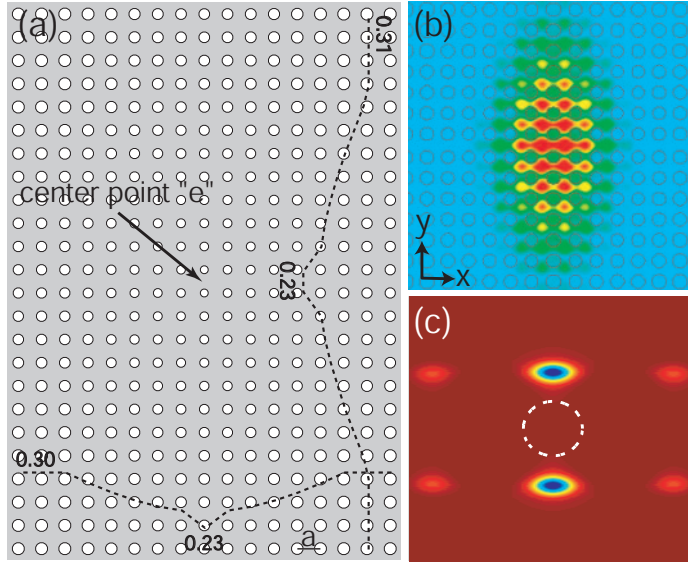


Figure 3.1: (a) Graded square lattice cavity designed in ref. [21]; dotted lines show the grade in hole radius (r/a) along the central \hat{x} and \hat{y} axes of the cavity. For the A_2 mode $(a/\lambda_o = 0.25)$: (b) Magnetic field amplitude (H_z) in the center of the PC membrane, and (c) Fourier transformed dominant electric field component (E_x) . The dashed circle in (c) denotes the cladding light cone, showing that vertical radiation has been significantly suppressed.

have made the creation of high quality semiconductor microphotonic structures possible.

In chapter 2, high- Q PC cavities were designed by considering the Fourier space properties and symmetry of cavity modes. An important feature of these designs is their robustness, in that perturbations to the size and shape of *individual* holes do not deteriorate the Q significantly. Vertical radiation losses, which are characterized by the presence of power at in-plane momentum components (\mathbf{k}_\perp) that lie within the light cone of the slab waveguide cladding, are reduced by choosing modes of a specific symmetry. In particular, the modes selected are those that are odd about mirror planes normal to the direction of the mode's dominant Fourier components. For the square lattice cavities studied in chapter 2, one such mode is a donor-type mode (labeled A_2 due to its symmetry) centered in the dielectric between two rows of air holes (point e in fig. 3.1). Further improvements to both the in-plane and vertical loss are achieved by grading the lattice as shown in fig. 3.1(a). Figure 3.1(b)-(c) shows the magnetic field amplitude and Fourier transformed dominant electric field component for the resulting A_2 mode as calculated by finite-difference time-domain (FDTD) simulations. FDTD calculations predict $Q \sim 10^5$ for this mode, with a modal volume $V_{\text{eff}} \sim 1.2(\lambda/n)^3$. Calculations show that the grade used in fig. 3.1(a) can be varied fairly significantly without degrading the Q to a value less than $\sim 2 \times 10^4$.

Table 3.1: Epitaxy for 1.3 μm PC microcavity lasers. 1.12 Q stands for quaternary GaInAsP layers, lattice matched to InP, with photoluminescence peak at 1.12 μm ($\text{Ga}_{0.15}\text{In}_{0.85}\text{As}_{0.32}\text{P}_{0.68}$). The quantum well layers are $\text{InAs}_{0.48}\text{P}_{0.52}$ and the barrier layers are $\text{Ga}_{0.24}\text{In}_{0.76}\text{As}_{0.32}\text{P}_{0.68}$. Total membrane thickness after undercutting the sacrificial InP layer is 252 nm.

Layer	Materials	Strain (rel. to InP)	Thickness	Doping (cm^{-3})
Separate confinement	1.12 Q	unstrained	810 Å	undoped
Half-barrier	GaInAsP	0.65% tens.	60 Å	undoped
Active region }	5 wells	1.5% comp.	60 Å	undoped
	4 barriers	0.65% tens.	120 Å	undoped
Half-barrier	GaInAsP	0.65% tens.	60 Å	undoped
Separate confinement	1.12 Q	unstrained	810 Å	undoped
Sacrificial buffer layer	InP	unstrained	15000 Å	undoped
Etch stop	InGaAs	unstrained	200 Å	undoped
Substrate	InP	unstrained	N/A	N/A

3.2 Fabrication of PC cavities in InP-based multi-quantum-well membranes

To measure the properties of the donor-type A_2 mode, graded square lattice PC cavities were fabricated in an active material that was grown by Dr. Jianxin Chen at Bell Laboratories through solid-source molecular beam epitaxy, as described elsewhere [113]. It consists of five InAsP compressively-strained quantum wells separated by InGaAsP barriers, as shown in table 3.1. The peak emission wavelength is at $\lambda=1284$ nm, and the epitaxy is designed so that, upon undercut of the 1.5 μm sacrificial InP layer, a 252 nm thick free-standing membrane will be formed (the thickness is chosen to be consistent with the emission wavelength of the quantum wells and the FDTD-calculated frequency of the cavity mode). The creation of the 2D PC membrane is accomplished through electron beam lithography, pattern transfer to a SiO_2 mask using an inductively coupled plasma reactive ion etch (ICP/RIE), and a high-temperature (205 $^\circ\text{C}$) Ar- Cl_2 ICP/RIE etch through the active material into a sacrificial InP layer. The sample is undercut by removing the InP layer with a $\text{HCl}:\text{H}_2\text{O}$ (4:1) solution. These fabrication steps are described in detail in the following sections. In addition, appendix C reviews some general considerations in the fabrication of microphotonic structures.

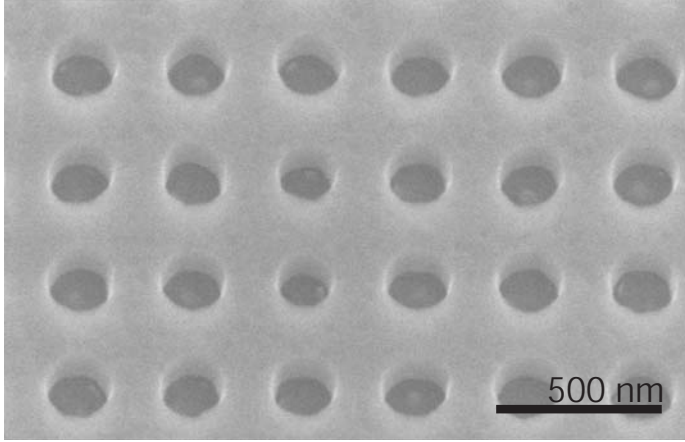


Figure 3.2: Angled view SEM image of the SiO₂ etch mask

3.2.1 Mask creation

A 200 nm thick SiO₂ mask layer is deposited on the epitaxial wafer by an Oxford Instruments Plasma Technology (OIPT) Plasmalab 100 plasma-enhanced chemical vapor deposition (PECVD) tool. The PC patterns are created through electron beam (e-beam) lithography of an ~ 350 nm thick layer of resist, typically Zeon Chemical's ZEP-520A. Each cavity consisted of a total of 32 rows and 25 columns of air holes, with a lattice spacing of $a = 305, 315, 325$, or 335 nm (normalized frequency of $a/\lambda \sim 0.25$ at $\lambda \sim 1.3 \mu\text{m}$), for total cavity dimensions on the order of $8 \times 11 \mu\text{m}$. The designed grade produces holes with radii between $r = 70$ - 110 nm.

To etch the SiO₂ mask layer, an OIPT Plasmalab 100 ICP/RIE tool with a C₄F₈ gas chemistry was used. The requirements of the process were that the etched sidewalls be as smooth and vertical in slope as possible. Due to the relatively poor dry etch resistance of the e-beam resist, a third requirement was to create a sufficiently low power etch to avoid excessive damage to the resist, so that the desired shape and size of the holes remained intact. Along with this, the low etch selectivity of the resist ($\sim 1:1$) placed an upper limit on the thickness of the oxide layer used.

The etch profile and sidewall roughness were examined as a function of ICP power (400-600 W), RF power (50-100 W), and C₄F₈:O₂ gas chemistry (between 20:0 sccm and 15:5 sccm), keeping a fixed chamber pressure ($P_{\text{ch}} = 6$ mTorr), lower electrode temperature ($\sim 20^\circ\text{C}$), and He backside cooling (20 Torr, ~ 20 sccm). To maintain the integrity of the ICP/RIE chamber, O₂ plasma cleans were periodically run between etches. For the process conditions examined, we did not observe significant changes in the sidewall roughness. For a given set of RF and ICP powers, we saw an increase in the sidewall verticality with increased C₄F₈ content, without any polymerization, so that a pure C₄F₈ gas chemistry was finally chosen. The RF and ICP powers were then adjusted to reduce

damage to the resist as much as possible without causing degradation of the sidewall profile. For the final process conditions chosen ($RF = 80$ W, $ICP = 600$ W, 20 sccm C_4F_8), an etch time of ~ 2 minutes etched through the oxide layer completely and produced a sidewall angle of $\sim 85^\circ$ as estimated through cross sectional SEM images. A scanning electron microscope (SEM) image of the etched SiO_2 mask layer is shown in fig. 3.2, where an O_2 plasma has been used to remove the remnants of the resist.

3.2.2 InAsP/InGaAsP membrane etch and undercut

The next step is an ICP/RIE etch through the InAsP/InGaAsP membrane layer into the InP sacrificial layer. From the standpoint of cavity Q , it is of critical importance that the etched sidewalls be both smooth and vertical, as sidewall roughness will produce scattering loss and an angled sidewall will break the vertical symmetry of the slab and causes radiative coupling to modes of the opposite symmetry (TM-like modes, for which there is no in-plane bandgap) [114]. As we shall discuss, the requirements on the ICP/RIE etch are also influenced by the ensuing undercut wet etch, as the necessity to undercut all of the holes in the lattice places a lower limit on the etch depth into the InP layer.

Dry etching of In-containing III-V semiconductors is typically accomplished using one of two gas chemistries [115]. The first, a CH_4/H_2 chemistry, is done at room temperature and can produce smooth etched morphologies, but with the drawbacks of a relatively slow etch rate ($\lesssim 60$ nm/min) and heavy polymer deposition during the process. Cl_2 -based plasmas have also been used, but the low volatility of $InCl_x$ products at room temperature necessitate some form of heating during the etch. This has been done in the past using a high-density ICP-produced Cl_2 plasma by Fujiwara et al. [116], where the production of smooth etched surfaces is most likely due to a combination of the plasma providing local surface heating of the sample and an increased efficiency in the sputter desorption of the $InCl_x$ products [115]. Alternately, a number of studies have successfully used a heated wafer table ($\gtrsim 150^\circ C$) with an Ar- Cl_2 chemistry to achieve a volatility of the $InCl_x$ products sufficient to etch InP-related compounds with vertical sidewalls and smooth surface morphologies. In a recent study [117], Rommel and his collaborators optimize this etch (using H_2 to control the sidewall profile) in an ICP/RIE system to produce sub-micron width racetrack resonators with a Q of 8,000. We adopt an etch similar to the process used in that work. An important difference between this work and much of the published work on InP etching is the geometry we are etching, as the small features (~ 150 nm diameter holes) likely inhibit both the flow of ionized source gases

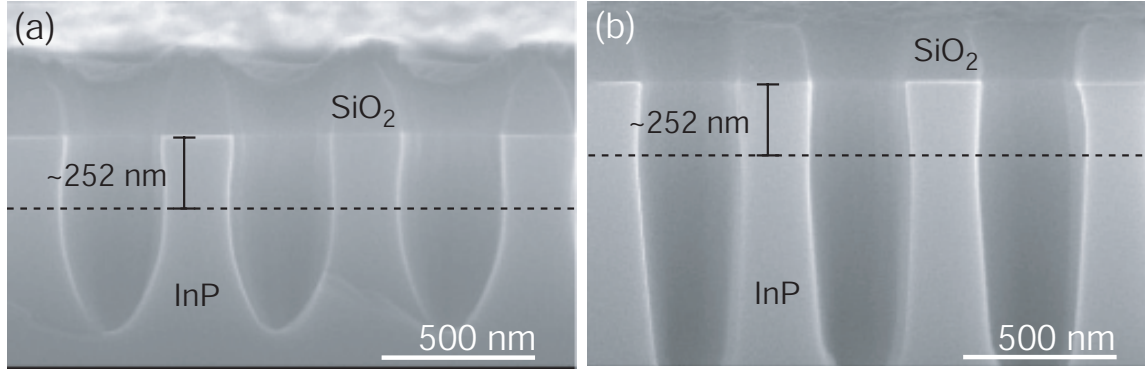


Figure 3.3: SEM cross sectional images of the InP etch for increasing wafer table temperature (a) $T=150\text{ }^{\circ}\text{C}$, $t_{\text{etch}}=120\text{ s}$, etch depth = 650 nm, and (b) $T=180\text{ }^{\circ}\text{C}$, $t_{\text{etch}}=165\text{ s}$, etch depth = 1 μm . For these etches, RF=100 W, ICP=300 W, $P_{\text{ch}} = 2\text{ mTorr}$, Ar:Cl₂=12:3 sccm. The top 252 nm, highlighted in each SEM image, corresponds to the active waveguiding layer thickness (final membrane thickness) in the actual InAsP/InGaAsP laser material used in the device fabrication.

to the etching surfaces as well as the removal of etched by-products. This will affect both the etch rates we observe (often a factor of two or more lower than the etch rates in open areas) and the resulting surface morphology.

We examined etched samples (initially etching pure InP rather than the InAsP/InGaAsP QW material) primarily as a function of gas composition (Ar:Cl₂ ratio between 9:6 sccm and 13:2 sccm), stage temperature (20-225 $^{\circ}\text{C}$), RF power (100-200 W), and ICP power (250-400 W). It quickly became apparent that elevated temperatures were indeed necessary, as the InP did not etch cleanly at room temperature. A preliminary etch with a stage temperature of 150 $^{\circ}\text{C}$ and an Ar:Cl₂ ratio of 12:3 sccm is shown in fig. 3.3(a). By further increasing the stage temperature (fig. 3.3(b)), the profile of the holes becomes more vertical and the total etch rate increases. We chose a stage temperature of 205 $^{\circ}\text{C}$ as temperatures above this value provided no added benefit to the sidewall smoothness and profile of the etched holes. With a stage temperature of 205 $^{\circ}\text{C}$, the Ar:Cl₂ gas ratio was varied around 12:3 sccm. It was found that higher concentrations of Cl₂ produce a slight amount of sidewall roughness, while lower concentrations produce a more pronounced overcut etch profile. With a stage temperature of 205 $^{\circ}\text{C}$ and an Ar:Cl₂ gas ratio of 12:3 sccm, the ICP and RF powers were then varied about values of 300 W and 100 W, respectively. Larger RF powers caused deterioration of the oxide mask, producing some sidewall erosion, while smaller RF powers reduced the etch anisotropy. We noticed little variation in etch quality as a function of ICP power over the range of ICP powers explored. The final InGaAsP material etch conditions that we settled

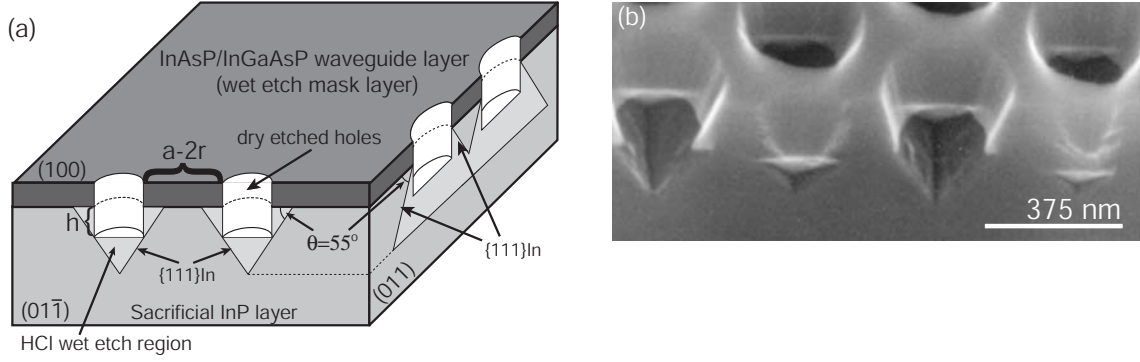


Figure 3.4: (a) Illustration of the shape of the etched surfaces resulting from the crystallographic nature of the InP wet etch (h = etch depth below waveguiding layer into InP sacrificial layer, r = hole radius, a = lattice spacing, $(a - 2r)$ = gap between holes). (b) SEM image of a partially undercut membrane (where the membrane layer was etched with a CAIBE system) showing the $\{111\}_{\text{In}}$ crystal plane facets. Both figures adapted from previous work [3].

on were: $T=205^\circ\text{C}$, $\text{Ar}:\text{Cl}_2=12:3$ sccm, $P_{\text{ch}}=2$ mTorr, $\text{RF}=100$ W, and $\text{ICP}=300$ W. With these process conditions and an etch time of 120 seconds, an etch depth of $1.5\ \mu\text{m}$ was achieved, with a selectivity of $\sim 20:1$ to the oxide mask.

To remove the sacrificial InP layer and undercut the membrane, an $\text{HCl}:\text{H}_2\text{O}$ (4:1) solution was used. HCl etches the InP layer at a much faster rate than it does the active waveguide layer (composed of lower Phosphorous (P) percentage alloys of InAsP and InGaAsP compounds), providing the necessary degree of etch selectivity [118]. The resolution and selectivity of the etch are improved by cooling the solution in an ice-water bath to $\sim 4^\circ\text{C}$, thereby reducing the material etch rates, and in particular, the total amount of waveguide material that is necessarily etched. The typical time to fully undercut the membrane was ~ 12 minutes (depending on the lattice spacing and hole size of the PC pattern). To protect the top sample surface, the remnants of the oxide mask layer were removed only after the undercut etch was performed.

The $\text{HCl}:\text{H}_2\text{O}$ solution etches InP with a strong crystallographic dependence [119]. The resulting etch shape is determined by the differences in etch rate of different crystallographic planes as well as boundary conditions imposed by masking layers (which limit the available etch angles). The etch shape will ultimately converge to one determined by the slowest set of etch planes, which are the Indium (In) rich $\{111\}$ planes ($\{111\}_{\text{In}}$) for the InGaAsP material system. For a (100) InP wafer, the $\{111\}_{\text{In}}$ planes are at an angle of $\sim 55^\circ$ from the surface normal as shown in fig. 3.4(a). For concave mask openings, this results in an etch cross section which is an overcut V-shape in the $(01\bar{1})$ plane and an undercut overhanging shape in the (011) plane. This is shown schematically

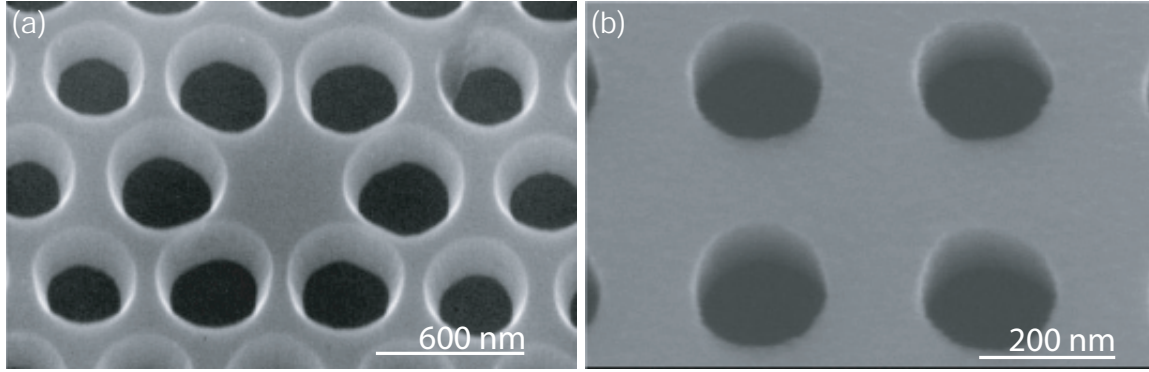


Figure 3.5: SEM micrographs of fully fabricated devices: (a) previous work using CAIBE for the membrane etch [3], and (b) the current work, using ICP/RIE for the membrane etch.

in fig. 3.4(a), and can also be seen clearly in the partially undercut holes of fig. 3.4(b). As in fig. 3.4(b), once the etch has proceeded to the $\{111\}_{\text{In}}$ planes, unless there is an overlap between the $\{111\}_{\text{In}}$ planes of adjacent holes, the etch will grind to a halt and the waveguiding layer will not completely undercut (longer etch times and/or higher temperatures may be employed to further undercut the structure, however, selectivity to the active waveguiding layer will have been lost). As a result, the ICP/RIE dry etch depth into the underlying sacrificial InP layer sets a lower limit on the radius (r) and lattice spacing (a) of holes that can be undercut. More precisely, using the nomenclature of fig. 3.4(a), the adjacent $\{111\}_{\text{In}}$ planes in the $(01\bar{1})$ plane overlap for $h \geq (a/2 - r) \tan(55^\circ)$, so that h increases as r decreases for a given a . This was a limitation of previous work done using an Ar:Cl₂ chemically assisted ion-beam etch (CAIBE) [3], where total etch depths were typically ~ 340 nm, corresponding to $h \sim 130$ nm. For the fabricated lattice spacings in that work, $a = 500$ nm, this produces a minimum possible undercut hole radius of $r/a = 0.32$. The ability to undercut smaller holes (preferably as small as $r/a = 0.20$) is of critical importance to the cavity Q , as holes that are too large in size will significantly raise the frequency of a given mode and hence the size of the cladding light cone, thereby increasing the amount of power radiating vertically [21]. Our etch depth of $\sim 1.5 \mu\text{m}$ ($h \sim 1.25 \mu\text{m}$) is not only deep enough to ensure that the $\{111\}_{\text{In}}$ crystal planes overlap for even the smallest desired holes ($r/a = 0.23$), but also aids the undercut process by reducing the total amount of material that needs to be removed.

Figure 3.5 compares the results of previous fabrication methods [3] with the current work. Both images show smooth membrane sidewalls, but the sidewall profile is considerably more sloped in the former work (this is also evident in fig. 3.4(b)). The higher degree of verticality and the ability

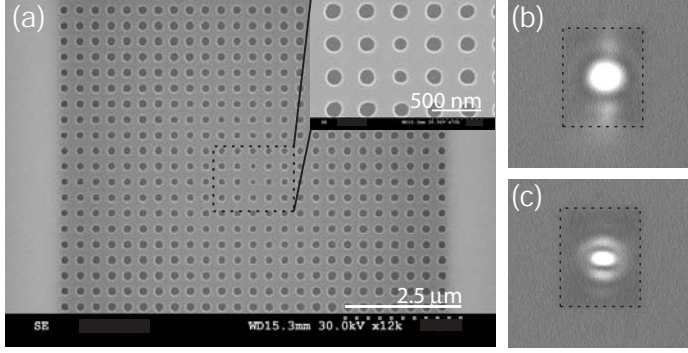


Figure 3.6: (a) SEM image of a graded lattice PC microcavity in the InAsP multi-quantum-well material. Lattice constant $a \sim 305$ nm, membrane thickness $d = 252$ nm. Optical image of cavity pumped with a (b) diffuse beam and (c) focused beam (dashed rectangle represents the physical extents of the undercut PC).

to undercut the smallest desired holes ($r/a = 0.23$) are the primary advantages of the present work. Although optimization of all of the masking steps was necessary to achieve this result, the ICP/RIE membrane etch is the critically important step that creates these advantages.

3.3 Photoluminescence measurements

Using the fabrication techniques described in the previous section, we created arrays of PC cavities within the InP-based MQW epitaxy. Devices are optically pumped (10 ns pulse width, 300 ns period) at room temperature with a semiconductor laser at 830 nm through a 20X objective lens, also used to collect emitted photoluminescence (PL) into an optical spectrum analyzer (OSA). A schematic of the setup that was used is shown in fig. 3.7. We initially pump the cavities with a broad pump beam (see fig. 3.6(b), area $\sim 21\mu\text{m}^2$) for two reasons: (i) the broad pump beam covers a significant portion of the cavity area, so that after diffusion of carriers, the majority of the cavity should be pumped and therefore non-absorbing, and (ii) use of a broad pump beam limits the effects of thermal broadening, which, as discussed below, are significant for focused pump beams.

A typical L-L (light-in versus light-out) curve using the broad pump beam condition is shown in fig. 3.8(a) for a device with $a = 335$ nm, where the power in the laser line is taken over a 10 nm bandwidth about the laser wavelength of $\lambda = 1298.5$ nm. In addition, the off-resonance background emission at $\lambda = 1310$ nm was measured over a similar 10 nm bandwidth. For low pump powers ($< 300\mu\text{W}$), the off-resonance emission and resonant wavelength emission linearly increase with pump power and are essentially identical in level, i.e., no resonance feature is observed. Above $300\mu\text{W}$, we begin to see a resonance peak in the spectrum and a characteristic super-linear transition from below threshold to above threshold follows. To estimate the position of threshold we extrapolate

Photoluminescence setup

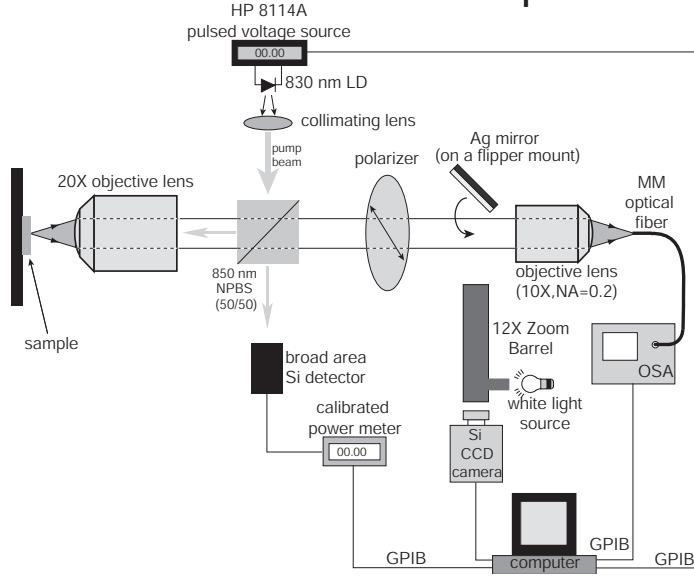


Figure 3.7: Schematic of the photoluminescence measurement setup. Acronyms used in this diagram: NPBS: non-polarizing beamsplitter, LD: laser diode, MM: multimode, OSA: optical spectrum analyzer

back the L-L curve from above threshold (fig. 3.8(b)), giving an approximate threshold pump level of $360 \mu\text{W}$. A plot of the off-resonance emission (fig. 3.8(c)) shows a (weak) slope change around $365 \mu\text{W}$ giving a similar estimate for the threshold value. The kink in the off-resonance background emission L-L curve can be attributed to the clamping of the carrier density (gain) in the region of the cavity mode and consequent saturation of the off-resonance (non-lasing modes') emission. The background emission continues to increase after crossing threshold (rather than completely saturating) as a result of the pumping of areas which are outside of the cavity mode volume and thus not affected by the gain clamping (non-equilibrium carrier distributions [120] may also play a role).

In order to estimate the cold cavity Q value of the PC microcavity mode we measured the linewidth of the resonance in the PL around threshold. The full-width half-maximum (FWHM) linewidth narrows from 0.138 nm (at the lowest pump level we could accurately measure the linewidth, $320 \mu\text{W}$) down to 0.097 nm at threshold. A simple steady state rate equation model [121] of the cavity photon and excited state populations estimates the threshold pump level (with this beam size) to be $\sim 350 \mu\text{W}$ for $Q \sim 10^4$ in this quantum well active material, close to the experimentally measured value. In this model the transparency carrier density occurs within 10% of the threshold carrier density for cavity modes with $Q > 10^4$. A PL spectrum (fig. 3.8(a), inset) for this device with the broad pump conditions, measured soon after detection of a resonance feature in the spectrum and below the estimated threshold level by about 10%, shows a resonance linewidth $\Delta\lambda = 0.100 \text{ nm}$, corresponding to a best estimate of the cold cavity $Q \sim 1.3 \times 10^4$. Above threshold

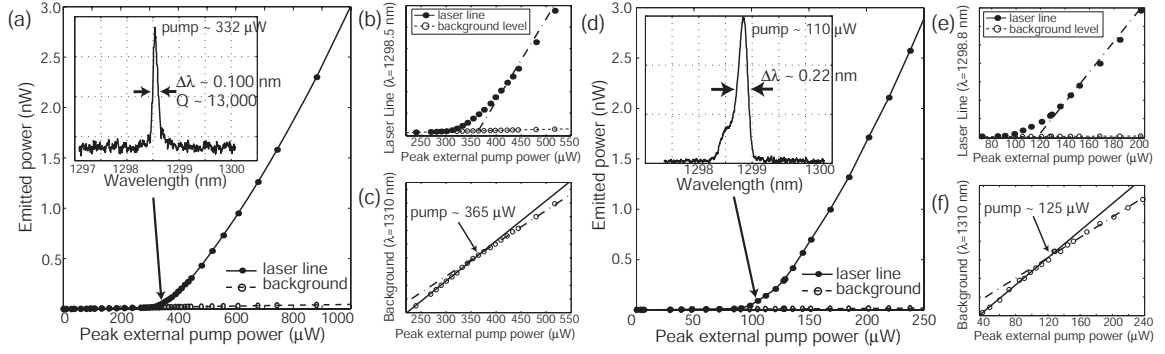


Figure 3.8: (a) L-L curve and subthreshold spectrum (inset) of a graded square lattice PC microcavity pumped with a spatially broad pump beam (10 ns pulse, 300 ns period), and zoomed-in plots of (b) laser threshold and (c) background emission for the same diffuse pump beam. (d) L-L curve and subthreshold spectrum (inset) taken with a focused pump beam spot, showing increased thermal broadening in comparison to the diffuse pump beam spectrum, and zoomed-in plots of (e) laser threshold and (f) background emission. The “guide” lines displayed in (b), (c), (e), and (f) are least-squares fits of the data taken over several points above and below the lasing transition region.

we do not see further linewidth narrowing due to the resolution limit of our scanning monochromator (0.08 nm); thermal broadening of the emission line during the pump pulse and incomplete saturation of the carrier density [120] may also play a role.

By using a more tightly focused beam (see fig. 3.6(c), area $\sim 8 \mu\text{m}^2$), the lasing threshold is considerably reduced. In fig. 3.8(d)-(f), we plot the L-L curve for the laser line and off-resonance background emission using such a pump beam. The plots are qualitatively similar to those for the diffuse pump beam; we begin to see a resonance feature when the pump power exceeds 95 μW . Estimates for the threshold pump power from the laser line curve and off-resonance background emission are 120 μW and 125 μW , respectively. Through further optimization of the pump beam, lasers with thresholds as low as $\sim 100 \mu\text{W}$ have been observed. From the subthreshold spectrum shown in the inset of fig. 3.8(d) it is readily apparent that the lineshape has thermally broadened (the measured linewidth is now 0.220 nm), as evidenced by its asymmetric shape on the short wavelength side. To reduce the effects of this thermal broadening, the duty cycle can be decreased to 1% (1 μs period and 10 ns pulse width), resulting in a less asymmetric resonance and subthreshold linewidth of approximately 0.13 nm. Conversely, we have also increased the duty cycle to 25% (1 μs period and 250 ns pulse width) and still observe lasing; heating in the membrane precludes lasing at even higher duty cycles.

To determine whether the laser mode described above is indeed the localized A_2 mode of fig. 3.1,

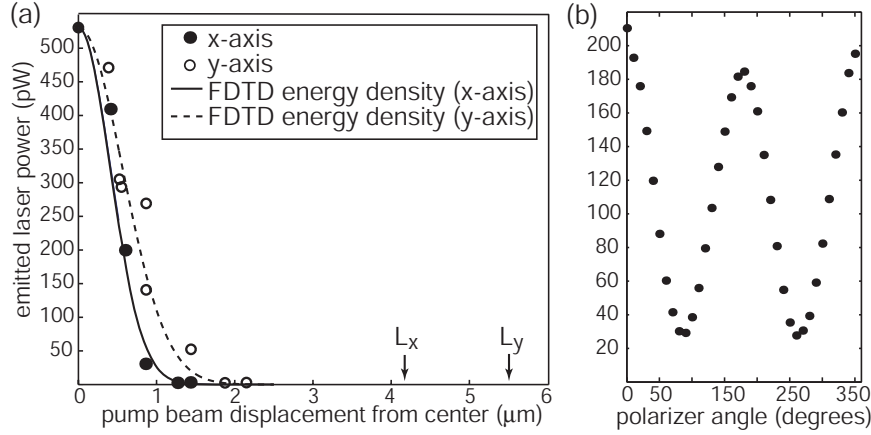


Figure 3.9: (a) Emitted laser power as a function of pump position along the \hat{x} and \hat{y} axes of the cavity. FDTD-generated Gaussian fits to the *envelope* of the electric field energy density of the cavity mode are shown for comparison (note that the effective mode volume is calculated from the *peak* electric field energy density). L_x and L_y correspond to the physical extent of the PC in the \hat{x} - and \hat{y} -direction, respectively. (b) Emitted laser power as a function of polarizer angle with respect to the \hat{x} axis of the cavity.

we have measured polarized intensity in the far-field as well as the sensitivity of the emitted laser power to pump position. The measurements show the mode to be predominantly polarized along the \hat{x} -axis (fig. 3.9(b)) of the cavity, consistent with FDTD results, and eliminating the possibility that the mode is of the other potential symmetry supported by the cavity (B_2 , as discussed in chapters 1 and 2). Furthermore, the lasing mode discussed above is the longest wavelength mode observed in the devices tested (higher frequency resonances are observed in some detuned devices), suggesting that it is the fundamental mode shown in fig. 3.1(b), and not a higher order version of it. In fig. 3.9(a) we show measurements of the emitted laser power as a function of the pump beam position (taken to be the center of the beam) relative to the center of the cavity (uncertainty in the pump position is $\sim 0.25 \mu\text{m}$). The measurements indicate the mode is highly localized within the center of the cavity, consistent with simulations.

3.4 Summary

In summary, this chapter reports on the observation of linewidths of $\Delta\lambda = 0.10 \text{ nm}$, corresponding to a cavity Q of 1.3×10^4 , in subthreshold measurements of graded square lattice photonic crystal microcavity lasers fabricated in an InAsP/InGaAsP multi-quantum-well membrane. In addition, lasing is seen at threshold peak external pump powers as low as $100 \mu\text{W}$. Measurements of the

emitted power as a function of pump position show the mode to be strongly localized and give an estimate of the modal localization that is consistent with FDTD results. This realization of a high Q , small mode volume microcavity is an important step in demonstrating the potential of PC microcavities for use in optoelectronics and quantum optics.

The Q values that we demonstrated in these PC microcavity lasers were at the time, the highest that had been seen in a PC microcavity, but were quickly exceeded by devices demonstrated by both the group of S. Noda at Kyoto University [51], and by our own group at Caltech, in devices I created in silicon membranes [52], which will be described in detail in the following chapter. To the best of my knowledge, within the InP material system, there has not yet been a demonstration of a PC microcavity with a Q higher than the devices described in this chapter.

More importantly, the measurements we performed on these devices give us some indication of the limitations of these spectrometer-based studies using cavities fabricated in an active material. The most obvious limitation is the resolution of the spectrometer; for the optical spectrum analyzer we used, this was 0.1 nm, but even for instruments with a longer path length, resolutions better than 0.01 nm are difficult to achieve. Of course, other resolving instruments, such as filters based on Fabry-Perot cavities (which can be commercially obtained in both free-space and fiber-based geometries), can be used to achieve much better resolution. That being said, it is still clear that there are other advantages to adopting a measurement technique that did not require an active medium. This would open up PC cavities fabricated in materials such as silicon (which had been shown to have relatively low material loss at telecommunications wavelengths) for investigation, and it would allow for a simple measurement of Q that would not be subject to the influence of material gain. Most importantly, developing a technique to efficiently get light into and out of the PC microcavities would make these devices much more functional and integrable within more sophisticated experiments or systems. In the next chapter, I describe our work with a fiber-based probe that enables such advances.

Chapter 4

Optical-Fiber-Based Measurement of an Ultrasmall Volume, High- Q Silicon Photonic Crystal Microcavity

4.1 Introduction

This chapter details the measurements of photonic crystal microcavities within silicon membranes. The cavity design is the graded square lattice geometry described in chapter 2 and examined experimentally within InP-based multi-quantum-well membranes in the previous chapter. From a device performance perspective, the primary result of importance in this chapter is the demonstration of a quality factor $Q \sim 40,000$ in a wavelength-scale PC cavity. Of equal importance, however, is the development of an optical-fiber-based probing technique that is utilized to study the spectral and spatial properties of resonant modes within these PC cavities. This technique, which essentially involves evanescent coupling between an optical fiber taper waveguide and the PC cavity, allows for quantitative measurements of two of the most important properties of a cavity mode, its Q and spatial localization (related to V_{eff}). From an experimentalist's perspective, other benefits of this fiber-based probing method are that it is relatively easy to implement and can be used to rapidly characterize all of the devices on a chip.

The majority of this chapter (sections 4.2-4.7) is largely based on three articles; (i) ref. [52], which describes our initial use of the fiber taper to demonstrate a high Q ($\sim 40,000$) and spatial localization consistent with an ultrasmall V_{eff} ($\sim 0.9(\lambda/n)^3$) in a PC cavity, (ii) ref. [53], which uses the fiber-based probe to study the robustness of the cavity Q in our graded lattice design with respect to perturbations in the lattice, and (iii) ref. [54], which is a review article that we have written on the use of the fiber taper as a probe for PC microcavities (and wavelength-scale semiconductor cavities

in general).

In section 4.8, I briefly review some of the work that I was not the primary investigator on, but which I had the opportunity to be a part of and is directly related to the work described in this and subsequent chapters. The first topic [57] describes the work of my colleague Paul Barclay in coupling light into our PC microcavities through use of an intermediate PC waveguide that is phase matched to the fiber taper. This technique is critical in achieving coupling to the cavities that is far more efficient than what is achieved through direct coupling from the fiber taper. The second topic I examine is the work of Matt Borselli [64], who used fiber tapers to investigate Si microdisk cavities. Matt was able to demonstrate Q/V ratios that were slightly higher than what we saw in the PC cavities, and more importantly, was able to show that the fiber taper can directly couple light into these devices in a relatively efficient manner. His work on these structures led to my subsequent adoption of them in experiments involving AlGaAs microcavities with embedded quantum dots (chapters 5-7).

4.2 Fabrication

We decided to fabricate our PC cavities within the silicon-on-insulator (SOI) material system, due to its relatively low material loss in the $1.5\ \mu\text{m}$ range and how readily available it is commercially. The material, obtained from the company SOITEC, consists of a 340 nm thick silicon (Si) layer on top of a $2\ \mu\text{m}$ silicon dioxide layer. As our goal was to test our devices through evanescent coupling with fiber tapers, we decided to fabricate our cavities on mesas that are isolated from the rest of the chip (the specific reasons for this, and recent developments that have obviated it, are discussed later within the chapter). The following processing steps were performed (additional details are given in appendix C): (1) electron beam lithography of the PC pattern and accompanying cutouts for removal of additional material from the mesa, (2) $\text{SF}_6/\text{C}_4\text{F}_8$ -based inductively-coupled plasma reactive ion etching (ICP-RIE) through the silicon membrane layer, (3) removal of the electron beam resist, (4) photolithography to define a mesa stripe that intersects the electron beam defined cutouts, (5) removal of material surrounding the mesa (dry etching of the top silicon, underlying oxide, and substrate silicon layers), (6) removal of the photoresist, and (7) wet etch (hydrofluoric acid) of the underlying oxide layer to form a free-standing membrane. Figure 4.1 shows scanning electron microscope (SEM) images of fully processed devices; in addition to being isolated to the mesa stripe, additional cutout material (defined in step (1) above) surrounding each cavity has been

removed to ensure that the taper interacts only with the cavity. Figure 4.2 shows close-up SEM images of a fabricated PC cavity. From these images, we can observe the quality of the dry etch processes that have been developed; the etched air holes are both smooth and vertical, each of which is necessary to achieve devices that exhibit high Q s.

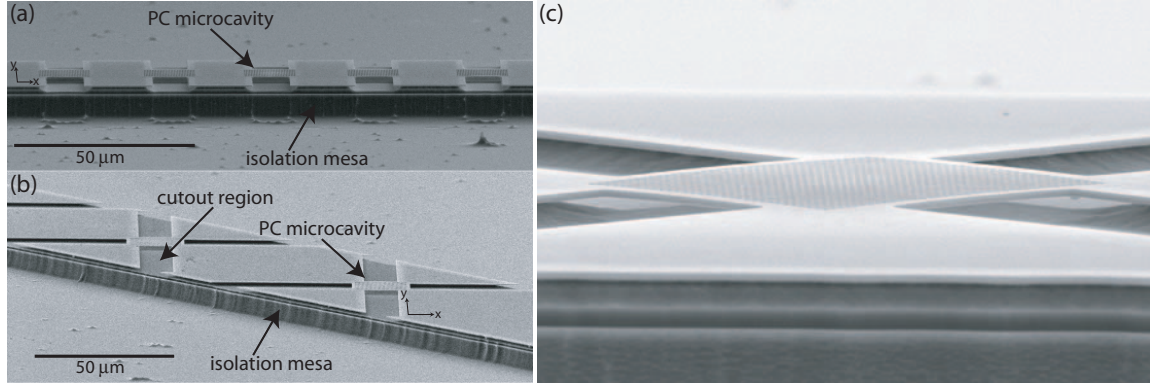


Figure 4.1: (a)-(b) Scanning electron microscope (SEM) images of photonic crystal microcavity arrays fabricated in silicon-on-insulator. The undercut PC microcavities are fabricated in a linear array that is isolated from the rest of the chip by several microns. The devices in (a) have additional material removed along the \hat{y} axis of the cavity, to allow for the fiber optic taper to be aligned along that axis. The devices in (b) have additional material ('cutout region') removed along both the \hat{x} and \hat{y} axes, to allow probing along either axis. (c) Close-up low-angle image of a single PC cavity within the array of devices in (b).

Within the linear array of devices, we fabricate two or three different lattice constants (with $a=380\text{-}430$ nm, so that $a/\lambda \sim 0.25$ for $\lambda=1600$ nm, to be consistent with simulation results for the grade square lattice cavity design), and for a given a , the average hole radius (\bar{r}/a) is varied. The combination of varying a and \bar{r}/a allows us to easily tune the cavity resonances through the range of the scanning tunable laser ($\lambda=1565\text{-}1625$ nm) that we use in our measurements.

4.3 Measurement setup

The fiber tapers we use consist of a standard single mode optical fiber ($9\text{ }\mu\text{m}$ core diameter, $125\text{ }\mu\text{m}$ cladding diameter) that has been simultaneously heated and stretched down to a minimum diameter (d) on the order of the wavelength of light (λ), so that for $\lambda \sim 1.6\text{ }\mu\text{m}$ as used in our experiments, $d \sim 1\text{-}2\text{ }\mu\text{m}$. To form the tapers used here, the heating mechanism is a hydrogen-based torch [122], but other techniques such as use of a CO_2 laser have also been studied by other groups [123]. In a taper with a suitably adiabatic transition region, the insertion loss through the taper can be quite

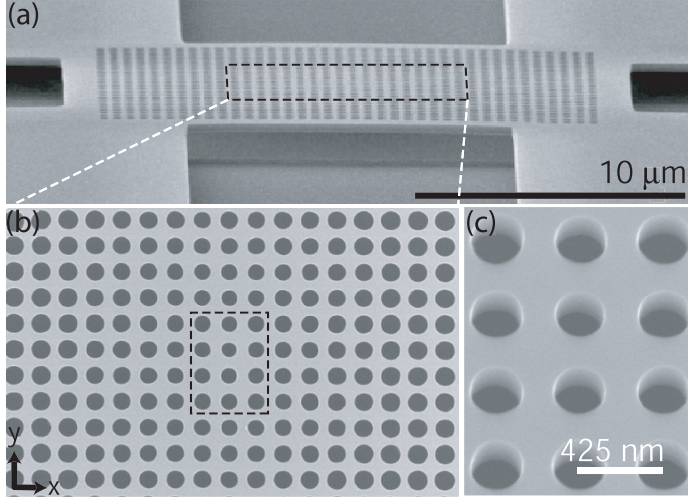


Figure 4.2: SEM micrographs of a fully fabricated PC microcavity. (a) Cross-sectional view. (b) Top view of the portion of the cavity contained within the dashed lines in (a). Total cavity dimensions are $\sim 13\mu\text{m} \times 16\mu\text{m}$. (c) Zoomed in angled view of the dashed line region in (b) showing the smoothness and verticality of the etched air hole side-walls, necessary to limit scattering loss and radiative coupling to TM-like modes.

low; the tapers we typically fabricate have an insertion loss of $\sim 10\%$. The taper is mounted onto an acrylic block in a u-shaped configuration (fig. 4.3(b)), and the block is then fastened to a DC motor-controlled \hat{z} -axis stage with 50 nm step size resolution. Mounting the taper in this fashion naturally keeps it under tension and prevents the taper position from excessively fluctuating due to environmental factors (such as fluctuating air currents in the laboratory). The microcavity chip is in turn mounted on a DC motor-controlled $\hat{x} - \hat{y}$ -axis stage with 50 nm step size resolution; in this way, the fiber taper can be precisely aligned to a microcavity. The taper-cavity interaction region is imaged with a microscope onto a CCD camera. The vertical separation between the taper and cavity can easily be calibrated by stepping the taper down in 50 nm increments until it just touches the cavity (this can be seen optically through the microscope), establishing the motor read-out corresponding to a zero gap. Determining the separation in this manner is made possible by the mechanical robustness of the taper, which allows it to withstand contact to the semiconductor chip without breaking.

The mounted taper is fusion spliced into the measurement setup (fig. 4.3(a)) so that a fiber-coupled scanning tunable laser with polarization-controlling paddle wheels is connected to its input and an InGaAs photodetector measures its output. The laser and photodetector output are attached to a computer via GPIB interfaces, so that the wavelength-dependent transmission of the taper can be recorded. In addition, the motorized stages on which the taper and PC chip are mounted are also GPIB controlled, so that the taper transmission spectrum can be monitored as a function of the taper's position with respect to the cavity. When the taper is laterally aligned over the central region of the cavity and positioned vertically within the cavity's near field (typically $< 1\mu\text{m}$), the cavity

modes appear as resonances within this transmission spectrum. As we shall discuss in section 4.4, measurements of the linewidth and depth of these resonances as a function of the taper's position with respect to the cavity can give us quantitative estimates of the cavity's Q and V_{eff} .

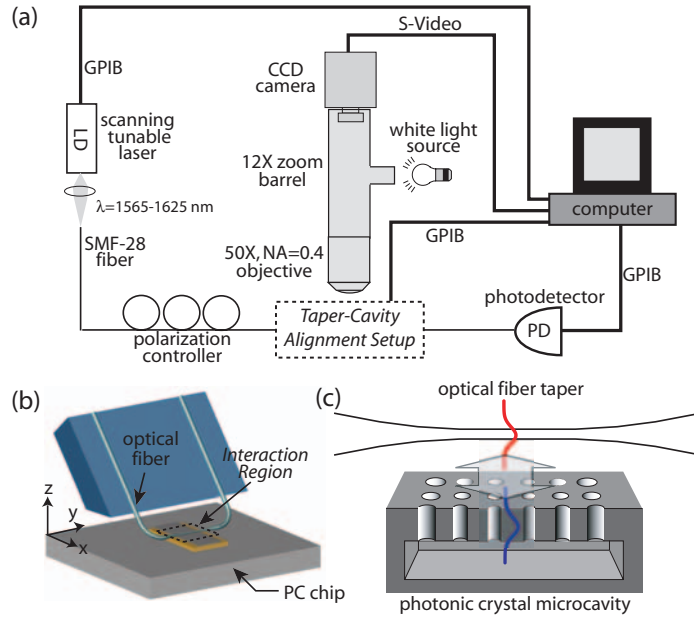


Figure 4.3: (a) Experimental measurement setup for probing optical microcavities with fiber tapers. (b) Taper-cavity alignment setup (dashed boxed region in (a)). The fiber taper is mounted in a u-shaped configuration and attached to a \hat{z} axis stage with 50 nm resolution, while the underlying PC chip can be positioned in the $\hat{x} - \hat{y}$ plane with 50 nm resolution. The fiber taper is spliced into the setup in (a), which allows for measurement of its wavelength-dependent transmission spectrum. (c) Zoomed-in depiction of the taper-cavity interaction region (dashed boxed region in (b)).

In principle, the curvature of the looped taper shown in fig. 4.3(b) could be made large enough so that only a small region of the fiber interacts with the PC chip, and the taper could then be used to probe a full two-dimensional (2D) array of cavities on a chip; since the work described in this thesis was completed, Chris Michael, a student in our group, has developed a technique and fiber mounting strategy to do this. For the fiber tapers we have used in the experiments described here, however, the region of the fiber that interacts with the chip is typically around 10 mm in length, and is roughly equal to the length of the tapered region of the fiber as defined when the taper is formed. One result of this relatively long 10 mm interaction length is that testing of a 2D array is not feasible, and linear (1D) arrays of devices are tested. In addition, because coupling to the cavity requires the taper to be positioned within a micron of the center region of cavity, control of the tip and tilt of the sample with respect to the taper is necessary; this is accomplished through use of a goniometer stage mounted to the motor-controlled $\hat{x} - \hat{y}$ sample stage. Finally, to prevent the taper from interacting with extraneous portions of the chip, the cavities are isolated to a mesa stripe that is several microns above the rest of the sample surface (fig. 4.1). By appropriately angling the goniometer stage with respect to the taper, it can be ensured that when the taper is brought into contact with the chip, it

only touches the cavity region.

4.4 Measurement results

The coupling between the tapered fiber waveguide and the PC microcavity can be understood using, for example, the coupling of modes in time approach as in Manolatou et al. [50]. The degree to which the taper mode couples to the cavity mode is a function of the parameter κ , which is approximately given by the field overlap between the two modes over their interaction length. More explicitly, for the taper aligned along the \hat{y} -axis of the cavity, it is given by:

$$\kappa = -\frac{i\omega\epsilon_0}{4} \int_0^L e^{-i\beta y} dy \left(\iint_{A_c} (n^2 - n_c^2) \mathbf{E}_c^* \cdot \mathbf{E}_t dx dz + \iint_{A_t} (n^2 - n_t^2) \mathbf{E}_c^* \cdot \mathbf{E}_t dx dz \right), \quad (4.1)$$

where ω is the resonant cavity mode frequency, ϵ_0 is the permittivity of free space, β is the propagation constant of the taper mode, n is the refractive index of the background air, n_c (n_t) is the refractive index profile of the cavity (taper), \mathbf{E}_c (\mathbf{E}_t) is the electric field vector of the cavity (taper), L is the interaction length of the coupling, and the integrals over A_c and A_t are two-dimensional integrals over the x - z cross section within the cavity and taper, respectively, for a given y value within the interaction length. From this formula, we see that κ is dependent upon: (i) the magnitude of the overlap between \mathbf{E}_c and \mathbf{E}_t , (ii) the relative phase between \mathbf{E}_c and \mathbf{E}_t , and (iii) the degree to which \mathbf{E}_c and \mathbf{E}_t share a common direction of polarization.

4.4.1 Polarization

Considering the latter point, for the taper aligned along the \hat{y} -axis of the cavity, as in fig. 4.4(a), the polarization-controlling paddle wheels are used to select a linearly polarized state of the taper whose dominant field component is aligned along the \hat{x} -axis of the cavity. Thus, modes that couple most strongly will have their \hat{x} field component overlap strongly with the \hat{x} component of the taper field. By aligning the taper along a different axis of the cavity, polarization selectivity can be realized. For the devices in Figs. 4.1(a) and 4.4(a), this is not possible, as aligning the taper along the \hat{x} -axis will couple the taper to multiple cavities. However, by fabricating the cavities at a 45° angle with

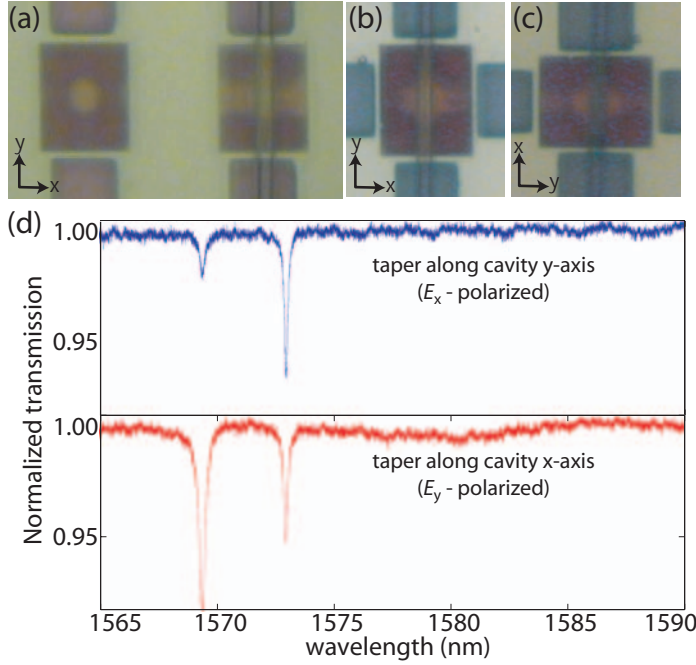


Figure 4.4: (a)-(c) Optical micrograph image of a fiber taper aligned along (a) the \hat{y} -axis of one of the cavities from fig. 4.1(a); (b)-(c) the \hat{y} and \hat{x} axes, respectively, of one of the cavities from fig. 4.1(b). (d) Normalized taper transmission when the taper is ~ 350 nm above a PC cavity of the type shown in fig. 4.1(b); (top) Taper aligned along the cavity's \hat{y} -axis (bottom) Taper aligned along the cavity's \hat{x} -axis.

respect to the isolation mesa stripe, as in fig. 4.1(b), the taper can be aligned along either of the orthogonal cavity axes without coupling to multiple devices. In fig. 4.4(b)-(c), we show the optical fiber taper aligned parallel to the \hat{y} and \hat{x} axes of one of the cavities from fig. 4.1(b). When the taper is laterally aligned with the center of the cavity and brought vertically close to it, we observe the cavity's resonances. As shown in fig. 4.4(d), the coupling is polarization selective, so that those resonances with dominant cavity field component E_x couple most strongly when the taper is aligned along the \hat{y} -axis of the cavity (fig. 4.4(b)), while those with dominant cavity component E_y couple most strongly when the taper is aligned along the cavity's \hat{x} -axis (fig. 4.4(c)). Thus, the shorter wavelength resonance in fig. 4.4(d) is more strongly polarized along the \hat{y} -axis, while the longer wavelength resonance is more strongly polarized along the \hat{x} -axis. This data is consistent with simulation and group theoretical results that predict that these square lattice microcavities support modes of types A_2 and B_2 symmetry, which are predominantly polarized along the \hat{x} and \hat{y} axes of the cavity, respectively [21]. The coupling depths of a few percent are typical values, and were found to be adequate to achieve a sufficient signal-to-noise ratio for all of the measurements presented in the upcoming sections.

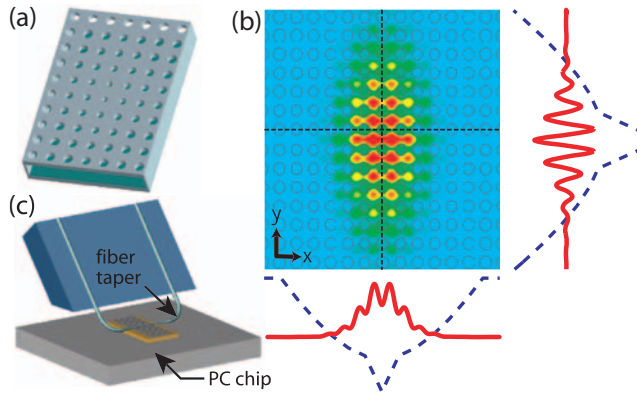


Figure 4.5: Summary of the design of the graded square lattice photonic crystal microcavity. (a) Schematic of the undercut, two-dimensional PC microcavity geometry. (b) Magnetic field amplitude ($|\mathbf{B}|$) in the center of the PC membrane for the A_2^0 mode. The dashed curves show the grade in hole radius (r/a) along the central \hat{x} and \hat{y} axes of the cavity (marked by dashed lines through the dielectric lattice), and the solid curves are slices of the field component B_z along these directions.

4.4.2 High- Q measurements

For future microcavity-enhanced experiments within our graded square lattice PC geometry, the fundamental TE-like mode of A_2 symmetry, which we label as the A_2^0 mode, is of particular interest, on account of its predicted ultrasmall V_{eff} and high Q factor. Let us briefly review some of the key features of this mode: the PC cavity geometry employed is shown in fig. 4.5(a-b), and was designed using group theoretical, Fourier space, and finite-difference time-domain (FDTD) analyses as described in detail in chapter 2. The cavity consists of a localized defect in a square lattice of air holes that are etched into an optically thin membrane of refractive index $n=3.4$. This geometry provides in-plane modal localization via distributed Bragg reflection due to the lattice and vertical confinement by total internal reflection at the membrane-air interface. The resulting TE-like A_2^0 defect mode shown in fig. 4.5(b) is predicted to have $Q \sim 10^5$ and $V_{\text{eff}} \sim 1.23 (\lambda_c/n)^3$. The important aspects of the cavity design are: (1) the dominant electric field component, E_x , is odd about the \hat{x} -axis, thereby reducing vertical radiation loss from the patterned slab, (2) a grade in the hole radius is used to both further confine the mode in-plane and reduce in-plane radiative losses, and (3) the design is relatively insensitive to perturbations to the cavity, as verified through simulations where the steepness of the grade and the average hole radius (\bar{r}) have been varied significantly without degrading the Q below $\sim 20,000$.

To experimentally locate a device for which this mode appears within the scan range of the laser we use (1565-1625 nm), we rely on the fact that it is the fundamental (and hence lowest frequency) mode within the region of $\omega - k$ space under consideration. In particular, for a given lattice constant a , we begin testing by examining the device with the largest \bar{r}/a . Typically, the

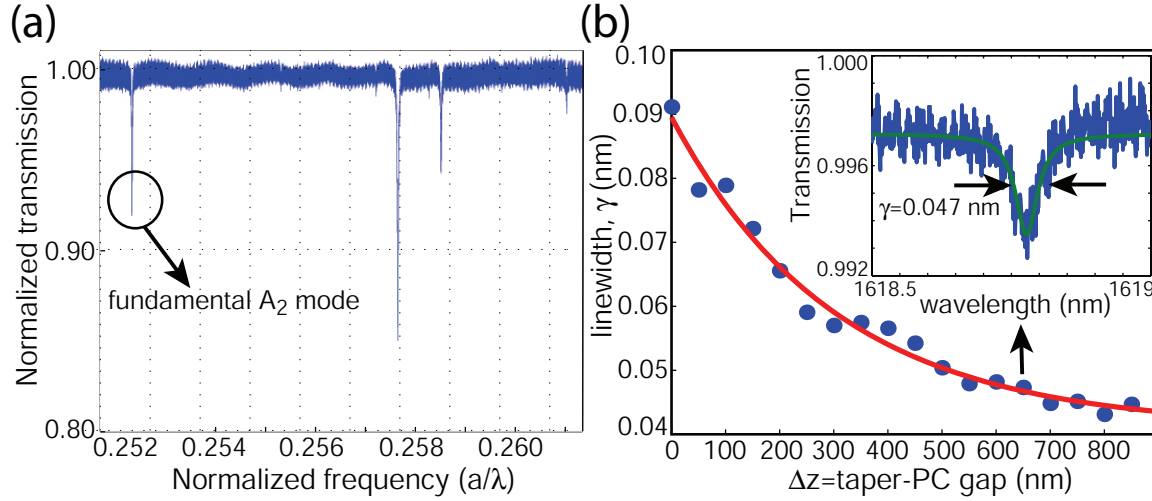


Figure 4.6: Fiber taper transmission measurements of the PC microcavities. (a) Taper transmission spectrum for a cavity with $a=409$ nm, where the data has been normalized to a background spectrum when the taper is far above the cavity. The highlighted long wavelength mode is the A_2^0 resonant mode. (b) Measured linewidth (dots) versus taper-cavity gap (Δz) for the A_2^0 mode ($a/\lambda_c \sim 0.263$) in a sample with $a=425$ nm. The taper is vertically positioned by a stepper motor with 50 nm encoder resolution. The solid curve is a fit to the experimental data. (inset) Normalized taper transmission versus wavelength when the taper is 650 nm above the cavity surface.

resonances of this device are at frequencies that are above that covered by the laser scan range, and hence, no resonances are observed in the taper's transmission spectrum. We then move on and test the next device in the array, which has a slightly smaller \bar{r}/a and is thus predicted to have lower frequency resonances than the previous device. This process is continued until we find a device for which a resonance is seen in the transmission spectrum. The first resonance which appears in the transmission spectrum (measuring from lowest frequency to highest frequency) is the A_2^0 mode; this identification procedure relies on having only small changes in \bar{r}/a between successive devices in the array, so that the cavity resonances can be smoothly tuned from frequencies above the laser scan range to frequencies within the scan range. However, this identification of the A_2^0 mode can be confirmed, both by comparing the measured resonance frequency with that predicted from FDTD simulations using the SEM-measured hole sizes, and as discussed later, by comparing the spatial localization of the cavity mode with that predicted from simulations. In addition, as described in the previous section, the polarization of the input light into the taper can be used to rule out modes that are not of the correct polarization.

Having identified a device for which the A_2^0 mode appears within the scan range of the laser (fig. 4.6(a)), we next examine its Q factor. In the inset of fig. 4.6(b), we show a wavelength scan of the

taper transmission showing the resonance dip of the A_2^0 mode for a device within the array shown in fig. 4.1(b), where the vertical taper-cavity separation $\Delta z = 650$ nm. An initial estimate of the Q of this resonance (centered at wavelength λ_0) is given by measuring its linewidth γ , with $Q = \lambda_0/\gamma$. For this device, $\lambda_0 \sim 1618.75$ nm and $\gamma \sim 0.047$ nm (where these values are determined by fitting the data to a Lorentzian curve), giving an estimate of $Q \sim 34,400$. This Q is a lower bound for the cold-cavity Q , due to the taper's loading effects on the cavity, which cause its linewidth to broaden. Loading by the taper results in out-coupling to the *forward* propagating fundamental taper mode which, upon interference with the power directly transmitted past the cavity, results in the observed resonant feature in the taper transmission. Parasitic taper loading effects could include coupling to radiation modes, higher-order taper modes, and the *backward* propagating fundamental taper mode. To estimate the taper loading effects on the A_2^0 cavity mode, we examine γ as a function of Δz . The resulting data (fig. 4.6(b)) shows that as Δz increases, the loading effects are reduced, until a regime is reached where the taper does not significantly affect the cavity mode and the measured linewidth asymptotically approaches the cold-cavity linewidth. Assuming that the loading is monoexponentially related to Δz , we fit the measured linewidth to the function $\gamma = \gamma_0 + \beta e^{-\alpha \Delta z}$, where γ_0 , β , and α are all fitting parameters. The resulting fit value of γ_0 is 0.041 nm, essentially identical to the directly measured linewidth when $\Delta z \gtrsim 800$ nm, and corresponds to a cold-cavity $Q \sim 39,500$.¹ To compare this result directly with numerical calculations, we repeat our previous FDTD calculations from chapter 2 but include an offset in \bar{r} of $r/a = 0.05$ to account for the increased size of the fabricated holes (as measured by SEM) relative to the design of fig. 4.5. Doing so yields a predicted $Q \sim 56,000$ and $a/\lambda_c \sim 0.266$, fairly close to the measured values, and $V_{\text{eff}} = 0.88(\lambda_c/n)^3$, smaller than the original design due to the better in-plane confinement provided by the larger hole radii.

4.4.3 Spatial localization measurements

As mentioned earlier, the extremely small volumes to which light is confined within PC microcavities is one of their distinguishing advantages over other optical microcavities, and is of critical importance in many applications, as the per photon electric field strength within the cavity is proportional to $1/\sqrt{V_{\text{eff}}}$. The ability to experimentally confirm such tight spatial localization using the same probe that maps the spectral properties (such as the Q) of the cavity modes is an important

¹Note that some parasitic taper loading effects may not diminish as a function of Δz as rapidly as does the coupling between the fundamental taper mode and cavity mode of interest. This could prevent the measured linewidth γ from reaching an asymptotic value as a function of Δz . In such cases, the best estimate of γ_0 is the linewidth for as large a Δz as can be reliably measured.

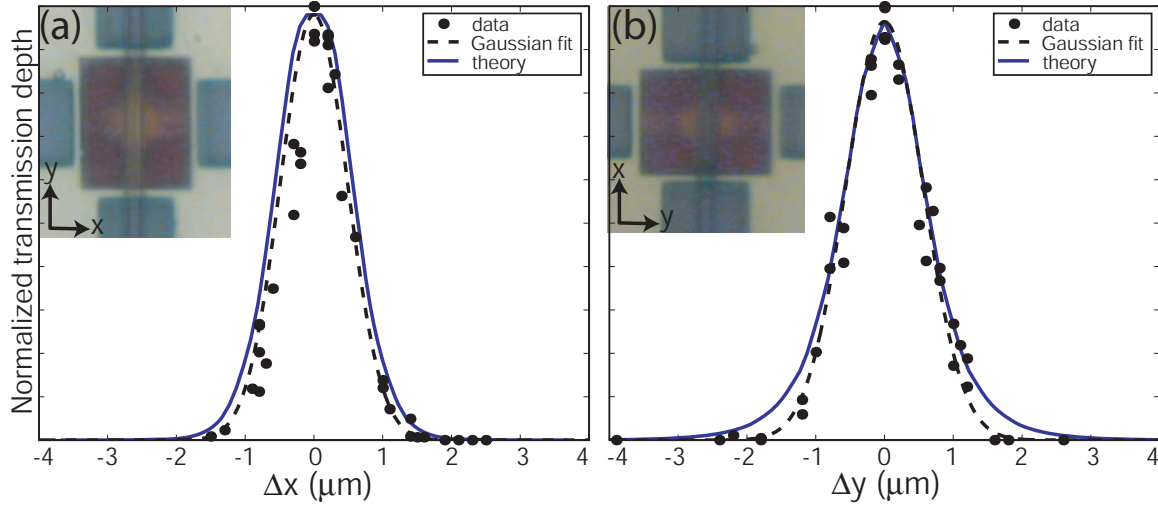


Figure 4.7: Mode localization data for the cavity whose Q was measured in fig. 4.6. The measured normalized taper transmission depth (black dots) is plotted as a function of taper displacement along the (a) \hat{x} -axis and (b) \hat{y} -axis of the cavity. The dashed line in (a)-(b) is a Gaussian fit to the data while the solid line is a numerically calculated coupling curve based upon the FDTD-generated cavity field and analytically determined fundamental fiber taper mode (taper diameter $d \sim 1.7 \mu\text{m}$)

demonstration of the versatility of the optical fiber taper. Here, the same near field probe is used to both excite the PC cavity modes and to map their spatial profile. Other works employing evanescent coupling from eroded monomode fibers to excite silica microsphere whispering gallery modes have used a secondary fiber tip to collect and map the mode profiles [124].

The spatial localization of the cavity mode is easily probed by examining the strength of coupling between it and the taper as the taper is laterally scanned above the surface of the cavity. The strength of coupling is reflected in the depth of the resonant dip in the taper transmission.² In the insets of fig. 4.7(a)-(b), we show the fiber taper aligned along the \hat{y} and \hat{x} -axis of the photonic crystal microcavity whose Q was measured to be $\sim 40,000$. The position of the taper is varied along the \hat{x} and \hat{y} axes of the cavity (at a fixed vertical taper-PC gap $\Delta z = 200 \text{ nm}$), respectively, allowing for measurements of the depth of coupling along these two orthogonal cavity directions. The depth of the resonant transmission dip for the A_2^0 cavity mode versus taper displacement is shown in Figs. 4.7(a) and 4.7(b), respectively. These measurements show the mode to be well localized to a micron-scale central region of the cavity, giving experimental confirmation that the A_2^0 mode of this cavity is both high- Q and small V_{eff} . As might be expected, they do not reveal the highly

²The maximum transmission depth achieved for the mode of interest was $\sim 10\%$, though coupling to other modes reached depths as large as $\sim 30\%$. Coupling in all cases was limited to the *under-coupled* regime [125, 20].

oscillatory cavity near field, but instead an envelope of the field, due to the relatively broad taper field profile. To compare this experimental data with FDTD calculations, we consider a simple picture of waveguide-cavity coupling [50], where the coupling coefficient (κ) is approximated, to save computation time, by taking the field overlap of the phase matched Fourier components of the FDTD-generated cavity field with the analytically-determined taper field (the modes of a cylindrical dielectric waveguide are derived in ref. [126], for example). The calculated resonant transmission depth as a function of taper displacement is shown in Figs. 4.7(a)-(b) as a solid line and agrees closely with the measured data, providing further confirmation that the mode studied is indeed the A_2^0 mode of interest. Assuming that the cavity mode is localized to the slab in the \hat{z} -direction (a good assumption based upon measurements that show the depth of coupling between the taper and cavity mode decreases exponentially as the taper-cavity separation is increased), the close correspondence between the measured and calculated in-plane localization indicates that $V_{\text{eff}} \sim 0.9(\lambda_c/n)^3$ for this high- Q mode, where this V_{eff} value was calculated through FDTD simulations which take into account the SEM-measured hole radii for this device.

Similar measurements of the higher-frequency resonant modes of the PC microcavity indicate that they are more delocalized in-plane in comparison to the A_2^0 mode, and sometimes contain multiple lobes within their coupling curves, as one might expect for higher-order modes of the cavity. As an example of this, we show in fig. 4.8(a)-(b) the depth of coupling to a higher order mode as a function of the taper's position along the \hat{x} and \hat{y} axes of the cavity, respectively. The node that appears within the coupling curve in fig. 4.8(a) results from the cavity and taper modes being precisely out of phase so that the integral determining κ in equation 4.1 is zero, and is a result of the measurement being sensitive to the fields within the cavity and taper rather than their intensities. These results indicate that the mode is likely fundamental along the \hat{y} -axis (its width is close to that measured in fig. 4.7(b)), while it is a higher order mode along the \hat{x} -axis. Simulations confirm that such modes are supported by the graded lattice geometry employed in this work.

With the exception of such cases where there is phase cancelation in κ , the resolution of the fiber taper probe is limited by the transverse profile of the taper mode. This is the reason why the measured coupling curves give an envelope of the cavity field rather than displaying its oscillatory nature; in the measurements of fig. 4.7, for example, the calculated full width at half maximum (FWHM) of the dominant taper field component at the center of the PC slab is $\sim \lambda_0$, while the cavity mode oscillates on the scale of a lattice constant a (fig. 4.5(b)), and $a/\lambda_0 \sim 0.25$. The taper used in these measurements had a diameter $d \sim 1.7 \mu\text{m}$ ($d/(\lambda_0/n) \sim 1.52$, where $n \sim 1.45$ is

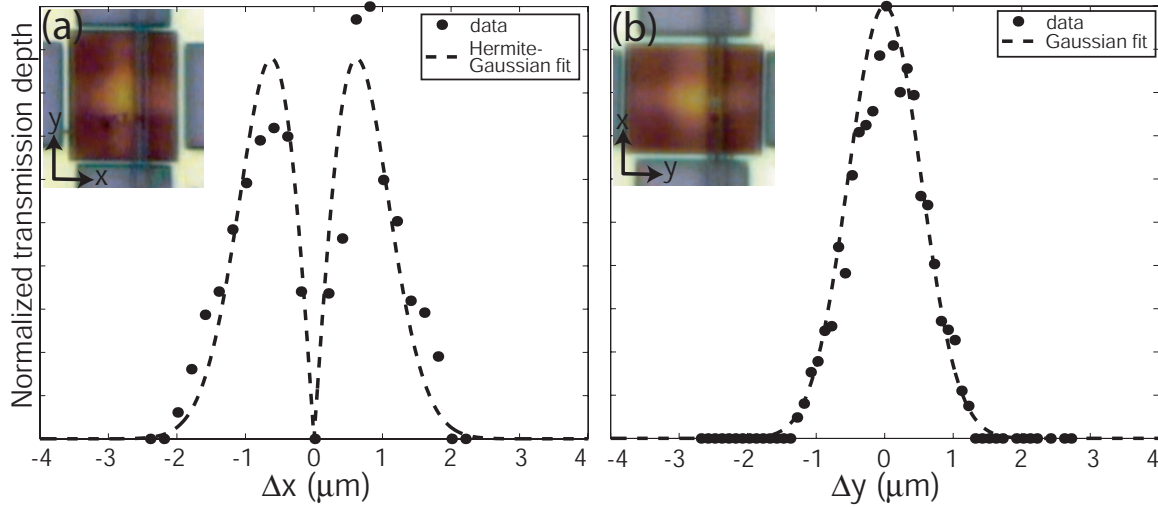


Figure 4.8: Mode localization data for a higher order mode of the graded square lattice PC cavity. The measured normalized taper transmission depth (black dots) is plotted as a function of taper displacement along the (a) \hat{x} -axis and (b) \hat{y} -axis of the cavity. The dashed line in (a) is a Hermite-Gaussian fit to the data and the dashed line in (b) is a Gaussian fit to the data.

the refractive index of the silica taper), and intuitively, it might be expected that better resolution could be achieved by further reducing its diameter. However, for the relatively small taper diameters ($\sim \lambda_0$) with which we operate, we note that the waveguiding properties of the taper begin to degrade below some minimum diameter so that, even if a smaller taper is used, it does not necessarily confine the mode any more tightly than a larger taper would.³ To better illustrate this, in fig. 4.9, we plot the calculated normalized FWHM of the dominant taper field component at the center of the PC slab for varying normalized taper diameter ($d/(\lambda_0/n)$) and taper-PC slab separation ($\Delta z/\lambda_0$). As expected, the smallest FWHM $\sim 1.23(\lambda_0/n)$ occurs when $\Delta z/\lambda_0=0$, that is, when the taper is touching the slab.⁴ We also see that reducing $d/(\lambda_0/n)$ below some minimum value begins to broaden the FWHM. Thus, for the spatial localization measurements, using smaller tapers will not appreciably improve the resolution of the measurement. Possibilities for future improvement might consist of partially aperturing the taper field (perhaps through a metallic coating on the taper), or forming the waveguide probe from a higher index material. As it stands with the current silica taper used, the width of the taper mode will limit the degree to which cavity modes of differing

³This simple point is very important when trying to compare the modal confinement properties of sub-micron diameter silica waveguides, now commonly called nanowire waveguides, with those of high-index contrast waveguides like PCs.

⁴In practice, a non-zero Δz , on the order of ~ 250 nm for $\lambda_0=1.6$ μm , is preferable for doing spatial localization measurements. This is due both to the relatively large amount of insertion loss that occurs when the taper touches the cavity, and also to allow the taper to be freely moved above the cavity.

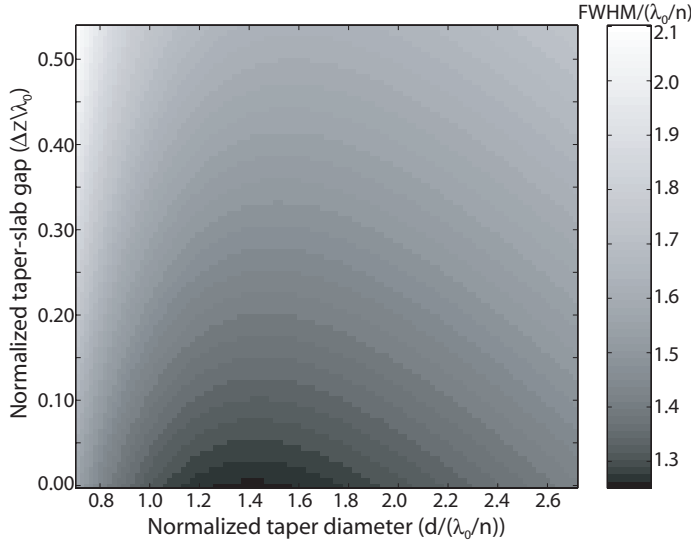


Figure 4.9: Resolution of the fiber taper. Plot of the normalized full-width at half-maximum ($\text{FWHM}/(\lambda_0/n)$) of the dominant taper electric field component at the center of the PC slab, as a function of normalized taper-slab gap ($\Delta z/\lambda_0$) and taper diameter ($d/(\lambda_0/n)$). λ_0 is the operating wavelength of the taper (and the resonant frequency of the cavity mode), and $n \sim 1.45$ is its material refractive index.

spatial localizations can be distinguished (differences in cavity localization will be blended out in the measured coupling curves, due to the effect of the convolution with the taper field). Nevertheless, we have been able to distinguish modes with localizations corresponding to differences in V_{eff} of $\sim 0.3(\lambda/n)^3$ in our work to this point.

4.5 Applications to quantum optics

To illustrate the potential applications of such a small V_{eff} and high- Q microcavity, we briefly consider two examples from quantum optics. The Purcell factor (F_P), a measure of the microcavity-enhanced spontaneous emission rate of an embedded active material, is given under suitable (maximal) conditions as (see appendix H and ref. [109]):

$$F_P = \frac{3}{4\pi^2} \left(\frac{\lambda_c}{n} \right)^3 \left(\frac{Q}{V_{\text{eff}}} \right). \quad (4.2)$$

For the A_2^0 mode ($Q \sim 40,000$, $V_{\text{eff}} \sim 0.9(\lambda_c/n)^3$), the predicted F_P is $\sim 3,500$, an extremely large value for a semiconductor-based microcavity (previous work on semiconductor microdisks [13] have predicted $F_P \sim 190$, for example).

Another application is in cQED, where strongly coupled atom-photon systems have been proposed as candidates to produce the quantum states required for quantum computing applications [60]. For such applications, the regime of strong coupling (see Appendices G-H and ref. [9]), where

the atom-photon coupling coefficient (g) exceeds the cavity and atomic decay rates (κ and γ_{\perp} , respectively), must be reached. Although strong coupling has been achieved in systems consisting of an alkali atom and an actively stabilized Fabry-Perot cavity [9], in future applications, where higher levels of integration are sought, chip-based cavities are of interest [60]. Using the measured Q and estimated V_{eff} for the A_2^0 mode studied here, the relevant parameters for a commonly-used Cesium (Cs) atomic transition ($\lambda_0 = 852$ nm, $\gamma_{\perp}/2\pi = 2.6$ MHz) [9], and the formulas (see appendix H)

$$\begin{aligned} g &= \eta \gamma_{\perp} \sqrt{\frac{3c\lambda_0^2}{4\pi\gamma_{\perp} V_{\text{eff}}}} \\ \kappa &= \frac{\omega}{2Q} \end{aligned} \tag{4.3}$$

we calculate $g/2\pi \sim 16$ GHz and $\kappa/2\pi \sim 4.4$ GHz, indicating that the coupled Cs-PC cavity system could achieve strong coupling.⁵ In addition, the calculated critical atom number ($N_0 = 2\kappa\gamma_{\perp}/g^2$) and saturation photon number ($m_0 = \gamma_{\perp}^2/2g^2$) are $N_0 \sim 8.8 \times 10^{-5}$ and $m_0 \sim 1.3 \times 10^{-8}$, a regime where a single atom would have a profound effect on the cavity field, and vice versa. More detailed calculations using the optical bistability state equation and quantum master equation have been performed [62], and confirm that it should be possible to detect single strongly coupled atoms in this system. Such experiments are being explored by Paul Barclay and Ben Lev in a collaborative effort between the Mabuchi and Painter groups at Caltech. In addition, calculations of the coupling and decay parameters for an InAs semiconductor quantum dot [127] indicate that the current PC microcavity would also be capable of reaching strong coupling in such a solid-state system. Calculations based on the quantum master equation are the focus of chapter 8, and so I will refrain from adding anything more on this here.

4.6 Fabrication-tolerant high- Q cavities

In this section, we investigate the robustness of the Q of the A_2^0 mode in our PC cavity design to imperfections in the lattice. The basic motivation for this work has been the observation that many fabricated PC cavities exhibited Q factors that were significantly smaller than the values expected from simulations. In some cases, this may have been due to issues such as surface state or bulk

⁵As V_{eff} is defined relative to peak electric field energy density, rather than electric field strength, a factor η must be included in g for dielectric cavities where the two values are not equal. $\eta \sim 0.42$ for our cavity.

material absorption, or due to problems with the etch used, resulting in angled sidewalls or rough etched surfaces. The robustness I study in this chapter does not cover such instances. Here, I focus purely on the response of the Q to variations in the size of the holes within the PC lattice. Although covering only one subset of the imperfections that can occur during fabrication, it is an important subset, as it is directly related to processes such as electron beam lithography, where incorrectly sized holes can result from variations in the beam current during the writing step, and plasma dry etching, where etches can undercut the mask and lead to larger holes than what were intended.

A range of designs have been employed in studies of high- Q PC microcavities [11, 21, 26, 51], and in many cases, the experimental achievement of high- Q is predicated on the ability to fabricate the design with a small margin for error. For example, in ref. [12], the discrepancy between the fabricated device and the intended design led to a theoretical degradation of Q from 3.0×10^4 to 4.4×10^3 , close to the measured Q of 2.8×10^3 . Extraordinary control over fabricated geometries has been demonstrated in recent work [51], where a shift of ~ 60 nm in the positions of holes surrounding the cavity defect region reduced Q s as high as 4.5×10^4 by over an order of magnitude. Here, we discuss a study of our PC microcavity design (chapter 2), which exhibits a degree of robustness, both theoretically and experimentally, to deviations from the nominal design sufficient for Q s above 10^4 to be maintained. This robustness in Q to changes in the PC cavity geometry is of practical importance for future experiments, to provide insensitivity to fabrication imperfections, as well as to maintain the flexibility in cavity design required to form resonant modes with a prescribed field pattern and polarization.

Radiative losses in planar waveguide PC defect microcavities can be separated into in-plane and out-of-plane components, quantified by the quality factors Q_{\parallel} and Q_{\perp} , respectively, with the total radiative Q given by $Q^{-1} = Q_{\parallel}^{-1} + Q_{\perp}^{-1}$. Q_{\parallel} is determined by the size and angular extent (in-plane) of the photonic bandgap, while Q_{\perp} is determined by the presence of in-plane momentum components (\mathbf{k}) within the waveguide cladding light cone, which are not confined by total internal reflection at the core-cladding interface. In chapter 2 and ref. [21], PC microcavities were designed using two mechanisms to avoid radiative loss: (i) use of a mode that is odd about mirror planes normal to its dominant Fourier components, in order to eliminate the DC ($\mathbf{k} = \mathbf{0}$) part of the in-plane spatial frequency spectrum and hence reduce vertical radiation loss, and (ii) use of a grade in the hole radius to further confine the mode and reduce in-plane radiative losses. The resulting PC microcavity design within the square lattice creates a TE-like donor-type defect mode (labeled A_2^0), as shown in fig. 4.5. FDTD simulations of this resonant mode predict a Q -factor of 10^5 and

an effective modal volume of $V_{\text{eff}} \sim 1.2(\lambda/n)^3$. We now show how use of mechanisms (i) and (ii) above create a level of robustness in the cavity design.

Use of an odd symmetry mode to suppress vertical radiation loss is, at a basic level, independent of changes in the size of the holes defining the defect cavity. This feature has been confirmed in the simulations of simple defect cavity designs in square lattice photonic crystals in chapter 2, where Q_{\perp} did not degrade below 10^4 , despite significant changes (as much as 40%) in the size of the (two) central defect holes. Perturbations that cause the cavity to be asymmetric create a mode which, though not strictly odd, will be a perturbation to an odd mode, and hence will still largely suppress DC Fourier components and exhibit high Q . However, for the square lattice photonic crystal structures considered here, perturbations to the central defect hole geometry can result in a degradation in Q_{\parallel} , due in part to the lack of a complete in-plane bandgap within the square lattice. This lack of a complete bandgap requires the defect geometry to be tailored so as to eliminate the presence of Fourier components in directions where the lattice is no longer reflective.

This tailoring was achieved in chapter 2 by a grade in the hole radius moving from the center of the cavity outwards. The grade, shown in fig. 4.5, serves to help eliminate couplings to in-plane radiation modes along the diagonal axes of the square lattice (the M -point of the reciprocal lattice) where the PC is no longer highly reflective, while simultaneously providing a means to keep the in-plane reflectivity high along the \hat{y} axis (the direction of the mode's dominant Fourier components). The use of a large number of holes to define the defect region ensures that no single hole is responsible for creating the potential well that confines the resonant mode, making the design less susceptible to fluctuations in the size of individual holes. Instead, the continuous change in the position of the conduction band edge resulting from the grade in hole radius creates an approximately harmonic potential well [25]. This smooth change in the position of the band edge creates a robust way to mode match between the central portion of the cavity (where the mode sits) and its exterior. In other work [51], softening of this transition is achieved by adjusting the position of two holes surrounding the central cavity region (which consists of three removed air holes in a hexagonal lattice). This method can achieve high- Q , but as mode-matching is achieved by tailoring only two holes it is more sensitive to perturbations than the adiabatic transition created by a grade in the hole radius. Finally, we note that even though a relatively large number of holes are modified to create the graded lattice, V_{eff} is *still* wavelength-scale, and remains between 0.8 - $1.4(\lambda/n)^3$ in all of the devices considered in this work. In addition, the methods used here to achieve robustness in Q are general and can be applied to cavities in other PC lattices [23].

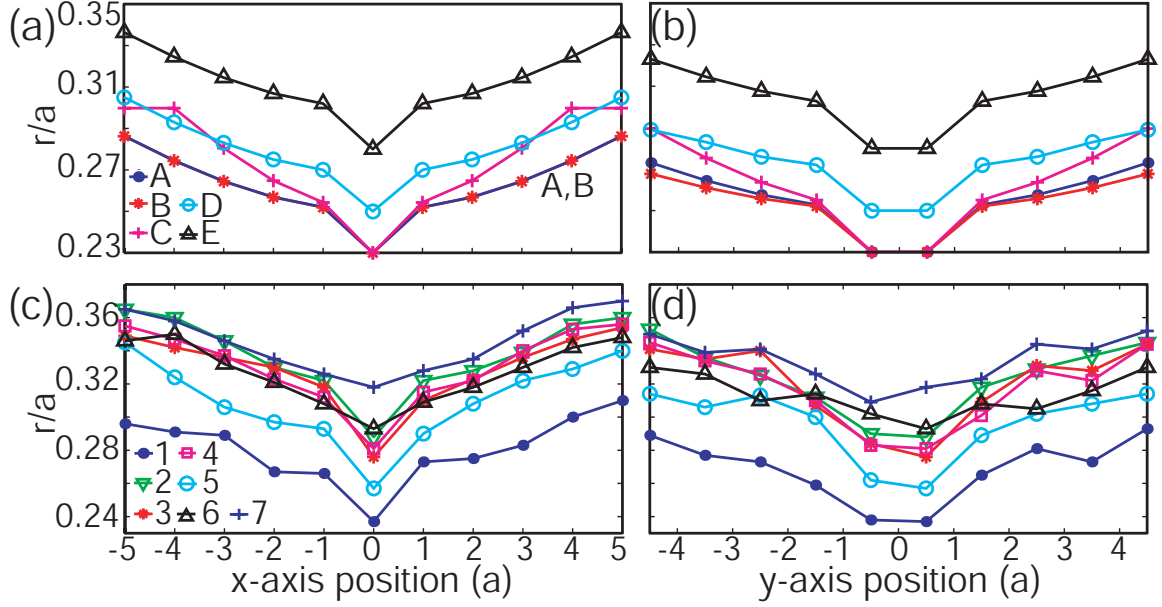


Figure 4.10: Grade in the normalized hole radius (r/a) along the central \hat{x} and \hat{y} axes of square lattice PC cavities. Cavity r/a profiles for (a,b) FDTD cavity designs and (c,d) microfabricated Si cavities.

To highlight these ideas, 3D FDTD simulations of cavities with varying grades and average normalized hole radius (\bar{r}/a) were performed. Figure 4.10(a)-(b) shows the grade in r/a along the central \hat{x} and \hat{y} axes for several designs (PC-A through PC-E), and table 4.1 lists the calculated resonant frequency, vertical, in-plane, and total Q factors. In all of these simulations, Q_{\perp} remains close to 10^5 , with PC-E showing more significant degradation largely as a result of the increased modal frequency (creating a larger-sized cladding light cone). In addition, an inappropriate choice of grade along the \hat{x} -axis can lead to increased in-plane losses via coupling to M -point modes. Nevertheless, the loss in any of the simulated devices did not cause Q to be reduced below 2×10^4 .

To test the sensitivity of the design to perturbations experimentally, cavities were fabricated in a $d=340$ nm thick silicon membrane through a combination of electron beam lithography, inductively-coupled plasma reactive ion etching, and wet etching. Figure 4.10(c)-(d) shows the values of r/a along the central \hat{x} and \hat{y} axes for a number of fabricated devices (PC-1 through PC-7), as measured with a SEM. Cavities are passively tested using the optical fiber taper probing method described in the previous sections.

Figure 4.11(a)-(b) shows measurements for devices PC-5 and PC-6, which have significantly different r/a profiles (fig. 4.10(c)-(d)). The inset of fig. 4.11(c) shows the normalized taper trans-

Table 4.1: Theoretical (PC-A through PC-E) and experimental (PC-1 through PC-7) normalized frequency (a/λ_o) and quality factor (Q) values for the A_2^0 mode of cavities with r/a profiles shown in fig. 4.10.

Cavity	d/a	a/λ_0	Q_{\perp}	Q_{\parallel}	Q
PC-A	0.750	0.245	1.1×10^5	4.7×10^5	9.0×10^4
PC-B	0.750	0.245	1.1×10^5	2.6×10^5	7.5×10^4
PC-C	0.750	0.247	1.0×10^5	3.7×10^5	8.0×10^4
PC-D	0.750	0.253	8.6×10^4	3.0×10^5	6.7×10^4
PC-E	0.750	0.266	6.2×10^4	6.5×10^5	5.6×10^4
PC-1	0.879	0.241	-	-	1.6×10^4
PC-2	0.850	0.255	-	-	1.8×10^4
PC-3	0.850	0.251	-	-	1.7×10^4
PC-4	0.842	0.251	-	-	2.4×10^4
PC-5	0.842	0.249	-	-	2.5×10^4
PC-6	0.800	0.263	-	-	4.0×10^4
PC-7	0.800	0.270	-	-	1.3×10^4

mission as a function of wavelength when the taper is 350 nm above cavity PC-5. By measuring the dependence of cavity mode linewidth (γ) on the vertical taper-PC gap (Δz) (fig. 4.11(a)), an estimate of the true cold-cavity linewidth (γ_0) is given by the asymptotic value of γ reached when the taper is far from the cavity. For PC-5, $\gamma_0 \sim 0.065$ nm, corresponding to $Q \sim 2.5 \times 10^4$. Figure 4.11(b) shows the linewidth measurement for PC-6. For this device, $\gamma_0 \sim 0.041$ nm, corresponding to a $Q \sim 4.0 \times 10^4$.

Linewidth measurements for each of the cavities PC-1 through PC-7 are compiled in table 4.1. The robustness of the Q to non-idealities in fabrication is clearly evident. Though all of the devices exhibit a general grade in r/a , the steepness of the grade and the average hole radius (\bar{r}/a) vary considerably without reducing Q below 1.3×10^4 . These high- Q values are exhibited despite the fact that many cavities are not symmetric (the odd boundary condition is thus only approximately maintained), and the frequency of the cavity resonance varies over a 10% range, between $a/\lambda_o = 0.243$ - 0.270 .

The measured Q values in table 4.1 are still lower than predicted from simulations. This discrepancy is likely due in part to slightly angled etched sidewalls that have been shown in calculations to lead to radiative coupling to TM-like modes [114]. This non-ideality helps explain why PC-1,

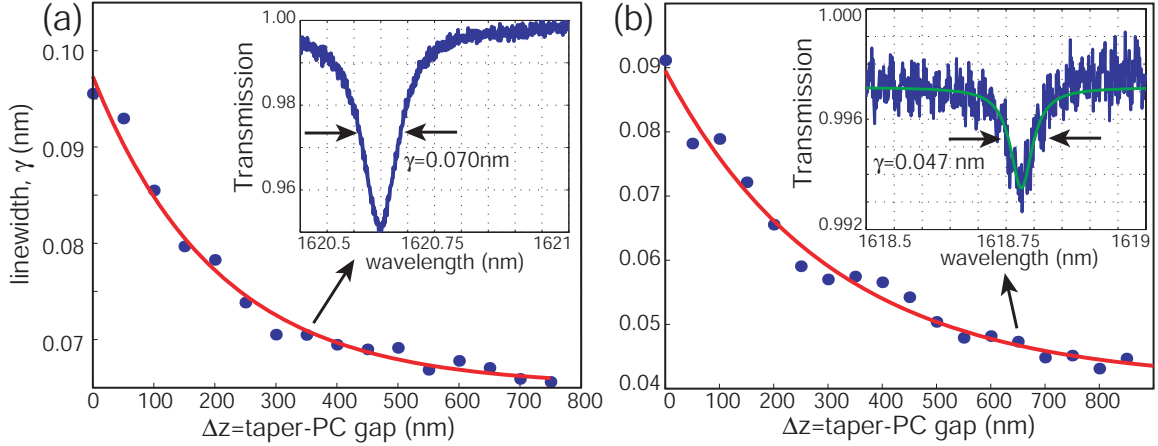


Figure 4.11: (a) Measured data (blue dots) and exponential fit (red curve) for linewidth vs. taper-PC gap of the A_2^0 mode in PC-5. (Inset) Taper transmission for this device when the taper-PC gap is 350 nm. (b) Same as (c) for PC-6 (here, the taper transmission in the inset is shown when $\Delta z = 650$ nm). The transmission curves are normalized relative to transmission in the absence of the PC cavity.

which is closest in r/a value to the desired design (PC-A), does not exhibit the highest Q experimentally. In particular, we have observed that the sidewall angle is poorer for smaller sized holes. On the other end of the spectrum, cavities with the largest hole sizes such as PC-7, which may have more vertical sidewalls, also begin to exhibit higher vertical radiation loss as a result of a larger modal frequency and cladding light cone. In addition, surface roughness is a potential source of loss; for PC-6, which exhibited the highest Q value, a chemical resist stripping process was used (rather than a plasma descum) and may have produced a cleaner, smoother surface. More recently, work on Si microdisk cavities [128] has indicated that absorption due to surface layers may be a limitation. Proper termination of etched surfaces is an important consideration for achieving higher Q s in these devices.

4.7 Fiber tapers as an optical probe for photonic crystal microcavities

The versatility of the optical fiber taper measurement technique has led us to think of it as a probe for studying the properties of microphotonic structures. In this section, we further elaborate on this idea, by comparing this method to some of the existing ways in which PC microcavities (and wavelength-scale semiconductor microcavities in general) are tested.

In general, measurements of PC microcavities are not necessarily straightforward, in large part due to their micron-scale V_{eff} values, which limit the ability to effectively couple to them from free-

space or through prism-based techniques, as can be done for larger microresonators such as Fabry-Perot cavities [9] and microspheres [129]. This difficulty has extended to other types of wavelength-scale cavities, such as small-diameter microdisks [13, 14]. Typically, there have been two techniques to probe Q factors in wavelength-scale cavities. In the first, the microcavities are fabricated in an active emitter material (such as a quantum well or quantum dot epitaxy), the cavities are optically pumped, and the emitted resonance linewidth is studied subthreshold, near material transparency [13, 43, 12]. This technique is limited both by difficulties in accurately establishing the pump power at which transparency occurs and by the necessity that the cavity contain embedded emitters. In particular, the latter requirement limits the variety of material systems in which the cavity can be fabricated (silicon, for example, would not be an easy option) and is not suitable for passive resonators in devices such as filters. For such devices, a second technique, consisting of fabricating an on-chip in-plane waveguide to couple to the cavity, is often used [130, 49]. In this approach, the problem of coupling light into the cavity is shifted to that of coupling light into the on-chip waveguide, a technically less challenging problem that can be done through a number of end-fire based approaches. A limitation of this technique is that it lacks a certain amount of flexibility due to the necessity of fabricating an in-plane waveguide for each cavity on the chip. In addition, both this approach and the emission-based approach described above do not provide a means to probe the V_{eff} of the cavity. To address this, several researchers have begun to investigate photonic crystal microresonators using near field scanning optical microscopy (NSOM), taking advantage of the sub-wavelength resolution that can be achieved in such measurements to map the localization of the cavity modes [131, 132].

The technique we have described in this chapter employs an *external* waveguide to couple to the cavity, where the external waveguide is a tapered optical fiber. Tapered optical fibers have been successfully used in the past to excite the resonances of larger sized microcavities, such as silica microspheres [32, 20] and microtoroids [56], and more recently, to excite the modes of a silicon-based PC waveguide [38, 40]. In these implementations, phase matching between the mode of the taper and the traveling wave mode of the resonator or the propagating mode of the waveguide was critical in achieving highly efficient coupling [55, 39]; in the former case, phase matching occurred primarily due to the silica-silica interface (same material index) between the taper and the microsphere, while in the latter, the dispersion of the PC waveguide was engineered to compensate for the disparate material indices ($n=3.4$ for silicon and $n = 1.45$ for silica) and achieve a PC waveguide effective index that matched that of the taper.

To study wavelength-scale cavities, we no longer rely on achieving phase matching, but rather just use the taper as a convenient means to produce a micron-scale evanescent field for sourcing and out-coupling the micron-scale cavity field. The taper effectively serves to bridge the disparate length scales from conventional fiber and free-space optics to chip-based microoptics, and does so entirely off the chip, so that on-chip structures do not require any additional complexity. Although the coupling we observe might not be as efficient as phase matched coupling, the power transfer is more than adequate enough to probe many of the important properties of the cavity. By using an external waveguide as the coupling element, this method is inherently non-invasive, can be used to rapidly characterize multiple devices on a chip, and the ability to vary the position of the taper with respect to the cavity (not an option for microfabricated on-chip waveguides) allows for quantitative investigation of not only the Q factor but also V_{eff} . Furthermore, the resonant coupling from the external waveguide is polarization selective, providing additional information about the cavity modes that is not easily obtainable through techniques such as NSOM. Knowledge of a mode's spectral position, polarization, Q , and V_{eff} will in many cases be enough to unambiguously determine the identity of the mode in comparison to simulation or theoretical results. Thus, in some respects, the versatility of the fiber-based approach that we have described in this chapter makes the technique an optical analog to electrical probes used to study microelectronic devices.

Another important aspect of this technique is the speed with which measurements can be made. In particular, the critical alignment step required in this work is making sure that the taper is not angled with respect to the surface of the chip, to ensure that coupling only occurs between the taper and the cavity, and not some extraneous part of the chip. Once this is done, and once the taper is aligned along the desired axis of the cavity, all of the devices within an array can be rapidly tested, and the spectral positions of resonances in successive devices can be determined within tens of seconds or faster. As an illustration of this, a movie showing the testing of two adjacent PC cavities has been made and is freely available on the internet (http://copilot.caltech.edu/research/PC_cav.avi). This ability to easily probe an array of devices on a chip greatly speeds up the testing process and shortens the turnaround time between device fabrication and measurement. Furthermore the simplicity of the measurement technique is another attractive feature; a single fiber taper serves as both the excitation and collection probe, and the taper is physically robust enough (will not break) so that no active servo control of the taper position is required to prevent it from touching the sample surface (in contrast to the more delicate probes used in NSOM techniques [132]).

Finally, we note that the optical fiber taper probe can be used to examine the spectral and spatial

properties of a number of wavelength-scale microcavities, and is not limited to just PC microcavities. The suitability of the fiber taper as a probe for a given microcavity will in large part be determined by the overlap between the cavity and taper fields; simply put, if that overlap is sufficiently large, an appreciable amount of power can be transferred from the taper to the cavity even without phase matching (in general, phase matching will not be achieved, because of the index mismatch between the silica fiber taper and the high refractive index semiconductors typically used in wavelength-scale cavities). For the A_2^0 PC microcavity mode studied in this work, the depth of coupling is typically limited to $\sim 10\%$ -20%, and at maximum levels of coupling, the cavity Q is degraded due to the taper loading effects seen in fig. 4.6. However, due to the low-loss nature of the optical fiber tapers (insertion losses are routinely as low as 10%), this is still a significant amount of coupling into the cavity, and from the measurement standpoint, coupling levels of a few percent are easily adequate to discern cavity resonances in the taper's transmission, and to then probe the Q and V_{eff} of the cavity. For applications requiring highly efficient power transfer from the fiber into the cavity, other approaches using an intermediate photonic crystal waveguide coupler have been developed [57], and will be briefly described in the following section.

As an example of the application of this probing technique to other types of wavelength-scale microcavities, fiber tapers have recently been used to probe the spectral and spatial properties of whispering gallery modes in $d < 10 \mu\text{m}$ diameter silicon microdisks [64] and AlGaAs microdisks with embedded quantum dots [69] (the latter of which will be described in detail in the second part of this thesis). Because the radiation losses in high-index-contrast microdisks are quite low ($Q_{\text{rad}} > 10^8$), measurements of Q in fabricated devices is a simple and elegant way to determine etch-induced and bulk material losses within a given materials system [65, 128], allowing one to optimize an etching process for the creation of low-loss structures. Because the fiber taper measurement is a passive measurement (light-emitting material is not required), this probing technique provides optical access to materials systems, such as silicon, which otherwise could only be accessed via end-fire coupling to microfabricated on-chip waveguides. We briefly review some of the results on Si microdisks in the following section.

4.8 Efficient optical fiber coupling to photonic crystal microcavities and microdisks

4.8.1 PC microcavities

To this point, we have demonstrated a PC microcavity that has a sufficiently high Q and small V_{eff} to enable strong coupling experiments in cQED, and we have shown that the Q is relatively robust to fabrication imperfections. To do these measurements, we have used fiber tapers as a way to couple light into and out of these devices. The above sections have detailed how the fiber taper can serve as a very versatile probe for studying the spectral and spatial properties of PC cavity modes.

One thing that was not shown in the measurements above is that the fiber taper is an efficient way to get light into and out of the PC cavities, and indeed, to this point, it has not been. In particular, depths of coupling between the taper and cavity have been limited to values around 10%, and at these highest levels of coupling, the Q s are significantly degraded (by about a factor of 2). It should be emphasized that whenever light is coupled out of a cavity, its Q is going to be degraded relative to its cold-cavity value. The important point is that the loss that is induced by coupling should be effectively funneled into some collection channel (this loss can euphemistically be called 'good' loss). For the direct fiber taper probing measurements, this clearly is not the case; the Q is degraded by almost a factor of 2, indicating that significant loss has been induced by the interaction with the taper, but only a small fraction of this loss has been collected, as evidenced by the small depths of coupling. The additional (uncollected) loss, which we call 'bad' loss, might be due to scattering or coupling into undesirable taper modes. For cavity QED applications, the goal is to obtain a requisite signal level without degrading the Q so far that the cavity is no longer in the strong coupling regime. The ability to do this is somewhat compromised by the amount of 'bad' loss present in the direct probing method; nevertheless, its simplicity makes it a candidate for use in future experiments.

The ability to efficiently source and extract light from the cavity is of particular importance for the low light intensities within the cavity in cavity QED experiments, where maximizing the amount of out-coupled signal from the interaction is necessary. In a standard Fabry-Perot cavity, the solution is perhaps obvious; one of the etalon mirrors is made to have slightly lower reflectivity. This causes a degradation of the cavity Q , but this additional loss is 'good' in the sense that it can be collected to comprise the measurement signal. Similarly, in a micropillar cavity, the top DBR mirror can be tailored to allow light to leak vertically into the air, where it can be efficiently collected into

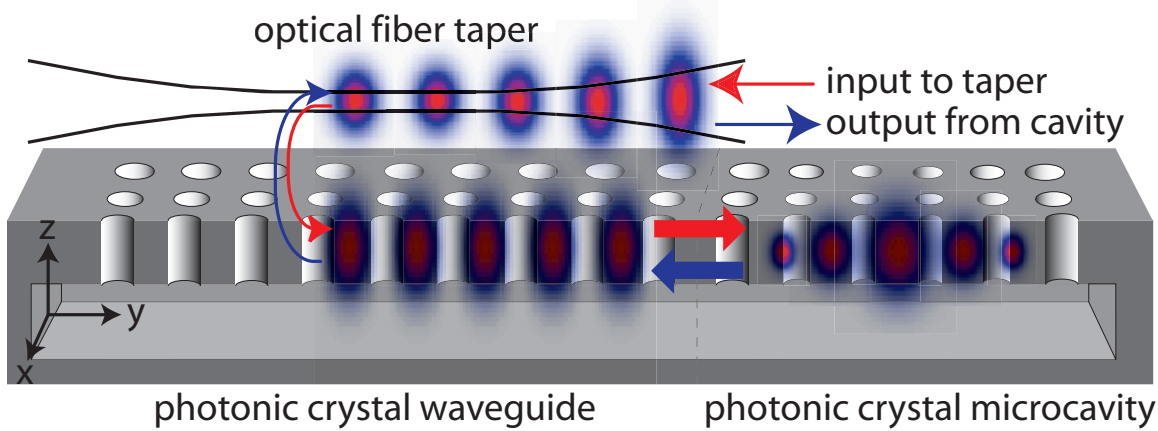


Figure 4.12: Fiber-coupled PC microcavity using an intermediate PC waveguide. (i) the taper adiabatically converts light injected into its input to a micron-scale field, (ii) light is contradirectionally coupled to a phase matched PCWG with high ($> 95\%$) efficiency, (iii) light tunnels from the end of the PCWG into a mode-matched PC cavity, (iv) coupling from the cavity back to the fiber follows the reverse process, so that the output from the cavity is detected in the reflected signal at the fiber input. Refer to the paper of Barclay et al., for details [57].

an optical fiber [133]. However, in PC microcavities, the solution is not necessarily straightforward; their wavelength-scale modal patterns are typically not suited for direct mode matching to the much larger standard free-space and fiber optics. One solution is to integrate the cavity with an on-chip photonic crystal waveguide (PCWG), and then use various end-fire-based approaches to couple into and out of the PCWG. Despite significant improvement in techniques for such end-fire coupling, losses of > 1 dB per coupling junction can still be expected in such systems [134].

To minimize the amount of 'bad' loss when coupling to the cavities while still taking advantage of the desirable properties of fiber tapers, my colleague Paul Barclay developed a technique that makes use of an intermediate photonic crystal waveguide (PCWG) [57]. In this approach (fig. 4.12(a)), light is first efficiently ($> 95\%$) transferred to the PC chip by phase matched evanescent coupling between an optical fiber taper and a PCWG [39]. This coupling is so efficient because the PCWG has been designed to phase match to the mode of the optical fiber taper (not the case in direct coupling between the fiber and cavity), and has a significant enough spatial overlap with it for near-complete power transfer over tens of microns. The PCWG is terminated by the PC cavity; the two devices have been designed to be mode matched so that coupling between them is also very efficient. Thus, light propagates through the PCWG, and when it reaches the PC cavity termination, some amount of the light that is resonant with the cavity mode tunnels into it (the amount of tunneling can be adjusted by tailoring the PCWG-PC cavity junction). This light can then interact with

material in the cavity (an atom or quantum dot, for example), and then tunnel back into the PCWG, where it will be transferred back into the reflected signal of the optical fiber for measurement. Experimental measurements of fabricated Si devices have yielded an unoptimized fiber-to-cavity coupling efficiency of 44% for a cavity with a loaded (unloaded) Q of 38,000 (47,000). Importantly, the limitations on the demonstrated coupling efficiency were not fundamental, but due to technical reasons, such as non-ideal taper-PCWG coupling and an imperfectly tailored PCWG-PC cavity transition region.

4.8.2 Microdisk cavities

Complementing the work described in the previous sections of this chapter, my colleague Matt Borselli has investigated silicon microdisk cavities, of the geometry shown in fig. 4.13. Microdisk cavities support whispering gallery modes (WGMs) in which light circulates around the periphery of the structure and is confined by total internal reflection at both the curved interface and the top and bottom surfaces. In comparison to microsphere cavities [19, 20, 135], microdisks are an optically thin dielectric slab in one dimension, which serves the dual purpose of dramatically reducing the number of modes within the structure, as well as the volume of those modes.

These microdisk cavities were of particular interest because they could support modes with very high radiation-limited quality factors ($Q_{rad} \sim 10^8$) for all but the smallest diameter structures (this was verified by finite-element-method simulations [136, 128, 137]). This is a result of the large refractive index contrast between the Si ($n \sim 3.4$) layer and the surrounding air ($n=1$). This large index contrast also suggests that modes with a much tighter spatial confinement (i.e., a smaller V_{eff}) than what is available in glass microcavities [19, 20, 56] can be supported. In addition to their potential Q and V_{eff} values, these cavities can be fabricated using the exact same fabrication processes developed above (section 4.2), and can be probed using optical fiber tapers.

Reference [64] describes the first set of results obtained from these devices. Cold-cavity Q s as high as $\sim 5 \times 10^5$ for $V_{eff} \sim 6(\lambda/n)^3$ were demonstrated, as were loaded Q s of $\sim 1.5 \times 10^5$ for a taper-cavity coupling depth of $\sim 50\%$. Since these initial results, Matt and another colleague, Tom Johnson, have gone on to show that they could reach Q s as high as 5.0×10^6 , albeit in larger volume devices [65], and have achieved critical coupling and overcoupling to these devices [128]. These high Q s have been achieved through additional improvements to the fabrication procedure described earlier, including the use of a resist reflow process to ensure very circular disk geometries [65], and a sequence of cleaning steps at the end of the disk fabrication aimed at the removal of

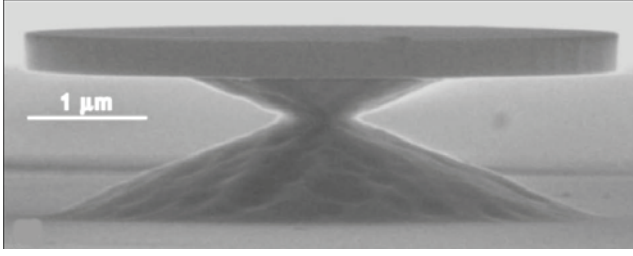


Figure 4.13: Scanning electron microscope image of a silicon microdisk cavity. Refer to the paper of Borselli et al., for further details [64].

highly absorbing surface layers from the devices [128].

From the perspective of the cavity QED experiments that have been a focus of this thesis, these Si microdisk cavities are extremely appealing, particularly in conjunction with integrated self-assembled quantum dots (QDs), where the field of the microdisk can optimally spatially overlap with the QD. Although PC cavities can ultimately result in similar or even better performance in terms of metrics such as Q/V_{eff} [52, 51, 28, 30], and can be effectively coupled to through the use of photonic crystal waveguides integrated with optical fiber tapers [57], these microdisk cavities are quite competitive on both the Q/V_{eff} and coupling fronts. More importantly, the simplicity of direct fiber coupling (rather than use of an intermediate element as is necessary for the PC cavities) and the relative ease of fabrication of these devices make them promising candidates for initial experiments. This is described in further detail in the upcoming chapters.

Part II

Fiber-Coupled Microdisk Cavities with Embedded Quantum Dots

The second part of this thesis studies the properties of AlGaAs microdisk cavities containing an integral layer of self-assembled InAs quantum dots. Chapter 5 presents initial measurements of high quality factors within $4.5\ \mu\text{m}$ diameter disks, as well as photoluminescence measurements of the devices. Chapter 6 examines the use of the fiber taper within photoluminescence measurements of the cavities, to create fiber-coupled microdisk lasers with high differential efficiencies. Chapter 7 extends the work of the previous chapters to consider small diameter ($D \sim 2\ \mu\text{m}$) disks with high quality factors, small mode volumes, and very low threshold powers. For cavity QED experiments, the most important results from these chapters are that the demonstrated microdisk cavities have the requisite combination of Q and V_{eff} for strong coupling to a single QD, and the fiber coupling technique provides an important tool that can enable future generations of experiments. Chapter 8 considers a first set of such experiments in detail, and in particular, presents quantum master equation simulations of the expected behavior of these devices.

Chapter 5

Optical Loss and Lasing Characteristics of AlGaAs Microdisk Cavities with Embedded Quantum Dots

5.1 Introduction

For future experiments in cavity QED with self-assembled quantum dots, the GaAs/AlGaAs system is the most appropriate choice of material, due to the relative maturity of the growth of InAs/InGaAs quantum dots [138, 139, 140] within this system. As the refractive index of GaAs and its alloys is relatively close to that of Si ($n_{GaAs} \sim 3.5$ and $n_{AlAs} \sim 2.9$ at $\lambda \sim 1.25 \mu\text{m}$), the PC cavity design of chapter 2 remains applicable. Similarly, the high refractive index difference between GaAs/AlGaAs and air suggests that the radiation-limited Q s for microdisk cavities would be quite high for all but the smallest diameter disks. At the start of the work described in this chapter, what remained to be seen was whether the fabrication processes and material losses within this new system would be adequate to achieve a sufficiently high Q and small V_{eff} for strong coupling experiments.

Recently, multiple research groups have demonstrated vacuum Rabi splitting in a semiconductor system consisting of a single quantum dot (QD) exciton embedded in an optical microcavity [70, 71, 72]. These experiments have in many ways confirmed the potential of semiconductor microcavities for chip-based cavity quantum electrodynamics (cQED) experiments. For future experiments, such as those involving quantum state transfer in quantum networks [141], it will be important to further improve upon the parameters of such QD-microcavity systems over what was demonstrated in the above references. One clear improvement required is to move the system further within the regime of strong coupling. In particular, the ratio of g (the QD-photon coupling rate) to the larger of κ (the cavity decay rate) and γ_{\perp} (the QD decay rate) approximately represents the number of Rabi

oscillations that can take place before the effects of dissipation destroy coherent energy exchange [9]. In each of refs. [70, 71, 72], loss in the system was found to be dominated by the optical cavity, with $g \lesssim \kappa$. As the low-temperature homogeneous linewidth in self-assembled InAs QDs is typically a few μeV [142], corresponding to a QD dipole decay rate of $\gamma_{\perp}/2\pi \sim 1$ GHz, it will be advantageous to develop cavities with quality factors such that $\kappa/2\pi \lesssim 1$ GHz, with further improvements in Q serving mainly to improve the optical collection efficiency of emitted light. For the $\lambda \sim 0.9\text{-}1.2$ μm emission wavelength for InAs QDs [70, 71], this corresponds to an optical mode quality factor of $Q \sim 1 \times 10^5$ ($\kappa/2\pi = \omega/4\pi Q$). Achieving such low loss cavities is also important in light of the difficulty in fabricating a structure where the QD is optimally positioned for maximum coupling to the cavity mode.

In this chapter, we review results first presented in ref. [69], which details the creation of $D=4.5$ μm diameter AlGaAs microdisks that exhibit Q factors as high as 3.6×10^5 at $\lambda \sim 1.4$ μm , a value which, to our knowledge, exceeds the highest Q factors measured for AlGaAs microcavities to date [13, 14, 70, 71]. These AlGaAs microdisks contain embedded quantum dots-in-a-well (DWELL) [143, 144] that have a ground state emission at $\lambda \sim 1.2$ μm , so that passive, fiber-taper-based measurements are performed at $\lambda \sim 1.4$ μm , where the QDs are relatively non-absorbing. The characteristics of these devices are also investigated through photoluminescence measurements, and low threshold, room temperature QD lasers are demonstrated.

5.2 Overview of microdisk cavity modes

5.2.1 Analytic approximation

In a perfectly circular microdisk structure, the cavity modes circulate around the periphery of the device in traveling wave whispering gallery modes (WGMs). These WGMs are classified in terms of their polarization (TE or TM), radial order (p), and azimuthal number (m).¹ Unlike microspheres, where the WGMs can be solved for analytically, microdisk modes do not have an analytic solution. An approximate analytic solution can be easily found, however, and yields physical insight into the properties of these modes. Such an approach has been considered by many authors; here, I follow the derivation of Borselli et al., in ref. [65].

We begin with Maxwell's equations in a charge-free, current-free medium:

¹As the microdisks studied here are optically thin, only the first order TE and TM modes are considered.

$$\begin{aligned}
\nabla \times \mathbf{E} &= -i\omega\mu_0\mathbf{H}, \\
\nabla \times \mathbf{H} &= +i\omega n^2\varepsilon_0\mathbf{E}, \\
\nabla \cdot (n^2\varepsilon_0\mathbf{E}) &= 0, \\
\nabla \cdot \mu_0\mathbf{H} &= 0,
\end{aligned} \tag{5.1}$$

where we have assumed that the fields oscillate in time as $\exp(i\omega t)$. For a piecewise homogeneous medium, these equations can be used to derive the familiar wave equations:

$$\begin{aligned}
\nabla^2 \mathbf{E} + \frac{n^2\omega^2}{c^2}\mathbf{E} &= 0 \\
\nabla^2 \mathbf{H} + \frac{n^2\omega^2}{c^2}\mathbf{H} &= 0
\end{aligned} \tag{5.2}$$

As the form of equation (5.2) is the same for both \mathbf{E} and \mathbf{H} , from here on out we write everything in terms of a single vector field \mathbf{F} , which can stand for either of the two. In cylindrical coordinates (ρ, ϕ, z) , we can re-write this as:

$$\left(\frac{\partial^2}{\partial \rho^2} + \frac{1}{\rho} \frac{\partial}{\partial \rho} + \frac{1}{\rho^2} \frac{\partial^2}{\partial \phi^2} + \frac{\partial^2}{\partial z^2} + \left(\frac{\omega}{c} \right)^2 \right) \mathbf{F} = 0 \tag{5.3}$$

We now invoke the major approximation used, which is to separate the modes into TE and TM polarizations, which contain the field components $\{E_\rho, E_\phi, H_z\}$ and $\{H_\rho, H_\phi, E_z\}$, respectively. For actual structures, this separation is only approximate (it truly only holds within the center of the slab WG). It provides the significant simplification of making equation (5.3) a scalar wave equation in F_z , where F_z is H_z (E_z) for TE (TM) modes. We then use separation of variables [145] with $F_z = \Psi(\rho)\Omega(\phi)Z(z)$ to break up equation (5.3) into three equations, given as:

$$\begin{aligned}
\frac{\partial^2 \Omega}{\partial \phi^2} + m^2 \Omega &= 0 \\
\frac{\partial^2 Z}{\partial z^2} + \frac{\omega^2}{c^2} (n^2 - \bar{n}^2) Z &= 0 \\
\frac{\partial^2 \Psi}{\partial \rho^2} + \frac{1}{\rho} \frac{\partial \Psi}{\partial \rho} + \left(\frac{\omega^2 \bar{n}^2}{c^2} - \frac{m^2}{\rho^2} \right) \Psi &= 0
\end{aligned} \tag{5.4}$$

where \bar{n} is the effective index. The first equation can immediately be solved, giving the azimuthal dependence $\Omega(\phi) = \exp(im\phi)$, where m is the azimuthal mode number (eigenvalue). The second equation is nothing more than the standard equation for the mode of a slab waveguide, as discussed in detail within ref. [126], for example. The third equation is used to solve for the radial dependence of the cavity mode. The solutions to this equation are Bessel functions within the disk ($\rho < R$, where R is the disk radius), and Hankel functions outside of it ($\rho > R$). As discussed in ref. [65], the Hankel function solution can be approximated by a decaying exponential, so that the radial solution $\Psi(\rho)$ has the form:

$$\Psi(\rho) = \begin{cases} J_m(\frac{\omega}{c}\bar{n}\rho), & \rho \leq R \\ J_m(\frac{\omega}{c}\bar{n}R)\exp(-\alpha(\rho - R)), & \rho \geq R. \end{cases} \quad (5.5)$$

The decay constant α is given as $\alpha = \frac{\omega}{c}(\bar{n}^2 - n_0^2)^{1/2}$ ($n_0=1$ for an air-clad disk). Finally, the azimuthal mode number m is determined (for a given frequency ω , disk radius R , and effective index \bar{n}) by the boundary conditions on the fields at $\rho = R$. This yields the transcendental equation:

$$\frac{\omega}{c}\bar{n}J_{m+1}(\frac{\omega}{c}\bar{n}R) = (\frac{m}{R} + \eta\alpha)J_m(\frac{\omega}{c}\bar{n}R) \quad (5.6)$$

where $\eta = \bar{n}^2/n_0^2$ for a TE mode and $\eta = 1$ for a TM mode.

For very rough estimates, a back of the envelope calculation of m can be useful. One that is typically used is to require that m wavelengths fit in the circumference of the disk. Written explicitly, this is stated as:

$$m\frac{\lambda_m}{n_g} = 2\pi R \quad (5.7)$$

where λ_m is the resonant wavelength of mode m , and n_g is the group index of the waveguide mode, which can be determined from the slope of the waveguide dispersion curve (through solving the slab waveguide portion of equation (5.4) for ω as a function of $\beta=\bar{n}\omega/c$). The free spectral range (FSR), which gives the separation between adjacent modes, is then:

$$\Delta v = v_{m+1} - v_m = \frac{c}{2\pi R n_g} \quad (5.8)$$

This is nothing more than the standard equation for the FSR of a Fabry-Perot cavity with the round-trip length of the cavity equal to the circumference of the microdisk.

5.2.2 Finite-element method simulations

To quantitatively study the properties of the microdisk cavities, we use finite-element eigenfrequency simulations based on the Comsol FEMLAB commercial software. The specific implementation I have used is based on the work of Matt Borselli [128, 137], who in turn received assistance from Sean Spillane [136]. By assuming azimuthal symmetry of the disk structures, only a two-dimensional cross section of the disk is simulated, albeit using a full-vectorial model. That is, the explicit azimuthal symmetry package offered within the software is not appropriate, because it forces the calculated modes to be azimuthally symmetric (i.e., $m=0$). Instead, we essentially solve the wave equation (5.3) assuming an azimuthal dependence of $\exp(im\phi)$. We seek solutions close to some nominal wavelength λ_{nom} , and specify an m value as found by solution of the transcendental equation (5.6). The FEMLAB solver then determines the precise frequency λ_0 at which the mode of azimuthal number m occurs. It also provides the spatial mode profile, which is used to calculate the cavity mode effective volume according to the already-mentioned formula:

$$V_{\text{eff}} = \frac{\int_V \epsilon(\mathbf{r}) |\mathbf{E}(\mathbf{r})|^2 d^3\mathbf{r}}{\max[\epsilon(\mathbf{r}) |\mathbf{E}(\mathbf{r})|^2]} \quad (5.9)$$

where $\epsilon(\mathbf{r})$ is the dielectric constant, $|\mathbf{E}(\mathbf{r})|$ is the electric field strength, and V is a quantization volume encompassing the resonator and with a boundary in the radiation zone of the cavity mode under study. The resonance wavelength λ_0 and radiation limited quality factor Q_{rad} are determined from the complex eigenvalue (wavenumber) of the resonant cavity mode, k , obtained by the finite-element solver, with $\lambda_0 = 2\pi/\Re(k)$ and $Q_{\text{rad}} = \Re(k)/(2\Im(k))$. For the microdisks studied in this chapter and in chapter 6, Q_{rad} is quite large ($> 10^{14}$), and the finite element simulations are only sparingly used. In chapter 7, however, we consider small enough diameter structures that Q_{rad} is a significant contributor to the overall Q of the devices. We will therefore consider these simulations

in greater detail within that chapter.

5.2.3 Standing wave whispering gallery modes

For the devices studied in this thesis, the high- Q modes are not traveling waves but are instead standing waves. This is a result of coherent coupling between the forwards and backwards propagating disk modes (i.e., modes of azimuthal number $\pm m$) as a result of surface roughness. The key behind this coherent coupling is that the modal loss (due to factors such as absorption, scattering, radiation, etc.) is low enough that the backscattering rate caused by the surface roughness is significant in comparison to it.

This modal coupling has been observed experimentally and explained by many other authors, including those of refs. [146, 147, 148, 135, 64]. Here, we present a simple analysis of this coupling. This analysis is essentially an abridged version of that which appears in a recent paper by Borselli et al. [65].

Maxwell's wave equation for the electric field vector in the microdisk structure is

$$\nabla^2 \mathbf{E} - \mu_0 \left(\epsilon^0 + \delta\epsilon \right) \frac{\partial^2 \mathbf{E}}{\partial t^2} = 0, \quad (5.10)$$

where μ_0 is the permeability of free space, ϵ^0 is the dielectric function for the ideal microdisk and $\delta\epsilon$ is the dielectric perturbation that is the source of mode coupling between the *cw* and *ccw* modes. Assuming a harmonic time dependence, the modes of the ideal structure are written as $\mathbf{E}_j^0(\mathbf{r}, t) = \mathbf{E}_j^0(\mathbf{r}) \exp(i\omega_j t)$, and are solutions of equation 5.10 with $\delta\epsilon = 0$. Solutions to equation (5.10) with $\delta\epsilon \neq 0$ (i.e., modes of the perturbed structure) are assumed to be written as

$$\mathbf{E}(\mathbf{r}, t) = e^{-i\omega_0 t} \sum_j a_j(t) \mathbf{E}_j^0(\mathbf{r}). \quad (5.11)$$

Plugging into equation (5.10), keeping only terms up to first order, and utilizing mode orthogonality, we arrive at the coupled mode equations

$$\frac{da_k}{dt} + i\Delta\omega_k a_k(t) = i \sum_j \beta_{jk} a_j(t) \quad (5.12)$$

$$\beta_{jk} = \frac{\omega_0}{2} \frac{\int \delta\epsilon \left(\mathbf{E}_j^0(\mathbf{r}) \right)^* \mathbf{E}_k^0(r) d\mathbf{r}}{\int \epsilon^0 |\mathbf{E}_k^0(\mathbf{r})|^2 d\mathbf{r}}. \quad (5.13)$$

Reference [65] presents a functional form for β in situations involving a small amount of surface roughness. We now explicitly assume that only two modes (the cw and ccw modes of a given polarization (TE or TM), azimuthal mode number m , and radial mode number p) are involved, and that the amplitude of the backscattering rates are equal, so that $|\beta_{cw,ccw}| = |\beta_{ccw,cw}| = |\beta|$. The coupled mode equations then read as

$$\frac{da_{cw}}{dt} = -i\Delta\omega a_{cw}(t) + i|\beta|e^{i\xi} a_{ccw}(t) \quad (5.14)$$

$$\frac{da_{ccw}}{dt} = -i\Delta\omega a_{ccw}(t) + i|\beta|e^{-i\xi} a_{cw}(t), \quad (5.15)$$

where we have taken $\beta = |\beta|e^{i\xi}$. These equations represent the time evolution of the two mode amplitudes (a_{cw}, a_{ccw}) of an isolated system, without loss or coupling to an external waveguide. The inclusion of such terms will be considered later in this thesis, in chapter 8.

These two coupled equations can be uncoupled by introducing the variables $a_{sw,1}$ and $a_{sw,2}$, which represent the standing wave mode amplitudes:

$$a_{sw,1} = \frac{1}{\sqrt{2}} \left(a_{cw} + e^{i\xi} a_{ccw} \right) \quad (5.16)$$

$$a_{sw,2} = \frac{1}{\sqrt{2}} \left(a_{cw} - e^{i\xi} a_{ccw} \right). \quad (5.17)$$

As we saw earlier within this chapter, for an ideal microdisk, a_{cw} and a_{ccw} have an azimuthal spatial dependence of $e^{im\phi}$ (where m is the azimuthal mode number and is a nonzero integer), so that $a_{sw,1}$ and $a_{sw,2}$ will have an azimuthal spatial dependence that will be a mixture of $\cos(m\phi)$ and $\sin(m\phi)$, with the precise dependence being a function of the phase ξ of the backscattering parameter β . Rewriting the coupled mode equations in terms of the standing wave mode amplitudes, we arrive at:

$$\frac{da_{sw,1}}{dt} = -i\Delta\omega a_{sw,1}(t) + i|\beta|a_{sw,1}(t), \quad (5.18)$$

$$\frac{da_{sw,2}}{dt} = -i\Delta\omega a_{sw,2}(t) - i|\beta|a_{sw,2}(t). \quad (5.19)$$

From these equations, we see that the standing wave modes resonate at frequencies $\pm|\beta|$ detuned from the original resonance frequency.

For cavity QED applications, one very important consequence of the distinction between traveling wave and standing wave modes is in the effective volume of the mode V_{eff} . Standing wave WGMs have approximately half the volume of the traveling wave WGMs, so that the coupling rate g between a single quantum dot and a single photon in a standing wave cavity mode is expected to be $\sqrt{2}$ times that when the quantum dot is coupled to a traveling wave cavity mode. This of course assumes the single QD is positioned at an antinode of the standing wave mode; alternately, if it happens to be positioned at a node, the coupling rate g will be zero. Chapter 8 considers the coupling of a QD to standing wave modes in a microdisk in much greater detail, invoking quantum master equation simulations [149] to aid in the analysis.

5.3 Fabrication

The specific devices we consider are AlGaAs/GaAs microdisk cavities with embedded quantum dots (QDs). The epitaxy used was grown by Professors Andreas Stintz and Sanjay Krishna at the Center for High Technology Materials (CHTM) at the University of New Mexico, and is shown in table 5.1. It consists of a single layer of InAs quantum dots embedded in an InGaAs quantum well [144], which is in turn sandwiched between layers of AlGaAs and GaAs to create a 255 nm thick waveguide. This DWELL (short for dot-in-a-well) material has a room temperature ground state emission peak at around 1190 nm (fig. 5.1(b)), and is grown on top of a $1.5 \mu\text{m}$ $\text{Al}_{0.70}\text{Ga}_{0.30}\text{As}$ layer that eventually serves as a support pedestal for the microdisk.

The cavities are created through: (i) deposition of a 200 nm SiN_x mask layer, (ii) electron beam lithography and subsequent reflow of the e-beam resist to produce smooth and circular patterns, (iii) $\text{SF}_6/\text{C}_4\text{F}_8$ inductively coupled plasma reactive ion etching (ICP-RIE) of the deposited SiN_x mask layer (fig. 5.2(a)), (iv) Ar-Cl_2 ICP-RIE etching of the $\text{Al}_{0.3}\text{Ga}_{0.7}\text{As}$ layer and removal of the remaining SiN_x layer, (v) photolithography and isolation of the microdisk onto a mesa stripe that

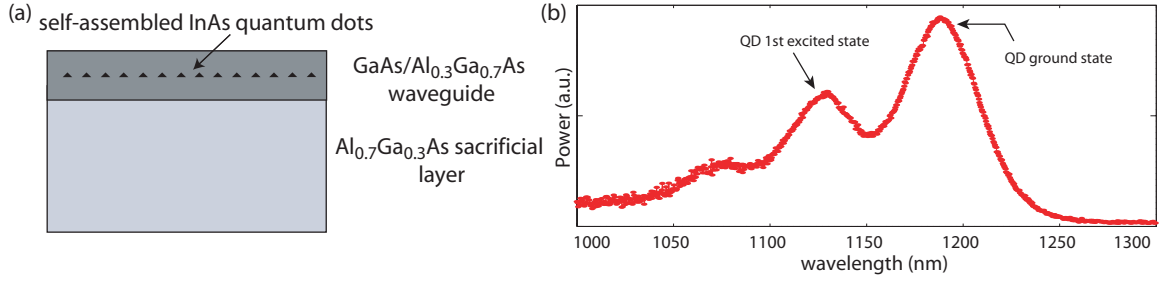


Figure 5.1: (a) Schematic of the DWELL epitaxy from which microdisk cavities are formed. (b) Photoluminescence from an unprocessed region of the 1DWELL material.

Table 5.1: Epitaxy for 1-DWELL microcavity lasers.

Layer	Materials	Thickness
Surface cap layer	GaAs	100 Å
Top waveguide layer	$\text{Al}_{0.30}\text{Ga}_{0.70}\text{As}$	400 Å
Top waveguide layer	GaAs	740 Å
Quantum well layer	$\text{In}_{0.15}\text{Ga}_{0.85}\text{As}$	60 Å
Quantum dot layer	InAs	2.4 monolayer
Barrier layer	$\text{In}_{0.15}\text{Ga}_{0.85}\text{As}$	10 Å
Bottom waveguide layer	GaAs	740 Å
Bottom waveguide layer	$\text{Al}_{0.30}\text{Ga}_{0.70}\text{As}$	500 Å
Sacrificial buffer layer	$\text{Al}_{0.70}\text{Ga}_{0.30}\text{As}$	15000 Å
Substrate	GaAs	N/A

is several microns above the rest of the chip (fig. 5.2(d)), and (vi) HF acid wet chemical etching of the underlying $\text{Al}_{0.7}\text{Ga}_{0.3}\text{As}$ layer to form the supporting pedestal (fig. 5.2(b)-(c)). The e-beam lithography and SiN_x etch steps are particularly important, as any roughness in the mask layer is transferred into the AlGaAs region. A resist reflow process originally developed for use with Si microdisks [65] is employed to create an initial mask pattern that is as circular as possible, and the subsequent SiN_x etch has been calibrated to produce as smooth a sidewall surface as possible (fig. 5.2(a)), without particular concern for its verticality. The subsequent Ar-Cl_2 etch is highly selective so that the angled mask does not result in erosion of the AlGaAs sidewalls. The fabricated

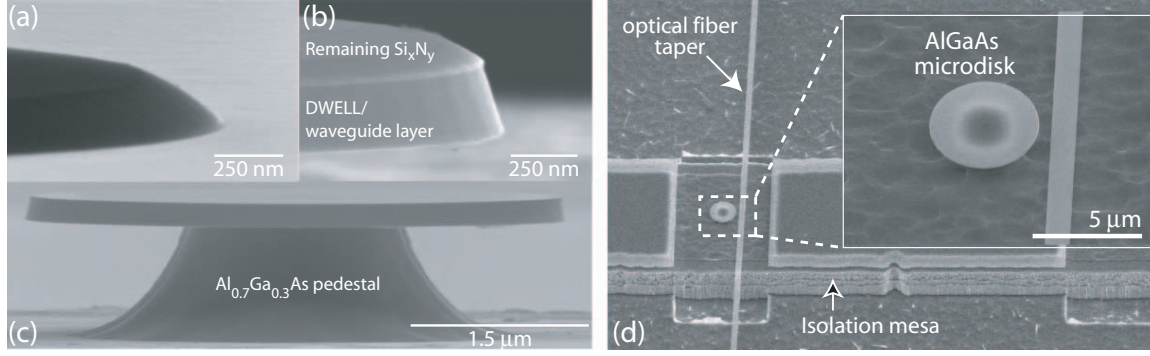


Figure 5.2: Scanning electron microscope (SEM) images of DWELL-containing microdisk cavities after the (a) SiN_x etch, and (b)-(c) AlGaAs etch and undercut. (d) Fully processed device, showing the isolation mesa that is incorporated in order to aid in the taper testing. An optical fiber taper aligned to the side of a microdisk is also visible in this image.

microdisks studied in this chapter are $D \sim 4.5 \mu\text{m}$ in diameter.² Additional fabrication details are given in appendix C.

5.4 Cavity Q measurements in the 1400 nm band

Initial passive measurements to measure the cold-cavity Q factor of the microdisk resonant modes were performed using the optical-fiber-based evanescent coupling technique. As was the case for measurements of the PC cavities in chapter 4, the optical fiber taper is formed by heating and adiabatically stretching a standard single mode fiber until it reaches a minimum diameter of $\sim 1 \mu\text{m}$. A fiber-coupled scanning tunable laser ($< 5 \text{ MHz}$ linewidth) operating in the 1400 nm band is spliced to the taper's input, and when the taper is brought within a few hundred nanometer (nm) of the cavity, their evanescent fields interact, and power transfer can result. A schematic illustrating the coupling geometry for this system is shown in fig. 5.3(a). The devices are tested in the 1400 nm band because it is significantly red detuned from the QD spectrum (fig. 5.1), so that absorption due to the DWELL layer will be negligible at these wavelengths.

The Q of a cavity mode is determined by examining the linewidth of the resulting resonance in the taper's wavelength dependent transmission spectrum. In fig. 5.3(b), we show a doublet resonance of a microdisk ($D=4.5 \mu\text{m}$, 1-DWELL structure) in the 1400 nm wavelength band when

²The AlGaAs sidewalls do show a pronounced angle; this angle does reduce the maximum achievable (radiation-limited) Q of the cavity modes, but for TE-like modes, this reduction does not prevent the devices from exhibiting radiation-limited Q s in excess of 10^8 (for $D \sim 4.5 \mu\text{m}$), even in the presence of the slant. As surface roughness is expected to be a more serious source of loss, the tradeoff between smoothness and verticality is acceptable.

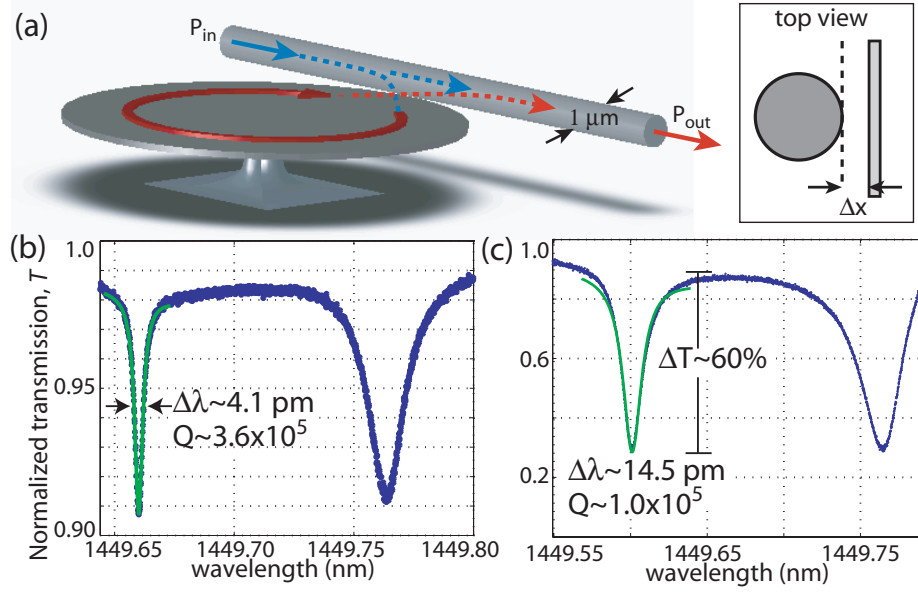


Figure 5.3: (a) Schematic geometry for probing the microdisk cavities through side-coupling via an optical fiber taper. (b) Normalized taper transmission ($T = P_{out}/P_{in}$) of a $4.5 \mu\text{m}$ diameter microdisk for a taper-disk lateral separation (Δx) of $\sim 800 \text{ nm}$. (c) Normalized taper transmission for the same device with $\Delta x \sim 200 \text{ nm}$. The overlying solid green curves are Lorentzian fits to the data.

the taper is $\sim 1 \mu\text{m}$ to the side of the disk; the separation is kept large in order to reduce taper loading effects [52, 64]. The double resonance peaks correspond to standing wave modes formed from mixtures of the degenerate clockwise and counterclockwise whispering gallery modes that couple and split due to the disk-edge surface roughness [64, 148, 146], as discussed earlier within the chapter. The linewidth ($\Delta\lambda$) of the shorter wavelength resonance corresponds to $Q \sim 3.6 \times 10^5$. Similarly, in fig. 5.3(c), we show the spectral response of the doublet when the taper is positioned much closer ($\sim 200 \text{ nm}$) to the edge of the disk, so that the amount of coupling has increased. The combination of increased coupling as well as parasitic loading due to the presence of the taper has increased the total loss rate of the resonant mode, yielding a loaded $Q \sim 1.0 \times 10^5$. The depth of coupling, however, has also considerably increased from 10% to 60%, corresponding to a photon collection efficiency η_0 (the ratio of “good” coupling to all other cavity losses including parasitic and intrinsic modal loss) of approximately 20% (see appendix E for the exact definition of η_0). It is believed that the high Q values achieved in these measurements are due to a combination of the resist reflow process that reduces radial variations and subsequent Rayleigh scattering in the disk, and the optimized dry etching processes that create very smooth disk-edge sidewalls.

The demonstrated Q is high enough that, if used in cQED, the cavity will have a decay rate

$\kappa/2\pi \sim 0.35$ GHz (at $\lambda \sim 1.2$ μm), lower than the aforementioned typical low temperature QD dipole decay rate of $\gamma_{\perp}/2\pi \sim 1$ GHz. After adjusting for the reduced wavelength of the QD resonance, the current devices ($D=4.5$ μm) have a $V_{\text{eff}} \sim 6(\lambda/n)^3$ for the standing wave resonant modes studied here.³ For a maximally coupled InAs QD (spontaneous emission lifetime $\tau \sim 1$ ns, oscillator strength $f \sim 18$ [110]), this mode volume corresponds to $g/2\pi \sim 11$ GHz (refer to Appendices D and H for the formulas used to calculate κ and g). Thus, even for the disk sizes considered here, an appropriately positioned QD would place the system deep within the strong coupling regime. Of additional importance is the fiber-based coupling technique used here. This method allows for the Q to be accurately determined in a way that does not rely upon the (weak) background emission from the QDs [70, 71, 72]; all that is required is a probe laser that can be slightly detuned from the QD absorption lines. Furthermore, the taper also acts as a coupler that transfers light from an optical fiber into the wavelength-scale mode volume of the cavity, where it can interact with the QDs, and as a subsequent output coupler. Such integration could markedly improve the collection efficiency in cavity QED experiments, particularly important for microdisk and photonic crystal cavities, which typically do not have a radiation pattern that can be effectively collected by free-space optics or a cleaved fiber [71]. Subsequent chapters further discuss the advantages of using the fiber taper coupler in such experiments.

5.5 Initial measurements of lasing behavior

In addition to the fiber-based passive measurements of the microdisks at $\lambda \sim 1.4$ μm , we performed some initial room temperature photoluminescence measurements to study the QD emission in the 1.2 μm wavelength band. The cavities ($D=5$ μm in this case) were optically pumped at room temperature using a pulsed 830 nm semiconductor laser, and the emitted laser light was collected by a microscope objective and spectrally resolved in an optical spectrum analyzer (OSA). The setup that was used was essentially identical to that used in chapter 3. Initial measurements were performed on cavities containing 3 DWELLs due to their higher modal gain, roughly three times that of a single DWELL layer [144]. Emission is observed for a small number (~ 2 -5) of modes in a given microdisk (fig. 5.4(a)). Figure 5.4(b) shows a typical light-in-light-out (L-L) curve for a 3-DWELL device pumped with a 300 ns period and 10 ns pulse width; the device exhibits lasing action with an estimated threshold value of ~ 22 μW .

³Our estimate of κ assumes that $Q \sim 3.6 \times 10^5$ is achievable at $\lambda \sim 1200$ nm. In chapter 6, we present measurements that show that such Q s are indeed achievable at the shorter wavelengths.

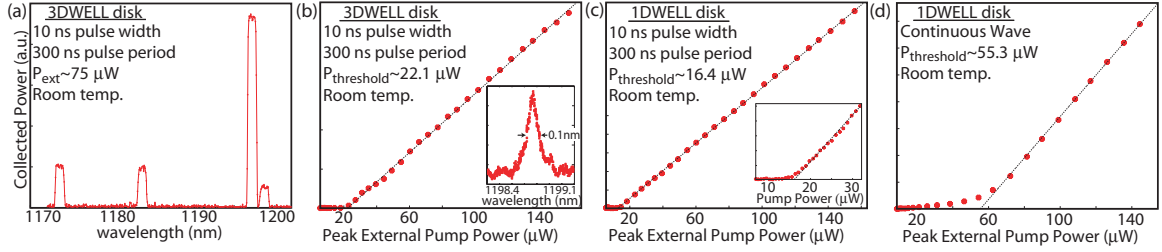


Figure 5.4: (a) Photoluminescence spectrum of a 3-DWELL microdisk device (OSA resolution bandwidth (RBW)= 1 nm). (b)-(d) L-L curves for: (b) pulsed 3-DWELL microdisk laser (inset shows the subthreshold spectrum of a cavity mode), (c) pulsed 1-DWELL microdisk laser (inset shows L-L curve near threshold), and (d) 1-DWELL microdisk laser under CW pumping conditions. The dashed lines are least-square linear fits to the above-threshold data.

The saturated ground state modal gain for single DWELL structures has been estimated to be $\sim 3.6\text{-}5.4 \text{ cm}^{-1}$ [144, 150]. Noting that modal gain approximately equals modal loss at threshold, this indicates that a *minimum* cavity $Q \sim 3\text{-}5 \times 10^4$ is required for this single layer of QDs to provide enough gain compensation to achieve lasing. The fiber-based linewidth measurements described earlier indicate that such Q factors should be achievable, and indeed, lasing from the QD ground states is observed in these single dot layer devices (fig. 5.4(c)). The laser threshold pump power for the 1-DWELL devices was measured to be as small as $16.4 \mu W$, significantly lower than the $750 \mu W$ threshold values recently reported for similarly sized microdisk QD lasers [151]. Furthermore, as shown in fig. 5.4(d), continuous wave (CW), room temperature lasing was also obtained, albeit with a somewhat higher laser threshold.

The laser threshold values we report here are the peak pump powers incident on the sample surface; the absorbed power is estimated to be roughly 16% of this value, determined by calculating the expected reflectivities at the disk interfaces and assuming an absorption coefficient of 10^4 cm^{-1} in the GaAs and quantum well layers [152]. The threshold absorbed pump power for the 1-DWELL lasers is thus $\sim 2.6 \mu W$. From this, the equivalent threshold current density, useful for comparing the performance of the microdisk lasers to previously demonstrated broad-area stripe lasers, can be estimated. Given the pump spot size ($\sim 16 \mu m^2$), and assuming an internal quantum efficiency ~ 1 , we arrive at an equivalent threshold current density of 11 A/cm^2 for the 1-DWELL devices. In comparison, the estimated *transparency* current density in previous work on broad-area 1-DWELL lasers was 10.1 A/cm^2 [144]. The proximity of the demonstrated laser threshold to this transparency value indicates that non-intrinsic optical losses within the microdisk cavity have largely been eliminated.

In conclusion, AlGaAs microdisks as small as $4.5 \mu m$ in diameter and supporting standing wave

resonant modes with Q factors as high as 3.6×10^5 in the 1400 nm wavelength band have been demonstrated. These cavities contain integral InAs quantum dots, and initial room temperature photoluminescence measurements have yielded laser threshold values as low as $16.4 \mu\text{W}$, nearing the transparency level of the material. In the following chapters, we will extend this work along two primary fronts: (i) use of the fiber taper within the photoluminescence measurements as a means to effectively collect (and source) light from the cavities, thereby creating fiber-coupled lasers, and (ii) consideration of smaller diameter disks, where the additional size reduction is important from the standpoint of increasing the peak electric field strength within the devices, to push cavity QED experiments further within the regime of strong coupling.

Chapter 6

Photoluminescence Measurements of Quantum-Dot-Containing Microdisks Using Optical Fiber Tapers

The ability to efficiently couple light into and out of semiconductor microcavities is an important aspect of many microphotonic technologies [153], and plays a vital role in chip-based implementations of cavity quantum electrodynamics (cQED) for quantum networking and cryptography [60, 9, 154]. While some geometries, such as micropillar cavities, exhibit highly directional emission that can be effectively collected [16, 109], coupling to wavelength-scale semiconductor microcavities is in general non-trivial [120, 155, 156, 154], due to a number of factors. These include the size disparity between the modes of the microcavity and those of standard free-space and fiber optics, the refractive index difference between semiconductors and glass or air, and the potentially complicated cavity mode profiles sustained by these devices. In this thesis, we have presented evanescent coupling through optical fiber tapers as a way to couple efficiently to semiconductor microcavities. As we have already discussed, such fiber tapers have been used as near-ideal coupling channels for glass-to-glass coupling with silica-based microcavities such as microspheres [32, 157, 20, 55] and microtoroids [56]. In addition, as described in chapters 4 and 5, our recent experiments have indicated that they can also serve as efficient couplers to high-refractive index semiconductor-based devices, such as photonic crystal waveguides [39], photonic crystal cavities [52, 57] and microdisks [64, 69]. While the work described in the previous chapter primarily utilized fiber tapers for passive measurements such as the characterization of cavity quality factors, in this chapter, which is largely based on ref. [75], we focus on using the fiber taper as an efficient coupler for injecting pump light into and extracting the light emitted by semiconductor quantum dots into microdisk whispering gallery modes. The immediate device application that we study

here is room-temperature, fiber-coupled microdisk-quantum-dot lasers, but the results described are directly applicable to future studies of cavity QED phenomena in semiconductor-based systems.

In section 6.1, we qualitatively describe the issues addressed in this chapter, as well as the experimental setup we use. In section 6.2, we briefly review passive measurements in the 1200 nm wavelength band to determine the optical losses of the optical resonant cavities under study. In section 6.3, we present experimental results demonstrating the improvements that result when free-space collection is replaced by fiber-based collection in photoluminescence measurements, while in section 6.4, we present initial results on microdisk lasers that employ both fiber pumping and fiber collection. Finally, in section 6.5, we consider some of the applications of this work to future experiments.

6.1 Preliminary discussion and experimental methods

The free-space collection from a whispering gallery mode (WGM) of a microdisk is a function of a number of factors, including the position and numerical aperture (NA) of the collection lens, and the radiation pattern and quality factor (Q) of the resonant mode. Optical losses from the microdisk include not only the (ideal) radiation due to radial tunneling of light from the disk periphery, but also scattering losses due to surface roughness imperfections at the disk edge and material absorption. For high-refractive index ($n \sim 3.5$) III-V semiconductor microdisks, surface roughness scattering is typically the dominant form of radiation from the microcavity. The intrinsic radiation loss of semiconductor microdisks is almost negligible in all cases, save the smallest of microdisks; the radiation Q of the lowest radial order WGM of the $D \sim 4.5 \mu\text{m}$ microdisks studied here is greater than 10^{14} at the QD emission wavelength of 1200 nm, and is greater than 10^6 for $D \sim 2.0 \mu\text{m}$ (FEMLAB calculations are shown in chapter 7). As such, any light that is collected through free-space methods is the result of scattering of the WGM off imperfections in the microdisk [155], a relatively inefficient and non-directional process. Bulk material absorption and absorption due to surface states may also play a role, particularly when considering devices in which the Q due to surface scattering can be in excess of 10^5 . This results in a situation where the more perfect the microdisk is made (through reduction in surface roughness), and the further the Q factor is improved, the more difficult it becomes to collect light from the resonant modes. Although there may be some potential in modifying the disk geometry [155, 154] to improve this situation (for example, by etching a shallow second-order grating in the microdisk surface), the ability to do this

while maintaining high Q factors could be of potential difficulty. The most successful method to date for increasing collection efficiency from semiconductor microdisk resonators seems to be placement of the collection optics in the plane of the disk [13, 14], resulting in more effective capture of the predominantly low-angle scattered light.

The fiber taper offers an attractive alternative because it provides a means to directly couple light out of the WGMs, without relying upon the weak intrinsic radiation of the microdisk or the non-directionality of surface roughness scattering. This evanescent near field coupling, which is a function of the integrated modal overlap of the microdisk and taper modes over the interaction region [50, 137], has been demonstrated to be appreciable in previous works with small diameter semiconductor microdisks [64, 69] where phase matching between the glass fiber taper waveguide and the semiconductor microdisk is not as limiting. While the fiber taper does load the cavity mode, and thus degrade its Q , the key point is that the added loss is primarily *good loss* in the sense that it can be efficiently collected into the taper mode of interest [55, 57]. This allows for the loaded Q to be maintained at a high value while simultaneously obtaining high collection efficiency [64, 69]. The situation is analogous to the case of a Fabry-Perot cavity where one mirror is intentionally made to have a slightly lower reflectivity for output coupling, which limits the Q of the cavity, but not beyond some acceptable level. While in that case, the cavity Q is fixed by the mirror reflectivities, here we have some flexibility over the Q and the amount of loading by adjusting the cavity-taper separation.

To compare free-space and fiber-taper-based collection, we use the experimental setup depicted in fig. 6.1, which consists of a fiber taper probing station that has been incorporated into a standard photoluminescence (PL) measurement setup. Passive measurements of the resonator modes are performed by connecting the input of the fiber taper to a 1200 nm band scanning tunable laser, with the polarization of the laser output at the taper-microdisk interaction region controlled using a paddle wheel polarization controller. The entire taper probing setup (motorized stages, microcavity chip, and fiber taper waveguide) is mounted onto a larger manually actuated X-Y-Z stage that is positioned underneath an ultra-long working distance objective lens (NA = 0.4). This microscope objective is part of a PL setup that provides normal incidence pumping and free-space collection from the samples. The pump laser in the majority of the measurements is a 830 nm laser diode that is operated in quasi-continuous-wave operation (280 ns pulse width, 300 ns period). The pump beam is shaped into a Gaussian-like profile by sending the laser beam through a section of single mode optical fiber, and is then focused onto the sample with a spot size that is slightly larger than the size

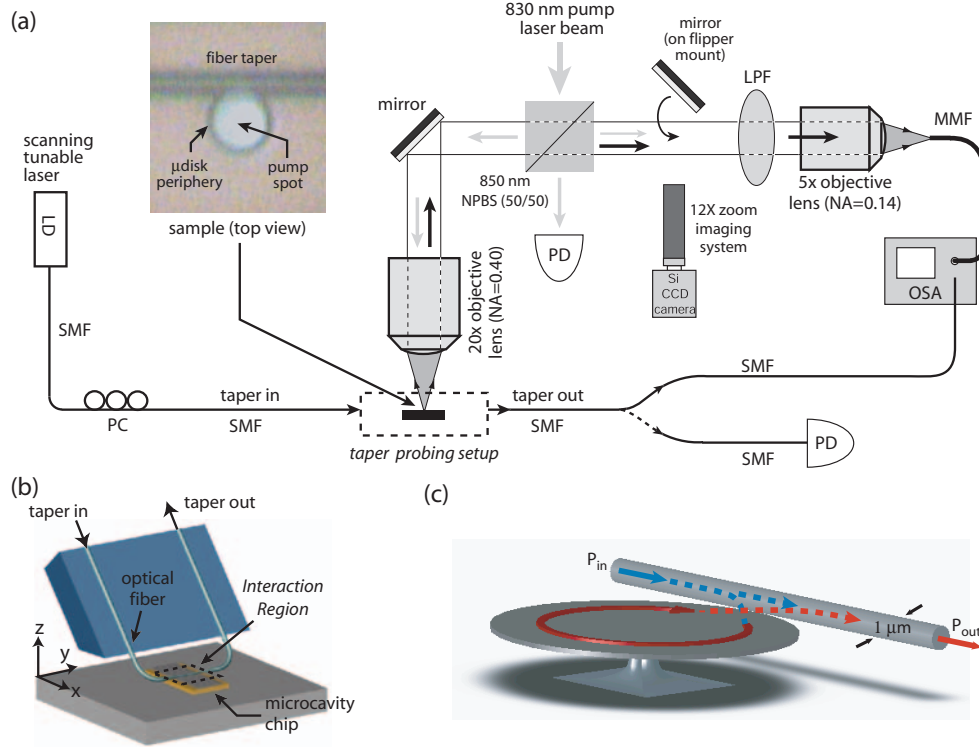


Figure 6.1: (a) Experimental setup for studying the QD-microdisk devices, where the pump laser and photoluminescence beams are shown as light gray and black arrows, respectively. The inset shows a fiber taper aligned to a microdisk that is being optically pumped from the top. Acronyms used in the diagram: polarization controller (PC), numerical aperture (NA), non-polarizing beam-splitter (NPBS), photodetector (PD), long-pass pump rejection filter (LPF), single mode fiber (SMF), multi-mode fiber (MMF), optical spectrum analyzer (OSA). (b) Schematic of the fiber taper probing geometry. (c) Schematic of the taper-to-microdisk interaction region, showing the resonant fiber taper coupling to WGMs of the microdisk.

of the microdisk (area $\sim 18 \mu m^2$). The free-space pump laser power is monitored by using a 830 nm wavelength 50/50 non-polarizing beamsplitter (NPBS) with a calibrated photodetector (PD) on one of the ports. The QD free-space photoluminescence in the 1200 nm band is collected at normal incidence from the sample surface using the same objective lens for pump focusing, is transmitted through the 830 nm NPBS and a long-pass pump rejection filter (LPF), and is finally collected into a multi-mode fiber (MMF) using an objective lens with NA = 0.14. The luminescence collected by this MMF is wavelength resolved by a Hewlett Packard 70452B optical spectrum analyzer. For fiber taper measurements, the fiber taper is strung across the sample and positioned in the near field of the microdisk from above, allowing simultaneous (normal incidence) free-space and fiber taper optical pumping and photoluminescence collection. The output of the fiber taper can either be connected to

an InGaAs photodetector (PD) for wavelength scans using the tunable laser source, or to the OSA for analysis of the photoluminescence from the microdisk. Alignment of the pump beam and the fiber taper to the microdisk is performed by imaging through the pump and collection objective lens, as shown in the inset (a mirror flips in-and-out of the free-space photoluminescence beam path to direct the image to a 12X zoom imaging system). All of the measurements presented here were performed with the sample maintained in a room temperature environment, with no active cooling or temperature control.

This integrated setup allows for a number of different measurements to be made. Passive measurements of the microdisk resonant modes are performed by sending a tunable laser into the taper's input and monitoring the wavelength-dependent transmission at the taper's output. Photoluminescence measurements can be done in any of four potential configurations (i) free space pumping, free space collection: here, the fiber taper plays no role, and the vertically emitted power from the disks is collected into a multimode optical fiber that is then fed into the optical spectrum analyzer (OSA); (ii) free space pumping, fiber taper collection: here, the output of the fiber taper is connected to the OSA; (iii) fiber taper pumping, free space collection: here, the input of the fiber taper is connected to a fiber-coupled pump laser; (iv) fiber taper pumping, fiber taper collection: here, the free-space optics used in the standard PL measurements play no role.

6.2 Measurement of cavity Q in the 1200 nm wavelength band

The devices studied in this work have been previously characterized in the 1400 nm band, and Q s as high as 3.6×10^5 have been measured (chapter 5). Those measurements were done at wavelengths significantly red detuned from the QD emission band, where QD absorption and material absorption in the GaAs/AlGaAs waveguide layers are expected to be quite small. To confirm that the cavity Q s are still high near the ground state QD emission wavelength (peaked near 1190 nm as shown in fig. 6.2(a)), we perform passive fiber-taper-based measurements [52, 64, 69] in the 1200 nm band.¹ The high- Q resonances within the transmission spectrum (fig. 6.2(b)), under closer inspection, are seen to be doublets (inset to fig. 6.2(b)), as was the case for the measurements in the 1400 nm band shown in chapter 7.

FEMLAB solutions of the WGM resonances of the microdisks studied in this chapter show

¹The WGMs in the 1400 nm wavelength band are expected to have very similar radiation and scattering losses as those in the 1200 nm band for the microdisk geometries studied here. Differences in Q at these two wavelengths are thus expected to be indicative of wavelength-dependent material absorption losses.

that the free spectral range (FSR) is ~ 40 nm for TE-polarized modes of low radial mode number ($q = 1, 2, 3, 4$) in the 1200 nm wavelength band. Higher radial order WGMs ($q \geq 5$) are expected to show up only very weakly in the fiber taper transmission owing to their relatively small radiation limited Q factors ($\lesssim 10^4$) and significantly larger overlap with the support pedestal. From the broad spectral wavelength scan shown in fig. 6.2(b), a pair of deeply coupled resonant modes separated by a full FSR are observed ($\lambda \sim 1222$ and 1263 nm), as well as several other deeply coupled resonant modes. Due to the extended nature of the higher order radial modes and their better phase matching to a low-index glass waveguide such as the fiber taper, the coupling to the lowest order $q = 1$ WGM is typically lower than that of the $q = 2$ mode for similar sized microdisks [137]. We believe that these doublet modes at $\lambda \sim 1222$ nm and $\lambda \sim 1263$ nm are first order ($q = 1$) radial modes, while the mode at $\lambda \sim 1242$ nm is probably a $q = 2$ radial mode. The broader and more weakly coupled intermediate modes are most likely higher order radial modes, $q = 3, 4$ (higher order slab modes in the vertical direction of microdisk are also a possibility, though less likely due to their reduced radiation Q). Examining the linewidth of the doublet resonances when the taper is relatively far away from the microdisk gives an estimate for the cold-cavity, unloaded Q of the modes. Q s as high as 2.2×10^5 at ~ 1260 nm and as high as 1.9×10^5 at ~ 1220 nm are measured in these microdisks (insets of fig. 6.2(b)), the latter of which is only 30 nm red detuned from the peak of the QD emission spectrum (fig. 6.2(a)). These Q factors are quite high for a wavelength-scale AlGaAs microcavity [13, 14, 71, 84, 158], and correspond to a cavity decay rate of $\kappa/2\pi \sim 0.6$ GHz for resonant modes with an effective mode volume of only $V_{\text{eff}} \sim 7(\lambda/n)^3$. Nevertheless, some degradation in the quality factors from those previously measured in the 1400 nm band is observed. These are believed to be at least in part due to absorption in the QD layers, as evidenced by the emission in the PL spectrum at these wavelengths (fig. 6.2(a)).

Additional measurements in the 980 and 850 nm wavelength bands on similar microdisk resonators formed in AlGaAs (without a QD layer) have indicated a trend of optical loss which significantly increases below a wavelength of $1 \mu\text{m}$. This trend in optical loss is similar to that reported in ref. [66], where material absorption that extended 350 meV within the bandgap was attributed to incorporation of oxygen impurities into the AlGaAs lattice. We are currently investigating this more carefully, in a project headed by Chris Michael in collaboration with the group of Evelyn Hu at UC Santa Barbara. This wavelength-dependent loss was one of the main reasons we wanted to test the devices in the 1200 nm band as well as the 1400 nm band; fortunately, as we have seen above, the achievable Q s at 1200 nm are still quite high.

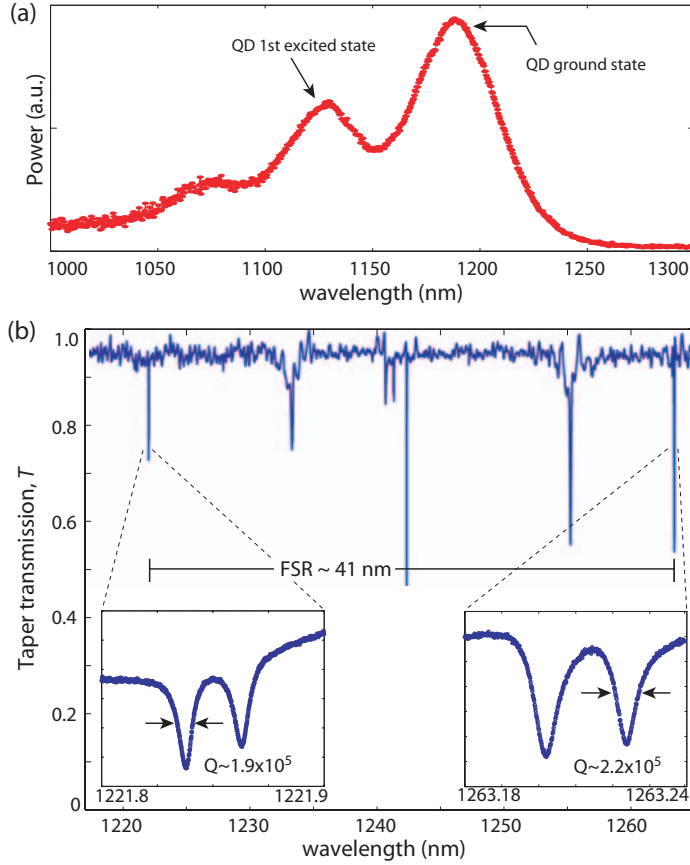


Figure 6.2: (a) Photoluminescence from an unprocessed region of the 1DWELL material. (b) Passive taper-based measurements of a microdisk in the 1200 nm band. The insets show high resolution scans for two sets of doublet modes for this device. These high resolution scans are taken when the taper-microdisk separation is a few hundred nm and the depth of coupling is $\sim 5\% - 10\%$.

6.3 Improved collection efficiency with fiber tapers

We now turn to the heart of the current work, which is a study of the gains in efficiency that can be achieved by using optical fiber tapers as a collection tool in PL measurements. This is initially done by comparing the amount of power obtained in free-space and fiber taper collection configurations, while maintaining identical free-space pumping conditions (in terms of pump-beam intensity and pump beam position). The free-space collection for a microdisk that has been pumped at normal incidence with $\sim 580 \text{ W/cm}^2$ at 830 nm is shown in fig. 6.3(a). This pump intensity is near the laser threshold for this device (see below), and we see that the peak height at $\lambda \sim 1193.5 \text{ nm}$ is $\sim 30 \text{ pW}$. For comparison to the fiber taper collection described below, an estimate of the optical losses in the free-space collection setup were made (after removal of the pump rejection filter). By measuring the collected pump laser power reflected off of the mirror-quality surface of the AlGaAs epitaxy, and assuming a 30% reflection coefficient from the AlGaAs surface, 43% of the reflected pump beam was collected into the OSA. Additional limitations in the normal incidence free-space collection stem from the finite numerical aperture of the collecting lens ($\text{NA}=0.4$) which covers only 4% of

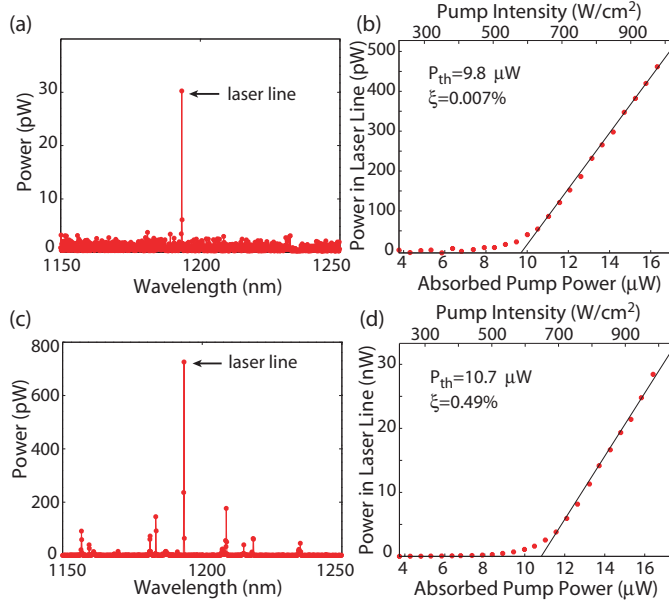


Figure 6.3: (a) Emission spectrum and (b) Light-in-light-out (L-L) curve for normal incidence free-space collection from a (free-space) optically pumped microdisk. Fiber taper collected (c) emission spectrum and (d) L-L curve from the same microdisk resonator, under identical pumping conditions. The emission spectra were taken near laser threshold at $\sim 580 \text{ W/cm}^2$ of incident pump beam intensity. The fiber taper collected power includes that from the forward propagating transmission channel only.

the full 4π steradians.

Next, we consider the use of the optical fiber taper as a collection optic in the PL measurements. To obtain an estimate of the amount of coupling between the taper and the microdisk, the free-space pump beam is blocked, and passive measurements at wavelengths that are slightly red detuned from the QD emission are performed as described above in section 6.2. Since the FSR for the low radial number WGMs of the microdisks studied here is $\sim 41 \text{ nm}$ in the 1200 nm wavelength band, the modes coupled to and studied passively are typically a single FSR red detuned from the lasing mode. For most experiments, the taper is placed in direct contact with the top edge or side of the microdisk, which increases the amount of coupling from that shown in fig. 6.2(b) to transmission depths between 30% and 60%. For this initial measurement, a resonance depth of $\sim 38\%$ is obtained for a cavity mode at $\lambda \sim 1238.1 \text{ nm}$, which gives us a qualitative estimate for the coupling to WGMs overlapping the peak of the gain spectrum.² This coupling depth corresponds to a taper collection efficiency $\eta_0 \sim 11\%$, where η_0 is defined (ref. [57] and appendix E) as the fraction of the optical power from the cavity resonant mode that is coupled into the fundamental fiber taper mode in the forward propagating transmission direction. Other loss channels from the microdisk include intrinsic loss of the cavity in absence of the taper, parasitic coupling into higher-order, non-collected modes of the fiber taper, and for the standing wave modes studied here, coupling into the backwards

²The coupling between the taper and microdisk can be different for different cavity modes, so this technique is used primarily as a qualitative guide.

propagating fundamental taper mode. For the moderate coupling depths measured here, the taper coupling efficiency into the forward and backward propagation directions is approximately equal, thus yielding an overall taper coupling efficiency of $\eta'_0 \sim 22\%$ for this WGM.

Once this level of coupling has been achieved, the tunable laser output is blocked, the free-space pump beam is unblocked, and the output of the fiber taper is disconnected from the photodetector and connected to the OSA to measure the emitted power from the microdisk. fig. 6.3(c) shows the resulting spectrum collected by the fiber taper in the forward propagating transmission direction. We see that at the wavelength $\lambda \sim 1193.5$ nm, the peak height is ~ 725 pW, which is nearly a factor of 25 times improvement over the peak height observed in normal incidence free-space collection. In addition, a significant amount of power is present within modes that were not detectable in the free-space case (the noise floor of the OSA was approximately 1 pW), due to the poor efficiency of collection in this configuration.

This straightforward comparison of the collected powers for a single pump power is not necessarily the most appropriate comparison, however. The reason for this is that the fiber taper loads the cavity, thus decreasing the Q of the resonant modes and increasing the threshold pump power, so that for a given pump power the laser is not equally above threshold in the two measurements. Another, more appropriate comparison is the differential collection efficiency above threshold, which we label ξ . This is determined by measuring a light-in-light-out (L-L) curve for the microdisk and taking the slope of this curve above threshold. In these curves, the light out is taken to be the total power within the laser line, while the light in is taken to be the estimated absorbed pump power. The absorbed pump power is determined by multiplying the pump beam intensity by the area of the microdisk to get an incident pump power (the beam overlaps the entirety of the disk), and then multiplying this value by the absorption of the microdisk at 830 nm. We estimate this absorption to be $\sim 10\%$, assuming an absorption coefficient of 10^4 cm^{-1} in the GaAs, quantum well, and QD layers [152], and a reflection coefficient of 30% at the GaAs-air interfaces at the top and bottom of the disk. The resulting L-L curves are shown in fig. 6.3(b),(d) for both free-space and fiber-taper collection. We see that the threshold pump power has indeed increased in the case of fiber-taper collection, but that the differential efficiency has also significantly improved and is more than 70 times that of the free-space value.

To study the tradeoffs between ξ and threshold more closely, in fig. 6.4(a) several L-L curves are plotted, each for a different taper position with respect to the microdisk (note that the microdisk studied here is not the same as the one studied above, but the qualitative behavior is identical). The

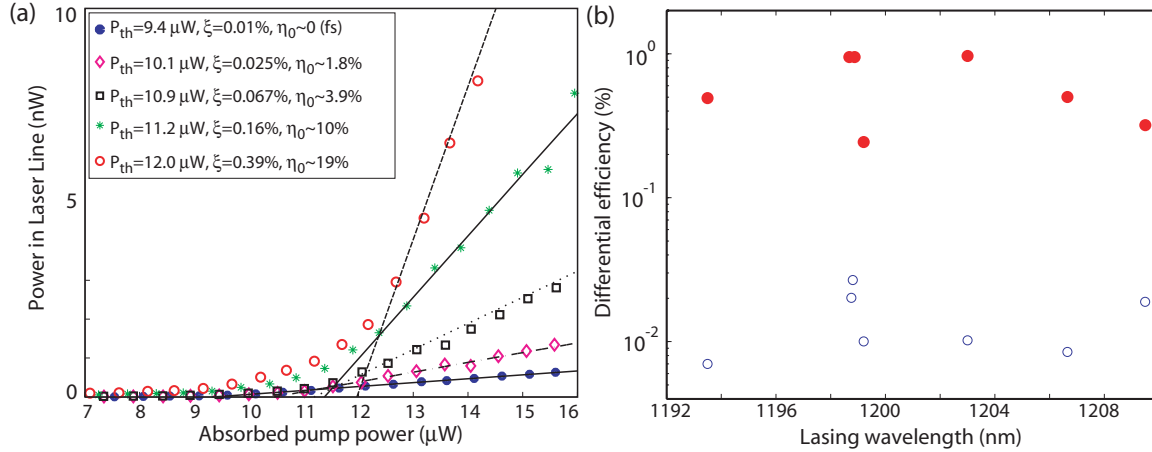


Figure 6.4: (a) L-L curves for free-space pumping and fiber taper collection at different taper positions. For each curve, we note the threshold pump power (P_{th}), the fiber taper collection efficiency (η_0) for a mode that is red detuned from the peak QD emission, and the above threshold differential efficiency (ξ). (b) Scatter plot of the differential efficiency for fiber taper (filled circles) and free-space collection (open circles) for a number of different microdisk lasers. For these measurements the fiber taper collected power included that from the forward propagating transmission channel only.

different taper positions correspond to a varying level of coupling between the microdisk and taper, which we again qualitatively estimate through measurements of the coupling to a microdisk WGM that is red detuned from the QD emission in the 1200 nm band. From fig. 6.4(a), we see that in general, both the threshold power and ξ increase with increasing η_0 . As might be expected, in the course of these measurements it was possible in some cases to load the microdisk strongly enough to degrade the initial laser mode's Q to the point that it no longer lases, and a different mode (with a higher loaded Q) begins to lase.

A number of different microdisk devices have been studied, and the results described above are fairly consistent from device to device, with ξ routinely 1-2 orders of magnitude larger when fiber taper collection is employed. A scatter plot for some of this data is shown in fig. 6.4(b). Despite the significant improvement obtained using the fiber taper, we see that the largest ξ measured is roughly 10 nW/μW, which means that only 1% of the pump photons are converted to a collected signal photon, and we should thus consider why ξ is far below unity. We first note that when considering collection into both directions of the fiber taper, ξ is actually 2% for the standing wave WGMs of the microdisks studied here. A measure of the fiber taper collection efficiency of the microdisk WGM laser light, η_0 , from the passive wavelength scans described above indicate that the external

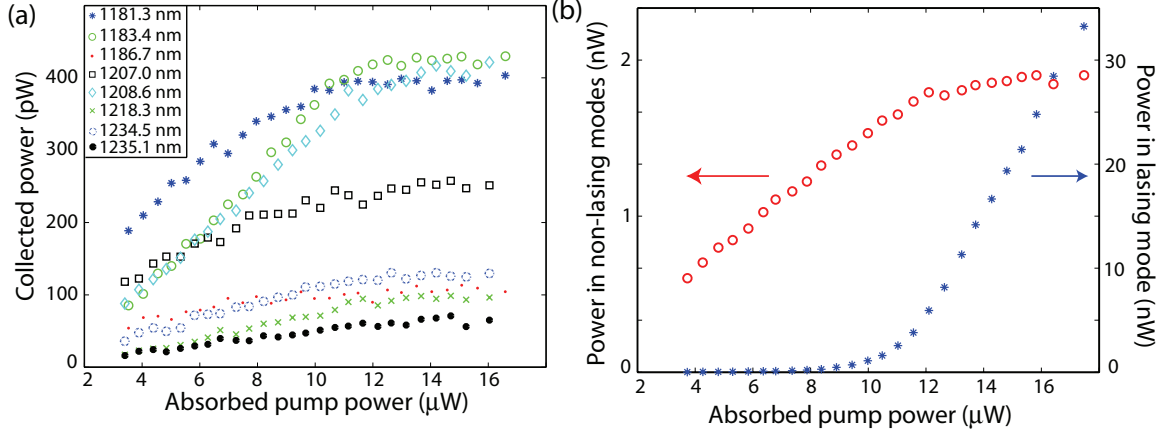


Figure 6.5: (a) L-L curves for non-lasing modes of the disk studied in fig. 6.3. (b) Total power in the non-lasing modes (shown by open circles), showing saturation for pump values close to the threshold value for the lasing mode (shown by asterisks). Note that the y-axis scale for the lasing mode is 15 times larger than that for the non-lasing modes.

fiber taper collection efficiency should be as high as $\sim 22\%$ (corresponding to 11% for the forward transmission direction only). The total loss through the fiber taper and all of the fusion-splices and connections in the fiber path was measured to be $\sim 1.6\text{dB}$, so that, if symmetric loss in the taper about the microdisk coupling region is assumed, $\sim 17\%$ of the WGM laser photons collected by the taper are lost before they reach the OSA. Taken together, these two factors put an estimate of the upper bound on the fiber-coupled external laser efficiency of 18% for collection into both directions of the fiber.

The roughly order of magnitude difference between the measured (2%) and expected (18%) differential laser efficiency may be a result of several factors involving the complex dynamics within the DWELL active region. Previous measurements of DWELL injection lasers in stripe geometries [144] indicate that the internal quantum efficiency of the quantum dots is $\eta_i^{QD} \sim 0.5$ (this is roughly the percentage of carriers captured by the QDs in the DWELL structure that contribute to stimulated emission above threshold). This factor can certainly change from growth to growth, and given that the laser threshold values are roughly 2-2.5 times higher than that measured in previous work on identically fabricated devices from a different wafer growth [69], we might qualitatively expect ξ to be reduced by a factor of $\sim 4 - 5$ due to η_i^{QD} .

Both the spectral and spatial distribution of carriers within the microdisk may also lead to reductions in the laser differential efficiency through incomplete clamping of the spontaneous emission into the non-lasing modes of the microdisk above threshold. To examine such effects in our struc-

tures, we measure L-L curves (fig. 6.5(a)) for a number of the most prominent non-lasing WGMs of the microdisk studied in fig. 6.3. We see that the emission into these modes is largely clamped above the threshold for the lasing mode (estimated to be $10.7\mu\text{W}$ of absorbed pump power). The aggregate effect is clearly seen in fig. 6.5(b), where the power into the non-lasing WGMs has been summed and plotted along with the L-L curve for the lasing mode. Such clamping has been reported by other authors for similarly sized microdisks [159], while smaller microcavity devices with a larger laser mode spontaneous emission rate, have exhibited a gradual rollover and/or incomplete clamping of spontaneous emission [120, 159, 160, 43]. Measurement of the background spontaneous emission into non-WGM, radiation modes of the microdisk was performed using free-space collection (the fiber taper is much more sensitive to WGM emission than to emission from the center of the microdisk into radiation modes), and did show incomplete clamping of the spontaneous emission. This sort of spatial hole burning has been predicted in numerical modeling of microdisk cavities [161]. If this is the case, the effective pump area is limited to a region about the WGM. Assuming that the WGM radial width is approximately (λ/n_{eff}) , where n_{eff} is the effective refractive index in the plane of the microdisk,³ this corresponds to a $7\mu\text{m}^2$ area in the devices under test here. Since the total disk area is $\sim 16\mu\text{m}^2$, then only 7/16 of the pump photons would be effectively pumping the WGM. Including this factor brings the expected value of ξ within the range of experimentally measured values.

Aside from reducing taper loss (loss $< 0.5\text{dB}$ can be easily achieved in our lab), η_0 is the main parameter that can be improved upon to increase ξ . This can be done by adjusting the geometry of the disk (using thinner disks, for example) to bring the index of the WGMs of the semiconductor microdisks closer to that of the silica fiber taper, so that more efficient coupling can be obtained. A study of such modifications in Si microdisk structures has been undertaken, and the regimes of critical coupling and overcoupling have been achieved [137]. In addition, if spatial hole burning is significant, another factor that could potentially be improved is the method of pumping. In particular, the pumping beam could be shaped to preferentially pump the perimeter of the microdisk (i.e., an annular-shaped beam could be used). Alternately, as discussed below, a fiber taper could be used to pump the microdisk.

³Finite-element simulations have shown this to be an accurate estimate.

6.4 Fiber-pumped microdisk lasers

In addition to improving the collection efficiency, optical fiber tapers have the potential for improving the pump efficiency of these QD-containing microdisks; such an effect has in fact been demonstrated in previous work on doped glass microcavities [162, 73, 74]. In particular, if the pump laser is resonant with a WGM of the microdisk, light can be absorbed with high efficiency, and in the case of critical coupling, complete power transfer can be achieved. This should be contrasted with the case of free-space pumping, where only a small percent (10% for the devices we have considered here) of the incident pump light is absorbed by the device, and some of this absorption is in a region (the center of the microdisk) that does not contribute to useful gain for the resonant WGMs [161].

For an initial demonstration, we use a tunable laser operating in the 980 nm band as a pump source. The 830 nm pump laser is not used because the absorption within the microdisk at this wavelength is too large to allow uniform pumping of the microdisk perimeter, as the pump light is absorbed before a single round trip around the cavity can be made. At 980 nm, the material absorption is still relatively high (the quantum well layer will be highly absorbing), so that the Q_{980} of WGM modes near the pump wavelength are not expected to exceed a few hundred. The pump laser is connected to the fiber taper input, and the fiber taper output is connected to the OSA. The taper is contacted to the side of the microdisk, and the pump wavelength and polarization are manually adjusted until the collected power in the OSA is maximized (this is necessary in order to resonantly couple to a mode within the pump wavelength band). A typical L-L curve and subthreshold spectrum are shown in fig. 6.6. We see that a significant amount of power is collected into the fiber taper, and that in particular, the subthreshold spectrum shows a number of well-resolved modes with a good signal-to-noise ratio. The estimated absorbed pump power in the microdisk displayed in fig. 6.6(a) corresponds to 66% of the input power in the fiber taper, and is found by taking the difference in the 980 nm band taper transmission between when the taper is displaced tens of microns above the microdisk (no coupling) and when it is in contact with the microdisk (strongly coupled). We note that the pump threshold value in this pumping geometry is only about a factor of two less than the *incident* pump power in the 830 nm free-space pumping, and is significantly larger than what might be expected (ideally, the pump power here should be less than the *absorbed* pump power in the 830 nm pumping). This is most likely a result of the relatively crude method we have employed to estimate the power absorbed in the microdisk; a much more accurate method for determining the coupled pump power uses the wavelength-dependent transmission of the

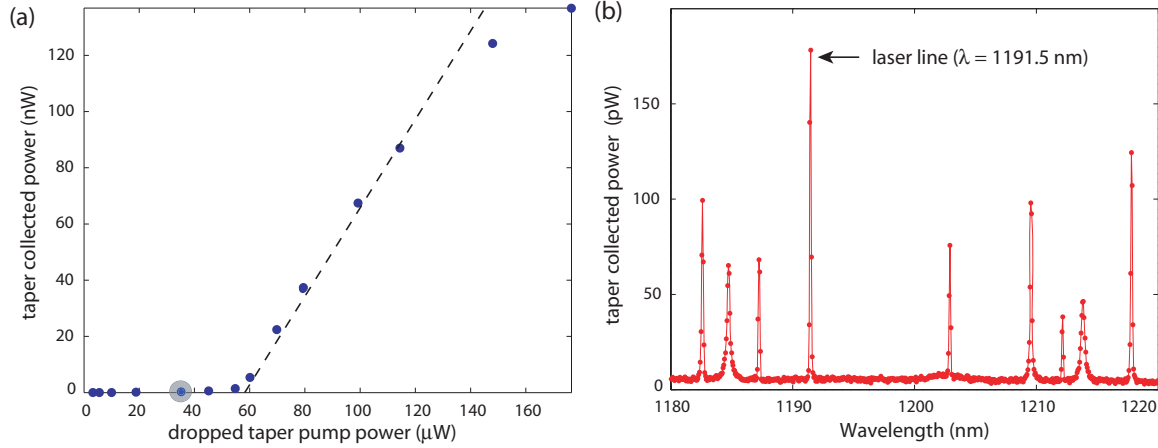


Figure 6.6: (a) L-L curve for a QD-microdisk device where the fiber taper is used for both pumping (at $\lambda = 967.6$ nm) and collection. The absorbed power was estimated to be 66% of the input power in the fiber taper. (b) Sub-threshold spectrum for this device taken at an estimated absorbed power of 37 μ W (highlighted point in (a)).

fiber taper to map out the resonance line due to the WGM at the pump wavelength. Here, the strong absorption of the microdisk in the 980 nm band makes it difficult to separate resonantly coupled power from scattering losses at the taper-microdisk junction. In order to more carefully study the efficiency of this fiber-pumping and fiber-collecting configuration, experiments in which an excited state of the quantum dots is resonantly pumped through the fiber taper are currently underway.

6.5 Discussion and future applications

As mentioned in the introduction, efficient optical access to wavelength-scale microcavities is of great importance to quantum optics and information processing applications currently being investigated within cavity QED systems. In almost any application involving the coherent transfer or manipulation of quantum information, loss is a significant detriment. As described in ref. [68], current implementations of linear optics quantum computing require a near-unity collection efficiency of emitted photons from a single photon source. The same is true for applications involving quantum repeaters in a quantum network [141]. A solution that is often proposed is to embed the single photon emitter within a microcavity with a high spontaneous emission coupling factor β , so that the majority of emitted photons are coupled into the microcavity mode. However, it is important to note that even for a $\beta = 1$ microcavity, it is still necessary to have a method to effectively collect all of the photons that are radiated by that one cavity mode [163]. Also, from a very practical perspec-

tive, efficient collection of emitted light from a microcavity is of premium importance for optical telecommunication wavelengths $> 1\mu m$, where the dark count rates from single photon counters are often 2-3 orders of magnitude larger than the Si single photon counters used at shorter wavelengths [164].

An efficient coupling channel can also enable a number of different types of experiments. Having access to this coupling channel makes the cavity transmission (and reflection) an experimentally accessible parameter whose behavior can be monitored to detect signatures of specific types of system behavior. In recent experimental measurements of coupling between a single quantum dot and a resonant mode of a semiconductor microcavity [71, 158, 70, 16, 109], spontaneous emission from the coupled system is the only parameter measured. Alternatively, using fiber tapers, vacuum Rabi splitting can be detected by simply measuring the transmission through the cavity as a function of the input wavelength to the cavity; such an experiment is directly analogous to the experiments done with cooled alkali atoms coupled to a Fabry-Perot cavity [77, 78]. Non-linear effects, such as optical bistability and photon blockade, and coherent control of the quantum system are also more easily observed through the optical transmission or reflection channel of a microcavity. Perhaps most importantly, by knowing the precise level of coupling between the fiber taper and the microcavity, the number of photons injected into the cavity can be precisely calibrated. This is obviously of paramount importance in experiments that involve few or single cavity photons. Finally, we note that although many of the advantages we have described are also applicable to in-plane waveguides that are microfabricated next to the cavities, the fiber taper provides a level of flexibility that, for example, allows for rapid device characterization, as described in detail in ref. [54].

Chapter 7

Cavity Q , Mode Volume, and Lasing Threshold in Small Diameter Microdisks with Embedded Quantum Dots

In this chapter, we continue our study of taper-coupled microdisk-QD structures by considering device performance as the disks are scaled down in size. In section 7.1, we use finite element simulations to examine the behavior of Q and V_{eff} as a function of disk diameter. We relate these parameters to those used in cQED, and from this, determine that disks of 1.5-2 μm in diameter are optimal for use in future experiments with InAs QDs. In sections 7.2 and 7.3, we present experimental measurements of fabricated devices. Through passive characterization (section 7.2), cavity Q s as high as 1.2×10^5 are demonstrated for devices with a predicted $V_{\text{eff}} \sim 2.2(\lambda/n)^3$. In addition, photoluminescence measurements (section 7.3) show that the devices operate as lasers with room temperature (RT), continuous-wave thresholds of $\sim 1 \mu\text{W}$ of absorbed pump power. Finally, the optical fiber taper is used to increase the efficiency of out-coupling by nearly two orders of magnitude, so that an overall fiber-coupled laser differential efficiency of $\xi \sim 16\%$ is achieved. We conclude by presenting some estimates of the number of QDs contributing to lasing and the spontaneous emission coupling factor (β) of the devices. The majority of this chapter is based on ref. [76].

7.1 Simulations

As described in chapter 5, finite-element eigenfrequency simulations [136, 128] using the Comsol FEMLAB software are used to study the radiation-limited quality factor (Q_{rad}) and mode volume (V_{eff}) of the microdisk cavities. Here, we consider how these parameters scale as a function of the disk size.

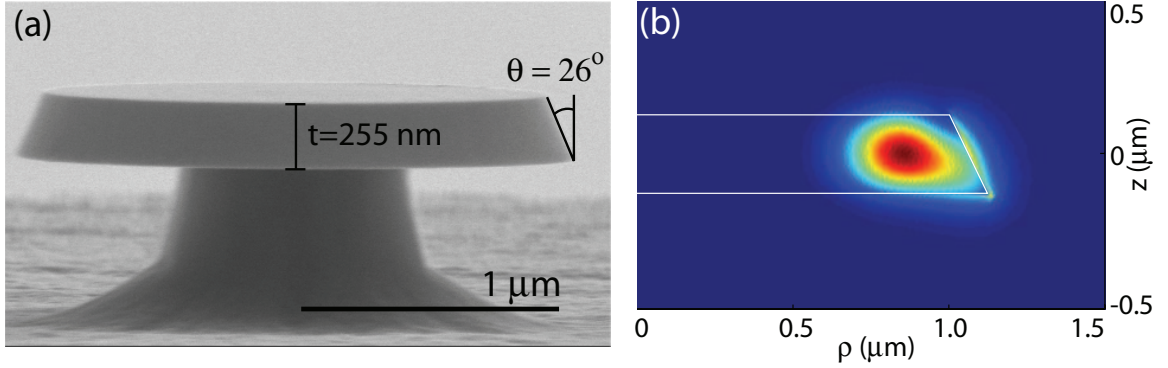


Figure 7.1: (a) Scanning electron microscope (SEM) image of a fabricated microdisk device. The disk thickness $t=255$ nm and sidewall angle $\theta = 26^\circ$ from vertical are taken as fixed in the finite-element simulations presented in the work. The measured average diameter for this device (i.e., the diameter at the center of the slab) is ~ 2.12 μm . (b) Finite-element-calculated $|\mathbf{E}|^2$ distribution for the $\text{TE}_{p=1,m=11}$ WGM of a microdisk with a diameter of ~ 2.12 μm at the center of the slab. For this mode, $\lambda \sim 1265.41$ nm, $Q_{\text{rad}} \sim 10^7$, and $V_{\text{eff}} \sim 2.8(\lambda/n)^3$.

Figure 7.1(a) shows a scanning electron microscope (SEM) image of a fabricated microdisk. The devices are formed using the same fabrication techniques discussed in chapter 5, where the emphasis of sidewall smoothness over verticality during fabrication leads to an etched sidewall angle that is approximately 26° from vertical. These parameters are included in the simulations as shown in fig. 7.1(b). Here, we will focus on resonant modes in the 1200 nm wavelength band, corresponding to the low temperature ($T=4$ K) ground state exciton transition of the QDs, relevant for future cavity QED experiments. We confine our attention to the more localized transverse electric (TE) polarized modes of the microdisk, and only consider the first order radial modes. In what follows we use the notation $\text{TE}_{p,m}$ to label whispering gallery modes (WGMs) with electric field polarization dominantly in the plane of the microdisk, radial order p , and azimuthal mode number m . The refractive index of the microdisk waveguide is taken as $n = 3.36$ in the simulations, corresponding to the average of the refractive indices of the GaAs and AlGaAs layers at $\lambda = 1200$ nm. In addition, the modes that we study are *standing wave* modes that are superpositions of the standard clockwise (CW) and counterclockwise (CCW) *traveling wave* modes typically studied in microdisks. As previously mentioned, the effective mode volume for a standing wave mode, as defined in Equation 5.9, is roughly half that of a traveling wave mode.

Figures 7.1(b) and 7.2 show the results of the finite element simulations. We see that V_{eff} for these standing wave modes can be as small as $2(\lambda/n)^3$ while maintaining $Q_{\text{rad}} > 10^5$. Indeed, for

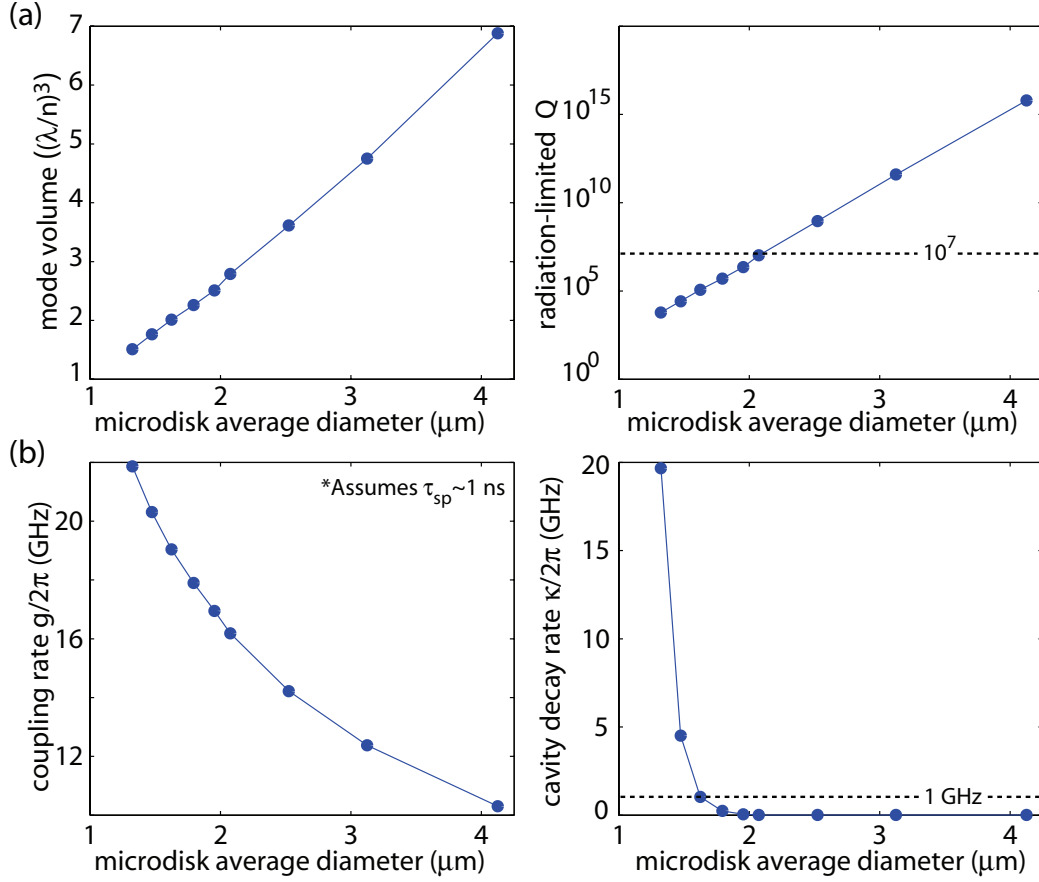


Figure 7.2: Finite-element method simulation results: (a) Modal volume V_{eff} (left) and radiation-limited cavity quality factor Q_{rad} (right) as a function of microdisk diameter (taken at the center of the slab), calculated for standing wave modes of disks of the shape shown in fig. 7.1. The modes studied are $\text{TE}_{p=1,m}$ WGMs with resonance wavelength within the 1200 nm band. (b) Coherent coupling rate $g/2\pi$ (left) and cavity decay rate $\kappa/2\pi$ (right) as a function of microdisk diameter. A QD spontaneous emission lifetime $\tau_{\text{sp}} = 1$ ns is assumed in the calculation of g .

microdisk average diameters $D > 2 \mu\text{m}$,¹ radiation losses are not expected to be the dominant loss mechanism as Q_{rad} quickly exceeds 10^7 , and other sources of field decay such as material absorption or surface scattering are likely to dominate. To translate these results into the standard parameters studied in cavity QED, we calculate the cavity decay rate $\kappa/2\pi = \omega/(4\pi Q)$ (assuming $Q = Q_{\text{rad}}$) and the coherent coupling rate g between the cavity mode and a single QD exciton. In this calculation, a spontaneous emission lifetime $\tau_{\text{sp}} = 1$ ns is assumed for the QD exciton, and $g = \mathbf{d} \cdot \mathbf{E}/\hbar$ is the vacuum coherent coupling rate (see appendix H) between cavity mode and QD exciton, given by [9, 110]:

¹The average diameter is taken at the center of the slab, or equivalently, is the average of the top and bottom diameters.

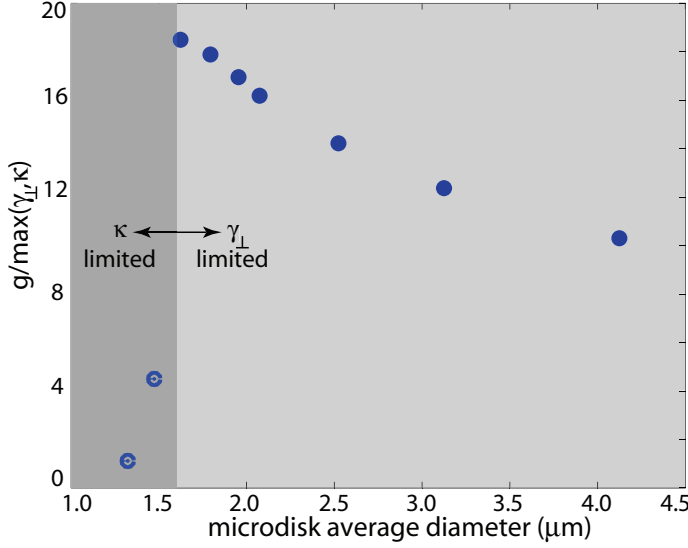


Figure 7.3: Ratio of the calculated coupling rate g to the maximum decay rate in the system, $\max(\gamma_{\perp}, \kappa)$, as a function of the microdisk diameter at the center of the slab. A fixed QD decay rate $\gamma_{\perp}/2\pi=1$ GHz is assumed, and the cavity decay rate κ is taken to be solely due to radiation loss.

$$g = \frac{1}{2\tau_{\text{sp}}} \sqrt{\frac{3c\lambda_0^2\tau_{\text{sp}}}{2\pi n^3 V_{\text{eff}}}}, \quad (7.1)$$

where c is the speed of light and n is the refractive index at the location of the QD. This formula assumes that the QD is optimally positioned within the cavity field, so that the calculated g is the maximum possible coupling rate. The resulting values for g and κ are displayed in fig. 7.2(b), and show that $g/2\pi$ can exceed $\kappa/2\pi$ by over an order of magnitude for a range of disk diameters. In addition, for all but the smallest-sized microdisks, $\kappa/2\pi < 1$ GHz. A decay rate of 1 GHz is chosen as a benchmark value as it corresponds to a linewidth of a few μeV at these wavelengths, on par with the narrowest self-assembled InAs QD exciton linewidths that have been measured at cryogenic temperatures [142]. Indeed, because dissipation in a strongly coupled QD-photon system can either be due to cavity decay or quantum dot dephasing, in fig. 7.3 we examine the ratio of g to the maximum decay rate in the system assuming a fixed QD dephasing rate $\gamma_{\perp}/2\pi=1$ GHz.² This ratio is roughly representative of the number of coherent exchanges of energy (Rabi oscillations) that can take place between QD and photon. We see that it peaks at a value of about 18 for a disk diameter $D \sim 1.5 \mu\text{m}$. For diameters smaller than this, loss is dominated by cavity decay due to radiation (so that $g/\max(\gamma_{\perp}, \kappa) = g/\kappa$), while for larger diameters, the dominant loss mechanism is due to dephasing of the QD ($g/\max(\gamma_{\perp}, \kappa) = g/\gamma_{\perp}$).

²Note that γ_{\perp} is in general greater than half the total radiative decay rate ($\gamma_{\parallel}/2 = 1/2\tau_{\text{sp}}$) for QD excitons, due to near-elastic scattering or dephasing events with, for example, acoustic phonons of the lattice.

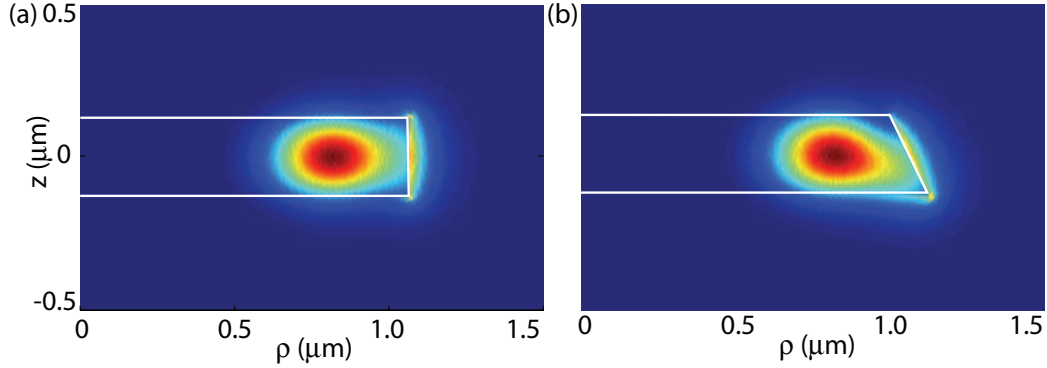


Figure 7.4: Finite-element-calculated $|E|^2$ distribution for the $TE_{p=1,m=11}$ WGM in (a) microdisk with a vertical sidewall and (b) microdisk with a slanted sidewall equivalent to what has been seen in experimentally fabricated devices.

For other types of atomic-like media besides the self-assembled InAs QDs considered here one need not assume a limit of $\gamma_{\perp}/2\pi = 1$ GHz, and we note that due to the exponential dependence of Q_{rad} and approximately linear dependence of V_{eff} on microdisk diameter, $Q_{\text{rad}}/V_{\text{eff}}$ rapidly rises above 10^7 for microdisks of diameter $D = 2.5 \mu\text{m}$. These values of Q_{rad} and V_{eff} are comparable to those found in recent high- Q photonic crystal microcavity designs [21, 26, 28, 30, 27]. In fact a similar scaling for high- Q planar photonic crystal microcavities, in which one may trade off a linear increase in V_{eff} for an exponential increase in Q , has recently been described by Englund et al., in ref. [29]. For our purposes here, however, we take the ratio $g/\max(\gamma_{\perp}, \kappa)$ with $\gamma_{\perp}/2\pi = 1$ GHz as our metric, and as such focus on 1.5-2 μm diameter microdisks.

Finally, we consider what effect the sidewall angle in our structures has on Q_{rad} . To do this, we compare Q_{rad} for the slanted structure with that for a disk with a vertical sidewall and diameter equal to the average diameter of the slanted disk. Figure 7.4 compares the electric field intensity for the $TE_{1,11}$ modes in each of these structures. We find the following: for the $TE_{1,11}$ modes, the vertical disk has $\lambda_0 \sim 1262$ nm, $Q_{\text{rad}} \sim 1.4 \times 10^7$, and $V_{\text{eff}} \sim 2.75(\lambda/n)^3$, while the slanted disk has $\lambda_0 \sim 1265$ nm, $Q_{\text{rad}} \sim 9.8 \times 10^6$, and $V_{\text{eff}} \sim 2.80(\lambda/n)^3$. For the $TE_{1,9}$ modes, the vertical disk has $\lambda_0 \sim 1435$ nm, $Q_{\text{rad}} \sim 4.8 \times 10^5$, and $V_{\text{eff}} \sim 2.14(\lambda/n)^3$, while the slanted disk has $\lambda_0 \sim 1438$ nm, $Q_{\text{rad}} \sim 3.7 \times 10^5$, and $V_{\text{eff}} \sim 2.20(\lambda/n)^3$. Although Q_{rad} is indeed smaller for the slanted disks, the reduction is likely modest in comparison to the losses that would be suffered if a more vertical dry etch was employed, due to the accompanying increase in surface roughness in such an etch (appendix C).

Table 7.1: Finite-element calculated $\text{TE}_{p=1,m}$ modes of a $D = 2 \mu\text{m}$ microdisk.

Mode label	λ_0	Q_{rad}	V_{eff}	application
$\text{TE}_{1,9}$	1438 nm	3.7×10^5	$2.2 (\lambda/n)^3$	passive RT testing
$\text{TE}_{1,10}$	1346 nm	1.9×10^6	$2.5 (\lambda/n)^3$	RT lasers
$\text{TE}_{1,11}$	1265 nm	9.8×10^6	$2.8 (\lambda/n)^3$	low-T cQED

7.2 Passive measurement of cavity Q

Similar to the devices studied in previous chapters, the samples used here were grown (by our collaborators at the University of New Mexico) through molecular beam epitaxy, and consist of a single layer of InAs QDs embedded in an $\text{In}_{0.15}\text{Ga}_{0.85}\text{As}$ quantum well, which is in turn sandwiched between layers of $\text{Al}_{0.30}\text{Ga}_{0.70}\text{As}$ and GaAs to form a 255 nm thick waveguide layer. This dot-in-a-well (DWELL) structure is grown on top of a 1.5 μm thick $\text{Al}_{0.70}\text{Ga}_{0.30}\text{As}$ buffer layer that is later undercut to form the disk pedestal. Growth parameters were adjusted [165] to put the material's RT ground state emission peak at $\lambda = 1317$ nm (fig. 7.5(a)). The basic reason for choosing a material with a red-shifted emission relative to what was used in previous investigations is to ensure that the low temperature (~ 10 K) emission of the QDs lies within the scan range of our 1200 nm tunable laser. This is essential for future cavity QED experiments employing near-resonant pumping of the QDs. Fabrication of the microdisk cavities follows the same process as was described in chapter 5.

We begin our measurements by using the fiber taper to passively probe the Q of the microdisks. Based on the simulations presented in section 7.1, we have focused on 2 μm diameter microdisks. Due to the small diameter of these microdisks, the finite-element-calculated free-spectral range of resonant modes is relatively large, with resonances occurring at 1265, 1346, and 1438 nm for the $\text{TE}_{p=1}$ WGMs with azimuthal mode numbers $m = 11, 10$, and 9, respectively. The simulations presented in section 7.1 were all done for the $\text{TE}_{1,11}$ mode in the $\lambda = 1200$ nm band due to the applicability of that wavelength region for future low temperature cavity QED experiments. However, for the current room-temperature measurements, the absorption due to the QD layer at those wavelengths is significant, so we probe the devices within the $\lambda = 1400$ nm band (~ 100 nm red detuned from the peak ground state manifold QD emission). At these longer wavelengths the radiation-limited Q_{rad} for a given disk diameter will be smaller than its value in the shorter $\lambda = 1200$ nm band. Table 7.1 summarizes the properties of the $\text{TE}_{p=1}$ WGMs within the 1200-1400 wavelength

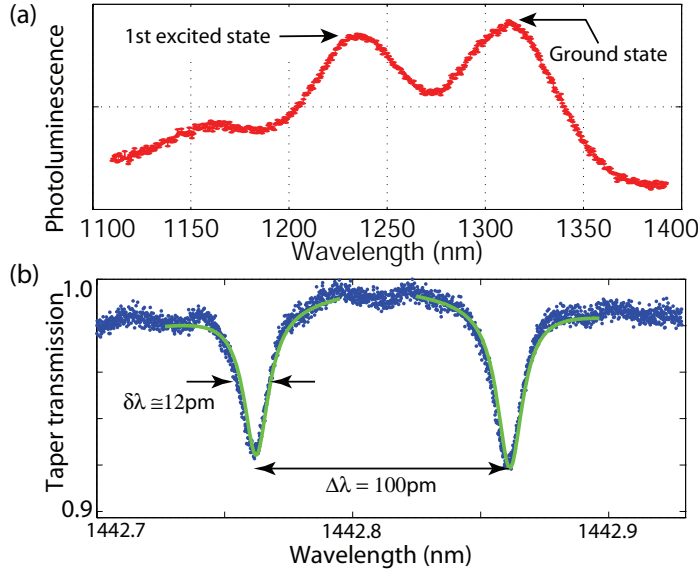


Figure 7.5: (a) Photoluminescence from an unprocessed region of the 1DWELL material whose growth has been tailored for $1.3\text{ }\mu\text{m}$ room-temperature emission. (b) Normalized transmission spectrum when a fiber taper is positioned a few hundred nm away from the edge of a $\sim 2\text{ }\mu\text{m}$ diameter microdisk fabricated from this material.

band for a $D = 2\text{ }\mu\text{m}$ microdisk with shape as shown in fig. 7.1.

Figure 7.5(b) shows a wavelength scan of the transmitted signal when a fiber taper is positioned a few hundred nanometers away from the disk edge. The doublet resonance appearing at $\lambda \sim 1440\text{ nm}$ in the spectrum is once again the signature of the standing wave modes described earlier. The measured linewidths correspond to Q factors of 1.2×10^5 , and in general, Q s of $0.9\text{--}1.3 \times 10^5$ have been measured for these $2\text{ }\mu\text{m}$ diameter microdisks. The Q s of these modes are approaching the radiation-limited value of 3.7×10^5 , and are some of the highest measured values for near-IR wavelength-scale microcavities in AlGaAs [71, 13, 69, 84]. The corresponding cavity decay rates are $\kappa/2\pi \sim 0.8\text{--}1.3\text{ GHz}$, over an order of magnitude smaller than the predicted coupling rate g for an optimally placed QD. In addition, these Q s, if replicated within the QD emission band at $\lambda = 1300\text{ nm}$ are high enough to ensure that room-temperature lasing should be achievable from the single layer of QDs in these devices [165]. From calculations of the intrinsic radiation loss, the shorter 1300 nm wavelength modes should in fact have a significantly increased Q_{rad} of 2×10^6 , although surface scattering may also slightly increase due to its approximate cubic dependence on wavelength [65].

7.3 Measurements of lasing behavior

The emission properties of the QD-containing microdisks are tested at room temperature by continuous-wave optical pumping through a high-NA objective lens at normal incidence and, initially, collecting

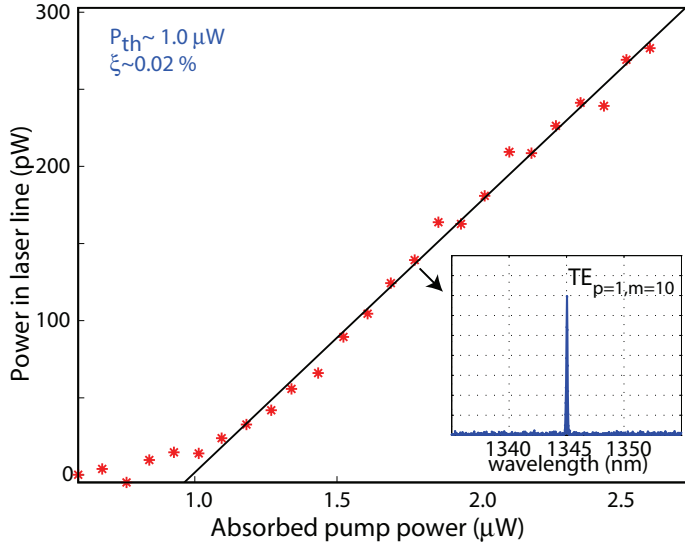


Figure 7.6: Light-in-light-out (L-L) curve for a device operated with free-space collection. The laser threshold absorbed pump power P_{th} is $\sim 1.0 \mu\text{W}$, and its differential efficiency $\xi \sim 0.02\%$. (inset) Spectrum from the device above threshold, showing emission at $\lambda \sim 1345 \text{ nm}$ corresponding to the $\text{TE}_{p=1,m=10}$ WGM.

the normal incidence emitted light through the same lens. A light-in versus light-out (L-L) curve for one of the $D \sim 2 \mu\text{m}$ microdisks with a resonant emission peak at $\lambda \sim 1345 \text{ nm}$ is shown in fig. 7.6, and displays a lasing threshold kink at approximately $1.0 \mu\text{W}$ of absorbed pump power. The laser mode wavelength corresponds well with the $\text{TE}_{p=1,m=10}$ mode from finite-element simulations (see table 7.1). The absorbed pump power is estimated to be 11% of the incident pump power on the microdisk, and was determined assuming an absorption coefficient of 10^4 cm^{-1} for the GaAs layers and quantum well layer. This threshold level is approximately two orders of magnitude smaller than those in recent demonstrations of RT, continuous-wave microdisk QD lasers [166, 167], although the active regions in those devices contain five stacked layers of QDs while the devices presented here contain only a single layer of QDs.

The low lasing threshold of the device presented in fig. 7.6 was consistently measured for the set of devices on this sample (approximately 20 devices). In fig. 7.7(a) we show another L-L curve, this time for a device that has a $\text{TE}_{p=1,m=10}$ WGM emission peak at $\lambda = 1330 \text{ nm}$ and has a threshold absorbed pump power of $1.1 \mu\text{W}$. As described in the previous chapter and in ref. [75], the same fiber taper used to measure the cavity Q can efficiently out-couple light from the lasing mode. We do this by maintaining the free-space pumping used above while contacting a fiber taper to the side of the microdisk as shown in the inset of fig. 7.7(b). From the corresponding L-L curve (fig. 7.7(b)) we see that the laser threshold under fiber taper loading has increased from $1.1 \mu\text{W}$ to $1.6 \mu\text{W}$, but in addition the differential laser efficiency ξ is now 4% compared to 0.1% when employing free-space collection (fig. 7.7(a)-(b)). Furthermore, because the microdisk modes are standing waves

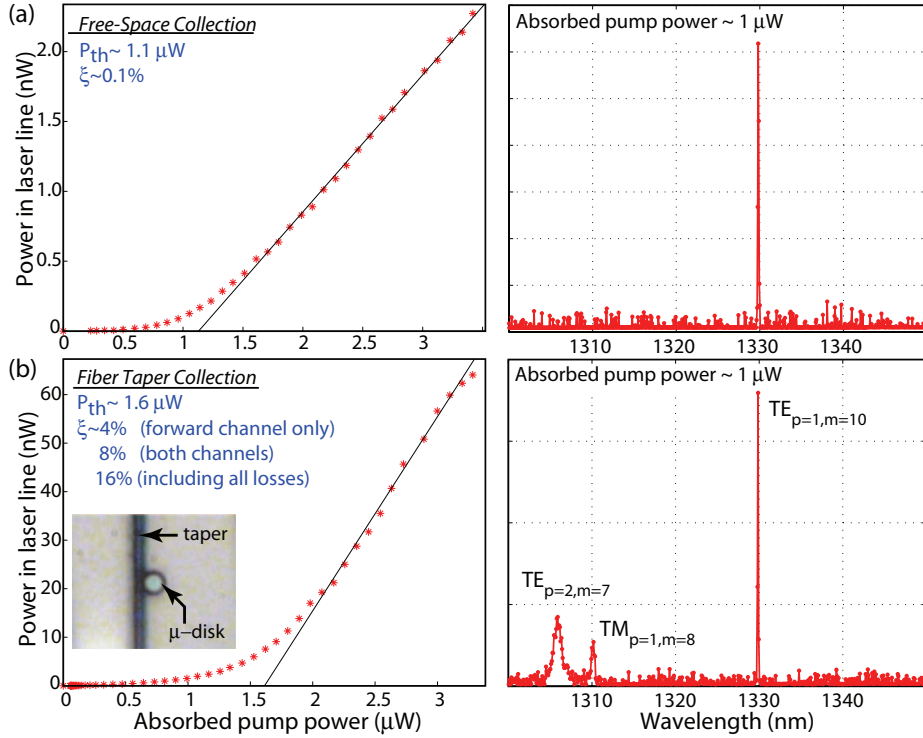


Figure 7.7: (a) (left) L-L curve for another microdisk device operated with free-space collection, with $P_{th} \sim 1.1 \mu\text{W}$ and $\xi \sim 0.1\%$. (right) Spectrum from the device near laser threshold, showing emission at $\lambda \sim 1330 \text{ nm}$. (b) (left) L-L curve for the same device using an optical fiber taper to collect the emission. P_{th} has increased to $1.6 \mu\text{W}$ while ξ increased to 4% for collection in the forward fiber taper channel. (inset) Optical microscope image of the taper output coupler aligned to the microdisk. (right) Spectrum of the fiber taper collected light below threshold.

they radiate into both the forwards and backwards channels of the fiber. With collection from both the forward and backward channels the differential efficiency was measured to be twice that of the single forward channel. Collecting from both channels and adjusting for all fiber losses in the system (roughly 50% due to fiber splices and taper loss), the total differential laser efficiency with fiber taper collection is 16%. Due to the difference in photon energy of the pump and microdisk lasers, this laser differential efficiency corresponds to a conversion efficiency of 28% from pump photons to fiber-collected microdisk laser photons. 28% is thus a *lower* bound on the fiber-taper collection efficiency and/or quantum efficiency of the QD active region.

In addition to the improved laser differential efficiency of the $TE_{p=1,m=10}$ laser mode when using the fiber taper to out-couple the laser light, we also see in the below-threshold spectrum of fig. 7.7(b) that two additional resonances appear at $\lambda = 1310 \text{ nm}$ and $\lambda = 1306 \text{ nm}$. The long wavelength mode is identified as $TM_{p=1,m=8}$ and the short wavelength mode as $TE_{p=2,m=7}$ from finite-element

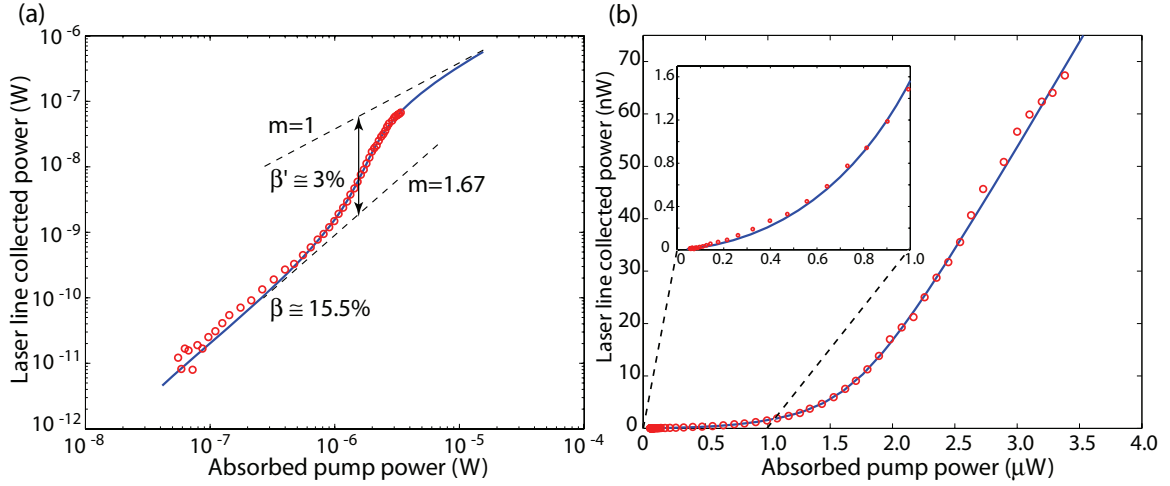


Figure 7.8: L-L curve experimental data (red circles) and rate-equation model fit (blue line) to data for the fiber taper coupled laser of fig. 7.7(b) : (a) log-log plot and (b) linear plot (inset shows deep subthreshold data and fit). $\beta' \sim 3\%$ is the spontaneous emission factor estimated directly from the slope change in the data, and thus includes a large non-radiative component, while $\beta \sim 15.5\%$ is the value used in the rate-equation model fit.

simulations. These modes are not discernible in the free-space collected spectrum due to their low radiation-limited Q factors (800 and 5000 for the $TE_{2,7}$ and $TM_{1,8}$, respectively), but show up in the taper coupled spectrum due to their alignment with the QD ground state exciton emission peak and the heightened sensitivity of the taper coupling method. The single-mode lasing and limited number of WGM resonances (6 when including the degeneracy of the WGMs) in the emission spectrum in these $D = 2 \mu\text{m}$ microdisks is a result of the large 80-100 nm free-spectral-range of modes in the 1300-1500 wavelength band. As a result, one would expect the spontaneous emission factor (β) of these microdisk lasers to be relatively high.

A log-log plot of the fiber taper coupled laser emission of fig. 7.7(b) is shown in fig. 7.8(a) along with a rate-equation model fit to the data. Of particular note is the well defined subthreshold linear slope of the log-log plot. In this case the sensitivity of the fiber taper collection allows for the subthreshold slope to be accurately estimated at $m=1.67$, corresponding to a near quadratic dependence of spontaneous emission intensity on pump power (fig. 7.8(b), inset) and indicating that there is likely significant non-radiative recombination. Assuming that radiative recombination occurs as a biparticle process,³ the larger than unity power law dependence of subthreshold emission on pump power is indicative of single-particle non-radiative recombination processes such as surface recom-

³As has been discussed recently in ref. [168] this may not be an accurate model for QD state filling, but for our simple analysis here it will suffice.

bination [121]. Given the close proximity of the WGM laser mode to the periphery of the microdisk and the above-band pumping, the presence of significant surface recombination is not surprising. Unfortunately, due to this large non-radiative component one can only provide a *weak lower bound* β' for the β -factor directly from the L-L curve. From fig. 7.8 we estimate $\beta \geq \beta' \sim 3\%$.

A rate-equation model (see appendix F) incorporating bi-particle spontaneous emission proportional to N^2 and surface recombination with a $N^{1.22}$ carrier dependence (the ratio of the power law dependence is set equal to the measured subthreshold slope of $m=1.67$) is fit to the data and shown as a solid curve in fig. 7.8. In this model the measured fiber taper collection efficiency was used, along with the previously measured and estimated QD density, maximum gain, and quantum efficiency from stripe lasers [165]. An estimate for the actual radiative β -factor of 15.5% was used, corresponding closely with the partitioning of spontaneous emission amongst the 6 localized and high- Q WGM resonances within the QD ground state manifold emission band.⁴ The reference spontaneous emission lifetime of the ground state QD exciton in bulk was taken as $\tau_{sp} = 1$ ns. The data was fit by varying *only* the effective surface recombination velocity. As seen in fig. 7.8, the fit is quite good over the entire subthreshold and threshold regions of the laser data. The inferred surface recombination velocity from the fit is $v_s \sim 75$ cm/s, extremely slow for the AlGaAs material system [152] but perhaps indicative of the fast capture rate of carriers and subsequent localization into QDs [170, 171]. Due to the large perimeter-to-area ratio in these small $D = 2$ μm microdisks, even with this low velocity the model predicts that laser threshold pump power is dominated by surface recombination with an effective lifetime $\tau_s \sim 300$ ps. Such a surface recombination lifetime has also been estimated by Ide and Baba et al., in their recent work on QD-microdisk lasers [151].

The number of QDs contributing to lasing in these small microdisks can also be estimated. From the finite-element simulations the area of the standing wave WGM lasing mode in the plane of the QD layer is approximately $1 \mu\text{m}^2$, and the predicted QD density for this sample is $300 \mu\text{m}^{-2}$, so that ~ 300 QDs are spatially aligned with the cavity mode. Assuming a RT homogeneous linewidth on the order of a few meV [142], compared to a measured inhomogeneous Gaussian broadening of 35 meV, and considering the location of the lasing mode in the tail of the Gaussian distribution, we estimate $< 10\%$ of these dots are spectrally aligned with the cavity mode. By this estimate, on the order of 25 QDs contribute to lasing.

⁴This estimate was based upon considering Purcell enhancement at RT for QDs spatially and spectrally aligned with the WGMs ($F_P \sim 6$), and suppression of spontaneous emission for QDs spatially and spectrally misaligned from the WGMs ($F_P \sim 0.4$). This estimate is consistent with FDTD calculations of similar sized microdisks [169].

Chapter 8

Prospects for Strong Coupling Between a Single Quantum Dot and Standing Wave Whispering Gallery Modes of a Semiconductor Microdisk Cavity

8.1 Introduction

In the previous three chapters, we have demonstrated AlGaAs microdisk cavities that, in principle, can be used for strong coupling experiments with semiconductor quantum dots. By this, we mean that the cavities have sufficiently high Q and small V_{eff} values that the maximum coupling rate between a single photon and a single QD in the cavity is larger than the decay rate of the cavity mode and the QD exciton. Of course, in practice, experimentally accessing the strong coupling regime will require addressing a number of technical issues, as will be reviewed in the subsequent chapter (chapter 9). In this chapter, we will assume that these experimental challenges can be overcome, and will focus on what we should expect to see when the experiments are conducted.

Recent demonstrations of vacuum Rabi splitting in systems consisting of a semiconductor microcavity and a single quantum dot (QD) [70, 71, 72] represent an important milestone in investigations of cavity QED in solid-state materials. The experimental configuration utilized in these experiments is schematically shown in fig. 8.1(a); the microcavity-QD system is incoherently pumped with an excitation beam at an energy above the bandgap of both the QD and the surrounding cavity material (usually GaAs or some form of its alloy AlGaAs). This pump light is absorbed and generates carriers in the GaAs system that can eventually (through phonon relaxation) fill the QD; under weak enough pumping conditions, a single electron-hole pair can fill the QD, forming a bound

exciton state. The electron-hole pair eventually recombines, leading to spontaneous emission that is modified by the presence of the microcavity. When the cavity is of small enough volume, the coupling (g) between the QD exciton and the cavity can be large, and if the cavity decay rate κ and QD decay rate γ_{\perp} are smaller than g , the system is said to be strongly coupled [9], in that the QD exciton and cavity mode are no longer truly separate entities but are instead bound together. In the experiments described in refs. [70, 71, 72], the evidence of this strong coupling has been presented in the form of spontaneous emission measurements from the QD-microcavity system, which display a double-peaked structure, rather than the single peak associated with either the cavity mode or QD exciton alone. This vacuum Rabi splitting [172, 173] is one signature of the strong coupling regime in cQED.

Applications of strongly coupled QD-microcavity systems to areas such as nonlinear optics [174, 175, 176, 177, 178] will also require an ability to effectively couple light into and out of the microcavity-QD device. That is, rather than measuring the spontaneous emission of the system alone, it is also important to have access to the cavity's response (transmission or reflection). This is true if, for example, one wants to examine the effect of a coupled QD-cavity system on the propagation of a subsequent beam through the cavity [174, 79], or if one wants to use the phase of the emerging transmitted signal within some type of logic gate [179]. Indeed, in 'traditional' cavity QED experiments, it is the cavity's transmitted or reflected signal that is typically observed [77, 17, 18, 78].

As we have described in previous chapters within this thesis, following demonstrations of coupling to *silica*-based cavities such as microspheres [32, 20] and microtoroids [56], we have shown that optical fiber tapers [122, 32] are an effective means to couple light into and out of wavelength-scale, semiconductor microcavities such as photonic crystals and microdisks. In addition, the microdisk cavities we have demonstrated are very promising for semiconductor cQED experiments, with cavity Q s in excess of 10^5 for devices with $V_{\text{eff}} \sim 2-6(\lambda/n)^3$. These Q values are significantly larger than those utilized in refs. [70, 71, 72], and as a result, the devices that we consider are poised to operate well within the strong coupling regime, where coherent interactions between the QD and photon occur. It is envisioned that initial experiments in this fiber-coupled microcavity-QD system (fig. 8.1(b)) will examine vacuum-Rabi splitting through measurements of the transmission spectrum past the cavity; such measurements will be directly analogous to recent measurements of vacuum Rabi splitting from one-and-the-same atom in a Fabry-Perot cavity [78].

The goal of this chapter is to provide a theoretical basis, accompanied by numerical simulations,

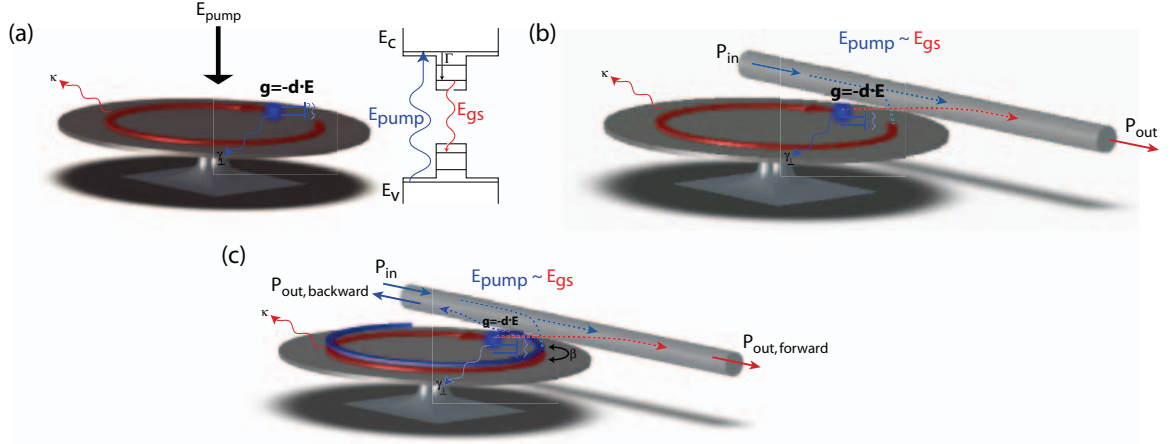


Figure 8.1: Illustrations of the various experimental configurations utilized in studying coupling between a semiconductor microcavity (microdisk in this case) and a single QD. g =QD-microcavity coupling rate, κ =cavity decay rate, and γ_{\perp} =QD decay rate. (a) Incoherent pumping ($E_{\text{pump}} > E_{\text{gs}}$) above the bandgap of the microcavity material. Here, strong coupling between a single QD and the microcavity mode is observed through measurements of vacuum Rabi splitting in the spontaneous emission from the QD. (b) Near-resonant driving ($E_{\text{pump}} \sim E_{\text{gs}}$) using a fiber taper to couple light into and out of the microdisk. Evidence of coupling between the QD and microcavity will be observed through measurements of the transmitted signal through the fiber taper as a function of input wavelength. (c) Near-resonant driving of a realistic microdisk-QD system, including both clockwise and counterclockwise propagating modes of the disk, and potential coupling, at a rate β , between the two modes due to surface scattering.

for the experiments to be performed with single QDs in fiber-coupled microdisk cavities. Of particular concern is the proper treatment of the whispering gallery modes (WGMs) in the cavities. More specifically, for a given polarization (TE or TM), the WGMs have a degeneracy of 2, as modes with azimuthal number $\pm m$ have the same frequency, but circulate around the disk in opposite directions. The WGMs are typically excited through an external waveguide (such as a fiber taper), and in a perfect WGM resonator, the forward propagating mode through the waveguide excites only the clockwise propagating mode in the resonator (see fig. 8.1(b)). As we have described several times within this thesis, imperfections in the resonator will change this, as they cause backscattering that can couple the clockwise (*cw*) and counterclockwise (*ccw*) propagating modes (fig. 8.1(c)). If the loss rates in the system (due to material absorption, other scattering and radiation loss, etc.) are low enough, the backscattering can lead to coherent coupling of the *cw* and *ccw* modes, producing a pair of standing wave modes. Our interest is to then study the interaction of a single quantum dot with the microdisk WGMs in the presence of this backscattering (which has been present in all of our

experiments to this point), and determine the spectral response of the system for varying degrees of quantum-dot-cavity coupling (g), backscattering (β), and modal loss (κ). We examine how the phase of the backscattering parameter affects the coupling between one or both cavity modes and the QD, and how the QD itself serves to couple the cavity modes together.

The organization of this chapter is as follows: in section 8.2, we review the simple classical coupled mode theory for modal coupling in microdisk cavities in absence of a QD. The starting point is the analysis from section 5.2, where we have derived the coupled mode equations for backscattering-induced coupling between the clockwise and counterclockwise propagating modes in a microdisk. In section 8.2, we further develop this theory by including input-output coupling from a waveguide (appendix E). Section 8.3 presents the quantum mechanical analysis of this system in the presence of a QD. We review the quantum master equation for this system and look at semiclassical approximations for specific choices of the backscattering parameter. As we have previously noted, standing wave WGMs have half the effective modal volume of traveling wave modes, and it is therefore expected that the peak electric field strengths they sustain are $\sqrt{2}$ times larger; this is explicitly confirmed in the derivation of the quantum master equation and associated Heisenberg equations of motion. In section 8.4, we present the results of numerical solutions of the quantum master equation for parameters that are accessible in current experiments. Finally, in section 8.5, we consider low power switching as one potential experiment beyond the observation of vacuum Rabi splitting in a fiber-coupled microdisk-QD system.

8.2 Modal coupling of two whispering gallery modes due to surface scattering

We start by reviewing the simple (classical) coupled mode theory for surface-roughness-induced coupling of the cw and ccw whispering gallery modes in an empty microcavity [146, 135, 147, 148] (without a quantum dot). Our analysis begins where we left off in section 5.2, with the coupled mode equations:

$$\frac{da_{cw}}{dt} = -i\Delta\omega a_{cw}(t) + i|\beta|e^{i\xi}a_{ccw}(t), \quad (8.1)$$

$$\frac{da_{ccw}}{dt} = -i\Delta\omega a_{ccw}(t) + i|\beta|e^{-i\xi}a_{cw}(t), \quad (8.2)$$

These equations represent the time evolution of the two mode amplitudes $\{a_{cw}, a_{ccw}\}$ of an isolated system, without loss or coupling to an external waveguide. For the experiments considered in our work, the waveguide coupler will be an optical fiber taper through which light is traveling in the forward propagating mode. Light will then be coupled into the clockwise WGM of the microdisk structure, and this can be included (appendix E) through the addition of the term ks to equation (8.1), where k is a coupling coefficient, and $|s|^2$ is the normalized input *power* (the mode amplitudes a_{cw}, a_{ccw} are normalized to *energy*). Loss is introduced to the coupled mode equations by use of the phenomenological *field* decay rate κ_T , taken to be the same for both the *cw* and *ccw* modes (though in general this does not have to be the case). This total field decay rate is broken into a contribution from intrinsic microdisk absorption and scattering loss (κ_i) and a contribution due to coupling back into the waveguide (κ_e), so that $\kappa_T = \kappa_i + \kappa_e$. Assuming lossless coupling and time reciprocity, it can be shown [125] that $|k|^2 = 2\kappa_e$. The coupled mode equations then read:

$$\frac{da_{cw}}{dt} = -(\kappa_T + i\Delta\omega)a_{cw}(t) + i|\beta|e^{i\xi}a_{ccw}(t) + is\sqrt{2\kappa_e} \quad (8.3)$$

$$\frac{da_{ccw}}{dt} = -(\kappa_T + i\Delta\omega)a_{ccw}(t) + i|\beta|e^{-i\xi}a_{cw}(t), \quad (8.4)$$

Here, the phase of the coupling coefficient was chosen to reflect the $\pi/2$ phase shift that occurs when light is coupled from the waveguide into the cavity. These two coupled equations can be rewritten as uncoupled equations in terms of the variables $a_{sw,1}$ and $a_{sw,2}$, which represent the standing wave mode amplitudes

$$\begin{aligned} a_{sw,1} &= \frac{1}{\sqrt{2}}(a_{cw} + e^{i\xi}a_{ccw}) \\ a_{sw,2} &= \frac{1}{\sqrt{2}}(a_{cw} - e^{i\xi}a_{ccw}). \end{aligned} \quad (8.5)$$

For an ideal microdisk, a_{cw} and a_{ccw} have an azimuthal spatial dependence of $e^{im\phi}$ (where m is the azimuthal mode number and is a nonzero integer), so that $a_{sw,1}$ and $a_{sw,2}$ will have an azimuthal spatial dependence that will be a mixture of $\cos(m\phi)$ and $\sin(m\phi)$, with the precise dependence being a function of the phase ξ of the backscattering parameter β .

The transmitted and reflected signals can be determined in either the basis of $\{a_{cw}, a_{ccw}\}$ or $\{a_{sw,1}, a_{sw,2}\}$; because our formulation of the problem has an external waveguide input s that is a

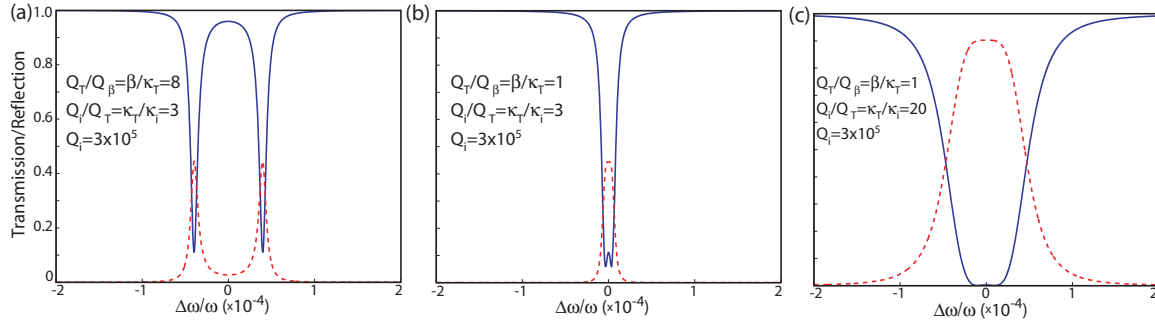


Figure 8.2: Normalized transmitted (solid line) and reflected (dashed line) signal for standing wave whispering gallery modes, determined through steady state solution of the coupled mode equations given in equation (8.3). (a) $\beta/\kappa_T = 8$, $\kappa_T/\kappa_i = 3$ (b) $\beta/\kappa_T = 1$, $\kappa_T/\kappa_i = 3$, and (c) $\beta/\kappa_T = 1$, $\kappa_T/\kappa_i = 20$. $Q_i = 3 \times 10^5$ in all cases.

source for a_{cw} , it is most natural to solve for these quantities in the traveling wave mode basis, and they are given by $|t|^2 = |-s - i\sqrt{2\kappa_e}a_{cw}|^2$ and $|r|^2 = |\sqrt{2\kappa_e}a_{ccw}|^2$ (appendix E). Steady state solutions for the normalized transmitted and reflected signals from the cavity for a number of different parameters are shown in fig. 8.2. For $\beta > \kappa_T$ (fig. 8.2(a)), we see the formation of a distinct pair of resonances, located at $\omega = \omega_0 \pm \beta$. These dips correspond to standing wave resonances that result from a backscattering rate (β) that exceeds all other losses in the system (κ_T), so that coherent coupling between the cw and ccw modes can take place. As we see in fig. 8.2(b)-(c), for $\beta \sim \kappa_T$, the resonances begin to overlap and are no longer distinguishable.

For cavity QED applications, one very important consequence of the distinction between traveling wave and standing wave modes is in the effective volume of the mode (V_{eff}), as the peak electric field strength (per photon) in the cavity scales as $1/\sqrt{V_{\text{eff}}}$. In particular, we recall the definition of V_{eff} as:

$$V_{\text{eff}} = \frac{\int \epsilon |\mathbf{E}(\mathbf{r})|^2}{\max[\epsilon |\mathbf{E}(\mathbf{r})|^2]}. \quad (8.6)$$

Standing wave WGMs have approximately half the volume of the traveling wave WGMs, so that the coupling rate g between a single quantum dot and a single photon in a standing wave cavity mode is expected to be $\sqrt{2}$ times that when the quantum dot is coupled to a traveling wave cavity mode. This of course assumes the single QD is positioned at an antinode of the standing wave mode; alternately, if it happens to be positioned at a node, the coupling rate g will be zero.

These arguments again rely upon having a physical system in which the coupling between *cw* and *ccw* modes is sufficiently strong enough compared to all other loss rates to allow for coherent modal coupling to form standing wave modes. They have also assumed that the QD does not introduce loss into the system. This is clearly not the case if the QD is strongly coupled to a cavity mode. In strong coupling, energy oscillates back and forth between the QD and the cavity, so that QD decay terms can also cause loss. In this case, we might expect that standing wave modes can be maintained provided that the modal coupling rate β exceeds not only κ_T , but also the QD spontaneous emission rate γ_{sp} and non-radiative dephasing rate γ_p . To verify our physical intuition and understand the system in better detail, we consider a quantum master equation approach [149] to take into account the QD-field interaction.

8.3 Quantum master equation model

We begin by considering the Hamiltonian for an empty microdisk cavity (resonance frequency ω_c) with field operators \hat{a}_{cw} and \hat{a}_{ccw} and mode coupling parameter β , written in a frame rotating at the driving frequency ω_l (see appendix G for details):

$$H_0 = \Delta\omega_{cl}\hat{a}_{cw}^\dagger\hat{a}_{cw} + \Delta\omega_{cl}\hat{a}_{ccw}^\dagger\hat{a}_{ccw} - \beta\hat{a}_{cw}^\dagger\hat{a}_{ccw} - \beta^*\hat{a}_{ccw}^\dagger\hat{a}_{cw} + i(E\hat{a}_{cw}^\dagger - E^*\hat{a}_{cw}), \quad (8.7)$$

where $\Delta\omega_{cl} = \omega_c - \omega_l$. Here, the clockwise (cw) propagating mode is driven by an intracavity field $E = -i\sqrt{2\kappa P_{in}}$, where $\kappa = \omega_c/2Q$ is the cavity field decay rate and P_{in} is the input power into the cavity. In this and all equations that follow, Planck's constant $\hbar = 1$. From this Hamiltonian, the classical coupled-mode equations without dissipation can easily be derived through an application of Ehrenfest's theorem and assuming that quantum mechanical expectation values correspond to classical variables (i.e., $\langle \hat{a}_{cw} \rangle = a_{cw}$, for example).

Modeling the QD as a two-level system, we add the term H_1 to the Hamiltonian (appendix G):

$$H_1 = \Delta\omega_{al}\hat{\sigma}_+\hat{\sigma}_- + ig(\hat{a}_{cw}^\dagger\hat{\sigma}_- - \hat{a}_{cw}\hat{\sigma}_+) + ig(\hat{a}_{ccw}^\dagger\hat{\sigma}_- - \hat{a}_{ccw}\hat{\sigma}_+) \quad (8.8)$$

where $\Delta\omega_{al} = \omega_a - \omega_l$ (ω_a is the frequency separation between the ground and first excited state of the QD). The equation of motion for the system's density matrix ρ can then be found from the

equation:

$$\frac{d\rho}{dt} = \frac{1}{i}[H_0 + H_1, \rho] + L\rho \quad (8.9)$$

where the term $L\rho = (L_1 + L_2 + L_3)\rho$ allows for the inclusion of decay through cavity loss (at a rate κ), quantum dot spontaneous emission (at a rate $\gamma_{||}$, which we previously called γ_{sp}), and phase-destroying collisional processes (at a rate γ_p), which are of particular importance for quantum dots, as unlike atoms, they are embedded in a semiconductor matrix that can serve as a phonon bath. These loss terms are given by (refs. [149, 180] and appendix G):

$$L_1\rho = \kappa(2\hat{a}_{cw}\rho\hat{a}_{cw}^\dagger - \hat{a}_{cw}^\dagger\hat{a}_{cw}\rho - \rho\hat{a}_{cw}^\dagger\hat{a}_{cw}) + \kappa(2\hat{a}_{ccw}\rho\hat{a}_{ccw}^\dagger - \hat{a}_{ccw}^\dagger\hat{a}_{ccw}\rho - \rho\hat{a}_{ccw}^\dagger\hat{a}_{ccw}) \quad (8.10)$$

$$L_2\rho = \frac{\gamma_{||}}{2}(2\hat{\sigma}_-\rho\hat{\sigma}_+ - \hat{\sigma}_+\hat{\sigma}_-\rho - \rho\hat{\sigma}_+\hat{\sigma}_-) \quad (8.11)$$

$$L_3\rho = \frac{\gamma_p}{2}(\hat{\sigma}_z\rho\hat{\sigma}_z - \rho) \quad (8.12)$$

From this master equation, we can numerically calculate the steady state density matrix ρ_{ss} and relevant operator expectation values such as $\langle \hat{a}_{cw}^\dagger \hat{a}_{cw} \rangle_{ss}$, which will then allow us to determine the transmission and reflection spectrum of the coupled QD-cavity system, using formulas that are analogous to those used in the classical model of section 8.2. These calculations are the subject of the following section. For now, however, we consider what intuition may be gained by further analytical study of the master equation. We take operator expectation values ($\langle \hat{A} \rangle = Tr(\hat{\rho}\hat{A})$ and $\langle \dot{\hat{A}} \rangle = Tr(\hat{\rho}\dot{\hat{A}})$) to arrive at:

$$\begin{aligned} \frac{d}{dt} \langle \hat{a}_{cw} \rangle &= -i\Delta\omega_{cl} \langle \hat{a}_{cw} \rangle + i\beta \langle \hat{a}_{ccw} \rangle + g \langle \hat{\sigma}_- \rangle - \kappa \langle \hat{a}_{cw} \rangle + E \\ \frac{d}{dt} \langle \hat{a}_{ccw} \rangle &= -i\Delta\omega_{cl} \langle \hat{a}_{ccw} \rangle + i\beta^* \langle \hat{a}_{cw} \rangle + g \langle \hat{\sigma}_- \rangle - \kappa \langle \hat{a}_{ccw} \rangle \\ \frac{d}{dt} \langle \hat{\sigma}_- \rangle &= -\left(i\Delta\omega_{al} + \gamma_{\perp}\right) \langle \hat{\sigma}_- \rangle + g(\langle \hat{\sigma}_z \hat{a}_{cw} \rangle + \langle \hat{\sigma}_z \hat{a}_{ccw} \rangle) \\ \frac{d}{dt} \langle \hat{\sigma}_z \rangle &= -2g(\langle \hat{\sigma}_- \hat{a}_{cw}^\dagger \rangle + \langle \hat{\sigma}_+ \hat{a}_{cw} \rangle) - 2g(\langle \hat{\sigma}_- \hat{a}_{ccw}^\dagger \rangle + \langle \hat{\sigma}_+ \hat{a}_{ccw} \rangle) \\ &\quad - \gamma_{||}(1 + \langle \hat{\sigma}_z \rangle) \end{aligned} \quad (8.13)$$

where we have noted that $[\hat{\sigma}_+, \hat{\sigma}_-] = \hat{\sigma}_z$, and have taken $\gamma_{\perp} = \gamma_{||}/2 + \gamma_p$.

In the semi-classical approximation, we assume that expectation values of products of operators equal the product of the expectation values ($\langle \hat{\sigma}_z \hat{a}_{cw} \rangle = \langle \hat{\sigma}_z \rangle \langle \hat{a}_{cw} \rangle$, for example). Writing $\beta = |\beta|e^{i\xi}$, these equations then reduce to

$$\begin{aligned}
\frac{d}{dt} \langle \hat{a}_{cw} \rangle &= -i\Delta\omega_{cl} \langle \hat{a}_{cw} \rangle + i|\beta|e^{i\xi} \langle \hat{a}_{ccw} \rangle + g \langle \hat{\sigma}_- \rangle - \kappa \langle \hat{a}_{cw} \rangle + E \\
\frac{d}{dt} \langle \hat{a}_{ccw} \rangle &= -i\Delta\omega_{cl} \langle \hat{a}_{ccw} \rangle + i|\beta|e^{-i\xi} \langle \hat{a}_{cw} \rangle + g \langle \hat{\sigma}_- \rangle - \kappa \langle \hat{a}_{ccw} \rangle \\
\frac{d}{dt} \langle \hat{\sigma}_- \rangle &= -\left(i\Delta\omega_{al} + \gamma_{\perp}\right) \langle \hat{\sigma}_- \rangle + g(\langle \hat{\sigma}_z \rangle \langle \hat{a}_{cw} \rangle + \langle \hat{\sigma}_z \rangle \langle \hat{a}_{ccw} \rangle) \\
\frac{d}{dt} \langle \hat{\sigma}_z \rangle &= -2g \langle \hat{\sigma}_- \rangle \left(\langle \hat{a}_{cw}^{\dagger} \rangle + \langle \hat{a}_{ccw}^{\dagger} \rangle \right) - 2g \langle \hat{\sigma}_+ \rangle \left(\langle \hat{a}_{cw} \rangle + \langle \hat{a}_{ccw} \rangle \right) \\
&\quad - \gamma_{\parallel} (1 + \langle \hat{\sigma}_z \rangle)
\end{aligned} \tag{8.14}$$

From equation 8.5 of section 8.2, we expect that the first two equations above can be uncoupled if written in terms of standing wave operators:

$$\begin{aligned}
\hat{a}_{sw,1} &= \frac{1}{\sqrt{2}} \left(\hat{a}_{cw} + e^{i\xi} \hat{a}_{ccw} \right) \\
\hat{a}_{sw,2} &= \frac{1}{\sqrt{2}} \left(\hat{a}_{cw} - e^{i\xi} \hat{a}_{ccw} \right).
\end{aligned} \tag{8.15}$$

Re-writing the operator evolution equations in terms of these quantities, we arrive at:

$$\begin{aligned}
\frac{d}{dt} \langle \hat{a}_{sw,1} \rangle &= -i\left(\Delta\omega_{cl} - |\beta|\right) \langle \hat{a}_{sw,1} \rangle + g \frac{1+e^{i\xi}}{\sqrt{2}} \langle \hat{\sigma}_- \rangle - \kappa \langle \hat{a}_{sw,1} \rangle + E \\
\frac{d}{dt} \langle \hat{a}_{sw,2} \rangle &= -i\left(\Delta\omega_{cl} + |\beta|\right) \langle \hat{a}_{sw,2} \rangle + g \frac{1-e^{i\xi}}{\sqrt{2}} \langle \hat{\sigma}_- \rangle - \kappa \langle \hat{a}_{sw,2} \rangle + E \\
\frac{d}{dt} \langle \hat{\sigma}_- \rangle &= -\left(i\Delta\omega_{al} + \gamma_{\perp}\right) \langle \hat{\sigma}_- \rangle + \frac{g \langle \hat{\sigma}_z \rangle}{\sqrt{2}} \left(\langle \hat{a}_{sw,1} \rangle (1+e^{-i\xi}) + \langle \hat{a}_{sw,2} \rangle (1-e^{-i\xi}) \right) \\
\frac{d}{dt} \langle \hat{\sigma}_z \rangle &= -\sqrt{2}g \langle \hat{\sigma}_- \rangle \left(\langle \hat{a}_{sw,1}^{\dagger} \rangle (1+e^{i\xi}) + \langle \hat{a}_{sw,2}^{\dagger} \rangle (1-e^{i\xi}) \right) \\
&\quad - \sqrt{2}g \langle \hat{\sigma}_+ \rangle \left(\langle \hat{a}_{sw,1} \rangle (1+e^{-i\xi}) + \langle \hat{a}_{sw,2} \rangle (1-e^{-i\xi}) \right) - \gamma_{\parallel} (1 + \langle \hat{\sigma}_z \rangle)
\end{aligned} \tag{8.16}$$

These equation indicate that, in this basis, we have a modified QD-photon coupling strength for each standing wave mode, which have shifted in frequency in comparison to the traveling wave modes and are now centered at $\omega_c \mp |\beta|$. For the first mode, corresponding to field operator $\hat{a}_{sw,1}$,

the effective coupling strength is $g_{sw,1} = g(1 + e^{i\xi})/\sqrt{2}$, while for the second mode, corresponding to field operator $\hat{a}_{sw,2}$, the effective coupling strength is $g_{sw,2} = g(1 - e^{i\xi})/\sqrt{2}$. These coupling strengths are thus dependent on the phase ξ of the backscattering parameter β ; they can be as large as $\sqrt{2}g$ and as small as zero. This result is consistent with what we would expect based upon the physical intuition that the superposition of traveling wave modes will result in a pair of standing wave modes whose volume V_{eff} is one-half that of the traveling wave modes. The two modes are phase shifted from each other in the azimuthal direction by $\pi/2$, and as a result, if the QD is positioned in the antinode of one mode ($\xi=0$, so that $g_{sw,1} = \sqrt{2}g$), it is within a node of the other mode (so that $g_{sw,2} = 0$), and vice versa for the situation when $\xi=\pi$. Note that these results can also easily be seen by substituting the equations for the standing wave field operators into the original Hamiltonian $H_0 + H_1$ (the two approaches are equivalent).

The semiclassical rate equations can be solved in steady state to yield information about the cavity response as a function of drive strength and detunings. In the case of a single cavity mode coupled to a two-level system, this leads to the standard optical bistability state equation (OBSE) (refs. [181, 182] and appendix G). Such a semiclassical solution might be of increased importance in the current work because of the potentially large system size that needs to be considered in the numerical simulations of the quantum master equation, due to the presence of two cavity modes. This will be particularly true when considering relatively large driving fields, which could be of interest in nonlinear spectroscopy of the system, for example, as in ref. [183]. For now, we consider a couple of simple examples, beginning with the case of $\xi=0$. Defining the following parameters:

$$\begin{aligned}
 n_s &= \frac{\gamma_{\perp} \gamma_{\parallel}}{4g^2}, \\
 C &= \frac{g^2}{2\kappa\gamma_{\perp}}, \\
 Y &= \frac{E}{\kappa} n_s^{-1/2}, \\
 X_{sw,1} &= \langle \hat{a}_{sw,1} \rangle n_s^{-1/2}, \\
 X_{sw,2} &= \langle \hat{a}_{sw,2} \rangle n_s^{-1/2},
 \end{aligned} \tag{8.17}$$

we solve (in steady state) the semiclassical equations of motion in the standing wave basis (equation 8.16) to arrive at the following expression:

$$\begin{aligned}
X_{sw,1} &= \frac{Y}{1 + \frac{4\sqrt{2}C}{2X_{sw,1}^2 + (\frac{\Delta\omega_{cl}}{\gamma_{\perp}})^2 + 1} + i\left(\frac{\sqrt{2}(\Delta\omega_{cl} - \beta)}{\kappa} - \frac{4\sqrt{2}C\left(\frac{\Delta\omega_{cl}}{\gamma_{\perp}}\right)}{2X_{sw,1}^2 + (\frac{\Delta\omega_{cl}}{\gamma_{\perp}})^2 + 1}\right)} \\
X_{sw,2} &= \frac{Y}{1 + i\left(\frac{\Delta\omega_{cl} + \beta}{\kappa}\right)}
\end{aligned} \tag{8.18}$$

We are most interested in obtaining an expression for the transmission (or reflection) past the cavity and into our collection fiber, which will be the quantity measured in experiment. In the formalism presented in section 8.2, the transmission and reflection are given in terms of the traveling wave mode operators. These operators can easily be recovered here by adding and subtracting $X_{sw,1}$ and $X_{sw,2}$, as the standing wave mode operators are related to the traveling wave mode operators through equation (8.15).

As discussed earlier, the cases of $\xi = 0$ and $\xi = \pi$ (which is identical except that the roles of $X_{sw,1}$ and $X_{sw,2}$ are swapped) essentially involve coupling between a single standing wave WGM and the QD. For most choices of ξ , however, both WGMs will couple to the QD, but obtaining an equation analogous to the OBSE for an arbitrary ξ is somewhat algebraically tedious. As a simple example, we consider $\xi = \pi/2$. In this case, it is perhaps easiest to start with the semiclassical equations of motion in the traveling wave basis (equation 8.14), from which we derive:

$$\begin{aligned}
Y &= \sqrt{2}X_+ \frac{|\beta|}{\kappa} + \frac{\sqrt{2}X_+}{\left(1 + \frac{|\beta|/\kappa}{1 + i\frac{\Delta\omega_{cl}}{\gamma_{\perp}}}\right)} \left[\left(1 - \frac{|\beta|}{\kappa} + \frac{4C}{2X_+^2 + (\frac{\Delta\omega_{cl}}{\gamma_{\perp}})^2 + 1}\right) + i\left(\frac{\Delta\omega_{cl}}{\kappa} - \frac{4C\left(\frac{\Delta\omega_{cl}}{\gamma_{\perp}}\right)}{2X_+^2 + (\frac{\Delta\omega_{cl}}{\gamma_{\perp}})^2 + 1}\right) \right] \\
X_- &= \frac{\frac{|\beta|}{\kappa}X_+ + Y/\sqrt{2}}{1 + i\frac{\Delta\omega_{cl}}{\gamma_{\perp}}}
\end{aligned} \tag{8.19}$$

where $X_+ = \left(\langle \hat{a}_{cw} \rangle + \langle \hat{a}_{ccw} \rangle\right)n_s^{-1/2}$ and $X_- = \left(\langle \hat{a}_{cw} \rangle - \langle \hat{a}_{ccw} \rangle\right)n_s^{-1/2}$. From X_+ and X_- , $\langle \hat{a}_{cw} \rangle$ and $\langle \hat{a}_{ccw} \rangle$ can easily be found, and the transmitted and reflected signals from the cavity can be calculated.

8.4 Solutions to the steady state quantum master equation in the weak driving regime

The quantum master equation (QME) presented in the previous section is solved numerically using the Quantum Optics Toolbox [81, 82] for Matlab. In addition to the general framework provided by the Toolbox, the accompanying manual [81] provides many basic programs that are the basis of the calculations presented below; the PhD theses of Ben Lev [184] and Kevin Birnbaum [185] were also very helpful in this regard. We begin by considering steady state solutions, and calculate the transmitted and reflected signals from the cavity in the weak driving regime. As a starting point, we eliminate the quantum dot from the problem by taking the coupling rate $g = 0$. As expected, the resulting solutions (not displayed here) are identical to those obtained using the classical coupled mode equations and presented in fig. 8.2. Having confirmed that the QME solution is consistent with the classical solution in the empty cavity limit, we move on to study interactions with the quantum dot. To connect these simulations to ongoing experiments, we choose physical parameters consistent with the devices that we have described in this thesis.

In fig. 8.3(a), we plot the calculated V_{eff} as a function of D_{avg} for traveling wave modes of a microdisk, as calculated by finite-element method simulations (see chapters 5 and 7 for a review of these simulations). From these values for V_{eff} we can calculate the maximum QD-photon coupling strength $g = \mathbf{d} \cdot \mathbf{E}/\hbar$, given by (see refs. [9, 110] and appendix H):

$$g = \frac{1}{2\tau_{\text{sp}}} \sqrt{\frac{3c\lambda_0^2\tau_{\text{sp}}}{2\pi n^3 V_{\text{eff}}}}, \quad (8.20)$$

where τ_{sp} is the spontaneous emission lifetime of the QD exciton, which we take as 1 ns in our calculations, consistent with what has been seen experimentally [142]. The results are plotted in fig. 8.3(b), and we see that $g/2\pi$ can be as high as ~ 16 GHz. We note that in these calculations of g , the *traveling wave* mode volume was used, because it is the value that is entered directly into the quantum master equations presented in section 8.3. However, as we shall see below, in the presence of strong backscattering, standing wave modes are formed, and when coupled to a single QD, the resulting vacuum Rabi splitting is consistent with an effective coupling strength of $g\sqrt{2}$, as expected due to the decreased volume of the standing wave modes.

As discussed in chapter 7, for such modes, $Q_{\text{rad}} > 10^5$ for all but the smallest diameter disks

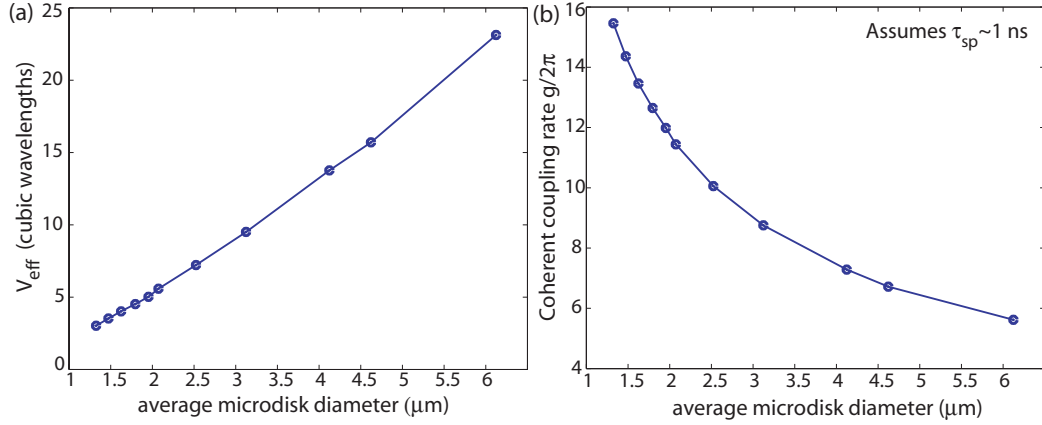


Figure 8.3: Finite-element method simulation results: (a) Modal volume V_{eff} as a function of microdisk diameter (taken at the center of the slab), calculated for traveling wave modes. The modes studied are $\text{TE}_{p=1,m}$ WGMs with resonance wavelength within the 1200 nm band. (b) Coherent coupling rate $g/2\pi$ as a function of microdisk diameter. A QD spontaneous emission lifetime $\tau_{\text{sp}} = 1$ ns is assumed in the calculation of g .

($D_{\text{avg}} < 1.5 \mu\text{m}$). We have confirmed this in experiments, with Q s as high as 3.6×10^5 achieved, so that cavity decay rates $\kappa/2\pi$ on the order of 1 GHz can reasonably be expected. Such devices exhibited doublet splittings that were on the order of 10-100 pm, corresponding to a backscattering rate $|\beta|/2\pi = 1$ -10 GHz. This rate can thus be very close in magnitude to do the QD-photon coupling rate, and we thus expect the simulation results to be particularly helpful in interpreting future experimental data.

8.4.1 $\beta > g > (\kappa, \gamma_{\perp})$

The first situation we study is one in which the backscattering rate β exceeds the coupling rate g , which in turn exceeds the cavity and QD decay rates κ and γ_{\perp} . We choose $\beta/2\pi = 9.6$ GHz, with $g/2\pi = 6$ GHz, $\kappa/2\pi = 1.2$ GHz (corresponding to $Q = 100,000$), and $\tau_{\text{sp}} = 1$ ns ($\gamma_{\parallel}/2\pi \sim 0.16$ GHz). The unperturbed cavity frequency (i.e., the resonance frequency of the *traveling wave* modes) is fixed at $\omega_c = 0$, and three different QD-cavity detunings, $\Delta = \omega_a - \omega_c = \{0, \beta, -\beta\}$ are considered. For each value of Δ , we calculate the steady state transmission and reflection spectra from the cavity in three different limits: (i) $g=0$; here, there is no QD-cavity coupling, and the response should be that of an empty cavity, (ii) $g/2\pi = 6$ GHz, $\gamma_p/2\pi = 0$ GHz; here, we neglect all non-radiative dephasing, which becomes a better and better approximation as the temperature of the QD-microcavity sample is lowered, and (iii) $g/2\pi = 6$ GHz, $\gamma_p/2\pi = 2.4$ GHz; here, we allow for a significant amount of non-

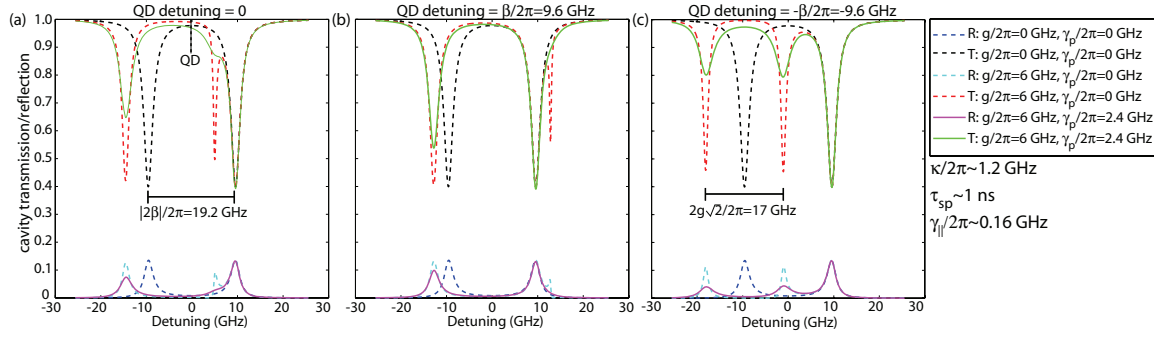


Figure 8.4: Normalized transmitted and reflected signal for a QD coupled to a microdisk cavity, calculated through numerical solution of the steady state quantum master equation under weak driving (< 0.03 photons/sec input power). (a) $\Delta = \omega_a - \omega_c = 0$, (b) $\Delta = \beta$, and (c) $\Delta = -\beta$. ω_c is the resonance frequency of the traveling wave whispering gallery modes. In these plots, $g/2\pi = 6$ GHz, $\beta/2\pi = 9.6$ GHz, $\kappa/2\pi = 1.2$ GHz, and $\tau_{sp} = 1$ ns.

radiative dephasing, corresponding to a QD exciton linewidth of ~ 10 μeV (at an energy of 1 eV), which is consistent with what has been observed experimentally at temperatures of around 10-20K [142].

The results are plotted in fig. 8.4. In all of the results, we see that the primary function of γ_p is to damp and broaden the resonances, in some cases significantly, but as expected, γ_p does not cause the features to shift in position. In fig. 8.4(a), we see that the presence of the QD has caused the lower frequency mode to shift slightly, while the higher frequency mode has not changed position. In fig. 8.4(b), the higher frequency mode remains unshifted, and the lower frequency dip has shifted even less. Finally, in fig. 8.4(c), the higher frequency mode again remains unshifted, while the lower frequency mode has split into two resonances.

The interpretation of these results is as follows: as a result of the modal coupling due to backscattering, which has formed standing wave modes through a superposition of the initial traveling wave modes, only the lower frequency mode of the doublet has any spatial overlap with the QD, and thus, we should only expect the low frequency mode to exhibit any frequency shifts or splittings. In fig. 8.4(a), the QD, spectrally located at $\Delta = 0$, is detuned from both modes (which are located at $\pm\beta$), and thus, although the low frequency mode exhibits a frequency shift, we do not see the symmetric vacuum Rabi splitting that would occur on resonance. As expected, due to the spatial misalignment, the higher frequency mode remains unshifted. In fig. 8.4(b), the QD is now on resonance with the higher frequency mode, so that it is detuned from the low frequency mode by 2β . Thus, the shift exhibited by the low frequency mode is smaller than that in fig. 8.4(a). Finally in

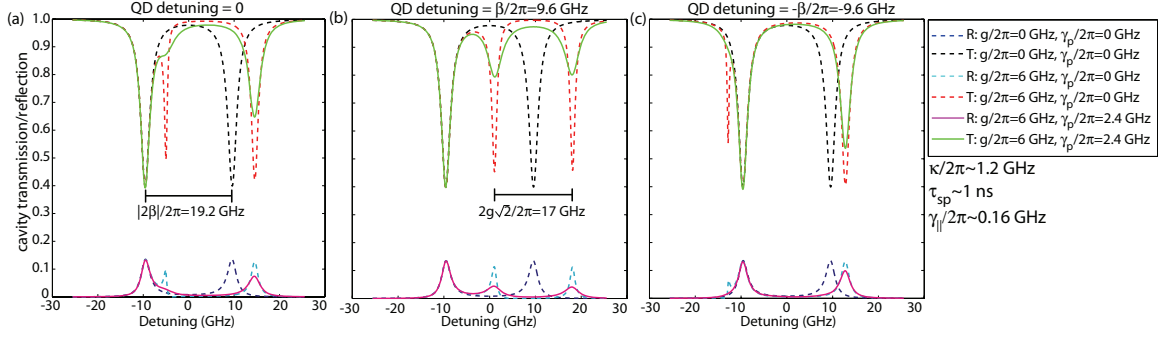


Figure 8.5: Normalized transmitted and reflected signal for a QD coupled to a microdisk cavity, calculated through numerical solution of the steady state quantum master equation under weak driving (< 0.03 photons/sec input power). These plots are calculated using identical parameters as those used in fig. 8.4, with the exception that the phase of the backscattering parameter β has been changed from $\xi=0$ to $\xi=\pi$, so that $\beta/2\pi=-9.6$ GHz.

fig. 8.4(c), the QD is on resonance with the low frequency mode, and is also spatially aligned with it, so that we see the familiar vacuum Rabi splitting of this resonance. We note that the separation Ω_R in this case is $2g\sqrt{2}$ rather than $2g$; this is consistent with the mode volume of the standing wave modes being one half that of the traveling wave modes, as $g \sim 1/\sqrt{V_{\text{eff}}}$.

The question then arises as to what parameter preferentially selected the low frequency mode to be spatially aligned with the QD over the high frequency mode. That parameter is the phase of the backscattering rate β , which we called ξ in the previous section. For the example above, $\xi = 0$. We now consider what happens if we take $\xi = \pi$, so that β is negative. Our expectation is that this phase shift should switch which mode is spatially aligned with the QD, so that the higher frequency mode should now be selected. This prediction is confirmed in fig. 8.5, as we see that the results are the mirror image of those in fig. 8.4, where now the high frequency mode is spatially aligned with the QD and exhibits frequency shifts and vacuum Rabi splitting.

Finally, we consider an intermediate backscattering phase $\xi = \pi/2$. Here, we expect both modes to have an equal (but non-optimal) spatial alignment with the QD. For example, for modes with a $\cos(m\phi)$ and $\sin(m\phi)$ azimuthal dependence, this would correspond to having the QD located at a position where $\cos(m\phi)=\sin(m\phi) <$, e.g., $m\phi=\pi/4$. The results, displayed in fig. 8.6, show that this is indeed the case. In fig. 8.6(a), for example, we see a symmetric spectrum, consistent with both modes being equally spatially coupled to the QD and equally (and oppositely) spectrally detuned from it. In fig. 8.6(b)-(c), we see that the spectra are no longer symmetric, as the QD is on resonance with the high frequency mode in fig. 8.6(b), and with the low frequency mode in fig. 8.6(c). In each

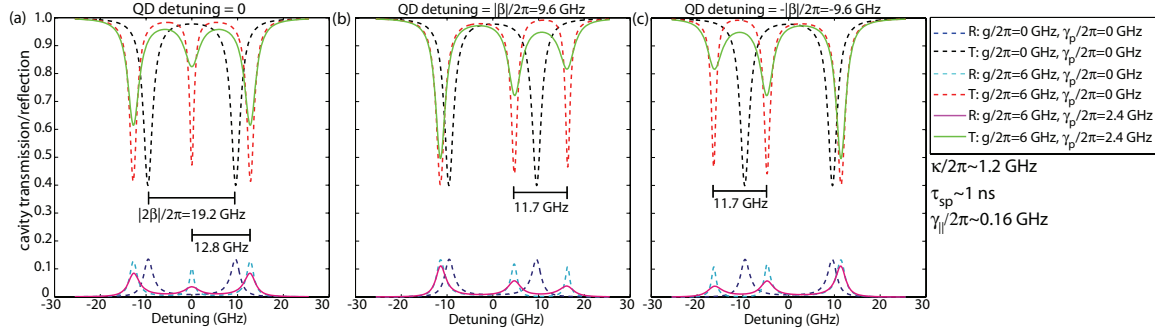


Figure 8.6: Normalized transmitted and reflected signal for a QD coupled to a microdisk cavity, calculated through numerical solution of the steady state quantum master equation under weak driving (< 0.03 photons/sec input power). These plots are calculated using identical parameters as those used in fig. 8.4, with the exception that the phase of the backscattering parameter β has been changed from $\xi=0$ to $\xi=\pi/2$, so that $\beta/2\pi=i*9.6$ GHz, where $i = \sqrt{-1}$.

case, we see Rabi splitting about the mode on resonance with the QD, and only a small shift for the non-resonant mode. The Rabi splitting between the peaks is no longer at the maximum value of $2g\sqrt{2}$, but at a value closer to $2g$. This makes sense because the maximum value of g is still larger than it would be for a traveling wave mode by a factor of $\sqrt{2}$, but this gain is negated by having the QD positioned away from the peak of the field.

The situation described by fig. 8.6(a), where the QD is equally spatially coupled to the two cavity modes, and spectrally positioned in between them, might be particularly interesting, due to the presence of a transmission dip at zero laser-QD detuning. It is anticipated that this resonance can be used as a means to inject photons into the system for applications such as nonlinear switching. The advantage of this configuration, in comparison to a QD coupled to a single mode, is that the position of this zero detuning resonance is fixed, regardless of the input power. This is in contrast to what one observes for a QD coupled to a single cavity mode, where the position of the transmission dips will shift as a function of driving power, so that the amount of power that can be coupled into the cavity at a given frequency is limited.

8.4.2 $g > \beta > (\kappa, \gamma_{\perp})$

Here, we switch regimes slightly to one in which the QD-cavity coupling rate dominates all other rates in the system, including the backscattering rate β . In particular, we choose $g/2\pi=12$ GHz, with $\beta/2\pi=4.8$ GHz, $\kappa/2\pi=1.2$ GHz, and $\tau_{sp}=1$ ns ($\gamma_{||}/2\pi \sim 0.16$ GHz). The qualitative behavior that we expect to see is identical to that of the previous section, as both g and β represent coherent

processes, so that their relative values compared to each other are not as important as their values in comparison to the dissipative rates in the system. This is seen in fig. 8.7(a), where the QD is spectrally located at $-\beta$, so that it is resonant with the low frequency mode of the standing wave doublet. Predictably, the interaction with the QD causes this resonance to split, with a splitting $\Omega_R=2g\sqrt{2}$. The higher frequency mode remains unaffected, as the choice of $\xi=0$ causes it to be spatially misaligned from the QD.

8.4.3 $\kappa > g > \beta > \gamma_{\perp}$

Now, we take the cavity loss rate $\kappa/2\pi=9.6$ GHz to exceed both $g/2\pi=6$ GHz and $\beta/2\pi=1.2$ GHz (in addition, $\gamma_{\parallel}/2\pi=0.16$ GHz and $\gamma_p/2\pi=0$ or 0.7 GHz), so that $\kappa > \gamma_{\perp}$. In the absence of a QD, we know that when $\kappa \gg \beta$, we expect to see a single transmission dip rather than a doublet. This is confirmed in simulation by the black dotted line in fig. 8.7(b). With the addition of a QD, taken to be resonant with the center frequency of the single cavity transmission dip, we expect to see this single dip split into two, with the dips not being completely resolved due to having $\kappa > g$. This is confirmed in fig. 8.7(b), where the splitting $\Omega_R/2\pi = 14.8$ GHz lies between the expected splitting for a purely traveling wave cavity mode ($\Omega_R=2g$) and the expected splitting for a purely standing wave cavity mode ($\Omega_R=2g\sqrt{2}$), and lies closer to the latter due to the degree to which κ exceeds β .

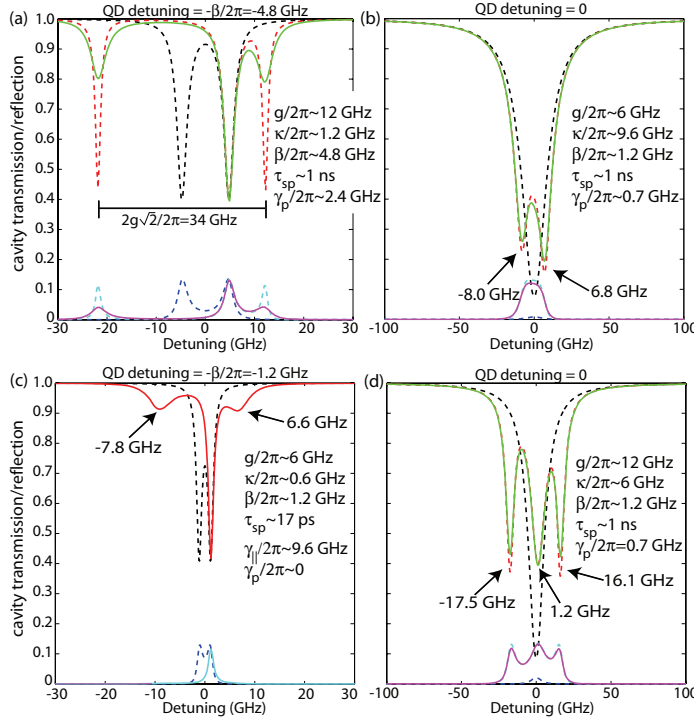


Figure 8.7: Normalized transmitted and reflected signal for a QD coupled to a microdisk cavity, calculated through numerical solution of the steady state quantum master equation under weak driving. (a) $g > \beta > (\kappa, \gamma_{\perp})$, (b) $\kappa > g > \beta > \gamma_{\perp}$, (c) $\gamma_{\parallel} > g > \beta > \kappa$, and (d) $g > \kappa > \beta > \gamma_{\perp}$.

8.4.4 $\gamma_{\parallel} > g > \beta > \kappa$

Here, the roles of κ and γ_{\parallel} are swapped in comparison to the previous subsection, so that $\gamma_{\parallel}/2\pi=9.6$ GHz is the dominant dissipative rate, exceeding both $g/2\pi=6$ GHz and $\beta/2\pi=1.2$ GHz (the transverse decay rate $\gamma_{\perp} \sim 4.8$ GHz $\sim g$). Unlike our previous example, in absence of a QD, we do expect to see a pair of standing wave modes form, as $\beta > \kappa$. This is confirmed in fig. 8.7(c) (plot with the black dashed lines). Now, we introduce a QD that is spectrally aligned with the low frequency mode at $-\beta$. Because QD decay is so large in this case, however, we expect that the standing wave character of the modes is going to largely be erased when coupled to the QD; standing wave modes form only when the decay processes in the system are small enough that coherent coupling can take place between the *cw* and *ccw* propagating modes. When a QD is introduced, we expect the energy to oscillate between the QD and the cavity modes, and that standing wave modes can still form if the energy decay is not too large, both when the system is primarily ‘QD-like’ and ‘cavity-like.’ Clearly, for $\gamma_{\parallel} \gg \beta$, this is not the case.

To confirm this intuition, we examine the calculated transmission spectrum in fig. 8.7(c). The low frequency mode does indeed split, but the splitting $\Omega_R/2\pi = 14.4$ GHz is much less than the expected splitting of $2g\sqrt{2}$ for standing wave modes, and lies much closer to the $2g$ splitting for traveling wave modes. The situation thus mimics that of the previous example. One major difference is the relatively poor contrast (transmission depth) exhibited by the split resonances; this is due to the fact that the dominant loss channel in this case, QD decay, is not collected in this measurement, unlike cavity loss (for which a large fraction is collected).

8.4.5 $g > \kappa > \beta > \gamma_{\perp}$

8.4.5.1 Steady state analysis

Finally, we consider an intermediate scenario where QD-cavity coupling $g/2\pi = 12$ GHz is the dominant rate in the system, but where cavity decay $\kappa/2\pi=6$ GHz exceeds the backscattering rate $\beta/2\pi=1.2$ GHz. Again, in absence of a QD, we see a single transmission dip (fig. 8.7(d)), as $\kappa > \beta$. If a QD is now spectrally aligned to the center of this dip ($\Delta=0$), however, we see three dips appear within the transmission spectrum of fig. 8.7(d), as opposed to the two dips that appeared in fig. 8.7(b). The central dip is at frequency of 1.2 GHz $=\beta/2\pi$, and corresponds to the frequency of one of the two standing wave modes that can form through an appropriate combination of the traveling wave modes. As this mode is spatially misaligned from the QD, we do not expect its frequency to

have shifted due to interaction with the QD. The other two dips correspond to the splitting of the low frequency standing wave mode from its original position at $-\beta/2\pi = -1.2$ GHz. The splitting of $\Omega_R/2\pi = 33.6$ GHz is very close to the maximum possible value of $2g\sqrt{2}$, which is the expected value for standing wave modes (indeed, if the QD was actually spectrally aligned at $-\beta/2\pi = -1.2$ GHz, Ω_R would be even closer to $2g\sqrt{2}$).

However, the question remains as to why the picture presented is largely consistent with a QD interacting with a standing wave mode when, in absence of a QD, the system is consistent with a traveling wave mode. The basic reason is as described above; when interacting with a QD, the system oscillates between being ‘QD-like’ and ‘cavity-like’, and in each phase, undergoes decoherence due to the corresponding decay channel. As a result, the fast cavity decay rate in this example is somewhat mitigated by the very slow QD decay rate, to the point that coherent coupling between the clockwise and counterclockwise traveling wave modes can be achieved and standing wave modes can be formed.

8.4.5.2 Time-dependent analysis

The density matrix calculations presented above are all steady state calculations ($\frac{d\rho}{dt} = 0$). To get a feeling for the time-dependence of the system, we can use the Quantum Optics Toolbox to numerically integrate the differential equation for the density matrix [81, 82]. One of the first things we can look at is the evolution of the cavity transmission spectrum as a function of time, to understand the time required to reach steady state. The results are plotted in fig. 8.8, along with the already calculated steady state solution. We see that the time-dependent solution approaches the steady state solution in a time of about 0.1 ns, which is on the order of the Rabi oscillation time $\tau_R \sim 1/g$.

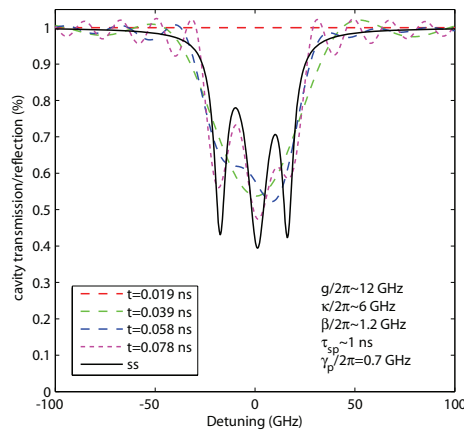


Figure 8.8: Normalized transmitted signal for a QD coupled to a microdisk cavity, calculated as a function of time through numerical integration of the quantum master equation under weak driving.

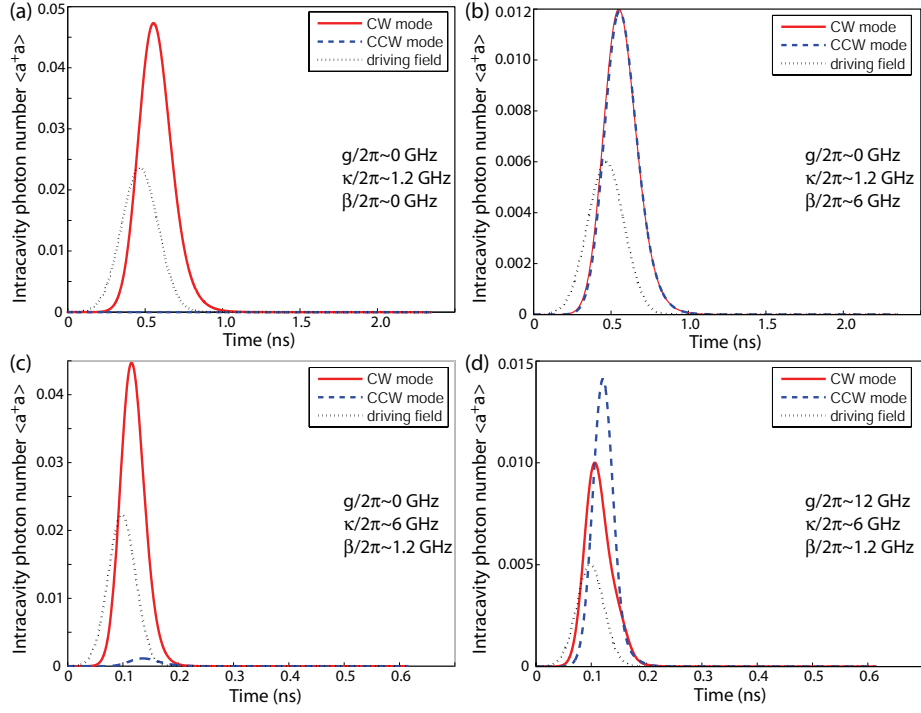


Figure 8.9: Number of intracavity photons in the microdisk clockwise (solid red curves) and counterclockwise (dashed blue curves) propagating WGMs, calculated by numerical integration of the quantum master equation. A driving field consisting of a Gaussian pulse in time is used (shown as a black dashed line), with $\omega_l = -\beta$. (a) $g/2\pi=0$, $\kappa/2\pi=1.2$ GHz, $\beta/2\pi=0$ GHz, (b) $g/2\pi=0$, $\kappa/2\pi=1.2$ GHz, $\beta/2\pi=6$ GHz, (c) $g/2\pi=0$, $\kappa/2\pi=6$ GHz, $\beta/2\pi=1.2$ GHz, and (d) $g/2\pi=12$ GHz, $\kappa/2\pi=6$ GHz, $\beta/2\pi=1.2$ GHz.

For the purposes of better understanding why the cavity spectrum appears as it does (and in particular, why the mode splitting is consistent with that expected for a QD interacting with a standing wave mode instead of a traveling wave mode), we examine the intracavity photon number ($\langle \hat{a}^\dagger \hat{a} \rangle$) for the clockwise and counterclockwise modes as a function of time. Rather than using a constant (time-independent) driving field, the cavity is driven by a short pulse (Gaussian in shape, with a drive power of 0.1 photons/sec), and is centered at a frequency $\omega_l = -\beta$. For an ideal microdisk structure (no surface roughness) that is not coupled to a QD ($g = 0$), the forward propagating mode of the fiber taper will only couple to the clockwise mode of the microdisk. This is confirmed in fig. 8.9(a), as $\langle \hat{a}_{ccw}^\dagger \hat{a}_{ccw} \rangle$ remains zero for all times, while $\langle \hat{a}_{cw}^\dagger \hat{a}_{cw} \rangle$ rises as light is coupled into the clockwise mode, and decays due to cavity radiation after the drive field is switched off. Next, we consider the empty cavity ($g = 0$) with $\beta/2\pi=6$ GHz and $\kappa/2\pi=1.2$ GHz, so that $\beta > \kappa$. As we have described in the previous sections, in this regime, we expect to see coupling between the

propagating WGMs to form standing wave modes. We thus expect to see non-zero photon numbers for both clockwise and counterclockwise modes, with the count rates damped due to cavity loss. This behavior is confirmed in fig. 8.9(b).

We now move on to the situation considered in steady state in section 8.4.5.1, starting without the QD. As the cavity decay rate $\kappa/2\pi=6$ GHz is significantly larger than the backscattering rate $\beta/2\pi=1.2$ GHz, we expect that the clockwise mode will suffer significant decay before an appreciable amount of power can be coupled into the counterclockwise mode. This is confirmed in fig. 8.9(c). Now, we introduce a QD with $\gamma_{||}/2\pi=0.16$ GHz, and spectrally located at zero detuning (for simplicity, we have taken $\gamma_p=0$ in this calculation). The calculated steady state transmission spectrum (fig. 8.7(d)) indicated that the QD mediates coupling between the clockwise and counterclockwise modes, allowing for standing waves to form, with the low frequency mode (at $\Delta\omega = -\beta$) spatially aligned with the QD. This behavior is confirmed in fig. 8.9(d), where we see that the photon number for the counterclockwise mode increasing much more quickly than it does in fig. 8.9(c), confirming that energy transfer occurs through some process other than backscattering. Once the driving field is switched off, the photon count rates in the two modes die down, as a result of both cavity and QD decay.

The density matrix calculations performed up to this point show the evolution of the system in an ensemble-averaged sense. To provide us with further physical insight, quantum trajectory calculations can be considered [149]. In these simulations, the Schrodinger wavefunction for the system is calculated under the influence of a non-Hermitian Hamiltonian H_{eff} , defined in terms of collapse operators for the cavity modes and the QD. At random times within this evolution, the wavefunction is subject to collapses, corresponding to detection events. The quantum trajectory approach thus models the conditional evolution of a system, and can provide insight into what will be observed in a measurement (such as the homodyne photocurrent). If the results of many trajectories are averaged, the results of the density matrix calculations can be reproduced. This latter point has been examined in quantum trajectory simulations of the systems studied in fig. 8.9, where 50 trajectories have been averaged, and it has been confirmed that the results match those of the density matrix calculations well. As only weak driving has been thus far considered, the computational benefit of using a wavefunction-based approach rather than the density matrix is minimal. However, for future studies, both the physical insight into the dynamics of these systems and the reduction in computational cost of the quantum trajectory method may be very important.

8.4.6 $\beta = 0; g > \kappa > \gamma_{\perp}$

The basic result that the above examples demonstrate is that the QD can effectively serve as a means to couple the cavity modes, even in instances where the backscatter parameter is small relative to other rates in the system. As a final illustration of this, we consider the situation where the backscatter parameter is zero. In absence of the QD, we then see a single Lorentzian dip in the transmission spectrum through the fiber taper. When the QD is added, one would might expect to just see this Lorentzian dip split into two dips separated by $2g$. From fig. 8.10, we see that the mode does split, but that the splitting exceeds $2g$ (it is actually $2g\sqrt{2}$). Furthermore, we also see the presence of a Lorentzian dip at the original cavity frequency, but with the transmission contrast reduced in amplitude.

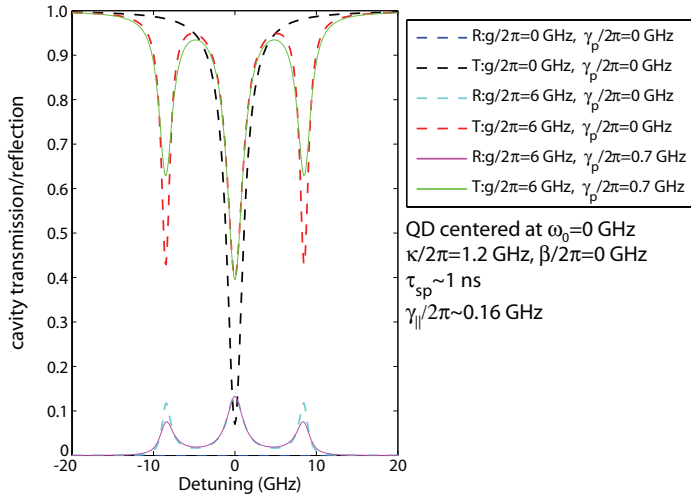


Figure 8.10: Normalized transmitted and reflected signal (steady state), for the case where the ‘passive’ modal coupling between clockwise and counterclockwise WGMs (β) is zero. Coupling to the atom serves to mediate coupling between the cavity modes.

The interpretation of these results is that the QD has effectively served to mediate coupling between the two traveling wave modes, creating a pair of standing wave resonances. The standing wave mode that is spatially aligned with the QD splits into the resonances at $\pm g\sqrt{2}$, while the other standing wave mode does not overlap with the QD at all, and appears as an unperturbed resonance at the original cavity frequency. Unlike the standing wave modes formed through surface-roughness-induced backscattering, this standing wave mode has not shifted in frequency with respect to the original traveling wave modes because it sees the exact same dielectric function as the traveling wave modes.¹

¹Standing wave modes that form through backscattering from structural variations see different dielectric functions, one which includes more of the air regions and the other that includes more of the dielectric regions, resulting in frequencies that are shifted above and below the original resonance frequency, respectively.

8.5 Potential for low power switching in the microdisk-QD system

The ultrasmall volumes sustained by these semiconductor microcavities offer the potential to observe phenomena in nonlinear optics at very small input powers, due to the large per photon electric field strengths within the devices. The saturation photon number, m_0 , which represents the average number of intracavity photons needed to saturate the QD transition, can give us some idea of how low these powers might be. This quantity is given by [9]:

$$m_0 = \frac{\gamma_{\perp} \gamma_{\parallel}}{4g^2} \quad (8.21)$$

where γ_{\perp} is the transverse relaxation rate given by $\gamma_{\perp} = \gamma_{\parallel}/2 + \gamma_p$ (note that m_0 was called n_s previously). Let us first consider the case where γ_p is small, so that the QD is radiative-limited, and $m_0 = \gamma_{\parallel}^2/8g^2$. For $g/2\pi \sim 10$ GHz, which is certainly reasonable for the microdisk cavities we study, and $\gamma_{\parallel}/2\pi \sim 0.16$ GHz ($\tau_{\text{sp}} \sim 1$ ns), which is typical for self-assembled InAs QDs, $m_0 \sim 10^{-5}$. This value indicates the degree to which one photon in the cavity can affect a single QD.

To study this in a bit more detail, we use steady state solutions to the semiclassical optical bistability state equation (OBSE) and the quantum master equation (QME) to look at the cavity response as a function of the drive strength. For our purposes here, we will restrict ourselves to looking at a single (standing wave) cavity mode coupled to the QD; as we saw in the previous sections, this can occur within our system if the phase of the backscattering parameter is such that the QD is only spatially aligned with one of the two standing wave cavity modes. This simplification is also necessary as our calculations here are not done in the weak driving limit, so that a significant number of Fock space basis elements are needed to describe the cavity mode; this would become computationally untenable in the case of two cavity modes. The QME and OBSE for a single cavity mode coupled to a two-level system are discussed in appendix G.

We begin by considering a system with $(g, \kappa, \gamma_{\parallel}, \gamma_p)/2\pi = (6, 2.4, 0.16, 0)$ GHz, and with the atom, cavity, and driving field all on resonance. The corresponding saturation photon number (equation (8.21)) and cooperativity parameter (equation (8.17)) are $m_0 \sim 9 \times 10^{-5}$ and $C \sim 94$. The critical atom number [9], which describes the number of atoms (or QDs in this case) needed to have an appreciable effect on the intracavity field, is given by $N_0 = 1/C$ and is 0.01 in this example. We first plot, on a linear scale, the normalized steady state intracavity field $X_{\text{ss}} = \langle \hat{a} \rangle m_0^{-1/2}$ as

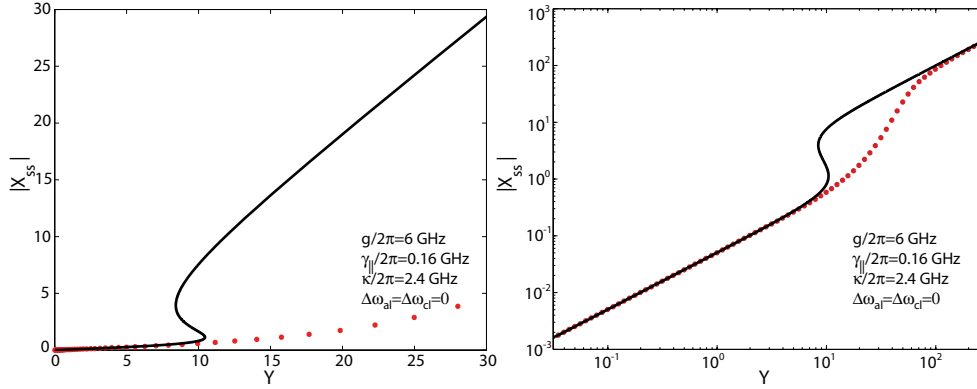


Figure 8.11: Steady state solutions to the semiclassical Maxwell-Bloch equations (solid line) and quantum master equation (dots), showing normalized intracavity field amplitude $|X_{ss}|$ as a function of normalized drive field $|Y|$. In these simulations, $\omega_a = \omega_c = \omega_l$, and $g/2\pi = 6$ GHz, $\kappa/2\pi = 2.4$ GHz, $\gamma_p = 0$, and $\gamma_{||}/2\pi = 0.16$ GHz. Correspondingly, $m_0 \sim 9 \times 10^{-5}$ and $C \sim 94$.

a function of the normalized drive field $Y = (E/\kappa)m_0^{-1/2}$ in fig. 8.11(a). The semiclassical solution displays bistability, so that in the intermediate (multi-valued) portion of the curve, the top and bottom branches are stable solutions, and the middle branch is unstable. However, the quantum master equation solution looks very different, and the bistability has been washed away.² Plotted on a logarithmic scale over a wider range (fig. 8.11(b)), we confirm the absence of bistability in the quantum master equation solution, but see that it does follow the semiclassical solution in regions of small Y and large Y .

In an experiment, we will measure the transmission or reflection response of the cavity as a function of drive power through the taper input. This is plotted in fig. 8.12, where we have displayed the cavity reflection as a function of the average number of intracavity drive photons and the input drive power, for a number of different cavity decay rates (we have assumed critical coupling between the taper and cavity). We again see that the quantum master equation solutions do not match the prediction of optical bistability that the semiclassical equation solutions make, but do indicate that switching between near-zero and unity reflection can occur for relatively small input powers, on the order of tens of nanoWatts. We note that there is a general trade-off between the contrast in reflection, which increases as the cavity Q increases, and the switching power. Similar behavior can be observed in the transmitted signal by setting the laser drive frequency $\omega_l = \pm g$.

In order to achieve radiative-limited operation of the QDs, low temperatures ($T \lesssim 10$ K) are required. It is interesting to consider whether functional devices can be created that operate at room

²This discrepancy has been observed and discussed by several authors in the context of atomic cQED [176, 186].

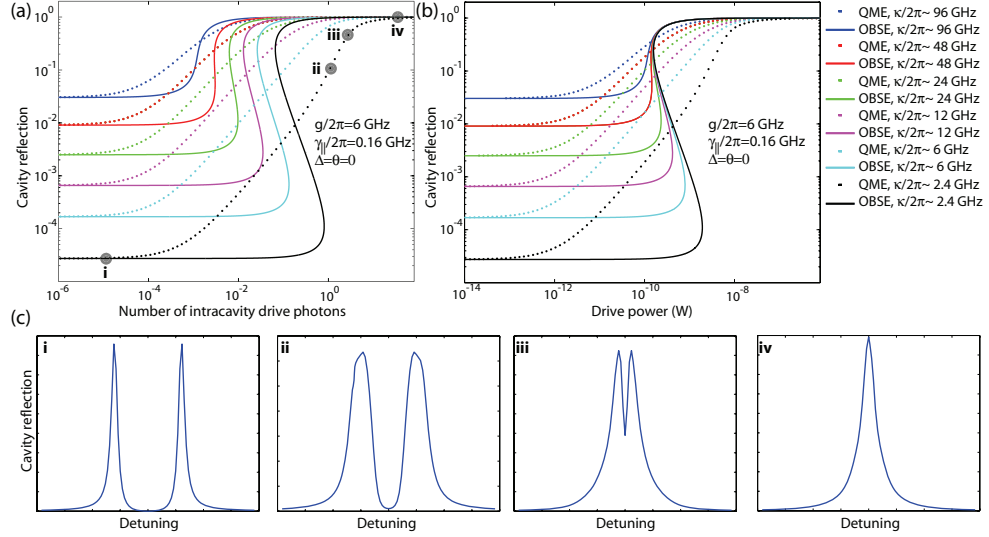


Figure 8.12: Steady state solutions to the semiclassical Maxwell-Bloch equations (solid lines) and quantum master equation (dots), showing cavity reflection as a function of (a) average number of intracavity drive photons (b) input drive power, for varying cavity decay rates. In these simulations, $\omega_a = \omega_c = \omega_l$, and $g/2\pi=6$ GHz. We assume $\gamma_p=0$, and $\gamma_{||}/2\pi=0.16$ GHz. The cavity reflection spectrum at selected drive strengths, indicated by the gray circles in (a) and labeled i-iv, are shown in (c).

temperature, where non-radiative dephasing of the QD broadens its linewidth, to values on the order of ~ 5 meV (for a QD exciton line at ~ 1 eV). Equation (8.21) predicts $m_0 \sim 0.4$ for $g/2\pi \sim 10$ GHz, indicating that a single photon can still have an appreciable effect on a single QD. However, the significant non-radiative dephasing would also suggest that any switching devices will not function as efficiently as they do at low temperature.

We first plot X_{ss} as a function of Y (fig. 8.13(a)) for a system with $g/2\pi=17$ GHz and $\kappa/2\pi=0.1$ GHz. We now see that neither the semiclassical nor the quantum master equation solutions display bistability, and that the two solutions match much more closely than they did in the previous example. Despite the absence of bistability, the shape of the curve is very similar to the quantum master equation solution in the radiative-limited case, indicated the potential for switching between low reflection and high reflection values at relatively low powers.

The reflected signal from the cavity as a function of average number of intracavity drive photons and input drive power for a couple of different combinations of κ and g are plotted in fig. 8.14. These solutions indicate that low switching powers can still be achieved, but that the reflection contrast is significantly diminished as a result of the non-radiative dephasing. Relatively large cavity Q s ($> 10^6$) are then needed to achieve ~ 20 dB of contrast. As mentioned above, switching in the

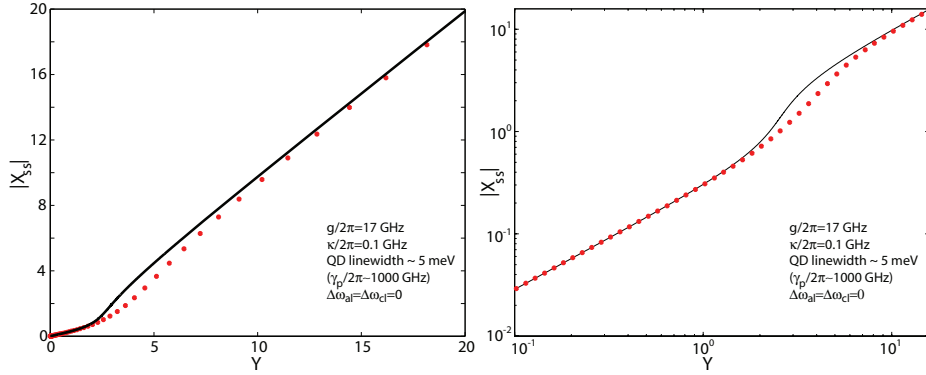


Figure 8.13: Steady state solutions to the semiclassical Maxwell-Bloch equations (solid line) and quantum master equation (dots), showing normalized intracavity field amplitude $|X_{ss}|$ as a function of normalized drive field $|Y|$, for a system with large non-radiative dephasing (linewidth ~ 5 meV).

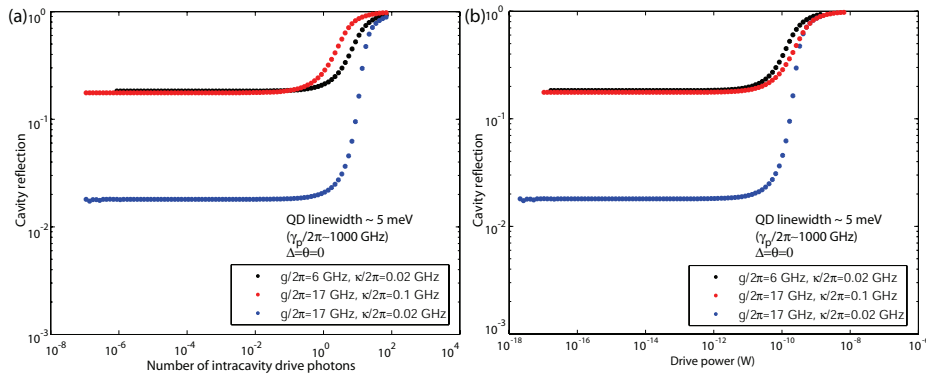


Figure 8.14: Steady state solutions to the quantum master equation, showing cavity reflection as a function of (a) average number of intracavity drive photons and (b) input drive power (right), for a system with large non-radiative dephasing (linewidth ~ 5 meV). In these simulations, $\omega_a = \omega_c = \omega_l$.

transmitted signal can be achieved by tuning the drive field to $\omega_l = \pm g$.

The simulations presented above are just a preliminary examination of switching possibilities in these fiber-coupled microcavity-QD systems. A more detailed bifurcation analysis of the semiclassical model and quantum trajectory analysis to study the time-dependent properties of the system must be conducted better understand the system and the various types of behavior that can be accessed for different parameter regimes. The recent analysis of Armen and Mabuchi [178] will be quite useful in this regard.

Chapter 9

Conclusions and Future Outlook

In this concluding chapter, we briefly summarize some of the remaining challenges to accessing the strong coupling regime in our experiments. Addressing these challenges is an on-going effort, and is essentially the primary focus of my current research.

Semiconductor microcavity-QD vacuum Rabi splitting has been demonstrated in the experiments of three groups in late 2004 [70, 71, 72]. The procedure in these experiments is as follows: 1) the sample is cooled within a liquid He cryostat, in order to reduce non-radiative dephasing in the QDs, 2) the sample is incoherently pumped at energies above the bandgap of the dominant material in the microcavity (e.g., 870 nm for GaAs), in order to efficiently generate carriers that can fill the QDs, and 3) spontaneous emission from the device is collected through free-space optics and dispersed by a spectrometer onto a linear array of detectors (typically a CCD for measurements below 1 μm , or an InGaAs detector array for wavelengths above 1 μm). The primary technical hurdles in such experiments are creating a sufficiently high- Q cavity to be within the strong coupling regime, and achieving spectral and spatial alignment of a single QD with the cavity mode. In addition, efficient collection of emitted light can be difficult, and is particularly necessary for work at longer wavelengths ($> 1 \mu\text{m}$), where the InGaAs detector dark count rates are significantly greater than those of Si detectors used at shorter wavelengths [164].

We are interested in being able to observe vacuum Rabi splitting within the spontaneous emission spectrum of incoherently pumped devices, but beyond this, our goal is to use the fiber taper to provide efficient near-resonant pumping. Initial experiments will examine the spectral response of a coupled microcavity-QD system as a function of the frequency of a weak probe beam, providing a slightly different measurement of vacuum Rabi splitting than has been accomplished in refs. [70, 71, 72]. Such fiber-taper-based measurements have been discussed in detail in the context of microdisk cavities in chapter 8. Beyond vacuum Rabi splitting, further experiments will explore

phenomena like switching or other nonlinear optical effects in a strongly coupled microcavity-QD system. In such measurements, the fiber taper (or some other form of efficient input-output coupling) is basically a necessity.

Incorporating the fiber taper within a liquid He cryostat is thus a critically important step, and one that is specific to the experiments we wish to conduct. As mentioned in the preface to this thesis, our initial hope was to create fiber-pigtailed devices using the taper mounting technique developed by Paul Barclay for use in ultra-high-vacuum chambers and atomic physics experiments [80]. Our attempts at using such structures were unsuccessful, due to the mechanical failure of the epoxy joints (used to affix the taper onto the microcavity chip) at low temperatures. On the positive side, the fiber taper itself showed no degradation (in terms of its transmission properties, for example) at low temperatures. Current efforts are focused on utilizing low-temperature-compatible micropositioners to actively position the taper with respect to the cavity in the same way we do so at room temperature.

The other principal technical challenges that we face are common to the field as a whole, rather than our specific experiments. As mentioned above, foremost amongst these is achieving spectral and spatial alignment of a single QD with the cavity mode. Let us first consider spectral alignment. Unlike atomic systems, for which the transition wavelength of interest is known (e.g., 852.3 nm for the Cs D2 transition) and as a result, so is the desired cavity mode resonance wavelength, there is typically a non-uniform size distribution of QDs within a sample. For example, the inhomogeneous linewidth of the QD exciton ground state transition in our samples is ~ 50 nm. Devices are then fabricated to have cavity mode resonances lying within this inhomogeneous QD spectrum, and precise spectral alignment is achieved through some tuning mechanism of the cavity mode and/or the QD exciton line. This is sometimes accomplished through temperature tuning [187], where the differing tuning rates of the QD exciton line and the cavity mode can be exploited to tune the two into resonance. There are significant limitations here, however; in ref. [187], for example, the InAs quantum dot shifts by ~ 1 nm when the sample temperature is changed between ~ 4 K and 40 K, while the cavity mode shifts by less than one-quarter of this. The tuning range is limited by the maximum sample temperature at which QD non-radiative dephasing is acceptable; even at 20 K, non-radiative dephasing can be significant [142]. If the QD exciton and cavity mode are more widely separated than what can be compensated for through temperature tuning, the cavity geometry can be slightly modified, through etching away a thin layer of material to blue-shift the resonances, for example [188, 48]. One drawback of this method is that it has to be done outside

of the cryostat, and therefore lacks the flexibility and of an *in situ* tuning mechanism. Red shifting of the cavity modes can be accomplished through deposition of a thin dielectric layer by a process such as PECVD (again, not an *in situ* process), or through condensation (of an introduced gas such as Xenon, for example) on the sample surface within the cryostat [189, 190].

Spatial alignment of the QD with the cavity mode is typically achieved by playing the percentages, rather than any sort of active positioning technique. For example, the material we use in our experiments typically has a QD areal density of around $100\text{--}300\ \mu\text{m}^{-2}$. For a microcavity mode with an area of $1\ \mu\text{m}^2$ (e.g., a standing wave mode in a $2\ \mu\text{m}$ diameter microdisk), this means that 100–300 QDs are expected to be spatially located within the cavity mode. By choosing cavity modes that are located within the long wavelength tail end of the QD spectrum, a small number of these QDs (ideally one) will be within temperature tuning range of the cavity mode. Of course, just because a single QD is on-resonance with the cavity mode and is spatially located within it does not mean the coupling is optimal. Optimal coupling is achieved if the electric dipole vector is aligned parallel to the cavity field, and if the QD is located at a field maximum. For cavity geometries like photonic crystals and microdisks, the field is highly oscillatory in-plane, so that relatively small displacements ($\sim 200\ \text{nm}$) of the QD with respect to the position of the field maximum can cause the observed coupling strength g to be significantly smaller than the maximum achievable coupling strength g_0 . As our experiments (and the vast majority of the experiments within the field) stand, we have no way to account for this other than to create a number of devices and hope to have some number of those devices exhibit sufficiently good QD positioning for strong coupling to be obtained. A more deterministic approach for achieving QD-cavity alignment is really contingent upon continued progress in the growth of QDs. There has recently been some exciting progress in this area by the group at the University of California at Santa Barbara [158]. In this work, very dilute samples of QDs (QD density $\sim 0.01\ \mu\text{m}^{-2}$) are grown, so that at most one QD will be located within the cavity mode. Furthermore, above each QD, a stack of five red-shifted QDs was grown all the way up to the sample surface, so that the in-plane position of the QDs within the sample could be ascertained by imaging the material (with an SEM, for example). Alignment features are then fabricated on the sample surface, and PC cavities are aligned to these features in such a way so that a single QD is appropriately positioned within each of the cavities. For future demonstrations, it will be of great use if the QD positions can not only be identified, but specified, within a regular 2D matrix, for example. This will ultimately be necessary for applications involving the integration of multiple QD-cavity systems, such as in quantum networks [141]. This topic is of interest to a number of

other important applications (such as lasers), and as such, ordered quantum dot growth is an active area of research. Techniques under consideration include growth on patterned substrates [191, 192], where recent work [193] has shown great promise, with the QDs in a hexagonal array (spacing of 5 μm) displaying an inhomogeneous spectral width of 7.6 meV and a homogeneous spectral width of 140 μeV .

Appendix A

Quantum Cascade Photonic Crystal Surface-Emitting Injection Lasers

A.1 Introduction

In this appendix, I review the results of a collaborative project between our group at Caltech and the quantum cascade (QC) laser group at Bell Laboratories, aimed at the development of photonic crystal microcavity lasers within quantum cascade heterostructures. The results I described are the focus of refs. [34, 35, 36]. Unlike the main part of this thesis, the focus here was not on the development of high- Q , small- V_{eff} resonators for cavity QED, but to instead utilize other important properties of planar PC cavities, such as their scalability and potential for surface emission, to create novel QC lasers, termed QC-PCSELs (quantum cascade, photonic crystal surface-emitting lasers). In addition, another main distinction in comparison to the PC lasers studied in chapter 3 is that these QC PC lasers are electrically injected devices. As electrical injection is a desirable characteristic for many devices, some of the techniques utilized in this work are of potential significance for applications involving high Q , small V_{eff} PC lasers.

Research in semiconductor heterostructures has led to the development of a number of optoelectronic devices in which the flow of electrons is controlled with great precision [194]. The quantum cascade laser [195, 196], one product of such progress in electronic bandstructure engineering, operates based upon intraband optical transitions (within conduction band states, or subbands) where electrons flow through a semiconductor superlattice "staircase", emitting a photon at each step. Such devices are hence unipolar (single carrier), and thus operate in a fundamentally different manner than standard semiconductor lasers, which rely upon electron-hole recombination for light generation. QC lasers have established themselves as the leading tunable coherent semiconductor source

in the mid- and far-infrared (IR) ranges of the electromagnetic spectrum [197, 198, 199].

However, due to the transverse magnetic (TM) polarization of intersubband transitions, QC lasers are intrinsically only in-plane emitters. The electric field vector is perpendicular to the semiconductor layers, and surface emission, desirable for several applications, cannot be easily achieved. The PC microcavity that we employ acts both as a source of optical feedback and as the means for diffracting light vertically from the chip to provide surface emission. In addition to enabling surface emission, our devices are greatly scaled down from standard QC devices, enabling miniaturization and on-chip integration of QC lasers, with potential applications such as multi-wavelength two-dimensional laser arrays for spectroscopy envisioned. In addition, QC PC lasers are an interesting system for research on photonic bandgap structures, as their unipolar nature, operation through electrical injection, and long emission wavelengths (and hence larger device feature sizes) are unique and advantageous aspects in comparison to previously studied interband PC lasers. In particular, the demonstration of an electrically-injected PC microcavity laser is an important step in the development of PC technology for practical applications.¹ In our QC PC lasers, an etched pattern penetrates through the laser active region, deep into the bottom waveguide cladding. This etch produces the same 2D PC pattern in the lower refractive index bottom cladding as in the waveguide core, allowing for efficient vertical confinement of the guided mode [201]. This design reduces the diffraction of radiation into the substrate, while providing a high-index contrast semiconductor-air 2D grating for strong in-plane feedback. As a result, our devices use only 10 periods of the photonic lattice (less than eight wavelengths in diameter), hence, their classification as microcavity lasers.

A.2 Basic design and fabrication

The details of the device design and measurement are given elsewhere (ref. [34] and references therein). For our purposes here, the key background information is an overview of the principles of the device operation and an understanding of the PC design strategy. fig. A.1(a) shows a schematic view of a QC-PCSEL device. Electronic current transport through a cascade of active regions and injectors within the QC heterostructure results in photon emission at $\lambda \sim 8 \mu\text{m}$. Optical feedback is provided by a PC microcavity consisting of an array of air holes that has been etched through the active region and bottom cladding of the QC heterostructure. The lattice of air holes provides distributed Bragg reflection (DBR) in two dimensions parallel to the chip.

¹At the time of publication of this work, the QC PC lasers described here were the first electrically injected PC microcavity lasers. Since that time, electrically injected PC lasers at near-IR wavelengths have also been demonstrated[200].

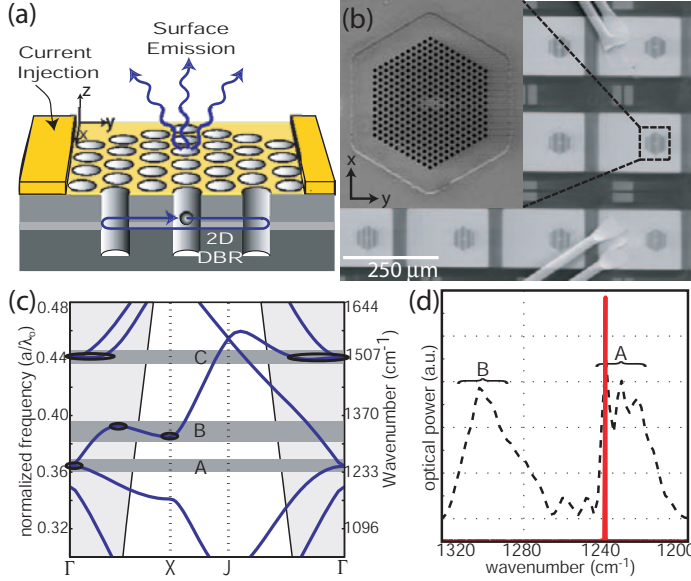


Figure A.1: (a) Schematic of a QC-PCSEL device. (b) Scanning electron microscope (SEM) image of an array of QC-PCSELs (inset shows a zoomed in top-view of a device). (c) Calculated two-dimensional in-plane TM bandstructure. The flat-band regions (*A*, *B*, and *C*) are indicated by dark gray bands. (d) Sub-threshold (dashed) and lasing (solid) emission spectra from a QC-PCSEL with lattice geometry tailored for emission centered at the *A* flat-band region.

The PC lattice consists of a hexagonal array of air holes, chosen primarily due to its connected nature (unlike a lattice of rods, for example), necessary for efficient electrical injection. The intersubband transitions in quantum wells are naturally TM-polarized (electric field normal to the epitaxial layers). Using the plane-wave expansion method [202], we thus calculate the in-plane bandstructure for TM modes, shown in fig. A.1(c) for a device with hole radius (r) to lattice constant (a) ratio $r/a = 0.30$, and with an effective index $n_{\text{eff}} = 3.35$ taken to account for vertical waveguiding. Highlighted in this bandstructure are three frequency regions of interest, labeled *A*, *B*, and *C*, which overlap flat-band regions. These flat-band regions are formed through mixing of forward and backward propagating plane waves at high-symmetry points of the PC reciprocal lattice. In these flat-band regions, low-loss resonant modes can be localized in finite lattice structures (such as our cavities) due to the reduction in group velocity over an extended region of wavevector space. Regions *A*, *B*, and *C* are specifically highlighted because they surround the flat-band regions in the frequency range close to the second-order Bragg condition. Close to the second-order Bragg condition, light can radiate into the air for surface emission, as coupling occurs to plane waves with near-zero in-plane momentum. These are the components which lie above the air-light cone (light gray region of fig. A.1(c)) and can radiate vertically. Choosing $a \sim 3 \mu\text{m}$ for a hexagonal lattice with $r/a=0.30$ aligns these flat-band regions with the QC material gain spectrum ($\lambda \sim 8 \mu\text{m}$).

Vertical optical confinement is determined by the semiconductor and metal layers comprising the QC laser structure. A key element of our design is the use of a surface-plasmon waveguide

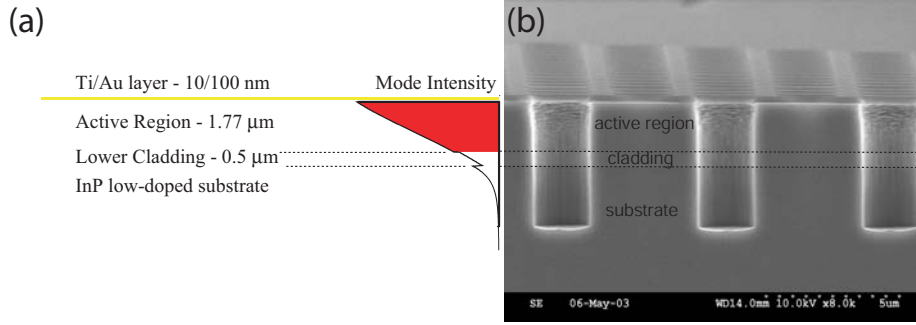


Figure A.2: (a) QC epitaxy and surface plasmon waveguide mode. (b) Cross-sectional SEM of an etched QC PC laser.

for vertical confinement [203]. This waveguide exhibits an electric field intensity maximum at the top semiconductor-metal interface (fig. A.2(a)). Particularly relevant to this work is the thinner epitaxial material (2.4 μm compared with 5.2 μm for a standard waveguide) and the absence of AlInAs cladding layers. Both of these characteristics dramatically ease the etching process, which must penetrate into the bottom InP cladding to suppress radiation into the substrate [201].

The PC patterns are created by electron beam lithography, mask transfer to a dielectric oxide layer, and transfer into the heterostructure material by inductively-coupled plasma reactive ion etching. The deep etch through the vertical waveguide core region into the bottom cladding layer (see appendix C) produces a high index contrast semiconductor-air grating (fig. A.2(b)), reducing substrate radiation losses and ensuring that only a small number of PC periods (less than 8 optical wavelengths in diameter) are required to provide strong optical feedback, in contrast to traditional second order grating based devices which typically employ a shallow etch (weak grating) and require several hundred periods of the lattice.

After etching of the PC pattern, an insulating silicon nitride layer is deposited surrounding the PC cavities, and top and back metal contact layers are evaporated, with the etched sidewalls sufficiently vertical to prevent electrical shorting. In addition, a thin metal layer, used to create the bound surface plasmon mode in the vertical direction of the waveguide, is evaporated on the surface of the cavities. An array of fully-processed QC-PCSEL devices is shown in fig. A.1(b).

A.3 Electroluminescence and lasing measurements

As described in ref. [34], low-temperature electroluminescence measurements of microfabricated devices reveal three sets of emission peaks, corresponding to regions A, B, and C in fig. A.1(c).

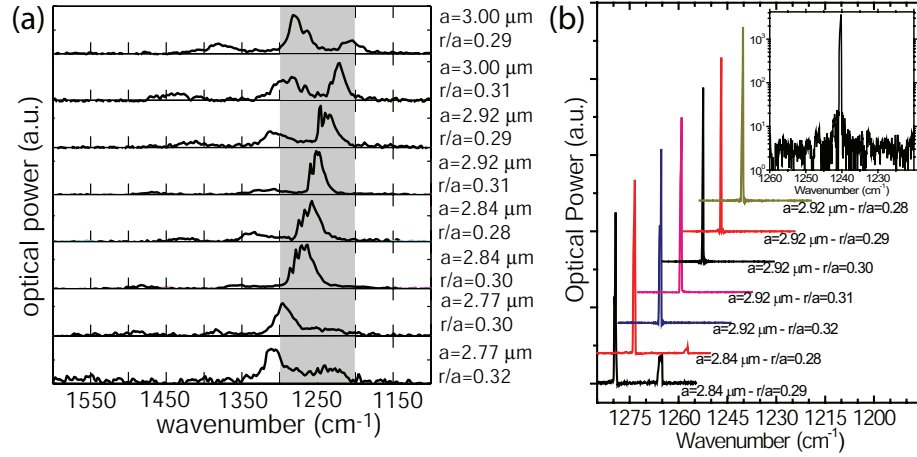


Figure A.3: (a) Emission spectra from devices with different a and r/a . The gray shaded area corresponds to the FWHM of the QC gain spectrum. (b) Tuning of the laser emission wavelength as a function of a and r/a for several different devices located on the same semiconductor chip. The lasers operate predominantly in single mode (see inset) with a side-mode suppression of at least 20 dB.

Laser emission was achieved (operating in pulsed mode with 50 ns pulse width at 5 kHz repetition rate), and is seen to tune with the hole radius and lattice spacing of the PC cavity in accordance with simulation predictions (fig. A.3). Figure A.1(d) shows the subthreshold and lasing emission spectra for a device with lattice geometry chosen to align the gain peak to the A flat-band region. Lasing always originated from the highest frequency (wavenumber) resonance within the A-peak. The majority of the devices exhibit single mode laser emission in pulsed mode. By selecting devices with different values for a or r , multi-wavelength emission from the same semiconductor chip is achieved (fig. A.3).

As described in ref. [36], a careful analysis of the experimental data (spectral information, far-field emission measurements and polarized intensity measurements) and numerical simulations shows a close correspondence between theory and simulation, and provides a unique identification of the lasing mode. The first step in the process of identification of the laser mode is to determine its symmetry. Here, we consider the behavior of the laser mode under reflection about the cavity's \hat{x} and \hat{y} axes (see fig. A.1(b) for the definition of these axes with respect to the cavity). The polarized spatial distribution of the laser's vertically emitted field intensity is studied by placing a polarizer in front of a micro-bolometer camera fitted with a lens (fig. A.4(a-b)). The nodal lines (lines of near-zero intensity in the images) along the \hat{x} and \hat{y} axes of fig. A.4(b) for the \hat{y} -polarized intensity pattern are consistent exclusively with an electromagnetic field mode which is odd (parity -1) under

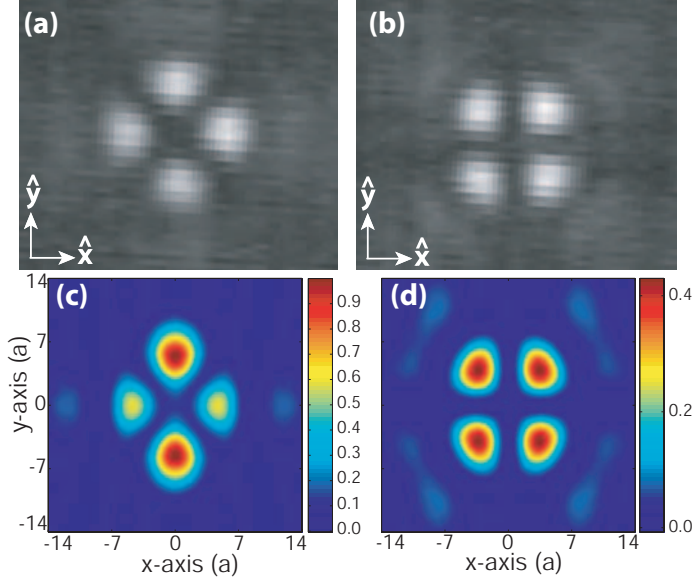


Figure A.4: (a) Polarized emission pattern (taken in a plane close to the near field of the PC cavity surface) of a typical lasing device for an electric field polarization along the (a) \hat{x} -axis and (b) \hat{y} -axis of the cavity. FDTD-generated (c) \hat{x} -polarized and (d) \hat{y} -polarized vertical emission pattern at a few wavelengths above the PC cavity.

a mirror symmetry about the \hat{y} -axis and which is even (parity +1) under a mirror symmetry about the \hat{x} -axis. Such a mode is said to have B_1 symmetry, using the nomenclature of chapter 1. A similar conclusion is reached by studying the \hat{x} -polarized intensity pattern of fig. A.4(a), which has anti-nodes along both the \hat{x} - and \hat{y} -axis. Thus, the two polarized intensity patterns of fig. A.4(a-b) indicate that the laser emission is single mode and of B_1 symmetry.

To better understand the vertical emission characteristics of the PC microcavity modes, full 3D-FDTD simulations were performed. The hole depth was taken to be 5 microns and a 200 nm thick idealized 'perfectly conducting' metal top contact was used to guide the TM surface wave (at a wavelength of $8\text{ }\mu\text{m}$ this is a reasonable approximation for a gold metal contact [204, 93]). To reduce the size and time of the simulation, the cavity was limited to 6 periods of the hexagonal lattice as opposed to the 10 periods used in the experiment. Mirror boundary conditions were used to project the modes of the hexagonally symmetric cavity onto a basis compatible with the symmetry of a rectangle whose principal axes lie along the \hat{x} - and \hat{y} -axis of the PC microcavity.

The highest frequency resonant mode of the A-peak was found to be of B_1 symmetry (we refer to this mode simply as the B_1 mode from here on). This is consistent with the experimentally measured emission spectrum (fig. A.1(d)) and with the laser near field symmetry (fig. A.4(a-b)). Figure A.5(a-b) shows the electric field component normal to the semiconductor-metal surface (E_z) and its in-plane spatial Fourier transform (\tilde{E}_z) for the B_1 mode. It is interesting to note that this mode has only a small overlap with the central region of the PC cavity, a characteristic which

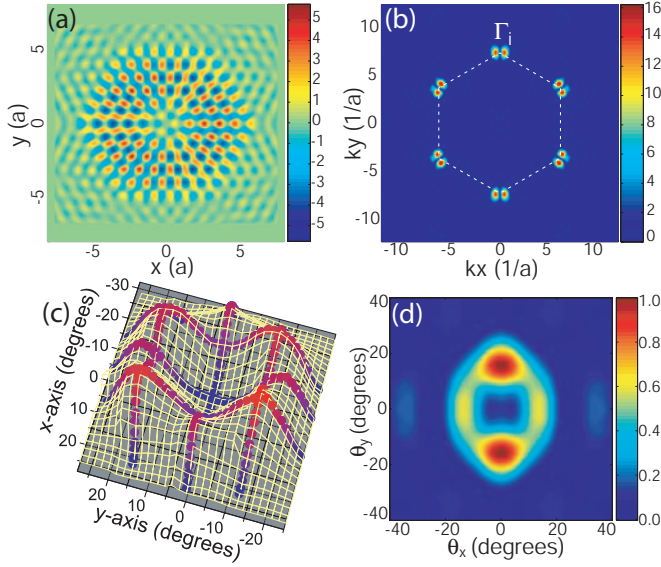


Figure A.5: FDTD-generated plot of (a) E_z and (b) \tilde{E}_z for the B_1 mode in the plane of the PC cavity just beneath the metal contact in the semiconductor active region. (c) Far-field emission pattern of the PC microcavity laser. The experimental data is shown as blue/red dots, and an interpolation of the line scans (shown as a light yellow grid) is used to generate an approximate 2D intensity image. (d) FDTD simulation of the far-field intensity pattern for the high-frequency mode within the A-peak set of resonances.

may partially explain its preferential selection as the lasing mode, due to the expected in-plane spreading resistance in the etched PC region and consequent higher current injection and gain in the periphery of the PC. Calculations of the vertically emitted radiation field, taken in a plane several wavelengths above the cavity surface, were performed by eliminating the non-propagating FDTD near field components and introducing, to simulate the experimental conditions, a 30° collection angle cut-off for the imaging optics. The resulting \hat{x} - and \hat{y} - polarized intensity patterns of the B_1 mode are shown in fig. A.4(c-d), and closely match the polarized micro-bolometer camera images (fig. A.4(a-b)).

As a final consistency check, far-field emission measurements and calculations were performed. Figure A.5(c) shows a typical far-field intensity pattern of the B_1 lasing mode, measured by scanning a $300 \times 300 \mu\text{m}$ nitrogen-cooled HgCdTe detector in a plane parallel to the semiconductor chip surface at a distance of approximately 10 cm without any intermediate optics. The theoretical far-field emission pattern was calculated by transforming the FDTD generated radiation field into the far-field [205] and is shown in fig. A.5(d). The increased intensity of the two lobes on the \hat{y} -axis in fig. A.4(c) of the \hat{x} -polarized intensity and in fig. A.5(d) of the far-field pattern is likely a result of inadvertent symmetry breaking of the hexagonal symmetry of the PC cavity in the FDTD simulation.² In this case, the computed near field under the metal contact is still very symmetric, as shown in fig. A.5(a). The symmetry breaking in the measured far field (experimentally we observe

²This may result from discretization error in employing the mirror boundary conditions and/or the rectangular boundary of the simulation volume.

the opposite effect, more intensity in the \hat{y} -polarization), is possibly a result of the rectangular metal contact geometry and/or non-uniform current injection.

The FDTD-calculated radiative quality factor (Q) of the B_1 mode was found to be roughly a factor of two higher than the Q value of the neighboring A-peak resonant modes, helping explain why it is the first mode to lase. The calculated in-plane, top, and substrate radiation rates, as given by effective cavity quality-factors, were $Q_{||}=600$, $Q_t=10,000$, and $Q_s=7,000$, respectively. An estimate for the Q value associated with internal loss in the metal and semiconductor at 8 microns ($\alpha_i = 40 \text{ cm}^{-1}$) is $Q_a=800$. Thus, the total vertical extraction efficiency of the PC microcavity laser is estimated to be $\eta_t = Q_t^{-1} / (Q_{||}^{-1} + Q_t^{-1} + Q_s^{-1} + Q_a^{-1}) = 3\%$. The vertical extraction of light in this case is due to the radiation of small in-plane Fourier components near the Γ -point of the hexagonal PC reciprocal lattice (fig. A.5(b)), as in second-order Bragg diffraction. The coupling of radiation from the bottom semiconductor-metal interface to the top metal-air interface (from which the radiation finally escapes) is mediated through the air holes [204], as well as through the metal itself (although this last effect has not been included in our simulations).

These PC microcavity lasers combine the electronic bandgap engineering exploited in QC lasers and the optical dispersion engineering of photonic crystals. The result is a photonic crystal injection laser that may open new horizons in device design and application in the mid- to far-IR ranges of the electromagnetic spectrum. In particular, multi-wavelength surface emission makes these devices interesting from the perspective of spectroscopy applications, as many trace gases and complex molecules can be probed in this wavelength region [206, 207]. The open cavity architecture of these holey devices makes them interesting from the perspective of integration with fluids; microfluidic technology [208, 209] can, in principle, be integrated with these devices to allow for precise delivery of these fluids to the cavity regions. The introduction of the fluid should affect the L-I characteristic (light out versus injected current) of the device, for example, through a modification of the laser threshold current. Electrical readout (a kind of 'detectorless' spectroscopy) within these systems is a promising possibility with QC-PCSEL-based devices.

Significant improvements in device performance must be made in order for these applications to become accessible. In particular, the operating temperature must be increased, and the threshold current needs to be reduced. Current efforts, led by Raviv Perahia at Caltech, are focused on reducing current spreading in the devices as a means to help achieve these goals.

Appendix B

Finite-Difference Time-Domain Simulations

The photonic crystal cavities studied in this thesis are numerically investigated through the finite-difference time-domain (FDTD) method, reviewed in detail by Taflové [6]. The FDTD algorithm discretizes Maxwell's equation, replacing derivatives with finite differences that are second order accurate. The implementation that is commonly used is based on the Yee algorithm [210], which is essentially a direct solution to Maxwell's curl equations, solving for both the electric and magnetic fields in time and space. The Yee algorithm follows a grid (fig. B.1(a)) in which every electric field component (E) is surrounded by four circulating magnetic field components (H), and vice versa. This arrangement means that Faraday's and Ampere's laws (which are integral forms of Maxwell's equations) are automatically satisfied, as are Gauss's divergence laws. In terms of boundary conditions, this arrangement naturally assures the continuity of tangential field components across material boundaries that follow the cartesian grid.

FDTD is very appropriate for modeling structures such as our PC cavities, where the refractive index varies significantly on the sub-wavelength scale; other techniques that approximate Maxwell's equations with a wave equation usually require a slowly varying refractive index. In addition, because it does not require matrix inversion techniques, FDTD can be used to do full three-dimensional modeling of microphotonic structures. Accurate estimates of important properties such as the frequency, quality factor, and modal volume can be obtained.

The code that we use was originally written by Brian D'Urso, an undergraduate in Professor Axel Scherer's group at Caltech, and has since been modified by a number of graduate students. Full three-dimensional simulations of PC cavities are typically performed in the following fashion. To reduce the simulation time, only one-eighth of the cavity volume is simulated (the upper octant, for

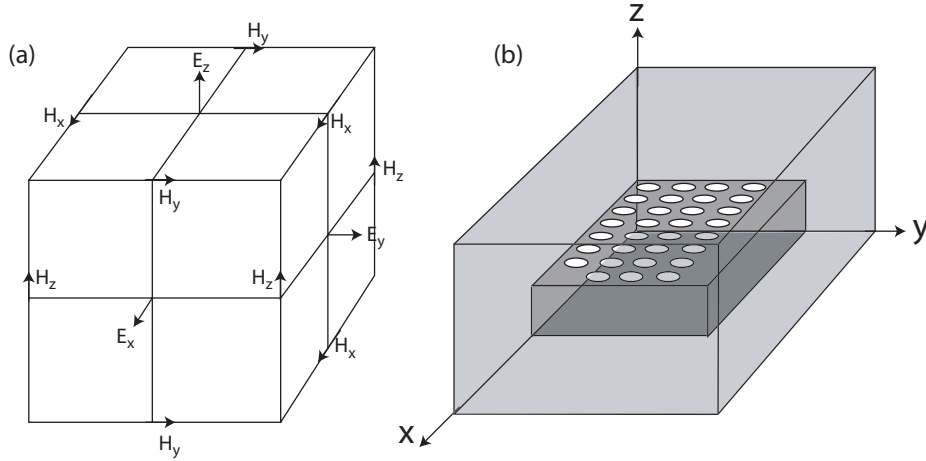


Figure B.1: Setup for FDTD simulations. (a) Yee space lattice, as formulated in ref. [210]. Figure adapted from ref. [6] (b) Typical simulation volume for 3D photonic crystal cavities. Mirror boundary conditions are applied along the planes $x=0$, $y=0$, and $z=0$; Mur's absorbing boundary conditions are applied along the other three faces of the simulation volume.

example), with mirror conditions chosen for three of the cavity boundaries. Absorbing conditions are chosen for the other three boundaries, and an air region, typically on the order of two-thirds of a free-space wavelength, is placed above the cavity to allow the field to adequately decay before it reaches the boundary. In the in-plane dimensions, the field has already decayed within the photonic crystal region so that only a small air region (or no air region at all) is needed in those dimensions. Figure B.1(b) shows a schematic of this. To adequately represent the field within the structure, we choose a discretization of 20 points per lattice constant (which typically translates to about 80 points per free space wavelength for the devices we study). With this resolution, the total number of grid points is typically on the order of 2×10^6 (200x200x50, for example).

To calculate the cavity mode field patterns in chapter 2, a two-step process is used. We first calculate the time evolution of an initial field placed within the cavity, and record this time evolution at some small number of judiciously chosen spatial points (~ 5 -10). The initial field is a delta function in time and has a Gaussian spatial profile, and is chosen to have the polarization of interest (TE or TM). Modes of a specific symmetry can be chosen through proper choice of the mirror boundary conditions; alternately, if a full structure is simulated, the initial field is spatially located off-center to allow for excitation of modes of both even and odd spatial symmetry. The field as a function of time is fourier transformed to give its spectral content. Cavity modes appear as peaks within this spectrum.

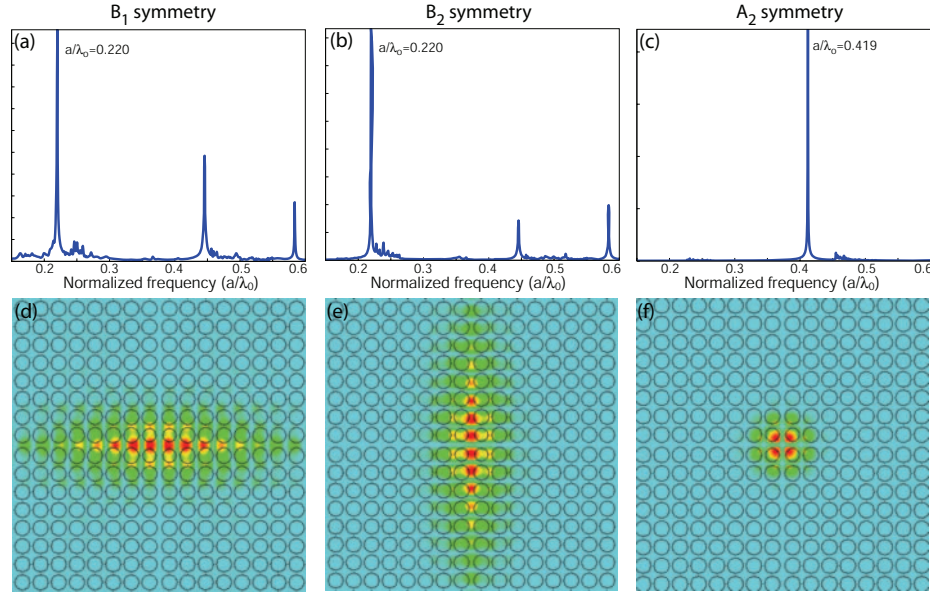


Figure B.2: FDTD spectra and mode field patterns for TM-polarized donor type defect modes in a square lattice photonic crystal. (a)-(c) Spectra for modes of (a) B_1 , (b) B_2 , and (c) A_2 symmetry. (d)-(f) $|\mathbf{E}|$ for the specified modes in (a)-(c)

Figure B.2(a)-(c) shows examples of such spectra, taken from ref. [37]. The system studied here is a simple square lattice donor-type defect centered about point e in the lattice (see chapters 1 and 2 for the labeling of high symmetry points in the square lattice), where we are focused on TM-polarized modes due to their applicability for QC lasers. From the group theory analysis of chapter 1 (extended to cover TM modes), we know that the two X -point donor type defect modes off the first conduction band are predicted to have B_1 and B_2 symmetry, and the donor type mode off the M -point of a higher frequency band is predicted to have A_2 symmetry. This knowledge allows us to specify the mirror boundary conditions; a separate simulation is run for each symmetry type (three simulations in all here).

The second step of the process is to determine the spatial field profiles for the cavity modes. To solve for the field profile for a given mode, we take the modal frequency determined through the spectral calculation described above, and use it as the center frequency for a bandpass filter. The initial field (chosen to have the appropriate polarization) is then convolved in time with the bandpass filter [211], whose width is slowly decreased as the initial field evolves and begins to stabilize. The cavity Q is calculated by determining the stored energy in the cavity (U) and the radiated power to the boundaries (P_d), with $Q = \omega U / P_d$. Example modal field patterns generated by this technique are shown in fig. B.2(d)-(f).

In the design of high- Q cavities presented in chapter 2, we made frequent use of the spatial Fourier transform of the cavity mode as a diagnostic tool for understanding radiation losses within a given design. In these calculations, we Fourier transform the complex field pattern $\mathbf{E}(\mathbf{r})$. By doing so, we capture all of the spatial Fourier components, regardless of the time at which the snapshot of the field is taken. The real, physical electric field can be written in terms of this complex field pattern as $\mathbf{E}(\mathbf{r}, t) = (\mathbf{E}(\mathbf{r})e^{-i\omega_0 t} + \mathbf{E}^*(\mathbf{r})e^{i\omega_0 t})/2$. To generate the complex field pattern, we take snapshots of the real field at times t and $t + T/4$, where $T/4$ is a quarter period ($T = 2\pi/\omega_0$), so that $\mathbf{E}(\mathbf{r}) = \mathbf{E}(\mathbf{r}, t) + i\mathbf{E}(\mathbf{r}, t + T/4)$. Typically, the times are chosen so that they coincide with the magnetic field maximum (at time t , for example) and the electric field maximum (at time $t + T/4$).

Appendix C

Fabrication Notes

In this appendix, I have compiled some notes that, for the most part, focus on the etching of materials using an inductively coupled plasma reactive ion etch (ICP-RIE) tool. The initial part gives a general overview of some of the considerations taken into account when processing these materials when the focus is on the creation of microphotonic structures. I then consider fabrication within specific material systems that are relevant to this thesis, including Si, GaAs/AlGaAs, and the quantum cascade heterostructures considered in appendix A. As fabrication of photonic crystal cavities within the InP-based multi-quantum-well material was considered in detail in chapter 3, no specific further consideration of those devices is given here.

C.1 Process flow and general considerations

The process flow for fabricating a device such as a photonic crystal microcavity (fig. C.1) typically consists of 1) deposition of a hard mask layer (occasionally not required), 2) spin coating of the sample in electron beam resist and subsequent electron beam lithography, 3) plasma etching (also known as dry etching) of the mask layer, and 4) plasma etching of the primary material layer (typically a semiconductor layer in the applications we consider). For some devices, such as the passive PC resonators and optically pumped lasers described in this thesis, these steps are followed by a wet etch step to undercut the devices. For more complicated structures, such as electrically-contacted devices, a number of additional fabrication steps are required.

The creation of low loss optical devices requires an optimization of the steps listed above. For the plasma etching steps, there are a number of factors to take under consideration. One of the most important is the mask layer used during the etching; the strength and quality of the mask layer determines what types of etches can be used. Due to the small feature sizes needed for most of

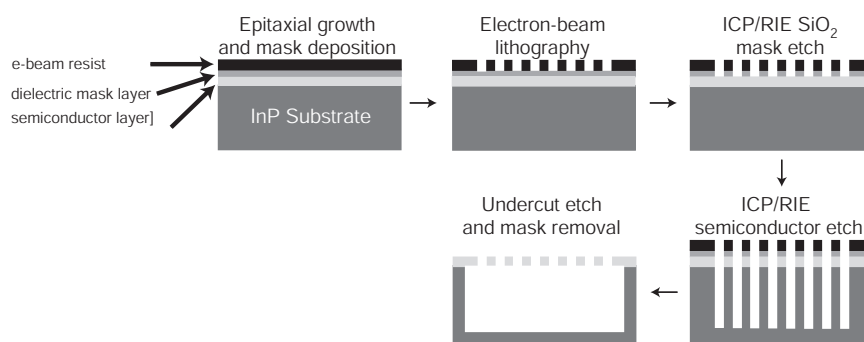


Figure C.1: Process flow for fabrication of microphotonic devices such as photonic crystals.

our structures, the starting point will always be an electron beam mask. A relatively soft mask (such as an electron beam resist mask) that is easily damaged through the dry etching procedures necessitates the use of a low impact dry etch, while harder masks such as dielectric layers provide greater etch selectivity and the ability to use a wider variety of etches, but come at the expense of having to develop a method to fabricate the dielectric mask. For semiconductor etches that are deeper than a few hundred nanometers, a hard mask is typically a necessity. For most of the devices we consider in this thesis (with the exception of the QC lasers), the required etch depth is just a couple hundred nanometers (corresponding to a half-wavelength of light in the material). In such cases, direct etching into the semiconductor using the electron beam resist is a possibility, although the benefits (and drawbacks) of this simpler approach must be weighed against the merits of using a dielectric mask. To use a dielectric mask, one has to develop a suitable etch recipe for transferring the pattern from the electron beam resist to the dielectric layer, and this can be, in some cases, as difficult as etching the semiconductor layer directly.

Once a masking material is chosen, the plasma etching processes can be calibrated. Plasma etching is used because of the anisotropic etch profiles that it can create; PC cavities, for example, require vertical sidewalls to sustain high Q s. Wet etching, on the other hand, can produce very smooth etched surfaces, but the etch profiles are often slanted and control of feature sizes can be difficult (due to undercutting of the mask layer). The system we use for plasma etching is an Oxford Instruments Plasma Technology (OIPT) ICP-RIE, which has the advantage of allowing for independent control of the plasma density (through variation of the ICP power) and the kinetic energy of the resulting ions (through application of RF power to the wafer table/electrode upon which the sample sits). This allows for the development of processes that employ a precise combination of chemical etching and physical etching (ion milling) to create anisotropic, smooth sidewalls. In addition,

we have control over gas chemistry (Ar, N₂, H₂, O₂, Cl₂, SF₆, and C₄F₈ are our available gases), chamber pressure, and sample temperature (either through control of the temperature of the lower electrode or the application of He to the backside of the sample). Typically, we begin development of an etch process by starting with an etch recipe provided by OIPT, or by searching the technical journals (particularly the *Journal of Vacuum Science and Technology B*) to see what work has been done by other groups. This essentially serves to give us a starting point, but the final etch is often quite different from this initial recipe. One reason for this is that the low loss, micro-optical structures of interest to us are often quite different than the applications for which many previous etch recipes have been developed, so that the requirements on the etch can also be significantly different. In addition, structures such as PCs contain very small confined spaces whose etch behavior is markedly altered relative to that of more open structures (both the delivery of source gases and the removal of etched by-products can be modified within these confined regions). Finally, most etch recipes in the literature are calibrated using photoresist, a dielectric layer, or a metal layer as an etch mask. While we will often use a dielectric etch mask immediately before etching of a semiconductor layer, the initial mask, where the cavity geometry is first defined, and from which the dielectric mask is created, is usually an electron beam layer.

Before considering the specific processes employed to create the structures studied in this thesis, let us review some of the process parameters involved in the plasma etching. The gas chemistry used is determined by the material system being etched; chlorine-based chemistries, for example, are known to be effective in etching III-V heterostructures, while fluorine-based chemistries are often used for silicon, silicon dioxide, and silicon nitride. Reference [212], for example, lists many of the common etch chemistries used to etch semiconductor materials. Once a chemistry is selected, gas flows must be chosen. Here, the important things to consider are the ratio of the gas flows (for example, the ratio of Ar to the ratio of Cl₂ when etching GaAs) and the total gas flow. The total gas flow needs to be chosen in such a way that a sufficient amount of gas reaches the sample (so that the etch is not reactant-limited), but should not be so high that the gas does not have a sufficient amount of time to react with the material. Typical total gas flows are on the order of 20-30 sccm (standard cubic centimeters per minute) for the processes we have used. The ratio of the gas flows will, among other things, affect the etched sidewall angle and smoothness; examples of this will be shown below.

The chamber pressure is another important process parameter. Typically, the chamber is held at a baseline pressure of $\sim 10^{-7}$ torr when no process is being run; typical process pressures are ~ 10

mTorr. The effect of the chamber pressure on the etch behavior can be somewhat difficult to gauge. In principle, if the etch is one in which chemical etching is the dominant mechanism, an increased chamber pressure will increase the concentration of the reactive elements and can speed up the etch (though the etch rate may eventually saturate). If the etch is primarily a physical milling process, an increased pressure will also initially increase the etch rate, but may eventually cause it to slow, as the increased pressure may cause collisions between ions that will reduce the kinetic energy with which they bombard the surface.

The ICP power level sets the density of ionized atoms. In addition, it can have an effect on the sample temperature; dense plasmas generated by high ICP powers can cause heating of the sample, which can dramatically influence the etch rate, sidewall profile, and sidewall roughness. This effect has been exploited in our etching of QC heterostructures, as described below in section C.4. The RF power level sets a DC Bias, which is basically a potential difference between the plasma coils and the lower electrode upon which the sample sits. This DC Bias drives the ions into the sample; a large DC Bias will impart significant kinetic energy into the ions, making physical etching a dominant process. A large ion milling component will significantly affect the etch mask as well, so that high DC Bias etches typically require use of a hard dielectric etch mask. In addition, a high DC Bias can heat the sample.

C.2 Si-based devices

We have been able to create high aspect ratio Si PC structures through direct transfer using an electron beam resist; this has basically been made possible as a result of the relative ease with which Si can be etched and the relatively thin (~ 350 nm) waveguide layer we employ in our devices. The starting point for our process was an OIPT recipe that called for a relatively low RF power (50 W), a high ICP power (1200 W), and a C_4F_8/SF_6 etch chemistry. This was a very appealing etch in that it did not require the special operating conditions that other Si etches do (such as cryo-cooling or gas chopping).

The first step in the etch calibration was to determine the gas flows to be used. This was done by fixing a total gas flow and varying the ratio of C_4F_8 to SF_6 . The behavior of the etch as a function of this ratio was very controllable; higher SF_6 flows would increase the verticality of the etch (though flows that are too high would undercut the mask), while C_4F_8 could be used to smoothen the sidewalls and counteract the chemical etching by SF_6 . After a suitable flow ratio was chosen,

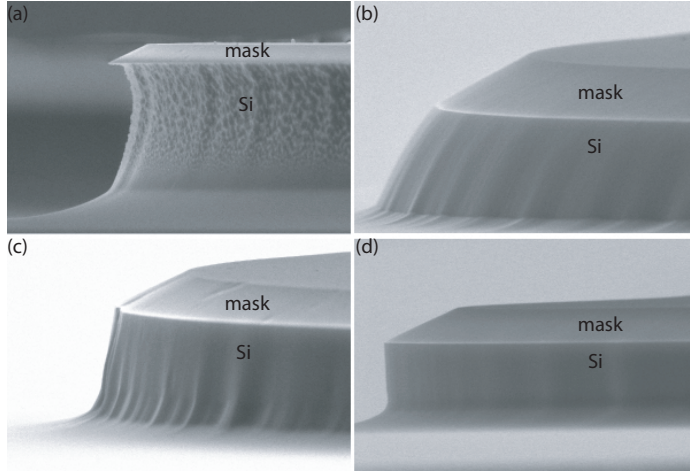


Figure C.2: SEM images of the Si ICP-RIE etch with varying gas flow and RF power. (a) RF=50 W, C_4F_8 =11 sccm, SF_6 =12 sccm (b) RF=50W, C_4F_8 =22 sccm, SF_6 =12 sccm (c) RF=50W, C_4F_8 =11 sccm, SF_6 =12 sccm (d) RF=20W, C_4F_8 =11 sccm, SF_6 =12 sccm.

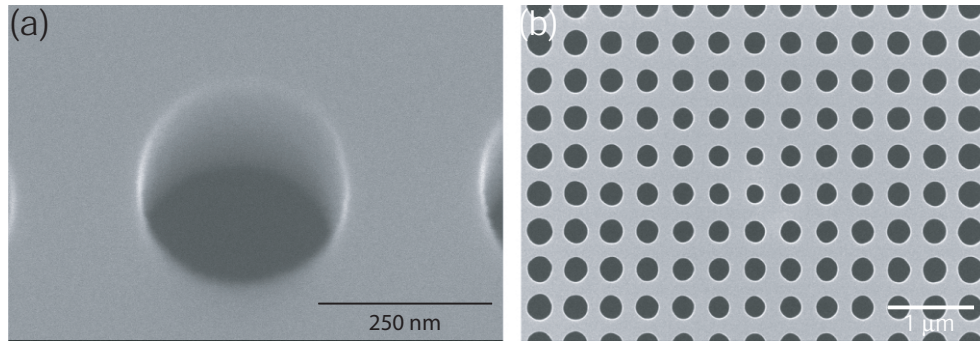


Figure C.3: (a) Angled and (b) top view SEM images of the Si etch used in fabrication of high- Q PC cavities.

the RF power was varied to limit mask erosion as much as possible. Figure C.2 shows SEM images of an etched sidewall as function of different process parameters. The initial etch calibration was done using a photoresist mask consisting of a relatively large circle. After a reasonable etch had been achieved with this mask, PC patterns in an electron beam resist were used in the final etch optimization. The primary modification here in comparison to the process used in fig. C.2(d), for example, is a further reduction in RF power and a bit of an increase in the C_4F_8 gas flow. Figure C.3(a) shows an angled SEM image of an etched PC pattern, showing the sidewalls to be both smooth and vertical. Figure C.3(b) is a top view SEM image of an etched structure, indicating that the holes are smooth and circular, which is a good indication that the etch that has been employed does not significantly damage the electron beam mask, thereby allowing faithful transfer of the PC pattern into the Si layer.

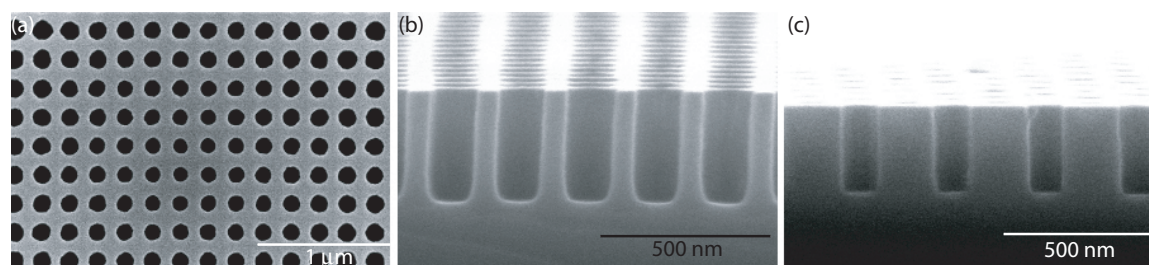


Figure C.4: Top view and cross sectional SEM images of AlGaAs PC cavities fabricated using an SiO₂ etch mask.

C.3 AlGaAs-based devices

As briefly mentioned in the preface, the GaAs/AlGaAs system dry etches with an ease that, qualitatively, is somewhere between Si (easy) and InP (hard). At the time we began our work on etching AlGaAs structures, we had already developed an etch recipe for InP using an SiO₂ mask (chapter 3), and our hope was to simply use this mask. We would then use some form of an Ar/Cl₂ chemistry to plasma etch the AlGaAs layer, and the PC membrane would be undercut with a dilute HF acid wet etch. In general, fabrication processes can be difficult to reproduce, as the condition of the etch chamber is continuously changing over time, particularly for chambers (such as ours) in which multiple materials are etched. As a result, even after a process has nominally been completely developed, there is often some kind of re-calibration period needed prior to fabrication of a new set of devices, particularly if it has been a few weeks since the last round of fabrication. When I started doing SiO₂ etches for the purpose of AlGaAs fabrication, it had been about 8 months since our InP-based PC microcavity laser work, and our ICP-RIE had mostly been used for Si etching during that time. For reasons that were never completely explainable, we were unable to replicate our previous success with the SiO₂ etch; the etch now seemed to burn the resist somewhat, and produced misshapen holes, even after many attempts at modifying the etch to make it less damaging to the resist. We were able to develop a subsequent AlGaAs etch that could produce smooth, vertical sidewalls for a range of hole sizes, but the problems we had with the lack of circularity in the holes seemed to be significant enough to warrant investigation of other masks. Figure C.4 shows the results of our AlGaAs processing with an SiO₂ etch mask. The AlGaAs etch employed was a simple derivative of the InP etch described in chapter 3, but now done at room temperature, with modifications to the Ar/Cl₂ gas flows (the Ar/Cl₂ ratio was now typically 10/5 sccm) and slight adjustments to the RF and ICP powers.

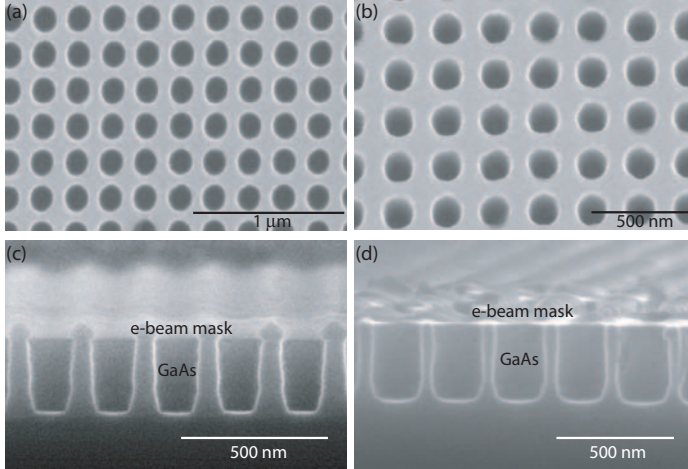


Figure C.5: SEM images of AlGaAs photonic crystals using direct pattern transfer from an electron beam mask. (a) top view, (b) angled view, and (c)-(d) cross sectional view, showing the different sidewall angles for different hole sizes.

Another possibility was to transfer the PC pattern directly from the electron beam resist to the AlGaAs layer. We spent a few weeks working this out, and developed a reasonably good AlGaAs etch that was able to do this while maintaining good hole shapes and without overly damaging the resist. This etch was again a derivative of the InP etch, performed at room temperature, with significantly lower RF powers (now ~ 70 W) and an Ar/Cl₂ gas ratio of $\sim 10/5$ sccm. The electron beam resist seemed to be less adversely affected by the Ar/Cl₂ chemistry (in terms of the hole shape) than the C₄F₈/O₂ chemistry used to etch the SiO₂, even though the RF power and DC Bias levels used were fairly similar. However, maintaining sidewall verticality over the range of hole sizes used in our graded lattice designs was difficult, and it was clear that the etch did undercut the electron beam mask, so that producing a desired hole size would take some amount of calibration (this seemed particularly difficult in that the hole size varies widely in our graded lattice design). As angled sidewalls can cause a significant increase in loss in planar photonic crystals [114], we decided that a dielectric etch mask would probably be a necessity. The advantage in using a dielectric mask is that the range of RF powers that can be used is significantly larger (with the electron beam mask, we had to limit the RF power to avoid etching the mask away too quickly or beginning to burn the mask). Nevertheless, the direct transfer approach, summarized by the SEM images in fig. C.5, remains a potentially viable option, particularly if further optimization can be done to help improve the sidewall verticality.

In order to etch a dielectric mask without burning the electron beam resist, we wanted to adopt an etch that would be similar to what we used for Si, where we were able to transfer the PC patterns into the Si device layer while only using an electron beam mask. This did not seem far-fetched,

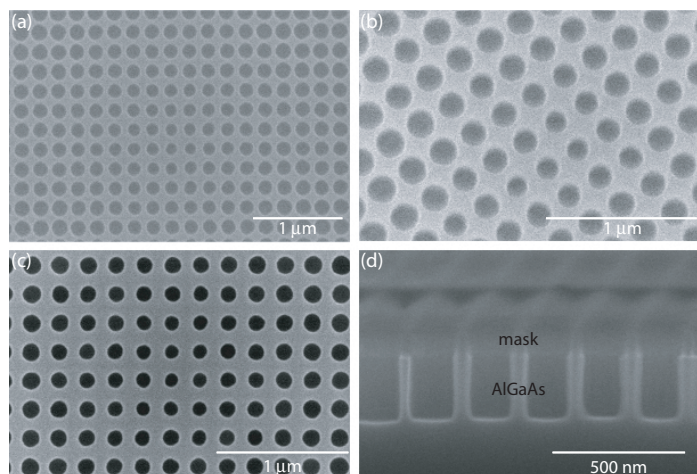


Figure C.6: SEM images of photonic crystal patterns in a SiN_x mask and subsequent transfer into AlGaAs. (a)-(b) Top view and angled image of the SiN_x mask. (c)-(d) Top view and cross sectional image of the AlGaAs layer using the SiN_x as an etch mask.

as both Si and SiO_2 can be dry etched using a fluorinated chemistry. However, when we tried to etch the SiO_2 with this low RF power etch, it was not very successful; the etch proceeded very slowly and the sidewalls were not vertical. Another option for the mask was SiN_x , which we could also deposit with our PECVD. The nitride mask was a great choice, primarily because it could be effectively etched using essentially the same conditions as what we used for Si. The etch rate was certainly much slower than what it was for Si, but on the positive side, the resist was not burned or misshapen during the etch, and we had a sufficiently thick resist layer to be able to etch through the nitride mask (~ 200 nm thick). Results for the nitride etch are shown in fig. C.6(a)-(b); typical process conditions were quite similar to the Si etch described above. Once this etch was developed, we used an AlGaAs etch (fig. C.6(c)-(d)) that was essentially identical to that used when we tried an SiO_2 mask, as the SiN_x had nearly the same etch selectivity.

We used the SiN_x and AlGaAs etches developed for PC cavities as a basis for etching the microdisk structures investigated in the second part of this thesis. The main difference in the etches were the gas chemistries and RF powers used; we typically decreased the chemical nature of the etches (increased C_4F_8 for the SiN_x , decreased Cl_2 for the AlGaAs), and slightly reduced the applied RF power. With the microdisk cavities, the primary objective is to make the disk sidewall smooth; this has led to us adopting etches where sidewall verticality has been sacrificed in favor of smoothness.

The SiN_x etch can be a bit unpredictable in practice. In particular, if the C_4F_8 flow is too low, the etched sidewalls can be very rough. Figure C.7 shows the results of some poor etches; the sidewall roughness in the mask is clearly transferred into the AlGaAs layer. As the state of our etching

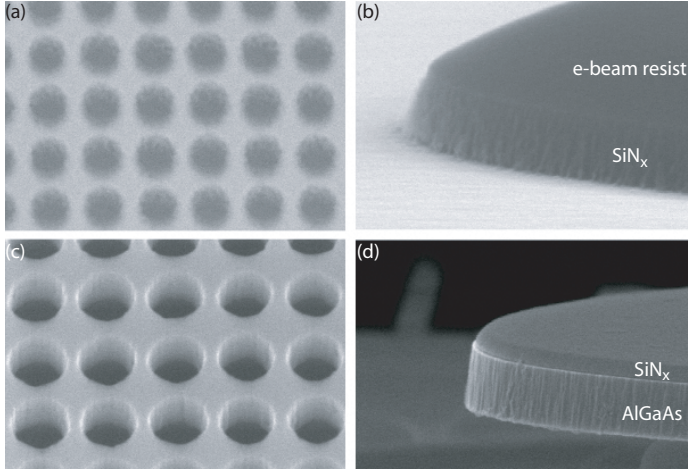


Figure C.7: SEM images of photonic crystal and microdisk patterns when the SiN_x etch does not turn out properly, most likely because of too low a flow of C_4F_8 . (a)-(b) SiN_x PC and microdisk mask and (c)-(d) AlGaAs layer using the SiN_x as an etch mask.

chamber is essentially constantly varying in time, we typically have to re-calibrate the SiN_x etch before each new processing batch. This usually involves a couple of practice etches that are used to determine the precise C_4F_8 and SF_6 flows and RF power that will etch the material appropriately given the current state of the etch chamber. In addition, chamber cleaning runs are periodically run, in principle, to reset the condition of the chamber.

C.4 ICP-RIE etching of quantum cascade heterostructures

The quantum cascade lasers discussed in appendix A required a dry etch optimization to be able to create relatively deep ($\sim 4\text{-}5\ \mu\text{m}$), etched features ($\sim 2\ \mu\text{m}$ diameter holes) with vertical sidewalls in an InP-based heterostructure. The starting point was a 500 nm thick SiO_2 mask (etched at Bell Laboratories) that had smooth and relatively vertical sidewalls ($> 85^\circ$). Our efforts on developing this etch are reported in ref. [35].

Dry etching of In-containing III-V semiconductor materials is typically accomplished using one of two gas chemistries [115]. The first, using a CH_4/H_2 mixture, is performed at room temperature but is relatively slow ($< 60\ \text{nm/min}$) and suffers from heavy polymer deposition during the process. Cl_2 -based plasmas have also been used, but the low volatility of InCl_x products at room temperature requires some form of heating to be employed. One method for producing smoothly etched, vertical sidewalls in an InP-based semiconductor system is direct heating of the wafer table ($> 150^\circ\text{C}$). Such a process was employed to etch the near-IR PC lasers of chapter 3, for example.

The Cl_2 -based plasma etch that we discuss in this appendix does not make use of direct wafer table heating, but rather uses the high density plasma produced by the ICP system to provide local

surface heating of the sample and an increased efficiency in the sputter desorption of the InCl_x products [115]. Such an etch has been used by Fujiwara et al., to etch 8 μm diameter, 3.6 μm deep holes in a photonic bandgap structure [116].

The ICP-RIE etch was studied as a function of ICP power (300-500 W) and RF power (100-350 W), with the chamber pressure ($P_{ch} = 3$ mTorr) and Ar: Cl_2 gas chemistry (12 sccm:8 sccm) kept fixed, and no He backside cooling. The final ICP and RF powers chosen were 350 and 250 W, respectively, and produced vertical sidewalls with an acceptable amount of sidewall roughness (fig. C.8). Lower RF powers produced extremely pitted (and slightly angled) sidewalls throughout both the core and cladding layers (which we attribute to the decreased volatility of the InCl_x etch products, resulting from the lower sample temperature and/or lower desorption rate caused by the reduced RF power), while higher RF powers created smooth sidewalls in the lower cladding and InP layers but increased roughness in the core layer (attributed to pitting that occurs in Al-containing layers that are etched at too hot a temperature). Similar effects on the sidewall roughness were observed as the ICP power was varied. These results suggest that the sample temperature (generated by the plasma) is a leading factor affecting sidewall roughness. The percentage of Cl_2 in the gas mixture, which can also play a role, has been varied between 30% and 50%, with a value of 35% (7 sccm) finally chosen as the best compromise between decreased sidewall roughness (seen for lower Cl_2 percentages) and improved sidewall angle (seen for higher Cl_2 percentages). For our typical etch times ($t \sim 4.75$ min), etch depths of 5 μm are achieved.

Using the plasma as a mean of increasing the sample temperature indicates that the etch rate (and therefore etch depth) will be a nonlinear function of time, as some amount of time is required for the temperature to reach a value hot enough for the InCl_x compounds to be sufficiently volatile. This has been observed experimentally, as etch times under 3 min have produced devices with angled holes and non-volatile InCl_x etch products. Note that the change in sample temperature as a function of time for a number of different process parameters has been investigated in detail by Thomas III et al. [213], and confirms that some minimum etch time (dependent upon the RF and ICP powers) is required for the sample to reach the requisite temperature ($> 150^\circ\text{C}$).

Our etch creates a nearly 90° sidewall angle but suffers from roughness in the core layer. We believe that this is the result of the elevated sample temperature created by the high density plasma, which probably causes pitting of Al-containing layers. In the optimal case, control of the sample temperature (or some other critical process parameter) as a function of time would be employed to allow for varying etch conditions depending on the layer composition. This will be of particular

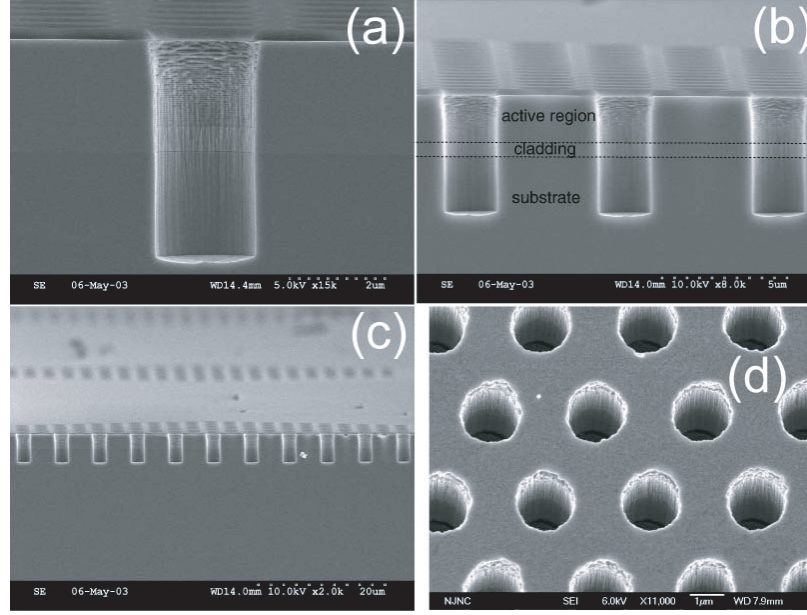


Figure C.8: SEM images of a typical QC-PCSEL device after the semiconductor etch, but before the deposition of electrical contacts. (a)-(c) Images of a cleaved device at different magnifications, showing (a) the verticality and relative smoothness of the etch, (b) the etch depth compared to the active region thickness of the QC device, and (c) the uniformity of the etch across the whole device. (d) SEM image of a device from the top surface.

use in standard vertical waveguide designs that have both top and bottom semiconductor cladding layers (often composed of AlInAs).

Appendix D

Cavity Q and Related Quantities

There are a number of physical quantities related to a cavity quality factor (Q) that appear in the literature. I have made an attempt to summarize some of these quantities in this appendix.

The definition of a cavity's quality factor is essentially $Q = \omega\tau_{ph}$, where ω is the cavity mode frequency and τ_{ph} is the photon lifetime within the cavity ($\tau_{ph} = 1/\Delta\omega$, where $\Delta\omega$ is the spectral width of the cavity mode). Q is defined in terms of the energy of the field, so that $1/\tau_{ph} = \omega/Q$ is an energy decay rate. The field's decay rate is one-half this amount, so that:

$$\kappa = \frac{\omega}{2Q}. \quad (\text{D.1})$$

Written like this, κ has units of radians/second. To convert this to Hz, we divide by 2π . I have tried to adopt the convention of explicitly writing $\kappa/2\pi$ when quoting cavity decay rates in units of Hz, to avoid any confusion.

It is sometimes convenient to consider a cavity decay length L_{ph} , which can be defined through

$$\tau_{ph} = \frac{L_{ph}}{c/n} \quad (\text{D.2})$$

where c/n is the speed of light within the cavity. More precisely, n is not the material refractive index but instead is the group index of the mode within the cavity, n_g . The Q of the cavity can be written in terms of L_{ph} as:

$$Q = \frac{2\pi n_g L_{ph}}{\lambda} \quad (\text{D.3})$$

Typically, a decay length L_{ph} might not be quoted, but rather, an inverse decay length $\alpha = L_{ph}^{-1}$ is. This is in particular true for structures such as waveguides, for which a loss per unit length (sometimes in units of cm^{-1} for example, and other times in units such as dB/cm) is a common metric. Equation (D.3) above is then important for being able to compare waveguide loss to a cavity Q . Perhaps more important, material absorption losses are often quoted in terms of a loss per unit length, and equation (D.3) then tells us how to compute the equivalent absorption-limited Q .

A cavity's Q physically represents the number of cycles the optical field undergoes before its energy decay to a value that is $1/e$ time its original value. This is nothing more than saying that the cavities energy decays in time as $e^{-\omega t/Q}$, or equivalently

$$\frac{dU}{dt} = -\frac{\omega}{Q}U \quad (\text{D.4})$$

Where U is the stored energy within the cavity, and $P_d = -\frac{dU}{dt}$ is the dissipated power. This leads to another common definition of Q ,

$$Q = \omega \frac{U}{P_d} \quad (\text{D.5})$$

If we write the cavity frequency $\omega = \frac{2\pi}{T}$, where T is period of the field, this equation can be rewritten as

$$Q = 2\pi \frac{U}{U_{l,c}} \quad (\text{D.6})$$

where $U_{l,c}$ is the energy loss per cycle (period). For traveling wave mode cavities, such as Fabry-Perots or WGM-based devices, it is common to quote a cavity finesse F , which is given by

$$F = \frac{U}{U_{l,rt}} \quad (\text{D.7})$$

where $U_{l,rt}$ is the energy loss per round trip length (where the round trip length is $2L$ for a Fabry-Perot cavity of length L and $2\pi R$ for a WGM cavity of radius R). The finesse is then related to the Q (modulo 2π) by the ratio of $U_{l,c}$ to $U_{l,rt}$. This ratio is simply the number of optical cycles within a round trip length L_{rt} , which is $L_{rt}/(\lambda/n_g)$. Plugging into equation (D.7), we have:

$$F = \frac{Q}{2\pi} \frac{\lambda}{n_g L_{rt}} \quad (\text{D.8})$$

Finally, our equation for the decay length L_{ph} (equation (D.3)), can be used to simply write the finesse as:

$$F = \frac{L_{ph}}{L_{rt}} \quad (\text{D.9})$$

A cavity finesse of 1 then means that the field decays to its $1/e$ point after one complete round trip.

Appendix E

Resonator-Waveguide Coupled Mode Theory

In this appendix, I briefly review some of the key equations of the coupling of modes in time approach of Haus et al. [125] that is often used to study resonator-waveguide coupling. There are many references that treat this topic; the discussion below has been primarily influenced by refs. [50, 57, 55]. Other helpful works include refs. [214, 215, 216].

E.1 Traveling wave mode resonator

We first consider coupling between a single mode waveguide and a single mode of a cavity; an example of this would be coupling between the forward propagating mode of a waveguide and the clockwise propagating WGM of a microdisk resonator, as shown in fig. E.1. The cavity's intrinsic loss rate is γ_i , and its loss rate into the waveguide is γ_e . Note that the γ 's are energy decay rates,

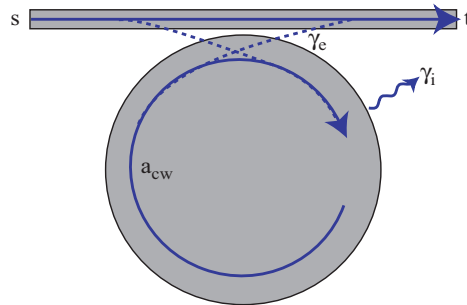


Figure E.1: Schematic for single mode coupling between a resonator and waveguide. The cavity's intrinsic energy loss rate is γ_i , and its energy loss rate into the waveguide is γ_e . The cavity, whose mode amplitude is called a_{cw} , is excited by a waveguide mode s , and the transmitted field past the cavity is t . Note that a_{cw} is normalized to energy, while s and t are normalized to power.

related to the field decay rates by a factor of 2, as discussed in appendix D. The waveguide input field is labeled s , and it couples to a cavity mode of amplitude a_{cw} . The transmitted field past the cavity is t , with s and t normalized to power, and a_{cw} normalized to energy [125].

The time evolution of the mode amplitude a_{cw} is given by:

$$\frac{da_{cw}}{dt} = i\omega_0 a_{cw} - \frac{\gamma_T}{2} a_{cw} + k_e s \quad (\text{E.1})$$

where γ_T is the total energy decay rate of the cavity mode (equal to $\gamma_0 + \gamma_e$ above), and k_e is the waveguide-resonator coupling coefficient.¹ The above equation simply states that the mode amplitude a_{cw} oscillates in time with a frequency ω_0 (first term on the right hand side), decays with a loss rate γ_T (second term), and is driven by an input field s with coupling coefficient k_e (third term).

The transmitted signal t will have a contribution due to that portion of the input signal s that does not couple into the cavity, and a contribution from the signal coupled out of the cavity. We thus expect $t = \alpha_1 s + \alpha_2 a_{cw}$, where α_1 and α_2 are coefficients to be determined. We can determine α_1 and α_2 through a power conservation argument, where we equate the power transfer into the cavity with the change in the cavity's internal energy plus the dissipated power. That is, we write:

$$|s|^2 - |t|^2 = \frac{d|a_{cw}|^2}{dt} + \gamma_0 |a_{cw}|^2 \quad (\text{E.2})$$

Plugging in equation (E.1) along with $t = \alpha_1 s + \alpha_2 a_{cw}$ yields three equations for the variables α_1 and α_2 (which are complex). We have

$$\begin{aligned} 1 - |\alpha_1|^2 &= 0 \\ |\alpha_2|^2 &= \gamma_e \\ -\alpha_1 \alpha_2^* &= k_e \end{aligned} \quad (\text{E.3})$$

One simple choice of solution is $\alpha_1 = -1$, $\alpha_2 = k_e^*$ (with $|k_e|^2 = \gamma_e$), giving the transmitted signal as:

¹Coupling coefficients are often denoted by the symbol κ . However, we have already reserved κ for the field decay rate, so we choose k instead.

$$t = -s + k_e^* a_{cw} \quad (\text{E.4})$$

From equations (E.1) and (E.4), we can find the steady state (normalized) transmission through the waveguide, given by $T = |t/s|^2$. Before doing this, we expand our formalism a bit to let $\gamma_T = \gamma_e + \gamma_0 + \gamma_p$, where γ_p is a loss term representing parasitic coupling between the waveguide and resonator (for example, coupling-induced scattering into radiation modes). From this, we solve for T , and arrive at:

$$T = \left| \frac{\gamma_e - (\gamma_0 + \gamma_p) - 2i\Delta\omega}{\gamma_e + (\gamma_0 + \gamma_p) + 2i\Delta\omega} \right|^2 \quad (\text{E.5})$$

where $\Delta\omega = \omega - \omega_0$, the difference between the drive frequency and the cavity resonance frequency. As a function of ω , T is a Lorentzian centered at $\omega = \omega_0$.

On resonance ($\Delta\omega=0$), we can rewrite this equation as

$$T = \left(\frac{1-K}{1+K} \right)^2 \quad (\text{E.6})$$

where K is called the coupling parameter [55, 57], and is defined as

$$K = \frac{\gamma_e}{\gamma_0 + \gamma_p} \quad (\text{E.7})$$

K is the ratio of coupling into the waveguide with coupling into intrinsic and parasitic loss channels. $K=1$ is called critical coupling (corresponding to complete power transfer, where waveguide-cavity coupling equals intrinsic and parasitic loss), while $K < 1$ ($K > 1$) is called the undercoupled (overcoupled) regime. These important regimes are discussed in many other works [125, 20, 55, 214].

Experimentally, we always measure $Q_T = \omega_0/\gamma_T$, although we have control over γ_e by controlling the taper-cavity separation. In practice, we can increase the taper-cavity separation to the point that γ_e is quite small, giving us an estimate of the cold-cavity quality factor Q_i (assuming that γ_p

also becomes quite small as the separation becomes large). Without changing the taper-cavity separation, we can get an estimate of Q_{i+p} , the Q due to intrinsic decay and parasitic waveguide-cavity coupling, by knowing K , or equivalently, the transmission depth on resonance (equation (E.6)). In particular,

$$\begin{aligned} Q_{i+p} &= \frac{\omega_0}{\gamma_0 + \gamma_p} = \frac{\omega_0}{\gamma_0 + \gamma_e + \gamma_p} \cdot \frac{\gamma_0 + \gamma_e + \gamma_p}{\gamma_0 + \gamma_p} \\ &= Q_T(1 + K) \end{aligned} \quad (\text{E.8})$$

Another important parameter is called the ideality I , which is the ratio of the coupling into the waveguide mode of interest with the coupling into all waveguide channels. That is,

$$I = \frac{\gamma_e}{\gamma_e + \gamma_p} \quad (\text{E.9})$$

$I=1$ implies that the resonator-waveguide coupling is ideal in the sense that all coupling is into the desired waveguide channel.

Next, let us consider the case of an emitter within the cavity. A fraction β of the emitter's spontaneous emission will be coupled into the cavity mode of interest. The fraction of these photons that are then coupled into the waveguide mode of interest is given by the parameter η_0 , with

$$\eta_0 = \frac{\gamma_e}{\gamma_e + \gamma_0 + \gamma_p} \quad (\text{E.10})$$

This can easily be rewritten in terms of the coupling parameter K as:

$$\eta_0 = \frac{1}{1 + 1/K} \quad (\text{E.11})$$

We see that η_0 approaches unity as the system is driven into the overcoupled regime; at critical coupling ($K=1$), $\eta_0 = 50\%$. In the literature, much attention is paid to β , with a high- β cavity often seen as a solution to efficiently collecting photons from an emitter, such as a self-assembled quantum dot within a high-index semiconductor. Although it is somewhat obvious, we note here

that η_0 also plays an important role, with $\beta\eta_0$ giving the total fraction of emitted photons that are actually collected into the channel of interest, which could be the forward propagating fundamental taper mode in our experiments, or some well-defined free-space collection channel for experiments with a Fabry-Perot cavity.

The ratio of the total (loaded) quality factor Q_T to the intrinsic quality factor Q_i can be written in terms of η_0 and I as:

$$\begin{aligned}\frac{Q_T}{Q_i} &= \frac{\gamma_0}{\gamma_0 + \gamma_e + \gamma_p} = \frac{\gamma_0 + \gamma_e + \gamma_p}{\gamma_0 + \gamma_e + \gamma_p} - \frac{\gamma_e + \gamma_p}{\gamma_0 + \gamma_e + \gamma_p} \\ &= 1 - \frac{\gamma_e}{\gamma_e + \gamma_0 + \gamma_p} \frac{\gamma_e + \gamma_p}{\gamma_e} \\ &= 1 - \frac{\eta_0}{I}\end{aligned}\tag{E.12}$$

Finally, we consider two quantities of importance to many processes that occur within optical microcavities. The internal cavity energy U can be written as the product of the dropped power into the cavity, P_d , and the photon lifetime due to intrinsic and parasitic losses, τ_{i+P} . Noting that $P_d = (1 - T)P_{in}$, where P_{in} is the input power into the waveguide, and plugging in for T in terms of the coupling parameter K , we have:

$$\begin{aligned}U &= (1 - T)P_{in}\tau_{i+P} \\ &= \frac{4K}{(1 + K)^2}P_{in}\frac{Q_{i+P}}{\omega_0} \\ &= \frac{4K}{1 + K}P_{in}\frac{Q_T}{\omega_0}\end{aligned}\tag{E.13}$$

Equations (E.12) and (E.11) can then be used to relate U to the intrinsic quality factor Q_i , ideality I , and coupling parameter K . This yields:

$$U = \frac{4K}{(1 + K)^2}(I + K(I - 1))\frac{Q_i}{\omega_0}P_{in}\tag{E.14}$$

This quantity is maximized when $K = I/(2 - I)$, for which $U = I(Q_i/\omega_0)P_{in}$.

The circulating intensity within the cavity, \mathfrak{S} , is given as $\mathfrak{S} = (U/V_{\text{eff}})v_g$, where v_g is the group index of the cavity mode. For critical coupling ($K = 1$) with unity ideality ($I = 1$), we can simply

write this as:

$$\begin{aligned}
 \mathfrak{S} &= v_g \frac{U}{V_{\text{eff}}} \\
 &= \frac{c}{n_g} \frac{Q_i}{\omega_0 V_{\text{eff}}} P_{\text{in}} \\
 &= P_{\text{in}} \frac{\lambda_0}{2\pi n_g} \frac{Q_i}{V_{\text{eff}}}
 \end{aligned} \tag{E.15}$$

E.2 Standing wave mode resonator

We next briefly consider the case where the resonator supports a standing wave mode rather than a traveling wave mode. This is true, for example, in the photonic crystal microcavities studied in the first part of this thesis. The main difference is that the standing wave mode decays equally into the forward *and* backward propagating modes of the waveguide. If we continue to consider γ_e to be the loss rate into the forward propagating waveguide mode, the total loss rate γ_T is given as $\gamma_T = 2\gamma_e + \gamma_0 + \gamma_p$. The formula for the normalized transmission is then determined through an analogous set of equations as used above, with:

$$T = \left| \frac{\gamma_e - (\gamma_e + \gamma_0 + \gamma_p) - 2i\Delta\omega}{\gamma_e + (\gamma_e + \gamma_0 + \gamma_p) + 2i\Delta\omega} \right|^2 \tag{E.16}$$

On resonance ($\Delta\omega=0$), we can rewrite this equation as:

$$T = \left(\frac{1-K}{1+K} \right)^2 \tag{E.17}$$

where the coupling parameter K is now written as

$$K = \frac{\gamma_e}{\gamma_e + \gamma_0 + \gamma_p} \tag{E.18}$$

We see that the form of $T(K)$ is exactly the same as what is was for coupling to a traveling wave mode, but the range of values that K can attain is restricted to $K \leq 1$.

In coupling to a standing wave mode, there is now a reflected signal coming out of the input

port, with the normalized reflection R given as $R = |r_s|^2$. In this equation, $r = k_e^* a_{sw}$, where a_{sw} is the standing wave mode amplitude. We then arrive at:

$$R = \left| \frac{2\gamma_e}{\gamma_e + (\gamma_e + \gamma_0 + \gamma_p) + 2i\Delta\omega} \right|^2 \quad (\text{E.19})$$

so that on resonance, this is rewritten in terms of K as:

$$R = \frac{4K^2}{(1 + K)^2} \quad (\text{E.20})$$

Finally, we consider the parameter η_0 . Assuming that photons are only collected from one of the waveguide modes, it is defined as:

$$\eta_0 = \frac{\gamma_e}{2\gamma_e + \gamma_0 + \gamma_p} \quad (\text{E.21})$$

and can again be rewritten in terms of the coupling parameter K as:

$$\eta_0 = \frac{1}{1 + 1/K} \quad (\text{E.22})$$

provided that K is defined as in equation (E.18). We see that $\eta_0 \leq 50\%$, which makes sense because the cavity mode equally decays into the forwards and backwards channels of the waveguide, so that at most 50% of the cavity photons can be collected out of any one channel. For the experiments we have conducted thus far (chapters 6 and 7), collection from both channels can be easily achieved, so that this is not a significant limitation. However, this might not always be the case, particularly if the cavity-waveguide unit is to be a node within a more complex system.

Appendix F

Laser Rate Equations

A rate equation approach [152, 217, 218] is often a simple way to study aspects of the steady state and dynamical behavior of lasers. Although a full quantum mechanical approach can be more rigorous, rate equation techniques are typically relatively simple and easier to solve, while still including fluctuations (i.e., spontaneous emission into the laser mode), albeit at a relatively basic level. In contrast, purely semi-classical theories, beginning at the level of the Maxwell-Bloch equations, for example, neglect fluctuations altogether [219]. In what follows, we present an overview of a simple rate equation model used in the fits of our 2 μm diameter microdisk-quantum-dot lasers studied in chapter 7. There are a number of good treatments of rate equation modeling in the literature; I have personally benefitted from studying the text of Coldren and Corzine [152].

For semiconductor lasers, the rate equations are often a pair of equations that describe the time evolution of the carrier number (N) and photon number in the cavity mode of interest (N_p) within the structure. Here, we are considering a semiconductor material where light emission occurs as a result of electron-hole recombination, and where the active material maintains charge neutrality, so that the electron number N_e is equal to the hole number N_h , and we keep track of a single carrier number N . The rate of change of N will be given by the difference between carrier generation processes and carrier recombination processes. Carrier generation (occurring at a rate L) can occur through current injection or optical pumping, for example. Recombination processes can include stimulated and spontaneous emission (R_{st} and R_{sp}) and non-radiative recombination (R_{nr}) (carrier leakage can also be a factor, although we do not consider it here). Calling the volume of the active region V , we can write this explicitly as:

$$\frac{dN}{dt} = L - (R_{nr} + R_{sp} + R_{st})V \quad (\text{F.1})$$

The rate of change of N_p will be given by difference in photon generation and photon removal processes. Photon generation will be due to stimulated and spontaneous emission, while photon removal will be due to cavity loss. We can write this equation as:

$$\frac{dN_p}{dt} = (R_{st} + \beta R_{sp})V - \frac{N_p}{\tau_{ph}} \quad (\text{F.2})$$

where $\gamma_{ph} = 1/\tau_{ph}$ is the photon number loss rate from the cavity ($=\omega/Q$). As we have mentioned in other parts of this thesis, β is called the spontaneous emission coupling factor, and is the fraction of spontaneous emission emitted into the cavity mode of interest. In this equation, we have not explicitly made use of the modal confinement factor Γ , which basically takes into account the fact that the volume of the cavity mode of interest will often be different than the volume of the active region. This is because our equations are in terms of carrier number and photon number; if we had instead written them in terms of densities, use of Γ would be necessary, because the photon number N_p is not taken over the active region volume V , but rather a mode volume.

From this point, an essentially phenomenological approach is often used to describe the different recombination processes; the specifics often depend on the gain medium under consideration. For our purposes in chapter 7, the gain medium is a single layer of quantum dots. Let us first consider stimulated recombination R_{st} . By a stimulated process, we mean that photon generation requires the presence of seed photons. It is therefore taken to be proportional to the photon number N_p ; for example, $R_{st} = v_g g_l N_p$ as in Coldren and Corzine [152], where v_g is the group velocity of the cavity mode and g_l is the gain per unit length. Equivalently, it can be written in terms of a gain per unit time g as $R_{st} = g N_p$. Next, the spontaneous recombination term R_{sp} is often taken to be a bi-particle process (electron-hole recombination), so that $R_{sp} = B N^2$, where B is called the bimolecular recombination rate. Non-radiative recombination is usually a combination of processes with varying power law dependencies on N . One process is surface recombination, which is often taken as $R_{sr} = A N$, where A is some material-dependent coefficient. Another process is Auger recombination, the transfer of kinetic energy from an electron-hole pair to another electron (or

hole). It is often taken as $R_A = CN^3$, where C is called the Auger recombination coefficient.

The rate equations we use to model the microdisk lasers of chapter 7 are:

$$\frac{dN}{dt} = L - \left[\frac{N^{1.22}}{\tau_s} + \frac{N^2}{\tau'_{sp}} \right] - gN_p \quad (\text{F.3})$$

$$\frac{dN_p}{dt} = (g - \gamma_{ph})N_p + \frac{\beta N^2}{\tau'_{sp}} \quad (\text{F.4})$$

Here, we have assumed an N^2 dependence for radiative recombination, no Auger recombination, and have taken the surface recombination term to have a $N^{1.22}$ dependence (as discussed in chapter 7, this is done to match the measured subthreshold slope of the light-in-light-out curve). In these equations, the proportionality coefficients in front of the N -dependent terms have been written as lifetimes, with τ_s being the surface recombination lifetime and τ'_{sp} being the Purcell-factor-modified (appendix H) spontaneous emission lifetime of the quantum dots (where the unmodified lifetime is taken to be 1 ns).

In our microdisk cavities, carrier generation is accomplished through optical pumping, where the measured quantity is the pump power incident on the sample surface, P_{inc} . L is related to P_{inc} through:

$$L = \frac{P_{inc}\eta_{abs}\eta_{int}}{E_{ph,pump}} \frac{A_m}{A_{pump}} \quad (\text{F.5})$$

where η_{abs} is the fraction of incident pump power that is absorbed, η_{int} is the internal efficiency of carrier generation, $E_{ph,pump}$ is the energy per pump photon, A_m is the modal area, and A_{pump} is the pump beam area. Basically, $P_{inc}\eta_{abs}A_m/A_{pump}$ gives the absorbed pump power by the disk, dividing by $E_{ph,pump}$ converts this to an absorbed photon number rate, and multiplying by η_{int} converts this to a carrier generation rate.

The surface recombination lifetime τ_s is taken as:

$$\tau_s = \frac{1}{2(2\pi R\rho_{A,QD})v_s} \quad (\text{F.6})$$

Here, $\rho_{A,QD}$ is the areal quantum dot density, a quantity estimated by the material growers (300

μm^{-2} for the QD material we use), so that $2\pi R\rho_{A,QD}$ gives a linear QD density along the perimeter of the device (the additional factor of 2 in the equation takes into account the degeneracy of the QD ground state). v_s is a surface recombination velocity, which we take as a fit parameter.

The gain per unit time g is taken to have the form:

$$g = g'(N - N_{tr}) \quad (\text{F.7})$$

where g' is the differential gain and $N_{tr} = \rho_{A,QD}A_m$ is the transparency carrier number (the total number of available states is $2\rho_{A,QD}A_m$ due to degeneracy, and the transparency level is half of this). g' is taken to be the maximum modal gain if all QD ground states interacting with the cavity mode are inverted divided by the total number of QD states.

We thus solve the rate equations (equation (F.3)) in steady state to give us the steady state photon number $N_{p,ss}$ as a function of pump power. To match our experimental data, the collected laser power (L_{out}) is related to $N_{p,ss}$ through:

$$L_{out} = \eta_{coll} E_{ph} \gamma_{ph} N_{p,ss} \quad (\text{F.8})$$

where E_{ph} is the emitted photon energy ($E_{ph} = \hbar\omega$) and η_{coll} is the collection efficiency. Finally, we have:

$$\eta_{coll} = \xi \frac{E_{ph,pump}}{E_{ph}} \eta_{int} \quad (\text{F.9})$$

where ξ is the laser's differential efficiency (which we directly measure, as discussed in chapter 7), and $E_{ph,pump}/E_{ph}$ is the ratio of the energies of the pump and emission photons. The steady state solutions to the rate equations, using the relationships outlined above, produce the solid fits to the experimental data in fig. 7.8.

Appendix G

The Jaynes-Cummings Model

The interaction of an atom with an electromagnetic field is approached in a number of different ways, depending on how the atom and field are treated (classically or quantum mechanically). Semiclassical models treat the field classically and the atom quantum mechanically. The Jaynes-Cummings model [220, 221, 222] treats both quantum mechanically, but makes several simplifying assumptions. In particular, the atom is treated as a two-level system, and driving and dissipation terms are not included. In this appendix, I first briefly review the Jaynes-Cummings model. I then consider extensions of this model to include driving and damping terms, following the quantum master equation approach as outlined by Carmichael in his books [149, 180].

G.1 The Jaynes-Cummings Hamiltonian and eigenvalue spectrum

The Jaynes-Cummings Hamiltonian H_{JC} can be written as:

$$H_{\text{JC}} = H_{\text{atom}} + H_{\text{field}} + H_{\text{int}}, \quad (\text{G.1})$$

where H_{atom} , H_{field} , and H_{int} are terms due to the free atom, the free field, and the atom-field interaction, respectively. The first two terms can be written as:

$$H_{\text{atom}} = \frac{1}{2} \hbar \omega_a \hat{\sigma}_z \quad H_{\text{field}} = \hbar \omega_f \left(\hat{a}^\dagger \hat{a} + \frac{1}{2} \right) \quad (\text{G.2})$$

where $\hat{\sigma}_z$ is the Pauli spin operator (inversion), ω_a and ω_f are the atomic transition and electromagnetic field frequencies, and \hat{a} (\hat{a}^\dagger) is the electromagnetic field annihilation (creation) operator. The

$\frac{1}{2}\hbar\omega_f$ term is often left out of the free-field Hamiltonian, as it is just adds a constant energy shift to the eigenstates.

The dipole interaction term is $H_{\text{int}} = -\hat{\mathbf{d}} \cdot \hat{\mathbf{E}}$, where $\hat{\mathbf{d}}$ is the dipole operator, and can be written as $\hat{\mathbf{d}} = \mathbf{d}_{eg}|e\rangle\langle g| + \mathbf{d}_{eg}^*|g\rangle\langle e|$. Here, $|g\rangle$ and $|e\rangle$ are the ground and excited states of the atom, and we have assumed that they are states of definite parity, so that the dipole operator only contains off-diagonal terms. The terms $|e\rangle\langle g|$ and $|g\rangle\langle e|$ are just the Pauli matrices σ_+ and σ_- , so that:

$$\hat{\mathbf{d}} = \mathbf{d}_{eg}\hat{\sigma}_+ + \mathbf{d}_{eg}^*\hat{\sigma}_- \quad (\text{G.3})$$

Quantizing the electromagnetic field [223], we write the electric field operator as:

$$\hat{\mathbf{E}}(\mathbf{r}) = iE_{\text{max}}(\mathbf{f}(\mathbf{r})\hat{a} - \mathbf{f}^*(\mathbf{r})\hat{a}^\dagger) \quad (\text{G.4})$$

where $\mathbf{f}(\mathbf{r})$ describes the spatial variation of the electric field (it is essentially a normalized version of the electric field), and E_{max} is the amplitude of the field (see appendix H). From this equation, along with the expression for $\hat{\mathbf{d}}$, we write the interaction term H_{int} as

$$H_{\text{int}} = i\hbar g(\hat{a}^\dagger\hat{\sigma}_- - \hat{a}\hat{\sigma}_+) \quad (\text{G.5})$$

where g is the atom-field coupling rate, which we consider in further detail in appendix H. In this equation for H_{int} , we have neglected the $\hat{a}\hat{\sigma}_-$ and $\hat{a}^\dagger\hat{\sigma}_+$ terms, which are processes that do not conserve energy (the former process corresponds to annihilation of a photon while having the atom transition from the excited to the ground state, for example). This is essentially the rotating wave approximation. Thus, our final form for the Jaynes-Cummings Hamiltonian, including all three terms, is:

$$H_{\text{JC}} = \frac{1}{2}\hbar\omega_a\hat{\sigma}_z + \hbar\omega_f\left(\hat{a}^\dagger\hat{a} + \frac{1}{2}\right) + i\hbar g(\hat{a}^\dagger\hat{\sigma}_- - \hat{a}\hat{\sigma}_+) \quad (\text{G.6})$$

The energy eigenvalues of this system can be determined by considering product states of the

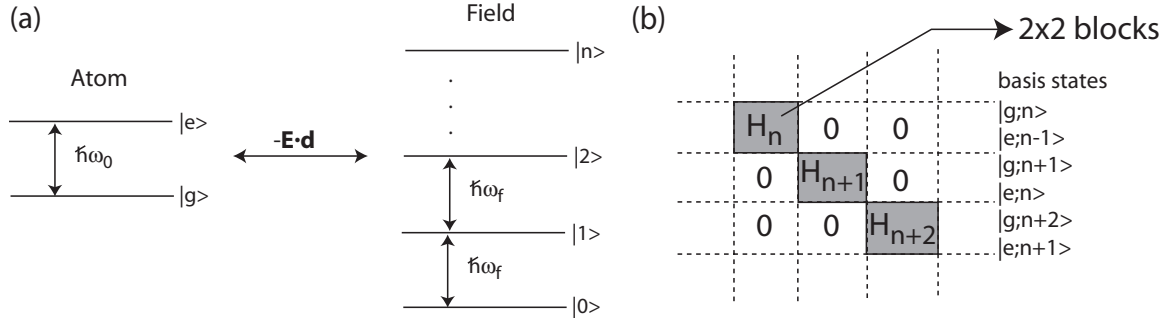


Figure G.1: (a) Schematic for atom-field coupling and (b) block diagonal form for the Hamiltonian in the Jaynes-Cummings model.

form $|g;k\rangle$ ($|g;k\rangle = |g\rangle \otimes |k\rangle$), where the atom is in either the excited or ground state, and the field has k photons. We have:

$$H_{JC}|g;n\rangle = -\frac{1}{2}\hbar\omega_a|g;n\rangle + \hbar\omega_f\left(n + \frac{1}{2}\right)|g;n\rangle - i\hbar g\sqrt{n}|e;n-1\rangle \quad (\text{G.7})$$

$$H_{JC}|e;n-1\rangle = \frac{1}{2}\hbar\omega_a|e;n-1\rangle + \hbar\omega_f\left(n - \frac{1}{2}\right)|e;n-1\rangle + i\hbar g\sqrt{n}|g;n\rangle. \quad (\text{G.8})$$

In matrix form, the Hamiltonian is block diagonal, with 2×2 blocks. The form for the n th block (fig. G.1(b)) is:

$$H_n = \hbar \begin{pmatrix} (n + \frac{1}{2})\omega_f - \frac{\omega_a}{2} & -ig\sqrt{n} \\ ig\sqrt{n} & (n - \frac{1}{2})\omega_f + \frac{\omega_a}{2} \end{pmatrix}. \quad (\text{G.9})$$

The eigenvalues for this matrix are

$$E_{n,\pm} = \hbar \left(n\omega_f \pm \frac{\Omega}{2} \right) \quad (\text{G.10})$$

$$\Omega = \sqrt{(\omega_f - \omega_a)^2 + 4ng^2} \quad (\text{G.11})$$

The corresponding eigenstates, which we write as $|n, \pm\rangle$, are mixtures of $|g;n\rangle$ and $|e;n-1\rangle$:

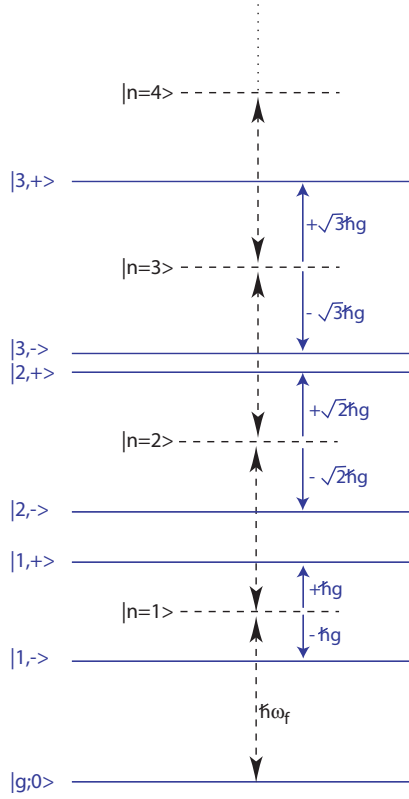


Figure G.2: Energy level spectrum for the Jaynes-Cummings model ($\omega_f = \omega_a$). The unperturbed field states are shown as black dashed horizontal lines and are labeled as $|n = 1 \rangle$, for example. The eigenstates of the Jaynes-Cummings Hamiltonian are labeled as $|n, \pm \rangle$, and are shown as solid horizontal lines.

$$|n, - \rangle = -\sin\theta_n |g; n \rangle + \cos\theta_n |e; n-1 \rangle \quad (\text{G.12})$$

$$|n, + \rangle = \cos\theta_n |g; n \rangle + \sin\theta_n |e; n-1 \rangle \quad (\text{G.13})$$

$$\tan(2\theta_n) = \frac{2g\sqrt{n}}{\omega_f - \omega_a} \quad (\text{G.14})$$

From this, we see that for vary large detunings, or alternately, very small coupling strengths g , the eigenstates are essentially product states.

On-resonance ($\omega_f = \omega_a$), the eigenvalues and eigenstates are:

$$E_{n,\pm} = \hbar(n\omega_f \pm g\sqrt{n}) \quad (\text{G.15})$$

$$|n, - \rangle = -\frac{1}{\sqrt{2}}(|g; n \rangle - |e; n-1 \rangle) \quad (\text{G.16})$$

$$|n, + \rangle = \frac{1}{\sqrt{2}}(|g; n \rangle + |e; n-1 \rangle). \quad (\text{G.17})$$

The eigenvalue spectrum for the coupled atom-field system (on-resonance) is shown schematically

in fig. G.2. We see that the field's harmonic oscillator spectrum, consisting of energy levels separated by $\hbar\omega_f$, has been modified, with each energy level splitting into a pair of levels, separated by a spacing of $\Delta E = 2g\sqrt{n}$. The splitting of the first excited state ($n=1$) is $2g$, and is called the vacuum Rabi splitting.

G.2 The damped, driven Jaynes-Cummings model

The Jaynes-Cummings Hamiltonian of the previous section examines the interaction of a single mode electromagnetic field (such as the mode of an electromagnetic cavity) with a two-level atom, and basically models an isolated system. An experiment will typically differ from this in two primary ways. There will often be some probe field that is used to study the system; the probe might be a weak classical field that is swept in frequency, for example. In addition, the atom-cavity system will be unavoidably coupled to the environment, which will cause dissipation. This may come in the form of cavity loss or spontaneous emission of the atom, for example. In this section, we review how the Jaynes-Cummings model is expanded to account for these effects.

G.2.1 Driving field

From the previous section, we recall that the Jaynes-Cummings Hamiltonian is written as:

$$H_{\text{JC}} = \frac{1}{2}\hbar\omega_a\hat{\sigma}_z + \hbar\omega_c\left(\hat{a}^\dagger\hat{a} + \frac{1}{2}\right) + i\hbar g(\hat{a}^\dagger\hat{\sigma}_- - \hat{a}\hat{\sigma}_+) \quad (\text{G.18})$$

where here we have relabeled the field to oscillate at frequency ω_c , to explicitly indicate that we are considering it to be the mode of an electromagnetic cavity. The driving field modifies H_{JC} by adding a term H_{drive} , given as:

$$H_{\text{drive}} = i\hbar \left[E \begin{bmatrix} \hat{\sigma}_+ \\ \hat{a}^\dagger \end{bmatrix} e^{-i\omega_l t} - E^* \begin{bmatrix} \hat{\sigma}_- \\ \hat{a} \end{bmatrix} e^{i\omega_l t} \right] \quad (\text{G.19})$$

where E and ω_l are the amplitude and frequency of the driving field. The top row in the equation (involving $\hat{\sigma}_+$ and $\hat{\sigma}_-$) applies to the case of the field driving the atom, and the bottom row (involving \hat{a}^\dagger and \hat{a}) is when the field drives the cavity mode. The introduction of this time-dependent term

into the Hamiltonian can be handled by transforming to a frame that rotates at the same frequency as the driving field (ω_l). That is, we will apply a unitary transformation $\hat{U} = \exp(-i\omega_l t(\hat{\sigma}_z/2 + \hat{a}^\dagger \hat{a}))$. In general, we know that if some unitary operator \hat{U} acts on the state vector, the transformed Hamiltonian, H_r , is written in terms of the original Hamiltonian H_S as [224]:

$$H_r = i\hbar \dot{\hat{U}} \hat{U}^\dagger + \hat{U} H_S \hat{U}^\dagger. \quad (\text{G.20})$$

We apply this to the Hamiltonian $H_S = H_{JC} + H_{\text{drive}}$, and make use of the operator expansion theorem [225]:

$$\exp(x\hat{A})\hat{B}\exp(-x\hat{A}) = \hat{B} + x[\hat{A}, \hat{B}] + \frac{x^2}{2!}[\hat{A}, [\hat{A}, \hat{B}]] + \dots \quad (\text{G.21})$$

This yields the following form for the driven Jaynes-Cummings Hamiltonian (written in a frame rotating at ω_l):

$$H_r = \hbar\Delta\omega_{cl}\hat{\sigma}_+\hat{\sigma}_- + \hbar\Delta\omega_{cl}\hat{a}^\dagger\hat{a} + i\hbar g(\hat{a}^\dagger\hat{\sigma}_- - \hat{a}\hat{\sigma}_+) + i\hbar \left[E \begin{bmatrix} \hat{\sigma}_+ \\ \hat{a}^\dagger \end{bmatrix} - E^* \begin{bmatrix} \hat{\sigma}_- \\ \hat{a} \end{bmatrix} \right] \quad (\text{G.22})$$

where $\Delta\omega_{cl} = \omega_c - \omega_l$ and $\Delta\omega_{al} = \omega_a - \omega_l$. In deriving this equation, we have noted that $\hat{\sigma}_+\hat{\sigma}_- = (I + \hat{\sigma}_z)/2$. As described in ref. [226], the addition of the driving term to the Jaynes-Cummings Hamiltonian can modify the eigenvalue spectrum considerably. In particular, when the cavity is driven by the external field, the energy levels undergo a driving-field-dependent Stark shift, with the standard Rabi splittings of $\pm g\sqrt{n}$ being replaced by the quasienergies $\pm g\sqrt{n}[1 - (2E/g)^2]^{3/4}$ (when the atom, cavity, and driving field all at the same frequency). This can have a direct impact on experiments, where the atom-cavity system is often probed by a driving field that is swept in frequency [9, 182]. If the probe beam has a small amplitude (where the ratio of E to g is the important metric), its effects on the atom-cavity system would be expected to be small, and measurements of features such as vacuum Rabi splitting should yield the $2g$ splitting in accordance with the Jaynes-Cummings model.¹ However, if the probe beam has a large amplitude, the energy level structure of

¹The $2g$ splitting of the first excited state is maintained down to an arbitrarily weak driving field E ; this is one reason for the terminology ‘vacuum Rabi splitting’.

the Jaynes-Cummings model will be significantly altered. This can, for example, affect the ability to access and observe higher excited states of the Jaynes-Cummings system.

G.2.2 Dissipation terms and the quantum master equation approach

Dissipation in the Jaynes-Cummings system can be addressed by considering the interaction of this system with a reservoir. The treatment we follow below is entirely based on Carmichael's books [149, 180]. Our intent here is to briefly outline some of the important steps in this approach.

The Hamiltonian for the system plus reservoir is given as $H_S + H_R + H_{SR}$, where H_S and H_R are system and reservoir Hamiltonians, and H_{SR} is the Hamiltonian for the interaction of the two [180]. The interest in the reservoir is purely in terms of its effects on the system, so that a density matrix approach is well suited to study this problem. In particular, rather than considering the full density matrix of the system plus reservoir χ , a reduced density matrix $\rho = \text{Tr}_R[\chi]$ is considered, where the trace is taken over all of the reservoir states.

As χ is a density matrix, we know that:

$$\frac{d\chi}{dt} = \frac{1}{i\hbar}[H, \chi]. \quad (\text{G.23})$$

A convenient form for the equation of motion of χ can be determined by first transforming to the interaction picture to separate out the motion due to $H_S + H_R$ from that due to H_{SR} , and then formally integrating equation (G.23) to arrive at:

$$\frac{d\tilde{\chi}}{dt} = \frac{1}{i\hbar}[\tilde{H}_{SR}, \tilde{\chi}(0)] - \frac{1}{\hbar^2} \int_0^t dt' [\tilde{H}_{SR}(t), [\tilde{H}_{SR}(t'), \tilde{\chi}(t')]]. \quad (\text{G.24})$$

Here, the \sim is to note that all of the quantities are in the interaction picture. Our interest is in the reduced density matrix ρ , which is found by tracing over the reservoir states, so that:

$$\frac{d\tilde{\rho}}{dt} = -\frac{1}{\hbar^2} \int_0^t dt' \text{Tr}_R [\tilde{H}_{SR}(t), [\tilde{H}_{SR}(t'), \tilde{\chi}(t')]]. \quad (\text{G.25})$$

The first term from equation (G.24) has been dropped (it can essentially be thought of as a constant offset in the Hamiltonian). From this point, two important simplifying assumptions are made. The

first is called the Born Approximation, where we assume that the total density matrix (χ) can be written as the product of density matrices for the system (ρ) and reservoir R , and furthermore, that the effect of the system on the reservoir is negligible, so that R does not vary in time ($R(t) = R(0)$). This yields:

$$\frac{d\tilde{\rho}}{dt} = -\frac{1}{\hbar^2} \int_0^t dt' \text{Tr}_R \left[[\tilde{H}_{\text{SR}}(t), [\tilde{H}_{\text{SR}}(t'), \tilde{\rho}(t')R(0)]] \right]. \quad (\text{G.26})$$

The second major simplifying assumption is the Markov approximation, where we assume a memoryless system behavior due to the interaction with the reservoir. Carmichael's books consider this point in much greater detail [149, 180]. Assuming this point to be valid, its effect on equation (G.26) is to change the $\tilde{\rho}(t')$ within the integrand to $\tilde{\rho}(t)$.

From this point, specific models for the system, reservoir, and system-reservoir interaction Hamiltonians are employed. Many times, the reservoir is modeled as a collection of harmonic oscillators. The system-reservoir interaction Hamiltonian will often be written as $H_{\text{SR}} = \hbar \sum_j s_j \Gamma_j$ where s and Γ are system and reservoir operators, respectively. System operators might be the field annihilation and creation operators \hat{a} and \hat{a}^\dagger , or atomic raising and lowering operators $\hat{\sigma}_+$ and $\hat{\sigma}_-$, for example. Reservoir operators might be of the form $\Gamma = \sum_j \kappa_j \hat{r}_j$, for example, where the κ_j is the coupling coefficient linking the j th reservoir oscillator (characterized by annihilation and creation operators \hat{r}_j and \hat{r}_j^\dagger) to the field.

For the systems of interest to us, there are three primary dissipative channels: (i) atomic spontaneous emission, at a rate γ_{\parallel} , into modes other than the cavity mode of interest, (ii) photon leakage out of the cavity at a rate 2κ (so that the cavity's field decay rate is κ , as in appendix D), and (iii) non-radiative damping through phase-destroying processes, at a rate γ_p . These loss terms are given by [149, 180]:

$$L_1 \tilde{\rho} = \kappa (2\hat{a} \tilde{\rho} \hat{a}^\dagger - \hat{a}^\dagger \hat{a} \tilde{\rho} - \tilde{\rho} \hat{a}^\dagger \hat{a}) \quad (\text{G.27})$$

$$L_2 \tilde{\rho} = \frac{\gamma_{\parallel}}{2} (2\hat{\sigma}_- \tilde{\rho} \hat{\sigma}_+ - \hat{\sigma}_+ \hat{\sigma}_- \tilde{\rho} - \tilde{\rho} \hat{\sigma}_+ \hat{\sigma}_-) \quad (\text{G.28})$$

$$L_3 \tilde{\rho} = \frac{\gamma_p}{2} (\hat{\sigma}_z \tilde{\rho} \hat{\sigma}_z - \tilde{\rho}). \quad (\text{G.29})$$

The equation for the reduced density matrix in the interaction picture is then:

$$\frac{d\tilde{\rho}}{dt} = (L_1 + L_2 + L_3)\tilde{\rho}. \quad (\text{G.30})$$

Finally, we need to transform back to the Schrodinger picture from the interaction picture. We do this by noting that

$$\tilde{\rho}(t) = e^{\frac{iH_S t}{\hbar}} \rho(t) e^{-\frac{iH_S t}{\hbar}} \quad (\text{G.31})$$

so that differentiating this equation yields:

$$\dot{\tilde{\rho}}(t) = e^{\frac{iH_S t}{\hbar}} \dot{\rho}(t) e^{-\frac{iH_S t}{\hbar}} + \frac{i}{\hbar} [H_S, \tilde{\rho}] \quad (\text{G.32})$$

$$e^{-\frac{iH_S t}{\hbar}} \dot{\tilde{\rho}}(t) e^{\frac{iH_S t}{\hbar}} = \dot{\rho}(t) + \frac{i}{\hbar} [H_S, \rho] \quad (\text{G.33})$$

$$\dot{\rho} = \frac{1}{i\hbar} [H_S, \rho] + e^{-\frac{iH_S t}{\hbar}} \dot{\tilde{\rho}}(t) e^{\frac{iH_S t}{\hbar}} \quad (\text{G.34})$$

Putting it all together, we get the following master equation for the density matrix, often used as a starting point in cavity QED studies:

$$\frac{d\rho}{dt} = \frac{1}{i\hbar} [H_S, \rho] + \kappa(2\hat{a}\rho\hat{a}^\dagger - \hat{a}^\dagger\hat{a}\rho - \rho\hat{a}^\dagger\hat{a}) \quad (\text{G.35})$$

$$+ \frac{\gamma_{||}}{2}(2\hat{\sigma}_-\rho\hat{\sigma}_+ - \hat{\sigma}_+\hat{\sigma}_-\rho - \rho\hat{\sigma}_+\hat{\sigma}_-) \quad (\text{G.36})$$

$$+ \frac{\gamma_p}{2}(\hat{\sigma}_z\rho\hat{\sigma}_z - \rho) \quad (\text{G.37})$$

with

$$H_S = \hbar\Delta\omega_{al}\hat{\sigma}_+\hat{\sigma}_- + \hbar\Delta\omega_{cl}\hat{a}^\dagger\hat{a} + i\hbar g(\hat{a}^\dagger\hat{\sigma}_- - \hat{a}\hat{\sigma}_+) + i\hbar \left[E \begin{bmatrix} \hat{\sigma}_+ \\ \hat{a}^\dagger \end{bmatrix} - E^* \begin{bmatrix} \hat{\sigma}_- \\ \hat{a} \end{bmatrix} \right]. \quad (\text{G.38})$$

From this master equation, the time evolution of operator expectation values can be easily found by noting that $\langle \hat{A} \rangle = \text{Tr}(\hat{\rho}\hat{A})$ and $\langle \dot{\hat{A}} \rangle = \text{Tr}(\hat{\rho}\dot{\hat{A}})$ for a system operator \hat{A} . For example, if the driving field excites the cavity, these time-evolution equations are (here, we take $\hbar = 1$):

$$\frac{d}{dt} \langle \hat{a} \rangle = -\left(i\Delta\omega_{cl} + \kappa\right) \langle \hat{a} \rangle + g \langle \hat{\sigma}_- \rangle + E \quad (\text{G.39})$$

$$\frac{d}{dt} \langle \hat{\sigma}_- \rangle = -\left(i\Delta\omega_{al} + \gamma_{\perp}\right) \langle \hat{\sigma}_- \rangle + g \langle \hat{\sigma}_z \hat{a} \rangle \quad (\text{G.40})$$

$$\frac{d}{dt} \langle \hat{\sigma}_z \rangle = -2g(\langle \hat{\sigma}_- \hat{a}^\dagger \rangle + \langle \hat{\sigma}_+ \hat{a} \rangle) - \gamma_{\parallel}(1 + \langle \hat{\sigma}_z \rangle) \quad (\text{G.41})$$

To derive these equations, the identities $[\hat{\sigma}_+, \hat{\sigma}_-] = \hat{\sigma}_z$, $\hat{\sigma}_+ \hat{\sigma}_- + \hat{\sigma}_- \hat{\sigma}_+ = I$, and $\hat{\sigma}_{\pm}^2 = 0$ are useful, as is utilizing the cyclic property of the trace operator ($Tr(\hat{A}\hat{B}\hat{C}) = Tr(\hat{C}\hat{A}\hat{B}) = Tr(\hat{B}\hat{C}\hat{A})$). In addition, we have taken $\gamma_{\perp} = \gamma_{\parallel}/2 + \gamma_p$.

In the semi-classical limit, expectation values of operator products are replaced by products of operator expectation values (i.e., $\langle \hat{\sigma}_z \hat{a} \rangle = \langle \hat{\sigma}_z \rangle \langle \hat{a} \rangle$). These Maxwell-Bloch equations can then be solved in steady state, for example, to yield the optical bistability state equation (OBSE) [181, 182]. For reference, the solution is:

$$X = \frac{Y}{1 + \frac{2C}{X^2 + (\frac{\Delta\omega_{al}}{\gamma_{\perp}})^2 + 1} + i\left(\frac{\Delta\omega_{cl}}{\kappa} - \frac{2C\left(\frac{\Delta\omega_{al}}{\gamma_{\perp}}\right)}{X^2 + (\frac{\Delta\omega_{al}}{\gamma_{\perp}})^2 + 1}\right)} \quad (\text{G.42})$$

where

$$\begin{aligned} n_s &= \frac{\gamma_{\perp}\gamma_{\parallel}}{4g^2}, \\ C &= \frac{g^2}{2\kappa\gamma_{\perp}}, \\ Y &= \frac{E}{\kappa} n_s^{-1/2}, \\ X &= \langle \hat{a} \rangle n_s^{-1/2}. \end{aligned} \quad (\text{G.43})$$

n_s and C are called the saturation photon number and critical atom number (also known as the single atom cooperativity), which represent the number of photons (on average) needed to saturate the atomic transition and the number of atoms needed to dramatically affect the response of the cavity, respectively [9].

Appendix H

The Purcell Factor F_p and Atom-Photon Coupling Rate g

H.1 The Purcell factor

The degree to which a microcavity can influence the spontaneous rate of an emitter within it is known as the Purcell effect [227]. When the emitter (a radiating dipole) is on resonance with a cavity mode, this rate can be enhanced; when off-resonance, it can be inhibited [228]. Purcell enhancement (or inhibition) of spontaneous emission is one of the hallmarks of cavity QED within the *weak coupling* regime, where it is still appropriate to treat the emitter and the field as separate entities and their interaction as a perturbation. In *strong coupling*, the usual interpretation of spontaneous emission as an irreversible process no longer holds. The Jaynes-Cummings model reviewed in appendix G is the starting point for the treatment of emitter-field interactions in the strong coupling regime.

Placing a radiating dipole within a cavity causes the spontaneous emission rate to change due to the cavity's modification of the spectral density of modes (related to its Q) and the amplitude of the vacuum field interacting with the dipole (related to V_{eff}). We therefore expect the Purcell enhancement to scale with Q and V_{eff} . A simple derivation of this enhancement has been given by Gérard and Gayral [109]; we repeat this derivation here. We begin with the statement of Fermi's Golden Rule [224]:

$$\frac{1}{\tau_{\text{sp}}} = \frac{2\pi}{\hbar^2} |W_{ge}|^2 \rho(E_{ge}) \quad (\text{H.1})$$

W_{ge} is the dipole matrix element between the initial (ground) and final (excited) states of the two-

level system, with

$$W_{ge} = \langle \hat{\mathbf{d}} \cdot \hat{\mathbf{E}} \rangle_{ge} \quad (\text{H.2})$$

where $\hat{\mathbf{d}}$ is the electric dipole operator, $\hat{\mathbf{E}}$ is the electric field operator, and the subscript ge indicates that the matrix element connects the ground and excited states of the emitter. $\rho(E_{ge})$ is the density of photon modes at the emitter's transition energy E_{ge} . We recall that Fermi's Golden Rule is only applicable under the assumption that the dipole can effectively be thought of as coupling to a continuum of modes. When the dipole is embedded in a uniform dielectric material, this is clearly the case. When it is embedded within a cavity, we must satisfy the condition that the dipole's emission line be spectrally narrow compared to the cavity resonance.

Let us begin by calculating the spontaneous emission rate when the emitter is in a uniform dielectric of index n . The density of modes ρ is obtained by the usual procedure of counting the number of modes within some box of volume V [224]. This yields:

$$\rho_0 = \frac{\omega^2 n^3 V}{3\pi^2 c^3} \quad (\text{H.3})$$

where the factor of $1/3$ represents the random orientation of the modes within a uniform dielectric with respect to the dipole (this factor is derived in Yariv's Quantum Electronics book [223], for example). The spontaneous emission rate is then given by:

$$\frac{1}{\tau_{sp,0}} = \frac{2\pi}{\hbar^2} |\langle \hat{\mathbf{d}} \cdot \hat{\mathbf{E}} \rangle_{ge}|^2 \frac{\omega^2 n^3 V}{3\pi^2 c^3} \quad (\text{H.4})$$

with the electric field operator written as [223]

$$\hat{\mathbf{E}}(\mathbf{r}) = iE_{max}(\mathbf{f}(\mathbf{r})\hat{a} - \mathbf{f}^*(\mathbf{r})\hat{a}^\dagger) \quad (\text{H.5})$$

In this equation, \hat{a} and \hat{a}^\dagger are the field annihilation and creation operators, respectively, and $\mathbf{f}(\mathbf{r})$ is describes the spatial variation of the electric field (it is essentially a normalized version of the

electric field). E_{max} is the amplitude of the field, a per photon electric field strength written as:

$$E_{max} = \sqrt{\frac{\hbar\omega}{2\epsilon_0 n^2 V}} \quad (\text{H.6})$$

If we plug this into equation (H.4), we arrive at:

$$\frac{1}{\tau_{sp,0}} = \frac{ne^2 |\hat{\mathbf{r}}_{ge}|^2 \omega^3}{3\pi \hbar \epsilon_0 c^3} \quad (\text{H.7})$$

where I have taken $\hat{\mathbf{d}} = e\mathbf{r}$. Equation (H.7) is the standard expression for the spontaneous emission rate into a uniform dielectric material of index n .

When the emitter is placed in a cavity with a mode volume V_{eff} , E_{max} is given by the same expression as in equation (H.6), but with V (the quantization volume for the uniform dielectric material) replaced by V_{eff} . We next write $|W_{ge}|^2 = e^2 |\hat{\mathbf{r}}_{ge}|^2 E_{max}^2 \eta^2$, where $\eta = \mathbf{d} \cdot \mathbf{E} / |\mathbf{d}| E_{max}$ describes not only the orientation of the dipole with respect to the cavity field, but also the spatial dependence of the dipole within the cavity field (that is, even if the dipole is aligned with the field, if it is positioned at some place other than an antinode of the field, $\eta < 1$). If the cavity mode has a linewidth $\Delta\omega_c$, corresponding to a quality factor $Q = \omega_c / \Delta\omega_c$, we can write its density of states as:

$$\rho_c = \frac{2Q}{\pi\omega_c} \frac{\Delta\omega_c^2}{4(\omega - \omega_c)^2 + \Delta\omega_c^2} \quad (\text{H.8})$$

which is a Lorentzian function that has been normalized so that $\int_{\omega} \rho_c(\omega) d\omega = 1$. If we plug this, along with our expression for $|W_{ge}|^2$ into equation (H.1), we arrive at:

$$\frac{1}{\tau_{sp,c}} = \frac{2Qe^2 |\hat{\mathbf{r}}_{ge}|^2 \eta^2}{\hbar \epsilon_0 n^2 V_{\text{eff}}} \frac{\Delta\omega_c^2}{4(\omega - \omega_c)^2 + \Delta\omega_c^2} \quad (\text{H.9})$$

The ratio of equations H.9 and H.7 gives us the Purcell enhancement:

$$\frac{\tau_{sp,0}}{\tau_{sp,c}} = \frac{3}{4\pi^2} \left(\frac{Q}{V_{\text{eff}}} \right) \left(\frac{\lambda}{n} \right)^3 \frac{\Delta\omega_c^2}{4(\omega - \omega_c)^2 + \Delta\omega_c^2} \eta^2 \quad (\text{H.10})$$

When the emitter is spatially aligned with an antinode of the field, is spectrally aligned with the field ($\omega = \omega_c$), and oriented along the field, we arrive at the Purcell factor F_p quoted in chapter 4:

$$F_p = \frac{\tau_{sp,0}}{\tau_{sp,c}} = \frac{3}{4\pi^2} \left(\frac{Q}{V_{\text{eff}}} \right) \left(\frac{\lambda_c}{n} \right)^3 \quad (\text{H.11})$$

We again note that the above is valid when the dipole emission linewidth is narrow in comparison to the cavity mode linewidth. If this is not the case, the Q used in F_p will not be the cavity Q but instead will be the emitter's $Q = \lambda_e/\gamma_e$, where γ_e is the emitter linewidth.

H.2 Atom-photon coupling rate

The coupling strength between a single two-level system and an optical field is given by the dipole matrix element divide by Planck's constant. That is:

$$g = \frac{|\langle \hat{\mathbf{d}} \cdot \hat{\mathbf{E}} \rangle|}{\hbar} \quad (\text{H.12})$$

For the purposes of this thesis, the above formula is used to calculate quantities like the optimal coupling strength between an atom, or quantum dot, and a single photon within a resonant cavity. For these calculations, it is assumed that the dipole and the field are aligned, so that $g = d_{ge}E_{\text{max}}/\hbar$, where the per photon field strength E_{max} of equation (H.6) is used, along with some value for the strength of the electric dipole d_{ge} as found in literature.

In many cases, d_{ge} will not be the piece of information readily available; rather, the spontaneous emission rate between the two levels τ_{sp} will be. Using equation (H.7), we can easily relate the two quantities, and then arrive at an expression for g . Doing so yields

$$g = \frac{1}{2\tau_{\text{sp}}} \sqrt{\frac{3c\lambda_0^2\tau_{\text{sp}}}{2\pi n^3 V_{\text{eff}}}}, \quad (\text{H.13})$$

As defined above, g has units of radians/second; dividing by 2π express it units of Hz, which are often the units for which g is quoted. To be explicit, I have adopted the convention of writing $g/2\pi$ when quoting values in units of Hz, to try to eliminate any confusion.

Within the literature, the decay rates γ_{\parallel} and γ_{\perp} are sometimes used. γ_{\parallel} is a radiative decay rate, equal to $1/\tau_{\text{sp}}$. γ_{\perp} is a transverse decay rate, and is most generally written as $\gamma_{\perp} = \frac{\gamma_{\parallel}}{2} + \gamma_p$, where γ_p is due to non-radiative decay (for example, phase-destroying collisional processes). For strong coupling, it is the total emitter decay rate, γ_{\perp} , that must be exceeded by the coherent coupling rate g . Within single atom systems, the decay is essentially purely radiative, so that $\gamma_{\perp} = \frac{\gamma_{\parallel}}{2}$ is taken. For these systems, g is then often written in terms of γ_{\perp} rather than τ_{sp} . Doing so yields

$$g = \gamma_{\perp} \sqrt{\frac{3c\lambda_0^2}{4\pi n^3 V_{\text{eff}} \gamma_{\perp}}}, \quad (\text{H.14})$$

Within the literature, the decay times T_1 and T_2 are often quoted [223]; by our definitions above, $T_2 = 1/\gamma_{\perp}$ and $T_1 = 1/\gamma_{\parallel}$.

In semiconductor-based structures such as quantum dots, an oscillator strength is often quoted [110, 70]. This oscillator strength f is a dimensionless quantity given by

$$f = \frac{2m\omega |\langle \hat{\mathbf{r}}_{ge} \rangle|^2}{\hbar}, \quad (\text{H.15})$$

It is found through a calculation of the optical susceptibility $\chi(\omega)$ of an atom ($P(\omega) = \chi(\omega)E(\omega)$, where $P(\omega)$ is the field-induced polarization), and subsequent comparison to the expression generated by the classical damped, driven harmonic oscillator model of the atom. Reference [229] presents such a derivation. The QD-coupling rate g can then be written in terms of the oscillator strength as:

$$g = \sqrt{\frac{e^2 f}{4\epsilon_0 n^2 V_{\text{eff}}}}, \quad (\text{H.16})$$

Bibliography

- [1] O. Painter, K. Srinivasan, J. D. O'Brien, A. Scherer, and P. D. Dapkus. Tailoring of the resonant mode properties of optical nanocavities in two-dimensional photonic crystal slab waveguides. *J. Opt. A*, 3(6) S161–S170, November 2001.
- [2] O. Painter and K. Srinivasan. Polarization properties of dipole-like defect modes in photonic crystal nanocavities. *Opt. Lett.*, 27(5) 339–341, March 2002.
- [3] O. Painter. *Optical Nanocavities in Two-Dimensional Photonic Crystal Planar Waveguides*. PhD thesis, California Institute of Technology, 2001.
- [4] J. D. Joannopoulos, R. D. Meade, and J. N. Winn. *Photonic Crystals*. Princeton University Press, Princeton, New Jersey, 1995.
- [5] K. Sakoda. *Optical Properties of Photonic Crystals*. Springer-Verlag, Berlin, Germany, 2001.
- [6] A. Taflove and S. C. Hagness. *Computational Electrodynamics: the finite-difference time-domain method*. Artech House, Boston, Massachusetts, 2000.
- [7] O. Painter, J. Vučković, and A. Scherer. Defect modes of a two-dimensional photonic crystal in an optically thin dielectric slab. *J. Opt. Soc. Am. B*, 16(2) 275–285, February 1999.
- [8] O. Painter, R. K. Lee, A. Yariv, A. Scherer, J. D. O'Brien, P. D. Dapkus, and I. Kim. Two-dimensional photonic band-gap defect mode laser. *Science*, 284 1819–1824, June 1999.
- [9] H. J. Kimble. Strong interactions of single atoms and photons in cavity QED. *Physica Scripta*, T76 127–137, 1998.
- [10] P. Michler, editor. *Single Quantum Dots*. Springer Verlag, Berlin, 2003.
- [11] J. Vučković, M. Lončar, H. Mabuchi, and A. Scherer. Design of photonic crystal microcavities for cavity QED. *Phys. Rev. E*, 65(1), January 2002.

- [12] T. Yoshie, J. Vučković, A. Scherer, H. Chen, and D. Deppe. High quality two-dimensional photonic crystal slab cavities. *Appl. Phys. Lett.*, 79(26) 4289–4291, December 2001.
- [13] B. Gayral, J.-M. Gérard, A. Lemaître, C. Dupuis, L. Manin, and J. L. Pelouard. High- Q wet-etched GaAs microdisks containing InAs quantum boxes. *Appl. Phys. Lett.*, 75(13) 1908–1910, September 1999.
- [14] P. Michler, A. Kiraz, L. D. Zhang, C. Becher, E. Hu, and A. Imamoglu. Laser emission from quantum dots in microdisk structures. *Appl. Phys. Lett.*, 77(2) 184–186, 2000.
- [15] J.-M. Gérard, B. Sermage, B. Gayral, B. Legrand, E. Costard, and V. Thierry-Mieg. Enhanced spontaneous emission by quantum boxes in a monolithic optical microcavity. *Phys. Rev. Lett.*, 81(5) 1110–1113, August 1998.
- [16] G. S. Solomon, M. Pelton, and Y. Yamamoto. Single-mode spontaneous emission from a single quantum dot in a three-dimensional microcavity. *Phys. Rev. Lett.*, 86(17) 3903–3906, 2001.
- [17] C. J. Hood, T. W. Lynn, A. C. Doherty, A. S. Parkins, and H. J. Kimble. The atom-cavity microscope: single atoms bound in orbit by single photons. *Science*, 287(5457) 1447–1453, February 2000.
- [18] P. W. H. Pinsky, T. Fischer, P. Maunz, and G. Rempe. Trapping an atom with single photons. *Nature*, 404 365–368, March 2000.
- [19] D. W. Vernooy, V. S. Ilchenko, H. Mabuchi, E. W. Streed, and H. J. Kimble. High- Q measurements of fused-silica microspheres in the near infrared. *Opt. Lett.*, 23(4) 247–249, February 1998.
- [20] M. Cai, O. Painter, and K. J. Vahala. Observation of critical coupling in a fiber taper to a silica-microsphere whispering-gallery mode system. *Phys. Rev. Lett.*, 85(1) 74–77, July 2000.
- [21] K. Srinivasan and O. Painter. Momentum space design of high- Q photonic crystal optical cavities. *Opt. Express*, 10(15) 670–684, July 2002.
- [22] J. Vučković, M. Lončar, H. Mabuchi, and A. Scherer. Optimization of the Q factor in photonic crystal microcavities. *IEEE J. Quan. Elec.*, 38(7) 850–856, July 2002.

- [23] K. Srinivasan and O. Painter. Fourier space design of high- Q cavities in standard and compressed hexagonal lattice photonic crystals. *Opt. Express*, 11(6) 579–593, March 2003.
- [24] O. Painter and K. Srinivasan. Localized defect states in two-dimensional photonic crystal slab waveguides: a simple model based upon symmetry analysis. *Phys. Rev. B*, 68 035110, July 2003.
- [25] O. Painter, K. Srinivasan, and P. E. Barclay. A Wannier-like equation for photon states of locally perturbed photonic crystals. *Phys. Rev. B*, 68 035214, July 2003.
- [26] H.-Y. Ryu, M. Notomi, and Y.-H. Lee. High-quality-factor and small-mode-volume hexapole modes in photonic-crystal-slab nanocavities. *Appl. Phys. Lett.*, 83(21) 4294–4296, November 2003.
- [27] Z. Zhang and M. Qiu. Small-volume waveguide-section high Q microcavities in 2D photonic crystal slabs. *Opt. Express*, 12(17) 3988–3995, August 2004.
- [28] B.-S. Song, S. Noda, T. Asano, and Y. Akahane. Ultra-high- Q photonic double-heterostructure nanocavity. *Nature Materials*, 4 207–210, February 2005.
- [29] D. Englund, I. Fushman, and J. Vučković. General recipe for designing photonic crystal cavities. *Opt. Express*, 13(16) 5961–5975, August 2005.
- [30] E. Kuramochi, M. Notomi, S. Mitsugi, A. Shinya, T. Tanabe, and T. Watanabe. Ultrahigh- Q photonic crystal nanocavities realized by the local width modulation of a line defect. *Appl. Phys. Lett.*, 88 041112, January 2006.
- [31] J. M. Geremia, J. Williams, and H. Mabuchi. Inverse-problem approach to designing photonic crystals for cavity QED experiments. *Phys. Rev. E*, 66 066606, December 2002.
- [32] J. C. Knight, G. Cheung, F. Jacques, and T. A. Birks. Phase-matched excitation of whispering-gallery-mode resonances by a fiber taper. *Opt. Lett.*, 22(15) 1129–1131, August 1997.
- [33] P. E. Barclay, K. Srinivasan, and O. Painter. Design of photonic crystal waveguides for evanescent coupling to optical fiber tapers and integration with high- Q cavities. *J. Opt. Soc. Am. B*, 20(11) 2274–2284, November 2003.

- [34] R. Colombelli, K. Srinivasan, M. Troccoli, O. Painter, C. Gmachl, D. M. Tennant, A. M. Sergent, D. L. Sivco, A. Y. Cho, and F. Capasso. Quantum cascade surface-emitting photonic crystal laser. *Science*, 302 1374, November 2003.
- [35] R. Colombelli, K. Srinivasan, M. Troccoli, O. Painter, C. Gmachl, D. M. Tennant, A. M. Sergent, D. L. Sivco, A. Y. Cho, and F. Capasso. Fabrication technologies for quantum cascade photonic crystal microlasers. *Nanotechnology*, 15 675–681, March 2004.
- [36] K. Srinivasan, O. Painter, R. Colombelli, C. Gmachl, D.M. Tennant, A.M. Sergent, D.L. Sivco, A. Y. Cho., M. Troccoli, and F. Capasso. Lasing mode pattern of a quantum cascade photonic crystal surface-emitting microcavity laser. *Appl. Phys. Lett.*, 84(20) 3990, May 2004.
- [37] K. Srinivasan and O. Painter. Design of two-dimensional photonic crystal defect states for quantum cascade laser resonators. www.arxiv.org/abs/physics/0410068, 2004.
- [38] P. E. Barclay, K. Srinivasan, M. Borselli, and O. Painter. Experimental demonstration of evanescent coupling from optical fibre tapers to photonic crystal waveguides. *IEE Elec. Lett.*, 39(11) 842–844, May 2003.
- [39] P. E. Barclay, K. Srinivasan, M. Borselli, and O. Painter. Efficient input and output optical fiber coupling to a photonic crystal waveguide. *Opt. Lett.*, 29(7) 697–699, April 2004.
- [40] P. E. Barclay, K. Srinivasan, M. Borselli, and O. Painter. Probing the dispersive and spatial properties of planar photonic crystal waveguide modes via highly efficient coupling from optical fiber tapers. *Appl. Phys. Lett.*, 85(1), July 2004.
- [41] S. L. McCall, A. F. J. Levi, R. E. Slusher, S. J. Pearton, and R. A. Logan. Whispering-gallery mode lasers. *Appl. Phys. Lett.*, 60(3) 289–291, January 1992.
- [42] H.-Y. Ryu, S.-H. Kim, H.-G. Park, J.-K. Hwang, Y.-H. Lee, and J.-S. Kim. Square-lattice photonic band-gap single-cell laser operating in the lowest-order whispering gallery mode. *Appl. Phys. Lett.*, 80(21) 3883–3885, May 2002.
- [43] K. Srinivasan, P. E. Barclay, O. Painter, J. Chen, A. Y. Cho, and C. Gmachl. Experimental demonstration of a high quality factor photonic crystal microcavity. *Appl. Phys. Lett.*, 83(10) 1915–1917, September 2003.

- [44] K. Srinivasan, P. E. Barclay, O. Painter, J. Chen, and A. Y. Cho. Fabrication of high- Q photonic crystal microcavities in InAsP/InGaAsP multi-quantum well membranes. *J. Vac. S. Tech. B*, 22(3) 875, May 2004.
- [45] M. Lončar, A. Scherer, and Y. Qiu. Photonic crystal laser sources for chemical detection. *Appl. Phys. Lett.*, 82(26) 4648–4650, June 2003.
- [46] M. Lončar, M. Hochberg, A. Scherer, and Y. Qiu. High quality factors and room temperature lasing in a modified single-defect photonic crystal cavity. *Opt. Lett.*, 29(7) 721–723, April 2004.
- [47] E. Chow, A. Grot, L. W. Mirkarimi, M. Sigalas, and G. Girolami. Ultracompact biochemical sensor built with two-dimensional photonic crystal microcavity. *Opt. Lett.*, 29(10) 1093–1095, May 2004.
- [48] D. Dalacu, S. Frederick, A. Bogdanov, P. J. Poole, G. C. Aers, R. L. Williams, M. W. McCutcheon, and J. F. Young. Fabrication and optical characterization of hexagonal photonic crystal microcavities in InP-based membranes containing InAs/InP quantum dots. *J. Appl. Phys.*, 98 023101, July 2005.
- [49] S. Noda, A. Chutinan, and M. Imada. Trapping and emission of photons by a single defect in a photonic bandgap structure. *Nature*, 407(6804) 608–610, October 2000.
- [50] C. Manolatou, M. J. Khan, S. Fan, P. R. Villeneuve, H. A. Haus, and J. D. Joannopoulos. Coupling of Modes Analysis of Resonant Channel Add-Drop Filters. *IEEE J. Quan. Elec.*, 35(9) 1322–1331, September 1999.
- [51] Y. Akahane, T. Asano, B.-S. Song, and S. Noda. High- Q photonic nanocavity in a two-dimensional photonic crystal. *Nature*, 425 944–947, October 2003.
- [52] K. Srinivasan, P. E. Barclay, M. Borselli, and O. Painter. Optical-fiber-based measurement of an ultrasmall volume, high- Q photonic crystal microcavity. *Phys. Rev. B*, 70 081306R, August 2004.
- [53] K. Srinivasan, P. E. Barclay, and O. Painter. Fabrication-tolerant high quality factor photonic crystal microcavities. *Opt. Express*, 12(7) 1458–1463, April 2004.

- [54] K. Srinivasan, P. E. Barclay, M. Borselli, and O. Painter. An optical fiber-based probe for photonic crystal microcavities. *IEEE J. on Sel. Area. in Comm.*, 23(7) 1321–1329, July 2005.
- [55] S. M. Spillane, T. J. Kippenberg, O. J. Painter, and K. J. Vahala. Ideality in a fiber-taper-coupled microresonator system for application to cavity quantum electrodynamics. *Phys. Rev. Lett.*, 91(4) 043902, July 2003.
- [56] D. K. Armani, T. J. Kippenberg, S. M. Spillane, and K. J. Vahala. Ultra-high- Q toroid microcavity on a chip. *Nature*, 421 925–928, February 2003.
- [57] P. E. Barclay, K. Srinivasan, and O. Painter. Nonlinear response of silicon photonic crystal microcavities excited via an integrated waveguide and fiber taper. *Opt. Express*, 13(3) 801–820, January 2005.
- [58] M. Notomi, A. Shinya, S. Mitsugi, G. Kira, E. Kuramochi, and T. Tanabe. Optical bistable switching action of Si high- Q photonic-crystal nanocavities. *Opt. Express*, 13(7) 2678–2687, April 2005.
- [59] Y. Akahane, T. Asano, B.-S. Song, and S. Noda. Fine-tuned high- Q photonic-crystal nanocavity. *Opt. Express*, 13 1202–1214, February 2005.
- [60] H. Mabuchi and A. C. Doherty. Cavity quantum electrodynamics: coherence in context. *Science*, 298 1372–1377, November 2002.
- [61] B. Lev. Fabrication of micro-magnetic traps for cold neutral atoms. *Quantum information and computation*, 3(5) 450–464, 2003.
- [62] B. Lev, K. Srinivasan, P. E. Barclay, O. Painter, and H. Mabuchi. Feasibility of detecting single atoms with photonic bandgap cavities. *Nanotechnology*, 15 S556–S561, 2004.
- [63] K. Hennessy, C. Reese, A. Badolato, C. F. Wang, A. Imamoglu, P. M. Petroff, E. Hu, G. Jin, S. Shi, and D. W. Prather. Square-lattice photonic crystal microcavities for coupling to single InAs quantum dots. *Appl. Phys. Lett.*, 83(18) 3650–3652, November 2003.
- [64] M. Borselli, K. Srinivasan, P. E. Barclay, and O. Painter. Rayleigh scattering, mode coupling, and optical loss in silicon microdisks. *Appl. Phys. Lett.*, 85(17) 3693–3695, October 2004.

- [65] M. Borselli, T. J. Johnson, and O. Painter. Beyond the Rayleigh scattering limit in high- Q silicon microdisks: theory and experiment. *Opt. Express*, 13(5) 1515–1530, March 2005.
- [66] M. M. Karkhanehchi, D. A. Barrow, A. C. Bryce, C. J. Hamilton, and J. H. Marsh. The Influence of Single-Photon Absorption on the Performance of the Two-Photon Waveguide Autocorrelator. *IEEE J. Quan. Elec.*, 33(6) 933–937, June 1997.
- [67] E. Knill, R. Laflamme, and G. J. Milburn. A scheme for efficient quantum computation with linear optics. *Nature*, 409(6816) 46–52, January 2001.
- [68] A. Kiraz, M. Atature, and A. Imamoglu. Quantum-dot single-photon sources: Prospects for applications in linear optics quantum-information processing. *Phys. Rev. A*, 69 032305, 2004.
- [69] K. Srinivasan, M. Borselli, T. J. Johnson, P. E. Barclay, O. Painter, A. Stintz, and S. Krishna. Optical loss and lasing characteristics of high-quality-factor AlGaAs microdisk resonators with embedded quantum dots. *Appl. Phys. Lett.*, 86 151106, April 2005.
- [70] J. P. Reithmaier, G. Sek, A. Loffer, C. Hoffman, S. Kuhn, S. Reitzenstein, L. V. Keldysh, V. D. Kulakovskii, T. L. Reinecke, and A. Forchel. Strong coupling in a single quantum dot-semiconductor microcavity system. *Nature*, 432 197–200, November 2004.
- [71] T. Yoshie, A. Scherer, J. Hendrickson, G. Khitrova, H.M. Gibbs, G. Rupper, C. Ell, Q.B. Schenkin, and D.G. Deppe. Vacuum Rabi splitting with a single quantum dot in a photonic crystal nanocavity. *Nature*, 432 200–203, November 2004.
- [72] E. Peter, P. Senellart, D. Martrou, A. Lemaître, J. Hours, J. M. Gérard, and J. Bloch. Exciton photon strong-coupling regime for a single quantum dot embedded in a microcavity. *Phys. Rev. Lett.*, 95(067401), August 2005.
- [73] M. Cai, O. Painter, K. J. Vahala, and P. C. Sercel. Fiber-coupled microsphere laser. *Opt. Lett.*, 25(19) 1430–1432, October 2000.
- [74] L. Yang, D. K. Armani, and K. J. Vahala. Fiber-coupled erbium microlasers on a chip. *Appl. Phys. Lett.*, 83(5) 825–827, August 2003.

- [75] K. Srinivasan, A. Stintz, S. Krishna, and O. Painter. Photoluminescence measurements of quantum-dot-containing semiconductor microdisk resonators using optical fiber taper waveguides. *Phys. Rev. B*, 72(20) 205318, November 2005.
- [76] K. Srinivasan, M. Borselli, O. Painter, A. Stintz, and S. Krishna. Cavity Q , mode volume, and lasing threshold in small diameter AlGaAs microdisks with embedded quantum dots. *Opt. Express*, 14(3) 1094–1105, February 2006.
- [77] R. J. Thompson, G. Rempe, and H. J. Kimble. Observation of normal-mode splitting for an atom in an optical cavity. *Phys. Rev. Lett.*, 68(8) 1132–1135, February 1992.
- [78] A. Boca, R. Miller, K. M. Birnbaum, A. D. Boozer, J. McKeever, and H. J. Kimble. Observation of the vacuum Rabi spectrum for one trapped atom. *Phys. Rev. Lett.*, 93 233603, December 2004.
- [79] K. M. Birnbaum, A. Boca, R. Miller, A.D. Boozer, T. E. Northup, and H. J. Kimble. Photon blockade in an optical cavity with one trapped atom. *Nature*, 436 87–90, July 2005.
- [80] P. E. Barclay, K. Srinivasan, M. Borselli, T. J. Johnson, O. Painter, B. Lev, and H. Mabuchi. Fiber-coupled silicon nitride microcavities for integration with atom chips. 2006. manuscript in preparation.
- [81] S. M. Tan. Quantum optics and computation toolbox for MATLAB, and accompanying user guide. <http://www.qo.phy.auckland.ac.nz/qotoolbox.html>, 2002.
- [82] S. M. Tan. A computational toolbox for quantum and atomic optics. *Journal of Optics B: Quantum and Semiclassical Optics*, 1 424–432, 1999.
- [83] T. J. Kippenberg, S. M. Spillane, and K. J. Vahala. Demonstration of ultra-high- Q small volume toroid microcavities on a chip. *Appl. Phys. Lett.*, 85(25) 6113–6115, December 2004.
- [84] A. Löffler, J. P. Reithmaier, G. Sek, C. Hofmann, S. Reitzenstein, M. Kamp, and A. Forchel. Semiconductor quantum dot microcavity pillars with high-quality factors and enlarged dot dimensions. *Appl. Phys. Lett.*, 86 111105, March 2005.
- [85] N. G. Stoltz, M. Rakher, S. Strauf, A. Badolato, D. D. Lofgreen, P. M. Petroff, L. A. Col-dren, and D. Bouwmeester. High-quality factor optical microcavities using oxide apertured micropillars. *Appl. Phys. Lett.*, 87 031105, July 2005.

- [86] S. P. Ogawa, M. Imada, S. Yoshimoto, M. Okano, and S. Noda. Control of light emission by 3D photonic crystals. *Science*, 305 227–229, July 2004.
- [87] W. M. J. Green, J. Scheuer, G. DeRose, and A. Yariv. Vertically emitting annular Bragg lasers using polymer epitaxial transfer. *Appl. Phys. Lett.*, 85(17) 3669–3671, October 2004.
- [88] J. Scheuer, W. M. J. Green, G. DeRose, and A. Yariv. Lasing from a circular Bragg nanocavity with an ultrasmall modal volume. *Appl. Phys. Lett.*, 86(25) 251101, 2005.
- [89] Y. Xu, W. Liang, A. Yariv, J. G. Fleming, and S.-Y. Lin. High-quality-factor Bragg onion resonators with omnidirectional reflector cladding. *Opt. Lett.*, 28(22) 2144–2146, November 2003.
- [90] K. Sakoda. Symmetry, degeneracy, and uncoupled modes in two-dimensional photonic crystals. *Phys. Rev. B*, 52(11) 7982–7986, September 1995.
- [91] W. Ludwig and C. Falter. *Symmetries in Physics: Group Theory Applied to Physical Problems*. Number 64 in Springer-Verlag Series in Solid-State Sciences. Springer-Verlag, New York, NY, 2nd edition, 1996.
- [92] M. Tinkham. *Group Theory and Quantum Mechanics*. International Series in Pure and Applied Physics. McGraw-Hill, Inc., New York, NY, 1964.
- [93] J. D. Jackson. *Classical Electrodynamics*. John Wiley & Sons, Inc., New York, NY, 2nd edition, 1975.
- [94] E. Yablonovitch, T. J. Gmitter, R. D. Meade, A. M. Rappe, K. D. Brommer, and J. D. Joannopoulos. Donor and acceptor modes in photonic band-structure. *Phys. Rev. Lett.*, 67(24) 3380–3383, June 1991.
- [95] O. J. Painter, A. Husain, A. Scherer, J. D. O’Brien, I. Kim, and P. D. Dapkus. Room Temperature Photonic Crystal Defect Lasers at Near-Infrared Wavelengths in InGaAsP. *J. Lightwave Tech.*, 17(11) 2082–2088, November 1999.
- [96] J. C. Slater. Electrons in perturbed periodic lattices. *Physical Review*, 76(11) 1592–1601, 1949.
- [97] C. Kittel and A. H. Mitchell. Theory of donor and acceptor states in silicon and germanium. *Physical Review*, 96(6) 1488–1493, December 1954.

- [98] J. M. Luttinger and W. Kohn. Motion of electrons and holes in perturbed periodic fields. *Physical Review*, 97(4) 869–883, February 1955.
- [99] G. H. Wannier. Dynamics of band electrons in electric and magnetic fields. *Reviews of Modern Physics*, 34(4) 645–655, October 1962.
- [100] N. F. Johnson and P. M. Hui. Theory of propagation of scalar waves in periodic and disordered composite structures. *Phys. Rev. B*, 48(14) 10118–10123, October 1993.
- [101] M. Charbonneau-Lefort, E. Istrate, M. Allard, J. Poon, and E. H. Sargent. Photonic crystal heterostructures: Waveguiding phenomena and methods of solution in an envelope picture. *Phys. Rev. B*, 65 125318, March 2002.
- [102] E. Istrate, M. Charbonneau-Lefort, and E. H. Sargent. Theory of photonic crystal heterostructures. *Phys. Rev. B*, 66 075121, August 2002.
- [103] G. H. Wannier. The structure of electronic excitation levels in insulating crystals. *Physical Review*, 52 191–197, August 1937.
- [104] A. Baldereschi. Valley-orbit interaction in semiconductors. *Phys. Rev. B*, 1(12) 4673–4677, June 1970.
- [105] P. C. Sercel and K. J. Vahala. Analytical formalism for determining quantum-wire and quantum-dot band structure in the multiband envelope-function approximation. *Phys. Rev. B*, 42(6) 3690–3710, August 1990.
- [106] W. Kohn and J. M. Luttinger. Theory of donor states in silicon. *Physical Review*, 98(4) 915–922, May 1955.
- [107] J. E. Sipe. Vector $\mathbf{k} \cdot \mathbf{p}$ approach for photonic band structures. *Phys. Rev. E*, 62(4) 5672–5677, October 2000.
- [108] S. G. Johnson, S. Fan, A. Mekis, and J. D. Joannopoulos. Multipole-cancellation mechanism for high- Q cavities in the absence of a complete photonic band gap. *Appl. Phys. Lett.*, 78(22) 3388–3390, May 2001.
- [109] J.-M. Gérard and B. Gayral. Strong Purcell effect for InAs quantum boxes in three-dimensional solid-state microcavities. *J. Lightwave Tech.*, 17(11) 2089–2095, November 1999.

- [110] L. C. Andreani, G. Panzarini, and J.-M. Gérard. Strong-coupling regime for quantum boxes in pillar microcavities: Theory. *Phys. Rev. B*, 60(19) 13276–13279, November 1999.
- [111] H. Benisty, D. Labilloy, C. Weisbuch, C. J. M. Smith, T. F. Krauss, D. Cassagne, A. Beraud, and C. Jouanin. Radiation losses of waveguide-based two-dimensional photonic crystals: Positive role of the substrate. *Appl. Phys. Lett.*, 76(5) 532–534, 2000.
- [112] C. Reese, B. Gayral, B. D. Gerardot, A. Imamoglu, P. M. Petroff, and E. Hu. High- Q photonic crystal microcavities fabricated in a thin GaAs membrane. *J. Vac. S. Tech. B*, 19(6) 2749–2752, Nov/Dec 2001.
- [113] W.-Y. Hwang, J.N. Baillargeon, S. N. G. Chu, P. F. Sciortino, and A. Y. Cho. GaInAsP/InP distributed feedback lasers grown directly on grating substrates by solid-source molecular beam epitaxy. *J. Vac. S. Tech. B*, 16(3) 1422–1425, 1998.
- [114] Y. Tanaka, T. Asano, Y. Akahane, B.-S. Song, and S. Noda. Theoretical investigation of a two-dimensional photonic crystal slab with truncated air holes. *Appl. Phys. Lett.*, 82(11) 1661–1663, March 2003.
- [115] C. Youtsey and I. Adesida. *Dry Etching of InP and Related Materials*, in *Handbook of Advanced Plasma Processing Techniques*, pages 479–483. Springer, Berlin, 2000.
- [116] Y. Fujiwara, K. Kikuchi, M. Hashimoto, H. Hatate, T. Imai, Y. Takeda, H. Nakano, M. Honda, T. Tatsuta, and O. Tsujii. Fabrication of Two-Dimensional InP Photonic Band-Gap Crystals by Reactive Ion Etching with Inductively Coupled Plasma. *Jap. J. Appl. Phys. 1*, 36(12B) 7763–7768, December 1997.
- [117] S. L. Rommel, J.-H. Jang, W. Lu, G. Cueva, L. Zhou, G. Pajer, R. Whaley, A. Lepore, Z. Schellanbarger, and J. H. Abeles. Effect of H_2 on the etch profile of InP/InGaAsP alloys in $Cl_2/Ar/H_2$ inductively coupled plasma reactive ion etching chemistries for photonic device fabrication. *J. Vac. S. Tech. B*, 20(4) 1327–1330, Jul/Aug 2002.
- [118] P. Mounaix, P. Delobelle, X. Mélique, L. Bornier, and D. Lippens. Micromachining and mechanical properties of GaInAs/InP microcantilevers. *Materials Science and Engineering B*, 51 258–262, 1998.
- [119] S. Adachi and H. Kawaguchi. Chemical etching characteristics of (001)InP. *J. Electrochem. Soc.*, 128(6) 1342–1349, June 1981.

- [120] R. E. Slusher. Optical processes in microcavities. *Semiconductor Science and Technology*, 9(11) 2025–2030, 1994.
- [121] G. P. Agrawal and N. K. Dutta. *Semiconductor Lasers*. Van Nostrand Reinhold, New York, NY, 1993.
- [122] T. A. Birks and Y. W. Li. The shape of fiber tapers. *J. Lightwave Tech.*, 10(4) 432–438, April 1992.
- [123] T. E. Dimmick, G. Kakarantzas, T. A. Birks, and P. St. J. Russell. Carbon dioxide laser fabrication of fused-fiber couplers and taper. *Appl. Opt.*, 38(33) 6845–6848, November 1999.
- [124] J. C. Knight, N. Dubreuil, V. Sandoghdar, J. Hare, V. Lefèvre-Seguin, J. M. Raimond, and S. Haroche. Mapping whispering-gallery modes in microspheres with a near-field probe. *Opt. Lett.*, 20(14) 1515–1517, July 1995.
- [125] H. A. Haus. *Waves and Fields in Optoelectronics*. Prentice-Hall, Englewood Cliffs, New Jersey, 1st edition, 1984.
- [126] A. Yariv. *Optical Electronics*. Saunder College Publishing, a division of Holt, Rinehart and Winston, Inc., Orlando, Florida, 5th edition, 1997.
- [127] C. Becher, A. Kiraz, P. Michler, A. Imamoğlu, W. V. Schoenfeld, P. M. Petroff, Lidong Zhang, and E. Hu. Nonclassical radiation from a single self-assembled InAs quantum dot. *Phys. Rev. B*, 63 121312, 2001.
- [128] M. Borselli, T. J. Johnson, and O. Painter. Measuring the role of surface chemistry in silicon microphotronics. *Appl. Phys. Lett.*, 88 13114, March 2006.
- [129] L. Collot, V. Lefevre-Seguin, M. Brune, J. M. Raimond, and S. Haroche. Very high- Q whispering gallery mode resonances observed on fused-silica microspheres. *Europhysics Letters*, 23(5) 327–334, 1993.
- [130] B. E. Little, S. T. Chu, H. A. Haus, J. Foresi, and J. P. Laine. Microring resonator channel dropping filters. *J. Lightwave Tech.*, 15(6) 998–1005, 1997.
- [131] K. Okamoto, M. Loncar, T. Yoshie, A. Scherer, Y. M. Qiu, and P. Gogna. Near-field scanning optical microscopy of photonic crystal nanocavities. *Appl. Phys. Lett.*, 82(11) 1676–1678, 2003.

- [132] B. C. Buchler, P. Kramper, M. Kafesaki, C. M. Soukolis, and V. Sandoghdar. Near-field optical investigations of photonic crystal microresonators. *IEICE Trans. Electron.*, E87-C(3) 371–377, March 2004.
- [133] M. Pelton, C. Santori, J. Vuckovic, B. Zhang, G. S. Solomon, J. Plant, and Y. Yamamoto. Efficient source of single photons: a single quantum dot in a micropost microcavity. *Phys. Rev. Lett.*, 89 233602, December 2002.
- [134] M. Notomi, A. Shinya, K. Yamada, J. Takahashi, C. Takahashi, and I. Yokohama. Structural tuning of guiding modes of line-defect waveguides of silicon-on-insulator photonic crystal slabs. *IEEE J. Quan. Elec.*, 38(7) 736–742, July 2002.
- [135] M. L. Gorodetsky, A. D. Pryamikov, and V. S. Ilchenko. Rayleigh scattering in high- Q microspheres. *J. Opt. Soc. Am. B*, 17(7) 1051–1057, June 2000.
- [136] S. M. Spillane, T. J. Kippenberg, K. J. Vahala, K. W. Goh, E. Wilcut, and H. J. Kimble. Ultrahigh- Q toroidal microresonators for cavity quantum electrodynamics. *Phys. Rev. A*, 71 013817, January 2005.
- [137] M. Borselli. *High- Q Microresonators as Lasing Elements for Silicon Microphotonics*. PhD thesis, California Institute of Technology, 2006.
- [138] D. Bimberg, M. Grundmann, and N. N. Ledentsov. *Quantum Dot Heterostructures*. John Wiley and Sons, New York, 1st edition, 1999.
- [139] P. M. Petroff, A. Lorke, and A. Imamoglu. Epitaxially self-assembled quantum dots. *Physics Today*, 54 46–52, May 2001.
- [140] G. W. Bryant and G. S. Solomon. *Optics of Quantum Dots and Wires*. Artech House, Boston, 2005.
- [141] J. I. Cirac, P. Zoller, H. J. Kimble, and H. Mabuchi. Quantum state transfer and entanglement distribution among distant nodes in a quantum network. *Phys. Rev. Lett.*, 78(16) 3221–3224, April 1997.
- [142] M. Bayer and A. Forchel. Temperature dependence of the exciton homogeneous linewidth in $\text{In}_{0.60}\text{Ga}_{0.40}\text{As}/\text{GaAs}$ self-assembled quantum dots. *Phys. Rev. B*, 65 041308(R), 2002.

- [143] S. Krishna, S. Raghavan, A. L. Gray, A. Stintz, and K. J. Malloy. Characterization of rapid-thermal-annealed InAs/In_{0.15}Ga_{0.85}As dots-in-well heterostructure using double crystal x-ray diffraction and photoluminescence. *Appl. Phys. Lett.*, 80(21) 3898–3900, May 2002.
- [144] G. T. Liu, A. Stintz, H. Li, T. C. Newell, A. L. Gray, P. M. Varangis, K. J. Malloy, and L. F. Lester. The influence of quantum-well composition on the performance of quantum dot lasers using InAs/InGaAs dots-in-a-well (DWELL) structures. *IEEE J. Quan. Elec.*, 36(11) 1272–1279, November 2000.
- [145] R. Haberman. *Elementary Applied Partial Differential Equations with Fourier Series and Boundary Value Problems*. Prentice-Hall, Englewood Cliffs, New Jersey, 1997.
- [146] D. S. Weiss, V. Sandoghdar, J. Hare, V. Lefèvre-Seguin, J.-M. Raimond, and S. Haroche. Splitting of high- Q Mie modes induced by light backscattering in silica microspheres. *Opt. Lett.*, 20(18) 1835–1837, September 1995.
- [147] B. E. Little and S. T. Chu. Estimating surface-roughness loss and output coupling in microdisk resonators. *Opt. Lett.*, 21(7) 1390–1392, September 1996.
- [148] T. J. Kippenberg, S. M. Spillane, and K. J. Vahala. Modal coupling in traveling-wave resonators. *Opt. Lett.*, 27(19) 1669–1671, October 2002.
- [149] H. J. Carmichael. *An Open Systems Approach to Quantum Optics*. Springer-Verlag, Berlin, 1993.
- [150] P. G. Eliseev, H. Li, G. T. Liu, A. Stintz, T. C. Newell, L. F. Lester, and K. J. Malloy. Ground-state emission and gain in ultralow-threshold InAs-InGaAs quantum dot lasers. *IEEE J. Sel. Top. Quan. Elec.*, 7(2) 135–142, March 2001.
- [151] T. Ide, T. Baba, J. Tatebayashi, S. Iwamoto, T. Nakaoka, and Y. Arakawa. Lasing characteristics of InAs quantum-dot microdisk from 3K to room temperature. *Appl. Phys. Lett.*, 85(8) 1326–1328, August 2004.
- [152] L. A. Coldren and S. W. Corzine. *Diode Lasers and Photonic Integrated Circuits*. John Wiley & Sons, New York, NY, 1995.
- [153] Y. Yamamoto and R. E. Slusher. Optical Processes in Microcavities. *Physics Today*, 46(6) 66–73, June 1993.

- [154] W. L. Barnes, G. Björk, J.M. Gérard, P. Jonsson, J. A. E. Wasey, P. T. Worthing, and V. Zwiller. Solid-state single photon sources: light collection strategies. *Eur. Phys. J. D*, 18 197–210, 2002.
- [155] A. F. J. Levi, R. E. Slusher, S. L. McCall, J. L. Glass, S. J. Pearton, and R. A. Logani. Directional light coupling from microdisk lasers. *Appl. Phys. Lett.*, 62(6) 561–563, February 1993.
- [156] J.U. Nöckel. Optical feedback and the coupling problem in semiconductor microdisk lasers. *Phys. Stat. Sol. (a)*, 188(3) 921–928, 2001.
- [157] N. Dubreuil, J. C. Knight, D. K. Leventhal, V. Sandoghdar, J. Hare, and V. Lefèvre. Eroded monomode optical fiber for whispering-gallery mode excitation in fused-silica microspheres. *Opt. Lett.*, 20(8) 813–815, April 1995.
- [158] A. Badolato, K. Hennessy, M. Atature, J. Dreiser, E. Hu, P. M. Petroff, and A. Imamoglu. Deterministic coupling of single quantum dots to single nanocavity modes. *Science*, 308 1158–1161, May 2005.
- [159] R. E. Slusher, A. F. J. Levi, U. Mohideen, S. L. McCall, S. J. Pearton, and R. A. Logan. Threshold characteristics of semiconductor microdisk lasers. *Appl. Phys. Lett.*, 63(10) 1310–1312, 1993.
- [160] M. Fujita, R. Ushigome, and T. Baba. Large Spontaneous Emission Factor of 0.1 in a Microdisk Injection Laser. *IEEE Photonics Tech. Lett.*, 13(5) 403–405, May 2001.
- [161] K. Nozaki and T. Baba. Carrier and photon analyses of photonic microlasers by two-dimensional rate equations. *IEEE J. on Sel. Area. in Comm.*, 23(7) 1411–1417, July 2005.
- [162] V. Sandoghdar, F. Treussart, J. Hare, V. Lefèvre-Seguin, N. Dubreuil, J.-M. Raimond, and S. Haroche. Very low threshold whispering-gallery-mode microsphere laser. *Phys. Rev. A*, 54(3) R1777–R1780, September 1996.
- [163] J.-M. Gérard and B. Gayral. Towards high-efficiency quantum-dot single photon sources. *Proceedings of SPIE*, 5361 88–95, 2004.

- [164] G. Ribordy, N. Gisin, O. Guinnard, D. Stucki, M. Wegmuller, and H. Zbinden. Photon counting at telecom wavelengths with commercial InGaAs/InP avalanche photodiodes: current performance. *Journal of Modern Optics*, 51(9-10) 1381–1398, July 2004.
- [165] A. Stintz, G. T. Liu, H. Li, L. F. Lester, and K. J. Malloy. Low-threshold current density 1.3- μm InAs quantum-dot lasers with the dots-in-a-well (DWELL) structure. *IEEE Photonics Tech. Lett.*, 12(6) 591–593, 2000.
- [166] T. Ide, T. Baba, J. Tatebayashi, S. Iwamoto, T. Nakaoka, and Y. Arakawa. Room temperature continuous wave lasing InAs quantum-dot microdisks with air cladding. *Opt. Express*, 13(5) 1615–1620, February 2005.
- [167] T. Yang, O. Schekin, J. O’Brien, and D. G. Deppe. Room temperature, continuous-wave lasing near 1300 nm in microdisks with quantum dot active regions. *IEEE Elec. Lett.*, 39(23), November 2003.
- [168] H. J. Pask, H. D. Summer, and P. Blood. Localized recombination and gain in quantum dots. In *Tech. Dig. Conf. on Lasers and Electro-Optics, CThH3*, Baltimore, MD, 2005. Optical Society of America.
- [169] J. Vučković, O. Painter, Y. Xu, A. Yariv, and A. Scherer. FDTD Calculation of the Spontaneous Emission Coupling Factor in Optical Microcavities. *IEEE J. Quan. Elec.*, 35(8) 1168–1175, August 1999.
- [170] T. S. Sosnowski, T. B. Norris, H. Jiang, J. Singh, K. Kamath, and P. Bhattacharya. Rapid carrier relaxation in $\text{In}_{0.40}\text{Ga}_{0.60}\text{As}/\text{GaAs}$ quantum dots characterized by differential transmission spectroscopy. *Phys. Rev. B*, 57(16) R9423–R9426, April 1998.
- [171] D. A. Yarotski, R. D. Averitt, N. Negre, S. A. Crooker, A. J. Taylor, G. P. Donati, A. Stintz, L. F. Lester, and K. J. Malloy. Ultrafast carrier-relaxation dynamics in self-assembled InAs/GaAs quantum dots. *J. Opt. Soc. Am. B*, 19(6) 1480–1484, June 2002.
- [172] J. J. Sanchez-Mondragon, N. B. Narozhny, and J. H. Eberly. Theory of spontaneous-emission line shape in an ideal cavity. *Phys. Rev. Lett.*, 51(7) 550–553, August 1983.
- [173] G. S. Agarwal. Vacuum-field Rabi splittings in microwave absorption by Rydberg atoms in a cavity. *Phys. Rev. Lett.*, 53(18) 1732–1734, October 1984.

- [174] Q. A. Turchette, C. J. Hood, W. Lange, H. Mabuchi, and H. J. Kimble. Measurement of conditional phase shifts for quantum logic. *Phys. Rev. Lett.*, 25(18) 4710–4713, December 1995.
- [175] P. R. Rice and H. J. Carmichael. Single-atom cavity-enhanced absorption I: photon statistics in the bad-cavity limit. *IEEE J. Quan. Elec.*, 24(7) 1351–1366, July 1988.
- [176] C. M. Savage and H. J. Carmichael. Single-atom optical bistability. *IEEE J. Quan. Elec.*, 24(8) 1495–1498, August 1988.
- [177] P. Alsing and H. J. Carmichael. Spontaneous dressed-state polarization of a coupled atom and cavity mode. *Journal of Optics B: Quantum Optics*, 3 13–32, 1981.
- [178] M. A. Armen and H. Mabuchi. Low-lying bifurcations in cavity quantum electrodynamics. *quant-ph/0602170*, 2006.
- [179] L.-M. Duan and H. J. Kimble. Scalable photonic quantum computation through cavity-assisted interactions. *Phys. Rev. Lett.*, 92 127902, March 2004.
- [180] H. J. Carmichael. *Statistical Methods in Quantum Optics I: Master Equations and Fokker-Planck Equations*. Springer-Verlag, Berlin, 2003.
- [181] L. A. Lugiato. Theory of optical bistability. *Progress in Optics*, 21 69–216, 1984.
- [182] H. J. Kimble. *Structure and Dynamics in Cavity Quantum Electrodynamics*, pages 203–266. Academic Press, Boston, 1994.
- [183] R. J. Thompson, Q. A. Turchette, O. Carnal, and H. J. Kimble. Nonlinear spectroscopy in the strong-coupling regime of cavity QED. *Phys. Rev. A*, 57(4) 3084–3104, April 1998.
- [184] B. L. Lev. *Magnetic Microtraps for Cavity QED, Bose-Einstein Condensates, and Atom Optics*. PhD thesis, California Institute of Technology, 2005.
- [185] K. M. Birnbaum. *Cavity QED with Multilevel Atoms*. PhD thesis, California Institute of Technology, 2005.
- [186] C. J. Hood, M. S. Chapman, T. W. Lynn, and H. J. Kimble. Real-time cavity QED with single atoms. *Phys. Rev. Lett.*, 80(19) 4157–4160, May 1998.

- [187] A. Kiraz, P. Michler, C. Becher, B. Gayral, A. Imamoglu, L. Zhang, E. Hu, W. V. Schoenfeld, and P. M. Petroff. Cavity-quantum electrodynamics using a single InAs quantum dot in a microdisk structure. *Appl. Phys. Lett.*, 78(25) 3932–3934, June 2001.
- [188] K. Hennessy, A. Badolato, A. Tamboli, P. M. Petroff, E. Hu, M. Atature, J. Dreiser, and A. Imamoglu. Tuning photonic crystal nanocavity modes by wet chemical digital etching. *Appl. Phys. Lett.*, 87 021108, July 2005.
- [189] S. Mosor, J. Hendrickson, B. C. Richards, J. Sweet, G. Khitrova, H. Gibbs, T. Yoshie, A. Scherer, O. B. Shchekin, and D. G. Deppe. Scanning a photonic crystal slab nanocavity by condensation of Xenon. *Appl. Phys. Lett.*, 87 141105, October 2005.
- [190] S. Strauf, M. T. Rakher, I. Carmeli, K. Hennessy, C. Meier, A. Badolato, M. J. A. DeDood, P. M. Petroff, E. L. Hu, E. G. Gwinn, and D. Bouwmeester. Frequency control of photonic crystal membrane resonators by monolayer deposition. *Appl. Phys. Lett.*, 88 043116, January 2006.
- [191] H. Lee, J. A. Johnson, M. Y. He, J. S. Speck, and P. M. Petroff. Strain-engineered self-assembled semiconductor quantum dot lattices. *Appl. Phys. Lett.*, 78(1) 105–107, January 2001.
- [192] A. Konkar, A. Madhukar, and P. Chen. Stress-engineered spatially selective self-assembly of strained InAs quantum dots on nonplanar patterned GaAs(001) substrates. *Appl. Phys. Lett.*, 72(2) 220–222, January 1998.
- [193] M. H. Baier, S. Watanabe, E. Pelucchi, and E. Kapon. High uniformity of site-controlled pyramidal quantum dots grown on prepatterend substrates. *Appl. Phys. Lett.*, 84(11) 1943–1945, March 2004.
- [194] F. Capasso. Band-gap engineering: from physics and materials to new semiconductor devices. *Science*, 235 172–176, September 1987.
- [195] J. Faist, F. Capasso, D. L. Sivco, C. Sirtori, A. L. Hutchinson, and A. Y. Cho. Quantum cascade laser. *Science*, 264 553–556, April 1994.
- [196] F. Capasso, R. Paiella, R. Martini, R. Colombelli, C. Gmachl, T. Myers, M. S. Taubman, R. M. Williams, C. G. Bethea, K. Unterrainer, H. Y. Hwang, D. L. Sivco, A. Y. Cho, H. C.

- Liu, and E. A. Whittaker. Quantum cascade lasers: ultrahigh-speed operation, optical wireless communication, narrow linewidth, and far-infrared emission. *IEEE J. Quan. Elec.*, 38(6) 511–531, June 2002.
- [197] F. Capasso, C. Gmachl, R. Paiella, A. Tredicucci, A. L. Hutchinson, D. L. Sivco, J. N. Bailargeon, A. Y. Cho, and H. C. Liu. New frontiers in quantum cascade lasers and applications. *IEEE J. Sel. Top. Quan. Elec.*, 6(6) 931–947, November 2000.
- [198] R. Kohler, A. Tredicucci, F. Beltram, H. E. Beere, E. H. Linfield, A. G. Davies, D. A. Ritchie, R. C. Iotti, and F. Rossi. Terahertz semiconductor heterostructure lasers. *Nature*, 417 156–159, May 2002.
- [199] M. Beck, D. Hofstetter, T. Aellen, J. Faist, U. Oesterle, M. Illegems, E. Gini, and H. Melchior. Continuous wave operation of a mid-infrared semiconductor laser at room temperature. *Science*, 295 301–305, January 2002.
- [200] H.-G. Park, S.-H. Kim, S.-H. Kwon, Y.-G. Ju, J.-K. Yang, J.-H. Baek, S.-B. Kim, and Y.-H. Lee. Electrically drive single-cell photonic crystal laser. *Science*, 305(5689) 1444–1447, September 2004.
- [201] B. D’Urso, O. Painter, J. O’Brien, T. Tombrello, A. Scherer, and A. Yariv. Modal reflectivity in finite-depth two-dimensional photonic-crystal microcavities. *J. Opt. Soc. Am. B*, 15(3) 1155–1159, March 1998.
- [202] K. Sakoda. Transmittance and Bragg reflectivity of two-dimensional photonic lattices. *Phys. Rev. A*, 52(12) 8992–9002, September 1995.
- [203] C. Sirtori, J. Faist, F. Capasso, D. L. Sivco, A. L. Hutchinson, and A. Y. Cho. Quantum cascade laser with plasmon-enhanced waveguide operating at 8.4 μm wavelength. *Appl. Phys. Lett.*, 66(24) 3242–3244, June 1995.
- [204] L. Martin-Morteno, F. J. Garcia-Vidal, H. J. Lezec, K. M. Pellerin, T. Thio, J. B. Pendry, and T. W. Ebbesen. Theory of extraordinary optical transmission through subwavelength hole arrays. *Phys. Rev. Lett.*, 86(6) 1114–1117, February 2001.
- [205] J. B. Judkins and R. W. Ziolkowski. Finite-difference time-domain modeling of nonperfect conducting metallic thin-film gratings. *J. Opt. Soc. Am. A*, 12(9) 1974–1983, September 1995.

- [206] L. M. Miller, G. D. Smith, and G. L. Carr. Synchrotron-based biological microspectroscopy: From the mid-infrared through the far-infrared regimes. *Journal of Biological Physics*, 29(2) 219–230, 2003.
- [207] K. E. Meissner, P. L. Gourley, T. M. Brennan, and B. E. Hammons. Intracavity spectroscopy in vertical cavity surface-emitting lasers for micro-optical-mechanical systems. *Appl. Phys. Lett.*, 69(11) 1517–1519, September 1996.
- [208] M. A. Unger, H. P. Chou, T. Thorsen, A. Scherer, and S. R. Quake. Monolithic microfabricated valves and pumps by multilayer soft lithography. *Science*, 288 113–116, April 2000.
- [209] G. M. Whitesides and A. D. Stroock. Flexible methods for microfluidics. *Physics Today*, 54 42–48, June 2001.
- [210] K. S. Yee. Numerical solution of boundary value problems involving Maxwell’s equations in isotropic media. *IEEE Trans. Antennas Propag.*, 14 302–307, 1966.
- [211] Z. Bi, Y. Shen, K. Wu, and J. Litva. Fast finite-difference-time-domain analysis of resonators using digital filtering and spectrum estimation techniques. *IEEE Trans. Microwave Theory Tech.*, 40(8) 1611, August 1992.
- [212] R. J. Shul and S. J. Pearton, editors. *Handbook of Advanced Plasma Processing Techniques*. Springer, Berlin, first edition, 2000.
- [213] S. Thomas III, E. W. Berg, and S. W. Pang. *In-situ* fiber optic thermometry of wafer surface etched with an electron cyclotron source. *J. Vac. S. Tech. B*, 14(3) 1807–1811, may/jun 1996.
- [214] A. Yariv. Universal relations for coupling of optical power between microresonators and dielectric waveguides. *IEEE Elec. Lett.*, 36(4) 321–322, February 2000.
- [215] S. M. Spillane. *Fiber-coupled Ultrahigh-Q Microresonators for Nonlinear and Quantum Optics*. PhD thesis, California Institute of Technology, 2004.
- [216] T. J. Kippenberg. *Nonlinear Optics in Ultrahigh-Q Whispering-Gallery Optical Microcavities*. PhD thesis, California Institute of Technology, 2004.
- [217] G. Björk and Y. Yamamoto. Analysis of semiconductor microcavity lasers using rate equations. *IEEE J. Quan. Elec.*, 27(11) 2386–2396, November 1991.

- [218] G. Björk, A. Karlsson, and Y. Yamamoto. Definition of a laser threshold. *Phys. Rev. A*, 50(2) 1675–1680, August 1994.
- [219] P. R. Rice and H. J. Carmichael. Photon statistics of a cavity-QED laser: A comment on the laser-phase transition analogy. *Phys. Rev. A*, 50(5) 4318–4329, November 1994.
- [220] E. T. Jaynes and F. W. Cummings. Comparison of quantum and semiclassical radiation theories with application to the beam maser. *Proceedings of the IEEE*, 51 89–109, 1963.
- [221] B. W. Shore and P. L. Knight. The Jaynes-Cummings model (topical review). *J. Mod. Opt.*, 40(7) 1195–1238, 1993.
- [222] D. Suter. *The Physics of Laser-Atom Interactions*. Cambridge University Press, Cambridge, United Kingdom, 1997.
- [223] A. Yariv. *Quantum Electronics*. John Wiley & Sons, New York, NY, 3rd edition, 1989.
- [224] C. Cohen-Tannoudji, B. Diu, and F. Laloe. *Quantum Mechanics*. John Wiley & Sons, Inc., New York, NY, 1977.
- [225] L. Mandel and E. Wolf. *Optical Coherence and Quantum Optics*. Cambridge University Press, Cambridge, United Kingdom, 1995.
- [226] P. Alsing, D.-S. Guo, and H. J. Carmichael. Dynamic Stark effect for the Jaynes-Cumming system. *Phys. Rev. A*, 45(7) 5135–5143, April 1992.
- [227] E. M. Purcell. Spontaneous emission probabilities at radio frequencies. *Phys. Rev.*, 69 681, 1946.
- [228] D. Kleppner. Inhibited Spontaneous Emission. *Phys. Rev. Lett.*, 47(4) 233–236, July 1981.
- [229] H. Haug and S. W. Koch. *Quantum theory of the optical and electronic properties of semi-conductors*. World Scientific Publishers, New Jersey, 4th edition, 2004.